

Technical Report

TR-13-05

Climate and climate-related issues for the safety assessment SR-PSU

Svensk Kärnbränslehantering AB

October 2014

Svensk Kärnbränslehantering AB

Swedish Nuclear Fuel
and Waste Management Co

Box 250, SE-101 24 Stockholm
Phone +46 8 459 84 00



ISSN 1404-0344

SKB TR-13-05

ID 1411747

Climate and climate-related issues for the safety assessment SR-PSU

Svensk Kärnbränslehantering AB

October 2014

Keywords: Climate, Global warming, Periglacial, Permafrost, Glacial, Sea-level, Safety assessment, Nuclear waste, SR-PSU, Forsmark.

A pdf version of this document can be downloaded from www.skb.se.

Preface

This document presents information on climate and climate-related issues relevant for the assessment of long-term safety of the SFR repository for low- and intermediate level nuclear waste. It supports the safety assessment SR-PSU.

The report was compiled by Assoc. Prof. Jenny Brandefelt, SKB, and Prof. Jens-Ove Näslund, SKB.

The report was reviewed by Dr. Mike C. Thorne (Mike Thorne and Associates Limited), Prof. Andrey Ganopolski (Potsdam Institute for Climate Research), Prof. Jordi Bruno (Amphos 21 Consulting Ltd) and Dr. Tommy Olsson (I T Olsson AB).

Stockholm, October 2014

Jens-Ove Näslund
Research coordinator Climate programme SKB

Summary

This report documents current scientific knowledge on climate and climate-related conditions, relevant to the long-term safety of a shallow geological repository for low- and intermediate-level nuclear waste. The documentation is made to a level required for an adequate treatment in the SR-PSU safety assessment made for the SFR repository in Forsmark, south-central Sweden. The accounts given in this report are based on research published in the general scientific literature as well as on research conducted and published by SKB. Furthermore, the handling of the current scientific knowledge on climate and climate-related conditions in the SR-PSU safety assessment is described and compared to the handling in earlier safety assessments performed by SKB.

Climate is not predictable on a 100,000 year timescale, i.e. the time-scale that is covered by the SR-PSU safety assessment. Therefore, a single most likely climate evolution cannot be predicted with enough confidence and detail for the analysis of long-term safety. Instead, *a range* of future climate developments must be considered in the safety assessment in order to cover the uncertainty in future climate development. This overall strategy for handling climate in safety assessments is the same in SR-PSU as in previous safety assessments performed by SKB. It is also a strategy that is approved by the Swedish regulating authorities and by the society, through the acceptance of the recurrent SKB programme for Research, development and demonstration.

In addition to the general approach described above, i.e. to use a range of possible future climate developments, different types of nuclear waste repositories require somewhat different treatments depending on the character of the waste materials (activity levels and lifetimes of the key radio nuclides and hence the total time that needs to be covered by the safety assessment), as well as on the repository concept (barrier material and repository depth). Because of this, the detailed methodology for handling the evolution of climate and climate-related processes in the SR-PSU safety assessment differs, in some respects, from the methodology used in previous safety assessments for the planned repository for spent nuclear fuel in Forsmark (e.g. the SR-Site assessment). The significantly shorter assessment period for SFR, 100,000 years instead of 1 million years, as well as the considerably shallower repository depth (c 60–140 m instead of 450–470 m), requires more focus on the expected climate development over the coming tens of thousands of years, including the possible timing of the earliest period of permafrost growth and freezing of SFR engineered structures.

In the present report, climate-related processes of importance for repository performance and safety are identified and described. These include i) development of permafrost and frozen ground, ii) isostatic and eustatic changes and the resulting relative sea level changes, iii) ice-sheet development and iv) surface denudation. Furthermore, the current knowledge on past and potential future evolution of climate and climate-related processes is documented. Finally, four possible future developments of climate and climate-related processes in Forsmark over the next 100,000 years (here called “climate cases”) are defined and presented. These include two cases describing prolonged interglacial conditions with climates dominated by global warming, one case with early periglacial conditions with permafrost development at Forsmark, and one case with repeated conditions reconstructed for the last glacial cycle, representing a development with only natural climate variability and glacial conditions at Forsmark within the coming 100,000 years. These climate cases together cover the expected maximum range within which climate and climate-related processes of importance for long-term SFR safety may vary over the 100,000 year time period analysed in the SR-PSU safety assessment. The *actual* development of climate and climate-related processes at the Forsmark site for the coming 100,000 years is expected to lie within the range covered by these climate cases.

Sammanfattning

Denna rapport dokumenterar nuvarande vetenskapliga kunskapsläge om klimat och klimatrelaterade förhållanden av relevans för långsiktig säkerhet för ett grunt geologiskt förvar för låg- och medelaktivt radioaktivt avfall. Dessa förhållanden dokumenteras till den nivå som krävs för ett ändamålsenligt omhändertagande i säkerhetsanalysen SR-PSU, vilken utförs för förvaret SFR i Forsmark, Uppland. Informationen i denna rapport är baserad på forskningsresultat som publicerats i den allmänna vetenskapliga litteraturen, såväl som på forskning som genomförts och publicerats av SKB. Hanteringen av den vetenskapliga kunskapen om klimat och klimatrelaterade förhållanden i säkerhetsanalysen SR-PSU beskrivs och jämförs med hanteringen av dessa frågor i tidigare säkerhetsanalyser utförda av SKB.

Klimat är inte förutsägbart på en 100 000-års tidsskala, vilket är den tidsrymd som analyseras i säkerhetsanalysen SR-PSU. Av den anledningen kan inte en mest sannolik framtida klimatutveckling förutsägas med tillräcklig tillförlitlighet och detaljeringsgrad för analysen av långsiktig säkerhet. Istället måste ett flertal tänkbara framtida klimatutvecklingar inkluderas i säkerhetsanalysen för att täcka upp osäkerheten i framtida klimatutveckling. Den övergripande strategin för att hantera klimat i säkerhetsanalyser är densamma i SR-PSU som i tidigare säkerhetsanalyser genomförda av SKB. Denna strategi är också godkänd av svenska berörda myndigheter samt av samhället i stort, genom deras godkännande av SKB:s program för forskning, utveckling och demonstration.

I tillägg till det allmänna angreppssätt som beskrivs ovan, med ett flertal möjliga framtida klimatutvecklingar, kräver olika typer av förvar för radioaktivt avfall delvis olika hantering. Avfallens karaktär (radioaktivitetsnivåer och livstid för de viktigaste radionukleiderna och följaktligen den totala tid som analyseras i säkerhetsanalysen) samt det aktuella förvarskonceptet (barriärmaterial och förvarsdjup) styr hur klimatfrågorna behöver hanteras i detalj. Av denna anledning, skiljer sig den detaljerade metodiken i säkerhetsanalysen SR-PSU i vissa avseenden från metodiken som användes i tidigare säkerhetsanalyser för det planerade förvaret för använt kärnbränsle i Forsmark (t ex säkerhetsanalysen SR-Site). Den avsevärt kortare analysperioden för SFR, 100 000 år istället för 1 miljon år, samt förvarets betydligt grundare djup (ca 60–140 m istället för 450–470 m), kräver större fokus på den förväntade klimatutvecklingen under de kommande tiotals tusen åren, inklusive den första möjliga tidpunkten för permafrosttillväxt och frysning av barriärstrukturerna i SFR.

I denna rapport identifieras och beskrivs klimatrelaterade processer av betydelse för förvarets funktion och den långsiktiga säkerheten. Dessa inkluderar i) utveckling av permafrost och frusen mark, ii) isostatiska och eustatiska förändringar vilka resulterar i förändringar av den relativa havsnivån, iii) utveckling av inlandsisar, och, iv) denudation vid markytan. Vidare dokumenteras nuvarande kunskap om forntida- och potentiella framtida utvecklingar av klimat och klimatrelaterade processer. Slutligen definieras och presenteras fyra tänkbara framtida utvecklingar av klimat och klimatrelaterade processer i Forsmark för de kommande 100 000 åren. Dessa inkluderar två fall med en förlängd period av interglaciala förhållanden, dominerade av olika grad av global uppvärmning, ett fall med tidiga periglaciala förhållanden med permafrosttillväxt i Forsmark, och slutligen ett fall med förhållanden rekonstruerade för den senaste glaciala cykeln, vilket representerar en utveckling med enbart naturlig variabilitet i klimat inklusive glaciala förhållanden vid Forsmark inom de kommande 100 000 åren. Tillsammans täcker dessa klimatfall den förväntade maximala spännvidden inom vilken klimat och klimatrelaterade processer, av betydelse för den långsiktiga säkerheten för SFR, kan variera under den 100 000 år långa period som analyseras i SR-PSU. Den faktiska utvecklingen hos klimat och klimatrelaterade processer i Forsmark under denna period förväntas ligga inom spännvidden som täcks av dessa fyra klimatfall.

Contents

1	Introduction	9
1.1	Purpose of the report	9
1.2	Climate and climate-related processes – importance for repository performance and safety	9
1.3	Strategy for managing climate and climate-related processes in safety assessments	10
1.3.1	Climate and climate-related changes	10
1.3.2	Strategy for handling evolution of climate and climate-related processes	11
1.4	Structure of the report	15
1.4.1	Overall report structure and authors	15
1.4.2	Structure for description of climate related processes	15
1.5	Publications supporting the SR-PSU Climate report	16
1.5.1	Publications produced for SR-PSU	16
1.5.2	Publications produced for SR-Site and SR-Can, in parts or in whole used for the SR-PSU Climate report	17
1.5.3	General scientific publications	17
1.6	Interactions between the climate programme and other SR-PSU programmes	17
1.7	Summary of main changes made since the SAR-08 safety assessment	18
2	Climate-related processes	19
2.1	Permafrost	19
2.1.1	Overview / general description	19
2.1.2	Controlling conditions and factors	19
2.1.3	Natural analogues / observations in nature	22
2.1.4	Model studies	24
2.1.5	Time perspective	36
2.1.6	Handling in the safety assessment SR-PSU	36
2.1.7	Handling of uncertainties in SR-PSU	37
2.1.8	Adequacy of references	38
2.2	Isostatic adjustment and shore-level changes	38
2.2.1	Overview/general description	39
2.2.2	Controlling conditions and factors	43
2.2.3	Natural analogues/observations in nature	44
2.2.4	Model studies	47
2.2.5	Time perspective	69
2.2.6	Handling in the safety assessment SR-PSU	70
2.2.7	Handling of uncertainties in SR-PSU	70
2.2.8	Adequacy of references	71
2.3	Ice-sheet dynamics	71
2.3.1	Overview/general description	71
2.3.2	Controlling conditions and factors	78
2.3.3	Natural analogues/observations in nature	82
2.3.4	Model studies	85
2.3.5	Time perspective	89
2.3.6	Handling in the safety assessment SR-PSU	90
2.3.7	Handling of uncertainties in SR-PSU	91
2.3.8	Adequacy of references	92
2.4	Surface denudation	92
2.4.1	Overview/general description	92
2.4.2	Controlling conditions and factors	96
2.4.3	Natural analogues/observations in nature	97
2.4.4	Model studies	98
2.4.5	Time perspective	100
2.4.6	Handling in the safety assessment SR-PSU	100

2.4.7	Handling of uncertainties in SR-PSU	101
2.4.8	Adequacy of references	101
3	Past and future climate evolution	103
3.1	Introduction	103
3.2	Glacial history, Weichselian climate and reconstructed last glacial cycle conditions at Forsmark	105
3.2.1	Weichselian glacial history and climate	106
3.2.2	Exemplified of Weichselian climates	111
3.2.3	Reconstructed last glacial cycle conditions at Forsmark	126
3.3	Projected future climate evolution	130
3.3.1	Atmospheric greenhouse-gas concentrations	131
3.3.2	Insolation	133
3.3.3	Climate evolution until 2100 AD	133
3.3.4	Climate evolution until 10 ka AP	143
3.3.5	Climate evolution until 100 ka AP	149
3.3.6	Exemplified climate conditions for a future warm climate	152
4	Climate cases for the SR-PSU safety assessment	161
4.1	Global warming climate case	166
4.1.1	Background	166
4.1.2	Ice-sheet evolution	166
4.1.3	Shore-level evolution	166
4.1.4	Permafrost evolution	167
4.1.5	Surface denudation	167
4.1.6	Evolution of climate domains	168
4.2	Early periglacial climate case	169
4.2.1	Background	169
4.2.2	Ice sheet evolution	169
4.2.3	Shore-level evolution	169
4.2.4	Permafrost evolution	169
4.2.5	Surface denudation	170
4.2.6	Evolution of climate domains	170
4.3	Extended global warming climate case	172
4.3.1	Background	172
4.3.2	Ice sheet evolution	172
4.3.3	Shore-level evolution	172
4.3.4	Permafrost evolution	174
4.3.5	Surface denudation	174
4.3.6	Evolution of climate domains	174
4.4	Weichselian glacial cycle climate case	175
4.4.1	Background	175
4.4.2	Ice-sheet evolution	175
4.4.3	Shore-level evolution	178
4.4.4	Permafrost evolution	180
4.4.5	Surface denudation	184
4.4.6	Evolution of climate domains	187
4.5	Summary of climate cases for the SR-PSU safety assessment	189
5	List of abbreviations	193
	References	195

1 Introduction

1.1 Purpose of the report

The purpose of this report is to document current scientific knowledge on climate and climate-related conditions, relevant to the long-term safety of a repository for low- and intermediate-level nuclear waste, to a level required for an adequate treatment in the safety assessment SR-PSU. The report also presents a number of dedicated studies on climate and selected climate-related processes of relevance for the assessment of long-term repository safety. Based on this information, the report presents a number of possible future climate developments for Forsmark, the site where the existing SFR1 is located and where the extension SFR3 is planned (Figure 1-1). The presented future climate developments (“climate cases”) are used as a basis for the selection and analysis of SR-PSU safety assessment scenarios in the SR-PSU main report (SKB 2014a). The present report is based on research published in the general scientific literature as well as research conducted and published by SKB.

1.2 Climate and climate-related processes – importance for repository performance and safety

Global climate variations associated with growth and decay of permafrost and ice sheets and sea-level variations influence both surface and geosphere conditions. Freezing of groundwater, changes in shorelevel and the presence of an ice sheet influence permeability, water turnover, groundwater pressure, groundwater flow and chemical composition. Further, the presence of an ice sheet influences rock stresses during different phases of a glaciation.

Climate-related processes addressed in the SR-PSU safety assessment are listed in Table 1-1. This table is intended to give an overview of the processes considered and possible impacts on repository safety associated with each process. Further, the climate cases describing the impact of these climate-related processes are also indicated. The handling of these processes in the SR-PSU safety assessment scenarios is described in the SR-PSU main report (SKB, 2014a, Section 3.5.1).

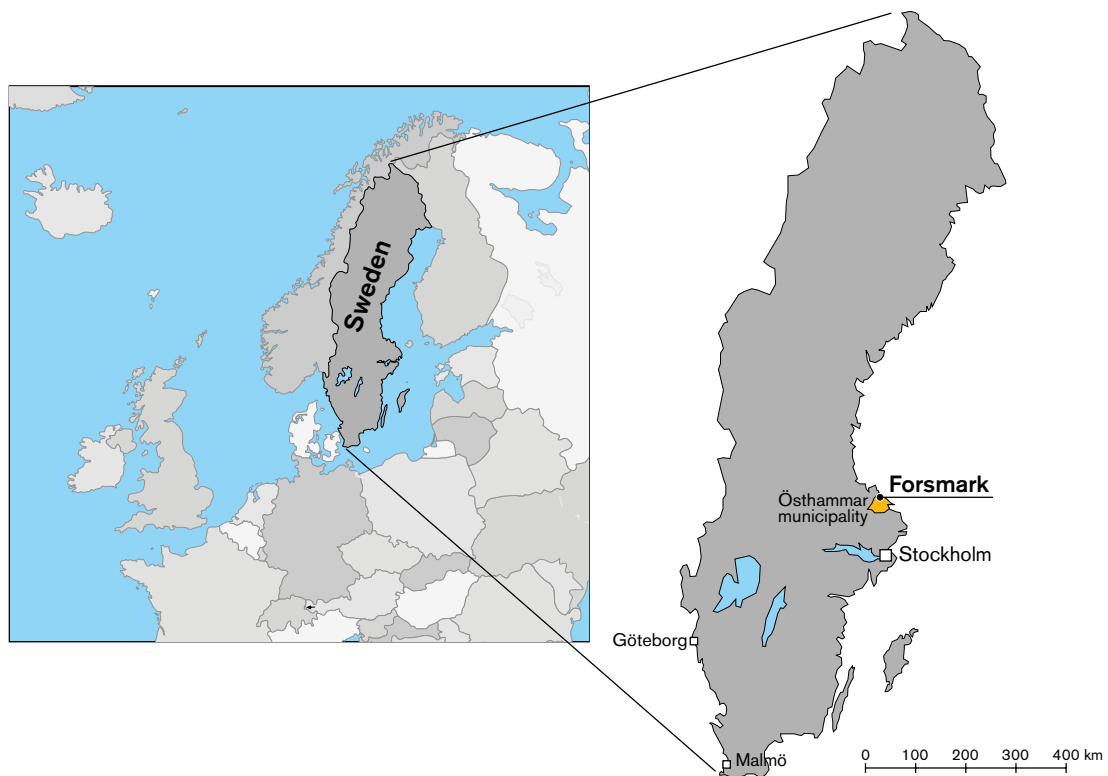


Figure 1-1. Location map.

Table 1-1. Climate-related processes addressed in the SR-PSU safety assessment. The table is intended to give an overview of the processes considered and associated possible impacts on repository safety. Climate cases describing the impact of these climate-related processes are also indicated. In addition, information from the climate programme has been used within several other SR-PSU activities, see Section 1.6.

Climate-related process (Section of this report)	Possible impact on repository safety	Climate cases which describe climatic conditions necessary for the impact of the climate-related process
Permafrost development (2.1)	Lowering of bedrock temperatures causing freezing of concrete and bentonite barriers	<i>Global warming</i> <i>Early periglacial</i> <i>Weichselian glacial cycle</i>
Shore-level displacement (2.2)	Drilling of wells in vicinity of the repository Groundwater flow	<i>Global warming</i> <i>Extended global warming</i> <i>Early periglacial</i> <i>Weichselian glacial cycle</i>
Ice sheet development (2.3)	High hydrostatic pressures affecting repository structures	<i>Weichselian glacial cycle</i>
Surface denudation (2.4)	Glacial erosion resulting in radioactive waste closer to the surface after de-glaciation	<i>Weichselian glacial cycle</i>
Global warming (3.3)	Ground water recharge by meteoric water over prolonged periods of time affecting groundwater geochemistry	<i>Global warming</i> <i>Extended global warming</i>

1.3 Strategy for managing climate and climate-related processes in safety assessments

1.3.1 Climate and climate-related changes

Climate-related changes such as variations in shore-level and the development of permafrost and ice sheets are the most important naturally occurring external factors affecting a repository for low- and intermediate-level nuclear waste in a time perspective up to 100,000 years (100 ka). Most of the processes occurring in the biosphere and geosphere are likely to be affected by climate and climate-related changes in one way or another.

Over the past 2.5 million years (Ma), Scandinavia has experienced multiple cycles of glaciation (e.g. Ehlers and Gibbard 2004). Cold periods that include ice sheets gradually growing to maximum extents are known as *glacials*. These periods alternate with periods of warm climate called *interglacials*, with ice sheets of similar extent to those of the present day. A *glacial cycle* consists of a glacial and an interglacial. Within the glacial periods, warmer *interstadial* periods occur, as well as cool *stadial* periods. The shifting between glacials and interglacials is depicted for instance in the variation of the content of the heavy oxygen isotope, ^{18}O , in deep-sea sediments (e.g. Lisiecki and Raymo 2005) which reflects both the sea-water temperature and the volume of water that has been bound in land-based ice sheets and glaciers globally, see Figure 1-2.

Figure 1-2 shows that over the last 900 ka, glacial–interglacial cycles of about 100 ka duration have dominated global climate variation. The time frame of one such 100 ka glacial–interglacial cycle also constitutes the approximate time period to be covered by the SFR safety assessment. Current scientific understanding of the climate system suggests that the climate evolution for the coming 100 ka will differ from the past climate variability seen in e.g. Figure 1-2. It is very likely that the anthropogenic release of CO_2 into the atmosphere, together with the future natural variation in insolation, will result in the present Holocene interglacial being considerably longer than previous interglacials, see Section 3.3.5.

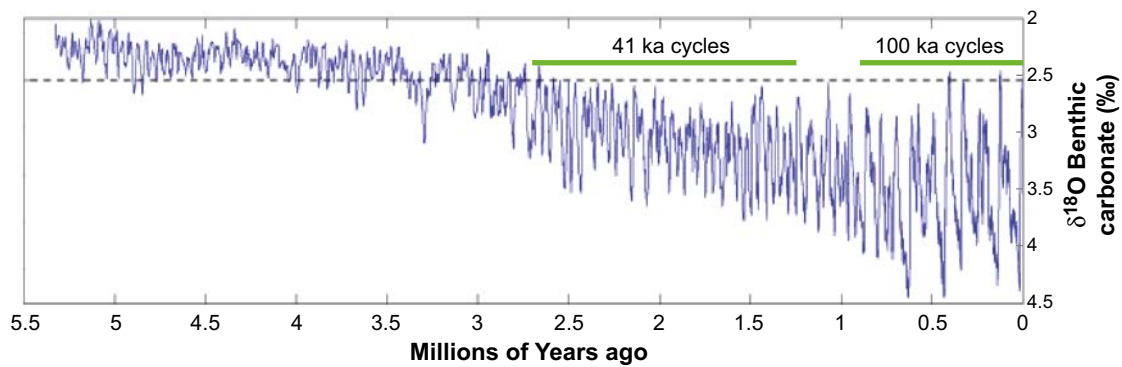


Figure 1-2. Variations of $\delta^{18}\text{O}$ in deep-sea sediments over the last 5.5 Ma (Lisiecki and Raymo 2005). High $\delta^{18}\text{O}$ values indicate large global ice volume and low sea water temperature, i.e. colder climate conditions, whereas low $\delta^{18}\text{O}$ values indicate the opposite. The last 900 ka have been dominated by 100 ka long glacial cycles. Modified from *Global Warming Art* (2007), after Lisiecki and Raymo (2005).

The choice of climate developments (“climate cases”; Chapter 4) analysed in the SR-PSU safety assessment is based on current knowledge of the past and potential future evolution of climate and climate-related processes. A review of current knowledge on past and future climate evolution is given in Chapter 3.

1.3.2 Strategy for handling evolution of climate and climate-related processes

The handling of climate and climate-related processes in safety assessments must be tailor-made for each repository concept and waste type to be analysed (Näslund et al. 2013). Further, climate is not predictable on a 100 ka timescale. Therefore, a range of future climate developments must be considered in the safety assessment in order to cover the uncertainty in future climate development. This range is determined based on scientific knowledge on past, present and future climate evolution, as well as knowledge of which processes are of importance for the functioning of the repository concept under consideration.

The overall strategy for handling climate in safety assessments, i.e. to make use of a range of possible future climate developments, is the same in SR-PSU as in previous recent safety assessments performed by SKB. However, in line with the above reasoning, the strategy for handling the evolution of climate and climate-related processes in the SR-PSU safety assessment differs in some respects from the strategy used in previous safety assessments for the planned repository for spent nuclear fuel in Forsmark (e.g. the SR-Site assessment). The differences are motivated by the different character of the waste materials (activity levels and lifetimes of the key radionuclides), and hence the total time that needs to be covered by the safety assessment, as well as by the repository concept (barrier material and repository depth), see further Näslund et al. (2013). The radioactivity of the nuclear waste in SFR decays to low levels in the first tens of thousands of years, motivating a total safety assessment period covering c 100 ka. In contrast, the safety assessment for a spent nuclear fuel repository needs to cover the next 1 Ma due to the considerably larger inventory of long-lived radionuclides. The shorter assessment period for SFR, as well as the considerably shallower repository depth (c 60–140 m instead of 450–470 m), requires more focus on climate development over the coming tens of thousands of years, including the possible timing of the earliest period of permafrost growth and freezing of SFR engineered structures. In comparison, the timing of this earliest development of shallow permafrost was not of relevance in the SR-Site assessment. Instead, the main question, regarding permafrost and freezing, related to the potential for freezing to reach the depth of the repository for the spent nuclear fuel (SKB 2011).

In previous safety assessments for low-and intermediate-level nuclear waste (SAR-08) and for spent nuclear fuel (SR-Can, SR-Site) a reconstruction of the last glacial cycle was used, together with a wide range of other climate cases, in order to analyse repository safety. In the present safety assessment, the methodology for analysing the effects of climate change for the SFR repository has been developed further in comparison with SAR-08. More focus has been put on determining the timing of the first potential future period of cold climate conditions. To this end, current scientific knowledge of relevance to this question has been given more weight in the definition of the set of

future climate evolutions relevant for the long-term safety of the SFR. In line with this approach, the climate case based on repetition of conditions reconstructed for the last glacial cycle has been given less focus. This is fully in line with the fact that this climate case was not constructed with the purpose of presenting the possible timing of first permafrost at the Forsmark site. This question was not of specific relevance in the safety assessment for which the climate case was originally developed. A dedicated study addressing this question is, on the other hand, included in the SR-PSU assessment. The main reasons for the difference in the range of future climate evolutions between the latest SKB safety assessment for spent nuclear fuel (SR-Site) and the current safety assessment for low- and intermediate-level nuclear waste (SR-PSU) are:

- The time frame of the safety assessment is 100 ka for low- and intermediate-level waste as compared to 1 Ma for spent nuclear fuel. Thus, the current safety assessment deals with a *specific* 100 ka period, with atypical characteristics in a 1 Ma time perspective, whereas safety assessments for high-level nuclear waste need to give weight to a *typical* c 100 ka period (typically including glacial conditions) in order to describe the full 1 Ma period.
- The scientific understanding of the effect of human activities on long-term climate evolution has been improved in the last decades. The next 100 ka are expected to be characterised by a prolonged interglacial lasting for 50, or even 100, ka due to elevated atmospheric CO₂ concentrations in combination with small amplitude incoming solar radiation variations.

Definition of climate change and climate domains

There are various definitions of *climate change*. In the present report, climate change is defined according to the definition by the Intergovernmental Panel on Climate Change (IPCC), namely as “any change in climate over time whether due to natural variability or as a result of human activity” (IPCC 2001). This differs from the definition used by the United Nation’s Framework Convention on Climate Change (UNFCCC) that defines climate change as “a change of climate that is attributed directly or indirectly to human activity that alters the composition of the global atmosphere, and that is in addition to natural climate variability over comparable time periods”. Since climate may change due to both natural variability and to anthropogenic influences, and both types of change are relevant to the long-term safety of the SFR, the definition of climate change in SR-PSU follows the one of IPCC.

It is not possible to predict the climate evolution over the next 100 ka. However, based on knowledge of climate variations in the past and on inferred future climate change, a range within which the climate of Sweden may vary can be estimated with reasonable confidence over this long time frame. Within these limits, characteristic climate-related conditions of importance for repository safety can be identified. The conceivable climate-related conditions can be represented as *climate-driven process domains* (Boulton et al. 2001), where such a domain is defined as “a climatically determined environment in which a set of characteristic processes of importance for repository safety appear”. In the following parts of the report these climate-driven process domains are referred to as *climate domains*. For Forsmark, a site on the Baltic Sea coast, a set of three climate domains were identified. These are denominated:

- The temperate climate domain.
- The periglacial climate domain.
- The glacial climate domain.

The purpose of identifying climate domains is to create a framework for the assessment of issues of importance for repository safety associated with particular climatically determined environments that may occur at the repository location in south-central Sweden. If a repository for low- and intermediate-level nuclear waste fulfils the safety requirements for plausible climate developments, including the transitions between climate domains, then the uncertainty regarding the precise extent in time and space of the climate domains is of less importance.

The temperate climate domain is defined as regions without permafrost or the presence of ice sheets. It is dominated by a temperate Baltic Sea coast climate in a broad sense, with cold winters and either cold or warm summers. Precipitation may fall at any time of the year. The precipitation falls either as rain or snow. The temperate climate domain has the warmest climate of the three climate domains. Within the temperate climate domain, a site may also at times be submerged by the sea. Climates dominated by global warming due to enhanced atmospheric greenhouse gas concentrations are included in the temperate climate domain.

The term periglacial is today used for a range of cold but non-glacial environments. In the periglacial environment, permafrost is a central, but not defining, element (French 2007). However, for the present work, the *periglacial climate domain* is defined strictly as regions that contain permafrost. Furthermore, the periglacial climate domain is a cold region but without the presence of an ice sheet. In this climate domain, permafrost occurs either in sporadic (less than 50% spatial coverage), discontinuous (between 50 and 90% coverage), or continuous form (more than 90% coverage). Although true for most of the time, regions belonging to the periglacial climate domain are not necessarily the same as regions with a climate that supports permafrost growth. For example, at the end of a period with periglacial climate domain the climate may be relatively warm, not building or even supporting the presence of permafrost. Instead, permafrost may be diminishing. However, as long as permafrost is present, the region is defined as belonging to the periglacial climate domain, regardless of the prevailing temperature at the ground surface. This way of defining the climate domain is used because the presence of the permafrost is more important for the safety function of the repository than the actual temperature at the ground surface. In general, the periglacial climate domain has a climate colder than the temperate climate domain and warmer than the glacial climate domain. Precipitation may fall either as snow or rain. Within the periglacial climate domain, a site may also at times be submerged by the sea.

The glacial climate domain is defined as regions that are covered by glaciers or ice sheets. Within the glacial climate domain, the glacier or ice sheet may in some cases be underlain by sub-glacial permafrost. In line with the definition of the periglacial climate domain, areas belonging to the glacial climate domain may not necessarily at all times have a climate that supports the presence of ice sheets. However, in general, the glacial climate domain has the coldest climate of the three climate domains. Precipitation normally falls as snow in this climate domain.

A simplified glacial cycle constructed for a coastal site impacted by major ice sheets using the above climate domains is presented in Figure 1-3.

Climate cases and safety assessment scenarios

Based on the scientific knowledge on the influence of enhanced atmospheric greenhouse gas concentrations and low-amplitude insolation variability in the next tens of thousands of years (see Section 3.3) a set of three climate cases was defined. These represent different levels of cumulative carbon emissions due to human activities. The *global warming climate case* (Section 4.1) represents medium-level carbon emissions. The *early periglacial climate case* (Section 4.2) represents low-level carbon emissions and the *extended global warming climate case* (Section 4.3) represents high-level carbon emissions due to human activities. To supplement this range of future climate developments a climate case based on a reconstruction of the last glacial cycle was defined. The *Weichselian glacial cycle climate case* (Section 4.4) represents a climate development dominated by natural variability as manifested during the past c 100 ka. As described earlier in Section 1.3.2, a future climate evolution over the next few tens of thousands of years based on a repetition of the last glacial cycle is not in agreement with current scientific understanding. Because of this and because of the shorter assessment period in the present assessment compared to the one for the repository for spent nuclear fuel, the *Weichselian glacial cycle climate case* is given less emphasis than in earlier safety assessments.

The climate domains were used to describe the climate evolution in Forsmark in the climate cases. The climate cases were in turn used as the basis for the construction of safety assessment scenarios (SR-PSU **Main report**; SKB 2014a) (Figure 1-4). The *global warming* and *early periglacial* climate cases were used for the *main scenario* aiming at describing a reasonable evolution of the repository system in the next 100 ka. The *extended global warming climate case* and the *Weichselian glacial cycle climate case* were treated as residual scenarios (SKB 2014a).

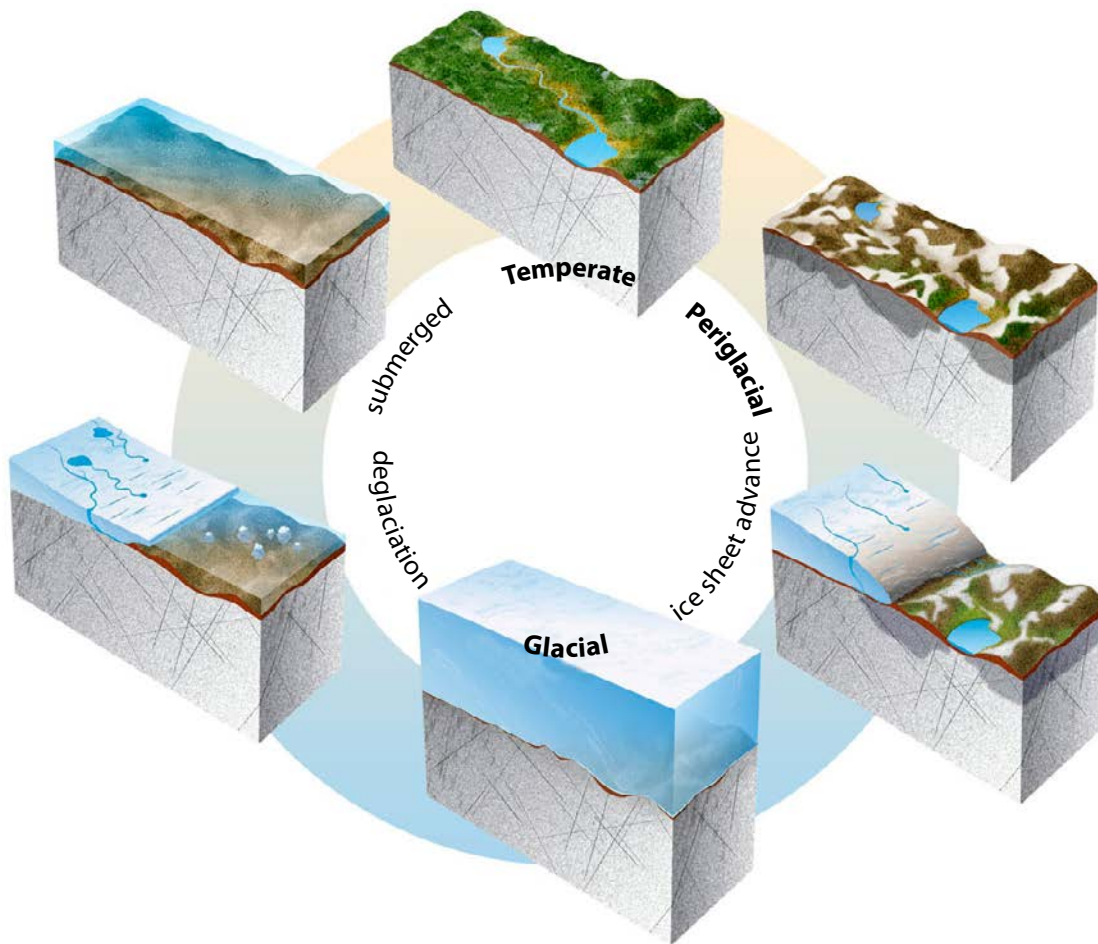


Figure 1-3. Simplified glacial cycle constructed from the climate domains (bold text) relevant for assessments of long-term repository safety at Forsmark. In addition to the climate domains, the illustration also depicts a terrestrial glacial advance and a marine deglaciation with subsequent submerged conditions (regular text), in line with the last glacial phase at the Forsmark site. Modified from Selroos et al. (2013).

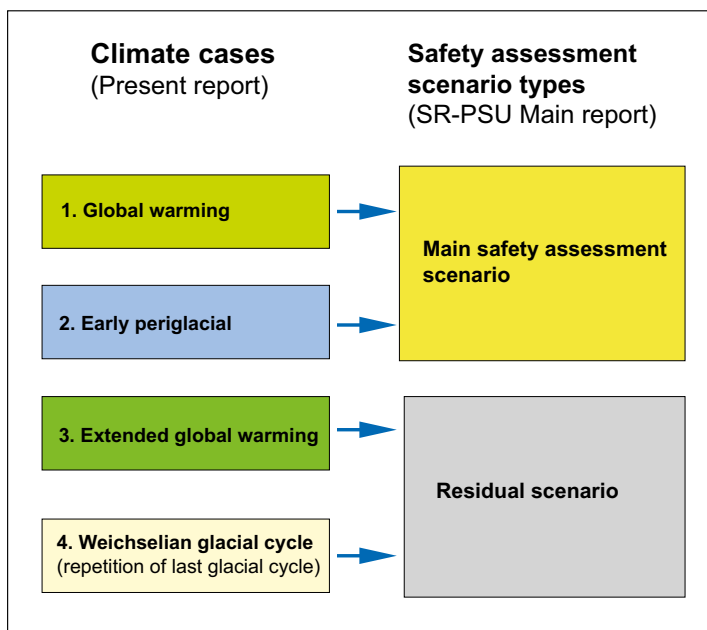


Figure 1-4. Relationship between the climate cases identified and described in the present report for the SR-PSU assessment, and the associated safety assessment scenario types analysed in the SR-PSU main report (SKB 2014a).

1.4 Structure of the report

1.4.1 Overall report structure and authors

Following this introductory chapter, the present report includes three main chapters:

- Identification and discussion of climate and climate-related issues, including reconstructions for the last glacial cycle and scenarios for the future development of the identified variables (Chapter 2).
- A description of current knowledge on past and future climate evolution, both globally and regionally in Forsmark (Chapter 3).
- A description of climate and climate-related conditions for the four climate cases used in SR-PSU (Chapter 4).

As further described in the SR-PSU **Main report** (SKB 2014a) the content of the present report has been audited by comparison with national Features-Events-Processes (FEP) databases from other assessment projects as compiled by the NEA (Nuclear Energy Agency), see the SR-PSU **FEP-report** (SKB 2014b). The models used for the reconstruction of the last glacial cycle and for the assessment of the potential for future cold climate conditions and permafrost in Forsmark, used in the definition of the SR-PSU climate cases, are documented in the SR-PSU **Model summary report** (SKB 2014c), whereas the data produced from the models are presented in the SR-PSU **Data report** (SKB 2014e). Results from the present climate report are used in the SR-PSU **Main report** (SKB 2014a) and in reports supporting the main report.

A list of abbreviations is found at the end of the report.

The present report was written and edited by Jenny Brandefelt and Jens-Ove Näslund, SKB. In this work, parts of the report have been produced by adaptation of text and figures from i) the SR-Site Climate report (SKB 2010a), ii) SR-PSU supporting reports (Brandefelt et al. 2013, Helmens 2013, Wohlfarth 2103), and iii) selected SR-Site supporting reports (Helmens 2009a, Jansson and Näslund 2009, Kjellström et al. 2009, Whitehouse 2009, Wohlfarth 2009, Hartikainen et al. 2010, Olvmo 2010). References to the original reports are made within all respective sections of the report. All experts that in this way contributed to the present report are included in the SR-PSU expert database.

1.4.2 Structure for description of climate related processes

In discussing each of the various climate-related issues, the following standardised structure has been adopted.

Overview/general description

Under this heading, a general description of the current knowledge regarding the climate-related issue is given.

Controlling conditions and factors

The external and internal conditions and factors that control each “issue” are discussed. *External* refers to systems that are not part of the described system/feature and that the described system/feature interacts with. For example, for “ice-sheet dynamics”, the atmosphere and the bed are external factors and relevant aspects of them are described. *Internal* refers to conditions and factors governing system/feature behaviour and that are generally included in models of the system/feature, e.g. for “ice-sheet dynamics” the creep process of ice. The external and internal conditions and factors are those that relate to the described behaviour of the system/feature, e.g. for “ice-sheet dynamics” air temperature, geothermal heat flow and ice properties.

A table summarising the influence of the climate-related issue on the geological barrier of the repository is presented. The table includes the geosphere variables influenced by the system/feature and the variables associated with the system/feature that are required to be known to quantify the interaction between the system/feature and the repository system, e.g. for “ice-sheet dynamics” basal temperature and melt-rate. In this context, the repository system includes both the geosphere and the engineered barriers.

Natural analogues/observations in nature

Under this heading observations in nature and, when applicable, present-day natural analogues regarding the process are summarised.

Model studies

In this section, model studies of the process are summarised. This documentation focuses on process understanding and, for instance, includes sensitivity analyses. The handling of external and internal controlling conditions and factors is described, e.g. if spatially and temporally varying internal conditions considered.

Time perspective

The time scales on which the system/feature operates and changes are documented.

Handling in the safety assessment SR-PSU

The handling of the documented interactions with the repository is discussed. As a result of the information under this subheading, mappings of the climate-related issues to the method, or methods, of treatment and, in relevant cases, applicable models are produced. The mappings are characterised on various time scales.

Handling of uncertainties in SR-PSU

Given the adopted handling in the safety assessment SR-PSU as described above, the treatment of different types of uncertainties associated with the issue, within that general framework, is summarised under the following headings.

Uncertainties in mechanistic understanding: The uncertainties in the general understanding of the issue are discussed based on the available documentation and with the aim of answering the question: Are the basic scientific mechanisms governing the issue understood to a level necessary for the suggested handling? Alternative models may sometimes be used to illustrate this type of uncertainty.

Model simplification uncertainties: In most cases, the quantitative representation of a process contain simplifications, for instance in a numerical model. These may result in a significant source of uncertainty in the description of the system evolution. Alternative models or alternative approaches to simplification for a particular conceptual model may sometimes be used to illustrate this type of uncertainty.

Input data and data uncertainties: The input data necessary to quantify the process for the suggested handling are documented. The treatment of important input and output data and associated data uncertainties are described in detail in SKB (2014g), to which reference is made as appropriate.

Adequacy of references

For the description of each climate-related issue, the qualification of key references is described.

1.5 Publications supporting the SR-PSU Climate report

1.5.1 Publications produced for SR-PSU

Within the SKB climate programme, three reports were produced to support the SR-PSU Climate report. A review of early Weichselian climate was performed by Wohlfarth (2013) to enhance knowledge on the last transition from interglacial to glacial climate conditions in Sweden, whereas Helmens (2013) re-examined the last interglacial–glacial cycle based on long proxy records from central and northern Europe. The aim of the two studies was to describe the complex course of events that took place when warm interstadial conditions, similar to those at present, turned into cold glacial conditions. Finally, Brandefelt et al. (2013) analysed the potential for cold climate conditions and permafrost in Forsmark in the next 60 ka. The purpose was to provide information to the descriptions of the SR-PSU climate cases and to the analysis of freezing of SFR structures discussed in the SR-PSU **Main report** (SKB 2014a).

1.5.2 Publications produced for SR-Site and SR-Can, in parts or in whole used for the SR-PSU Climate report

Within the SKB climate programme, twelve supporting reports and publications were produced to support the SR-Site Climate report. Many of the topics that were studied are by necessity linked to each other and in some cases therefore partly overlapping. Studies on climate, palaeoclimate and Weichselian glacial history were conducted (Helmens 2009a, Houmark-Nielsen 2009, Kjellström et al. 2009 (including erratum Feb 2010), Wohlfarth 2009). A special issue of *Boreas* (Wohlfarth and Näslund 2010), with papers on conditions in Scandinavia during a long period prior to the Last Glacial Maximum of the last glacial cycle, was published as a result of a workshop on this topic arranged by SKB in 2007 (Näslund et al. 2008). Permafrost development was studied by Hartikainen et al. (2010) whereas glacial hydrology was studied by Jansson and Näslund (2009). Surface denudation (i.e. weathering and erosion) was investigated by Olvmo (2010), while bedrock borehole temperatures, geothermal heat and palaeoclimate were studied by Sundberg et al. (2009). Various aspects of glacial isostatic adjustment have been studied, such as sea-level change and shore-level displacement (Whitehouse 2009) and crustal stresses under glacial conditions (Lund et al. 2009, Lund and Näslund 2009). In addition, Brydsten et al. (2009) studied extreme sea-levels at Forsmark up until the year 2100. The information on sea-level to the year 2100 has been updated for SR-PSU within the present report (Section 3.3).

The climate studies performed for SR-Site resulted in a number of scientific publications, or contributions to such publications in *peer-reviewed* journals, see SKB (2010a, Section 1.4.1).

1.5.3 General scientific publications

In addition to the above SR-PSU, SR-Site and SR-Can studies, a large number of papers from the general scientific literature have been used as input to the present SR-PSU Climate report.

1.6 Interactions between the climate programme and other SR-PSU programmes

Data and information from the climate programme have been used within many other parts of the SR-PSU safety assessment. The main flows of data within the climate programme and to other SR-PSU activities are summarised in Figure 1-5 and below.

Data on air temperature have been used to simulate the development of ice sheets (Section 2.3.4) and permafrost (Section 2.1.4 and Hartikainen et al. 2010) and for the evaluation of thermal gradients and geothermal heat flow (Sundberg et al. 2009).

Data from permafrost simulations have been used to make appropriate selections of conditions when studying groundwater flow under permafrost conditions as well as for studies of surface hydrology under a colder climate (Odén et al. 2013).

Data on shore-level change have been used for a description of the past and future evolution of the landscape as influenced by e.g. the isostatic recovery from the last glacial cycle (SKB 2014f), for instance in order to model future lake formation. Shore-level data are also used for studying groundwater flow in potential future situations when the isostatic uplift has progressed further. Data on permafrost and glacial development have also been used for investigating and for assessing the potential for freezing of various parts of the repository (SKB 2014a).

SKB (2014g) summarises the data flow to and from all SR-PSU activities.

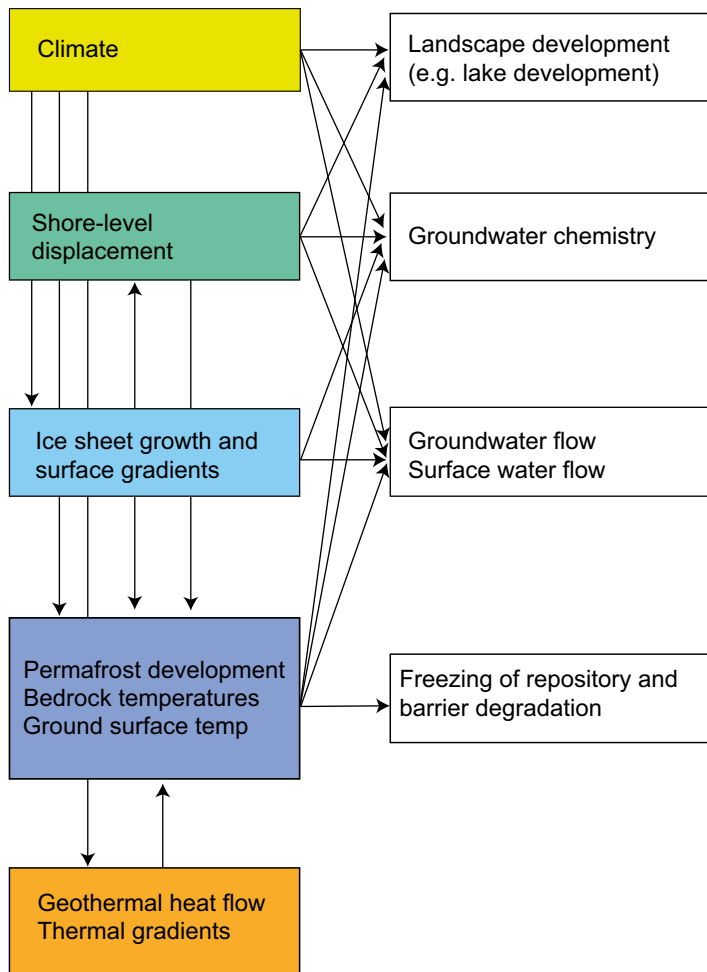


Figure 1-5. Main flows of climate- and climate-related data in SR-PSU. Coloured boxes show data within the climate programme. White boxes show other SR-PSU activities that use data from the climate programme.

1.7 Summary of main changes made since the SAR-08 safety assessment

Below is a summary of main changes in the SR-PSU Climate report compared with the SAR-08 safety assessment (SKB 2008). In addition to these major changes, all chapters and sections of the report have been updated.

- Complementary and up-to-date studies on Weichselian glacial history are included; these are used for the description of the reconstruction of the last glacial cycle and the SR-PSU *Weichselian glacial cycle*, *global warming* and *early periglacial* climate cases.
- In order to better describe possible future climate variability and to exemplify climates with the different climate domains, dedicated climate model simulations have been performed for selected periods during the last glacial cycle and for a future climate dominated by global warming.
- Detailed site-specific permafrost simulations have been performed in 2D, with an improved permafrost model, complementary to the 1D permafrost simulation performed for SR-Can used in SAR-08.
- Complementary information on shore-level displacement from 3D GIA simulations is included.
- Uncertainties in the palaeotemperature used for e.g. ice sheet- and permafrost simulations are better described.
- The knowledge and descriptions of possible future climate changes have been updated according to recent literature.
- A dedicated description of transitions between climate domains has been included.

2 Climate-related processes

2.1 Permafrost

2.1.1 Overview / general description

Permafrost is defined as ground that remains at or below 0°C for at least two consecutive years (French 2007). This definition is based exclusively on temperature, and disregards the texture, degree of compaction, water content, and lithologic character of the material. As a result, the term *permafrost* does not always equate to *perennially frozen ground*, since, depending on the pressure and composition of groundwater and on the adsorptive and capillary properties of ground matter, water in the ground may freeze at temperatures below 0°C. Therefore, permafrost encompasses the perennially frozen ground and a surrounding so-called *cryopeg*, i.e. a ground layer in which water remains unfrozen at sub-zero temperatures.

Permafrost and perennially frozen ground originate from the ground surface depending on a complex heat exchange process across the atmosphere-ground boundary layers and on an almost time-invariant geothermal heat flow from the Earth's interior. The heat exchange between the atmosphere and the Earth's surface is governed by shortwave and longwave radiative fluxes and sensible and latent heat fluxes.

Freezing of water is governed by thermal, hydraulic, mechanical, and chemical processes in the ground. In addition, freezing of water influences the thermal, hydraulic, mechanical, and chemical properties of the ground. Thermal properties change from those of unfrozen ground to those of frozen ground, affecting the heat transfer process. Ice formation in pores of the ground confines groundwater flow through the almost impermeable frozen ground, therefore altering the overall groundwater circulation pattern. Ice formation can also cause deformation of the ground and changes in the mechanical stress state. Frost weathering and degradation of the ground surface and patterned ground are additional consequences of cyclic freezing and thawing processes. Moreover, exclusion of salts in the freezing of saline groundwater can lead to increased salinity concentrations in adjacent unfrozen bedrock volumes.

Issues associated with permafrost development are comprehensively explained in Washburn (1979), Williams and Smith (1989), Yershov (1998), French (2007) and reviewed in e.g. Gascoyne (2000), Ahonen (2001) and Vidstrand (2003). Experimental investigations of thermal, hydrochemical and mechanical impacts of freezing on bedrock properties have been reported by e.g. Mackay (1997) and Ruskeeniemi et al. (2002, 2004), whereas model studies of present and future permafrost development influenced by increasing atmospheric greenhouse-gas concentrations can be found in e.g. Lunardini (1995), Kukkonen and Šafanda (2001) and Slater and Lawrence (2013). More recently, some model studies on thermo-hydro-mechanical impacts of freezing processes on bedrock properties with implications for interactions between glaciers and permafrost in a time frame of a glaciation cycle (~100 ka) have been conducted, e.g. Bauder et al. (2003), Hartikainen (2004, 2013), SKB (2006a), Person et al. (2007), Lemieux et al. (2008a, b, c) and Hartikainen et al. (2010). The effects of freezing of the geosphere on groundwater flow have been studied by e.g. Vidstrand et al. (2010, 2013).

2.1.2 Controlling conditions and factors

Climate and surface conditions

Heat exchange between the atmosphere and the Earth's surface is determined in the interplay of climate, topography, vegetation and snow cover, soil characteristics and water bodies. These factors can vary considerably with time and location. The main climatic parameters are incoming solar radiation (insolation), air temperature and humidity, wind, and precipitation. Absorption of incoming solar radiation by the Earth's surface governs the sensible and latent heat flux at the Earth's surface. Further, the longwave radiative flux is determined by the atmospheric and surface temperatures, respectively. Air temperature, which is commonly applied to map permafrost distribution, controls the longwave atmospheric radiation, the turbulent heat exchange, and evaporation and condensation. Wind, in turn, mainly influences the sensible heat exchange, but also latent heat exchange. Precipitation together with evapotranspiration and condensation determine groundwater recharge, affecting the groundwater content and flow and hence the terrestrial heat flux.

Topography has a significant impact on climate conditions. Generally, air temperature decreases as altitude increases, being affected by radiation, convection and condensation. The average air temperature decrease is approximately 0.65°C for every 100 metres increase in height (Danielson et al. 2003). In addition, inversions are common in hilly terrain causing low-slope low-lying areas to experience significantly lower temperatures than higher lying and steeper-slope areas. Furthermore, the slope angle and azimuth affect the flux of shortwave radiation, and where topographical differences are large a more patchy distribution of permafrost is expected.

Vegetation and snow cover are sensitive to climatic conditions and topography. The characteristic parameters of the surface cover are surface albedo, emissivity, and roughness controlling the absorption of incoming shortwave radiation, the longwave terrestrial radiation and the turbulent heat exchange, respectively, as well as the thermal properties and the thickness of the surface cover affecting terrestrial heat transfer. In general, vegetation and snow cover moderate the ground temperature and thus the aggradation and degradation of permafrost. Vegetation is an insulating cover limiting cooling in winter and warming in summer, hence reducing the amplitude of the annual cycle of ground temperature. Vegetation is also important for the creation of snow cover, which protects the ground from heat loss in winter. However, the high albedo of snow can lead to a snow surface temperature almost 2°C lower than the mean winter air temperature (Yershov 1998). As a rule, for a majority of the surface covers, permafrost can build from the ground surface if the annual mean air temperature is lower than a value ranging between -9 and -1°C (Washburn 1979, Williams and Smith 1989, Yershov 1998, French 2007). An exception occurs with peat layers, which can insulate the ground from warming in summer more effectively than from cooling in winter, with the resulting effect that permafrost can exist where the mean annual air temperature is above 0°C (Williams and Smith 1989).

Properties and thickness of the soil cover affect the terrestrial heat flow. Of importance are the porosity and water content of the soil, influencing the annual fluctuation of ground temperature and the thickness of the active layer, i.e. the seasonally thawing ground layer. The soil cover also acts as an insulating cover, since the thermal conductivity of the soil cover is lower than that of the underlying bedrock.

Water bodies, i.e. the sea, lakes, and watercourses, influence permafrost creation and distribution considerably since they have high values of specific heat. A talik, i.e. an unfrozen layer, can exist beneath water bodies that do not freeze to their bottom in winter. Depending on the characteristics of the climatic zone, the critical depth of a water body for it to remain unfrozen in winter is approximately 0.2 to 1.6 metres (Yershov 1998).

Sea water extensively reduces the development of costal permafrost. On the other hand, when the shore-level of a highly saline sea is rising, submerged permafrost and perennially frozen deposits can survive for a long time beneath a cold seabed (Washburn 1979, Yershov 1998).

The hydrological conditions on the ground surface affect the freezing of groundwater. For instance, under glaciated conditions, a warm-based overlying ice sheet may increase the subglacial groundwater pressure, in which case the freezing point may decrease to such a degree that the subglacial ground is kept unfrozen. A similar, but minor, effect may occur when cold ground is submerged and submarine freezing is reduced by the pressure of the overlying sea water. Furthermore, groundwater flow, whether carrying fresh glacial meltwater or saline seawater, can influence the freezing process by altering the chemical groundwater composition.

Table 2-1 summarises how geosphere variables are influenced by permafrost development.

Geosphere and repository

The ground temperature that defines the presence of permafrost and primarily governs the freezing of water in the ground, is principally controlled by the ground thermal energy balance in terms of heat transfer, geothermal heat production, the specific heat content and the amount of heat generated by phase change processes of water. Heat transfer within the ground can occur through conduction, convection and radiation (Sundberg 1988). In general, only conduction is regarded as important to permafrost evolution, since radiation is of importance only in unsaturated high-porosity ground at high temperatures, and convection is of importance only when groundwater and gas fluxes are large.

Heat conduction depends on the ground temperature gradient, ambient temperature conditions, and the thermal properties of the ground matter. Thermal conductivity, describing the ability of material to transport thermal energy, and heat capacity characterising the capability of material to store heat, depend on a number of variables such as mineralogy, porosity and groundwater content. Having typically three to four times higher conductivity than other common rock-forming minerals, quartz is the most important mineral for determining thermal characteristics of rock materials, as it typically has up to four times higher heat conductivity.

When the porosity is less than 1%, freezing of water has a minor effect on heat transfer in water-saturated ground. The degree of saturation has relevance to the thermal properties of ground due to the very low thermal conductivity and heat capacity of air, e.g. the thermal conductivity of 1%-porosity granite can decrease by over 10% with decreasing saturation (Clauser and Huenges 1995). In rock, heat capacity is not very dependent on ambient temperature and pressure conditions, whereas thermal conductivity is a rather variable function of both temperature and pressure. The thermal conductivity of granite decreases with increasing temperature by approximately 5 to 20% per 100°C and increases with increasing pressure by about 1 to 2.5% per 100 MPa (Seipold 1995). The pressure dependence of thermal conductivity is increased when rocks are unsaturated (Sundberg 1988, Clauser and Huenges 1995). Moreover, Allen et al. (1988) reported a strong correlation between lithology and permafrost depth, which could be directly explained by differences in thermal conductivity.

In addition to the thermal properties above, the hydrogeochemical and mechanical properties of the ground important for freezing of groundwater are permeability, porosity, adsorptive capacity of ground matter, chemical composition of groundwater and deformation properties of the ground.

Table 2-1. Influence of permafrost development on geosphere variables.

Geosphere variable	Climate issue variable	Summary of influence
Temperature	Permafrost depth	Permafrost is by definition a thermal condition hence having no influence on temperature.
Groundwater flow	Frozen/unfrozen fraction of groundwater	Freezing occurs at temperatures below the freezing point (SKB 2010c). Groundwater transformed from liquid to solid phase can be regarded as immobile. Filling fractures and pores, ice also affects the groundwater flow through permeability, which decreases with a reduction in the unfrozen fraction of groundwater.
Groundwater pressure	Frozen/unfrozen fraction of groundwater	The volume increase in the phase change of water from liquid to solid state causes an increase in the pressure of water which remains liquid. Moreover, freezing of water in porous ground matter can lead to cryosuction and depression of groundwater pressure in the unfrozen ground.
Groundwater composition	Frozen/unfrozen fraction of groundwater	When saline water is transformed from liquid to solid phase, the solutes are typically not incorporated in the crystal lattice of ice but transferred in the liquid phase. Therefore the salinity in the unfrozen fraction increases.
Rock stresses	Frozen fraction of groundwater	Deformations due to ice formation will lead to changes in rock stresses. The effect of the changes is strongest nearest to the surface where in situ stresses are lowest.
Fracture geometry	Frozen fraction of groundwater	Freezing can have some influence on the fracture geometry at shallow depths due to frost cracking. Close to the ground surface frost wedges can form down to depths of c 10 m. Otherwise, there can be widening of fractures due to freezing but the effect may be reversible as thawing takes place.

2.1.3 Natural analogues / observations in nature

At present, approximately 25% of the total continental land area of the Earth is occupied by permafrost. The permafrost distribution may be characterised into: i) continuous (more than 90% spatial coverage), ii) discontinuous (between 90 and 50% coverage), iii) sporadic (less than 50% coverage), and iv) subglacial forms. About one fifth of this permafrost is estimated to be subglacial in Antarctica and Greenland. Permafrost is abundant in Alaska, the northern parts of Canada and Russia, and in parts of China (French 2007). Along the coast of southern and south-western Greenland both continuous and discontinuous permafrost can be found (Mai and Thomsen 1993). The Northern Hemisphere distribution of permafrost is illustrated in Figure 2-1.

The deepest known permafrost occurs in the central part of Siberia in Russia, where thicknesses of up to 1,500 m have been reported (Fotiev 1997). The extensive region of continuous permafrost in central Siberia corresponds to areas that are believed not to have been covered by Quaternary ice sheets and that experienced cold climate conditions during the last glacial cycle and before. In coastal areas, submarine permafrost may also exist, such as in northern Siberia where the permafrost formed during ice-free periods of the last glacial cycle in regions subsequently covered by the Arctic Ocean. Furthermore, permafrost is frequently observed in mountainous terrain. For example, in the area of Tarfala in the Kebnekaise massif in northern Sweden, discontinuous permafrost has been reported to be 100 to 350 m thick at an altitude above 1,500 m a.s.l. (King 1984, Isaksen et al. 2001).

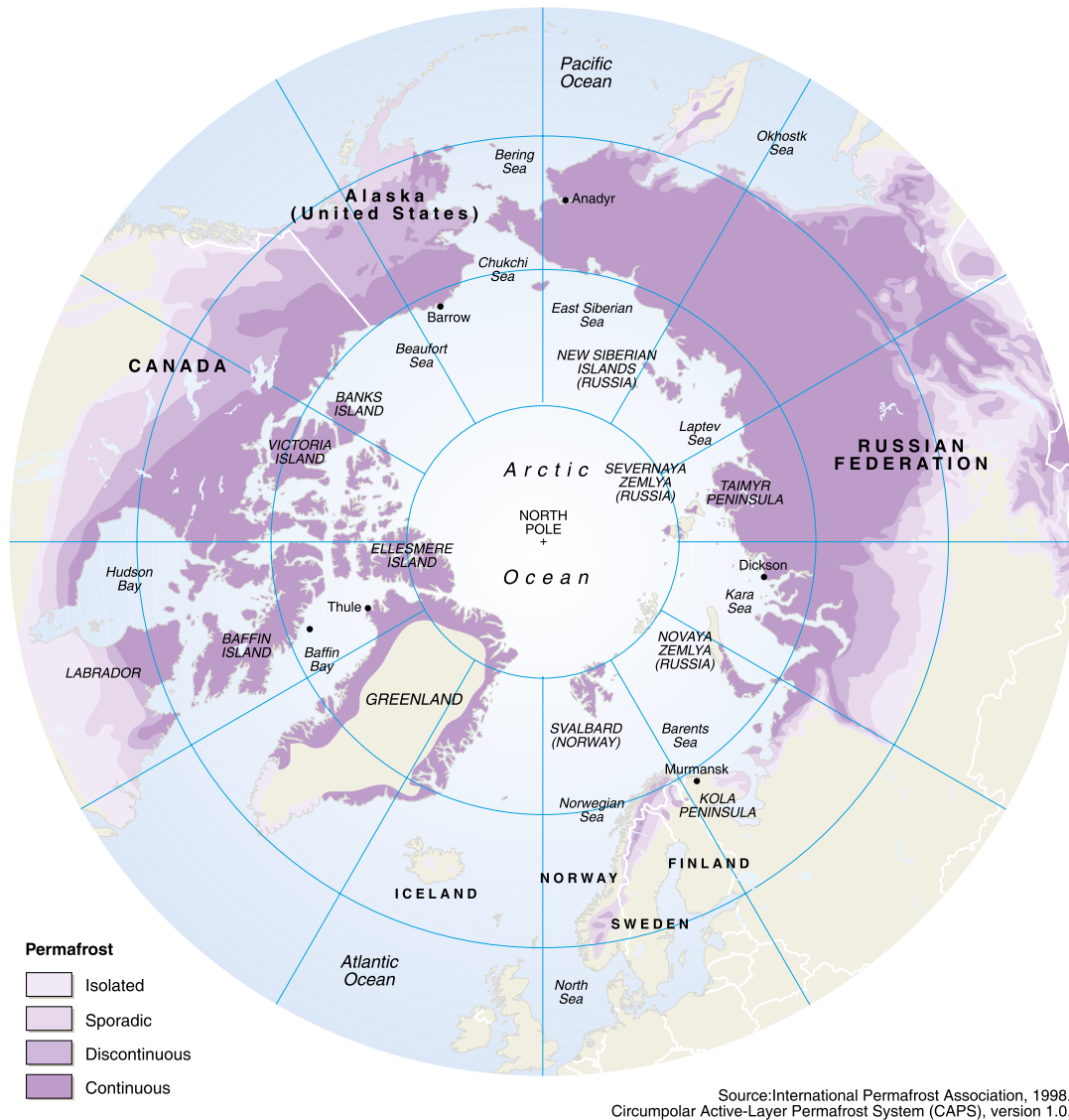


Figure 2-1. Permafrost distribution in the Northern Hemisphere. From UNEP/GRID-Arendal (2005).

SKB, together with co-funding parties from Finland (Geological Survey of Finland and Posiva), Great Britain (UK Nirex Ltd) and Canada (Ontario Power Generation and University of Waterloo), carried out a research project on permafrost at the Lupin gold mine in northern Canada (Ruskeeniemi et al. 2002, 2004). In this area, the depth of the permafrost extends to ~500–600 m. The main objective of the project was to provide data describing the subsurface conditions in a permafrost area with crystalline bedrock. Permafrost depth, temperatures, groundwater composition and hydraulic properties have been measured. The mean annual air temperature at this site is -11°C and the annual mean precipitation is low; ~270 mm (Ruskeeniemi et al. 2002). Based on a seismic refraction survey, the depth of the active layer has been interpreted to be ~1.5 m, varying between 1.2 and 1.8 m. The present permafrost depth is believed to have been developed over the last 5 ka. In the Lupin area, all shallow lakes freeze down to the bottom during winter. Lakes deeper than 2–3 m are expected to have unfrozen bottoms all year. The latter lakes may have the potential to support closed taliks. The large Lake Contwoyto, located about 1,300 m from the mine at surface, provides the most significant talik structure that may extend through the deep permafrost. However, direct observations beneath this lake are lacking.

In order to investigate the distribution of permafrost and locate salinity differences in the deep groundwaters, a number of electromagnetic soundings were conducted in the Lupin mine area. Furthermore, drillings were made from the deeper parts of the mine through the base of the permafrost, in order to sample groundwaters and to study the distribution of open fractures and hydraulic conditions. The main result of the electromagnetic sounding surveys was the identification of anomalies forming a subhorizontal layer at depths between 400 and 700 m. Paananen and Ruskeeniemi (2003) made the interpretation that this conducting layer represents saline or brackish water at the base of the permafrost. According to the temperature measurements made in the mine, the base of the permafrost occurs at a depth of 540 m. The drillings revealed the existence of a ~100 m thick unsaturated or dewatered zone below the permafrost. An alternative interpretation of the subhorizontal conductor at ~650 m depth could be that it represents the groundwater table (Ruskeeniemi et al. 2004). The dry zone below the permafrost could either be a natural result of very limited recharge through the permafrost or an effect of mine drainage. No pressurised water or gas flow was observed in the boreholes. The available data from water sampling do not provide any evidence of highly saline water below the permafrost (Ruskeeniemi et al. 2004).

Between 2009 and 2013, SKB, Posiva and NWMO conducted a comprehensive study on hydrology in western Greenland called the Greenland Analogue project (GAP). The main purpose of the project was to investigate the hydrological conditions at a site affected by the presence of the Greenland ice sheet, from the formation of meltwater at the ice-sheet surface and bed, through the groundwater flow in bedrock at KBS-3 depth (400–700 m), to the groundwater discharge through taliks into proglacial lakes (SKB 2010e, Harper et al. 2011). Background information on the site is available in terms of the hydrogeology and hydrogeochemistry (Wallroth et al. 2010), Holocene environmental change and climate development (Engels et al. 2010) and the periglacial environment (Clarhäll 2011).

Detailed temperature measurements in a deep bedrock borehole drilled at an elevated area at the very ice-sheet margin showed that the proglacial permafrost at this site is ~400 m deep. Measurements of basal thermal properties of the ice sheet showed warm-based conditions at all sites investigated, i.e. the basal ice temperature is at the pressure melting point and free water is available at the ice-sheet bed. This indicates that, at some distance in under the ice, the bedrock is likely fully thawed. However, a wedge of subglacial permafrost probably stretches in for some distance under the ice.

Investigations made in the deep borehole at the ice margin show that groundwater flows beneath the frozen ground. Sampling of groundwater has been made at three different depths (511, 563 and 574 m) in the borehole. The water samples will be subject to geochemical and isotope analyses in order to study e.g. if there is a glacial chemical signal at depth, and the characteristics of such a signal.

Through taliks are common in the GAP study area. From field observations and modelling, all larger proglacial lakes in the area are assumed to support a talik (SKB 2010e). How they contribute to the hydrogeology depends on the properties of the lake-bottom sediments, underlying bedrock and surrounding hydraulic gradients. A bedrock borehole has been drilled at the shore of a nearby proglacial lake, through the permafrost and into the through-talik that is located under the lake. In this borehole, water samples have been taken at a depth of 140 m. The samples have been subject to geochemical and isotope analysis. The same lake, and its surrounding catchment, has also been subject to detailed water balance studies showing that, at least for the hydrological year studied, the talik acts as a groundwater recharge area (Bosson et al. 2013). Regional-scale groundwater flow modelling studies are also being performed in the GAP study area (see e.g. Jaquet et al. 2012).

2.1.4 Model studies

In order to give input to the definition of the climate cases for SR-PSU, the potential for permafrost in Forsmark in the next 60 ka has been studied (Brandefelt et al. 2013). The purpose was to analyse the potential for climate conditions favourable for permafrost growth, and to analyse the resulting bedrock temperatures. These results were used to define the *global warming climate case* and the *early periglacial climate case* (see Sections 4.1 and 4.2). Further, earlier studies of the permafrost evolution reconstructed for the last glacial cycle in the Forsmark area were also used in the definition of the *Weichselian glacial cycle climate case* (see Section 4.4). A broad range of sensitivity tests made in these earlier studies, covering the range of uncertainties associated with various parameters of importance for permafrost development, were also used.

The simulations of permafrost for the reconstruction of the last glacial cycle were made with two types of models, a 1D permafrost model and a 2D permafrost model improved from the 1D model. The 1D modelling was performed for the SR-Can safety assessment (SKB 2006a), with some of the results used also for the SR-Site safety assessment (SKB 2010a, Engström et al. 2012). The 1D simulations were conducted specifically for the location of the planned spent nuclear fuel repository. The 2D modelling (Hartikainen et al. 2010) was conducted for the SR-Site safety assessment, and covered a 15 km long and 10 km deep vertical cross-section crossing both the site for the planned spent nuclear fuel repository and the location of the SFR. Reconstructed air temperature for the Forsmark region for the past 120 ka, based on the ice-sheet modelling of this period (Section 2.3.4), was used as input to the 1D and 2D permafrost modelling for the reconstruction of the last glacial cycle. The methodology is described in Appendix 1 of SKB (2010a).

The 2D simulations of permafrost for the next 60 ka (Brandefelt et al. 2013) were conducted along the same 15 km profile as for the SR-Site simulations (Hartikainen et al. 2010), but with an improved version of the permafrost model. All the simulations (SKB 2006a, Brandefelt et al. 2013, Hartikainen et al. 2010) use site-specific input data from the Forsmark site investigation programme. Details on the input data used for the 1D and 2D permafrost simulations are given in SKB (2006a, Section 3.4), Hartikainen et al. (2010) and Brandefelt et al. (2013, Section 2.4), respectively.

The purpose of the modelling studies was to analyse the main factors of importance for the development of permafrost and perennally frozen ground at Forsmark, and to exemplify how permafrost grows and degrades at this site. Further, in Brandefelt et al. (2013), the purpose is to analyse the potential for permafrost growth in Forsmark in the next 60 ka.

The permafrost models include mathematical expressions for freezing and thawing of saline groundwater-saturated bedrock. The bedrock is considered as an elastic porous medium and the groundwater as an ideal solution of water and ionic solvents. The models are based on the principles of continuum mechanics, macroscopic thermodynamics and the theory of mixtures being capable of describing heat transfer, freezing of saline water, groundwater flow and deformations of bedrock. In the 2D version of the model, the freeze-out and transport of solutes is included (Hartikainen et al. 2010). The models are described further in Hartikainen (2004), SKB (2006a), Hartikainen et al. (2010) and Brandefelt et al. (2013).

A 3D version of the model has also been used for simulating the development of permafrost and frozen ground at the Olkiluoto site in Finland (Hartikainen 2013).

To capture the most important factors and parameters affecting the development of permafrost, sensitivity analyses have been performed considering the following issues:

- Surface conditions.
- Subsurface conditions.
- Presence of heat from a KBS-3 repository.

Surface temperatures, together with the influence of surface covers such as snow, vegetation and water bodies, have been included as factors of importance in the surface conditions. The investigated bedrock conditions are thermal properties of the bedrock and the geothermal heat flow. The sensitivity simulations carried out with the 2D permafrost model (Hartikainen et al. 2010) are presented in SKB (2010a). The heat generated by the spent nuclear fuel repository has been included in most simulations, and is also analysed in a dedicated 2D sensitivity simulation. In this context, it should be noted that the repository depth was changed between SR-Can (for which the 1D simulations were made) where it was 400 m and SR-Site (for which the 2D simulations were made) where it is 450 m.

Despite this, the resulting permafrost and freezing depths are very similar between the two studies, as demonstrated later in the present report.

Main conclusion from the 1D and 2D permafrost modelling studies for the last glacial cycle

The conclusion drawn from the 1D permafrost investigations (SKB 2006a) was that the surface conditions can be seen as the driving force for the development of permafrost. This conclusion was strengthened by the 2D study (Hartikainen et al. 2010). In addition, the conclusion that the subsurface conditions and the heat from the spent nuclear fuel repository act as reducing factors for the development of permafrost and perennially frozen ground is also supported. The following main conclusions can be drawn from the 2D permafrost study performed for the SR-Site safety assessment for a spent nuclear fuel repository at 450 m depth in Forsmark:

- Given the temperatures reconstructed for the last glacial cycle, the study demonstrates how the site-specific spatial- and temporal development of permafrost and perennially frozen ground takes place at the Forsmark site, developing from sporadic-, to discontinuous- to continuous coverage in various combinations and extents. The results show that through taliks may form at the site under certain conditions, and that groundwater may flow in these taliks.
- The study provides a full range of sensitivity analyses of uncertainties in sub-surface and surface conditions, including the reconstructed input air temperature for the last glacial cycle.
- For the reconstruction of last glacial cycle conditions, the simulated maximum permafrost (the 0°C isotherm) depth over the KBS-3 repository is between 180 and 260 m depending on the surface conditions. The corresponding range for the entire 15 km profile is from 220 to 300 m.
- By making the very pessimistic combination of setting all known uncertainties (e.g. in air temperature, surface vegetation and snow conditions, bedrock thermal conductivity and heat capacity, and geothermal heat flow) as most favourable for permafrost growth, permafrost (i.e. the 0°C isotherm) reaches 450 m depth after 45 ka in the reconstruction of the last glacial cycle. However, the perennially frozen ground does not reach KBS-3 repository depth. It should be noted that the combination of assumptions in this case is quite unrealistic.
- The prevailing surface conditions, such as temperature and surface moisture, are the main factors governing the spatial and temporal development of permafrost and perennially frozen ground at the Forsmark site.
- Subsurface conditions, such as bedrock thermal properties, geothermal heat flow and groundwater salinity, modify the spatial and temporal development of permafrost and perennially frozen ground, but are of secondary importance for modelled permafrost depths compared with surface conditions.
- The variation in thermal properties along the profile as well as 2D groundwater flow only have a slight influence on permafrost (the 0°C isotherm) development. Therefore, the uncertainties introduced by excluding lateral variations in thermal properties, boundary conditions and convective heat transfer in the 1D model study (SKB 2006a) are considered insignificant.
- Under continuous permafrost conditions, the unfrozen groundwater content in the perennially frozen ground under lakes can exceed 10% down to a ~50 m depth. This may indicate that taliks are able to form under lakes through perennially frozen ground, if favourable groundwater flow conditions with open flow paths prevail. When the unfrozen groundwater content decreases below 10%, groundwater flow is reduced considerably, and taliks are not longer able to form or survive.
- Freezing can induce salt exclusion and salt transport when perennially frozen ground develops deeper than ~200 m. At shallower depths the impacts of freezing are difficult to see since the salinity of groundwater has been diluted prior to the development of perennially frozen ground. When salt transport occurs more slowly than the freezing zone advances, the salinity concentration is increased within the perennially frozen ground.
- The uncertainty in dealing with groundwater flow with this permafrost model remains, since the 3D flow network is omitted in the 2D model. However, the topography of the Forsmark site is too flat to generate significant hydraulic gradients, compared to e.g the gradients imposed by the ice sheet during glacial conditions, suggesting that this would only have a minor impact on the results for non-glacial conditions.
- The uncertainty regarding the neglect of salinity transport in the 1D model (SKB 2006a) seems to be insignificant, mainly due to the low rock porosity, although the present 2D model is not able to describe the groundwater flow realistically.

The potential for cold climate conditions and permafrost in Forsmark in the next 60 ka

Based on the two previous studies (SKB 2006a, Hartikainen et al. 2010), it can be concluded that permafrost growth can occur in Forsmark under cold climate conditions. It can also be concluded that the permafrost can penetrate deeper than the SFR repository structures, located at a depth of c 140–60 m below the surface. Since the functionality of the concrete and bentonite barriers of SFR may be influenced by freezing temperatures (SKB 2014d), the potential for permafrost and frozen ground at repository depth is of interest. Further, since the radionuclide inventory of SFR is dominated by relatively short-lived nuclides, possible radiation doses to man or the environment are strongly dependent on the earliest timing of permafrost growth to repository depth.

In order to assess the potential for cold climate conditions and permafrost growth at the SFR repository location in the next 100 ka a combined climate modelling – permafrost modelling study was performed by Brandefelt et al. (2013). Based on the known future insolation variations, with Northern Hemisphere summer minima at 17 ka and 54 ka AP, the study focused on the first 60 ka AP.

The latitudinal and seasonal distribution of incoming solar radiation (insolation) varies on millennial time scales due to variations in the Earth's orbit and axial tilt. These variations, together with variations in the atmospheric CO₂ concentration, are viewed as two main factors in determining the climate variation between interglacial (warmer) and glacial (colder) climates. Summer insolation at high northern latitudes is at a minimum 17 ka and 54 ka after present (AP). These periods were therefore identified as potential future periods of cold climate conditions in high northern latitudes in general and in south-central Sweden in particular. Due to human emissions of carbon to the atmosphere, the atmospheric CO₂ concentration is currently 392 ppmv (2011 AD), a substantial increase as compared to the range of atmospheric CO₂ concentrations of 180–295 ppmv found in ice cores for the last 400 ka. The future atmospheric CO₂ concentration is determined by i) future human carbon emissions to the atmosphere, ii) possible emissions due to feedbacks in the climate system, and iii) by the global carbon cycle.

Climate modelling for next 60 ka

To investigate the potential for cold climate conditions in south-central Sweden in the next 60 ka the future air temperature in Forsmark was estimated based on simulations with an Earth system model of intermediate complexity (EMIC), LOVECLIM version 1.2, and a state-of-the-art Earth System Model (ESM), Community Earth System Model version 1 (CESM1). To span the possible combinations of future orbital variations and possible future atmospheric CO₂ concentrations, three sets of simulations were performed. The first set consists of a suite of EMIC simulations performed for the future periods of minimum summer insolation at high northern latitudes (17 ka and 54 ka AP) with the atmospheric CO₂ concentration varying in the range 180–400 ppmv. These are equilibrium simulations with constant forcing conditions. The second set consists of two transient EMIC simulations with constant atmospheric CO₂ concentrations of 200 or 400 ppmv respectively and insolation variations for the full period from the present to 61 ka AP. The third set of simulations consists of two ESM equilibrium simulations with insolation for 17 ka and 54 ka AP and atmospheric CO₂ concentration set to 200 ppmv and 180 ppmv respectively. This set was used, in combination with published results from climate model intercomparisons, to estimate the uncertainty in the EMIC results due to the simplified model formulation. When the atmospheric CO₂ concentration is varied from 180 ppmv to 400 ppmv the annual average bias-corrected air temperature at 2 m height (T_{2m}) at Forsmark varies from 1.6°C to 5.7°C in the EMIC simulations for orbital year 17 ka AP and from 0.96°C to 5.3°C in the simulation for orbital year 54 ka AP (Figure 2-2). The insolation difference between orbital years 17 ka AP and 54 ka AP results in a difference in the annual average Forsmark T_{2m} of c 0.3°C–1.2°C, with a tendency towards larger differences for lower atmospheric CO₂ concentrations. These results indicate that the future atmospheric CO₂ concentration is more important than insolation variations for future cold climate conditions in Forsmark in the next 60 ka.

The ESM simulations reveal significant inter-model differences in the simulated climate, specifically in the regional climate, in line with earlier inter-comparison studies. Annual average Forsmark T_{2m} is 5.9°C and 7.7°C colder than the pre-industrial value in the ESM simulations for 17 ka AP and 54 ka AP, respectively. These values are 3.9°C and 4.4°C, respectively, lower than in the corresponding EMIC simulations.

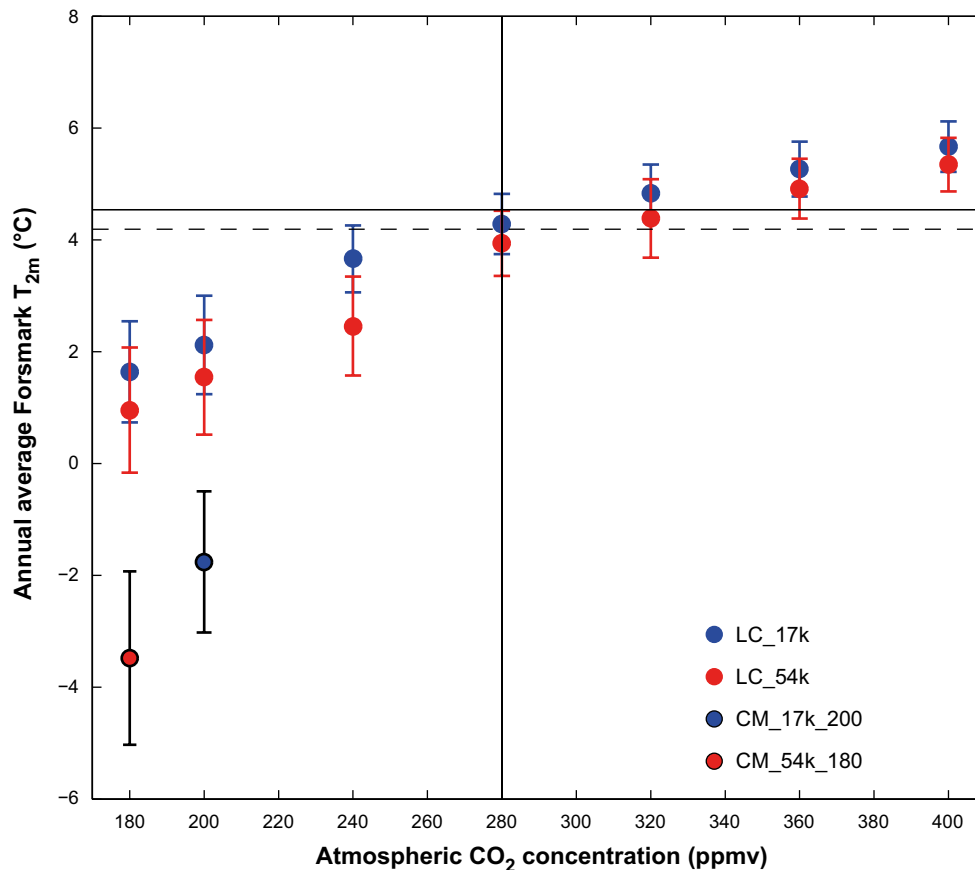


Figure 2-2. Annual average bias-corrected near-surface air temperature (T_{2m} , °C) in Forsmark in the EMIC (LC_) and ESM (CM_) simulations with constant forcing and boundary conditions for orbital years 17 ka AP (blue circles) and 54 ka AP (red circles). Annual average bias-corrected T_{2m} for the EMIC transient simulations is also displayed (cyan and magenta circles). T_{2m} is shown as a function of the atmospheric CO_2 concentration. The standard deviation of the annual average bias-corrected T_{2m} in Forsmark is indicated as error bars. The annual average bias-corrected T_{2m} in Forsmark in the EMIC simulation of pre-industrial (c 1850 AD) climate (+4.54°C; horizontal black line) and in the ESM simulation of pre-industrial climate (+4.19°C; horizontal black dashed line) is indicated. The pre-industrial atmospheric CO_2 concentration is indicated with a vertical line. The climate simulations are described in Brandefelt et al. (2013).

The climate models used in Brandefelt et al. (2013) do not include glacier and ice-sheet dynamics, which gives rise to a potential warm bias in the simulated climate. Comparison of the results presented here to an earlier study of future climate evolution with EMICs that include ice-sheet dynamics (Pimenoff et al. 2011) indicate a potential bias of up to 5°C in the results presented here. The uncertainties in the simulated Forsmark T_{2m} due to future glacier and ice-sheet growth, inter-model differences, internal variability and future greenhouse-gas concentrations are estimated. The collective uncertainty is taken to be larger for orbital year 54 ka AP, reflecting two factors. Firstly, inter-model differences generally increase when the difference between the simulated climate state and the present climate increases. Secondly, several earlier studies indicate that ice-sheet growth may occur at 40 ka to 50 ka AP if the atmospheric CO_2 concentration reaches pre-industrial or lower values (see further Section 3.3.5).

The results of the climate modelling are summarised in Table 2-2. To assess the potential for permafrost in Forsmark in the coming 60 ka AP, the uncertainty in the climate model results must first be assessed. Models of the Earth's climate system are designed to simulate the dynamics of the system. The complexity of climate system dynamics is however partly unresolved, both in terms of incomplete knowledge of some processes and in terms of insufficient resources to numerically resolve small-scale processes in the models. Further uncertainty in the results of such models exists due to the nonlinear nature of the climate system. To assess the uncertainty in the bias-corrected T_{2m} in Forsmark used as input to the permafrost model, a number of sources of uncertainty have been identified. A thorough description is given in Section 3.3 of Brandefelt et al. (2013).

Table 2-2. The minimum annual average bias-corrected Forsmark T_{2m} when all uncertainties are taken into account. See Section 3.3 of Brandefelt et al. (2013) for a detailed description.

Atmospheric CO ₂ concentration (ppmv)	180	200	240	280	320
Orbital year 17 ka AP	-7.4	-5.9	-2.3	0.3	0.8
Orbital year 54 ka AP	-11	-9.5	-6.5	-3.1	-2.6

2D permafrost modelling

To analyse the potential for permafrost development in the Forsmark region, the bias-corrected T_{2m} from the EMIC simulation with the coldest climate was used as input to a site-specific 2D permafrost model for Forsmark. This study provides a numerical estimation of the development of permafrost and perennially frozen ground along a profile covering a major portion of the Forsmark site and crossing the repository location, using site-specific surface and subsurface conditions. Special emphasis is put on the modelling of surface conditions, including climate (temperature and humidity), soil, vegetation, water bodies and topography, lateral variations in bedrock and surface physical properties. In addition, groundwater flow and salt transport processes are considered (in 2D).

The present study made use of an improved version of the 2D thermo-hydro-chemical model of permafrost and perennially frozen ground that was used for the SR-Site safety assessment for spent nuclear fuel (Hartikainen et al. 2010). The 2D model domain was set up in the same way as in Hartikainen et al. (2010), and covers the same 15 km long and 10 km deep vertical cross-section of the Forsmark site (Figure 2-3). The profile crosses the SFR repository which is the main focus for the present study. The permafrost model includes mathematical expressions for freezing and thawing of saline groundwater-saturated bedrock. The bedrock is considered as an elastic porous medium and the groundwater as an ideal solution of water and ionic solvents. The model is based on the principles of continuum mechanics, macroscopic thermodynamics and the theory of mixtures being capable of describing heat transfer, freezing of saline water, groundwater flow and deformations of bedrock. The freeze-out and transport of solutes is also included in the model.

A more detailed description of the 2D permafrost model used for the reconstruction of last glacial cycle permafrost conditions is found in Hartikainen et al. (2010). The improvement made to the model since the study by Hartikainen et al. (2010) is described below.

The improved version of the permafrost model includes seasonal freezing and thawing of the ground. Inter-annual variations in ground surface temperature are now expressed in terms of the monthly mean ground surface temperatures, T_s , which are determined by the monthly mean 2-m air temperatures, T_a , the freezing n -factor, n_{fr} , and thawing n -factor, n_{th} , as

$$T_s = \begin{cases} n_f T_a, & T_a < 0^\circ\text{C} \\ n_h T_a, & T_a \geq 0^\circ\text{C} \end{cases} \quad (2-1)$$

The n -factors are statistical relations between the annual mean 2-m air temperature and annual mean ground surface temperature (Lunardini 1978). Values for the n -factors used in this study are given in Table 2-7 in Hartikainen et al. (2010).

The improvement allows for the thermal offset, i.e. a decrease, in the annual mean ground temperature profile due to seasonal freezing and thawing of the ground (Goodrich 1978). The offset can be several degrees depending on the amount of freezing water in the ground, and may in some cases, lead to development of perennially frozen ground in locations where the annual mean air temperature is above 0°C.

Sub-surface properties and conditions

To capture the most important factors and parameters affecting the development of permafrost and frozen ground at the Forsmark site, detailed site-specific sensitivity analyses were previously performed considering surface and subsurface conditions (Hartikainen et al. 2010). Factors of importance, and analysed in the sensitivity studies, were air temperatures and the influence of surface covers such as snow, vegetation and water bodies.

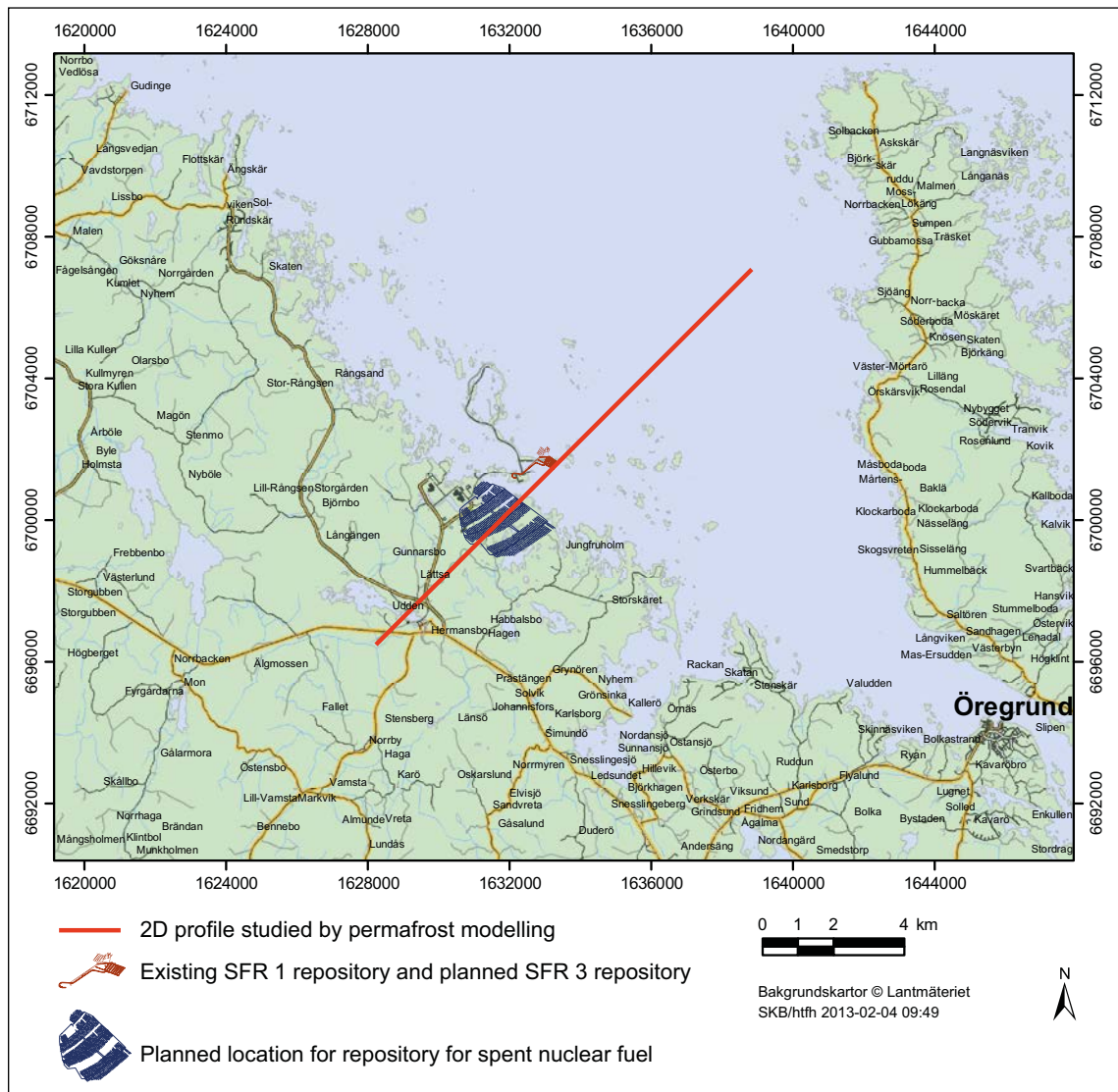


Figure 2-3. The ~15 km long profile analysed in the 2D permafrost modelling study (Brandefelt et al. 2013; red line), SFR repository location (brown), and the planned location of the repository for spent nuclear fuel.

The model domain encompasses an approximately 15 km long and 10 km deep vertical section consisting of six soil layers, 23 rock domains and 31 deformation zones as shown in Figure 2-3 and Figure 2-4. Figure 2-5 illustrates the thermally different rock mass domains, the deformation zones of the upper 2.1 km of the model domain, as well as the present-day level of the Baltic Sea. The soil layers are shown in Figure 2-6. The thermal and hydraulic properties of the soil domains are given in Hartikainen et al. (2010, Table 2-1), whereas Table 2-2 and Table 2-3 in the same publication give the thermal and hydraulic properties of the rock mass domains. Hydraulic properties of the deformation zones are presented in Hartikainen et al. (2010, Appendix D). The thermal properties of deformation zones are assumed identical to those of the corresponding rock mass domain. The bedrock below the depth of 2.1 km is assumed to have the same thermal and hydraulic properties as the rock domain in which the repository is located. The material properties of the bedrock are described in detail in Hartikainen et al. (2010, Appendices D and E). For the treatment of e.g. unfrozen groundwater content, see also Hartikainen et al. (2010). The numerical simulations were carried out using an unstructured finite element mesh of linear triangular elements. The mean grid spacing varied from less than 10 m close to the ground surface to about 300 m at the bottom of the model domain. The maximum time step for the adaptive time-integration scheme was limited to 100 years.

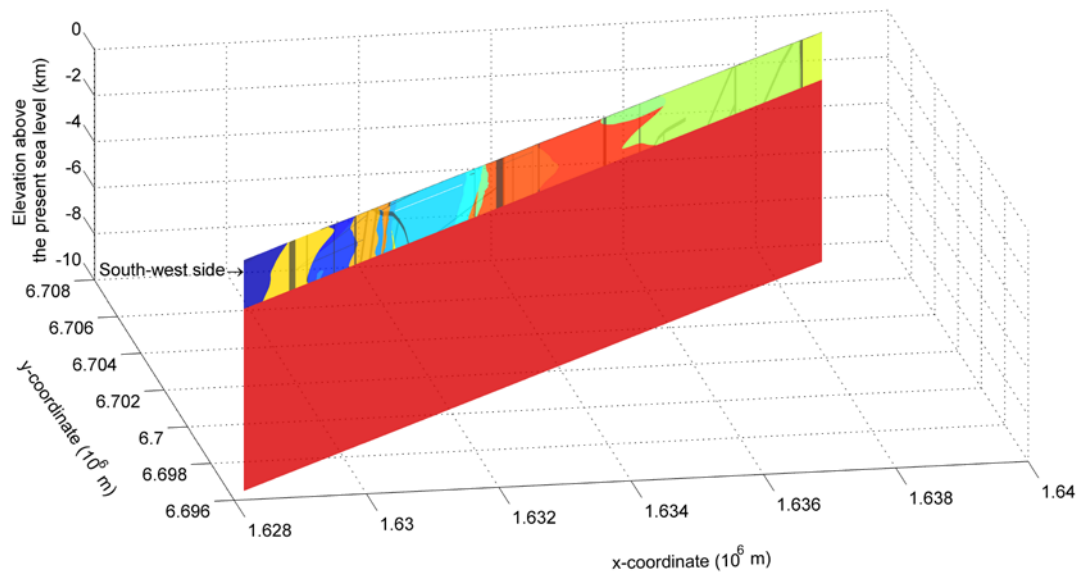


Figure 2-4. The model domain used in the 2D permafrost simulations. Colours from blue to red signify the 23 rock domains considered, and grey the 31 deformation zones. Physical and thermal characteristics for the rock domains and deformation zones were obtained from the site investigation programme at Forsmark, see Hartikainen et al. (2010). The six soil layers described in Hartikainen (2010, Appendix B) and Figure 2-6, are too thin to be seen in this figure. The x-axis is directed eastward and y-axis northward. The RT-90 coordinates of the south-west corner are $x = 1,628,228$ m, $y = 6,696,472$ m.

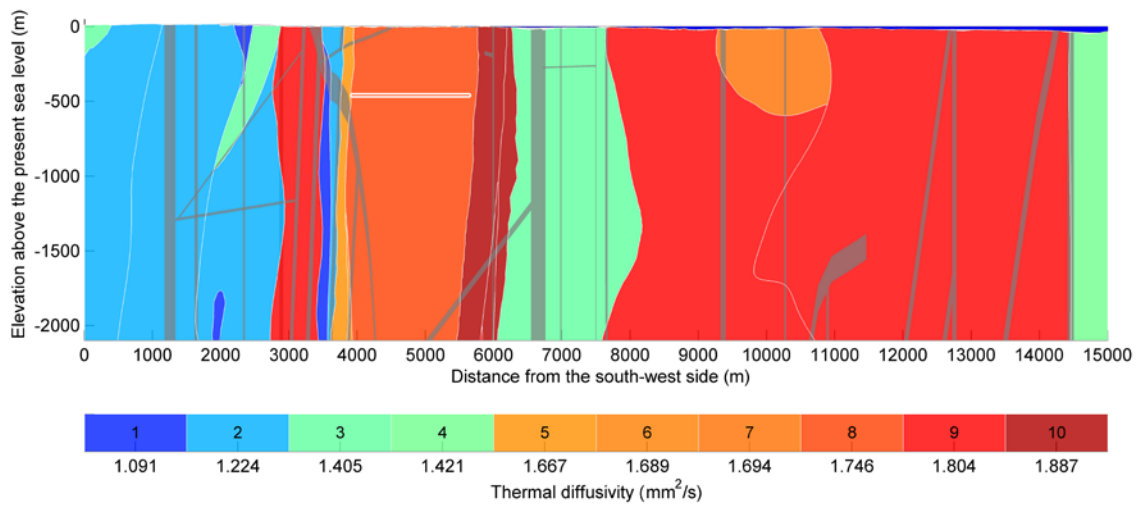


Figure 2-5. The upper 2.1 km of the 2D model domain. Colours from blue to red signify rock domains with different thermal diffusivities. Numbers from 1 to 10 indicate the rock domains of Table 2-2 in Hartikainen et al. (2010). The location of deformation zones is illustrated in grey and the repository for spent nuclear fuel in white, at a depth of 450 m starting at a distance of about 4,000 m along the profile. The thin blue layer on the top surface represents the present-day level of the Baltic Sea. Further description and references for these data are found in Hartikainen et al. (2010, Appendix C).

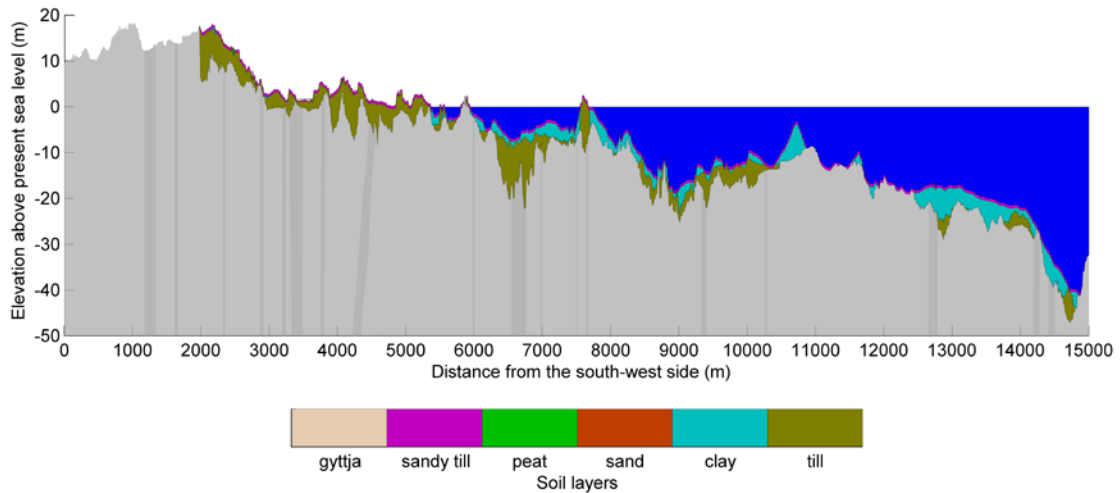


Figure 2-6. The soil layers of the 2D model domain. Grey represents bedrock and blue the present day Baltic Sea. The gytja, peat and sand layers are too thin to be seen in this figure. In addition, because the first 2,000 m of the model domain is outside the area of detailed site investigations, no information about the soil cover is used here. Further description and references for these data are found in Hartikainen et al. (2010, Appendix B). Note that the vertical axis has a scale which gives a strong vertical exaggeration of topography.

The geothermal heat flow is an important parameter for permafrost modelling. The geothermal heat flow, crustal radiogenic heat production and ground temperature to a depth of ~1 km are based on Sundberg et al. (2009), see also Hartikainen et al. (2010, Appendices B–F). For a description of how these parameters are modelled for depths from ~1 km to 10 km, see Hartikainen et al. (2010). Figure 2-7 shows the initial ground temperature calculated for mean thermal properties.

The initial salinity concentration of groundwater for depths to ~1.5 km is described in Hartikainen et al. (2010 Appendix F), and for depths from ~1.5 km to 10 km it is obtained as a stationary solution using present concentration values on the surface and at the depth of 1.5 km.

Figure 2-8 shows the initial salinity distribution in the model domain.

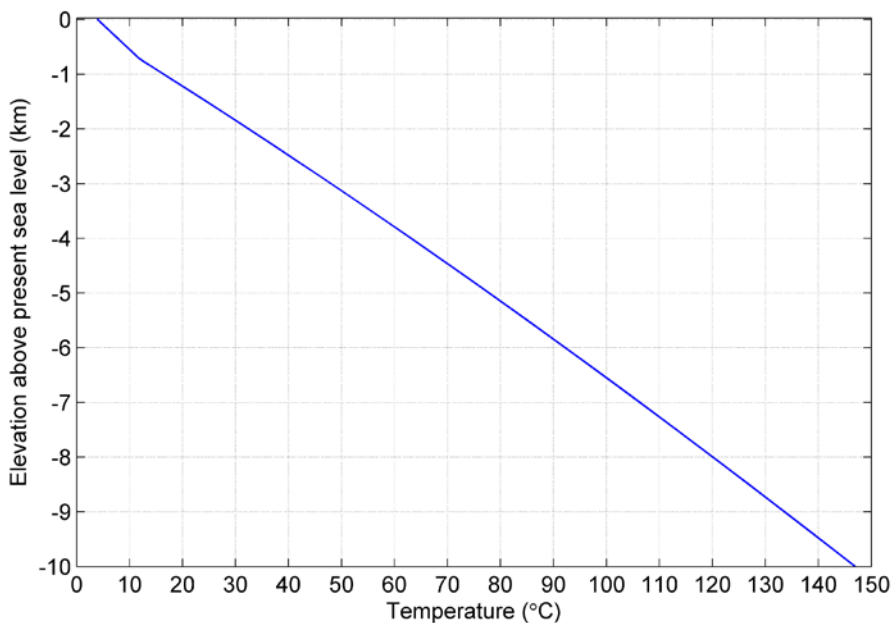


Figure 2-7. Distribution of initial ground temperature for the mean thermal properties used in the 2D permafrost modelling. For a description of these properties, see Hartikainen et al. (2010, Table 2-2).

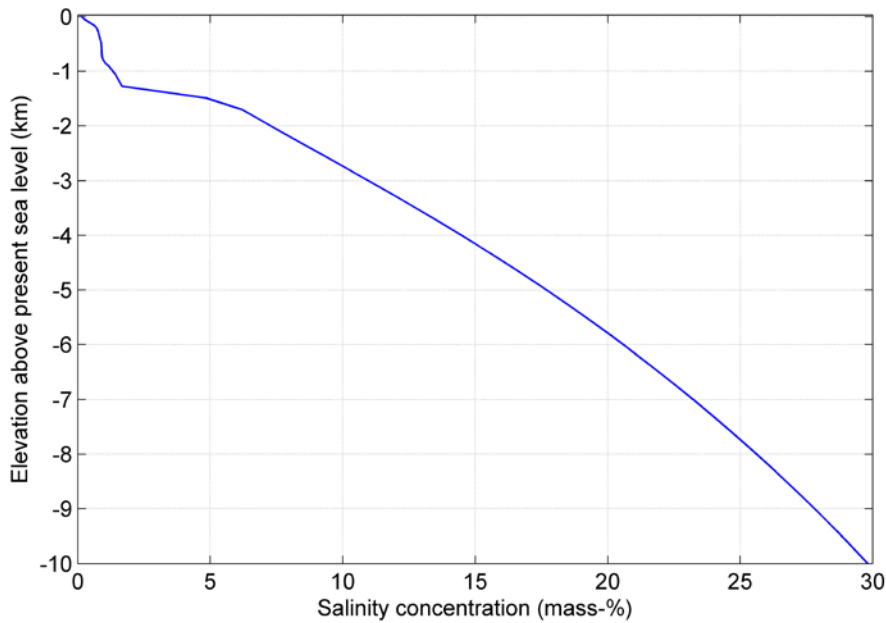


Figure 2-8. Distribution of the initial salinity concentration of groundwater (Hartikainen et al. 2010).

The present-day groundwater pressure is determined as hydrostatic pressure based on the initial conditions of ground temperature and groundwater salinity concentration as well as the hydrostatic pressure at the bed of the Baltic Sea. The results for initial groundwater pressure are shown in Figure 2-9.

In the present study, thermal conductivity and thermal diffusivity are set to the mean values given in Table 2-1 and Table 2-2 in Hartikainen et al. (2010). The uncertainty associated with these parameters is taken from Hartikainen et al. (2010). The geothermal heat flow is also set to the mean value given in Table 2-3 in Hartikainen et al. (2010). The uncertainty associated with this parameter is also taken from Hartikainen et al. (2010).

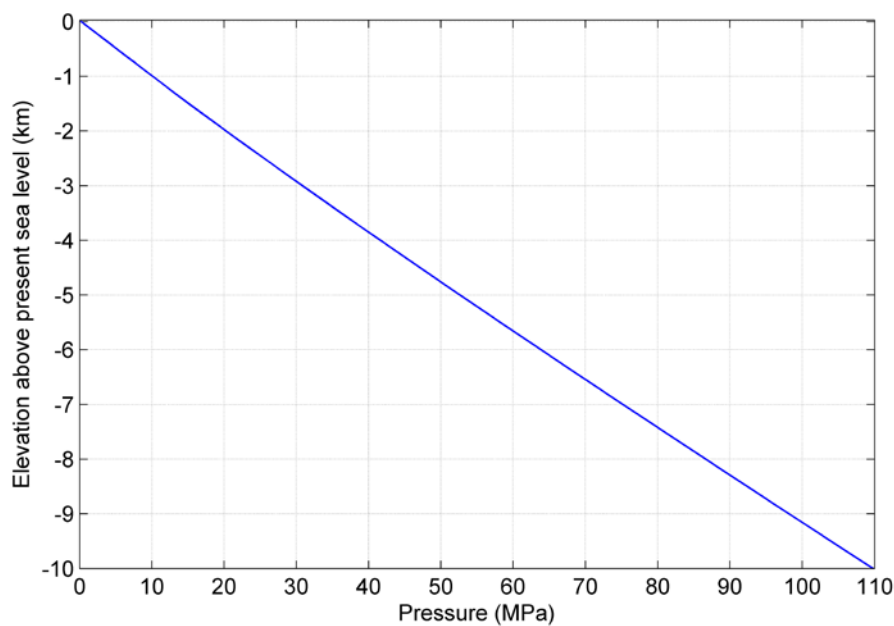


Figure 2-9. Distribution of initial groundwater pressure associated with the temperature and salinity concentrations shown in Figure 2-7 and Figure 2-8.

The planned SFR3 repository for short-lived low- and medium-level nuclear waste does not produce a significant amount of heat. In contrast to Hartikainen et al. (2010), the heat production from the planned nearby repository for spent nuclear fuel in Forsmark is, *not* included in the current simulations. This is a pessimistic assumption in terms of permafrost development and freezing, since the exclusion of heat from a nuclear waste repository may result in somewhat lower bedrock temperatures (Hartikainen et al. 2010, Section 5.2).

Surface properties and conditions

The uncertainty in future precipitation and surface conditions is taken into account by assuming conditions that in the previous studies were shown to be the most favourable for permafrost growth, i.e. a *dry climate* with *dry surface conditions* (Hartikainen et al. 2010). For more detailed definitions of these states see Hartikainen et al. (2010).

The impact of vegetation, snow cover and other climate factors on the ground surface temperature and permafrost development has been well investigated (Washburn 1979, Williams and Smith 1989, Yershov 1998, French 2007). In general, an annual mean air temperature ranging between -9 and -1°C is required to build up permafrost for a majority of surface covers, depending on other climatic conditions and topography. The surface conditions can be modelled by thermodynamic and hydrodynamic models using surface energy and water balance equations and information on climate conditions and topography, including radiation, precipitation, cloudiness and wind, and their annual and diurnal variation (Riseborough et al. 2008). However, these models are unsuitable for the long time spans associated with glacial cycles, since no climate data besides the air temperature can be adequately constructed. Therefore, an empirical approach based on *n*-factors (Lunardini 1978), i.e. statistical correlations between air and ground surface temperature, has been used to construct the ground surface temperature from the projected air temperature. For a detailed motivation for and description of the *n*-factors approach for treatment of surface conditions see Hartikainen et al. (2010).

In accordance with the conclusions from the previous permafrost simulations for Forsmark (Hartikainen et al. 2010), the permafrost model was set up under the assumption of dry climate conditions and dry surface conditions to promote permafrost at the site. A number of sensitivity simulations were performed to investigate the potential for frozen ground when the uncertainties in simulated Forsmark T_{2m} are taken into account.

According to Glacial Isostatic Adjustment (GIA) simulations, there is remaining isostatic uplift from the last glaciation of around 70 m (SKB 2010a, Section 4.5.2). In the permafrost simulations performed for the 54 ka AP period, this is taken into account by assuming the sea level to be 65 m lower than present. In this situation, no Baltic Sea water bodies exist within the permafrost model domain.

Near-surface air temperature

The monthly mean air temperature at 2 m height (T_{2m}) in Forsmark, derived from the EMIC simulation resulting in the coldest conditions in Forsmark, was used as input to the permafrost model. The sensitivity of the permafrost modelling to uncertainties in the climate model results was further analysed based on a suite of seven sensitivity simulations with the permafrost model. In these experiments the annual average Forsmark T_{2m} was lowered by 2 to 8°C as compared to the reference case. The amplitude and shape of the annual cycle of T_{2m} varies with the annual average T_{2m} . To account for this variation in the sensitivity experiments, a linear regression between the monthly average and annual average T_{2m} as determined for each month of the year using data from the EMIC simulation was adopted. The regression coefficients were thus used to determine the resulting annual cycle in Forsmark T_{2m} for each sensitivity experiment (Figure 2-10).

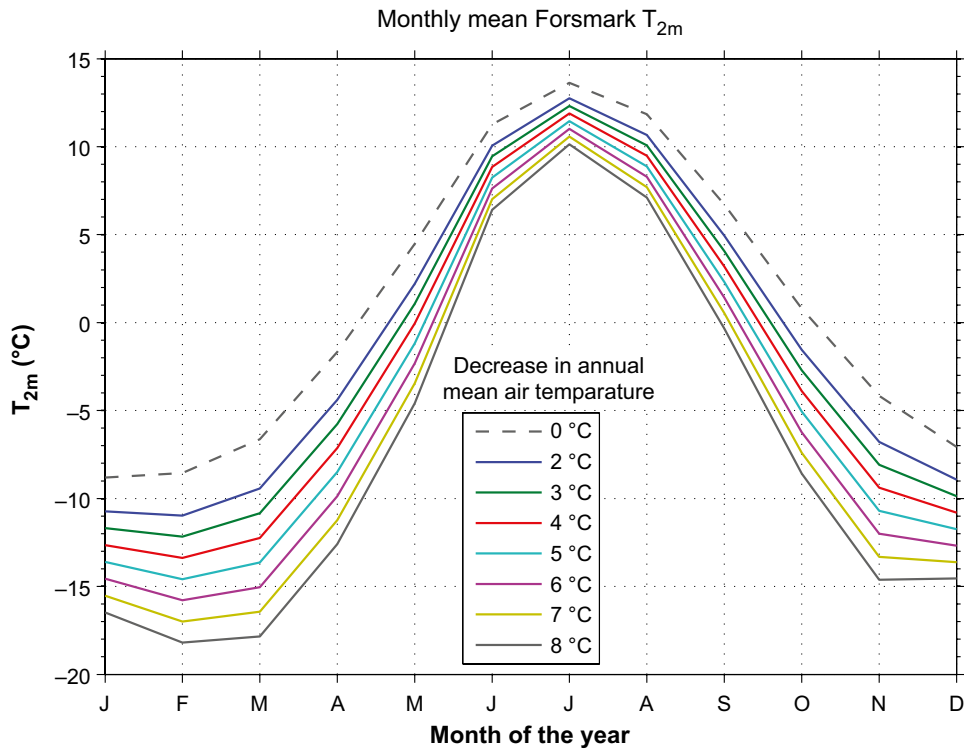


Figure 2-10. Monthly mean bias-corrected Forsmark T_{2m} (°C) in the LC_54k_180 simulation (dashed line) and in the sensitivity experiments (solid lines) performed with the permafrost model.

Sensitivity to model formulation improvement

The sensitivity of the results to the improvements made in the new version of the permafrost model was investigated. Thus, the results of the new version of the permafrost model were compared to experiments with identical forcing and boundary conditions performed with the old version of the model (described by Hartikainen et al. 2010). The new version, which includes an improved description of the influence of the annual temperature cycle on permafrost growth and thawing, simulates faster growth of permafrost and deeper equilibrium depths for the isotherms. The effect is larger for shallow depths than for deeper depths. For example, in the experiments with an annual average near-surface air temperature of -1°C , the equilibrium depth of the 0°C isotherm in the new model results is more than twice the depth in the old model version. In the experiment with -7°C annual average near-surface air-temperature on the other hand, the 0°C isotherm in the new model results is only c 7% deeper than in the old model version. Since the new version of the permafrost model describes the coupling between the air temperature and the bedrock in greater detail it is reasonable to believe that this version gives more reliable results. Therefore the results of this model version were used in the analysis. This choice further reduces the risk of using too shallow isotherm depths to analyse the potential for permafrost in Forsmark. The results are discussed in more detail in Section 3.4 of Brandefelt et al. (2013).

Potential for permafrost

The results of the permafrost modelling performed by Brandefelt et al. (2013) are summarised in Figure 2-11 which shows the maximum depth of the 0°C , -1°C , -2°C , -3°C , -4°C and -5°C isotherms at the SFR repository location after 10,000 years of permafrost model integration as a function of the annual average Forsmark T_{2m} simulated for a cold climate period at 54 ka AP. The permafrost modelling results are given here as a function of the annual average T_{2m} in Forsmark.

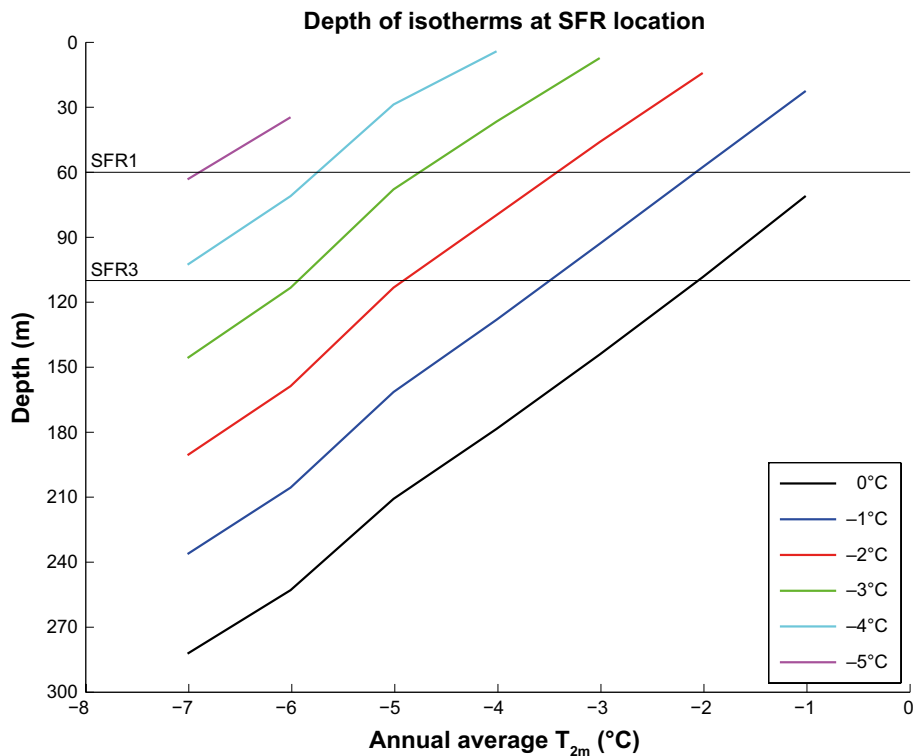


Figure 2-11. Depth (m) of the 0, -1, -2, -3, -4° and -5°C isotherms as a function of the annual average Forsmark T_{2m} . The depths of the existing SFR1 repository (c 60 m) and planned SFR3 repository (c 110 m) are indicated with black lines. The Forsmark annual average T_{2m} was c +5°C in the period 1961–1990 (Johansson et al. 2005).

Brandefelt et al. (2013) concluded that an annual average T_{2m} of c -5°C and c -6°C is required for the -3°C isotherm to reach the SFR1 and SFR3 depths, respectively. Further, based on the results of the climate modelling summarised in Table 2-2, it is concluded that an atmospheric CO_2 concentration of c 210 ppmv or less is required to get annual average Forsmark T_{2m} below c -5°C for orbital year 17 ka AP. Similarly, it is concluded that an atmospheric CO_2 concentration of c 250 ppmv or less is required to get annual average Forsmark T_{2m} below c -5°C for orbital year 54 ka AP. Based on a literature review of future atmospheric CO_2 concentrations (see Section 2.3.2 in Brandefelt et al. 2013), it is concluded that an atmospheric CO_2 concentration of c 250 ppmv or less at 54 ka AP cannot be excluded. Further, it is concluded that it is *not* likely that the atmospheric CO_2 concentration will be c 210 ppmv or less at 17 ka AP. To reach such low concentrations would require that human carbon emissions to the atmosphere end in the near future, such that natural processes can decrease the concentration to a pre-industrial value of 280–290 ppmv in the next 10 ka. After this the processes that produce the natural glacial–interglacial CO_2 variations seen in ice core data are required to reduce the concentration further by c 70 ppmv in c 7 ka. The required decrease rate of 10 ppmv per ka is almost twice the rapid decrease rate seen in ice core data for the last glacial inception around 100 ka BP (Lüthi et al. 2008). For further discussion of future atmospheric CO_2 concentrations, see Section 3.3.1.

For comparison, it was concluded that an annual average T_{2m} of c -1°C and c -2°C is required for the 0°C isotherm to reach the SFR1 and SFR3 depth respectively (Figure 2-11). Based on a literature review of future atmospheric CO_2 concentrations (see Section 2.3.2 in Brandefelt et al. 2013), it was concluded that, although unlikely, an atmospheric CO_2 concentration of c 260 ppmv or less at 17 ka AP cannot be excluded. For orbital year 54 ka AP, it was concluded that an annual average Forsmark T_{2m} below c -1°C or -2°C cannot be excluded even for atmospheric CO_2 concentrations above 280 ppmv.

In summary, a bedrock temperature of 0°C cannot be excluded at c 60 m and c 110 m depth at 17 ka AP or at 54 ka AP (Brandefelt et al. 2013). Under the assumptions made in the study, it is further concluded that it is very unlikely to get a bedrock temperature of –3°C or less at c 60 m and c 110 m depth at 17 ka AP, but that this possibility cannot be excluded at 54 ka AP. The main reason for the different conclusions for the two time periods is the decrease in atmospheric CO₂ concentrations between these times.

2.1.5 Time perspective

Changes in annual ground surface temperature can lead to development of permafrost and freezing of the ground. If the mean annual ground surface temperature at the SFR location is lowered to –7°C, the 0°C isotherm can reach 60 m depth in c 460 years and 110 m depth in c 820 years (Brandefelt et al. 2013, Tables 3-5 and 3-6). Similarly, the –3°C isotherm can reach 60 m depth in c 880 years and 110 m depth in c 2,700 years (Brandefelt et al. 2013, Tables 3-5 and 3-6).

Under periglacial conditions, permafrost can aggregate from some centimetres to some decimetres a year. The depth of the 0°C isotherm increases by up to c 0.15 m/yr in the first few centuries (Brandefelt et al. 2013, Figure 3-22).

Permafrost degradation can take place several times faster than aggregation (SKB 2010a, Figure 3-57), especially when the surface temperature is increased above 0°C and permafrost decays simultaneously from the bottom upwards and from the top downwards. High degradation rates may also occur at the transition from cold-based to warm-based conditions during ice-sheet overriding.

2.1.6 Handling in the safety assessment SR-PSU

The potential for cold climate conditions and permafrost in Forsmark in the next 60 ka has been investigated by means of numerical modelling. This investigation was based on the previous studies of the last-glacial-cycle evolution of permafrost performed for the SR-Can (SKB 2006a) and SR-Site (Hartikainen et al. 2010) safety assessments. Further, these previous studies were used to define parts of the SR-PSU *Weichselian glacial cycle* climate case and also to define the variability after 50 ka AP in the two base cases, the *global warming* and *early periglacial* climate cases.

A broad range of sensitivity experiments were conducted for SR-Can and SR-Site in order to describe the effects of uncertainties in bedrock, surface or climate conditions. The results of these were used in the dedicated investigations of the potential for permafrost in the next 60 ka. Two numerical permafrost models were used, a 1D model that was used for simulations of permafrost at the repository location, and a 2D model that investigated spatial development of permafrost along a profile that crossed the repository site. The permafrost models include a mathematical expression for freezing and thawing of saline-groundwater-saturated bedrock. The bedrock is considered as an elastic porous medium and the groundwater as an ideal solution of water and ionic solvents. The models are based on the principles of continuum mechanics, macroscopic thermodynamics and the theory of mixtures, and are capable of describing heat transfer, freezing of saline water, groundwater flow and deformations of bedrock. To capture the most important factors and parameters affecting the development of permafrost, sensitivity analyses were performed considering the following issues:

- Surface conditions and climate.
- Subsurface conditions.
- Presence of the spent nuclear fuel repository.

Surface temperatures, together with the influence of surface covers such as snow, vegetation and water bodies, have been included as factors of importance in the surface conditions. The investigated subsurface conditions are thermal properties of the bedrock and geothermal heat flow. The heat generated by the spent nuclear fuel was included in most simulations in SKB (2006a) and Hartikainen et al. (2010). In the dedicated simulations performed for SR-PSU (Brandefelt et al. 2013), the heat generation by the spent fuel was not included.

2.1.7 Handling of uncertainties in SR-PSU

Uncertainties in mechanistic understanding

There are no major uncertainties in understanding of mechanistic processes regarding permafrost development. Minor uncertainties in the 1D modelling experiments are associated with the fact that the exclusion of salts during the freezing of groundwater is not included. The process of freeze-out of salts is included in the 2D modelling.

Model simplification uncertainty

The major model simplification in the 1D permafrost modelling study was the exclusion of lateral variations in physical properties, boundary conditions and geometry. For example, full consideration of the anisotropy of thermal conductivity and heat capacity and the features of water bodies and topography, as well as the heat generation from the spent fuel, requires 3D modelling. However, this is to a large extent taken care of by the 2D modelling study reported here.

The 1D modelling approach could, in certain situations, result in somewhat higher temperatures than would be calculated using a 2D or full 3D approach. In the context of permafrost development, the effect of groundwater flow, cooling down the bedrock, is the most important factor here. However, compared with heat conduction, groundwater flow has only a minor role in permafrost development, as indicated by the 2D modelling results that included groundwater flow. Furthermore, the anisotropy of thermal properties is not a problem in 1D or 2D, since one can choose a combination of thermal properties that would give the lowest temperatures, or at least very close to the lowest temperatures. Therefore, it is unlikely that 3D simulations would yield notably lower temperatures than the range obtained in the full series of 1D and 2D sensitivity modelling cases that have been performed.

Input data and data uncertainty

Bedrock data

Some data uncertainty exists when it comes to thermal conductivity and heat capacity of rock at the Forsmark site. In the calculation of ground temperature and the rate of freezing, thermal conductivity is the most important input parameter in terms of thermal properties of the ground. Some uncertainty also exists in determination of hydraulic and mechanical properties of bedrock and salinity concentrations of groundwater versus depth, see appendices in Hartikainen et al. (2010) and references therein.

A considerable uncertainty in the 1D permafrost study is associated with determination of the *in situ* temperature and geothermal heat flow in the depth range of 1,000–10,000 m for the thermal boundary and initial conditions of the model. The *in situ* ground temperature has been measured in boreholes to a depth between 500 and 1,400 m at the Forsmark site. The temperature at the same depth in different boreholes differs over a range of 2°C (SKB 2005, 2006a, b). These thermal data have been used for ground temperature modelling which provided new and better constrained values on geothermal heat flow as well as estimates on the difference between ground- and air temperature for the site (Sundberg et al. 2009). The results from the ground temperature modelling were applied in the setup of the 2D permafrost model, which considerably reduced the uncertainty associated with determination of the ground surface temperature from the air temperature and the estimation of the *in situ* temperature and geothermal heat flow for the 1,000–10,000 m-depth for the thermal boundary and initial conditions.

In general the uncertainty in thermal characteristics of the bedrock and geothermal heat flow has a significantly smaller impact on modelled permafrost and freezing depths than uncertainties related to ground conditions and climate.

Surface conditions

The impacts of the surface conditions on the spatial (along the profile) development of permafrost and perennally frozen ground was investigated by Hartikainen et al. (2010) using site-specific information on climate and landscape features including water bodies and topography. In the SR-PSU study of Brandefelt et al. (2013), the results of the previous investigations were used to choose surface conditions that promote permafrost development in Forsmark. Thus, dry surface conditions and dry climate conditions were used in these simulations.

Near-surface temperature

In the SR-PSU study of Brandefelt et al. (2013), the annual cycle of near-surface air temperature in Forsmark was estimated based on climate model simulations and a literature review. All known uncertainties in the climate modelling results were taken into account under the pessimistic assumption that they all would result in cooling in Forsmark. These uncertainties include inter-model differences and internal variability, atmospheric greenhouse gas and aerosol concentrations and glacier and ice sheet dynamics, see Section 3.3 of Brandefelt et al. (2013). Thus, the full range of uncertainty in near-surface air temperature is taken into account in these simulations. The sum of all known uncertainties varies from 4°C, for climates similar to the present, to 12°C, for cold climates substantially different from the present climate.

Major uncertainties exist in the near-surface temperature used for the last-glacial-cycle permafrost modelling (SKB 2006a, Hartikainen et al. 2010), including uncertainties as to its representativeness for the last glacial cycle climate. A detailed discussion and description of these uncertainties are found in Appendix 1 of SKB (2010a). To cover the estimated uncertainties in air temperature reconstructed for the last glacial cycle, a large range of sensitivity cases and alternative air temperature variations have been analysed. This was also motivated by the fact that the variation in surface conditions and climate has a larger impact on modelled permafrost and freezing depth than bedrock thermal conditions and geothermal heat flow.

Input data for the permafrost modelling are described in Hartikainen et al. (2010, Appendix H) and SKB (2010a).

Repository heat

The heat from a repository for spent nuclear fuel was included in the 1D permafrost study made for SR-Can and in the 2D study made for SR-Site. Nonetheless, these simulations were used to define the evolution of climate domains in the period after 50 ka AP in the *global warming* and *early periglacial* climate cases and in the *Weichselian glacial cycle climate case* for SR-PSU. However, as described in Section 3.4.7 of the SR-Site Climate report (SKB 2010a), the temporal difference in the timing of the onset and termination of periglacial climate conditions is negligible since it is the surface conditions that are the main factor for the initiation and development of permafrost.

2.1.8 Adequacy of references

The SKB report produced for the handling of permafrost and freezing processes in SR-PSU (Brandefelt et al. 2013) has undergone the SR-PSU QA system handling, including a documented factual review procedure. Also the SKB report produced for SR-Site (Hartikainen et al. 2010) and the SR-Can Climate report (SKB 2006a), from which some studies are used, have undergone QA system handling including a factual review process. Other references used for the handling of the permafrost and freezing processes, in this report and in Brandefelt et al. (2013) are either peer-reviewed papers from the scientific literature or the textbooks (Yershov 1998, Lide 1999, French 2007).

2.2 Isostatic adjustment and shore-level changes

In addition to the descriptions in the present section, a detailed in-depth description of the physics of glacial isostatic adjustment (GIA), how it affects sea-level, and the methods which are employed to study and understand these processes are presented in Whitehouse (2009).

The major part of Section 2.2.1 is adapted from SKB (2006a, Section 3.3) written by P. Whitehouse, whereas some parts are adapted from Lund and Näslund (2009). Section 2.2.2 is adapted from SKB (2006a). Section 2.2.3 is from Lund and Näslund (2009), and Section 2.2.4 is adapted from SKB (2006a) and Whitehouse (2009).

2.2.1 Overview/general description

Shoreline migration, sea-level and shore-level

The spatial location of the shoreline varies in time. Shoreline migration is the result of eustatic changes relative to isostatic changes of the solid surface of the Earth. The shoreline location is determined by the height of the geoid surface, corresponding to the undisturbed ocean surface, relative to the solid surface of the Earth. The geoid is the equipotential surface of the Earth's gravitational field which best fits the undisturbed surface of the oceans. The shape of the geoid is governed by the gravitational field of the Earth and varies over time.

Sea-level is defined to be zero on land and positive in the oceans, where it corresponds to the depth of the ocean. Relative sea-level is the vertical height difference between the geoid at an arbitrary time and the present height of the geoid, where the height of the geoid is measured relative to the height of the solid surface. Relative sea-level is defined to be zero at the present day. It is positive during *transgression*, when the intersection of the geoid with the solid surface is higher than at present and negative during *regression*, when the intersection of the geoid with the solid surface is lower than at present. The relative sea-level is also termed *relative shore-level* in this report.

Relative sea-level changes are a result of *isostasy* and *eustasy*. Isostasy is the response of the solid Earth to loading or unloading by ice or water, and/or unloading and loading due to denudation and sedimentation. Eustasy refers to changes in sea-level arising from changes in ocean water volume, due to mass exchange between continental ice masses and the oceans and density changes associated with ocean temperature and salinity, and, the spatial distribution of ocean water changes.

The solid Earth

The solid Earth consists of the crust, the upper and lower mantle, and the outer and inner core. The lithosphere comprises the crust and part of the upper mantle. The average thickness of the lithosphere is c 100 km, although this value varies between less than 30 km for oceanic lithosphere and up to more than 200 km for continental lithosphere (Watts 2001). Lithospheric thicknesses in Fennoscandia range between ~60 km in the north-west and ~200 km in the south-east (Watts 2001). The lithosphere is less dense than the mantle below and responds approximately elastically to forces applied at the surface. The deformation of this layer is short-lived once the load is removed. The mantle responds viscoelastically to forces applied over a time scale of ~100 ka. The recovery of this layer to a state of isostatic equilibrium following loading takes several orders of magnitude longer than the recovery of the lithosphere. The rheological properties of the lithosphere and upper and lower mantle determine the precise magnitude and duration of solid Earth deformation, see further Sections 2.2.2 and 2.2.4.

Glacial isostatic adjustment

The redistribution of mass associated with the growth and decay of continental ice sheets gives rise to major glacial loading and unloading effects over time scales of several tens of thousands of years. For instance, during the decay of a major ice sheet, the unloading of mass results in a post-glacial rebound of the crust, which continues well after the disappearance of the ice. This process is well known from previously glaciated regions such as Canada and the United States, Fennoscandia, the British Isles and Siberia (e.g. Ekman 1991); areas where this process is still active today, some 10–15 ka after the last deglaciation. The response of Earth's crust, mantle and gravitational field is referred to as Glacial Isostatic Adjustment (GIA). The Earth's outer and inner cores are not affected by GIA processes. In previously glaciated terrain without strong tectonism, glacial isostatic adjustment is the most significant geodynamic process governing vertical deformation of the crust (e.g. Peltier 1994).

During the Last Glacial Maximum (LGM), around 20 ka ago, the Laurentide ice sheet of Canada and the United States, and the Fennoscandian ice sheet had maximum thicknesses of around 2.5–3 km, corresponding to a total of c 120–135 m of global sea-level lowering at the LGM deduced from coral-reef data (Yokoyama et al. 2000). When these large ice masses slowly formed, their weight resulted in a slow downwarping of Earth's crust. One important factor that governed both this process and the following glacial unloading is the physical properties of Earth's crust and mantle.

In the downwarping process, mantle material has to be displaced and flow laterally in order to make room for the flexing crust. At times of ice-sheet decay, mantle flow is reversed and the crust rebounds. Since the mantle viscosity is high, the downwarping and subsequent rebound are slow processes. Furthermore, it has been shown that a deglaciation of large Northern Hemisphere ice sheets results in deformation of the Earth's entire surface, producing a series of upwarps and downwarps away from the areas of the former ice sheets (Figure 2-12). However, the deformation is largest in the regions that were glaciated.

The glacial isostatic adjustment process manifests itself not only in the slow rebound regions of past ice sheets. Current melting of glaciers produces additional GIA effects. As an example, Iceland is currently undergoing rapid glacial rebound due to a mass loss of Vatnajökull and other smaller ice caps (e.g. Árnadóttir et al. 2009). Since the viscosity of the mantle is inferred to be three orders of magnitude lower beneath Iceland (Árnadóttir et al. 2009), than below, for example, Fennoscandia, uplift rates on Iceland are on the order of 20 mm/year, in spite of the much smaller volume of ice loss.

Outside the ice-sheet margin, an uplifted forebulge, or peripheral bulge, is formed (e.g. Mörner 1977, Fjeldskaar 1994, Lambeck 1995). The forebulge is caused by flexure and a lateral displacement of mantle material extending outside the ice margin, and it may stretch for several hundreds of kilometres beyond a major ice sheet. The uplift of the forebulge is considerably smaller than the downwarping of the crust beneath the central parts of the ice sheet; on the order of tens of metres. During and after deglaciation, the area of the forebulge experiences land subsidence, exemplified by the ongoing lowering of the Netherlands, southern England and the east coast of the United States. It is worth noting that land subsidence in these regions is also a result of ongoing marine sediment loading. The location of maximum forebulge uplift migrates toward the formerly glaciated region as the ice sheet withdraws. In addition to the formation of the forebulge, the elasticity of the lithosphere may result in a downwarping of the crust, not only under the ice sheet, but also to some extent outside the ice margin. This produces a flexural depression between the ice margin and the forebulge, a depression where lakes may form from glacial meltwater.

At present, the crust beneath the Antarctic and Greenland ice sheets is depressed in a similar way as previously occurred under the North American, Fennoscandian and Siberian ice sheets. In Greenland and Antarctica, the crust would also be subject to significant glacial rebound if these areas were to be deglaciated in the future.

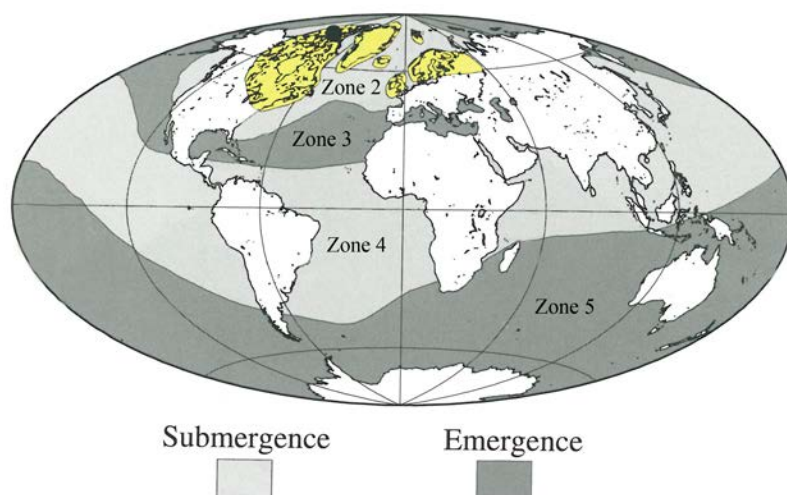


Figure 2-12. Calculated deformation resulting from an instantaneous unloading of Northern Hemisphere last glacial cycle ice sheets at 16 ka BP. The results show five sea-level zones with similar sea-level histories within each zone. Sea-level zone 1 is marked in yellow. The entire Earth is affected by the unloading through a series of elevated and subsided regions away from the areas of the former ice sheets. Modified from Clark et al. (1978).

GIA-induced relative sea-level changes

GIA-induced sea-level changes arise as a result of the gravitationally-consistent redistribution of water between ice sheets and ocean basins, and thus the evolution of surface loading. Any redistribution of surface mass alters the shape of the geoid, which in turn defines the position of the surface of the oceans. Relative sea-level changes exhibit complex global spatial and temporal patterns, and are strongly dependent upon the location relative to major ice sheets. Relative sea-level changes at locations far from ice sheets (hereafter referred to as far-field locations) are dominated by the eustatic signal; during deglaciation monotonic sea-level rise causes land inundation and the shift of shorelines inland. At locations close to ice sheets (hereafter referred to as near-field locations) the isostatic signal dominates; rebound of the solid surface from the time of deglaciation onwards causes land emergence and the migration of shorelines oceanwards. These are two end-member cases, and, in general, sea-level change, and hence shoreline migration, is governed by a complex interplay of isostatic and eustatic processes, operating on different time scales.

GIA-induced sea-level changes depend on the following factors (see Figure 2-13):

- The location and thickness of ice sheets.
- The depth and extent of the oceans.
- The structure and properties of the solid Earth and its response to surface loading.

Changes in surface loading arise due to the exchange of mass between ice sheets and ocean basins throughout a glacial cycle. The presence of ice-dammed lakes and the redistribution of sediments also contribute to changes in surface loading, although, in Fennoscandia, the short-lived nature of ice-dammed lakes, and their shallow depth, means that this perturbation to the pattern of surface loading probably has a negligible effect when considering the solid Earth response. The denudation of bedrock and redistribution of associated sediments persists over a much longer time scale, on the order of millions of years. On a regional scale, over a single glacial cycle, the effect of sediment redistribution upon solid Earth deformation is negligible in relation to the ice load, but over several glacial cycles, or locally, it may be of significance.

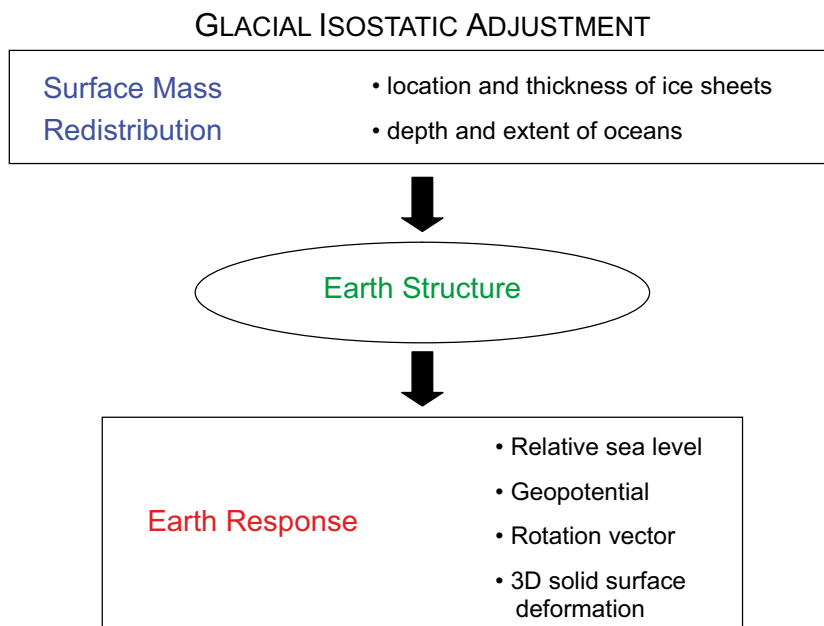


Figure 2-13. The theory of Glacial Isostatic Adjustment (GIA): inputs and outputs of the system.

The height of the geoid, or mean ocean surface, is dependent upon *direct* and *indirect* geoid perturbations (Milne et al. 2002), as well as changes in ocean water volume and the capacity of ocean basins. *Direct* effects refer to the deflection of the geoid due to the direct attraction of surface mass loads, such as ice sheets. *Indirect* effects refer to geoid perturbations arising due to the surface load-induced deformation. The volume of the oceans will vary as water is transferred to and from the ice sheets. Also changes in ocean capacity and bathymetry arise as a result of crustal and geoidal perturbations in response to ice and ocean loading. The ice-loading solid surface response includes the depression and rebound of the solid surface in the location of ice sheets, and the raising and lowering of glacial forebulges in areas surrounding the ice sheets. The ocean-loading response is similar to the ice-loading response. However, at continental margins ocean loading induces a levering of the continental lithosphere and a subsidence of offshore regions, this is referred to as *continental levering* (Clark et al. 1978) (see Figure 2-14). The combination of ice and ocean loading leads to a decrease in the volumetric capacity of the ocean basins during glaciation, and an increase during deglaciation due to the growth and decay of offshore peripheral bulges, resulting in a globally uniform rise or fall in sea-level, respectively. The ongoing fall in sea-level following the last deglaciation due to the migration of water from equatorial regions to subsiding peripheral bulge regions has been termed *equatorial ocean syphoning* (Mitrovica and Peltier 1991, Mitrovica and Milne 2002).

Changes in relative sea-level result in shoreline migration. A rise in relative sea-level and the consequent inland migration of the shore may be due to solid Earth subsidence, an increase in the height of the geoid (ocean surface) as a result of ice-sheet melting, or a combination of these processes. Similarly, a fall in relative sea-level and the consequent migration of the shore towards the ocean may be due to isostatic rebound, a fall in the height of the geoid due to ice-sheet build up, or a combination of these processes. In the vicinity of the Fennoscandian ice sheet, the effects of isostatic deformation and changes to the height of the geoid occur simultaneously, and may have opposite effects on the position of the shoreline. Further, the surface of the Baltic Sea does not solely depend on the height of the geoid, but also on the elevation of its sills relative to the Atlantic sea-level, and ice thicknesses at locations with potential connections to the sea; these may cause it to become isolated from the global ocean.

Indirectly, groundwater flow and composition are influenced by shoreline migration. If the site is not subject to permafrost, and it is not covered by an ice sheet, the sea, or a lake, then the groundwater surface follows a subdued version of the topography. Groundwater flow will be driven by topography, assuming precipitation exceeds evaporation. If the site is submerged the situation will be almost stagnant and groundwater flow will be driven by density variations only (SKB 2010c). Groundwater composition is affected, since relative sea-level affects the salinity of the Baltic Sea. Relative sea-level and the extent of the ice sheet determine whether there is a connection between the Baltic Sea and the ocean. This, together with the runoff to the Baltic basin, determines the salinity in the sea/lake water.

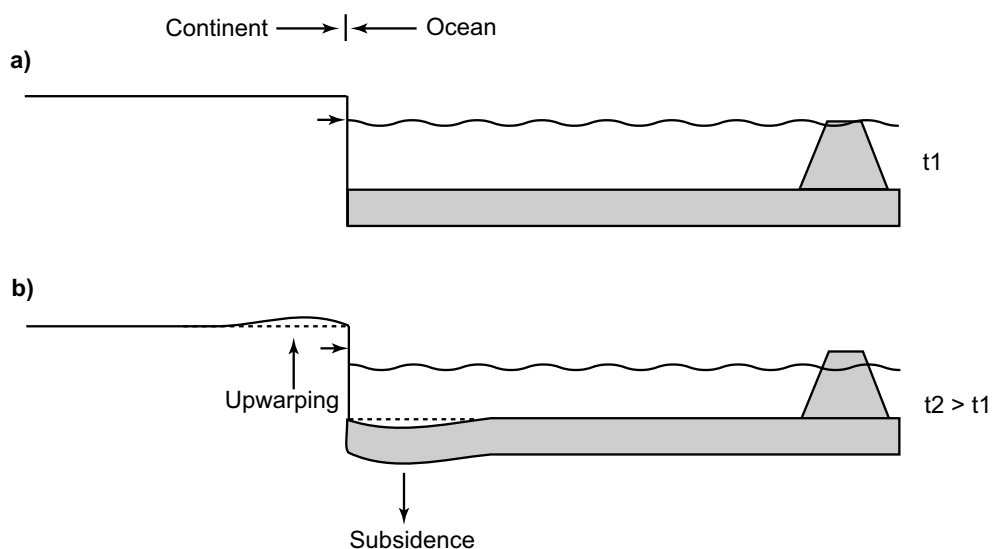


Figure 2-14. Continental levering: the migration of water into offshore regions following deglaciation results in offshore subsidence and onshore upwarping. Ocean floor subsidence results in sea-level fall at far-field sites.

2.2.2 Controlling conditions and factors

Loading

The main factors governing the evolution of relative sea-level during the last glacial cycle, and hence shoreline migration, throughout Fennoscandia are the loading history – both with regard to ice and ocean water – and the rheological parameters governing the response of the solid Earth to such a load.

Near-field relative sea-levels are very sensitive to variations in the evolution of the near-field ice sheet (Lambeck et al. 1998, Davis et al. 1999, Tamisiea et al. 2001, 2003, Milne et al. 2002, Kaufman and Lambeck 2002). There remain uncertainties in the details of ice loading during the last glacial cycle, especially with regard to estimates of ice thickness within Fennoscandia.

The details of far-field ice sheets are irrelevant for the prediction of relative sea-level change in Fennoscandia (Peltier 1998, Mitrovica et al. 2001b, Tamisiea et al. 2003, Bassett et al. 2005); mass changes in the far field mainly provide an influence on global-average sea-level. However, the overall characteristics of mass-changes in far-field ice sheets may also generate a long wavelength isostatic response in Fennoscandia. This response is likely to be dominated by the signal from a massive North American (Laurentide) ice-sheet complex. Due to the position of Fennoscandia on the Laurentide forebulge during the LGM (Mitrovica et al. 1994), the presence of the Laurentide ice sheet is estimated to have generated 25–30 m of solid Earth uplift in central Fennoscandia at this time (see Section 2.3.4). The magnitude of this signal does not vary greatly across Fennoscandia (unlike the relative sea-level signal due to local ice loading), and is not dependent upon the local geometry of the Laurentide ice sheet; only its volume.

During the last deglaciation an ice-dammed lake prevailed within the Baltic depression when non ice-covered sills were above sea-level and all other potential connections between the Baltic Sea and the North Sea were dammed by the ice-sheet ice (e.g. Björck 1995, Lambeck 1999). The surface of the ice-dammed lake was constrained by the height of the ice sheet above sea-level and the surrounding topography, i.e. the sill levels, and there is evidence to suggest that immediately prior to the draining of the so called Baltic Ice Lake its surface was 25 m above the contemporary relative sea-level (Björck 1995). Due to the relatively small volume of water released to the oceans as the ice lake drained the resulting perturbation of global sea-levels was insignificant (Lambeck 1999). The shallow depth and the short duration of the ice lake mean that its impact on isostasy was negligible in comparison with the ice load.

Another process that may impact the loading is erosion and sediment transfer. Erosion and transport of sediment took place beneath warm-based parts of the ice sheet during previous glacial cycles, and this mass redistribution has affected isostatic loading and topography. However, the average total depth of glacial erosion over all Late Pleistocene glacial cycles in lowland Precambrian parts of Fennoscandia is on the order of a few tens of metres, see Section 2.4. Therefore, on the time scale of one glacial cycle, the average unloading/loading effect of this process may be neglected. However, any local reshaping of the land will affect the evolution of the shoreline, and this needs to be taken into account.

Rheological parameters and topography

In order to determine the Earth's response to surface loading, its internal rheological and density structure must be specified. The characteristic time scale for loading during a glacial cycle will excite both elastic and viscous responses; therefore a viscoelastic (Maxwell) rheology is adopted. Such a system behaves elastically on a short time scale and viscously on a long time scale when placed under stress.

Parameters describing the rheological properties of the Earth's lithosphere and upper and lower mantle define its response to loading during a glacial cycle. The average density and elastic structure of the Earth are taken from Dziewonski and Anderson (1981). The lithosphere is generally regarded as elastic for the purposes of GIA studies; this has been shown to be a good approximation throughout the development of the subject (McConnell 1968).

The upper mantle lies below the lithosphere, extending to a depth of 660 km, and then the lower mantle extends to 2,900 km below the Earth's surface. The viscosity of the upper and lower mantle have been constrained to lie in the ranges $1 \cdot 10^{20}$ – $2.6 \cdot 10^{21}$ Pa s and $2 \cdot 10^{21}$ – $1 \cdot 10^{23}$ Pa s, respectively, as determined from previous GIA studies (Davis and Mitrovica 1996, Mitrovica and Forte 1997, Simons and Hager 1997, Lambeck et al. 1998, Davis et al. 1999, Milne et al. 2001, 2002, 2004, Mitrovica and Forte 2004). Lateral variations in radial viscosity structure may be derived from seismic shear-velocity models by converting velocities to temperatures, and then using temperature to estimate viscosity.

Present-day topography is used to constrain paleotopography. When calculating paleotopography, see Section 2.4, we assume that all changes to the shape of the land arise from the differential GIA response across the region; however topography is also affected by tectonic, erosional and depositional processes. However, the latter processes are judged to be of little significance compared with GIA effects.

The isostatic adjustment and shoreline migration described above may affect a number of geosphere variables of importance for a geological repository (Table 2-3).

2.2.3 Natural analogues/observations in nature

The GIA process may be observed by studying relative sea-level markers, both from the geological record and from tide gauge data, GPS observations of the 3D deformation of the solid surface, the time-variation of the gravity field as observed by satellites and land-based gravity surveys, and changes in the orientation of the Earth's rotation vector and length of day.

The geological data, including paleoshoreline positions, lake isolation and tilting information, cover a longer time period than the tide gauge data, but the tide gauge data are more accurate, both in terms of their vertical resolution and the dating of the information. In this context, shorelines or other geomorphological features that formed at the highest post-glacial sea-level, in front of the retreating ice sheet margin, provide the oldest estimate of former relative sea-level positions. However, the total amount of post-glacial uplift at a site is typically larger than can be inferred from, for example, raised beaches. A significant portion of the uplift takes place as the ice sheet starts to decay, *prior to the actual deglaciation* of a typical site situated at some distance from the maximum ice margin. The total maximum amount of glacial rebound that has occurred due to the decay of the Fennoscandian ice sheet is around 800 m (e.g. Mörner 1979) (Figure 2-15). This may be compared to the largest value of rebound as inferred from the highest marine limit, which is situated at ~280 m a.s.l. in the Swedish coastal region of the Gulf of Bothnia. Another related method to study glacial rebound is to analyse the amount and direction of tilt of paleoshorelines of glacial lakes that formed beyond the retreating ice margin. A selection of geological relative sea-level data for Fennoscandia can be found in e.g. Lambeck et al. (1998), Pässe (2001), Eronen et al. (2001), Kaufmann and Lambeck (2002), Whitehouse (2007¹), and references therein, but at present a complete compilation of such data does not exist.

Table 2-3. A summary of how geosphere variables are influenced by isostatic adjustment and shoreline migration.

Geosphere variable	Climate issue variable	Summary of influence
Rock stresses	Isostatic depression/rebound	The deformation of the Earth's crust will lead to altered rock stresses.
Groundwater pressure	Relative sea-level	If the site is not covered by the sea or a lake the groundwater pressures will be determined by topography and groundwater recharge. If the site is submerged the groundwater pressure will be determined by the depth of the sea/lake.

¹ Whitehouse P, 2007. A relative sea-level data base for Fennoscandia, Durham University, February 2007. Excel data base stored at SKB, SKBdoc 1265613.

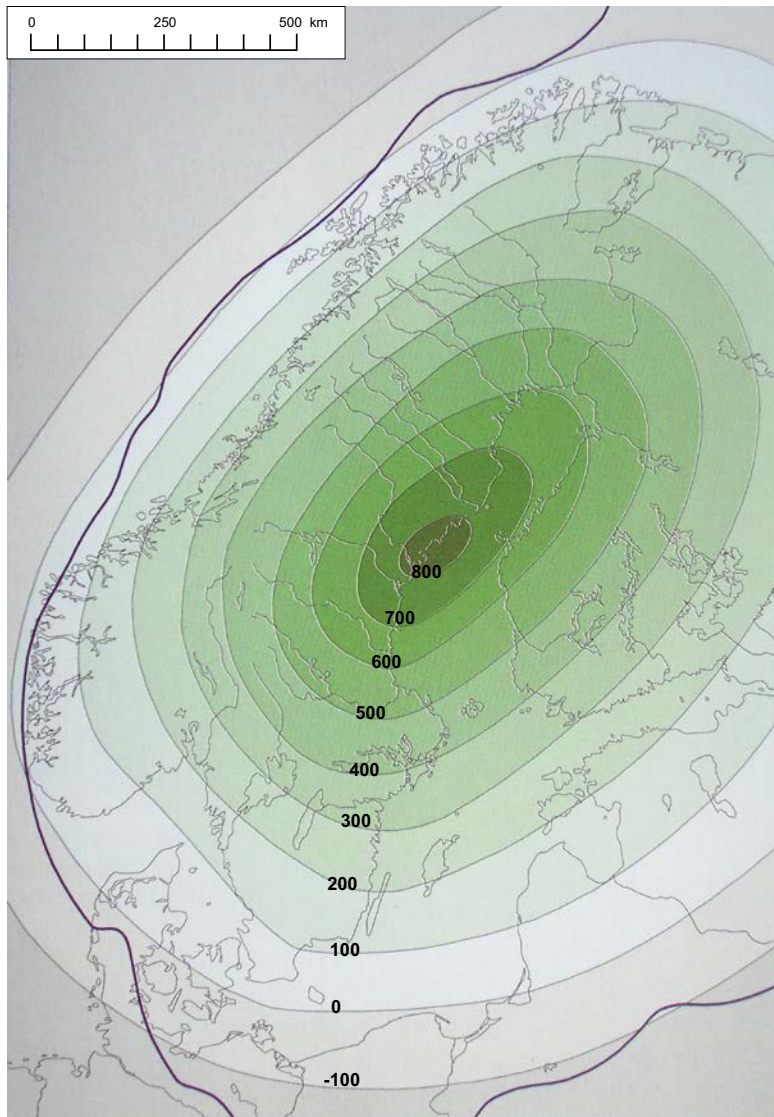


Figure 2-15. Total amount of glacial rebound (metres) that has taken place due to the deglaciation of the Weichselian ice sheet. The bold line shows the approximate maximum extent of the Weichselian ice sheet. Note that the total amount of rebound is more than twice as large as the amount of rebound that may be inferred from raised beaches formed at the highest post-glacial sea-level (see the text). After Fredén (2002).

Påsse (2001) developed an empirical model of glacio-isostatic rebound and shore-level displacement in Fennoscandia. The glacial isostatic component was estimated based on lake-tilting information and shore-level data from the area covered by the Scandinavian ice during the late Weichselian. The eustatic component was determined by iteration comparing a hypothetical glacial isostatic rebound evolution and empirical data on shore-level evolution. The resulting present day relative uplift rate displays a concentric spatial pattern over Fennoscandia, with a maximum rate of c 9 mm/yr in the northernmost part of the Baltic Sea. This relative uplift rate includes an eustatic contribution (sea-level rise) of c 1.1 mm/yr. The present day relative uplift rate, representing the present day shore-level change at Forsmark, is c 6 mm/yr. The present day glacial isostatic rebound at Forsmark is thus c 7.1 mm/yr according to Påsse (2001).

Care must be exercised when interpreting paleoshoreline data from the Baltic Sea; it is important to determine whether the data relate to sea-level or a lake level. An overriding problem with geological data in Fennoscandia is the lack of relative sea-level data prior to the LGM. Most of the evidence of shorelines prior to that time has been destroyed by the ice sheet. This makes it difficult to test relative sea-level estimates for the period before 20 ka before present. Furthermore, the fact that shorelines can only form in ice-free locations provides an important temporal constraint for the testing of shoreline migration estimates against undated shoreline data.

One way of making direct observations of ongoing post-glacial crustal deformation is to use high quality data from networks of continuously operating permanent GPS receivers. GPS data provide satellite-measured observations of changes in baseline distances which yield present-day rates of vertical and horizontal motion at a series of discrete positions. GPS data from the BIFROST project (Johansson et al. 2002) provide excellent spatial coverage of present-day solid Earth deformation throughout Fennoscandia to a high degree of accuracy. Typically, the GPS stations used in the BIFROST project were established within national land survey programmes with an initial aim of providing reference coordinates for other GPS measurements. The detailed analyses of data from such permanent GPS stations have provided new insight into the processes of post-glacial rebound or GIA in Fennoscandia and Canada (cf. Scherneck et al. 2001, Henton et al. 2006). The results provide information on both the rate of the vertical uplift component, as well as on the associated smaller horizontal component of crustal motion (e.g. Johansson et al. 2002) (Figure 2-16). The rates are averaged over the period of data collection, which is generally on the order of 10 years at the present, to yield estimates accurate to within ~ 0.4 mm/yr in the horizontal direction, and ~ 0.7 mm/yr in the vertical direction (Lidberg et al. 2010). The vertical component of GIA, interpolated to the Forsmark site from data of Lidberg et al. (2010), amounts to 8.4 ± 0.3 mm/yr.

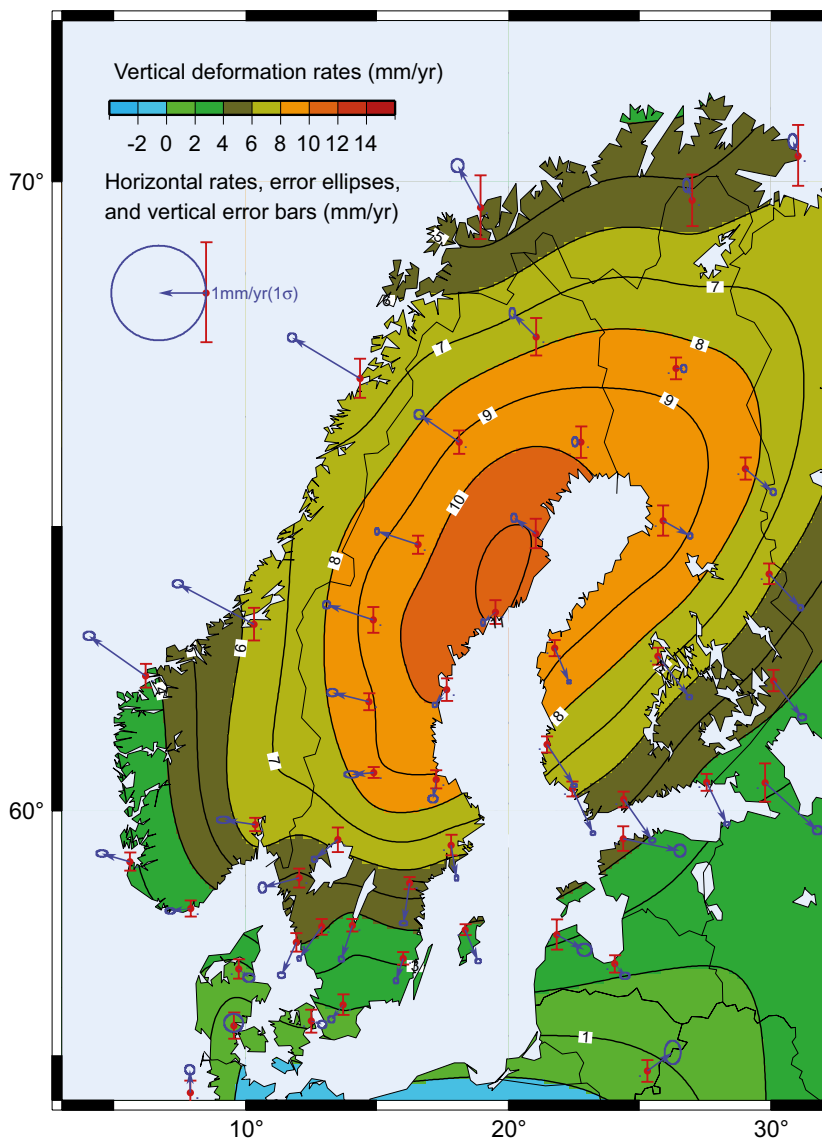


Figure 2-16. Present-day crustal deformation over Fennoscandia as observed by continuous GPS measurements within the BIFROST project (e.g. Scherneck et al. 2001). The rebound displays a concentric pattern with a maximum rebound rate of ~ 11 mm/yr located approximately in the area of the former maximum ice-sheet thickness. In the post-glacial upwarping process, a horizontal component of crustal deformation is also present (blue arrows), directed outward from the area of maximum depression. Modified from Lidberg (2007).

Uplift determined by these GPS observations shows the same concentric uplift pattern as that derived from sea-level and levelling measurements. The fastest rebound occurs approximately in the areas where the Laurentide and Fennoscandian ice sheets had their greatest thicknesses.

The maximum vertical uplift rate measured in this way in the area of the former Laurentide ice sheet is ~13 mm/yr (Henton et al. 2006), while the corresponding value for Fennoscandia is ~11 mm/yr (Figure 2-16). The largest horizontal displacements are generally found in the area of the ice margins of the maximum extent of the ice sheet. The difference between the maximum vertical uplift rates as observed from sea-level levelling measurements and from the analysis of GPS data is to a large extent covered by the uncertainty errors of the measurements, mainly in the sea-level measurements.

Since the GPS network yields an estimate for the full 3D deformation field, and the horizontal and vertical components of this field have different sensitivities to the ice history and Earth model, this opens up the possibility of constraining model parameters more accurately when these data are combined with sea-level observations. Combining the GPS data with sea-level data is particularly important when one considers that the GPS data are limited by their relatively short time span, and can only yield information about present-day deformation rates. The sea-level data are limited by their poor spatial coverage; a factor that is compensated for by the distribution of GPS observations throughout the interior of Fennoscandia.

Another, indirect, way of studying ongoing post-glacial rebound is by absolute gravity measurements (e.g. Lambert et al. 2001, Mäkinen et al. 2005), a method that may be used to estimate also the remaining uplift yet to be expressed in areas where the process is not complete.

2.2.4 Model studies

The GIA model

A recent review of GIA modelling in Fennoscandia is given by Steffen and Wu (2011). Another detailed review of present day GIA models is presented in Whitehouse (2009, Chapter 4). That chapter includes descriptions of different GIA approaches used by various research groups and the relative accuracy of these methods. Recent improvements of the GIA theory are described, as well as current shortcomings of the models. The various data sets used to calibrate and verify the accuracy of the modelling are also briefly discussed. A shorter description of GIA models is given here, followed by an account of the GIA simulations performed for the safety assessment.

The majority of GIA models solve the sea-level equation, which was originally developed by Farrell and Clark (1976), and describes the gravitationally-consistent redistribution of water from ice sheets to ocean basins, and thus the evolution of the distribution of water between oceans and land-based ice sheets. Any redistribution of surface mass alters the shape of the geoid, which in turn defines the redistribution of water in the ocean basins; therefore an iterative procedure is required to solve the sea-level equation. The magnitude of eustatic ocean volume changes due to water density changes associated with temperature and salinity changes is substantially smaller than that of eustatic ocean volume changes due to mass exchange between continental ice masses and the oceans, which is why ocean-water density variations are not taken into account in GIA modelling.

There have been many attempts to construct a dynamical model to explain the observed processes of GIA. Following Farrell and Clark (1976), early studies neglected the time dependence of ocean shorelines (Wu and Peltier 1983, Nakada and Lambeck 1989, Tushingham and Peltier 1991), and the ice loading was simply applied as a series of 'finite elements' (Clark et al. 1978, Peltier et al. 1978, Wu and Peltier 1983). In 1991, Mitrovica and Peltier (1991) derived a pseudospectral approach to solving the sea-level equation, and this method has been widely used throughout the field ever since. Models that take into account the time-varying nature of shorelines began to be developed in the early 1990s (Lambeck and Nakada 1990, Johnston 1993, Peltier 1994, 1998, Milne 1998, Milne et al. 1999, Peltier and Drummond 2002, Kendall et al. 2005), and the effects of Earth-rotation have also subsequently been considered (Han and Wahr 1989, Bills and James 1996, Milne and Mitrovica 1998, Peltier 1998, Mitrovica et al. 2001a, 2005). Initial investigations into the effect of lateral variations in Earth structure are also in the process of being developed (Kaufmann et al. 2000, Wu et al. 2005, Latychev et al. 2005b, Paulson et al. 2005, Whitehouse et al. 2006).

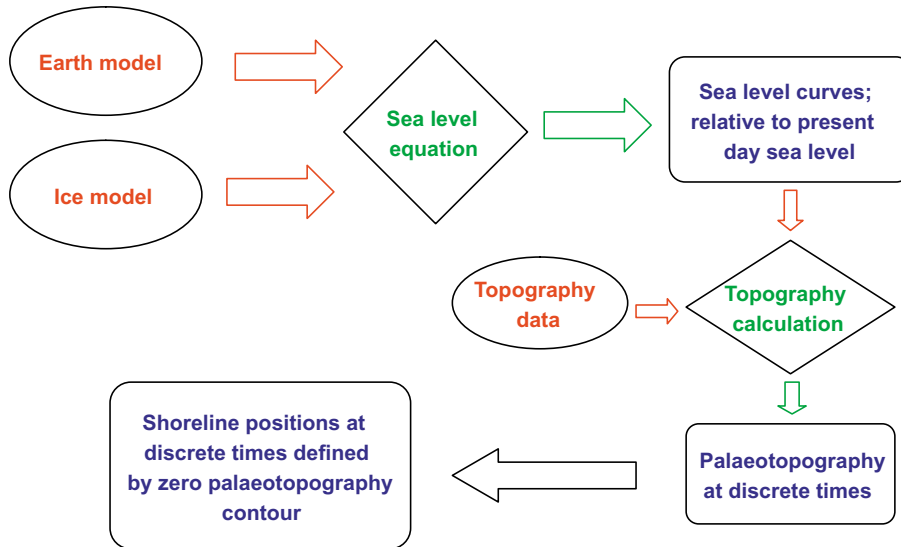


Figure 2-17. Flow chart outlining the inputs (in red), calculations (in green) and outputs (in blue) required to calculate paleoshoreline positions due to GIA processes.

The GIA model used in this study was developed by Milne (Milne 1998, Milne and Mitrovica 1998, Milne et al. 1999). Three refinements to the original sea-level equation presented by Farrell and Clark (1976) have been developed by Mitrovica and Milne (2003). Firstly, time-dependent shoreline positions are taken into account when calculating the ocean-loading function. Shorelines can change position by several hundreds of kilometres in flat terrains, and this must be accounted for in applying the ocean load. Secondly, the water influx into regions vacated by retreating, marine-based ice is carefully accounted for in the distribution of the load (Milne et al. 1999). And thirdly, changes to the rotational state of the Earth as a result of both surface and internal mass redistributions are considered. The model used to generate predictions of relative sea-level change in this study is based on a new general theoretical foundation that includes all these advances.

The sea-level equation

The sea-level equation takes account of changes to the height of the geoid and the Earth's solid surface. Local factors, such as changes to the tidal regime, the consolidation of sediments, and tectonic processes, are neglected in this study.

$$\Delta\zeta_{rsl}(\tau, \varphi) = \Delta\zeta_{eus}(\tau) + \Delta\zeta_{isos}(\tau, \varphi) + \Delta\zeta_{local}(\tau, \varphi) \quad (2-2)$$

In the above expression the left-hand side refers to changes in relative sea-level at time τ and location φ . The first term on the right-hand side is the time-dependent eustatic signal, the second term varies in space and time, and relates to the isostatic effects of glacial rebound, including both ice and water load contributions, and the third term refers to local factors, as described above. In order to solve Equation 2-2 in a gravitationally self-consistent manner, a pseudo-spectral algorithm (Mitrovica and Peltier 1991, Milne and Mitrovica 1998) is employed. Green's functions are constructed to determine the GIA-induced perturbations to the geopotential and solid surfaces due to loading. The resulting temporal convolutions are evaluated by describing the GIA loading history as a series of discrete Heaviside increments. The spatial convolutions are performed by transforming the problem to the spectral domain and employing the pseudospectral algorithm (Mitrovica and Peltier 1991, Milne and Mitrovica 1998).

The method by which relative sea-level is calculated at a certain position, at a certain time, may be broken down into a series of simplified steps. At the start of the model run, loading is applied to an Earth model that is assumed to be in isostatic equilibrium. Once an ice load is applied at each time step the resulting deformation of the solid Earth and the perturbation to the geoid are calculated. The new shape of the geoid determines the redistribution of water in the oceans and the new extent of the oceans. However, this redistribution of water in turn affects the shape of the geoid and

the deformation of the solid Earth in oceanic regions, therefore an iterative procedure is used to ensure the correct treatment of perturbations to the solid and geoid surfaces; recalculations of the perturbation to the geoid and the redistribution of water are carried out until there are no further changes, at which point loading for the next time step is applied. Loading is applied via forward time stepping.

The GIA model provides an estimate of relative sea-level as a function of location and time for the simulated period. In the method used here, relative sea-level is defined to be zero at the present day, and heights are given relative to this ‘zero level’ at all times in the past and future. Corrections are applied using present-day topography to determine the height of any point above or below sea-level at any given time. Assuming that the underlying topography is unaltered by erosion and sedimentation, the topography at location φ and time τ_p is calculated via the following equation:

$$T(\varphi, \tau_p) = T(\varphi, \tau_0) - \zeta_{rsi}(\varphi, \tau_p) \quad (2-3)$$

where T is topography, defined to be the height of the solid surface above sea-level at time τ , and ζ_{rsi} is relative sea-level at time τ . τ_0 refers to the present day, and φ is the location on the surface of the Earth. Shoreline positions at time τ_p are determined by the zero paleotopography contour at that time.

Ice loading

The global ice loading model used in this study is modified from the ICE3G deglaciation history (Tushingham and Peltier 1991), and has been calibrated using far-field relative sea-level data (Radtke et al. 1988, Fairbanks 1989, Bard et al. 1990, 1996, Chappell and Polach 1991, Chappell et al. 1996, Hanebuth et al. 2000, Yokoyama et al. 2000). A eustatic sea-level data set has been used to tune the mass of ice contained within far-field ice sheets. The near-field ice loading for Fennoscandia is the one described in Section 2.3.4 and has been derived using a thermodynamic ice-sheet model employing a proxy data paleo-temperature series for the last 120 ka from the Greenland GRIP ice core (Dansgaard et al. 1993), see Section 2.3.4. From this model, the extent and thickness of the Fennoscandian ice sheet at a series of discrete times from 116 ka BP to the present day has been derived and used.

The ice-loading history within Fennoscandia is the principal factor governing relative sea-level change in Fennoscandia. The loading history presented in Section 2.3.4 is perturbed to investigate the sensitivity of sea-level change to differences in ice thickness, the timing of deglaciation, the pattern of ice build-up, and the time scale over which loading is considered (Table 2-4). The extent of ice at each time step since the LGM has not been perturbed because the geometry of the ice sheets during this period are relatively well constrained by geological data. Details of the ice build-up prior to the LGM are less well constrained because geological evidence subsequently has been destroyed. However, for consistency, the ice extents for this period are also not altered.

An Earth model consisting of a 96 km-thick elastic lithosphere, an upper mantle of viscosity $0.5 \cdot 10^{21}$ Pa s, and a lower mantle of viscosity $1 \cdot 10^{22}$ Pa s has been used to investigate the response to the different loading models.

Table 2-4. Summary of ice-loading models used in this study. In all cases, the ICE3G global ice model is used to constrain the distribution and thickness of ice outside Fennoscandia.

Model	Description of loading model	Model run time
1	Weichselian glacial cycle as described in 2.3.4	116 ka
2	Two Weichselian glacial cycles run after each other to give a double glacial cycle	232 ka
3	Weichselian glacial cycle, loading only applied from 40 ka BP	40 ka
4	Weichselian glacial cycle with 90% ice thickness in Fennoscandia	116 ka
5	Weichselian glacial cycle with 80% ice thickness in Fennoscandia	116 ka
6	Weichselian glacial cycle with the timing of deglaciation advanced by 500 years	116 ka
7	Weichselian glacial cycle modified with ice thickness allowed to increase linearly between 60 ka BP and 20 ka BP	116 ka
8	Four relaxation models, as described in the isostatic memory section	Varies
9	Weichselian glacial cycle with all ice removed from Fennoscandia for the duration of the model run, as described in the section on far-field ice sheets	116 ka

In Figure 2-18a, the same Fennoscandian surface loading is used, but the model run is initiated at different times. Due to the assumption that the Earth is initially in isostatic equilibrium there will be some discrepancy between relative sea-level predictions at early times in a model started at 116 ka BP and one that has already been running for 100 ka because the Earth's response is dependent upon loading history as well as the instantaneous load (see the section on Isostatic Memory). Because the Earth has undergone a series of glacial cycles, a loading model that accounts for loading and unloading of the Earth during the previous cycle will give more realistic predictions for relative sea-level during the cycle of interest. However, the negligible difference between relative sea-level predictions from the single cycle, double cycle and 40 ka models (models 1, 2, and 3 in Table 2-4), for times between 25 ka BP and the present day, imply that no long-term error is introduced when a model with a later start time is used. It is important that the shortest possible time steps are used to ensure that the full loading history is captured; failure to do so will miss short time-scale fluctuations in ice distribution, leading to a decrease in the accuracy of the relative sea-level predictions.

The effect of altering the thickness of ice in the loading model is illustrated in Figure 2-18b. There is little difference in the shape and magnitude of predicted relative sea-level for the 80%, 90% and 100% loading models during the minor glaciation between ~65 ka BP and ~50 ka BP (models 5, 4 and 1 in Table 2-4), but comparing results from the 80% and 100% models at the LGM yields differences of ~100 m at Forsmark. The larger the range of ice thicknesses used, the greater the range of relative sea-level predictions, as illustrated by the range for Forsmark.

The timing of maximum relative sea-level is the same for all loading models except that where the timing of deglaciation is brought forward by 500 years (model 6 in Table 2-4). In this case, maximum relative sea-level also occurs 500 years earlier. Apart from this time shift, which decays to zero by the present day, there is otherwise no difference between predictions for this model, and the Weichselian glacial cycle. The magnitude of the maximum relative sea-level is identical to that predicted by the single cycle, double cycle and 40 ka loading models (models 1, 2 and 3 in Table 2-4).

In model 7 (Table 2-4), ice thickness is allowed to increase linearly between 60 ka BP and 20 ka BP. This model has been developed to test the postulate that there was a continuous ice sheet presence in Fennoscandia during this period, see also Section 3.2. The pattern of continuous, linear ice sheet growth is purely an assumption of this model sensitivity test; the maximum ice thickness of the Weichselian glacial cycle is never exceeded, but the cumulative effect of loading the Earth for a longer period results in a greater amount of isostatic depression throughout Fennoscandia, and a greater relative sea-level maximum (Figure 2-18c). Therefore the GIA signal is not only a function of the thickness and timing of ice loading at a given time, but also the evolution of the loading.

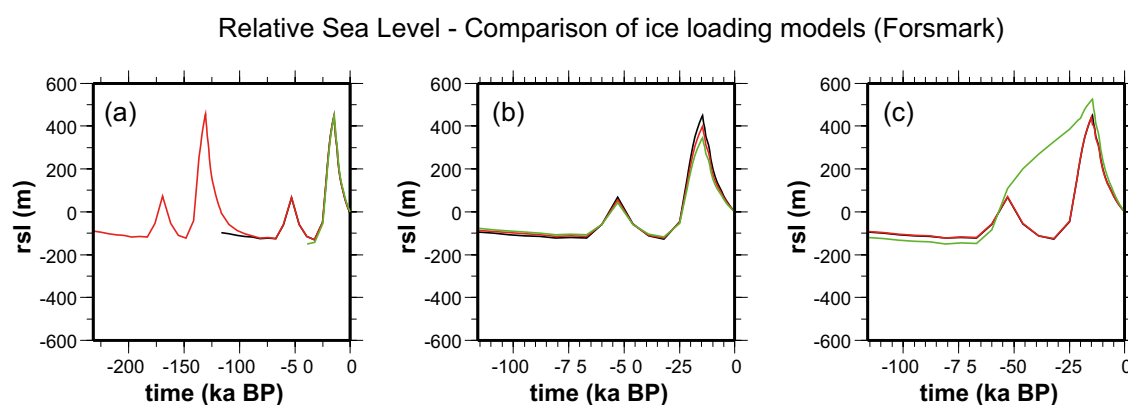


Figure 2-18. Predicted relative sea-level for Forsmark. See Table 2-4 for details of the ice loading models. An Earth model with a thin lithosphere and low upper mantle viscosity has been used in all cases (Model A, Table 2-5). a) black: model 1, red: model 2, green: model 3. b) black: model 1, red: model 4, green: model 5. c) black: model 1, red: model 6, green: model 7.

The rate of change of relative sea-level throughout the glacial cycle is similar for all the loading models, except for the model where the pattern of ice-sheet growth has been markedly altered prior to the LGM (model 7 in Table 2-4, Figure 2-18c). However, predictions of present-day uplift rates for the various models do highlight small differences between the models (see Figure 2-19). Uplift rates for the single cycle, double cycle, 40 ka loading model and the model where the timing of deglaciation is shifted by a small amount are virtually identical. Much lower rates are predicted for the case where only 90% or 80% of the ice thickness is used, although the lateral extent over which rebound occurs is similar to the standard loading models. The final model, where the pattern of ice-sheet growth has been altered, yields much greater present-day uplift rates, reflecting the fact that the solid Earth has to rebound from a position of greater isostatic depression at the LGM. In this final case, the area over which rebound is still taking place is greater than that predicted by the other loading models.

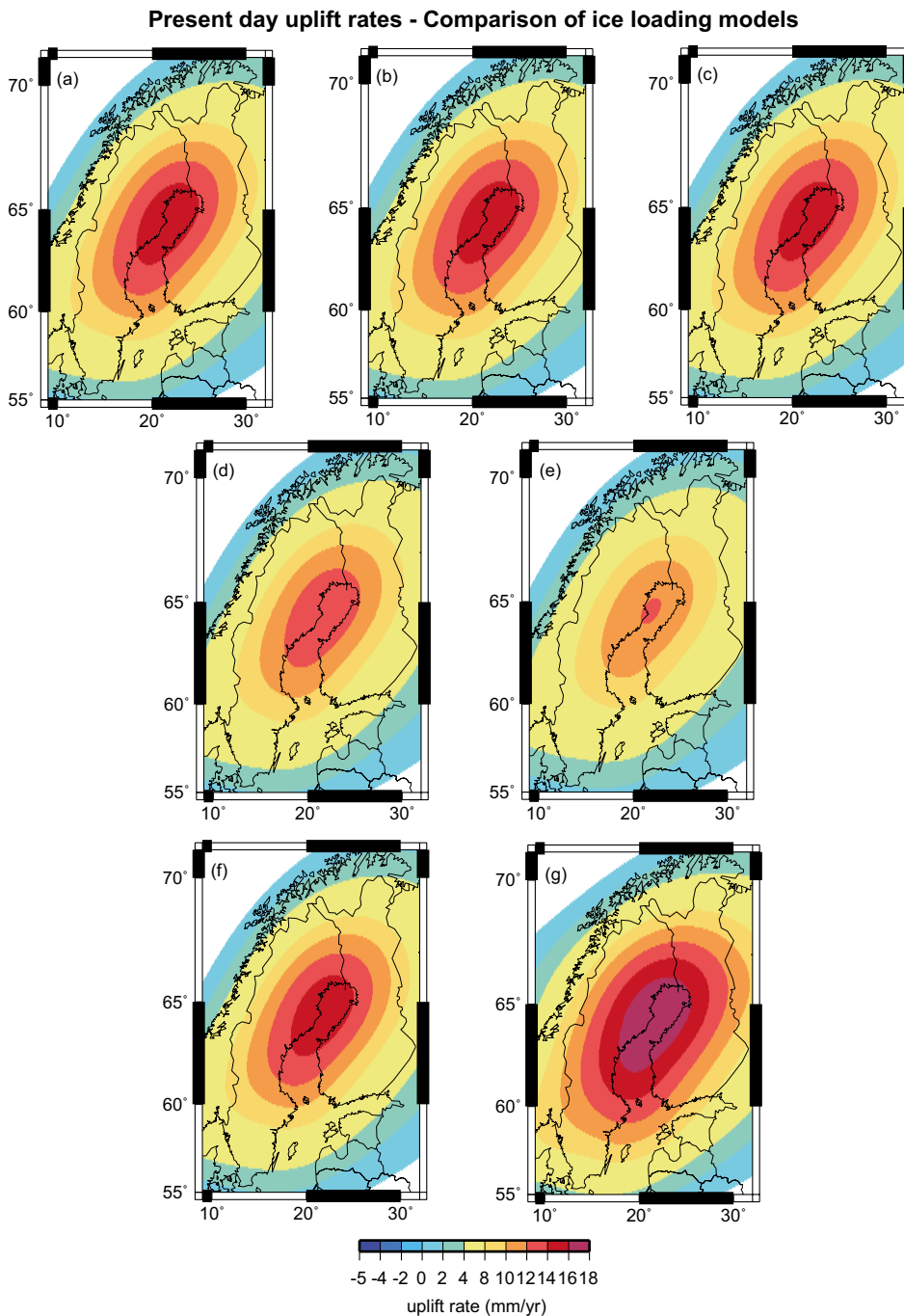


Figure 2-19. Predicted present-day uplift rates throughout Fennoscandia for the various ice-loading models. See Table 2-4 for details of the loading models. An Earth model with a thin lithosphere and a low upper mantle viscosity has been used in all cases (Model A). a) Loading model 1. b) Loading model 2. c) Loading model 3. d) Loading model 4. e) Loading model 5. f) Loading model 6. g) Loading model 7.

Comparisons between predictions from the GIA model, using the ice loading from the Weichselian glacial cycle (model 1 in Table 2-4), and observations of relative sea-level and present-day uplift rates in Fennoscandia show that the modelling overpredicts the GIA response (see Figure 2-20 and Figure 2-21). There may be several reasons for this; either the ice load has been too large in the ice loading history, as tested above with load models 4 and 5 reducing the Weichselian glacial cycle ice-sheet thickness to 90% and 80% respectively, or the misfit could be a result of assuming a laterally homogeneous (1D) Earth structure, discussed in the section *A GIA case study with a Fennoscandian 3D Earth structure* below, or a combination of the two.

Unlike the geological evidence relating to the spatial extent of the Weichselian ice sheet, very few constraints upon the ice-sheet thickness exist, and one explanation for the misfit could be that ice thicknesses in the loading model are too large. As pointed out by Denton and Hughes (1981), early ice-sheet modelling studies of steady-state ice sheets, including their own, produced ice thicknesses that were greater than one would expect for ice sheets during a natural glacial cycle. This has since been confirmed by GIA modelling, showing that such thick ice sheet profiles result in a poor fit to relative sea-level observations. Subsequent dynamical approaches to ice modelling outlined in Section 2.3, including the model used in the present study, produce considerably thinner ice sheets, for example at the LGM. These models yield a closer fit to relative sea-level observations when used as an input to GIA models, but in the present study there is still a misfit to explain. Some of this difference may be explained by the fact that there are still gaps in our knowledge of basal processes related to, for example, sliding and sediment deformation under ice sheets. Another explanation could be that the assumption of a uniform Earth structure results in too large a GIA response, see below.

Testing relative sea level data against GIA predictions

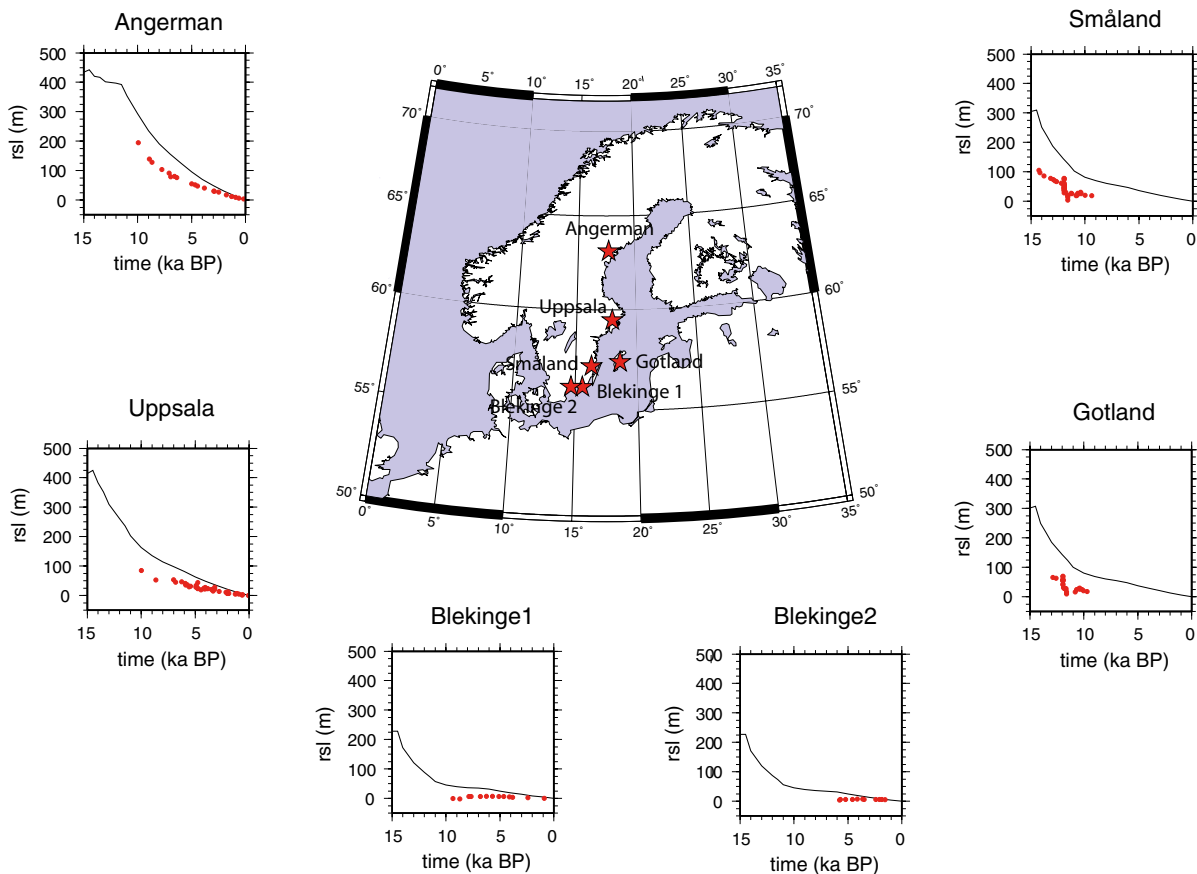


Figure 2-20. Comparison between predicted relative sea-level (black lines) from the GIA model, using the ice loading from the Weichselian glacial cycle (model 1 in Table 2-4), and observations from relative sea-level markers (red points) at six sites in Fennoscandia (red stars) for the last 15 ka. Data compiled from Lambeck et al. (1998).

Comparison of predicted and observed present day uplift rates

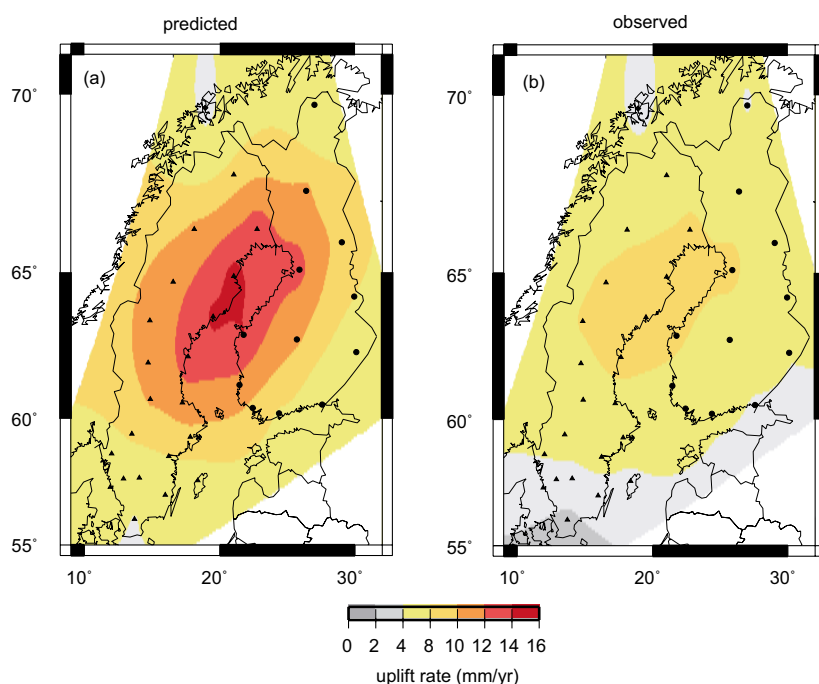


Figure 2-21. Comparison of predicted and observed present-day uplift rates. a) Predicted present-day uplift rates interpolated at GPS sites (black dots and triangles). Data generated using the Weichselian glacial cycle loading model (model 1 in Table 2-4) and an Earth model consisting of a 96 km-thick elastic lithosphere, an upper mantle of viscosity $0.5 \cdot 10^{21}$ Pa s, and a lower mantle of viscosity $1 \cdot 10^{22}$ Pa s (model A in Table 2-5). b) Observed present-day uplift rates interpolated at GPS sites. Data from the BIFROST project (Johansson et al. 2002).

Earth rheology

The second main factor governing sea-level change, together with the load history, is the Earth model. A three-layer, 1D radial structure is used in these experiments. A discussion of the reasonable joint parameter range for the rheological properties of the lithosphere and mantle can be found in Section 2.2.2. The details of the models used in this investigation are outlined below in Table 2-5.

For all of the loading models considered here, for the majority of the glacial cycle, there is less than ~20 m difference in predicted relative sea-level across all five Earth models (see Figure 2-22). However during the deglaciation of the Fennoscandian ice sheet, at around 14.5 ka BP, the difference in predictions for the five Earth models increases to ~100 m for Forsmark. At any one time, differences in geoid height at any fixed point will be negligible if the same loading model is used; any differences in the relative sea-level are therefore due to variations in the solid Earth response to loading.

Table 2-5. A summary of the five Earth models considered in this study.

Model	Model description	Lithospheric thickness (km)	Upper mantle viscosity (Pa s)	Lower mantle viscosity (Pa s)
A	Thin lithosphere	96	$0.5 \cdot 10^{21}$	$1 \cdot 10^{22}$
B	Thin lithosphere, strong lower mantle	96	$0.5 \cdot 10^{21}$	$4 \cdot 10^{22}$
C	Thick lithosphere	120	$0.5 \cdot 10^{21}$	$1 \cdot 10^{22}$
D	Thick lithosphere, strong lower mantle	120	$0.5 \cdot 10^{21}$	$3 \cdot 10^{22}$
E	Thick lithosphere, strong upper mantle	120	$0.8 \cdot 10^{21}$	$1 \cdot 10^{22}$

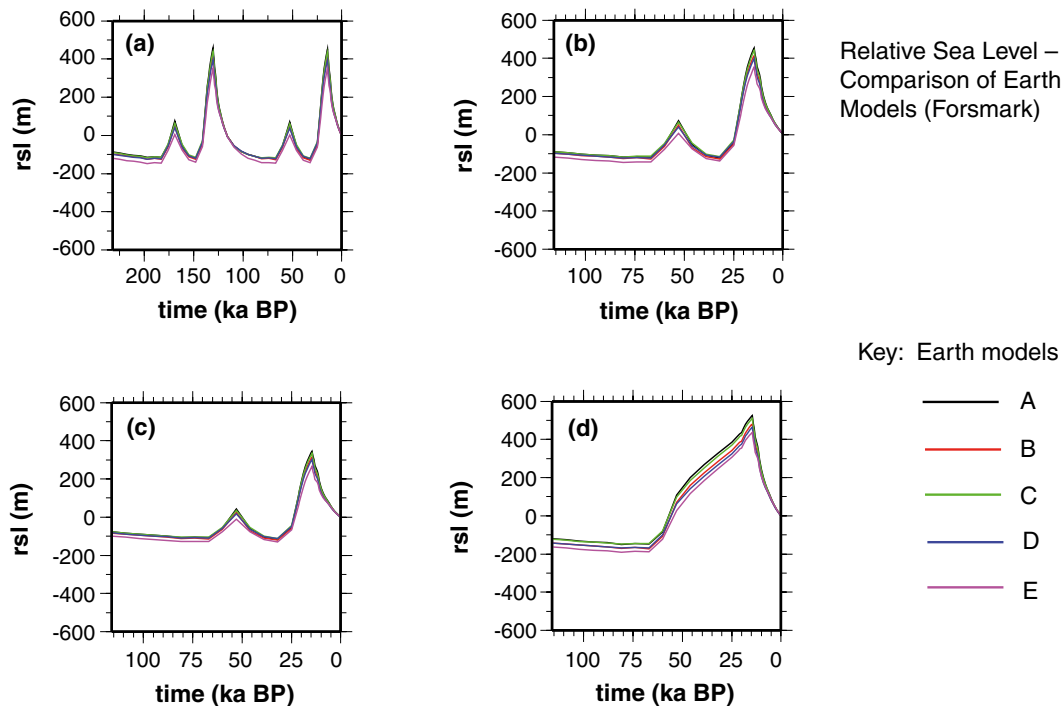


Figure 2-22. Comparison of Earth models. Predicted relative sea-level for Forsmark for all five Earth models under consideration. See Table 2-4 for details of the loading models. a): Double Weichselian glacial cycle – loading model 2. b): Single Weichselian glacial cycle – loading model 1. c): Single Weichselian glacial cycle modified with 80% ice thickness in Fennoscandia – loading model 5. d): Single Weichselian glacial cycle modified with a constant, linear increase in ice thickness in Fennoscandia between 60 ka BP and 20 ka BP – loading model 7.

The divergence in the predictions is short-lived, implying that the phenomenon is related to the elastic properties of the lithosphere. In general, an Earth model with a thinner lithosphere will undergo the greatest isostatic deformation, resulting in the most extreme relative sea-level prediction. From the results, it also seems that a model with a weaker lower mantle (e.g. models A and C) will undergo greater deformation than one with a stronger, or higher viscosity, lower mantle, while the model with the strongest upper mantle (model E), exhibits the smallest amount of solid Earth deformation.

Since the differences in relative sea-level predictions are short-lived, and very few relative sea-level data are available from this period, it is not possible to test these predictions against data in order to constrain the Earth parameters. Instead, present-day uplift rates must be used.

Earth models with a thinner lithosphere (models A and B in Table 2-5) are predicted to experience greater present-day uplift rates, although the extent over which rebound takes place will be slightly smaller than for models with a thicker lithosphere (see Figure 2-23 and Figure 2-24). Earth models with a weaker lower mantle (models A and C in Table 2-5) tend to experience greater present-day uplift rates, over a larger area, than models with the same lithospheric thickness but greater lower mantle viscosity (models B and D respectively in Table 2-5). The existence of a stronger upper mantle (model E in Table 2-5) also increases the predicted rate of uplift.

In reality, the Earth is not laterally homogeneous as assumed in these simulations, and variations in lithospheric thickness and mantle viscosity will perturb the GIA signal. Paulson et al. (2005) estimated that for realistic variations in mantle viscosity, present-day uplift rates may be altered by up to 10%. The effect of including a 3D Earth structure for Fennoscandia has been investigated by Whitehouse (2009, Section 4.5.4). Some of the results of this study are presented in the section *A GIA case study with a Fennoscandian 3D Earth structure* below.

Present day uplift rates - Comparison of Earth Models

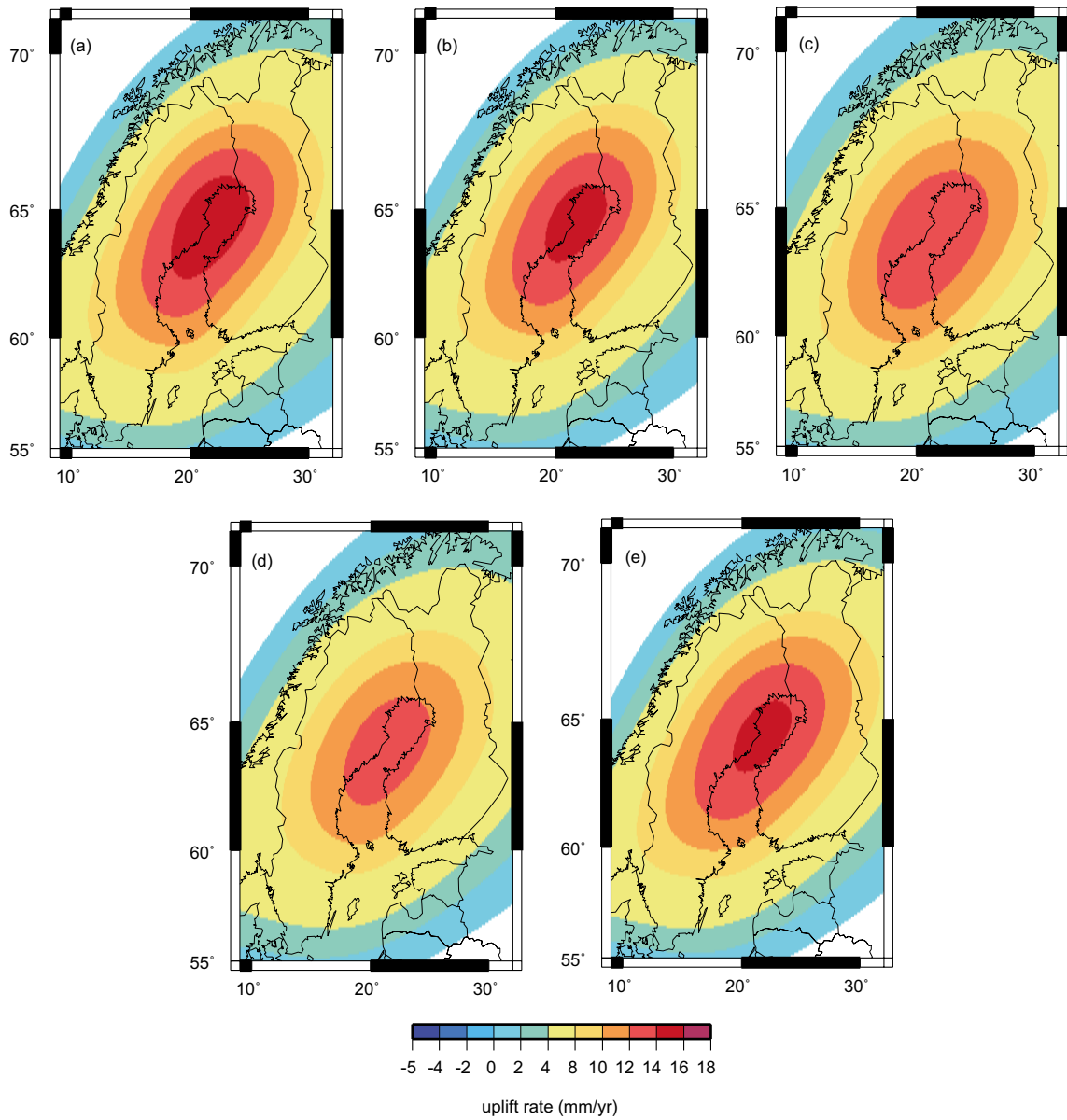


Figure 2-23. Comparison of Earth models. Predicted present-day uplift rates throughout Fennoscandia for the five Earth models under consideration. The loading model is defined to be a single Weichselian glacial cycle (Model 1) in all cases. a) Earth model A. b) Earth model B. c) Earth model C. d) Earth model D. e) Earth model E.

Present day uplift rates - Misfit between observations and predictions

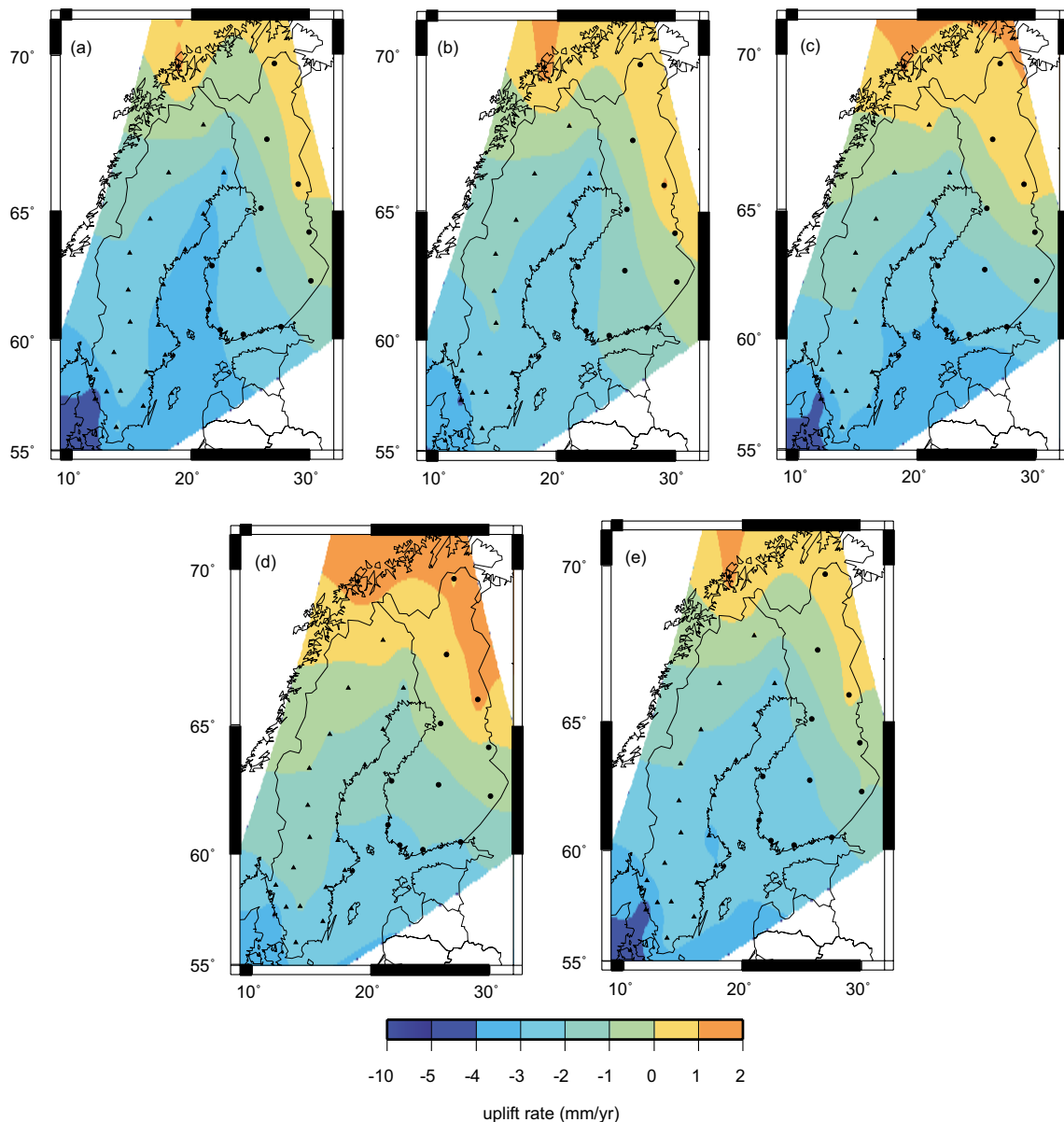


Figure 2-24. Residual present-day uplift rates (misfit between observations and predictions) throughout Fennoscandia for the five Earth models under consideration. The predictions of Figure 2-23 are interpolated at the BIFROST GPS sites and then subtracted from the observed signal (see Figure 2-25). Loading and Earth models as in Figure 2-23.

Isostatic memory

The time scale over which the GIA model is run has implications for the accuracy of relative sea-level predictions due to the viscous memory of the Earth model. The Earth is assumed to be in isostatic equilibrium at the start of a model run. In reality, the Earth is unlikely to reach such a state if the advance and decay of ice sheets continues with the same periodicity as seen in the past (Figure 1-2). Therefore, the model must be run for a long enough period that sufficient loading history is considered, and the initial condition of isostatic equilibrium does not affect predictions during the period of interest.

In order to investigate the sensitivity of the simulated isostatic deformation to the assumptions on ice sheet loading, four loading models were defined.

- The ‘standard’ model: Weichselian glacial cycle loading is applied for a single glacial cycle.
- The ‘double’ model: Weichselian glacial cycle loading is applied over two consecutive glacial cycles.
- The ‘40 ka’ model: Weichselian glacial cycle loading applied only from 40 ka BP.
- The ‘80%’ model: Weichselian glacial cycle loading modified with only 80% of the ice thickness in Fennoscandia being applied for a single glacial cycle.

In all four cases, the loading models were run using three different Earth models (A, C and D in Table 2-5 above), and following the final loading time step at 0 ka BP the relative sea-level calculations were allowed to run for another 60 ka into the future without any further change to the distribution of surface loads, thus enabling the system to return to equilibrium.

The vertical solid Earth response was calculated at six sites for each model run. These sites were chosen to lie roughly 250 km apart along a profile running approximately south from the present-day centre of isostatic uplift (see Figure 2-25) in order to investigate the solid Earth response at a range of distances from the previous centre of ice loading, and for a range of loading histories.

Deformation at each of the six sites is defined to be zero at the start of the model run. During the experiment, solid Earth deformation at each site was measured relative to the initial position, with negative values indicating a decrease in elevation due to isostatic subsidence. The timing and magnitude of maximum depression is recorded in each case, and when the deflection of the site returns to less than 1% of the maximum deflection, equilibrium is assumed. The isostatic signals at sites 1, 4 and 6 are shown for the complete simulation in Figure 2-26 and for the period from present day to 60 ka AP Figure 2-27. A more detailed summary of the results of these model runs are found in SKB (2010a, Figure 3-6).

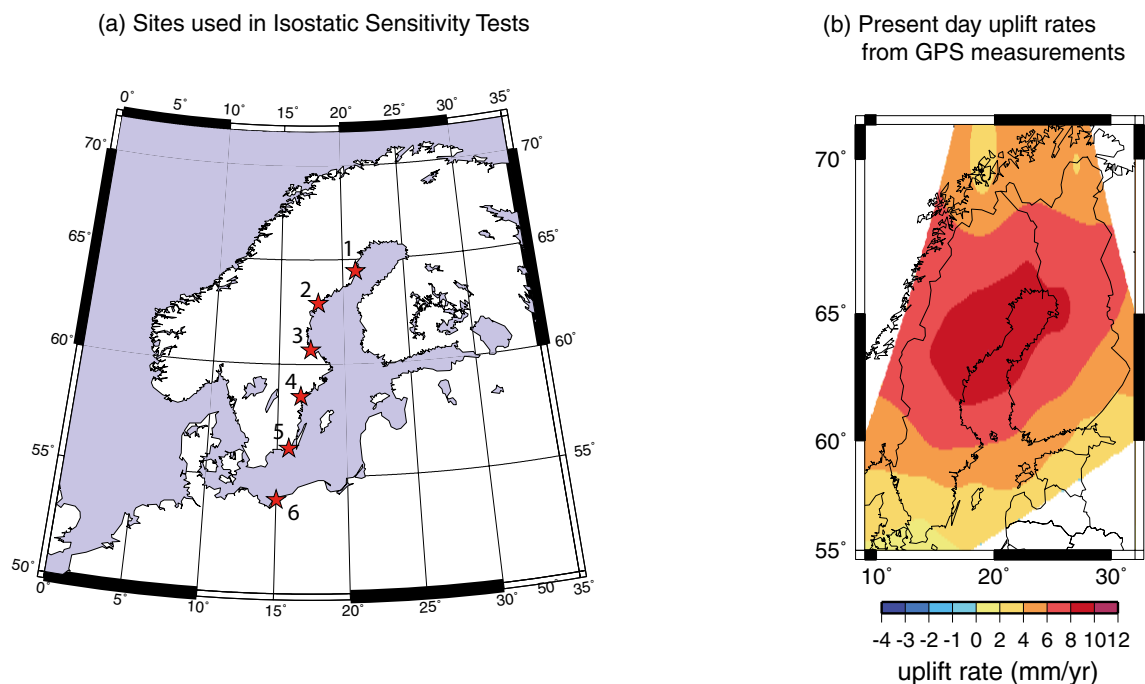


Figure 2-25. a) Map showing the location of the six sites (red stars) where the isostatic response is calculated and b) the present-day pattern of uplift in Fennoscandia from BIFROST GPS rates (Johansson et al. 2002).

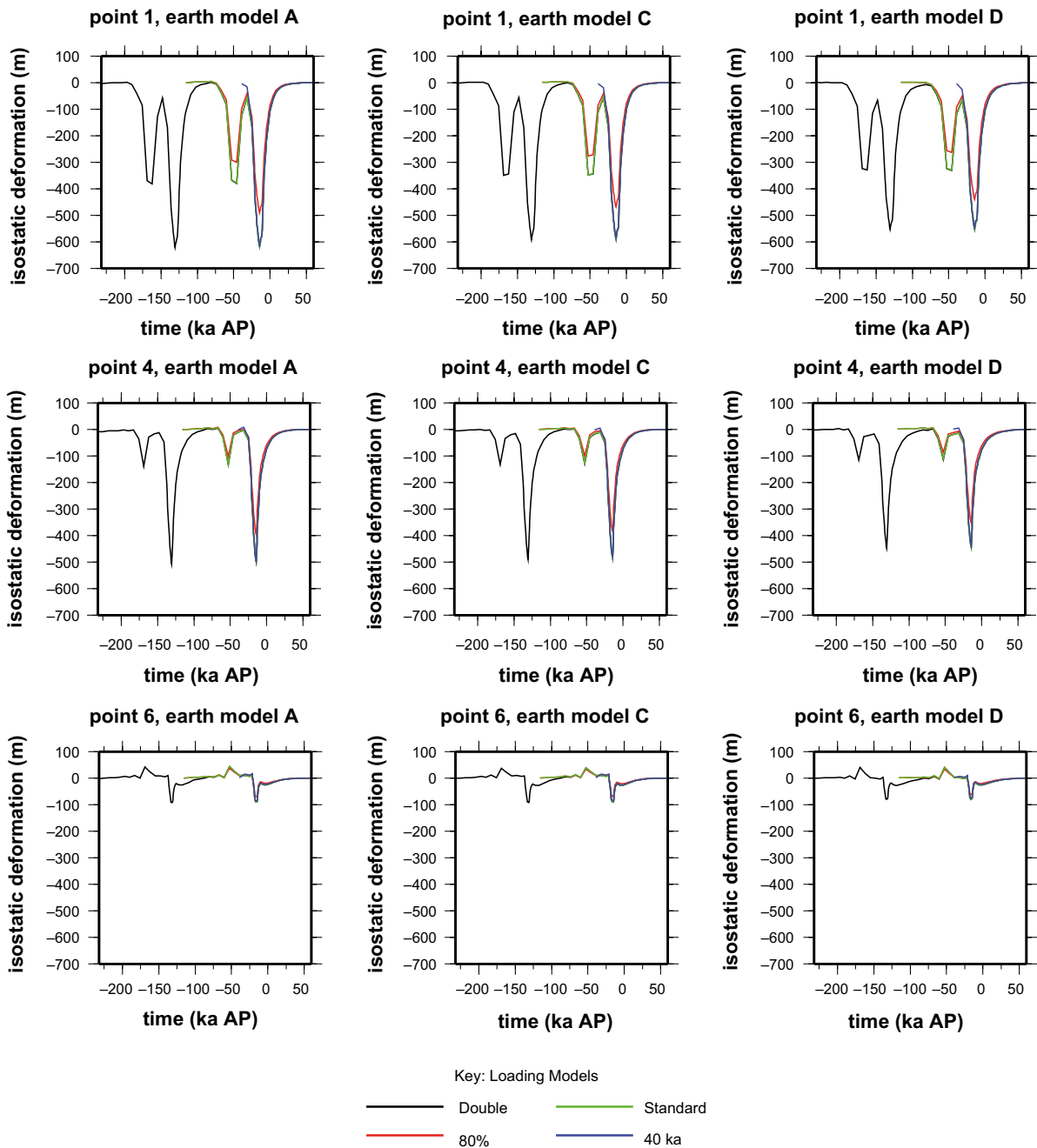


Figure 2-26. Isostatic deformation sensitivity tests. Solid Earth deformation at sites 1, 4 and 6 (see Figure 2-25) for the four loading models and three Earth models described in the isostatic recovery sensitivity tests.

For a given site and Earth model, there is little variation in the recovery time for the four different loading models. The shortest timescale loading model is initiated only ~25 ka before the timing of maximum deformation, and the difference in solid Earth deformation between this model and the double-cycle loading model is negligible from the time of maximum deformation onwards (see Figure 2-26). Therefore, the isostatic response of the Earth models is not dependent upon loading prior to ~25 ka before the timing of maximum deformation, and a loading model need only contain information from ~25 ka prior to the period of interest to ensure no distortion of the results due to initial conditions.

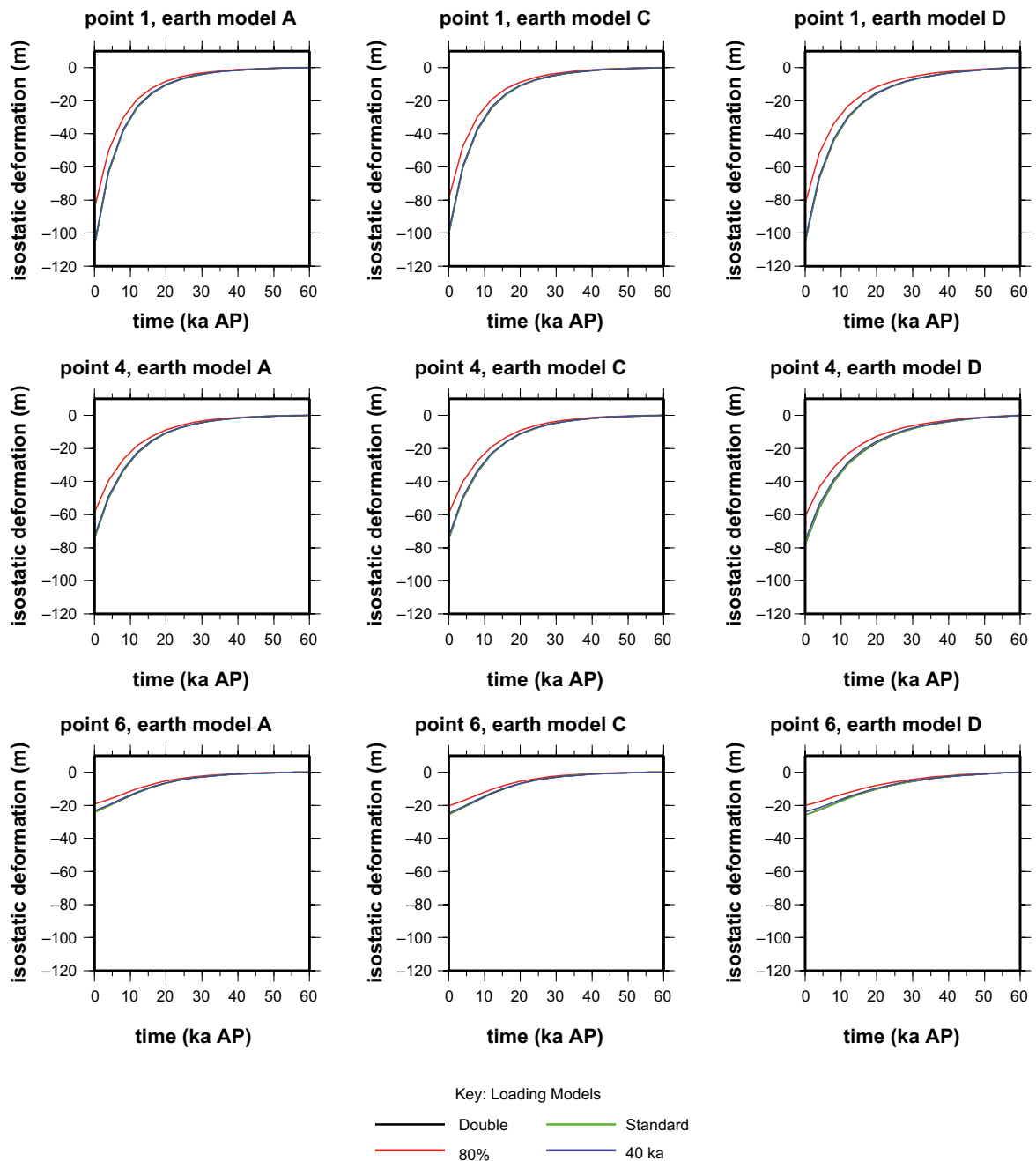


Figure 2-27. Isostatic deformation sensitivity tests. Solid Earth deformation projections between the present day and 60 ka AP at sites 1, 4 and 6 (see Figure 2-25) for the four loading models and three Earth models described in the isostatic recovery sensitivity tests.

Following unloading, the time to reach equilibrium varies between ~40 ka and ~75 ka. This range, and the observation that regions of maximum deformation recover more rapidly, may partly be attributed to the non-linear nature of solid Earth rebound. However, the distribution of relaxation times is principally an artefact of the method by which rebound is calculated: The rebound criterion states that deflection must return to within 1% of the maximum deflection. Therefore regions of greatest deformation seem to recover more rapidly as they only need return to a larger absolute deflection. The positive isostatic deformation at point 6 (Figure 2-26) indicates that this site was uplifted as part of a glacial forebulge prior to being loaded. For all sites, the time for recovery was found to be similar for Earth models A and C, but the model with the stiffer lower mantle (Earth model D) took consistently longer to reach maximum deformation and recover to equilibrium.

The ‘80%’ model was included in this study because it gives the closest fit to present-day uplift rates using the 1D GIA model. However, despite attaining a smaller maximum amount of deformation, the long-term rate of recovery for this loading model is not substantially different from that for models with 100% ice thickness. Therefore, the rate of isostatic recovery is not strongly dependent upon the magnitude of the load, but rather the timing of loading.

Importance of far-field ice sheets

Variations in the far-field Laurentide and Antarctic ice sheets perturb the shape and height of the global geoid signal, and generate an isostatic solid Earth response. Due to the distance of Fennoscandia from these ice sheets, the geoid signal will effectively be detected as a near-uniform rise or fall in the height of the geoid/ocean surface, dependent upon the surface mass change associated with these far-field ice sheets and distance from these surface masses. The solid surface signal due to far-field ice sheets will only be detectable in Fennoscandia if this region is located upon the forebulge of the deformation, as was the case during the maximum extent of the Laurentide ice sheet during the LGM (Mitrovica et al. 1994).

The magnitude of the solid Earth signal due to far-field ice sheet loading was calculated using a standard global ice-loading model for a single glacial cycle (Tushingham and Peltier 1991) with the ice removed from Fennoscandia during the last glacial cycle. Estimates of horizontal and vertical deformation at Forsmark are shown in Figure 2-28.

The positive sign of the predicted vertical deformation due to far-field ice loading at Forsmark (Figure 2-28a) indicates that the site was situated on the deformational forebulge of the Laurentide ice sheet, as predicted by Mitrovica et al. (1994). However, the calculated signal may overpredict reality, due to the neglect of any lateral structure in the Earth model; see section *A GIA case study with a Fennoscandian 3D Earth structure* below. The negative sign of the horizontal deformation indicates motion in an easterly direction. The non-zero magnitude of predicted deformation at the present day simply implies that the system has not yet returned to equilibrium following the removal of the far-field ice load.

The vertical deformation peaked at 18 ka BP, coincident with the maximum extent of the Laurentide ice sheet. The steady increase in the signal over time is a result of the gradual growth of the Laurentide ice sheet throughout the last glacial cycle. The magnitude of this deformation reached ~25 m for Earth models with a smaller lower mantle viscosity of $1 \cdot 10^{22}$ Pa s (models A, C and E), and only ~20 m for Earth models with a stronger lower mantle (models B and D). The strong lower mantle models demonstrate a slower, smaller response to loading, and a slower rate of recovery following unloading.

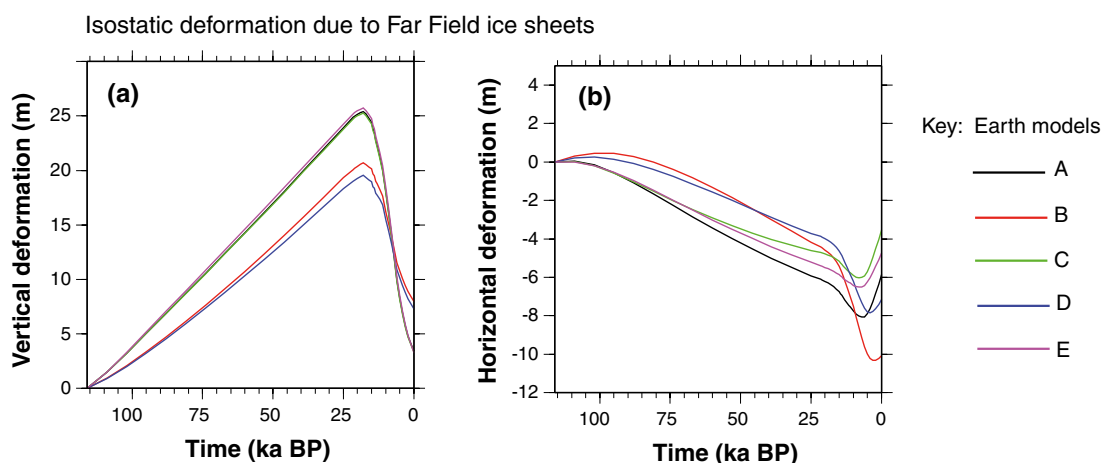


Figure 2-28. Solid surface deformation at Forsmark due to far-field ice loading. See Table 2-5 for a description of the Earth models used. a) vertical deformation, b) horizontal deformation.

This separation in the style of deformation according to lower mantle viscosity is also seen in the smaller horizontal signal (Figure 2-28b). When a stronger lower mantle is assumed, the magnitude of deformation is smaller during the majority of the glacial cycle, except during deglaciation, when the recovery of the solid Earth is delayed by ~ 10 ka for these models. The reason for this is unclear, but should provide a useful constraint upon lower mantle viscosities when testing predictions against data. In general, horizontal deformation peaks later than vertical deformation; at ~ 14.5 ka BP for models with a weaker lower mantle, and ~ 4 ka BP for models with a stronger lower mantle. A greater magnitude of horizontal deformation is predicted for models with a thinner lithospheric thickness of 96 km (as opposed to 120 km), but the absolute magnitude of the difference is small, and this phenomenon is not apparent in the vertical signal.

The magnitude of the far-field signal is small in comparison with predictions of near-field isostatic deformation (less than 10% of the total signal) during the Weichselian glaciation, but must not be neglected.

A GIA case study with a Fennoscandian 3D Earth structure

Note that in this 3D Earth structure case study, adapted from Whitehouse (2009), the overall aim is to investigate the sensitivity of GIA predictions to lateral Earth structure. To this end a comparison is made between dedicated 1D and 3D GIA simulations where the Earth structure has been specifically adjusted in order to give a relevant comparison between the two models. In turn, this means that the Earth structures have not been selected to give a best fit of e.g. uplift rates and shore-level displacement against observed data. Also note that the 1D–3D comparison study described here uses another ice sheet load history than the Weichselian glacial cycle used in the 1D simulations described in previous parts of Section 2.2.4.

State-of-the-art GIA models that account for 3D Earth structure use a range of geophysical observables to infer lateral variations in lithospheric thickness and mantle viscosity. Rayleigh wave dispersion data have been used to indicate variations in the thickness of the seismic lithosphere in Fennoscandia (Calcagnile 1982), while coherence studies have been used in the same region to study gradients of flexural rigidity and elastic thickness (Poudjom Djomani et al. 1999, Watts 2001, Pérez-Gussinyé et al. 2004). Fennoscandian lithospheric thickness variations, derived from elastic thickness estimates, are shown in Figure 2-29.

A first-order observation from GIA studies that include 3D Earth structure is that lateral variations in mantle viscosity affect the magnitude, but not the pattern, of GIA-related *uplift* rates, whereas they affect both the magnitude and direction of *tangential* velocity rates (Kaufmann and Wu 1998, 2002, Kaufmann et al. 2000, Latychev et al. 2005b, Whitehouse et al. 2006). A case study into the effect of including realistic Earth structure in Fennoscandian GIA models is presented here.

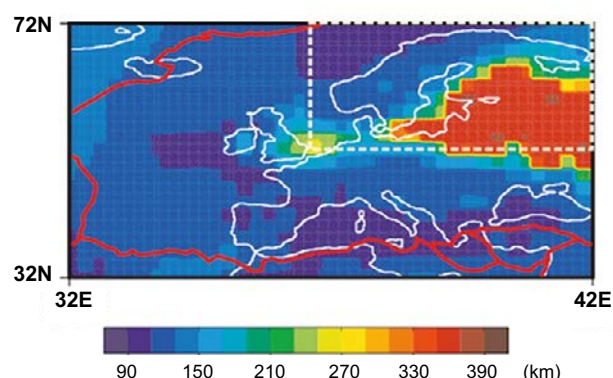


Figure 2-29. Lithospheric thickness derived from the elastic thickness model of Watts (2001) and Pérez-Gussinyé et al. (2004). This is part of a global model where the thicknesses have been scaled to ensure a global mean lithospheric thickness of 120 km. The red lines define plate boundaries. The dashed area is used to define a Fennoscandian regional model studied in Whitehouse (2009) (see text).

The sea-level theory presented in Mitrovica and Milne (2003) was implemented using the 3D finite volume model of Latychev et al. (2005a) to solve the sea-level equation on a spherical, rotating Earth. Even though this study focuses upon Fennoscandia, global calculations were carried out to ensure the correct redistribution of meltwater throughout the oceans. To give a global ice-loading history for the whole of the last glacial cycle that is tuned to fit global ice volumes as determined using far-field sea-level data (Bassett et al. 2005), the ICE-3G global ice model of Tushingham and Peltier (1991) was used for all ice sheets except in Fennoscandia where the ice model of Lambeck et al. (1998) was used, see Figure 2-30.

Calculations were initially carried out using a 1D Earth model with a lithospheric thickness of 120 km, an upper mantle viscosity of $5 \cdot 10^{20}$ Pa s, and a lower mantle viscosity of $5 \cdot 10^{21}$ Pa s. The calculations were then repeated using an Earth model that includes lateral variations in lithospheric thickness and mantle viscosity, and attempts to account for the presence of plate boundaries. The 3D Earth model was derived using estimates of elastic thickness as a proxy for lithospheric thickness, and seismic velocity anomalies as a proxy for mantle viscosity. Plate boundary zones are defined to be 200 km-wide bands of low ($2 \cdot 10^{20}$ Pa s) viscosity within the lithosphere. Portions of this model are shown in Figure 2-29.

A scaling method was used to ensure that the 1D and 3D Earth models have the same depth-averaged mean structure; thus permitting a meaningful comparison of the results. For the lithosphere, this means that the elastic thicknesses of the 3D model were multiplied by a uniform constant to ensure that the global mean lithospheric thickness is still 120 km. This results in the use of lithospheric thicknesses of more than 300 km for the Fennoscandian shield: these values are larger than independent estimates (e.g. Calcagnile 1982), but it should be noted that this study was carried out to explore the sensitivity of GIA calculations to variations in lateral Earth structure, and does not seek to accurately replicate the global 3D Earth structure.

For the mantle, the logarithm of the lateral viscosity perturbations at each depth (the calculations are carried out upon a finite volume grid) are multiplied by a uniform constant to ensure the mean for that depth is the same as in the 1D model. For further details of the construction of the Earth model see Whitehouse et al. (2006).

Figure 2-31 shows the predicted present-day uplift and horizontal deformation rates for Fennoscandia generated using the 1D Earth model. Uplift is centred upon the region of maximum ice-loading, and horizontal deformation exhibits a radial pattern of motion away from the centre of uplift.

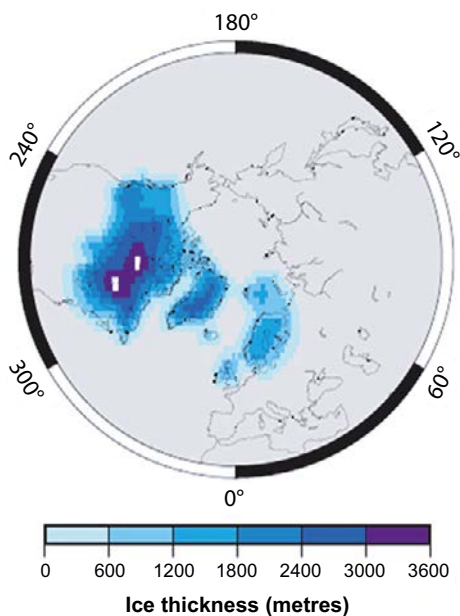


Figure 2-30. Ice thicknesses in the Northern Hemisphere at the LGM (20 ka BP). From the models of Tushingham and Peltier (1991) and Lambeck et al. (1998).

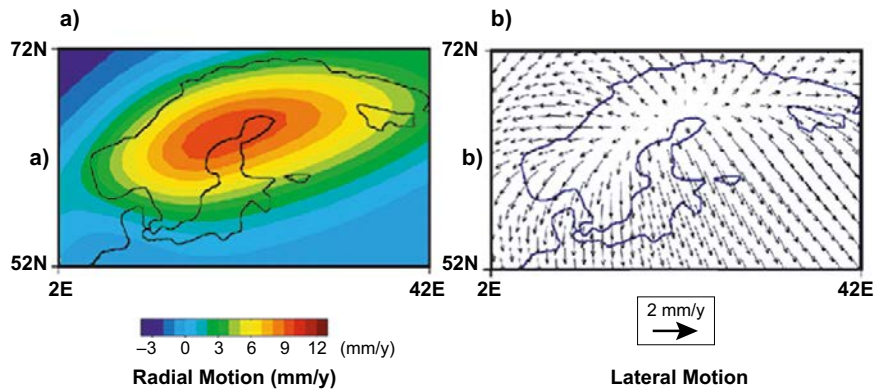


Figure 2-31. Predicted present-day uplift rates (a) and tangential rates (b) generated using the best-fitting 1D Earth model for Fennoscandia and the ice model discussed in the text. Tangential rates are given relative to a point on the north coast of the Gulf of Bothnia.

Figure 2-32 shows the misfit in present-day vertical and horizontal deformation rates between the 1D and 3D models. Note that the maximum differences of ~ 3 mm/yr for uplift rates and ~ 1 mm/yr for horizontal rates are greater than the current limit of observational uncertainty (e.g. from GPS measurements), implying that any inferences of Earth structure obtained from the inversion of geodetic data will be biased if a 1D profile is assumed.

In Figure 2-32 the 1D model predictions are subtracted from the 3D model predictions, therefore the blue region surrounded by the orange band in Figure 2-32a indicates that the 1D model predicts higher maximum uplift rates and lower minimum subsidence rates (more negative) than the 3D model. The differences are predominantly related to the magnitude of the predictions, and not the pattern, indicating that the introduction of lateral Earth structure has little effect upon the geometry of predicted uplift rates. However, in Figure 2-32b the change in the direction of the arrows indicates that both the magnitude and the pattern of horizontal deformation are perturbed with the introduction of realistic lateral Earth structure.

The question of whether it will be possible to constrain 3D Earth structure via GIA modelling remains open. The large number of degrees of freedom means that it is unlikely to be possible to carry out a unique inversion to determine the 3D viscosity structure using GIA observables. Wu et al. (2005) claim that the 3D Earth structure can be resolved using relative sea-level data from the centre of present-day rebound. However, this is disputed in other studies e.g. Spada et al. (2006) and Whitehouse et al. (2006), due to the similarity of the effect of lateral structure at different depths upon GIA observables. We investigate this aspect of GIA modelling below.

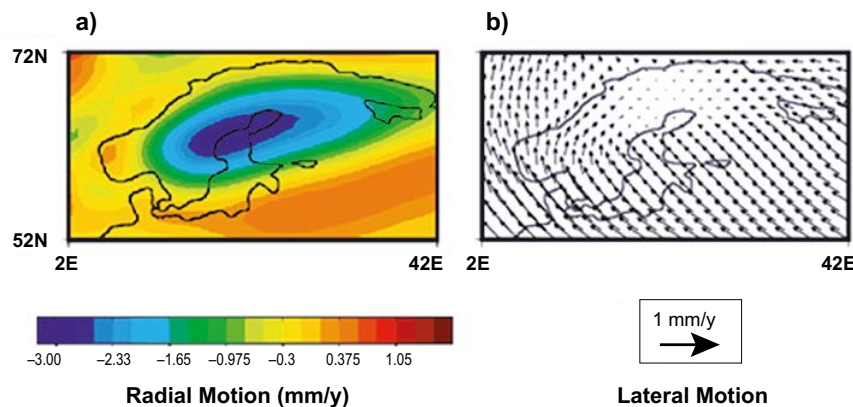


Figure 2-32. Misfit between (a) uplift rates and (b) tangential rates generated using a 3D Earth model and a 1D Earth model. 1D rates are subtracted from 3D rates.

Figure 2-33 again shows the difference (3D minus 1D) between predicted vertical (left) and horizontal (right) deformation rates. A different aspect of the 3D model is varied in each row. In the first row (Figure 2-33a) lithospheric thickness variations are permitted in the 3D calculations, but upper and lower mantle viscosities are held at the uniform values of the 1D model. In the second row (Figure 2-33b) a band of low viscosity is defined within the lithosphere along plate boundaries to replicate the weak stress-coupling across these regions. Other parameters are fixed at the 1D values. In the third row (Figure 2-33c) upper mantle viscosities are allowed to vary laterally whereas the lower mantle viscosity and lithospheric thickness are held fixed, while in the fourth row (Figure 2-33d) lower mantle viscosities are allowed to vary while the upper mantle viscosity and lithospheric thickness are fixed. In the first, third and fourth cases, weak plate boundary zones are not included.

The similarity of Figure 2-33a and c, both in the magnitude of uplift differences and the direction of the horizontal misfit arrows, indicates that lateral Earth structure at different depths can produce similar velocity perturbations in Fennoscandia. Therefore, it is unlikely that observations of present-day deformation rates will be able to uniquely infer the underlying Earth structure, or indeed identify the depth of any lateral heterogeneity.

The pattern in Figure 2-33d does not replicate the distribution of LGM ice-loading as in the previous cases, indicating a lesser dependence upon local ice-loading at lower mantle depths. Due to the transmission of stress, the lower mantle in Fennoscandia will play a part in supporting ice-loading in North America as well as Fennoscandia, and the pattern of horizontal perturbations, directed towards North America, reflects this.

The introduction of weak plate boundary zones induces a significant perturbation in horizontal deformation rates, but not vertical rates (Figure 2-33b). The reason for this is that the band of low viscosity decouples the transfer of stress across the plate boundary; the direction of the misfit arrows again reflect the non-negligible effect of North American ice-sheet loading upon surface deformation in Europe. Uplift rates have a strong local dependence upon loading; hence there is no perturbation to these rates when plate boundaries are introduced.

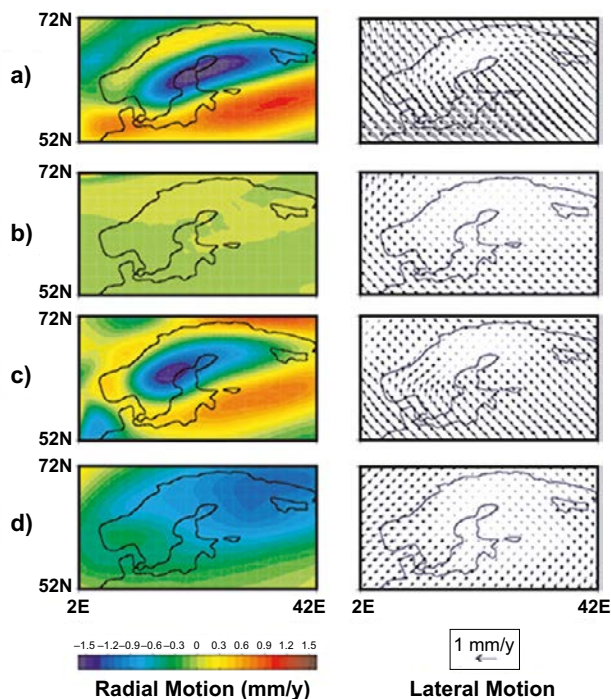


Figure 2-33. (a) Misfit due to lateral variations in lithospheric thickness. (b) Misfit due to the inclusion of weak plate boundary zones. (c) Misfit due to lateral variations in upper mantle viscosity. (d) Misfit due to lateral variations in lower mantle viscosity. Left column: difference in uplift rates. Right column: difference in horizontal rates. All plots show 3D predictions minus 1D predictions.

The effect of introducing lateral Earth structure at different depths has an approximately linear cumulative effect upon present-day deformation rates. This may be deduced by observing that within the region of uplift the sum of the perturbations in Figure 2-33 approximately equals the cumulative effect (Figure 2-32a).

Predictions of relative sea-level history for the last 10 ka are also compared for the 1D and 3D models. Figure 2-34a shows the perturbation to relative sea-level predictions at 10 ka BP due to the inclusion of lateral Earth structure (3D prediction minus 1D prediction). There is again a strong correlation between the pattern of ice loading and the region of maximum perturbations, and there is also a large positive misfit to the east of Fennoscandia in the region of maximum lithospheric thickness (Figure 2-29). Once again, the magnitude of perturbations due to the introduction of lateral Earth structure is greater than the observational uncertainty of relative sea-level data, which can be up to 10 m. Therefore, the results show that inverting relative sea-level data to yield inferences as to Earth parameters or ice-loading history will lead to biased results if lateral structure is neglected.

Along the Norwegian west coast there is very little difference in predictions of relative sea-level by the two models from 10 ka BP to the present day. In the top left plot of Figure 2-35 the relative sea-level history for a coastal site with good relative sea-level data (Bjugn: shown by the left-hand star in the bottom plot of Figure 2-35) is plotted for the whole of the Holocene. The black line is the prediction from the 1D model and the red line is the prediction from the 3D model. The similarity of the predicted sea-level history is characteristic for sites along the length of this coastline, indicating that introducing lateral Earth structure into the GIA model makes little difference to Holocene relative sea-level predictions for this region. Relative sea-level data from the Norwegian west coast may, therefore, form a data set that is insensitive to the 3D Earth structure of this region, and hence may be used to tune GIA model inputs such as 1D Earth structure and ice-load history. In this case, the poor fit to the data may be rectified by altering either the ice history or the depth-averaged viscosity profile of the Earth model.

The geographical region over which such data would be able to constrain input parameters is limited; it would be useful to also use relative sea-level data from within the Gulf of Bothnia to tune the GIA model. The predicted relative sea-level history for Ångermanälven is shown in the top right plot of Figure 2-35. Ångermanälven is the site of an extensive Holocene relative sea-level data set. It is situated on the east coast of Sweden (right-hand star in the bottom plot of Figure 2-35), in the centre of the region of maximum misfit for both uplift rates and relative sea-levels since 10 ka BP. The large difference between the relative sea-level history predicted by the 1D and 3D models during the last 10 ka indicates that using such data to tune GIA model inputs will lead to biased inferences of Earth structure and ice history if 3D structure is neglected.

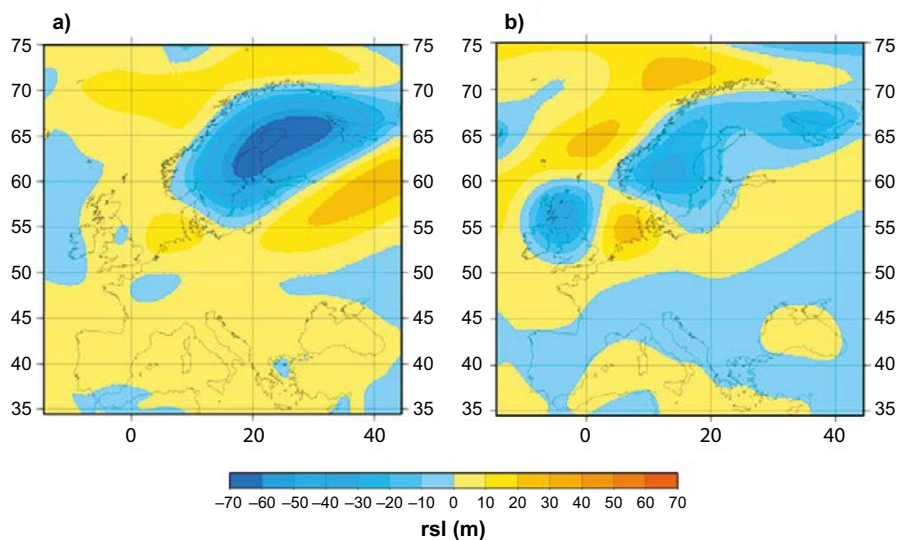


Figure 2-34. Difference in relative sea-level predictions at 10 ka BP. (a) 3D model minus 1D model. (b) 3D model minus 'regional' 1D model (see text).

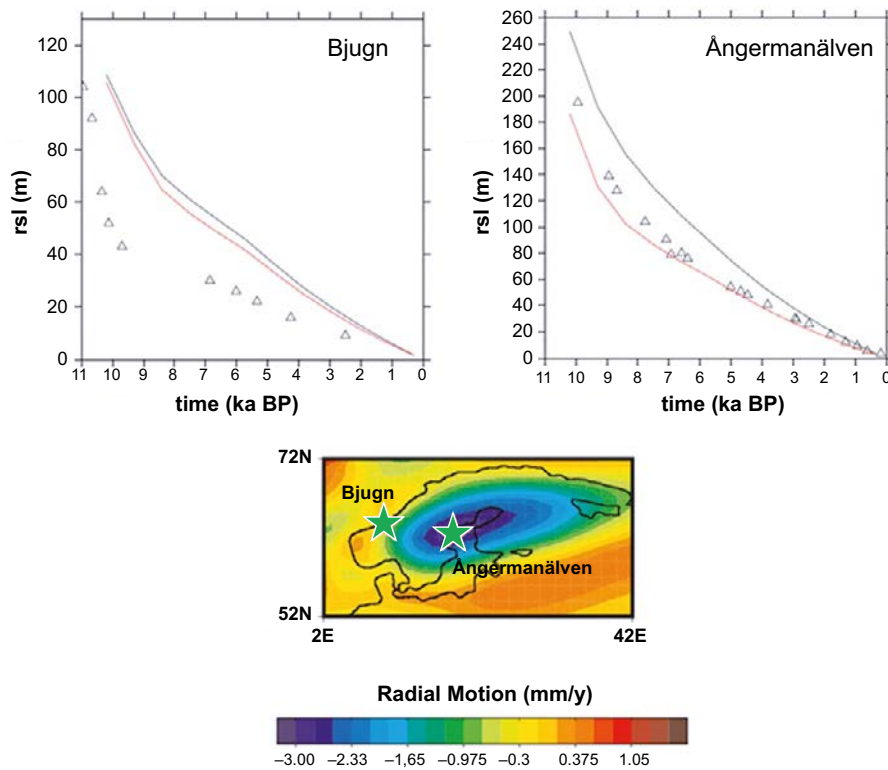


Figure 2-35. Top left: Predicted relative sea-level history at Bjugn for the last 10 ka. Black line: 1D model. Red line: 3D model. Top right: Predicted relative sea-level history at Ångermanälven for the last 10 ka. Line colours are as for Bjugn. Relative sea-level data are shown as triangles; see Lambeck et al. (1998) for references. Bottom plot: Location map for Bjugn and Ångermanälven overlaid upon the misfit in uplift rates (as for Figure 2-32a).

The difference in relative sea-level predictions for the 1D and 3D models is also plotted for Oskarshamn and Forsmark in Figure 2-36. To exemplify the magnitude of the error introduced by using a 1D Earth model instead of a 3D Earth model to predict relative sea-level, as done in the GIA studies, the difference at 10 ka BP is ~60 m at Forsmark (Figure 2-36).

The difference between 1D and 3D GIA simulations presented in this case study implies that ignoring lateral Earth structure and using a 1D Earth model in Fennoscandia leads to an over prediction of present-day uplift rates and the total amount relative sea-level change during deglaciation. This, in turn, conclusively shows that a significant part of the misfit between the 1D GIA model results and GPS observations arises from the 1D Earth structure approach. In addition, the misfit could also include a component of having too large an ice thickness in the Weichselian ice-sheet reconstruction. In line with this, one general interpretation of the results from the case study is that using a 1D model will lead to inferred LGM ice thicknesses that are too small. A second general interpretation is that the use of a 1D model will lead to overestimates of mantle viscosity or lithospheric thickness in an attempt to fit the observational GPS and relative sea-level data.

It is computationally demanding to solve the sea-level equation using a full 3D model; therefore there is ongoing work to determine to what extent we can continue to improve our understanding of GIA using flat Earth models or a suite of spherically-symmetric 1D models. Paulson et al. (2005) suggest that GIA observables within formerly-loaded regions are only sensitive to the local viscosity structure, and a global model that adopts the relevant local viscosity structure should be sufficient to model GIA in that region. The situation becomes more complex away from the centre of the former ice sheets because GIA in these regions seems to be dependent upon both the local viscosity structure and that beneath the ice sheets, which may be different. Thus, a model that allows for lateral variations in viscosity is required.

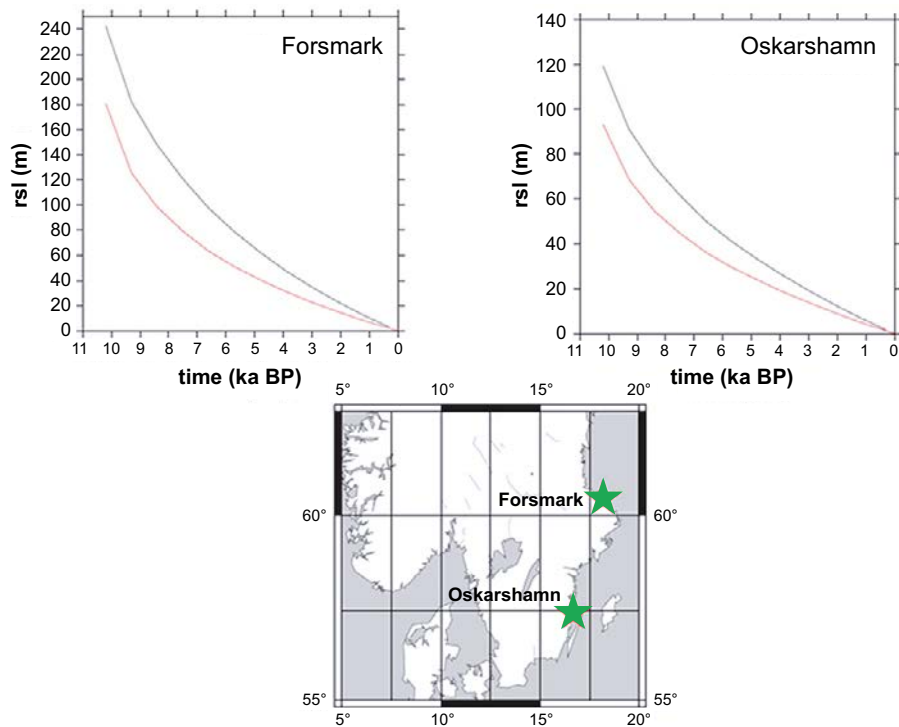


Figure 2-36. Predicted relative sea-level for Forsmark and Oskarshamn calculated using 1D (black line) and 3D (red line) Earth models. Note that both the 1D and 3D GIA simulations used for this plot use another ice load history than the 1D GIA simulations in the previous parts of Section 2.2.4. The results should only be used to exemplify the error introduced by using 1D instead of 3D GIA modelling. At Forsmark, the difference at 10 ka BP is ~60 m.

Modelling of future isostatic adjustment

The effect of sea-level rise and melting of the Greenland ice sheet in a future warmer climate (see Section 3.3) on Baltic shore-level was analysed in dedicated GIA simulations. In these simulations it is assumed that the Greenland ice sheet completely melts away at a linear rate during the coming 1,000 years, resulting in 7 m of global sea-level rise as a response to global warming. The rate of this melting may be different and likely non-linear and more complex than assumed here, however this does not influence the modelled long-term (glacial cycle time scale) shore-level signal at the Forsmark site.

In the GIA simulations made for the reconstruction of last glacial cycle conditions there was a discrepancy between the GIA results on modelled present-day uplift rates and present uplift rates as observed by GPS measurements. As described above and in Whitehouse (2009), it was shown that the discrepancy was partly due to the fact that a laterally homogeneous Earth model (2D Earth model) was used in the GIA simulations. A 3D modelling approach significantly reduces this discrepancy. Another contributing factor to the discrepancy can be a too large an ice load provided to the GIA model from the ice-sheet model. By sensitivity tests made in SR-Can using the GIA model, it was found that a reduction in ice thickness to 80% of the value in the reconstruction of last glacial cycle conditions yielded GIA results on present uplift rates that were in accordance with the observed present-day uplift. Even if a large part of the discrepancy now can be attributed to the 2D GIA modelling approach, an 80% reduction in ice-sheet thickness was used in the GIA modelling for a future warmer climate. However, this is judged as not having a large impact on the usefulness of the results on relative sea-level, given the large uncertainty interval presented for the results.

In line with the approach used in the GIA modelling of the reconstruction of the last glacial cycle, the GIA model was initiated by running one full glacial cycle in order to obtain realistic initial uplift rates. This was followed by linear melting of the Greenland ice sheet over 1,000 years, inducing corresponding changes in global sea-levels. This was followed by a 50 ka long period of no change to the loading model, simulating a warm global climate without a Fennoscandian ice sheet forming.

Finally a second full glacial cycle was added in the simulation. No contribution from thermal expansion of oceans or melting of glaciers and the West Antarctic ice sheet was included, which adds an uncertainty to the results, see below.

After the GIA simulation, the relative shore-level curve from the GIA model for the initial thousands of years was combined with extrapolation of observed shore-level data for the present day (Pässe 2001) in order to produce the final shore-level curve for a future warm climate (Figure 2-37). In the GIA simulation, the rise in global sea-level due to the melting of the Greenland ice sheet does not result in a sea transgression at Forsmark. This is due to the counterbalancing gravitational effect associated with the removal of the mass of the Greenland ice sheet (Milne et al. 2009, Whitehouse 2009).

Milne et al. (2009) studied the spatially variable change in sea-level assuming a melting of the Greenland ice sheet, and predicted a ~0 mm/yr sea-level change in the region of Fennoscandia. This is in line with the results of the GIA modelling performed for a future warmer climate, where the isostatic rebound is larger than the sea-level rise even when including a 1,000 year long complete melting of the Greenland ice sheet. The results show that the Forsmark site is situated above sea-level basically for the entire coming 100 ka under the assumptions made in this simulation.

However, here it is important to note that there are large uncertainties in the shore-level curve presented in Figure 2-37. They relate to uncertainties and assumptions made in the GIA modelling and also to the uncertainties in present knowledge on future global sea-level rise discussed above. The main uncertainty in future global sea-level rise is, as described above, related to the uncertain response of the Greenland and West Antarctic ice sheets to global warming and to the contribution from ocean thermal expansion and dynamics. The assumed complete collapse of the Greenland ice sheet covers the uncertainty in the response of the most sensitive ice sheet. Nevertheless, the uncertainty in the shore-level curve may be up to several tens of metres. Shore-level evolution in Forsmark until the year 2100 AD and until 10 ka AP is discussed in more detail in Sections 3.3.3 and 3.3.4, respectively.

It should further be noted that the SFR repository is located below sea-level today, with a maximum water depth of 7.2 m over SFR1 and 5.3 m over the planned SFR3 (layout L2). Under the assumptions made in producing the data in Figure 2-37, the duration for a complete transformation to terrestrial conditions above the repository (SFR 1 and 3) is c 1200 years. However, it is not only the timing for a full transition that is of most interest for the safety assessment. For example, permafrost development could start prior to a full transition. For comparison, the third quartile, when 75% of the surface above SFR 1 and 3 has become land, takes c 600 years and requires a relative sea level change of 3.8 m.

Given the uncertainties described above, it is possible that, in contrast to what is shown in Figure 2-37, there might be an initial period of sea transgression at the Forsmark site in the future, lasting some thousands of years, before the isostatic uplift component starts to dominate. This would arise if substantial contributions to sea-level rise occurred from thermal expansion and loss of West Antarctic ice.

The future evolution of global-average and Forsmark sea-level is given in Section 3.3.

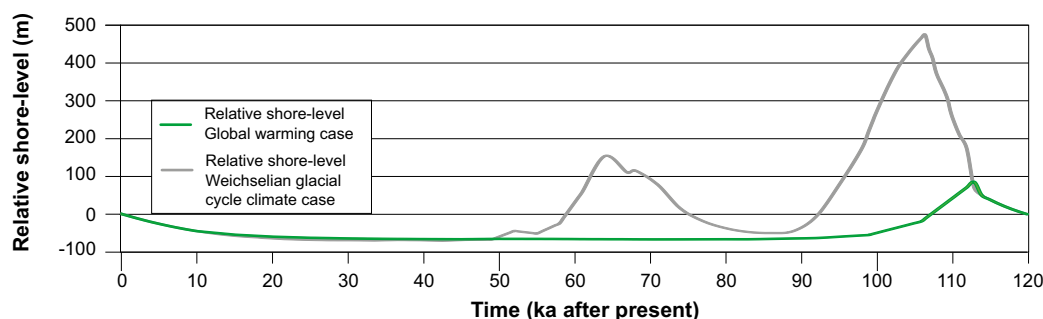


Figure 2-37. Shore-level evolution at Forsmark for a future warm climate. For comparison, the shore-level evolution for the reconstructed last glacial cycle, projected into the future as in the Weichselian glacial cycle climate case, see Section 4.4, is also shown. Negative numbers indicate that the area is situated above the contemporary sea-level. The curve was constructed by GIA modelling combined with results from observations of present-day uplift rates (Pässe 2001). There are significant uncertainties in the future shore-level development, which, in contrast to what is shown in the figure, may result in a sea transgression at Forsmark during the first thousands of years of the evolution.

2.2.5 Time perspective

Shoreline migration is an ongoing process. It is strongly coupled to the global distribution of water between the oceans and land-based ice sheets, and the isostatic response of the Earth to loading during a glacial cycle. This isostatic deformation is a slow process in relation to the rate at which ice sheets grow and decay during such a cycle.

As ice sheets grow, water is removed from the oceans and global eustatic sea-level falls. During the build-up to the last glaciation, eustatic sea-level fell at a mean rate of ~ 1.3 mm/yr between 120 ka BP and 20 ka BP (Fleming et al. 1998, Yokoyama et al. 2000, Clark and Mix 2002, Milne et al. 2002, Peltier 2002, Mitrovica 2003), although there were many departures from this rate during the build-up period, due to higher frequency climatic oscillations (Imbrie et al. 1984, Lambeck et al. 2002, Waelbroeck et al. 2002, Siddall et al. 2003). During deglaciation, the initial rate of eustatic sea-level rise between ~ 21 ka BP and 17 ka BP was only ~ 6 mm/yr, followed by an average rate of ~ 10 mm/yr for the next 10 ka (Fleming et al. 1998). Perturbations from this rate occurred during meltwater pulses at ~ 14.5 ka BP and ~ 11 ka BP. These are attributed to rapid melting events, during which rates of eustatic sea-level rise reached ~ 15 mm/yr (Fairbanks 1989, Bard et al. 1990, 1996, Clark et al. 1996, Fleming et al. 1998, Lambeck and Chappell 2001, Lambeck et al. 2002, Peltier 2005, Bassett et al. 2005). Rates of eustatic sea-level change fell to negligible values following the end of deglaciation around 5 ka BP. However, meltwater is not distributed uniformly throughout the oceans due to the alteration to the shape of the geoid following the redistribution of surface masses. Sea-level can actually fall at sites within $\sim 20^\circ$ of a melting ice sheet (Farrell and Clark 1976), therefore the rate of eustatic sea-level change is a poor indicator of local rates of sea-level change, especially for a local melt source.

The local rate of relative sea-level change incorporates both local changes in sea-level and the isostatic deformation of the solid Earth. The balance between rates of isostatic deformation and local sea-level change determine whether a site has advancing or retreating shorelines.

During the final build-up of the Fennoscandian ice sheet from ~ 32 ka BP, isostatic rates of solid Earth subsidence due to surface loading by ice are estimated to have reached values of 40 mm/yr (see Section 2.2.4). During future glacial cycles, modelling predictions imply that maximum rates will be attained immediately prior to the time of greatest ice thickness. In general, the time of maximum ice thickness is predicted to precede the time of maximum solid Earth deformation, with the latter being delayed by up to ~ 3 ka. During the period between maximum ice thickness and maximum deformation, the rate of solid Earth subsidence will decrease to zero.

There is usually a delay between the time of maximum deformation and the time at which a location becomes ice-free. Again, modelling predictions imply that as an ice sheet thins, rates of isostatic rebound will be low; < 20 mm/yr for this reconstruction of the Weichselian. Maximum rebound rates occur immediately following the final removal of an ice sheet, with uplift rates reaching ~ 75 mm/yr in this model at sites which had the greatest ice cover. The rate of rebound then decays exponentially with time; maximum rates at the centre of present-day uplift in Fennoscandia are ~ 10 mm/yr, and these are expected to decay to negligible values within the next 30 ka (see Section 2.2.4).

During a glacial cycle, immediately following the removal of ice, local uplift rates are far greater than the rate of local sea-level changes, consequently a situation of regression dominates, and shorelines migrate oceanwards. The rate of shoreline migration depends upon the local gradient of topography. A typical Swedish Baltic Sea shoreline with a gradient of 2 m of elevation per 1 km would experience 35 m/yr of oceanward shoreline migration for an uplift rate of 70 mm/yr, or 5 m/yr of oceanward shoreline migration for an uplift rate of 10 mm/yr (the present maximum in the Baltic region), assuming negligible changes in local sea-level.

A combination of decreasing rates of isostatic rebound and sea-level rise due to far-field melting slows the rate of regression with time, with a switch to transgression taking place if rates of local sea-level rise exceed the rate of local isostatic rebound. This situation is likely to arise during a global meltwater pulse at sites with low rebound rates, but will not be maintained because melting takes place on a shorter time scale than isostatic rebound. Rebound will once again become the dominant factor governing shoreline migration as sea-level changes become negligible. During the current interglacial period decaying uplift rates persist. These, along with processes related to ocean syphoning (see Section 2.2.1), act to maintain a situation of gradual oceanward shoreline migration throughout the majority of the Baltic region for the first few 10 ka of an interglacial so long as the higher interglacial temperatures do not give rise to a longer-term melting event, such as the destabilisation, and subsequent melting, of the Greenland ice sheet.

2.2.6 Handling in the safety assessment SR-PSU

Isostatic evolution and shoreline displacement have been investigated by means of numerical modelling. In this context, the main question for the safety assessment is whether the Forsmark site is submerged or not. The salinity in the lake/sea covering the site is also of interest. A 1D GIA model has been used to simulate shoreline migration. The evolution of the shoreline has been calculated for a glacial–interglacial cycle using a loading function based on the Weichselian ice sheet simulation described in Section 2.3.4. The GIA model used for generating the Weichselian glacial cycle is that developed by Milne (Mitrovica and Milne 2003). The *global* ice-loading function used in the study is modified from the ICE3G deglaciation history (Tushingham and Peltier 1991), and has been calibrated using far-field relative sea-level data. An eustatic sea-level history has been used to tune the mass of ice contained within far-field ice sheets. The Earth model is based on Maxwell rheology with a 1D radial three-layer structure. The lithosphere is represented by a 96 km thick layer with a very high viscosity and thus behaves as an elastic medium over GIA timescales, the density and elastic structure are from the preliminary reference Earth model (PREM) which has been determined to a high degree of accuracy by seismic methods (Dziewonski and Anderson 1981).

At the start of a GIA model run, the Earth is assumed to be in isostatic equilibrium. In reality, the Earth is unlikely to reach such a state if glaciations occur with similar periodicity as in the past. To correct for this, the GIA modelling has been initiated by a glacial loading history yielding shorelines comparable to those reported by Funder et al. (2002) at the peak of marine inundation in the Early Eemian about 130 ka before present.

Additional GIA simulations were also performed to describe shore-line variations for cases of global warming, assuming a complete melting of the Greenland ice sheet over a future period of 1000 years, see Section 2.2.4.

Complementary 3D GIA simulations have been made in order to quantify the error introduced by using a laterally homogeneous Earth model. The results show that the 1D modelling simulations probably over-predict the isostatic response to the ice-sheet load as well as present day uplift rates.

For the analysis of the biosphere and hydrological evolution, the shoreline evolution during the first thousands of years of the initial period with temperate climate domain is extrapolated from shoreline data (Pässe 2001), see Section 2.2.4. For further, detailed information on the GIA modelling, see the preceding parts of Section 2.2.4.

2.2.7 Handling of uncertainties in SR-PSU

Uncertainties in mechanistic understanding

The processes involved in GIA, and their effect upon shoreline migration, are well understood. There are no major uncertainties in our understanding of the mechanistic processes that cause shoreline migration.

Model simplification uncertainty

- Discussions of the uncertainty in the calculated shoreline are based on the sensitivity analysis and case study presented above. The assumption of a 1D Earth model is a simplification of the situation in Fennoscandia. A comparison between 1D and 3D GIA simulations (Whitehouse 2009) shows that the assumption of a laterally homogeneous (1D) Earth structure over Fennoscandia probably results in an over-prediction of the isostatic response to ice sheet load and present-day uplift rates. As an example, the 1D–3D GIA model comparison shows that the 1D simulation potentially overestimates the relative sea-level change over the last 10 ka by up to 60 m at Forsmark.
- The time discretisation of the basic loading model is fairly coarse (every 7 ka) between 116 ka BP and 21 ka BP, reflecting the lack of constraints upon ice history and sea-level prior to the LGM. If long time steps are used the loading function may be under- or over-estimated, leading to inaccuracies in relative sea-level, and hence shoreline migration, predictions for this period. A higher time resolution has been investigated, and discrepancies in relative sea-level predictions may be up to 50 m between a model that uses a time step of 7 ka and one that uses a time step of 1 ka, during periods of rapid change in ice-sheet geometry. However, using a coarse time scale during the early stages of a model run has a negligible effect upon predictions of relative sea-level change during the latter stages of a model run. A high resolution time scale has been used for ice loading since the LGM, i.e. for the period when the ice history is known reasonably accurately.

- At the beginning of a model run, the Earth is assumed to be in a state of isostatic equilibrium, with no deformation remaining from a previous glacial cycle or any other process that upsets the isostatic balance of the system. In reality, as the Earth enters each glacial cycle it will be pre-stressed, with deformation ongoing as a result of the previous loading event. GIA-induced deformation decays over a few tens of thousands of years, and after this period there will be a negligible difference between predictions from a model that started from equilibrium and one that was pre-stressed. However, in order to reproduce the relative sea-level evolution for the Weichselian as closely as possible the model was run twice in succession, with the second run taken to represent the Weichselian development. Nevertheless, a degree of inaccuracy remains at early times in the model since deformation will depend upon the details of the Saalian deglaciation, about which information is scarce.

Input data and data uncertainty

As demonstrated by the similarity of the shoreline predictions for a range of rheological parameters in Section 2.2.4, uncertainties in the lithospheric thickness and mantle viscosity parameters exist. However, these uncertainties are judged as being of limited significance compared to e.g. the major uncertainties in future eustatic change.

2.2.8 Adequacy of references

The SR-Site (SKB 2010a) and SR-Can (SKB 2006a) Climate reports, from which the studies are taken, has undergone QA system handling including a factual review process. Also the SKB report produced for the handling of isostatic adjustment and shore-level changes (Whitehouse 2009) has undergone the SR-Site QA system handling, including a documented factual review procedure. Other references used for the handling of ice-sheet dynamical processes are peer-reviewed papers from the scientific literature.

2.3 Ice-sheet dynamics

2.3.1 Overview/general description

Glaciers and ice sheets may form in climate regions where, in places, the winter snow precipitation is not completely melted away during summer. A glacier is an ice mass that has been formed by successive local accumulation of snow, with ice movement due to ice deforming under its own weight. An *ice sheet* is defined as a glacier that spreads out in all directions from a central dome, i.e. a large glacier (> 50,000 km² in area) that is not confined by the underlying topography. In reality, the flow pattern of ice sheets is not radial from a single dome. Instead, ice often flows out from a number of elongated *ice divides*, with the ice divides constituting the highest parts of the ice sheet.

Generally, ice-flow velocities are moderate to slow within an ice sheet, with ice moving a few tens of metres per year. However, certain well-defined parts of ice sheets, so called *ice streams*, exhibit significantly faster ice flow. Ice streams are typically some tens of kilometres wide and several hundreds of kilometres long. Ice velocities within present-day ice streams are several hundred metres per year, in some cases exceeding 1,000 m a⁻¹ (cf. Joughin et al. 2004). Since surrounding ice typically moves considerably slower, high velocity gradients across the ice stream margins produce distinct *shear zones* with heavy crevassing. Because of the high ice flux in ice streams, these features may drain large portions of ice sheets. Ice streams are often characterised by specific basal thermal and hydrological conditions, differing from those of the surrounding ice sheet.

The margin of an ice sheet may be either on land or in water. If the ice margin is positioned in the sea or in a lake, it is common that the outer part of the ice sheet is floating on the water, constituting an *ice shelf*. The boundary between the floating and grounded ice is the ice sheet *grounding-line*.

If the basal thermal and topographical conditions are favourable, sub-glacial melt water may accumulate in topographic lows beneath the ice, forming *sub-glacial lakes*. These are common features under the present Antarctic ice sheet, whereas none have so far been found beneath the Greenland ice sheet.

Mass balance

The growth and decay of ice sheets are determined by the *mass balance* of the ice mass. The mass balance constitutes the result of the mass gain, or *accumulation*, and the mass loss, or *ablation*, typically averaged over one year. The mass gain of an ice sheet is completely dominated by the process of snow accumulation. Most of the snow falls and accumulates during winter seasons, but snow may also accumulate during summer. For ice-sheet ablation on the other hand, a number of processes may be involved, the two most significant being surface melting of snow and ice (if the summer climate is warm enough) and calving of ice bergs from ice shelves (when the margin is at the sea). In addition, mass may also be lost from the ice sheet by melting of basal ice, and locally on the surface by sublimation of ice and snow. When a certain part of an ice sheet exhibits more accumulation than ablation during one year, that part is said to belong to the *accumulation area* of the ice sheet. This is in contrast to the *ablation area*, where there is a net loss of mass during one year. Central parts of ice sheets typically constitute accumulation areas, whereas in case of surface melting, lower parts of ice sheets constitute ablation areas (Figure 2-38). The line between the accumulation and ablation areas is called the *equilibrium line*.

If the total ice-sheet accumulation is greater than the total ablation during one year, the mass balance is said to be positive, whereas the opposite case produces a negative mass balance. If accumulation and ablation are equal, the mass balance is zero.

A positive mass balance over a number of years makes an ice sheet grow, whereas a negative mass balance reduces its size. However, changes in the size of ice sheets are very slow occurring over hundreds and thousands of years. The *response time* of an ice sheet is the time it takes for a steady-state ice sheet to come to a new steady-state condition after a climate change. It is often defined to represent the time to reach a near-steady state representing e.g. 90% of the change to equilibrium. Since climate is constantly changing, ice sheets are never in true steady-state, but are constantly adjusting their size and shape to the prevailing climate.

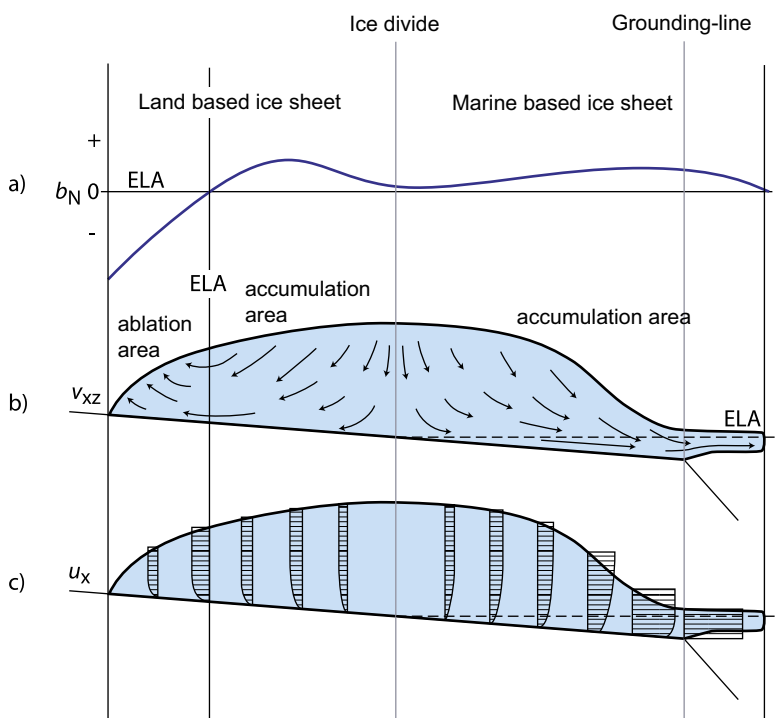


Figure 2-38. Schematic ice sheet cross section. Panel a) shows the surface net balance distribution (b_N), panel b) shows ice velocity trajectories (v_{xz}) as well as distribution of accumulation- and ablation areas, and panel c) shows the horizontal velocity component (u_x). ELA denotes equilibrium line altitude. Modified from Holmlund and Jansson (2003), after Denton and Hughes (1981).

Ice temperature. The temperature of the ice is of fundamental importance for the behaviour and characteristics of glaciers and ice sheets. Among other things, it has a strong effect on the movement, dynamics and hydrology of the ice. Two types of glacier ice can be defined based on temperature; 1) *Temperate ice* (or *warm ice*) with the ice temperature at the pressure melting point, and 2) *Polar ice* (or *cold ice*) with the ice temperature below the pressure melting point. Cold ice is harder than temperate ice and also impermeable to water unless crevasses are present.

Glaciers and ice sheets are often classified according to their thermal characteristics. A glacier where all ice has a temperature at the pressure melting point throughout the year is called a *temperate glacier* or *temperate ice sheet*, whereas a glacier in which all the ice is below the pressure melting point throughout the year is called a *polar glacier* or *polar ice sheet*. However, an ice sheet or glacier need not consist exclusively of temperate or polar ice. In many cases, it can contain both ice types, and in such a case it is called *polythermal*.

Of particular interest is the temperature of the ice at the ice-sheet bed, i.e. the basal thermal condition. An ice sheet can be *cold-based* or *warm-based*. A cold-based ice sheet has cold basal ice and it is frozen to its bed. There is no free water at the bed, and no sliding of basal ice over the substrate is taking place. A warm-based ice sheet is at the pressure melting point at the bed. Free water is, in this case, present at the ice-bed interface, and the ice may slide over the substrate. This has important consequences both for ice kinematics and landform development. A polar ice sheet may be either cold-based or warm-based. In the case of a warm-based polar ice sheet, it is typically only the lowermost part of the ice that is at the pressure melting point, whereas most of the ice sheet consists of polar ice. One part of a polar ice sheet may thus be cold-based at the same time as other parts are warm-based. This is the present case for the Greenland and Antarctic ice sheets. Warm-based and cold-based ice sheets are also called *wet-bed ice sheets* and *dry-bed ice sheets*.

Glaciers and ice sheets experience melting of basal ice where the basal ice temperature is at the pressure melting point. Heat for this melting can be added from geothermal heat flux and from frictional heating by internal deformation of basal ice. The thermodynamic situation at the base of an ice sheet is determined by the thermal properties of the ice. Energy can be transferred by diffusion along a temperature gradient in ice as in all materials. However, the solidus of the ice-water vapour phase space has a negative slope, which means that the melting or freezing temperature is depressed with increasing pressure by 0.09 K/Pa. As a general statement, freezing of liquid water occurs when temperature and pressure satisfy the generalised Clapeyron equation (e.g. O'Neill and Miller 1985):

$$\frac{p_w - p_i}{\rho_w - \rho_i} = \frac{L}{273.15} T + \frac{P_o}{\rho_w} \quad (2-4)$$

where p_w = water pressure, ρ_w = water density, p_i = ice pressure, ρ_i = ice density, L = ice density coefficient of the latent heat of fusion, T = temperature in degrees centigrade, and P_o = osmotic pressure. Equation 2-4 couples the effect of temperature and pressure. It is a general thermodynamic relationship not specific for the case of ice sheets and glaciers. However, the phase change of the ice-water system is not only controlled by temperature and pressure. Two other factors may also be of importance; 1) the presence of solutes in water, and 2) surface tension arising from interface curvature. Just as in the case with an increasing pressure, an increase in solutes in liquid water also depresses the melting/freezing point. This effect is referred to as the osmotic pressure (e.g. Padilla and Villeneuve 1992), and it is included in Equation 2-5. If liquid water is present at the base of an ice sheet, and it contains solutes, this will, together with the pressure, modify the ice melting point. The second factor constitutes an ice/water interfacial effect. The finer the grains in a sediment, the higher the curvature of the ice-water interface becomes, which in turn lowers the melting point (Hohmann 1997). For example, in clays, liquid water has been observed at temperatures down to -10°C (O'Neill and Miller 1985).

If the effect of phase curvature is taken into consideration the Clapeyron equation may be modified to (Raymond and Harrison 1975):

$$T = -\frac{273.15}{L} \left(\frac{1}{\rho_i} - \frac{1}{\rho_w} \right) p_w - \frac{273.15 \sigma_{iw}}{L \rho_i r_p} - \frac{273.15}{\rho_w L} P_o \quad (2-5)$$

where σ_{iw} = ice-water surface energy, and r_p = characteristic particle radius. Equation 2-5 is the fundamental equation for the ice-water phase transition given by Hooke (2004). In this equation, the first

of the three terms describes the effect of pressure on the ice-water phase transition; the second term describes the effect of interfacial pressure; and the third term the effect of osmotic pressure. Equation 2-5 thus gives the complete treatment of the ice-water phase transition. Commonly only the first term is used for calculations of the pressure melting point beneath glaciers and ice sheets, often rewritten in glaciological literature to give a simplified expression for calculating the pressure melting point (cf. Remy and Minster 1993):

$$T = -\frac{h}{1503} \quad (2-6)$$

where T = pressure melting point temperature ($^{\circ}\text{C}$), and h = ice thickness (m). The effect of the lowering of the pressure melting point described above is, in the case of an ice sheet, that the melting point is lowered by c 2 K beneath 3 km of ice. This is very important, since the basal conditions change drastically if the bed of an ice sheet becomes melted or frozen. This affects ice sheet flow by turning on and off basal sliding; governs if glacial erosion can take place or not; and of course has a profound impact on basal hydrology.

To demonstrate the effect of ice-sheet surface conditions on the temperature distribution within polar ice sheets, we start with a simplified case of a steady-state ice sheet with no ice flow, corresponding to an artificial situation at an ice divide (no horizontal flow) without any precipitation (no vertical flow). Figure 2-39a shows the vertical temperature profile through such an ice mass given a surface temperature of -20°C and a specified geothermal heat flux at the base. The resulting temperature profile is a straight line from the surface temperature down towards the bed. In this case the vertical temperature profile reaches the pressure melting point temperature near the bed, resulting in a warm-based polar ice sheet.

Next we consider the same case but with snow accumulation at the ice-sheet surface, which means we are introducing a vertically downward directed ice movement. Generally, this lowers the temperatures within the ice sheet as seen in Figure 2-39b. Due to the vertical velocity and cold surface climate, cold ice is advected downward, while the geothermal heat warms this descending ice. The upper part of the ice sheet develops an almost isothermal zone, whereas the ice warms quickly near the bed. In this example the ice sheet below this accumulation area has become cold-based. Higher precipitation rates at the surface, i.e. higher vertical velocities, result in an increased thickness of the isothermal zone and also decrease the basal temperature. Furthermore, lower air temperatures at the ice-sheet surface also decrease the ice-column temperatures, and vice versa.

If we instead consider an ablation area, with net mass loss at the surface, the vertical ice movement will be directed upwards. In this case, the upward vertical velocity produces a generally warmer ice column, in this example resulting in temperate conditions at the bed (Figure 2-39c).

The last case to consider is a more realistic situation, when we also have horizontal ice movement. Figure 2-39d shows a typical situation within the accumulation area of an ice sheet, but not located directly on an ice divide. The horizontal velocity component is advecting cold ice into the site, ice that was formed in higher, colder parts of the ice sheet. Compared with the situation in Figure 2-39b, the minimum temperature is now found at some depth below the surface, since the ice at the surface, formed locally at the site, is warmer (Figure 2-39d). This positive temperature gradient near the surface has been observed in several deep drill holes, see for example the Mirny, Century 13, and Byrd 9 drill hole temperatures in Figure 2-40. Furthermore, due to the horizontal ice movement, ice in the lower part of the ice sheet is warmed by internal friction, as this is where most of the internal deformation of the ice is taking place. In this example, the ice sheet has again become warm-based.

Including these processes, the resulting englacial and subglacial temperatures along a flow line are as shown in Figure 2-41. Typical polar ice-sheet accumulation rates and air temperatures are assumed. The lowest englacial temperatures are found in the highest central parts of the ice sheet, and the highest ice temperatures are found near the margin. Basal melting may take place in the interior part of the ice sheet and close to the margin, with a zone of basal frozen conditions in between. A narrow zone of basal frozen conditions at the margin may also occur due to decreasing vertical velocity (not shown in Figure 2-41).

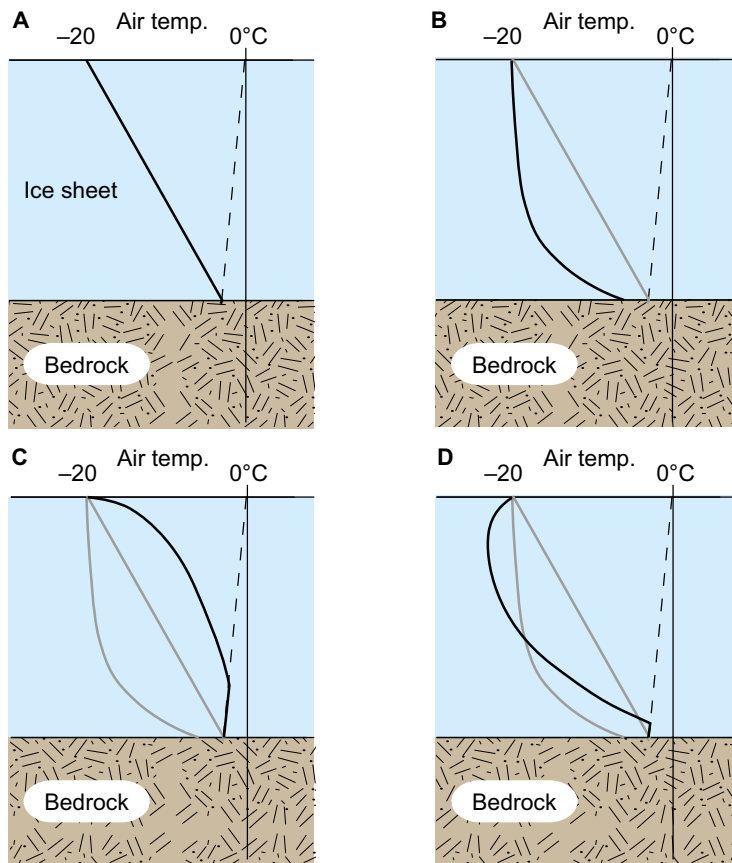


Figure 2-39. Vertical temperature profiles through a 2,000 m thick theoretical polar ice sheet. The dashed line denotes the pressure melting point temperature. a) No ice flow (dead-ice body), b) Vertical ice flow only – accumulation area (reflecting only a surface accumulation rate), and c) Vertical ice flow only – ablation area, d) Horizontal and vertical ice flow – accumulation area. Grey lines show the cases from the previous plates. Modified from Holmlund and Jansson (2003), after Sharp (1960).

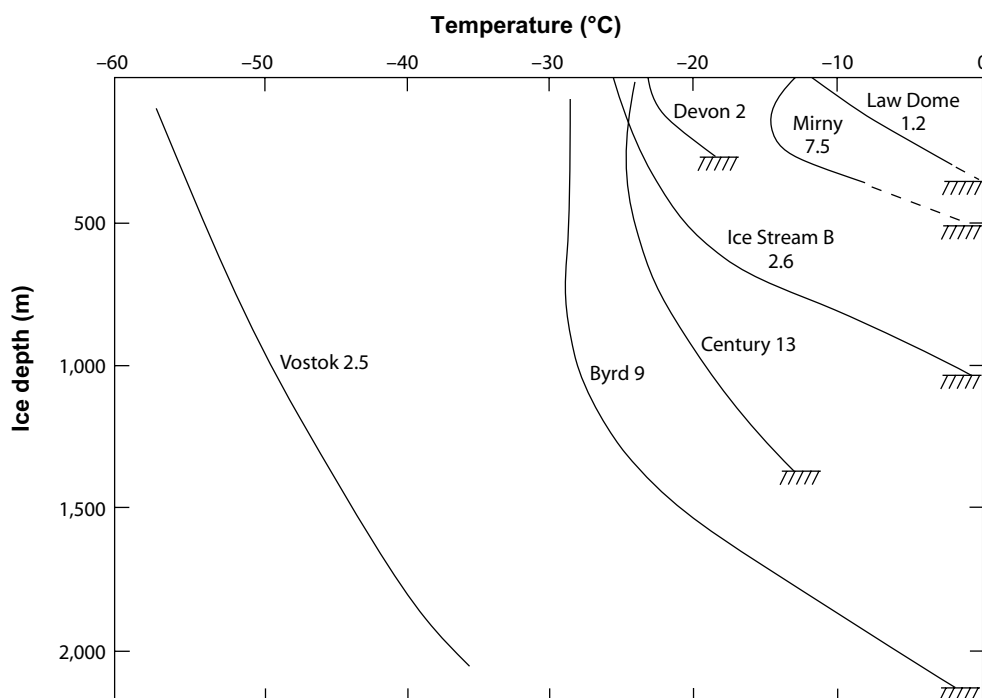


Figure 2-40. Borehole temperature data from the Greenland and Antarctic ice sheets. Modified from Holmlund and Jansson (2003), after Paterson (1994).

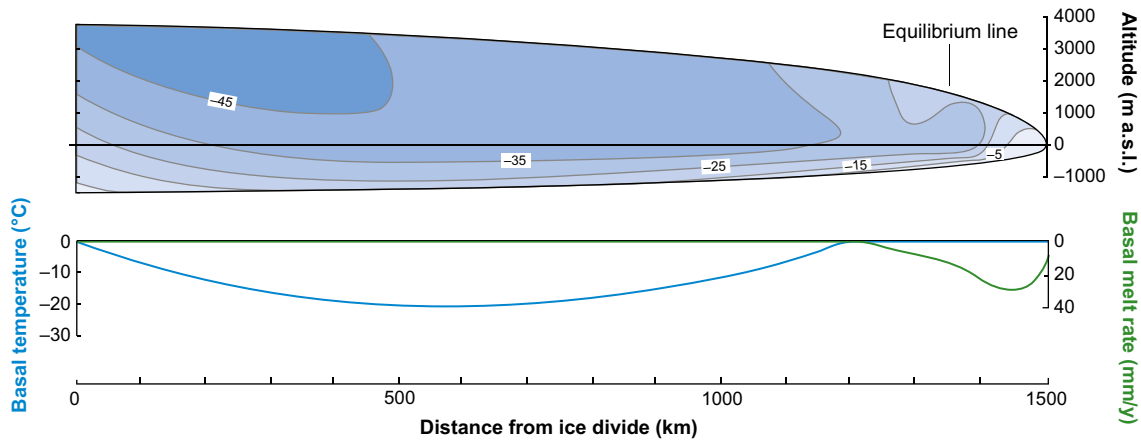


Figure 2-41. Example of modelled ice-sheet temperature distribution along a flow line. Ice temperatures are in °C. Basal melt rates are high near the terminus because of the strain heating effect from rapid ice flow in the region around the equilibrium line. Modified from Hooke (1977).

In nature, the topography of the landscape beneath the ice sheet is also of great importance for the basal temperature distribution. Topographic lows are more prone to experience basal melting conditions than topographic highs. This is both due to the fact that the pressure melting point is lowered more in depressions (due to the greater ice thickness and higher basal pressures) than over surrounding higher terrain, and due to the lower insulating capacity of thinner ice over topographic highs. The result is, for example, that the floor of a large valley in general is more likely to have experienced longer periods of basal melting than surrounding elevated areas (e.g. Näslund 1997).

An additional important process affecting ice temperature takes place if the air temperature allows surface melting during spring periods, for example at low elevations of an ice sheet in a warming deglaciation climate, or during times of early ice sheet formation. After the winter period with cold temperatures, the temperature in the upper snow/firn pack of the ice sheet is well below the freezing point. As surface melting starts, meltwater percolates down into the snow pack and re-freezes at some depth. During the re-freezing process, latent heat is released (334 kJ/kg, corresponding to the latent heat of fusion for ice) which warms the surrounding snow. As the process continues the entire snow pack can be transformed to temperate conditions during a few weeks. This is a very efficient process, and the result is that temperate ice instead of cold ice is formed at the location. This may have been an important process during build-up phases of Fennoscandian ice sheets, having an important effect on the thermal characteristics of early ice sheets (Näslund 1998).

Ice movement and thermodynamic feed-back. The stresses induced by the mass of overlying ice induce deformation or strain in the ice. The resulting ice movement, often referred to as *internal deformation*, is present in all glaciers (being one of the main criteria for the term *glacier*). The shear stress at the base of an ice sheet is calculated from:

$$\sigma = \rho gh \sin \alpha \quad (2-7)$$

where σ is the shear stress, g is the acceleration of gravity, h is the ice thickness, and α is the ice sheet surface slope. The most common flow law of ice describing the strain rate of ice under pressure is Glen's flow law (Glen 1955):

$$\dot{\epsilon} = \left(\frac{\sigma}{B} \right)^n \quad (2-8)$$

where $\dot{\epsilon}$ is the strain rate, σ is the shear stress, B is a viscosity parameter that increases as the ice gets more difficult to deform, a parameter depending on among other things ice temperature and crystal fabric, and n is an empirically determined constant (~ 3) that depends on the specific creep process that is operating. The main effect of Glen's flow law is that moderate increases in stress (ice thickness) result in a substantial increase in strain rate. For example, a doubling of the amount of stress results in 2^3 , that is 8, times higher deformation rate (Figure 2-42).

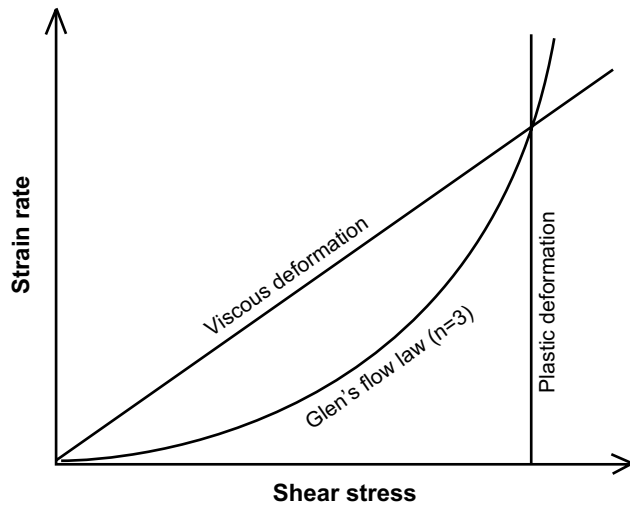


Figure 2-42. Deformation rate versus shear stress for various flow laws, including Glen's flow law for ice. Modified from Holmlund and Jansson (2003).

In ice sheets, the horizontal ice velocity increases from the ice divides, where it is zero, toward the margin. The steeper surface slope at the margin induces larger driving stresses which makes the ice deformation rate high. For an ice sheet with an ablation area, i.e. an ice sheet ending on land (Figure 2-38) the maximum horizontal velocity is at the equilibrium line, whereas in the case of a marine ice-sheet margin, the maximum velocity is at the ice sheet grounding-line (Figure 2-42).

The stress that acts on the uppermost layer of a glacier does not produce a plastic deformation. Instead the uppermost part of the ice, about 30–100 m thick depending on ice temperature, is brittle, often resulting in typical fractures, or *crevasses*. Most of the internal deformation takes place near the bed where stresses are highest. The overlying ice moves along more or less as a uniform block on top of the deforming ice. This is indicated as the internal deformation portion of the ice velocity in Figure 2-43.

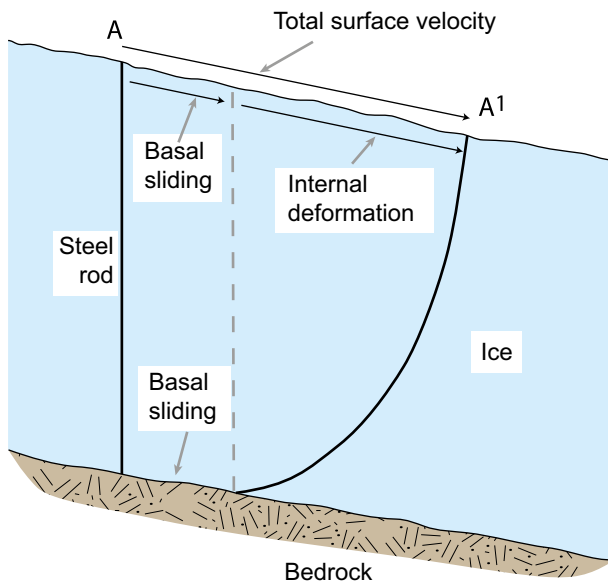


Figure 2-43. Internal deformation and basal sliding demonstrated by the deforming of a steel rod from time A to A'. Modified from Holmlund and Jansson (2003), after Sharp (1960).

There is also another process that may contribute to glacier movement. If the ice sheet is wet-based, the ice may slide over the substrate, and the substrate itself may deform, especially if the water pressure at the bed is high. The surface ice velocity is, in this case, the sum of the component from internal deformation and the component from basal sliding and deformation (Figure 2-43). For all practical purposes, one can assume that *basal sliding* does not occur if the bed is frozen. Therefore, not all glaciers, or all parts of an ice sheet, have the sliding ice-flow component. However, where it is present, it may be of great importance, for example in ice streams, which are typically warm-based. Here, the observed surface flow may be completely dominated by basal sliding (Engelhardt and Kamb 1998). High basal water pressures are favourable for intense basal sliding (Engelhardt et al. 1990), as well as smooth bed topographies and deformable, water-saturated tills (e.g. Kamb 2001, Iverson et al. 1995).

Within glaciers and ice sheets there are important thermodynamic feedback mechanisms, in the following exemplified by a discussion on ice streams. As seen above, the viscosity of the ice is affected by the ice temperature, with higher ice temperatures giving more easily deformable ice. At the same time, the internal deformation itself produces frictional heat, with higher velocities producing more heat. This gives a positive feedback mechanism; high internal deformation rates increase the temperature of the ice, which in turn makes the ice even easier to deform.

On the other hand, looking at the basal thermal conditions of ice streams, there may be additional thermodynamic processes acting. A fast-flowing warm-based ice stream may drain a lot of ice from the ice sheet. Over time this will reduce the thickness of the ice, also over the ice stream itself. The thinner ice insulates less well from cold surface temperatures, which leads to less melting at the bed, and eventually also to a shift from warm-based to cold-based conditions. This reduces the velocity of the ice stream considerably and the ice flux deformational heating reduces accordingly. The ice stream now drains much less ice than before, which in time results in increased ice thicknesses (Payne 1995). The larger ice thickness warms the bed, which again may become wet-based and basal sliding may start again. This process suggests that ice streams may have an inherited built-in unstable behaviour. It has been suggested as one explanation for the cyclic Dansgaard–Oeschger events recorded in glacial marine sediments (cf. Andrews and Barber 2002).

In addition, the dynamics of an ice sheet and, in particular, its ice streams, and the ice sheet response to changes in climate, are to a large degree governed by the prevailing subglacial hydrology. This field of knowledge is rapidly advancing, for instance through the Greenland Analogue Project providing observations and measurements from the western land-based sector of the Greenland ice sheet (SKB 2010e, Harper et al. 2011). One process that traditionally has not been incorporated in large-scale ice-sheet models is the coupling of longitudinal stresses within the ice (e.g. Pattyn 2003), i.e. upstream and downstream push and pull effects, a process of importance for proper modelling of ice streams and grounding-line features. Several recent ice sheet models have implemented this process.

2.3.2 Controlling conditions and factors

The upper boundary of the ice-sheet system is the ice-sheet surface, whereas the lower boundary is the ice-sheet bed, i.e. the interface between basal ice and substrate. In accordance with ice-sheet fluctuations, the lateral extent of these boundaries changes over time.

Upper boundary condition – Climate. The boundary condition at the ice-sheet surface is the prevailing climate, i.e. air temperature and precipitation, including its variation over time. The air temperature at the ice-sheet surface is determined mainly by the latitude, altitude and climate changes. The latitude at a site is fixed, but the altitude varies with the local thickness variations of the ice sheet and associated isostatic responses. The typical air temperature pattern over an ice sheet is with the lowest temperatures in the ice-sheet interior and higher surface temperatures closer to the margin. If temperatures are greater than 0°C during summer, surface melting takes place on the lower parts of the ice-sheet surface. This melting typically amounts to several m of ice per year, with large variations according to the prevailing temperature regime. Surface melt rates are lower closer to the equilibrium line. In general, during cold stages of ice-sheet growth, the amount of surface melt water production is small compared with the amounts of water produced during deglaciation under warmer climate conditions.

Most precipitation that falls on ice sheets falls as snow. During relatively warm climates at low ice-sheet elevations, precipitation may occur as rain. Snow accumulation and surface ablation are not distributed evenly over the ice-sheet surface. The precipitation pattern reflects ice surface elevation and degree of continentality, often giving a pattern of high accumulation rates close to the ice-sheet margin with diminishing values towards the interior. On mid-latitude ice sheets, like the former Fennoscandian ice sheet, the precipitation pattern is strongly affected by the prevailing west-wind belt and associated low-pressure tracks. This results in an orographic effect which gives most precipitation on the western side of large Fennoscandian ice sheets. Typical coastal accumulation rates of the Antarctic ice sheet are 0.3–0.6 m a⁻¹ (water equivalents), whereas the interior parts gets less than 0.1 m a⁻¹ in precipitation (Giovinetto and Zwally 2000), i.e. here polar desert conditions prevail. On an ice-sheet surface, regional and local variations of great magnitude in the amount of snow accumulation often occur, mainly due to wind re-distribution of snow in regions close to the ice-sheet margin (Figure 2-44).

To initiate ice-sheet growth in a non-glaciated region, the local climate needs to change. That can either occur due to global climate change, towards lower local summer temperatures, or higher winter precipitation rates, or, over long time scales, by tectonic uplift, or a combination of climate and tectonics. Generally, ice-sheet formation in Fennoscandia involves small alpine glaciers in the Scandinavian mountain range that grow into a mountain-centred ice sheet, and then grow to a full-scale ice sheet (Andersen and Mangerud 1989, Lundqvist 1992, Kleman et al. 1997). Increasing evidence suggests very dynamic ice sheet and climate behaviour during the last glacial cycle, with ice-sheet growth phases interspersed by extended periods with restricted ice coverage, see also Section 3.2.

Lower boundary condition – Ice-sheet bed. The lower boundary condition of the ice sheet system is the ice-sheet bed. The substrate typically either consists of bedrock, in Fennoscandia normally crystalline rocks, or bedrock covered by till. There are two important parameters to consider here; 1) the topography of the landscape and 2) the amount of geothermal heat flow.

The topography of the bed is of importance for the basal boundary conditions of ice sheets, as discussed above. Above all, an ice-sheet bed with strong relief produces basal thermal conditions with stronger lateral temperature gradients than an ice-sheet bed with smooth topography. The first case also implies larger spatial variations in basal melt water production.

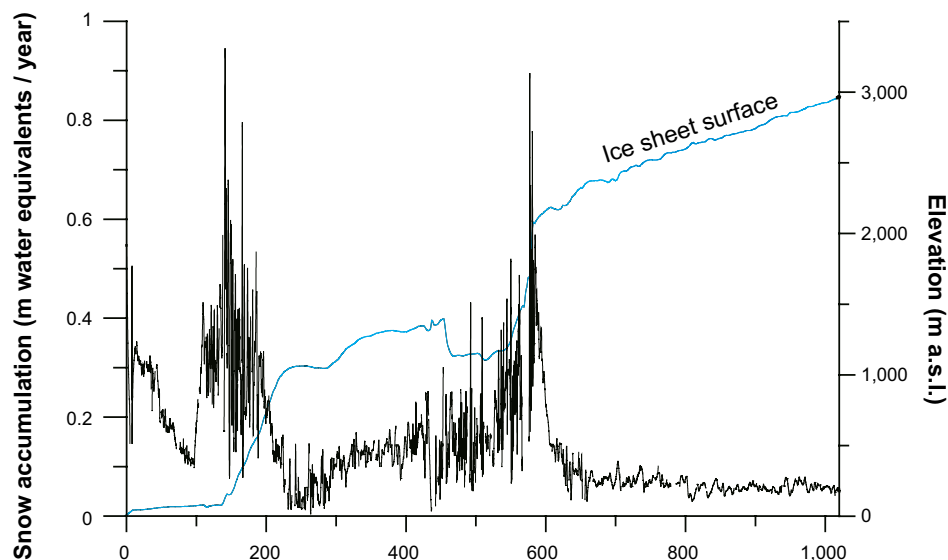


Figure 2-44. Accumulation rates and ice surface elevations along a profile in over the East Antarctic ice sheet. The accumulation is high in the coastal area and low in the interior. Due to wind redistribution of snow, exceptionally high values with strong variations are found in areas of nunataks and steep surface slope. From Richardson (2004).

The geothermal heat flux is also of great importance for the basal condition of ice sheets (e.g. Waddington 1987), affecting basal ice temperatures, hydrology, ice dynamics, and the erosional capacity of the ice. Typically, for a 3 km thick ice sheet at steady-state, a 20% error in geothermal heat flux generates a 6 K error in calculations of basal ice temperatures. This has direct implications on, for example, numerical ice-sheet modelling. If the geothermal heat flow is not realistic in the model setup, ice-sheet models will not produce useful data on basal melting and other characteristics. Numerical ice-sheet modelling studies have also shown that basal ice temperatures are sensitive to relatively small changes in geothermal heat flow (e.g. Greve and Hutter 1995, Siegert and Dowdeswell 1996).

For the modelling study presented in Section 2.3.4, Näslund et al. (2005) calculated a distributed, high-resolution geothermal heat flow data set for an approximate core area of the Fennoscandian ice sheet, and embedded this within lower-resolution data published for surrounding regions. In the following, a brief overview of the geothermal heat flux calculation is given.

The geothermal heat flow or surface heat flow density (HFD) in cratonic areas consists of two components: (1) heat produced within the mantle and core of the Earth and (2) heat produced within the crust. The contribution from the Earth's interior (so-called Moho- or reduced heat flow) arises from the cooling of the Earth and formation of a solid core, and from radiogenic heat production (e.g. Pollack et al. 1993). The crustal component consists of radiogenic heat production where heat is produced by the natural radioactive decay of primarily ^{238}U , ^{232}Th , and ^{40}K (Furlong and Chapman 1987). The Moho heat flow has a smooth spatial variation, possibly depending on mantle convection cell distribution (Beardsmore and Cull 2001), whereas the spatial variation in concentration of radioactively decaying nuclides in the lithosphere generates a heat flow with large spatial variations. The surface HFD can be estimated by a heat flow-heat production (Q-A) relationship of the form

$$Q = q_0 + DA_0 \quad (2-9)$$

(Birch et al. 1968, Lachenbruch 1968, Beardsmore and Cull 2001) where Q is the surface heat flow density (or geothermal heat flow), q_0 is the Moho heat flow, D represents the vertical distribution of heat-producing radionuclides in the lithosphere and A_0 is the radiogenic heat production from near-surface rocks.

The regional HFD pattern does not correlate with gravity variations (Balling 1984), magnetic anomalies (Riddihough 1972), or crustal thickness (Čermák et al. 1993). However, within the Baltic shield, as well as in other areas with similar geological settings, there is close correlation between HFD and regional geological units, with higher heat flow from acid (commonly granitic) areas and lower heat flow values from basic areas (e.g. Landström et al. 1979, Malmqvist et al. 1983).

The calculations of HFD values for Sweden and Finland were based on detailed data sets from numerous γ -emission measurements from bedrock and till. In Sweden, airborne surveys of γ -emissions have been carried out by the Geological Survey of Sweden (SGU), sampling data at 70 m intervals along flight lines with 17 km separation. In order to avoid shielding effects from vegetation and lakes, only data from exposed bedrock and till surfaces were used in the calculations. The Finnish data set is based on radiometric γ -emission measurements of 1,054 till samples providing full spatial coverage of the country (Kukkonen 1989).

The calculation of HFD is performed in several steps. First, the concentrations of ^{238}U , ^{232}Th , and ^{40}K are calculated from the γ -emission measurements, using information from detailed reference measurements over calibration plates with well-known isotopic concentrations. Near-surface heat production is then calculated from the concentrations of radionuclides. In addition, the Moho heat flow contribution needs to be considered. The distributed Moho heat flow by Artemieva and Mooney (2001) was added to the near-surface heat production data set. Finally, the HFD data set was re-sampled to a grid with 5 km resolution. To provide HFD coverage for the entire model domain, data for surrounding areas were added from the much coarser observed global HFD data set provided by Pollack et al. (1991). The resulting geothermal heat flow distribution is shown in Figure 2-45.

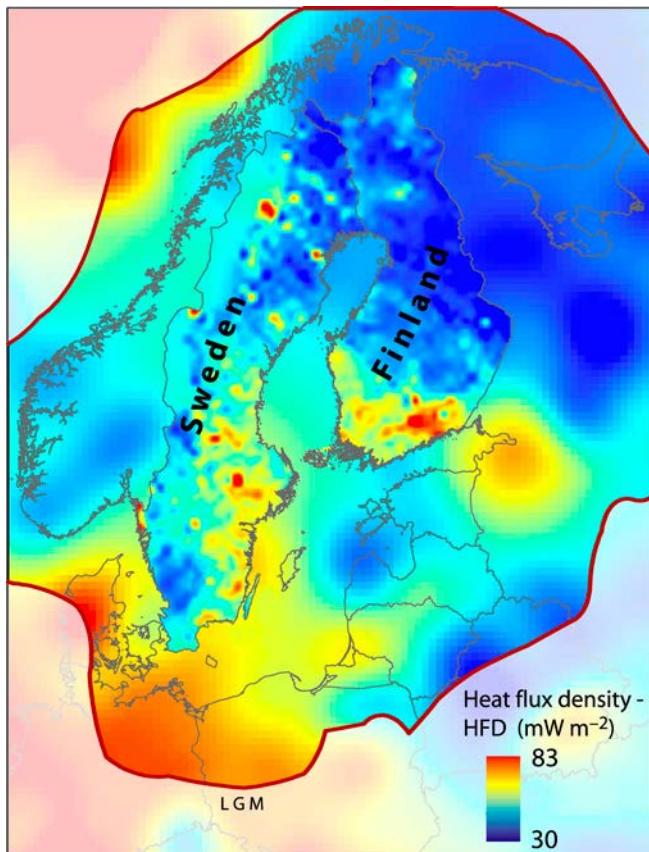


Figure 2-45. Geothermal heat flow distribution over Fennoscandia. From Näslund et al. (2005).

Within the LGM ice margin, the new data set shows that the geothermal heat flow varies by a factor of as much as 2.8 (geothermal heat flow values ranging between 30 and 83 mW/m², with an average of 49 mW/m²). This average value is 17% higher than 42 mW/m², which is the typical uniform value used in ice-sheet modelling studies of Fennoscandia. Using this new distributed data set on geothermal heat flow, instead of a traditional uniform value of 42 mW/m², yields a factor of 1.4 larger total basal melt water production for the last glacial cycle (Näslund et al. 2005). Furthermore, using the new data set in high-resolution modelling, results in increased spatial thermal gradients at the bed. This enhances and introduces new local and regional effects on basal ice temperatures and melt rates. The results show that regional to local variations in geothermal heat flow need to be considered for proper identification and treatment of thermal and hydraulic bed conditions under the Fennoscandian and other similar ice sheets (Näslund et al. 2005).

Ice properties. The exponent n in Glen's flow law (Equation 2-10) is dependent on the active creep process. Numerous field experiments and laboratory tests of glacier ice suggest that n should be ~ 3 . The typical creep process taken into account is a simple power-law creep, where the creep rate is proportional to the stress raised to some power greater than 1, for example:

$$\dot{\epsilon} \propto \sigma^n \quad (2-10)$$

On the other hand, with certain temperature, stress, and grain-size combinations, diffusional creep instead of power-law creep could take place in ice sheets (Duval et al. 1983), which would lower the value of n to less than 3. Other recent studies suggest that n should be between 1 and 2 for deformation at low stresses, low temperatures, and low cumulative strains (Alley 1992, Montagnat and Duval 2000). However, some of these conditions are likely to be important only down to depths of a few hundred metres in the coldest parts of ice sheets.

The viscosity constant B in Glen's flow law is dependent on a large number of parameters. Therefore, various modifications of Glen's flow law have been developed taking into account temperature, hydrostatic pressure, and crystal orientation. The last case is the most difficult, and it is done by introducing

an anisotropy enhancement factor. The *c*-axes of the ice crystals are, to a large degree, uniformly distributed in the upper part of the ice sheet, i.e. the ice is basically isotropic. When the ice over time is affected by the weight of the accumulating overlying ice mass, it is vertically compressed and longitudinally stretched, which results in a conical distribution of *c*-axes orientations. Subsequently, when the ice is affected by the simple shear close to the ice-sheet bed, the *c*-axes are typically re-oriented to a preferred single orientation. Development of *c*-axis fabrics has been obtained by re-crystallisation and ice-grain rotation. Since it is known from ice-core studies that the crystal orientation in ice sheets is not isotropic at depth, a non-isotropic flow law of ice improves, for example, ice-sheet modelling (e.g. Placidi et al. 2010).

The ice sheet dynamics described above may affect a number of geosphere variables of importance for the SFR (Table 2-6).

2.3.3 Natural analogues/observations in nature

Paleo-ice sheets

The mid-latitudes of the Northern Hemisphere have experienced repeated continental-scale glaciations during the Late Cenozoic. As previously mentioned, these periods are referred to as *glaciations* and the warm periods between the glacials are called *interglacials*. The present interglacial is called the Holocene, and, in north-western Europe, the last glaciation is named the Weichselian.

Table 2-6. A summary of how geosphere variables are influenced by ice sheet dynamics.

Geosphere variable	Climate issue variable	Summary of influence
Ground temperature	Basal ice temperature	During periods of cold-based ice coverage, low basal ice temperatures contribute to the formation of permafrost. During periods of warm-based ice coverage, basal ice temperatures at the pressure melting point contribute to permafrost degradation.
Groundwater flow	Basal thermal condition Basal melt rate Supply of surface melt water	If the ice sheet is cold-based no free water is available and there will be no groundwater recharge from basal melt water. If the ice sheet is warm-based, basal melting occurs at the ice/bed interface and groundwater recharge takes place. In addition, meltwater from the ice-sheet surface will, in both cases, be transported to the bed in frontal-near areas of the ice sheet. Groundwater recharge and flow will be determined by the presence of the ice sheet.
Groundwater pressure	Basal thermal condition Ice-sheet thickness Basal melt rate Supply of surface melt water	If the ice sheet is warm-based, the water pressure at the ice/bed interface may reach as much as the ice sheet overburden pressure, and in certain cases more. The groundwater pressure also depends on the melt water supply and the flow properties of the en- and sub-glacial hydrological systems. The groundwater pressure is also affected by the ice load compression of the bedrock pores and fractures.
Rock stresses	Basal condition Englacial ice temperatures Ice-sheet thickness	Rock stresses will be influenced by the ice load and the hydrostatic pressure. Independently of basal conditions there will be an increase in vertical stresses corresponding to the ice thickness. The horizontal stresses will also increase. If the ice sheet is warm-based the prevailing water pressures at the ice/bed interface will also alter rock stresses. The alteration of rock stresses also depends on the duration of the ice load and the slope of the ice-sheet surface. The slope of the ice-sheet surface near the front is in turn highly dependent on englacial ice temperatures and basal thermal conditions.
Groundwater composition	Glacial melt water composition	The glacial melt water is oxygen rich. The combination of abundant melt water supply and high water pressures may cause injection of glacial melt water to larger depths than oxygen-rich waters would penetrate in non-glacial conditions. Also, the consumption of oxygen close to the surface may be limited due to the lack of organic matter and microbiological activity.

Paleo-ice sheets have left geological traces in previously glaciated terrain in Fennoscandia, North America and Siberia, as well as abundant glacio-marine traces in adjacent ocean basins. Studies of North Atlantic marine sediments have shown that the first traces of eroding glaciers in Greenland and Fennoscandia date back to between 12 and 6.6 Ma BP (Jansen and Sjøholm 1991, Fronval and Jansen 1996), with larger ice sheets present in Fennoscandia from around 2.75 Ma BP. Over the last ~900 ka, glacial–interglacial cycles of about 100 ka duration have dominated global climate variation (see Figure 1-2). Before c 900 ka BP, cycles of 41 ka dominated (e.g. Raymo et al. 1998, McIntyre et al. 2001).

Geological information on till stratigraphy, interstadial deposits, glacial landforms in loose sediments and in bedrock have for a long time been used for making reconstructions of the Weichselian glacial history. A summary of that work is provided in Lokrantz and Sohlenius (2006). Section 3.2 describes several recent studies that have been used for the reconstruction of the Weichselian glacial history and of climate conditions during this glacial cycle.

Various types of glacial landforms may also be used to infer information on basal thermal conditions of paleo-ice sheets (e.g. Lagerbäck 1988a, Kleman et al. 1997, Kleman and Hättestrand 1999, Kleman and Glasser 2007).

Present ice sheets

At present there are two ice sheets on Earth, the Antarctic (14 Mkm²) and Greenland (1.7 Mkm²) ice sheets. Large portions of these quasi-stable ice sheets are more than 3 km thick. In both cases, the ice-sheet load has depressed the bed so that large portions are situated below sea-level. Offshore marine sediments show traces of waxing and waning Antarctic ice sheets of continental proportions back to 40–36 Ma BP (Haq et al. 1987, Hambrey et al. 1992), and Antarctic alpine glaciers may trace back to the Oligocene (Näslund 2001). The present configuration of the Antarctic ice sheet is thought to have been relatively stable for the last 15–11 Ma (cf. Shackleton and Kennett 1975, Marchant et al. 1993).

The spatial patterns of basal thermal characteristics of the Antarctic and Greenland ice sheets are complex due to ice-sheet dynamics, bed topography, and geothermal heat flux variability. For both ice sheets, parts of the bed are cold-based whereas other parts are warm-based, as seen from modelling studies (Figure 2-46), radar soundings and drillhole data. Ice-sheet modelling has also, together with geological field observations and remote sensing studies, showed that ice streams are prominent features of the Antarctic ice sheet, penetrating far into the ice-sheet interior (Figure 2-47). This has also been shown by remote sensing Interferometric Synthetic Aperture Radar (InSAR) studies (Joughin and Tulaczyk 2002). The outer coastal-near parts of these ice streams are typically wet-based, whereas their upstream parts, high in the catchment areas, often are cold-based.

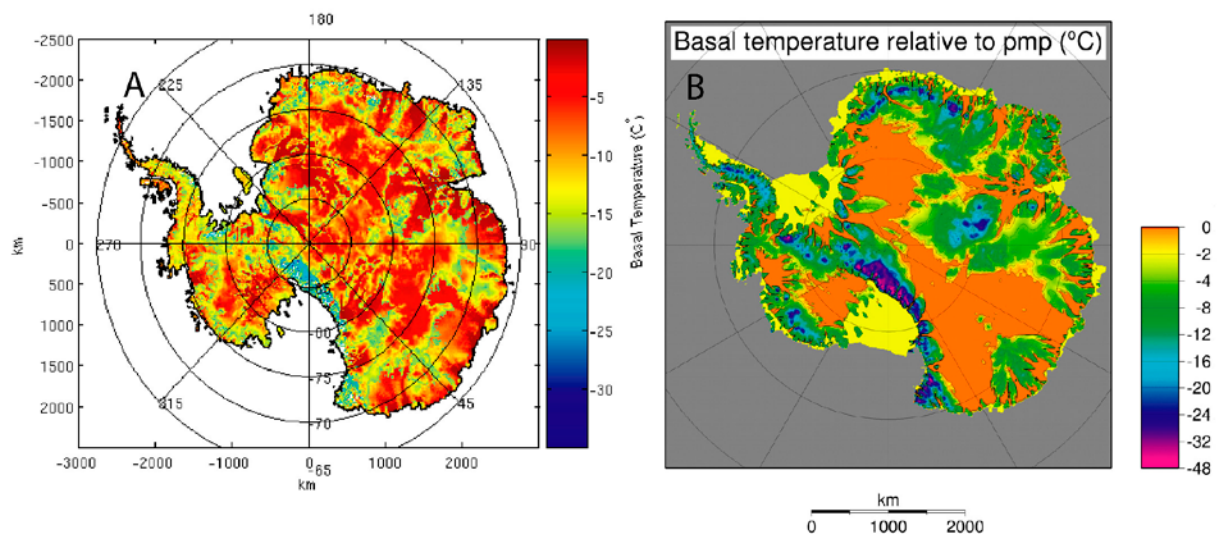


Figure 2-46. Two examples of modelled present-day Antarctic ice sheet basal temperatures. Temperatures are expressed relative to the pressure melting point (pmp). Figure a) is from Johnson (2004) and b) from Huybrechts (2006).

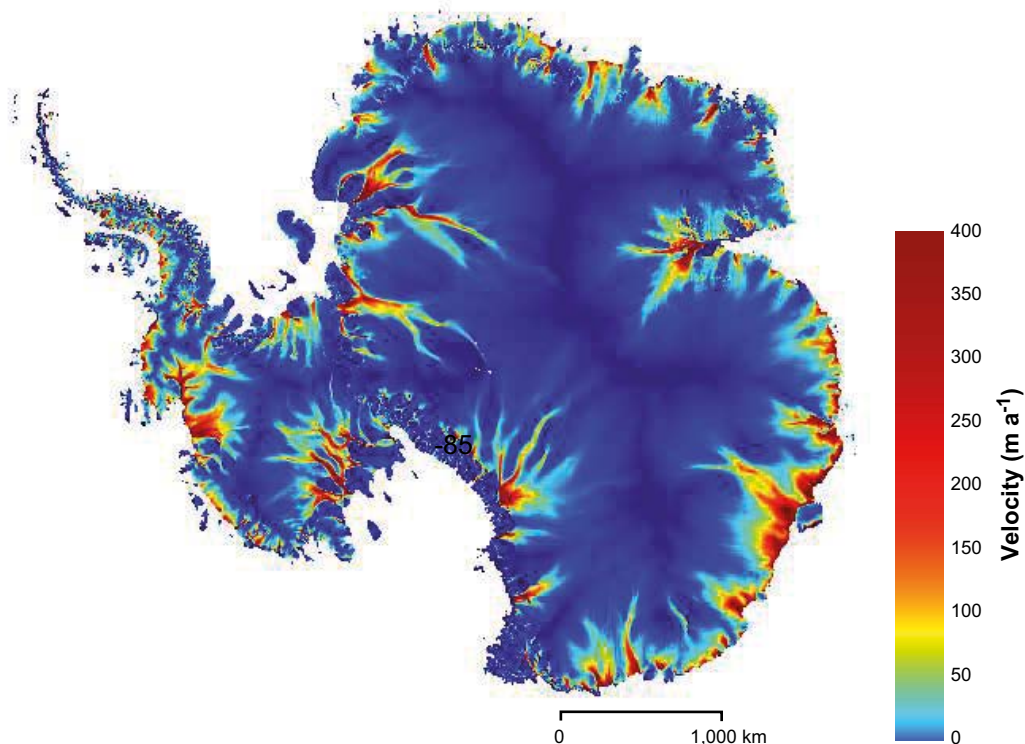


Figure 2-47. *Modelled Antarctic ice-surface velocities. Fast-flowing ice streams (red/yellow/green) reach far into the ice-sheet interior. From Johnson (2004) with numerical methods described in Staiger et al. (2005).*

During the main Pleistocene glacial periods, the Greenland and Antarctic ice sheets had a larger extent than at present. The major limiting factor on their maximum lateral extent is the bed topography; the Antarctic and Greenland ice-sheet margins are both today located close to the coastline. The continental crust does not extend out very far from the present-day coast lines, and, at the continental margin, the water depth quickly increases. When the ice sheets grow larger the grounding-line migrates outward, resulting in a larger area for the grounded part of the ice sheet. The grounding line cannot advance past the continental margin due to the larger water depths outside. The continental margin thus constitutes a definite constraint on the maximum spatial size of Antarctic and Greenland ice sheets during Late Cenozoic ice-sheet fluctuations. The situation was similar for part of the Fennoscandian ice sheet. From a bed topography point of view there were no constraints for ice-sheet growth from the Scandinavian mountain range towards the east (the Baltic depression is not deep enough to provide such a constraint), but Fennoscandian ice sheets, including the last Weichselian ice sheet, could not and did not extend farther west than the offshore continental margin (Svendsen and Mangerud 1987, Zweck and Huybrechts 2003).

Although the sizes of the Antarctic and Greenland ice sheets were greater during the Late Pleistocene glacials, the maximum thicknesses need not have been larger. On the contrary, because of atmospheric moisture starvation during the colder climates, the interior parts of the ice sheets probably were thinner during the coldest parts of the glacial cycles (e.g. Huybrechts 1990). In contrast, at the ice-sheet margins the ice-sheet thickness varies considerably during a glacial cycle. Areas where the ice thickness is zero during a warm interglacial period (i.e. at the exact margin) may experience an increase in ice thickness of several hundred metres, up to one kilometre, during a glacial maximum ice configuration (Näslund et al. 2000). In turn, this means that the temporal changes in basal conditions of the ice sheets, for example changes in basal ice temperatures from the present interglacial pattern, were highly complex. For example, due to the changed ice configuration affecting ice-sheet dynamics, some parts of the Antarctic ice sheet were warmer at the LGM ice configuration than at present, whereas, at the same time, other parts were colder (Figure 2-48) (cf. Näslund et al. 2000).

Recently, the coupling between the dynamic behaviour of the Greenland ice sheet and ice-sheet hydrological processes has been inferred from a number of studies, see e.g. SKB (2010e).

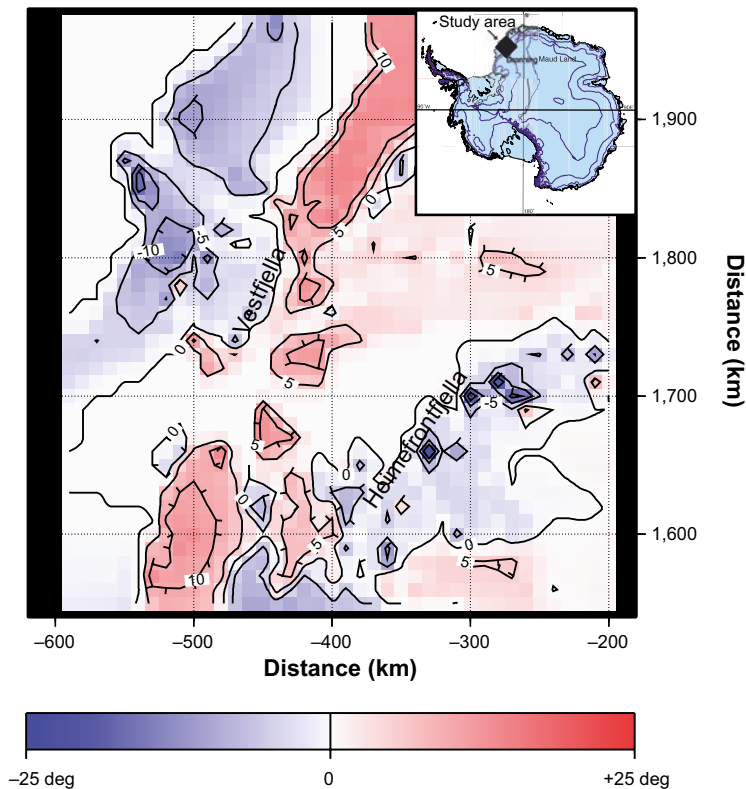


Figure 2-48. Modelled difference in basal temperature between the present-day ice configuration and a maximum Pleistocene ice sheet configuration for part of the Antarctic ice sheet. For this single change in ice configuration, ice-sheet thermodynamics induce complex changes in basal thermal pattern; some parts of the ice sheet become warmer at the bed the same time as other parts become colder. From Näslund et al. (2000).

2.3.4 Model studies

Ice-sheet modelling

Thermo-mechanical ice-sheet modelling is a well established and useful tool for studying a large array of ice-sheet-specific and ice-sheet-related issues. Although ice-sheet models have limitations, see e.g. SCAR (2007), they can be used to study characteristics and behaviour of present ice sheets, paleo-ice sheets, and in some cases also inferred future ice sheets. As computer capacity has increased, more sophisticated models have been able to be run at higher spatial resolution, which, in turn, has made it meaningful to compare detailed model output with various types of geological information, both for model verification and testing of glacial-geological hypotheses (e.g. Pattyn et al. 1989, Van Tatenhove and Huybrechts 1996, Näslund et al. 2003).

Reconstructions of paleo-ice sheet configurations, including ice thicknesses, may be done by two main groups of models. One group is thermo-mechanical ice-sheet models that are based on ice physics and thermo-mechanical interactions (e.g. Huybrechts 1986, Boulton and Clark 1990, Fastook 1994, Ritz et al. 1996, Payne and Dongelmans 1997, Marshall and Clarke 1997). The second group of models are isostatic rebound models that are used to invert observations of crustal rebound and shoreline locations to estimate paleo-ice thicknesses (e.g. Lambeck et al. 1998, Peltier 2004).

For the present study, UMISM (University of Maine Ice Sheet Model) (Fastook and Chapman 1989, Fastook 1990, 1994, Fastook and Prentice 1994, Johnson 1994) was selected for the simulation of last glacial cycle ice-sheet configurations. The UMISM code was selected since a large number of simulations of the last glacial cycle Fennoscandian ice sheet have been done with this model over the years (e.g. Fastook and Holmlund 1994, Holmlund and Fastook 1995, Näslund et al. 2003). The UMISM was part of the European Ice Sheet Modeling Initiative (EISMINT) model intercomparison experiment and yielded output in agreement with many other physically based ice-sheet models (Huybrechts et al. 1996, Payne et al. 2000), which further motivated the choice of this model.

The resulting reconstruction of last glacial cycle ice-sheet configurations for the Forsmark site, e.g. Figure 4-18 in SKB (2010a), shows large similarities with corresponding data for a North American

last glacial cycle scenario modelled using the Peltier model (Garisto et al. 2010). This indicates that the selection of the type of model is not critical for the general appearance of the ice sheets reconstructed for the last glacial cycle. In detail, however, the development of ice configurations over time in e.g. these two studies are expected to differ for several reasons, including that the studies deal with two different geographical areas and indeed two different ice sheets (the Weichselian ice sheet over Eurasia and the Laurentide ice sheet over North America). For instance, the last glacial cycle Laurentide ice sheet is known to have been considerably larger and thicker than the Weichselian ice sheet.

The ice-sheet system constitutes three main sub-systems: mass-balance, ice movement, and ice temperature. For these sub-systems the selected ice sheet model solves differential equations describing conservation of mass, momentum, and energy respectively. In addition, the ice-sheet model needs to contain a description of climate. A mass balance parameterisation for the spatial pattern of air temperature and precipitation is used in UMISM. The model includes a mathematical description of precipitation based on a number of other parameters; distance from the pole, saturation vapour pressure (function of altitude and lapse-rate), and surface slope. This is an empirical relationship developed from the Antarctic ice sheet (Fastook and Prentice 1994), but successfully applied also for simulations of Northern Hemisphere ice sheets (e.g. Fastook and Holmlund 1994, Holmlund and Fastook 1995, Näslund et al. 2003, Hooke and Fastook 2007, Kleman et al. 2013). Over a certain model domain, with a topography described by a Digital Elevation Model (DEM), this climate description gives a spatial pattern of air temperatures at ground level and a pattern of precipitation.

The UMISM also includes a simplified isostatic description for the behaviour of deforming bedrock due to the weight of the modelled ice-sheet configuration. This is not a full self-gravitational spherical Earth model as used in the Glacial Isostatic Adjustment (GIA) modelling in Section 2.2. Instead, it is a hydrostatically supported elastic plate model, considered adequate for the purpose of placing the ice-sheet surface at an appropriate altitude, and hence at an appropriate air temperature, for the mass balance calculations. Furthermore the UMISM also includes a subglacial hydrology model (Johnson 1994) that is able to transport basal meltwater under the ice sheet according to prevailing pressure potentials governed by ice-sheet thickness and basal topography.

A paleo-temperature record was employed to run the ice sheet model (Figure 2-49). For the reconstruction of the Weichselian ice sheet, see below, the temperature proxy record for the last 120 ka from the Greenland GRIP ice core has been used (Dansgaard et al. 1993). The temperature file that was used contains 50 year averages of the original time series. For a detailed description of this temperature data set, including its use in the ice-sheet modelling and its estimated uncertainties, see Appendix 1 of SKB (2010a).

In the modelling process, the variations in the proxy temperature are used to change the climate pattern (temperature and precipitation) over the model domain, initiating ice-sheet growth in Fennoscandia. Once glaciers/ice sheets are formed, the modelled thermo-dynamic ice-sheet system starts to evolve over time. In this way, the ice-sheet model simulates the behaviour of the ice sheet as it responds to the external forcing such as changing climate or sea-level, as well as internal dynamics, such as ice-stream variations caused by internal temperature oscillations at the bed.

The following are input parameters to the ice-sheet model in the simulations of the Weichselian ice sheet:

1. The thermodynamic properties of the ice, including flow laws, sliding laws, feedback mechanisms etc.
2. Upper boundary conditions: A mass-balance parameterisation providing a climate description constituting fields of annual air temperature and precipitation over the model domain.
3. Lower boundary conditions:
 - A. A DEM over Fennoscandia with a moderately high spatial resolution. For the reconstruction of the Weichselian ice sheet a grid size of 50 km was used. DEM data were taken from the ETOPO2 data base², depicting both continental topography and bathymetry;
 - B. Geothermal heat flux at the bed.
4. Sea-level changes during the last 120 ka.
5. Proxy air temperature for the past 120 ka (GRIP data).

² ETOPO2, 2001. Global Digital Elevation Model (ETOPO2) representing gridded (2 minute by 2 minute) elevation and bathymetry for the world. Data were derived from the National Geophysical Data Center (NGDC) ETOPO2 Global 2' Elevations data set from September 2001.

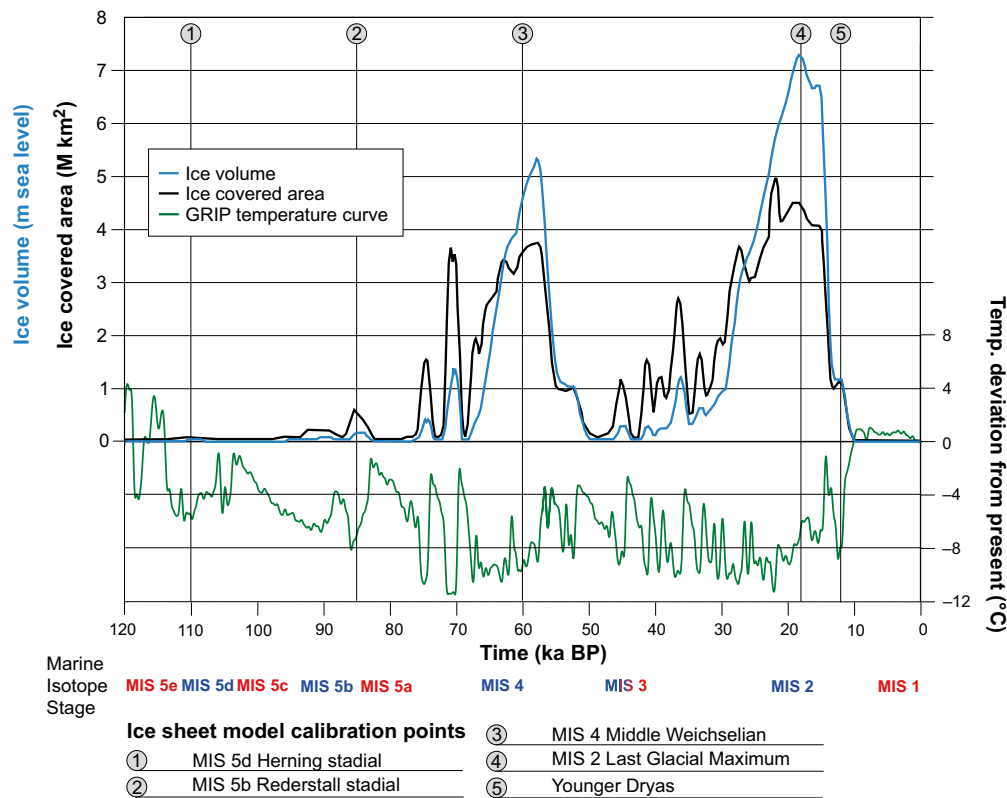


Figure 2-49. GRIP proxy temperature and reconstructed ice-covered area and ice volume for the reconstruction of the Weichselian ice sheet. Times of model calibration are shown, as well as Marine Isotope Stages (MIS) (warm stages in red and cold stages in blue).

The modelling starts 120 ka before present, and the model was run at a five year time step forward in time up to time zero (present). For each time step, output data were calculated for each grid cell and grid node. These data included:

1. Ice thickness.
2. Englacial and basal ice temperatures.
3. Ice velocity.
4. Direction of ice movement.
5. Isostatic depression of crust.
6. Amount of basal melting or freeze-on of water.

Model setup. A model domain was selected to cover the maximum extent of the Weichselian ice sheet over Fennoscandia, with a spatial DEM resolution of 50 km. The thermomechanical coupling between ice movement and ice temperature was enabled, as well as a function by which the amount of basal sliding is coupled to the amount of basal meltwater present at the ice-sheet bed. The n parameter in Glen's flow law (Section 2.3.2) was set to 3, whereas the value for the viscosity parameter B differed depending on ice temperature. Exemplified calculated values of B are seen in Figure 2-50. In the final model run, the model was run with a five year time step and data was saved from the model simulation at a 100 year interval.

The traditional way of specifying the basal thermal boundary condition in ice-sheet modelling is to apply a single, uniform value of geothermal heat flow for the entire model domain. The magnitude of this geothermal heat flow value has often been set according to the general geological setting for the area to be studied. Thermodynamic modelling of Fennoscandian ice sheets has, for instance, used a single geothermal heat flow value typical for the Pre-Cambrian shield, the most common reported value being 42 mW/m^2 (e.g. Boulton and Payne 1992, Huybrechts and T'siobbel 1995, Payne and Baldwin 1999). Others have used higher values, around $50\text{--}55 \text{ mW/m}^2$ (e.g. Hindmarsh et al. 1989, Forsström et al. 2003).

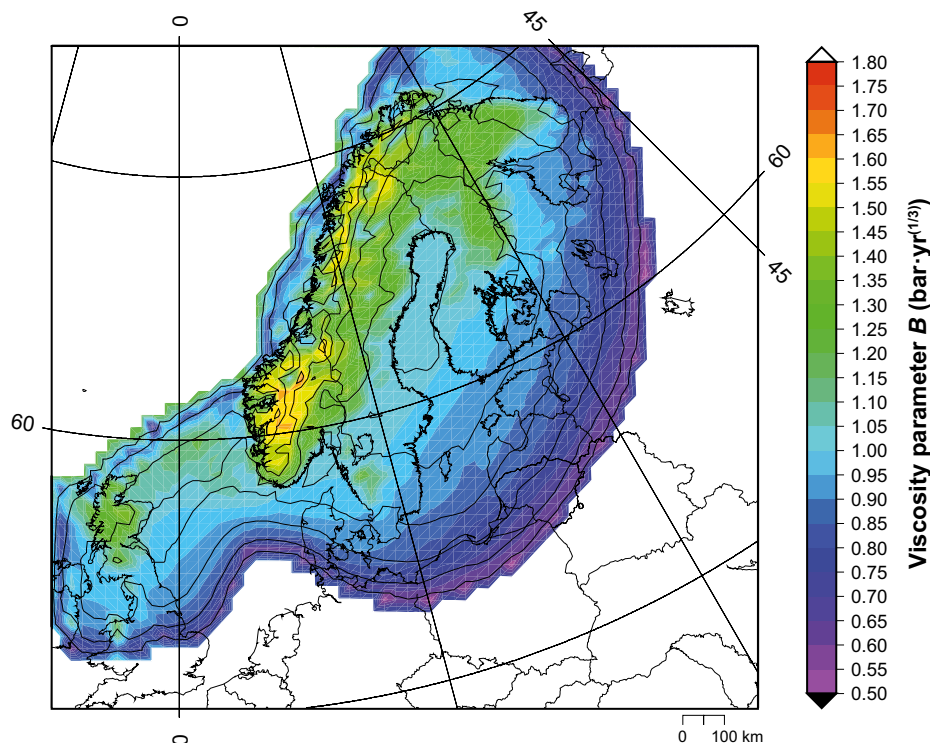


Figure 2-50. Calculated flow-law viscosity parameter B at 18.5 ka BP (at around the Last Glacial Maximum), shown as vertically integrated values up the ice column. Colder and harder ice is seen in the central parts of the ice sheet and over the Scandinavian mountain range (larger B values), while warmer and softer ice is seen closer to the ice margin (smaller B values). The black lines show ice thickness contours with a 500 m interval.

For the model reconstruction of the Weichselian ice sheet, the geothermal data set of Näslund et al. (2005) was used as the basal boundary condition. A so-called higher-order model, taking into account longitudinal push-and-pull effects within the ice sheet was used for specific studies of ice flow behaviour in relation to geothermal heat-flow anomalies in Sweden, see Näslund et al. (2005).

Model calibration. In studies in which ice-sheet modelling aims at simulating paleo-ice sheets, one needs to calibrate the behaviour of the model against known information on ice-sheet extents. The reason for this is that we do not have full knowledge on a number of the processes and boundary conditions involved, for example on climate, or ice-sheet basal processes. In the present reconstruction of the Weichselian ice sheet, the UMISM model was calibrated by making adjustments of the proxy air temperature (Figure 2-49). Over the years, a large number of such simulations of the Fennoscandian ice sheet have been done with the UMISM model using this proxy air temperature, which has given extensive experience of how to perform the model calibration. As mentioned above, the forcing in temperature for the ice-sheet model is based on the GRIP ice core (Dansgaard et al. 1993), see also SKB (2010a, Appendix 1). In the ice-sheet calibration process, the entire temperature time series was shifted and amplified (Figure 2-51) so as to obtain calibrated ice-sheet configurations that fitted as well as possible with geological observations on dated marginal positions. Model calibration was made for ice margins as described in Lokrantz and Sohlenius (2006) for MIS 5d (~110 ka BP), MIS 5b (~85 ka BP), MIS 4 (~60 ka BP), MIS 2 (~18 ka BP), and for the Younger Dryas (~12 ka BP) (Figure 2-51). Keeping all other input data constant in the calibration process, the modified temperature time series was obtained after model calibration results for Late and Middle Weichselian ice-sheet configurations in good agreement with dated ice-marginal positions and Early Weichselian configurations in reasonably good agreement with geological interpretations. The characteristics and applicability of the GRIP temperature time series for the present study is further described and discussed in SKB (2010a, Appendix 1).

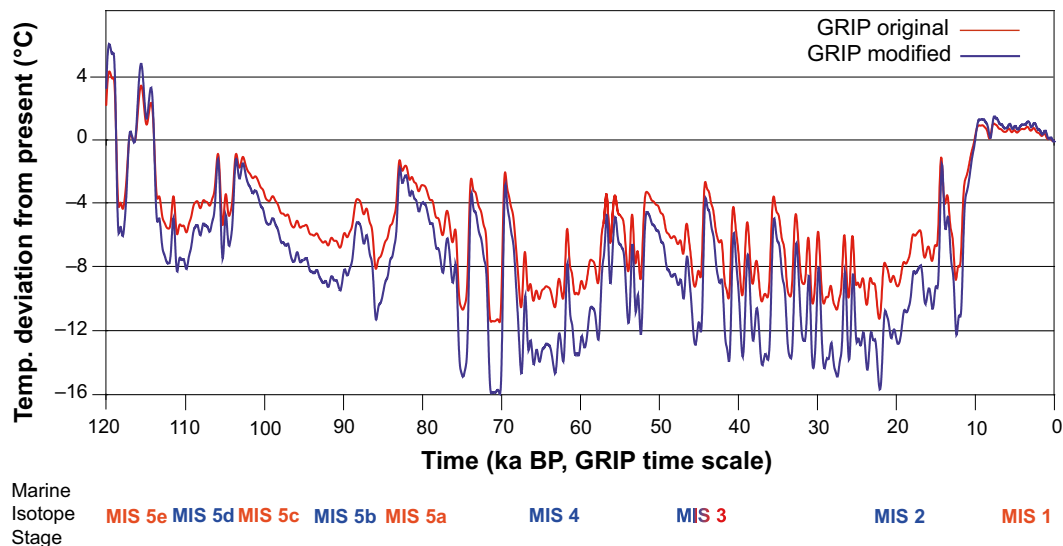


Figure 2-51. Proxy paleo-air temperature from the calibration process of the UMISM ice sheet model. The final calibrated time series used in the ice sheet modelling (blue) has larger amplitude than the original data (red), i.e. cold periods were even colder in the calibrated time series. Modifications of the temperature data set were performed for the complete time series. The temperature time series, and its uncertainties, are discussed in detail in SKB (2010a, Appendix 1).

The resulting calibrated reconstruction of the Weichselian ice sheet is seen in Figure 2-49 and Figure 2-52. Ice extends over the model domain during the cold stadials during Marine Isotope Stages (MIS) 5d, 5b, 4, and 2. During warmer interstadials, such as MIS 3, the ice cover is more restricted. As expected, there is a clear trend of more and more pronounced ice coverage during the stadials through the glacial cycle, with the LGM peak occurring at around 18 ka BP.

Different types of output data have been extracted and post-processed from the reconstruction of the Weichselian ice sheet, for example 1) basal and surface melt rates for groundwater modelling (Jaquet and Siegel 2006), 2) Basal and subaerial temperatures for permafrost modelling (Section 2.1 and Appendix 1 and 3 in SKB 2010a) ice-thickness variations for modelling of global isostatic adjustment (Section 2.2) and crustal stresses (Lund et al. 2009), and 4) 2D ice sheet profiles for modelling of groundwater flow under glacial conditions (Vidstrand et al. 2010), see also SKB (2010a, Appendix 2).

For more information on the ice-sheet model, see SKB (2010b) and for further descriptions of model simplifications and uncertainties, see Section 2.3.7.

2.3.5 Time perspective

It is generally agreed that ice sheets take longer to grow than to decay. However, our knowledge of the final deglaciation phase is much better than of inception phases, reflecting the fact that there are more geological traces from the last deglaciation than from earlier stages. Since ablation by surface melting is a more efficient process than snow accumulation, this suggests that the time for ice-sheet decay should be shorter than the growth time (Paterson 1994). In reality, this is also accentuated due to efficient ice shelf calving processes for marine parts of ice sheets, for example calving of the Fennoscandian ice sheet in the Gulf of Bothnia. In line with the present modelling results of the Weichselian ice sheet (Figure 2-49 and Figure 2-52), it is generally concluded that ice sheets may build up in a series of glacial build-up periods, peaking in a glacial maximum close to the end of the glacial. The Fennoscandian ice sheet seems to have exhibited such dynamic behaviour during the last glacial cycle, Section 3.2. This has also been inferred from studies of so called Heinrich events (cf. Heinrich 1988) recorded in North Atlantic marine sediments, suggesting that even large ice-sheet systems are dynamic features, responding relatively quickly to rapid changes in climatic forcing.

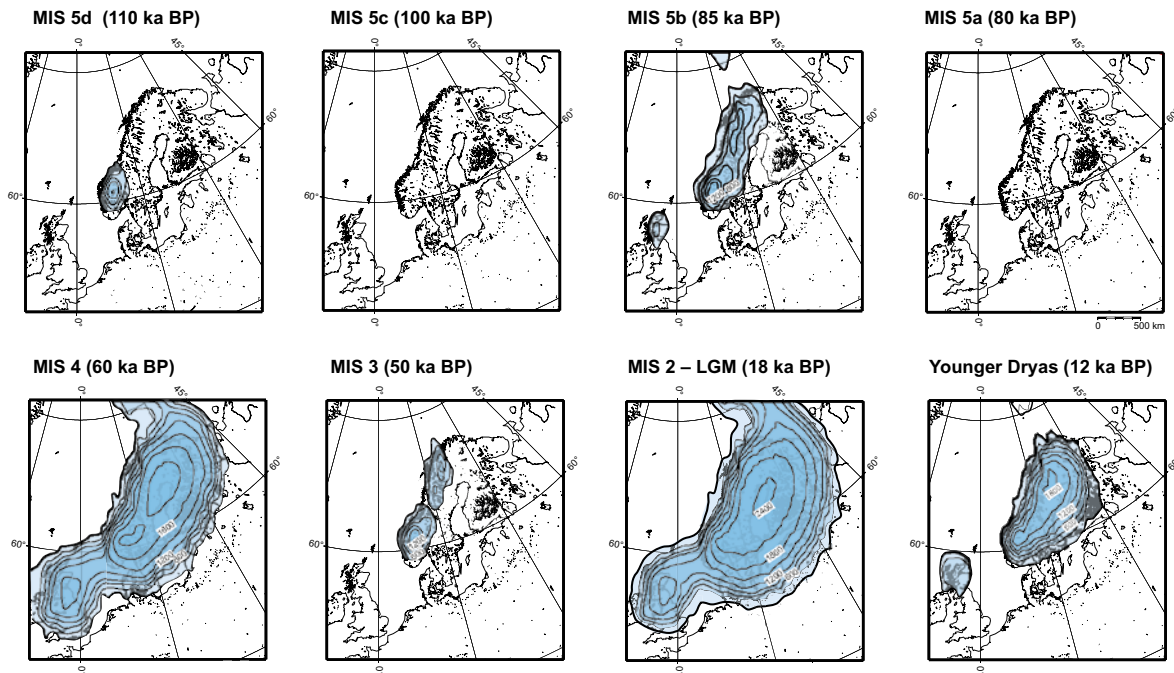


Figure 2-52. Selected maps of ice-sheet surface topography for the reconstructed Weichselian ice sheet. The ice sheet grows to its full LGM configuration in progressive phases of increasing maximum extent, with intervening periods of more restricted ice coverage. Contour lines show ice-surface elevation with a 300 m contour interval. All maps show present-day shoreline position.

During the last 900 ka, glacial cycles have typically lasted about 100 ka, with interglacials lasting around 10 to 20 ka (e.g. McIntyre et al. 2001, Tzedakis et al. 2009). As noted above and discussed in Section 3.2, the last glacial cycle was also characterised by a number of cold growth phases and intervening warmer periods with less ice, although from the geological record we still do not know how to date or correlate all observed interstadial localities (Lokrantz and Sohlenius 2006). A typical cold Weichselian stadial had duration of some ka, see e.g. Figure 2-49 and Section 3.2. The deglaciation of the Weichselian ice sheet from the LGM ice margin to the last ice remnants in the Scandinavian mountain range took about 8 ka. During the deglaciation, a number of temporary halts, and in some cases also readvances, took place, the most pronounced one occurring during the Younger Dryas (about 13–11.5 ka BP).

2.3.6 Handling in the safety assessment SR-PSU

The evolution of ice sheets is investigated by means of numerical modelling. The period from 50 ka AP to 100 ka AP in the *global warming and early periglacial climate case* was defined based on an ice-sheet model reconstruction of the Weichselian glaciation. This reconstruction was also used to define the *Weichselian glacial cycle climate case*. The thermo-dynamic ice sheet model used is capable of simulating realistic ice sheets which are typically not in balance with the climate. Derived ice temperatures, together with density variations with depth, control ice viscosity and ice flow. The thermodynamic calculation accounts for vertical diffusion, vertical advection and heating caused by internal shear. The climate input, forcing ice-sheet evolution, is the mean annual air temperature at sea-level, and its variation over time. The mass balance is determined from an empirical relationship based on a simple parameterisation of the ice sheet's effect on local climate (Fastook and Prentice 1994). Distributed temperatures over the model domain are determined from height above sea-level and distance from the pole.

The model simulation of the Weichselian ice sheet over Fennoscandia was controlled by the proxy temperature from the GRIP ice core, obtained from central Greenland (e.g. Dansgaard et al. 1993), see also SKB (2010a, Appendix 1), a typical method used in ice-sheet modelling of the Weichselian glacial cycle. The geothermal heat flow and its spatial variation have been shown to be of importance for obtaining realistic modelled basal ice temperatures and basal melt rates (Waddington 1987, Näslund et al. 2005). Basal temperatures and basal water conditions are in turn important for the overall ice flow

and ice dynamics. A detailed dataset of geothermal heat flux values, based on national measurements of gamma emissions in Sweden and Finland has been compiled (Näslund et al. 2005), and has for the first time been used as input to an ice-sheet model. This eliminates previous large uncertainties in geothermal heat flow, and associated uncertainties in modelled basal conditions of the ice sheet.

The ice-sheet model was calibrated so that modelled ice-sheet configurations were in agreement with dated geological information on ice-marginal positions (Section 2.3.4). For this purpose, geological information on the Weichselian glaciation history of Scandinavia was compiled by Lokrantz and Sohlenius (2006). For further information on the ice-sheet modelling, see the preceding parts of Section 2.3.

2.3.7 Handling of uncertainties in SR-PSU

Uncertainties in mechanistic understanding

Model simplification uncertainty. The most important simplifications made in the ice-sheet modelling in the model reconstruction of the Weichselian ice sheet are the following.

The proxy temperature driving the model is the GRIP Greenland temperature time series. First of all these data describe the climatic conditions for Greenland, but in the absence of similar paleoclimate data from Fennoscandia, or other closer areas, these are the best data available. With the applied modelling approach, the Greenland proxy data generate Fennoscandian ice sheets that are in fair agreement with geological information on LGM and Younger Dryas ice margin positions, even *without* model calibration, which is a justification that this approach is valid. There are also uncertainties introduced by the conversion from oxygen isotope values in the ice core to Greenland paleo-air temperatures (Johnsen et al. 1995), see also SKB (2010a, Appendix 1).

In order to improve the simulated Weichselian ice-sheet configurations, the model was calibrated against dated marginal positions as interpreted in studies of Quaternary geology and glacial history. One feasible way to make this calibration is to make use of the model input parameter estimated to have the largest uncertainty, in this case the last glacial cycle air temperature time series obtained from proxy data. In the present study, the air temperature was therefore selected for adjustment in the model calibration process. The full temperature time series was adjusted in a systematic way until a better fit was obtained between modelled and interpreted/observed ice-sheet configurations. For details, see Section 2.3.4. In the model, the amount of basal sliding is coupled to the thickness of the basal water layer of the ice sheet. This is a simplification, but is a reasonable way of handling the difficult topic of basal sliding and the coupling between glacier hydrology and ice-sheet dynamics. One thing that is excluded in the model is the possible presence of subglacial deformable sediments, for example in the Baltic depression, which may enhance ice velocities, especially in ice streams. The exclusion of the effects of such sediments could, in some cases, lead to some overestimation of ice thickness.

The UMISM model used in the present study employs the so-called shallow ice approximation. This means that the horizontal velocity only depends on the local driving stress. Horizontal englacial stresses are neglected, i.e. there are no push-and-pull effects within the ice sheet, as in nature. This is a reasonable and appropriate assumption for the major part of the ice sheet, with the exception of near-marginal locations and at ice divides. However, it is judged that the model has not been used in such detail that the results would be significantly different if a higher-order ice-sheet model (e.g. Pattyn 2003) had been used.

In the UMISM model, horizontal advection of heat was not included in the thermodynamic treatment of the ice. The result is that the model may overestimate basal ice temperatures to some extent. This is likely to be of importance only in fast-flowing situations like ice streams.

The hydrostatically supported elastic plate model included in the UMISM model is a simplification, but sufficient for adjusting bed- and ice-sheet surface elevations to obtain a reasonably good surface mass balance.

The UMISM model does not include an ice-shelf model. Instead, ice shelves are simulated by adjusting a marine calving rate directly at the dynamic grounding line.

The spatial resolution of model domain is approximately 50×50 km. This resolution may, in some cases, be too coarse to correctly depict smaller features in for example geothermal heat flow pattern.

Input data and data uncertainty

The proxy temperature. See section on Model simplification and uncertainty above, Section 2.3.4, and SKB (2010a, Appendix 1).

Digital elevation data. The accuracy and spatial resolution of the ETOPO2 DEM is sufficient for the 50×50 km and 10×10 km resolution ice-sheet model simulations performed.

Geothermal heat flux. The high-resolution data set on spatially varying geothermal heat flux is of high quality in the context of ice-sheet modelling. In the new data set, high resolution geothermal data are available only for Sweden and Finland, not for the entire area covered by the Weichselian ice sheet. However, this does not affect modelled basal conditions in Sweden, since basically all parts of Sweden are located down-stream from areas with high-resolution data. There are assumptions made in the calculation of the data set that could be refined to improve the data set in the future, for example using a varying lithospheric thickness in the calculation of surface heat flow. Also, denser data on γ -emission measurements from bedrock are available for parts of Sweden, which may be used for future versions of the data set. All in all, this new type of ice-sheet model input has improved ice-sheet modelling significantly from all previous reconstructions of paleo-ice sheets by numerical modelling.

Sea-level. The sea-level data used as input were derived from numerical ice-sheet modelling of all Northern Hemisphere ice sheets. The present volume of the Antarctic ice sheet was held constant. The maximum lowering of sea-level in this data set is 100 m, somewhat less than the ~ 120 – 135 m of global sea-level lowering at the LGM deduced from coral-reef data (Yokoyama et al. 2000). However, this is of minor importance since the position of the grounding-line in the western Atlantic part of the ice sheet is determined by the bed topography (i.e. continental shelf location), and the eastern part is advancing and retreating over the Baltic Sea which does not have contact with the Atlantic during such low global sea-levels.

2.3.8 Adequacy of references

The SR-Site and SR-Can Climate reports (SKB 2006a, 2010a), from which the studies are used, have undergone QA system handling including a factual review process. Other references used for the handling of ice-sheet dynamical processes are either peer-reviewed papers from the scientific literature or from a textbook (Paterson 1994).

2.4 Surface denudation

2.4.1 Overview/general description

The downwearing of the Earth's surface by exogenic processes is accomplished by weathering, erosion, and transportation of material. The combined effect of all weathering and erosion processes is referred to as denudation, i.e. denudation is the sum of the processes that result in the wearing away or the progressive lowering of continental relief. The energy needed for the denudation processes is gained from endogenic and exogenic sources. Glacial erosion is usually regarded as the main erosion process in Scandinavia during the Quaternary. However, as large parts of Scandinavia were not covered by ice during long periods of the Quaternary (e.g. Porter 1989), other denudation processes must also be considered to get the complete picture (Lidmar-Bergström 1997, Lidmar-Bergström et al. 1997, Pässe 2004).

Weathering

Weathering exerts the most fundamental control on denudation and is the driver of, or limiting factor, in landscape evolution (Turkington et al. 2005). Weathering can be defined as structural and/or mineralogical breakdown of rock through the cumulative effects of physical, chemical and biological processes operating at or near the surface (e.g. Reiche 1950, Selby 1993, Whalley and Warke 2005). The definition indicates that weathering occurs when minerals/rocks are exposed to temperature, pressure and moisture conditions characteristic of the atmosphere and hydrosphere, that is in an environment that differs significantly from the conditions in which most igneous and metamorphic rocks as well as lithified sedimentary rocks were formed. The alteration of rocks by weathering forms new materials (minerals) that are in equilibrium with conditions at or near the Earth's surface.

By definition weathering occurs *in situ* and does not directly involve erosion. This means that it leads to the formation of a residual material that differs from the parent, unweathered rock with respect to its physical and chemical properties. Weathering normally lowers the strength of rock and increases the permeability of the surface material and thus makes it more prone to mass wasting and easy to erode by running water, glaciers, wind etc. In addition, it is also an important prerequisite for the widespread development of flora and fauna on land by releasing nutrients for plants and other organisms.

Weathering is generally divided into physical-, chemical- and biological components. Physical or mechanical weathering occurs when volumetric expansion and related alterations of stresses lead to failure and disintegration of the rock. For example, volume changes due to decreased overburden and stresses can result in the creation of fractures at various scales. Crystallisation and volumetric alteration of salt crystals, freezing of water and freeze-thaw effects, as well as thermal fatigue due to repeated (diurnal) heating and cooling, may also cause physical weathering.

Chemical weathering comprises reactions between rock minerals and water. Examples are solution of minerals, carbonation, hydrolysis, hydration, and oxidation and reduction. Common to chemical weathering processes is that they depend on water composition, for example pH, salinity, CO₂ and redox potential. The prevailing temperature is another important parameter determining the type and efficiency of chemical weathering.

During temperate conditions in Sweden, weathering only occurs where the bedrock is exposed. Swantesson (1992) has estimated the postglacial weathering of bare bedrock surfaces in southern Sweden during the Holocene to be less than 0.02 m (i.e. a rate of less than 2 m Ma⁻¹). Weathering rates in tropical climates range between 2 and 48 m Ma⁻¹ (Thomas 1994). Although the weathering rates reported by Thomas (1994) have a large span, due to differences in temperature and humidity conditions, it can be seen that weathering is a slow process even under the most favourable tropical climatic conditions. Weathering of fresh bedrock under temperate climate conditions is a considerably slower process.

For a description of climatological-, hydrological- and geological factors affecting weathering, see Olvmo (2010, Section 3.3.3). Estimated denudation rates for the Forsmark region are presented and discussed below.

Erosion

Erosion can be defined as the removal and transport of bedrock and earth materials by a moving natural agent, such as air, water or ice. Erosion is often preceded by weathering and followed by transport and sedimentation. Air or water flowing over a bed of loose particles generates a shear stress that tends to initiate particle movement (Collinson 2005a). There is a critical boundary shear stress related to wind velocity and turbulence and water flow velocity above which particle movement occurs. With the exception of small grain sizes, the critical shear stress will increase as the grain size increases. For small grain sizes (less than 0.1 mm, silt and clay) increased cohesive strength and lower surface roughness means that higher velocities are required to initiate movement. In this section, a brief description is given of the main mechanisms of aeolian-, fluvial- and glacial erosion.

Aeolian erosion

Erosion of sediments by the wind, i.e. aeolian erosion, occurs in environments with sparse or non-existent vegetation, a supply of fine-grained sediments and strong winds, for example periglacial regions, semi-arid or arid regions, beaches and agricultural fields. Aeolian processes depend on weathering or other natural agents, e.g. rivers and waves, to supply sediments for transport. Particle movement is achieved due to wind shear stress and atmospheric turbulence. Particles begin to move when wind forces exceed the effect of weight and cohesion; the first particles to move dislodge or impact other grains and the number of particles in movement increase exponentially. However, the particles reduce the near-bed velocity of the wind and the transport reaches a dynamic equilibrium state in a few seconds. The mass flux of particles is related to the wind shear velocity, abrasion and the impact of particles moved by saltation and creep. The latter mobilise fine-grained material affected by cohesion but easily carried by the wind. Thus, the transport rate is limited both by wind shear velocity and supply of particles.

Fluvial erosion

Less than 0.005% of the global water is stored in rivers. Nevertheless, they are one of the most, if not the most, potent erosional forces operating on the Earth's surface. Rivers cut valleys, transport sediments and deposit their loads in a variety of depositional environments, such as flood plains and deltas. Vertical erosion by rivers is a striking feature of the world's mountainous areas where deep valleys dissect the landscape and form steep slopes, thereby creating the conditions for mass movement processes that are closely linked to fluvial vertical erosion.

Erosion and deposition of particles by water, i.e. fluvial erosion and deposition, is related to flow velocity. To generate water flow, a water supply and a flow gradient are required. Therefore, erosion by water generally requires a slope. However, erosion by water can also occur on bare surfaces as raindrops hit the surface and splash particles away. Fluvial erosion occurs on slopes, in ditches, brooks and rivers, and on beaches by wave action. Similarly to wind erosion, erosion by water depends on shear stress and turbulence, and particles begin to move when water fluid forces exceed the effects of weight and cohesion.

The material is transported in two distinct ways; it is either carried along with the fluid or in intermittent contact with the bed, described in e.g. Collinson (2005b). In the first case, fine-grained particles are supported by the upwards component of turbulence and carried away with the fluid in suspension. In the second case, generally referred to as bedload transport, coarser-grained material rolls (creep) or bounces (saltation) on the bed. Particles carried in suspension will enhance the erosive capability of the fluid by abrasion and particles moved by saltation or creep will set other grains in motion.

Fluvial erosion occurs on slopes and provides material that is transported to brooks and rivers, and into lakes and the sea. When freshwater reaches the sea, clay particles can flocculate into larger units and sedimentation is accelerated. Erosion by water on a slope increases with increased intensity of rain or snowmelt, increased inclination and length of the slope and decreased resistance to erosion of the soil. As for wind erosion, the presence of vegetation reduces the erosion rate.

Erosion on slopes can also be the result of mud flows, landslides, creep processes and avalanches. These processes result from the movement of masses of snow, earth and debris down a slope under the influence of gravity and can occur at scales from a few metres to several kilometres and at rates from metres per year to metres per second. The material can move by creep, sliding, flowing and falling. The movement of material is generally triggered by increased water content (for example from snowmelt), but earthquakes and volcanic eruptions can also cause material to move down a slope.

For more information on fluvial erosion, see Olvmo (2010, Section 4.1) and references therein.

Glacial erosion

Glacial erosion is complex and depends on material properties of ice and rocks, ice thermodynamics, friction and lubrication, chemical effects and subglacial hydrology. In addition, a precondition for efficient glacial erosion in bedrock is that the bedrock has been subject to pre-glacial, sub-aerial weathering processes.

In recent years, interpretations of geomorphological features (e.g. Kleman et al. 1997, 2008) measurements of cosmogenic radionuclides (e.g. Stroeven et al. 2002a) and ice-sheet modelling (e.g. Näslund et al. 2003) have resulted in a composite view on glacial erosion over Scandinavian. In some areas, over time dominated by basal frozen conditions, glacial erosion has been limited, whereas in other areas, where basal melting and sliding (see Section 3.1) have occurred, erosion may have been considerable.

Glacial erosion is traditionally divided into two components; plucking and abrasion. Plucking is the process by which rock fragments of different size are loosened, entrained and transported away from the glacier bed, while abrasion is the grinding of the substrate by rock fragments held in the moving glacier bed (cf. Sugden and John 1976, Benn and Evans 1998). The former is responsible for the characteristic irregular and fractured surfaces of lee sides of bedrock bumps and small hills in formerly glaciated areas.

Failure leading to loosening of fragments is known to be caused by stresses set up by differential ice load and high water pressures at the ice-bedrock interface (cf. Sugden and John 1976, Drewry 1986,

Benn and Evans 1998). Many minor fracture features, such as chattermarks and crescentic gouges, observed on glacially affected rock surfaces, indicate that normal stress at the glacier bed may be sufficient to cause failure in some rocks. However, the role of pre-existing weaknesses, such as joints, cracks and foliation, and also pre-glacial weathering should not be underestimated (cf. Ollmo and Johansson 2002). In addition, glacially induced cyclic water pressure variations may be important for bedrock crack propagation (e.g. Hooke 1991, Iverson 1991), a process by which rock fragments may be formed and eroded from the bedrock. Melting of ice on the stoss side and refreezing of meltwater on the lee side of obstacles at the ice-sheet bed may occur under certain thermal and pressure conditions. This so-called regelation process may also contribute to glacial erosion and transportation of subglacial till (e.g. Iverson 1993, 2000).

Abrasion is the process whereby the bedrock beneath a glacier is scoured by debris carried in the basal layers of the glacier (cf. Sugden and John 1976, Drewry 1986). The process leads to striation and polishing of bedrock surfaces (cf. Benn and Evans 1998) and is typical of the stoss side of rock bumps in formerly glaciated terrain. Many factors control the effectiveness of glacial abrasion. The relative hardness of the overriding clast and the bedrock is important and the erosion process is most effective when the overriding clast is considerably harder than the substratum. The force pressing the clast against the bed is decisive and depends in turn on the shape of clast as well as the motion of the clast during transport. Other factors related to the availability of clasts in the basal ice layers, such as clast concentration, removal of debris and availability of basal debris are also of major importance.

Also glaciers and ice sheets that are cold-based could contribute to a restricted amount of glacial erosion (Cuffey et al. 2000, Waller 2001, Bennett et al. 2003). This is achieved by e.g. movement, rotation and entrainment of debris in the basal ice at sub-freezing temperatures. However, this process is of very limited importance compared to other glacial erosional processes.

The magnitude of glacial erosion differs widely both in time and space. At a continental scale, the large-scale pattern of glacial erosion is controlled by the ice-sheet thermal regime and topography of the subglacial landscape. Based on a simple glaciological model (Sugden 1977, 1978) made a reconstruction of the thermal regime of the Laurentide ice sheet. The reconstructed thermal pattern shows an inner wet-based area and an outer cold-bed area, which broadly corresponds to the pattern of glacial erosion indicated by the distribution of erosional landforms. The most intense erosion as indicated by areas with high lake density coincides with the transition zone between wet-based and cold-based ice in the model, which probably favours plucking and debris entrainment.

Näslund et al. (2003) used a numerical ice-sheet model to study regional ice flow directions and glacial erosion of the Weichselian ice sheet in Fennoscandia. A new quantity, basal sliding distance, was introduced, describing the accumulated length of ice that has passed over the landscape by basal sliding. It was suggested that this entity could be used as a proxy for glacial erosion. The results indicate high basal sliding distance values in SW Sweden/SE Norway, in Skagerrak, and along the Gulf of Bothnia, implying relatively large amounts of glacial erosion in these regions. On elevated parts of the Scandinavian mountain range and on adjacent plains in the east, the basal sliding distance values are low, implying weaker glacial erosion, which is fairly in agreement with geological and geomorphological evidence (cf. Lagerbäck and Robertsson 1988, Riis 1996, Stroeven et al. 2002b, Ollmo et al. 2005). The method of estimating glacial erosion by simulated basal sliding distance (Näslund et al. 2003) was further developed by Staiger et al. (2005), who introduced a normalisation of the sliding values by the duration of ice cover over a particular site. Staiger et al. (2005) also set up a relationship between normalised sliding distance and rate of glacial erosion.

Another approach to the issue of glacial erosion is presented by Hallet et al. (1996) who made a comprehensive review of glacial erosion rates based on sediment yields. They found that rates of glacial erosion vary by many orders of magnitude from 0.01 mm yr^{-1} for polar glaciers and thin temperate plateau glaciers on crystalline bedrock, to 0.1 mm yr^{-1} for temperate valley glaciers also on resistant crystalline bedrock in Norway, to 1.0 mm yr^{-1} for small temperate glaciers on diverse bedrock in the Swiss Alps, and to $10\text{--}100 \text{ mm yr}^{-1}$ for large and fast-moving temperate valley glaciers in the tectonically active ranges of southeast Alaska. These major differences highlight the importance of the glacial basal thermal regime, glacial dynamics and topographic relief on the rates of glacial erosion.

Yet another approach was presented by Pässe (2004). In order to estimate the average glacial erosion in the bedrock in non-mountainous regions he used seismic data and well depth data on the thickness of the minerogenic Quaternary sediments in Sweden and Denmark. The average thickness of Quaternary sediments was estimated to be 16 m in the investigated area, which corresponds to 12 m of bedrock assuming that the whole volume is the result of glacial erosion of fresh bedrock. Since a great part of the sediments likely consist of glacially redistributed Tertiary regolith, this number probably is an overestimation of the glacial erosion depth in the bedrock. Considering this, Pässe concluded that the average glacial erosion during a full glacial period may be estimated to between 0.2 m and 4 m. This is in agreement with estimates of glacial erosion in the Precambrian basement based on geomorphological observations (Lidmar-Bergström 1997, Ebert 2009). The amount of Pleistocene glacial erosion of saprolites has been estimated between 10 and 50 m, whereas Pleistocene glacial erosion of fresh bedrock was estimated at some tens of metres (Lidmar-Bergström 1997), although with great variations.

However, in Fennoscandia as a whole, large spatial differences in thicknesses of Quaternary deposits occur and distinct patterns of glacial scouring and deep linear erosion are observed in places. Kleman et al. (2008) point to the relative roles of mountain ice sheets and full-sized Fennoscandian ice sheets for this zonation and use spatio-temporal qualitative modelling of ice sheet extent and migration of erosion and deposition zones through the entire Quaternary to suggest an explanatory model for the current spatial pattern of Quaternary deposits and erosion zones. According to Kleman et al. (2008), the Forsmark area is situated at the border between areas of bedrock scouring with thin patchy drift and areas of intermediate drift thickness.

For the period of the Quaternary that is dominated by 100 ka long glacial cycles, i.e. for the past ~1 Ma, the Forsmark region has been covered by ice sheets for ~10% of the time (Kleman et al. 2008, Figure 9).

Glacial meltwater erosion may be an effective agent both in subglacial and proglacial environments. The sediment concentrations of glacial meltwater streams are often high and the flow is often very rapid and turbulent, which mean that flows transitional between debris flows and normal stream flow are common (Benn and Evans 1998). The erosivity of glacial streams is therefore often high both on bedrock and in sediments. Apart from the high erosivity, the mechanisms of glacial meltwater erosion are the same as normal fluvial erosion including abrasion, cavitation, fluid stressing and particle entrainment from cohesionless beds as well as chemical erosion.

The formation of glacially overdeepened valleys and basins has been described in a recent publication by Fisher and Haeberli (2012), as well as methods of modelling glacial erosion (Fisher and Haeberli 2010). A review on deep glacial erosion of tunnel valleys in northern Europe was given by Stumm (2010).

The relative efficacy of fluvial and glacial erosion on a global basis, are presented in Koppes and Montgomery (2009). Olvmo (2010) presented a description of erosional and weathering processes relevant for Scandinavian conditions and the Forsmark area in a 0.1 to 1 Ma time perspective. Estimated denudation rates for the Forsmark region are presented and discussed below.

2.4.2 Controlling conditions and factors

As mentioned above, weathering and erosion are complex processes affected by the prevailing environmental conditions. Given the characteristics of the rock, the degree of weathering depends on the availability of weathering agents such as salt, moisture, biota (e.g. microorganisms and lichens), and on the microclimatic conditions to which the rock is exposed. Weathering occurs in all climates, but high temperatures and humid conditions increase weathering rates. In areas where frost and/or permafrost occur, freezing and freeze-thaw effects are important geomorphic processes. However, weathering in periglacial environments is also affected by salt (in combination with freezing), wetting and drying, thermal fatigue and biological agents (French 2007).

During temperate climate conditions, the dominant erosion process is fluvial erosion. During permafrost climate conditions, when the climate can be expected to be dryer and vegetation sparse, aeolian erosion and solifluction may also be important processes. During spring when the snow melts, there may be significant erosion of sediments in the active layer in periglacial permafrost areas. During glacial climate conditions, the erosion is mainly affected by the basal conditions of the ice sheet. In areas where the ice is frozen to the bed, the ice acts to preserve its subsurface and practically no

erosion occurs, whereas in areas of basal melting erosion of bedrock and pre-existing sediment is likely to occur, with more erosion generally associated with faster ice flow. In sub-glacial tunnels, where melt water flows towards the ice-sheet margin, the erosion of loose sediments and bedrock can be of significance.

The topographic relief in Scandinavia is generally not dramatic outside the Scandinavian mountains (e.g. Lidmar-Bergström and Näslund 2005). The resistance to denudation of the Precambrian rocks that dominate in Scandinavia is rather uniform, as compared with, for example, the variation between the Caledonian bedrock types in the Scandinavian mountains. Although the relief locally may be steep at many places, the relatively homogeneous denudation resistance has contributed to the moderate to low relief of the Precambrian rock basement. The relative relief is exceptionally low (less than some tens of metres) along significant portions of the eastern Baltic Sea coastline of southern and south-central Sweden, due to the present remnants of the *sub-Cambrian peneplain* (a denudation surface formed in crystalline rock with a typical relief of less than 20 m (Rudberg 1954, Lidmar-Bergström 1995), interpreted to have been formed down to sea-level prior to the Cambrian). The low relief favours low subaerial erosion rates, for example, the most important subaerial erosion process, fluvial erosion, increases with steeper topographical gradients.

One main reason why a deep dissection of the landscape could not occur by fluvial erosion in Forsmark is because of the coastal location of the site, situated just a few m above the Baltic Sea. The sea-level acts as the base-level for fluvial erosion, i.e. fluvial erosion cannot cut deeper than sea-level. The expected maximum lowering of the Baltic sea-level during glacial cycles (18 m) sets, together with the present altitude of the ground surface above the repository, a maximum limit to the amount future fluvial erosion at the Forsmark site.

Table 2-7 summarises how geosphere variables are influenced by surface denudation.

2.4.3 Natural analogues/observations in nature

The current landforms in Scandinavia are a result of the interaction between tectonic processes, weathering, erosion and sedimentation and consequently the traces of these processes can be observed and interpreted in nature. In Scandinavia, large-scale bedrock landforms outside the mountain range, such as denudation surfaces and landscapes of weathering and stripping of saprolites, are common, and reflect the varying phases of weathering, erosion, and sedimentation that have occurred in association with tectonic events and climate change (e.g. Lidmar-Bergström 1997, Lidmar-Bergström and Näslund 2002).

Table 2-7. Influence of surface denudation on geosphere variables.

Geosphere variable	Influence present (Y(N)	Summary of influence
Groundwater flow	Yes	The process refers to weathering and erosion at the surface. Even if there is no absolute boundary between surface- and groundwater this process only includes the action of surface water. Denudation could under certain circumstances affect permeability and thus the degree of infiltration, which would, marginally, change groundwater boundary conditions.
Groundwater composition	Yes	Surface weathering may to some degree change groundwater composition. The effect is judged as negligible for the safety assessment.
Rock stresses	Yes	The removal of bedrock by denudation changes the stress field. However, since the denudation rate is very low, the influence is judged as negligible for the safety assessment period.
Fracture geometry	Yes	Weathering may change fracture aperture in the upper metre of bedrock, for instance by widening of fractures due to freezing. The influence is judged as negligible in relation to repository safety.

During the late Cenozoic glacial cycles, ice sheets have repeatedly covered parts or the whole of Scandinavia, producing glacial erosional landforms in bedrock (e.g. Rudberg 1954) and in surficial deposits (e.g. Kleman et al. 1997, 2008). Traditionally, it has been thought that a considerable part of the bedrock relief is the result of glacial erosion. However, as mentioned above, it has been shown that the amount of glacial erosion of the Precambrian basement in general is on the order of a few tens of metres (Lidmar-Bergström 1997), and in this context valleys are more eroded than the surrounding terrain. However, within the Scandinavian mountain range, valleys may have experienced several hundred metres of glacial erosion (Kleman and Stroeven 1997). Furthermore, during the last decades our understanding of ice-sheet thermodynamics has showed that large portions of ice sheets may be cold-based and thus have a negligible erosive effect. Over the same period, numerous glacial geological studies have shown that the occurrence of preglacial saprolite remnants is solid evidence that ice sheets under certain circumstances cause very restricted glacial erosion, or even have a preserving effect on pre-glacial landforms (Lagerbäck 1988a, b, Kleman 1994), whereas under other conditions they may be fully erosive.

2.4.4 Model studies

Estimates of denudation rates can be made either through numerical models that per se describe the processes involved in the denudation, for instance the processes resulting in glacial erosion, or estimates may be based on interpretation and GIS-modelling of the development over time of landforms. A review of numerical modelling of glacial erosion is found in Fisher and Haerberli (2010), while the latter approach may be exemplified by Olvmo (2010), who has used this method in a study of the long-term denudation history of southern Sweden.

The long-term denudation history of southern Sweden is interesting for two reasons. Firstly, it may be a guide to understand the denudation rate through time in the Forsmark area. Secondly, it is important because the different landforms and surfaces that have been recognised, such as the sub-Cambrian peneplain mentioned above, may be used as reference surfaces to understand, at least at a regional scale, the magnitude and patterns of glacial erosion.

Some examples from Sweden of calculated long-term denudation rates can be found. Many of them use remnants of the sub-Cambrian peneplain as a reference surface. In eastern Småland and southern Östergötland, the maximum denudation of the tectonically uplifted sub-Cambrian peneplain is approximately 100 m. Once overlying sedimentary cover rocks had been removed, denudation and removal of the denudation products would have required a period of between 2 and 50 Ma (Lidmar-Bergström et al. 1997). On the Swedish west coast, a so-called *Sub-Cretaceous etch surface* has been incised into the sub-Cambrian peneplain by weathering. In places, it has resulted in a maximum bedrock lowering of 135 m. The time required for this amount of denudation has been suggested to be between 3 and 68 Ma (Lidmar-Bergström et al. 1997), with the denudation occurring during the Jurassic-Early Cretaceous. Finally, saprolite thicknesses of 50 m in Skåne were interpreted to have been produced by weathering over a time interval of 1–25 Ma (Lidmar-Bergström et al. 1997).

Given the specific tectonic and climatic evolution, including phases of denudation, sedimentation, and stripping of saprolites, the above examples clearly show that the evolution of the sub-Cambrian peneplain in southern Sweden into a younger incised landscape has been a very slow process, and that the total amount of material removed from the crystalline bedrock has not been large considering the very long time periods involved. The total maximum denudation of bedrock in areas of Precambrian crystalline basement in southern Sweden during the last 540 Ma is on the order of a few hundred metres. A significant part of this denudation took place during Mesozoic tropical climate conditions, considerably more favourable for chemical deep weathering than, for instance, the present temperate climate.

A more detailed account of the long-term landform development and associated denudation in southern Sweden is given in Olvmo (2010).

A study on landform development and associated denudation in the Forsmark and Laxemar regions has been performed, reported in Olvmo (2010). In the following, a summary of the study in the Forsmark region is given.

From a geomorphological point of view, the investigated region (Figure 2-53) can be divided into four distinctive areas, i) a central area, hosting the Forsmark site, characterised by very low topographic relief, ii) a coastal region SE of Forsmark with coast-parallel lineaments, iii) a southern part with more pronounced relief characterised by east-west trending fault scarps, and iv) an area with hilly

relief in the northwest. The relief in the central area, including the Forsmark site, is characteristic of the sub-Cambrian peneplain and is consistent with the interpretation by Lidmar-Bergström (1997). The relative relief in this area is less than 20 m (Figure 2-53), although with some shallow valleys present in the peneplain. Around Forsmark (within c 10 km) the relief is extremely low, often less than 10 m. South of this central flat area, a more dissected landscape appears. Here the peneplain is broken into blocks, tilted in different directions. Some of the blocks are elevated and partly dissected by weathering and erosion. In the southern part of the study area, the elevated rims of these uplifted blocks give rise to east-west trending horst ridges, whereas in the Stockholm region the peneplain is highly dissected and give rise to a *joint valley landscape*, consisting of plateaux bounded by shallow straight, structurally controlled valleys. In the coastal low-lying areas between Forsmark and Uppsala, the relief is quite considerable along coast-parallel tectonic lineaments. This is obvious in the relative relief map (Figure 2-53) where relative relief locally rises to 50 m along these fracture zones. In this area, some 15 km southeast of Forsmark, the coastal landscape is more dissected. The area coincides with areas with a high frequency of rock outcrops which may suggest that glacial erosion has been more effective in this region than at Forsmark, probably as a result of the closeness to the Baltic Sea depression which may have influenced the ice-sheet flow.

The Forsmark area is situated on the sub-Cambrian Peneplain not far from the present extension of the Lower Paleozoic sedimentary cover rocks. Exhumation of the peneplain has probably occurred during the Pleistocene glaciations and possibly as late as the Weichselian glaciation as indicated by the occurrence of clayey tills in the area. The major bedrock landforms in the area are probably close to the original peneplain surface. The area is extremely flat over large distances and many landforms in the Quaternary drift cover are prominent features in the landscape.

In this context, it is worth noting that the relief map (Figure 2-53) shows the ground surface relief, i.e. it comprises the relief of both bedrock and overlying Quaternary deposits. The uncertainty introduced by not having removed these deposits in the analysis is however in general not large, exemplified by the fact that within the terrestrial parts of the Forsmark site (Figure 2-3), the average soil thickness is only 4 m (SKB 2010d, Section 5.1.2). Locally in the investigated area (Figure 2-53), larger sediment thicknesses of up to c 100 m may occur, typically where large eskers are found. However, parts of these sediment thicknesses do have an expression in the relief map, such as the north-south trending eskers located north of Uppsala (Figure 2-53). If the esker sediments could be removed from the DEM, the resulting relative relief would not necessarily be greater than with the present eskers included. Nevertheless, this uncertainty is taken care of by the analysis of a case with considerably greater relief than in Figure 2-53, see below.

Glacial erosion has reshaped some of the forms in the bedrock and may be responsible for evacuation of regolith along structurally controlled valleys. This is especially true in the coastal areas some 15 km southeast of Forsmark, where glacial erosion may have been effective along fracture zones. Based on the conclusion that the sub-Cambrian peneplain is well-preserved and probably coincident with the present relief, the total amount of glacial erosion caused by repeated Pleistocene glaciations in the area on average is probably less than 10 metres, but is probably above that in the coastal zone southeast of Forsmark. The very low relief of the landscape today, together with the fact that the bedrock consists of crystalline basement rocks, implies that the present denudation rate is extremely low and corresponds to the low rates found in low relief shield areas reported in the literature.

Future glacial erosion at Forsmark

The effect of a future glacial cycle would probably be very limited in areas dominated by the well-preserved sub-Cambrian peneplain, such as at Forsmark. Given the long-term denudation history up to present, the expected amount of glacial erosion during a future glacial cycle is limited. For the Forsmark region, i.e. an area significantly larger than the specific repository location, Olvmo (2010) estimated that glacial erosion could amount to 2–5 m for a future glacial cycle comparable with the last one. Lidmar-Bergström (1997) estimated the *total* amount of glacial erosion for all Late Cenozoic ice sheets in low-land terrain in Sweden to be around 10 m. If extreme assumptions are excluded, which is a valid approach for the low relief of the Forsmark site, about 1 m of glacial erosion for one glacial cycle was estimated by Pässe (2004). Based on all these estimates, and the topographic and geological characteristics of the repository location, the amount of glacial erosion in fresh bedrock for one glacial cycle is here estimated to 1–2 m. More glacial erosion is expected in topographic low positions and/or along major fracture zones, especially if such features are located along the general ice flow direction.

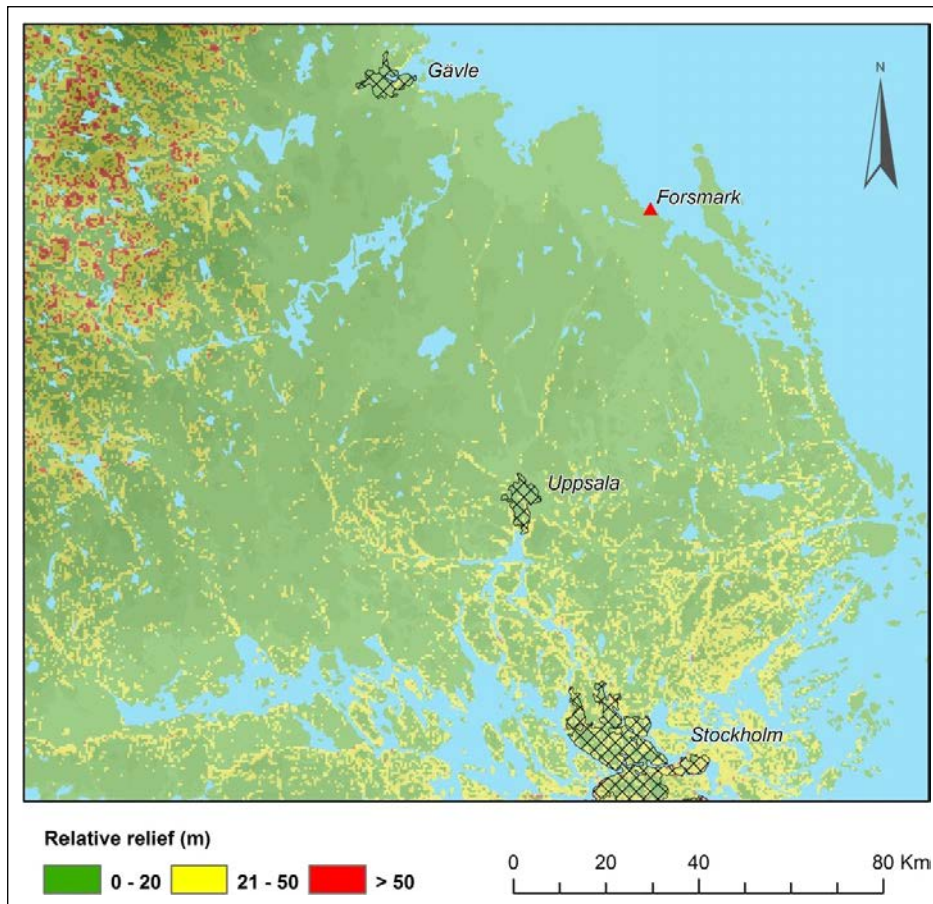


Figure 2-53. Relative relief of the ground surface in the Forsmark study area.

The dissected coastal areas south-east of Forsmark, with sometimes considerable relief, may experience stronger glacial erosion during a glaciation with a similar flow pattern as during the Late Weichselian. In this area, c 15 km from Forsmark, glacial erosion of more than 10 m in one glacial cycle would be expected locally in topographic lows (Olvmo 2010).

Conclusions

The Forsmark area has a very low topographic relief resulting in a setting not prone to effective denudation. Given this, and the denudation rates estimated by Lidmar-Bergström (1997), Påsse (2004) and Olvmo (2010), a glacial erosion value of 1–2 m per glacial cycle (similar to the last one), is expected. If looking only at the non-glacial component of denudation, the long-term denudation rate of the site is low as a consequence of the very low relief and the proximity to base level (sea-level). The numbers estimated for the long-term denudation rates (Olvmo 2010) are in agreement with reports of denudation rates in geological shield areas and lie within the range 0 to 10 m/Ma.

2.4.5 Time perspective

Weathering, erosion and sedimentation are active processes over most of the Earth’s surface. In Sweden, the maximum total denudation can be expected to be limited in lowland areas of low relative relief. For the region around Forsmark it is estimated to be up to 20 m Ma⁻¹. The rate of weathering and erosion vary in time and space.

2.4.6 Handling in the safety assessment SR-PSU

Present-day knowledge on denudation processes suggests that denudation generally will be limited in lowland parts of Scandinavia during the assessment period. In areas where the bedrock is highly

fractured, weathering and erosion can be expected to be significantly more rapid than the estimated averages. The impact of weathering and erosion on groundwater flow and rock stresses is considered to be insignificant over the time period of relevance in the assessment.

For a shallow repository, such as SFR, it is not meaningful (or requested by the regulators) to try and describe how the repository evolves during and after ice-sheet coverage. It is however requested to assess the radiological *consequences* of a potential repository collapse, following ice sheet coverage. In this context, the consequences of a repository affected by e.g. heavy glacial erosion and/or glacial tectonics are covered by the safety assessment scenarios analysed in SR-PSU that include a case that assumes completely degraded concrete and no geosphere retention (SKB 2014a). Therefore, the potential impact of glacial erosion on the SFR repository during the 100 ka assessment period is not described in great detail in the present report. It should be noted, however, that the amount of glacial erosion over SFR is not likely to be significant for the 100 ka assessment period.

2.4.7 Handling of uncertainties in SR-PSU

Rates of weathering and erosion vary as environmental conditions change. The rates of weathering and erosion also depend on rock and sediment characteristics and topography. In spite of the uncertainties in future environmental conditions, there is no reason to believe that denudation in the Forsmark region would diverge significantly from the values estimated above.

Uncertainties in mechanistic understanding

There are uncertainties in the understanding of the detailed mechanisms of weathering and erosion. However, for the safety assessment, the approach of using also indirect estimates of the amount of erosion and weathering over long time-scales (i.e. the development of large-scale landforms), means that the total knowledge is sufficient for estimating the amount of weathering and erosion of fresh bedrock during the assessment period.

Model simplification uncertainties in SR-PSU

Not relevant for this process.

Input data and data uncertainties in SR-PSU

Not relevant for this process.

2.4.8 Adequacy of references

The SKB report produced for the handling of surface denudation (Olvmo 2010) has undergone the SR-Site QA system handling, including a documented factual review procedure. Also the SR-Can Geosphere process report (SKB 2006b), from which some of the studies are used, has undergone QA system handling including a factual review process. Other references used for the handling of surface denudation processes are either peer-reviewed articles from the scientific literature or from textbooks (Sugden and John 1976, Drewry 1986, Paterson 1994, Thomas 1994, Benn and Evans 1998, French 2007).

Table 2-8. Expected future denudation at the repository location in Forsmark in a 100 ka time perspective. If looking at a larger region around Forsmark, locally higher denudation values are expected in topographic lows and along major fracture zones.

Parameter	~100 ka timescale (one glacial cycle)
A. Glacial erosion (average value over landscape)	1–2 m
B. Non-glacial denudation	0–0.6
C. Total denudation (A+B)	1 to 2.6 m

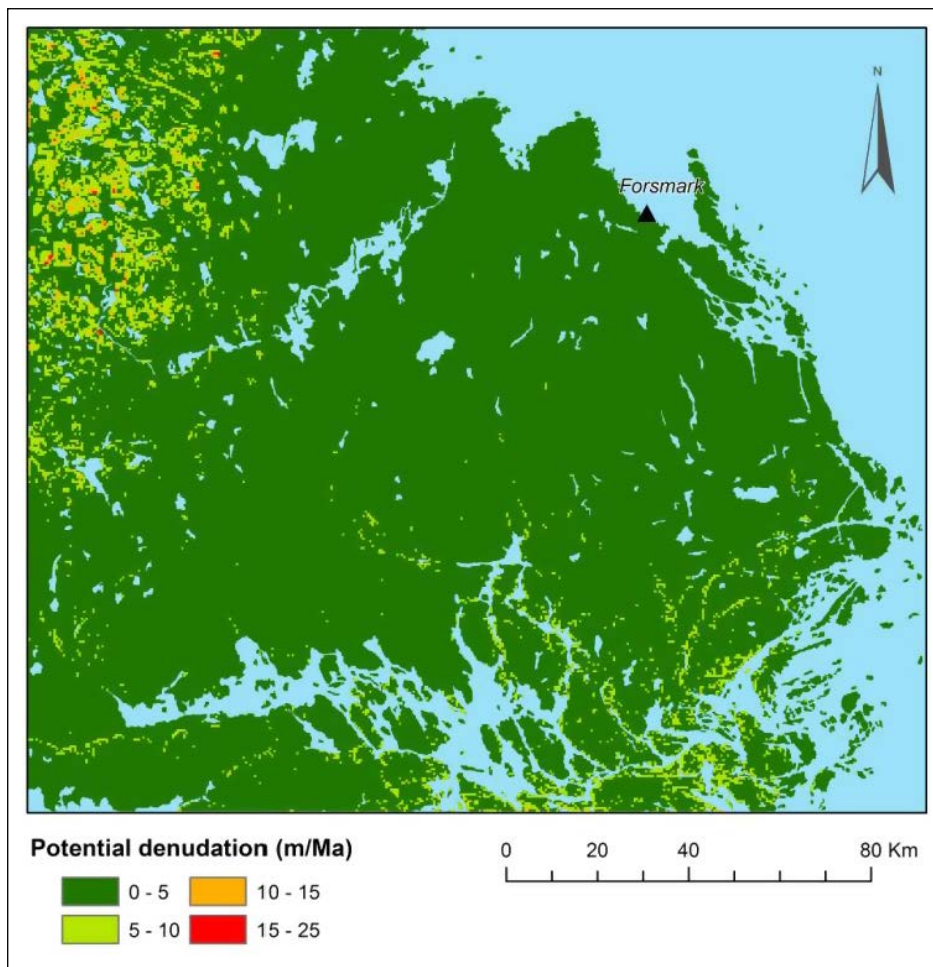


Figure 2-54. Calculated potential future non-glacial denudation in the Forsmark region. At Forsmark, calculated values of the non-glacial denudation component are low, up to 5 m/Ma. From Olvmo (2010).

3 Past and future climate evolution

3.1 Introduction

The scientific basis for the selection and definition of the climate cases utilised in the SR-PSU safety assessment is given in this section. The current knowledge on past and future climate evolution is described, based both on reviews of international scientific literature and on studies performed for SKB to extend current knowledge in areas of major interest for the safety assessment.

Geological records show that over the Quaternary period the Earth's climate has varied from warm (interglacial) to cold (glacial) periods characterised by extensive ice sheets in high northern latitudes. For the past ~900 ka interglacials have occurred every 80 to 120 ka (Abe-Ouchi et al. 2013, Crowley and Hyde 2008, Huybers 2011, Lisiecki 2010). To illustrate these variations, atmospheric CO₂ concentrations as measured in Antarctic ice cores and stacked $\delta^{18}\text{O}$ as measured in marine sediment records, a proxy for global ice volume, are displayed in Figure 3-1.

Understanding of the dynamics of past climate evolution and variability is essential to assess future climate evolution.

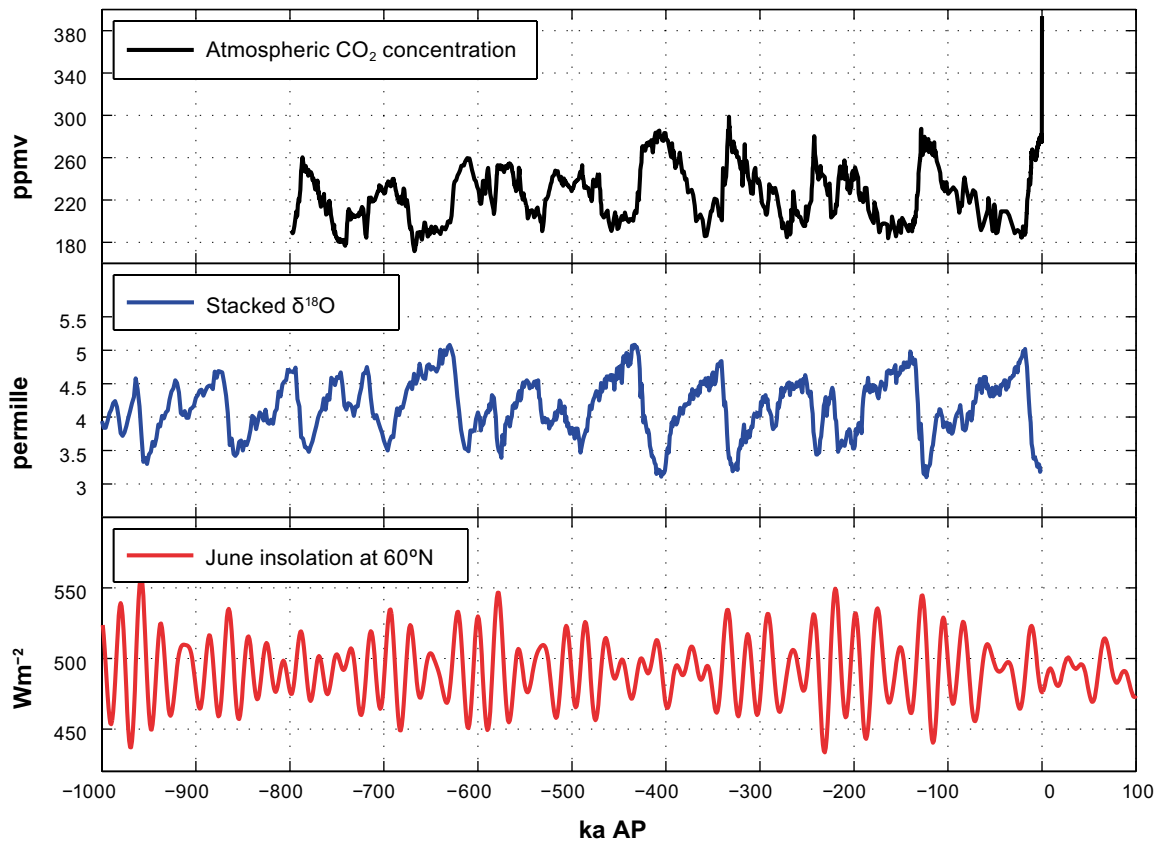


Figure 3-1. CO₂ composite record (upper panel; Lüthi et al. 2008) complemented with the observed annual average atmospheric CO₂ concentration in 2012 AD (393.8 ppmv; www.esrl.noaa.gov). High values of CO₂ correspond to a warmer climate (interglacial state). A stack (middle panel; Lisiecki and Raymo 2005) of 57 benthic $\delta^{18}\text{O}$ records; the $\delta^{18}\text{O}$ is a proxy for the global ice volume. High values of $\delta^{18}\text{O}$ correspond to a colder climate (glacial state). June insolation at 60°N (lower panel; Berger 1978, Berger and Loutre 1991).

The latitudinal and seasonal distribution of incoming solar radiation (insolation) is the major external driver of the Earth's climate. This distribution changes over time due to variations in the Earth's orbit. These include variations in the eccentricity of the Earth's orbit, the obliquity (i.e. the tilt of the Earth's axis of rotation), and in the precession of the equinoxes, with dominant frequencies at about one cycle per 100 ka (eccentricity), 41 ka (obliquity) and 21–23 ka (precession). The ~100 ka timescale in the glacial/interglacial cycles of the last ~900 ka (Figure 1-2) is commonly attributed to control by these variations in the Earth's orbit. Milankovitch proposed that the Earth is in an interglacial state when it's rotational axis both tilts to a high obliquity and precesses to align the Northern Hemisphere summer with Earth's nearest approach to the Sun. June insolation at 60°N is displayed in Figure 3-1 for reference. Statistical analyses of long climate records supported this theory (Hays et al. 1976, Huybers 2011, Huybers and Wunsch 2005, Lisiecki and Raymo 2007), however many questions remain about how orbital cycles in insolation produce the observed climate response (Huybers 2011, Imbrie et al. 2011, Lisiecki 2010).

The amplitude and the saw-tooth shape of the variations in the climatic records however imply that non-linearities and amplifications, e.g. through ice/snow albedo, atmosphere and ocean circulation and the carbon cycle, exist. A number of modelling studies have been performed to enhance understanding of the physical mechanisms associated with deglaciation and glaciation (see e.g. Mysak 2008 for a review of modelling studies of glacial inception). Studies with so called Earth System Models of Intermediate Complexity (EMICs) that include simplified descriptions of the main components of the climate system, i.e. atmosphere, ocean, sea ice, ice sheets and sometimes vegetation, indicate that the combination of orbital insolation variations and glacial–interglacial atmospheric CO₂ variations give a reasonable agreement between simulated and reconstructed glacial cycles (e.g. Ganopolski et al. 2010, Loutre and Berger 2000).

The most contentious problem is why late Pleistocene climate records are dominated by 100-ka cyclicity. Insolation changes are dominated by 41-ka obliquity and 23-ka precession cycles whereas the 100-ka eccentricity cycle produces negligible 100-ka power in seasonal or mean annual insolation. Recently, Abe-Ouchi et al. (2013), used comprehensive climate and ice-sheet models to simulate the ice-sheet variation for the past 400 ka forced by the insolation and atmospheric CO₂ content. Their model realistically simulates the saw-tooth characteristic of glacial cycles (Figure 3-1), the timing of the terminations and the amplitude of the Northern Hemisphere ice-volume variations, as well as their geographical patterns at the LGM and the subsequent deglaciation (Abe-Ouchi et al. 2013). They conclude that insolation and internal feedbacks between the climate, the ice sheets and the lithosphere–asthenosphere system explain the 100 ka periodicity.

To geologists of the future, the present interglacial, the Holocene, will look different from the previous major interglacial – the Eemian, which began around 130 ka BP (e.g. Solomon et al. 2011). During previous interglacials, the atmospheric CO₂ concentration reached a peak value of about 300 ppmv and thereafter began to fall; in the present interglacial, CO₂ will instead rise by an amount that will be determined by human activities. Marcott et al. (2013) reconstructed regional and global temperature anomalies for the past 11.3 ka from 73 globally distributed records (Figure 3-2).

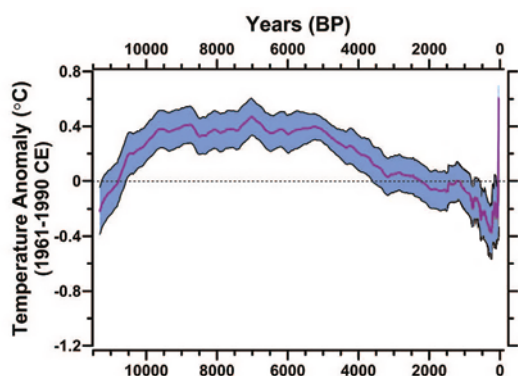


Figure 3-2. Globally stacked surface temperature anomalies with respect to the period 1961–1990 AD (purple line) with one standard deviation uncertainty (blue band). Modified from Marcott et al. (2013).

This reconstruction is based on records of relatively low temporal resolution, which is why only longer-term variations are reconstructed. They conclude that early Holocene (10 ka to 5 ka BP) warmth is followed by $\sim 0.7^{\circ}\text{C}$ cooling through the middle to late Holocene (<5 ka BP), culminating in the coolest temperatures of the Holocene during the Little Ice Age, about 200 years ago. They further state that current global temperatures of the past decade have not yet exceeded peak interglacial values but are warmer than during $\sim 75\%$ of the Holocene temperature history.

An up-to-date overview of scientific knowledge on past, present and future climate evolution was recently released by Working Group 1 of the Intergovernmental Panel on Climate Change (IPCC) Fifth Assessment Report (AR5; IPCC 2013). IPCC (2013) comes to the following conclusions.

- Warming of the climate system is unequivocal, and, since the 1950s, many of the observed changes are unprecedented over decades to millennia. The atmosphere and oceans have warmed, the amounts of snow and ice have diminished, sea level has risen, and the concentrations of greenhouse gases have increased.
- The atmospheric concentrations of CO_2 , methane, and nitrous oxide have increased to levels unprecedented in at least the last 800,000 years. CO_2 concentrations have increased by 40% since pre-industrial times, primarily from fossil fuel emissions and secondarily from net land use change emissions.
- Continued emissions of greenhouse gases will cause further warming and changes in all components of the climate system. Limiting climate change will require substantial and sustained reductions of greenhouse-gas emissions.
- Global surface temperature change for the end of the 21st century is likely to exceed 1.5°C relative to 1850 to 1900 for all emission scenarios.
- Most aspects of climate change will persist for many centuries even if emissions of CO_2 are stopped. This represents a substantial multi-century climate change commitment created by past, present and future emissions of CO_2 .

In this chapter, current knowledge on climate evolution during the penultimate interglacial, the Eemian and the Weichselian glacial is described. Further, current knowledge on future climate evolution on timescales from 100 years to 100 ka is described. This knowledge was used as a basis for the selection and description of a range of climate cases relevant for the safety assessment SR-PSU (Chapter 4).

3.2 Glacial history, Weichselian climate and reconstructed last glacial cycle conditions at Forsmark

The Weichselian glacial cycle, and specifically the transition from the warm Eemian interglacial into the cold Weichselian glacial is of interest in assessments of long-term repository safety, since the present Holocene interglacial will eventually end and a transition to colder climates will occur. As discussed in Section 3.3.5 the timing of this future event is uncertain. However, regardless of this timing, the present-day understanding and view of the most recent interglacial–glacial transition is of interest in this context. Therefore, a review of Early Weichselian climate in Europe, including the transition from the Eemian interglacial into the early cold and warm phases of the Weichselian glacial, is presented in Wohlfarth (2013). Furthermore, a re-examination of the full last interglacial–glacial cycle has been made based on long proxy records from central and northern Europe (Helmens 2013). In addition, ice-marginal fluctuations during the Weichselian glaciation in Fennoscandia were previously reviewed in Lokrantz and Sohlenius (2006). Section 3.2.1 gives a summary of the information in these publications. The different warm and cold phases of e.g. the last glacial cycle are divided into numbered so-called Marine Isotope Stages (MIS). For a better understanding of the temporal aspect in the description of the last glacial cycle below, these stages are summarised and described in Table 3-1.

Table 3-1. Summary and description of Marine Isotope Stages, ages, stadials and interstadials of the Eemian, Weichselian and Holocene. Regional variations from the denoted warm/cold state occur and there is a wide range of regional names used for each of the stadials/interstadials, see e.g. Lokrantz and Sohlenius (2006), Helmens (2013) and Wohlfarth (2013).

Marine Isotope Stage	Age (ka BP)	Stadial/ Interstadial	Warm/Cold	Name (several other names are also used)	Weichselian phase
MIS 5e	...–115(110)	Interglacial	Warm	Eemian	–
MIS 5d	115(110)–105	Stadial	Cold	Herning (Melisey I)	Early Weichselian
MIS 5c	105–93	Interstadial	Warm	Brørup (St Germain 1c)	Early Weichselian
MIS 5b	93–85	Stadial	Cold	Rederstall (Melisey II)	Early Weichselian
MIS 5a	85–74	Interstadial	Warm	Odderade (St Germain II)	Early Weichselian
MIS 4	74–59	Stadial	Cold	Middle Weichselian stadial	Middle Weichselian
MIS 3	59–24	Interstadials/ Stadials	Warm/Cold	Middle Weichselian interstadials	Middle Weichselian
MIS 2	24–12	Stadial	Cold	Stadial including Last Glacial Maximum	Late Weichselian
MIS 1	12–0	Interglacial	Warm	Holocene	–

3.2.1 Weichselian glacial history and climate

The review by Wohlfarth (2013) addresses the transition from the last interglacial into the last glacial period in Europe, which corresponds to the time interval between approximately 122 and 70 ka BP. Based on state-of-the-art paleoclimatic and paleoenvironmental information from selected terrestrial, marine and ice-core records, questions regarding the magnitude, duration, and cyclicity of early glacial stadial and interstadial episodes are discussed. The end of the last interglacial, i.e. the Eemian or MIS 5e, and the transition into the last glacial period was initially triggered by a decrease in incoming summer insolation at high northern latitudes. The change in orbital configuration subsequently led to a series of time-transgressive changes (e.g. gradual vegetation replacement; changes in sea-surface temperature, salinity, strength of the North Atlantic Current). As Northern Hemisphere ice sheets started to grow and expand these changes became progressively more pronounced.

The sequence of events leading from the last interglacial (the Eemian, MIS 5e) into the last glacial has been described using climate models of different complexity and using various boundary conditions, paleodata series, and comparisons between model outputs and paleodata. One possible scenario involves the development of summer sea ice in the northern North Atlantic already during the later part of the Eemian interglacial, as a response to decreasing summer insolation. This would have accelerated a vegetation shift, which in turn would have led to a decrease in albedo. More extensive sea ice could, through brine formation, have increased the Atlantic meridional overturning circulation, which would have supplied more moisture to the cold high northern latitudes. This in turn would have favoured the growth of ice sheets.

A response of the vegetation in northern Europe to the decrease in summer insolation and to increased summer sea ice may be seen as early as 122–120 ka BP, but became most distinct around 115 ka BP, when North Atlantic sea-surface temperatures show signs of a first minor cooling. This cold event (labelled sea surface cooling event C26, see Figure 3-3) defines the MIS 5e/5d transition in marine cores and seems to correlate with Greenland stadial GS26. This first distinct, but minor cooling event on Greenland is paralleled by cold temperatures in Antarctica, which implies synchronous cooling in both hemispheres. However, while Antarctica remained cold, Greenland started to warm just before 110 ka, suggesting the start of the so-called bipolar see-saw mechanism. The first marked cooling over Greenland at 110–108 ka BP (GS25, Figure 3-3) was accompanied by a distinct drop in North Atlantic sea-surface temperatures (C24 event), by an increase in ice-rafted debris and by marked vegetation changes in southern Europe. This shift in vegetation defines the end of the terrestrial Eemian in southern Europe, which in comparison to marine records, occurred during MIS 5d. Paleorecords thus suggest that the response of the vegetation to North Atlantic cooling events was delayed in southern Europe by at least 5 ka as compared to northern Europe (Figure 3-3).

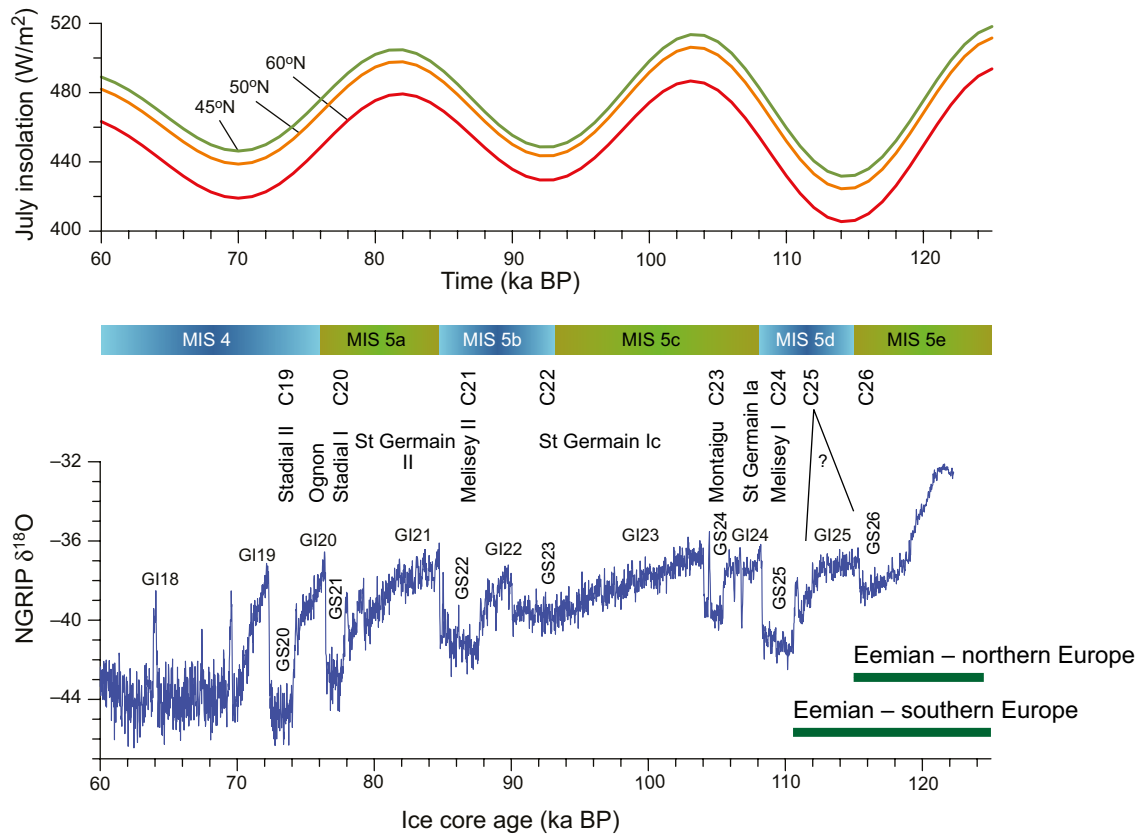


Figure 3-3. Summer insolation at 60°, 50° and 45° N (Berger 1978, Loutre M F, personal communication) compared to the NGRIP $\delta^{18}O$ record (NorthGRIP community members 2004). The North Atlantic sea surface cooling episodes (C26 to C19) and the terrestrial vegetation zones are according to Sánchez Goñi (2007). The correlation between marine and terrestrial events and the NGRIP record was inferred from Figure 13.1 in Sánchez Goñi (2007). The correlation between marine isotope stages (MIS 5e–4) and the NGRIP isotope record is tentative and partly follows Sánchez Goñi (2007) and partly Chapman and Shackleton (1999). The end of the terrestrial Eemian is according to Müller and Kukla (2004) and Sánchez Goñi (2007). GS = Greenland stadials; GI = Greenland interstadials. Note that the correlation of C25 and C26 to Greenland stadials is not entirely clear. C26 likely corresponds to GS26. From Wohlfarth (2013).

The decrease in summer insolation at high northern latitudes thus led to a series of feedback mechanisms, which gradually became stronger as ice sheets grew larger. The initiation of the bipolar see-saw mechanism at around 110–112 ka BP seems to have triggered the series of abrupt and recurrent shifts between warmer interstadials and colder stadials that characterised the last glacial. While tundra and steppe-tundra seem to have developed in response to severe stadial conditions, the vegetation response to warmer interstadial temperatures was regionally different.

The overall conclusion from the reviews of Wohlfarth (2013) and Helmens (2013) is thus that the transition from the warm Eemian interglacial state (MIS 5e) to full glacial conditions during e.g. MIS 4 was complex, involving climate variability on different temporal and spatial scales. One aspect of this variability was manifested as the shifts between cold stadials and warm interstadials of multi-millennial duration during the Early Weichselian (MIS 5d–a) (Figure 3-3). More specifically, MIS 5 was characterised by three long mild forested interstadials (MIS 5e, 5c and 5a), both in temperate and northern boreal Europe (Figure 3-3). These periods were interrupted by two cold and dry stadials (MIS 5d and 5b) with mountain-centered glaciation over Fennoscandia. This is shown also in Figure 3-4. Also suggested in Figure 3-4 is that the Weichselian ice sheet did not reach south-central Sweden and the Forsmark region during the Early Weichselian stadial periods. Superimposed on these longer-lasting climate fluctuations, millennial-scale climate fluctuations were present (Figure 3-3).

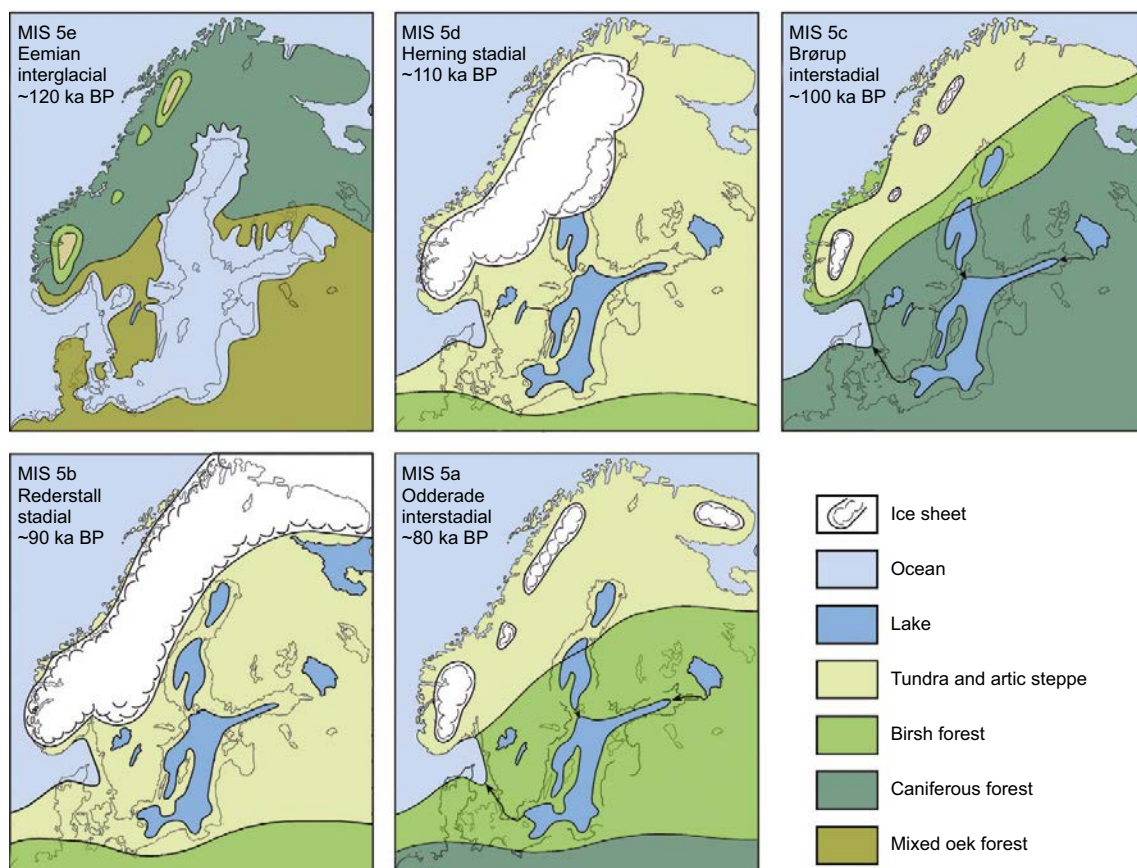


Figure 3-4. Conceptual maps illustrating the development of the Weichselian ice sheet during the Eemian and Early Weichselian (MIS 5e–a). According to this reconstruction, the Weichselian ice sheet did not reach south-central Sweden and Forsmark during these periods of ice-sheet growth. Modified after Lundqvist (1992) and Mangerud et al. (2011). From Wohlfarth (2013).

The duration of the Weichselian stadials and interstadials can be estimated based on records with independent chronologies (Wohlfarth 2013). The stadials lasted between about 1000 and 4000 years, whereas interstadials had a length of between 2000 and 16,000 years. The magnitude of temperature shifts at the last interglacial/glacial transition and between stadials and interstadials varied greatly, depending on the location of the paleo-archive and the methods and proxies used for estimating climate conditions. Summer and winter sea-surface temperatures reconstructed from marine sediment cores at 55°N for example suggest a temperature drop of 3°C and 2°C, respectively at the MIS 5e/5d transition. Stadial/interstadial shifts in summer and winter temperatures are estimated at between 2–3°C and 2–4°C, respectively. Temperature reconstructions from an Iberian Margin sediment core further to the south show even larger temperature differences of up to 10°C between stadials and interstadials (Sánchez Goñi et al. 2008). Biological proxies derived from terrestrial sites indicate similar summer temperatures during stadials and interstadials, or only slightly higher temperatures during interstadials. In contrast, winter temperatures seem to have been several degrees C colder during stadials as compared to interstadials. Probably the most detailed record of stadial/interstadial temperature shifts is derived from Greenland ice cores, where temperatures rose by between 8 and 16°C across stadial/interstadial transitions. These data are representative for high northern latitudes. Lower latitudes are expected to have experienced smaller shifts in temperature, as seen in climate modelling of past (e.g. Braconnot et al. 2007) and future climates (e.g. IPCC 2013).

Helmens (2013) compared five Late Pleistocene terrestrial climate proxy records from central, temperate and northern, boreal Europe. The records comprise the classic proxy records of La Grande Pile (NE France) and Oerel (N Germany) and more recently obtained records from Horoszki Duże (E Poland), Sokli (N Finland) and Lake Yamozero (NW Russia). The Sokli sedimentary sequence from the central area of Fennoscandian glaciation has escaped major glacial erosion in part due to non-typical bedrock conditions. Multi-proxy studies on the long Sokli sequence drastically change classic ideas of glaciation, vegetation and climate in northern Europe during the Late Pleistocene.

The comparison allows a re-examination of the environmental history and climate evolution of the last interglacial-glacial (MIS 5–2), and it shows that environmental and climate conditions during MIS 5 (c 130–70 ka BP) were different from those during MIS 4–2 (c 70–15 ka BP). As mentioned above, MIS 5 was characterised by three long warm intervals interrupted by two shorter cold and dry intervals. Subsequently, MIS 4–2 shows open vegetation both in central and northern Europe (Helmens 2013). It includes two glacial maxima (MIS 4 and 2) with sub-continental scale glaciation over northern Europe and dry conditions in strongly continental eastern European settings. During the cold MIS 4 and 2, south-central Sweden and the Forsmark region were ice covered. This is in contrast to the MIS 3 period, during which climate oscillations of millennial scale (so-called Dansgaard–Oeschger events) dominated. Summer temperatures approaching present-day values are recorded for various warming events during MIS 3 (Helmens 2013), i.e. during the Middle Weichselian (Table 3-1). Mild climate conditions in early MIS 3 at around c 50 ka BP were accompanied by large-scale deglaciation of the Weichselian ice sheet. Ice-free conditions with *Betula*-dominated vegetation (including tree birch) persisted over large parts of Fennoscandia, possibly interrupted by glaciation, into the middle part of MIS 3 to c 35 ka BP.

Overall, MIS 5 was mostly mild with warmest or peak interglacial conditions at the very start during MIS 5e. MIS 4–2 was mostly cold with most extreme or peak glacial conditions in the closing phase during MIS 2. Additionally, the reviewed data (Helmens 2013) reveals restricted ice cover during MIS 3 and indicates that climate variability during parts of the last interglacial-glacial cycle was expressed mostly in terms of changes in degree of continentality possibly due to changes in sea-ice cover.

There are still unsolved questions related to an ice-free interstadial period during parts of MIS 3, many of them concerning the datings of various interstadial and ice-advance phases. Nevertheless, it seems clear that the Weichselian ice sheet was considerably more dynamic during the MIS 3 period of the Middle Weichselian than previously thought, in line with the variable climate. One implication of such a revised MIS 3 glacial history is that the Forsmark site was free of ice for a considerable amount of time during the Middle Weichselian, prior to the LGM. If so, the climate at the end of MIS 3 at Forsmark probably was of a periglacial character, allowing permafrost conditions to develop and be maintained, see below.

After the MIS 3 period, during MIS 2, the ice sheet advanced to its last Glacial Maximum (LGM). During the LGM, the entire area of Fennoscandia was covered by the Weichselian ice sheet, including south-central Sweden and the Forsmark region. The ice volume was at its largest at ~20–21 ka BP, with the ice margin located in Germany and Poland. The ice reached its maximum LGM position at different times in different regions.

After the LGM, the ice sheet started to retreat across e.g. northern Germany and Poland. The timing of the deglaciation is well dated and the ages have been converted into calibrated years. Several re-advances took place during the deglaciation of the Danish and Norwegian coast. Furthermore, from Quaternary geological information it is known that temporary halts in the ice sheet retreat took place several times in southern and south-central Sweden during the last deglaciation (e.g. Lundqvist and Wohlfarth 2000, Fredén 2002). For instance, the deglaciation was interrupted during the Younger Dryas stadial (12.5–11.5 ka BP) and there were ice re-advances and stillstands in the middle part of Sweden and southern Finland. Correspondingly, coastal areas in the west were characterised by large re-advances. The ice-marginal deposits formed during the Younger Dryas can be identified all around Fennoscandia. A description of the characteristics of these stillstands during the last deglaciation in Fennoscandia is found in SKB (2010a, Section 4.2.2). After the Younger Dryas, the ice retreated towards the Fennoscandian mountain range more or less continuously.

Figure 3-5 presents the comparisons between marine- and terrestrial-based climate proxy records from central and northern Europe for the last 140 ka as compiled by Helmens (2013), i.e. the figure encompasses and describes the environmental conditions during the Eemian interstadial, the Weichselian glaciation and the present Holocene interstadial.

Note that the typical Quaternary ice-sheet configuration over Fennoscandia was considerably smaller than that of a full ice-sheet configuration, and also considerably smaller than during the Younger Dryas. For average Quaternary ice-sheet conditions, the ice sheet is centred over the Scandinavian mountain range (e.g. Porter 1989, Kleman et al. 2008), resulting in ice-free conditions in south-central Sweden including Forsmark.

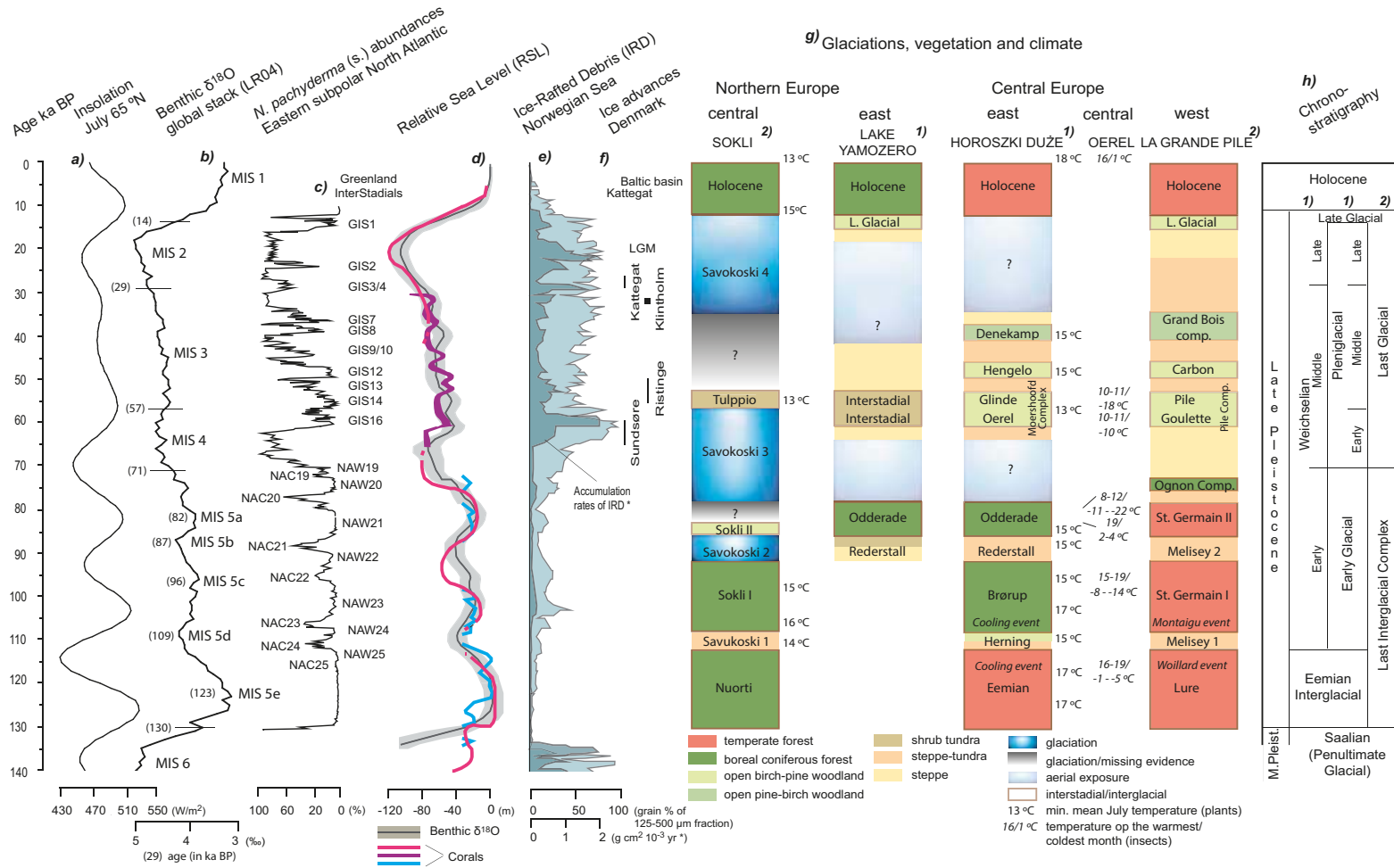


Figure 3-5. Compilation figure showing comparisons between marine- and terrestrial-based climate proxy records from central and northern Europe for the last 140 ka, i.e. encompassing the Eemian interstadial, the Weichselian glaciation and the present Holocene interstadial. Marine and ice-core chrono-stratigraphic units are given to the left and European chrono-stratigraphy (with two alternative chrono-stratigraphic subdivisions) is to the right. The marine and ice-core stratigraphies include Marine Isotope Stages (MIS in (b)), North Atlantic Cold and North Atlantic Warm events (NAC and NAW in (c); McManus et al. 1994), and Greenland InterStadials (GIS in (c); Johnsen et al. 1992, Dansgaard et al. 1993). Also shown to the left are variations in July insolation at 65°N latitude (Berger and Loutre 1991). References to the different types of data, and notes on methodological issues, are found in Helmens (2013, Figure caption 8). From Helmens (2013).

For more detailed descriptions of the Weichselian glacial history, see Lokrantz and Sohlenius (2006), Lundqvist (2007), Wohlfarth (2010, 2013), Helmens and Engels (2010), Lambeck et al. (2010), Mangerud et al. (2011), Lundqvist et al. (2011, Figure III.3) and Helmens (2013).

3.2.2 Exemplified of Weichselian climates

During the Weichselian, climate shifted many times between warmer and colder periods, as reflected in the growth and decay phases of the Weichselian ice sheet, see Section 3.2.1. The variability and range within which the climate shifted during the last glacial cycle could be expected also during future glacial cycles. Therefore, quantitative descriptions of prevailing climate conditions for periods with fundamentally different climates during the Weichselian are given below for Sweden and the Forsmark region.

The aim of the following descriptions of Weichselian climates is not to give a full review of all that is known on climate and climate variability during the last glaciation. Instead, the intention is to provide examples of Weichselian climates by selecting climate reconstructions for both stadial and interstadial phases and to cover a broad time span of the glacial cycle.

Early Weichselian (117–74 ka BP)

The Fennoscandian climate during the Early Weichselian (MIS 5d–5a, 117–74 ka BP) varied significantly, as described in Section 3.2.1.

Past environmental and climate conditions have been reconstructed for MIS 5d (the Herning stadial 117–105 ka BP, Table 3-1) by analyses of insect remnants and botanical and zoological macro remains from the Sokli sediment sequence (Engels et al. 2010), as well as of pollen from the same sediment sequence (Helmens et al. 2012). The results show that, for the ice-free stadial conditions at the investigated site, the summer July air temperature may have been ~7°C, which is ~6°C colder than the present summer mean temperature (13°C), and indicative of arctic climate conditions.

During MIS 5c (the Brørup interstadial, 105–93 ka BP), summer temperatures inferred from plant macrofossil remnants indicate surprisingly warm conditions for northern Fennoscandia (Väliranta et al. 2009, Engels et al. 2010). Minimum July temperatures were as high as 16°C, which is 3°C warmer than at present (Väliranta et al. 2009). At that time, open birch woodland existed at the site within a subarctic climate. This result is in contrast to other (lower-resolution) reconstructions from northern Fennoscandia which indicate MIS 5c temperatures 6–7°C lower than present, see Engels et al. (2010). However, several central European sites indicate that there was a phase during the MIS 5d interstadial that was characterised by high summer temperatures, and a comparison between the high-resolution reconstructions from western Europe and the results presented in Engels et al. (2010) suggests that the north–south July air temperature gradient between the mid- and high-latitudes was much weaker during MIS 5c than at present.

One suggested reason for the warm climate conditions during this interstadial is that the contemporary astronomical forcing resulted in a weaker north-south temperature gradient and a longer growing period, creating more favourable climate conditions than at present (Väliranta et al. 2009).

Middle Weichselian (74–24 ka BP)

Examples of Fennoscandian climates during the MIS 3 interstadial (59–24 ka BP) have been studied by use of geological information (Helmens 2009a, Wohlfarth 2009) and by climate modelling (Kjellström et al. 2009, including erratum Feb 2010). MIS 3 covers a long time period that includes both rapid millennial-scale climate shifts and longer trends in changing climate, see Wohlfarth (2009) and Helmens (2013). A few examples of climates occurring during MIS 3 are given below.

Early MIS 3 (at ~50 ka BP)

A comprehensive environmental reconstruction of early MIS 3 conditions, at around 50 ka BP, was made based on multi-proxy analysis on a two metre thick laminated, lacustrine clay-silt sequence obtained at the Sokli site in northern Finland (Helmens 2009a). The analyses included lithological characteristics; organic content (loss-on-ignition, LOI); plant microfossils (pollen, spores, algal

and fungal remains); macrofossils of plants (e.g. seeds, moss remains) and of aquatic animals (e.g. statoblasts of Bryozoa); head-capsules of chironomids (i.e. aquatic insects); and diatoms and other siliceous microfossils (e.g. phytoliths, chrysophyte stomatocysts). Additionally, geomorphic evidence and analyses of DEM data were employed in the environmental reconstruction. Mean July temperatures were reconstructed by applying transfer functions to the pollen, chironomid and diatom records.

The results have been surprising in various aspects, seriously challenging previous concepts on environmental conditions during early MIS 3 in the near-central area of the Weichselian glaciation. Helmens (2009a) shows not only ice-free interstadial conditions during parts of MIS 3, but also climate warming as compared to present-day temperatures. The laminated sediments seem to have been deposited in a sheltered embayment of a glacial lake impounded along the ice front of the Weichselian ice sheet. Throughout the deposition of the lacustrine sediments, the reconstructed terrestrial ecosystem on the deglaciated land is low-arctic shrub tundra very similar in composition to modern tundra in the continental sector of northern Fennoscandia. The distributional ranges of pine and tree birch were probably only a few hundred kilometres south or south-east of the Sokli site. This is concordant with the sparse evidence for the presence of boreal tree taxa during MIS 3 in the Baltic countries and further east in Europe, but contradicts with the commonly inferred treeless tundra or grass-dominated steppe conditions in central Europe.

Mean July air temperatures in the magnitude of present-day values are reconstructed from the chironomid and diatom records as well as on the basis of fossils from aquatic plants and Bryozoa. Temperature inferences based on the terrestrial pollen are consistently lower than the temperatures reconstructed from the fossil aquatic assemblages. It is possible that the regional terrestrial and the local aquatic systems responded differently to the climatic and landscape features at around 50 ka BP. Warmest and moistest conditions are recorded in the lower part of the laminated lacustrine sequence. This is consistent with the pattern of the Greenland millennium-scale Dansgaard–Oeschger interstadials in which abrupt warming is followed by a gradual cooling. The chironomid-inferred mean July air temperatures are around 13°C (i.e. the current temperature) $\pm 1.15^\circ\text{C}$ in the lower part of the lake sequence and around $12 \pm 1.15^\circ\text{C}$ in the upper part. The mean July air temperatures inferred from the terrestrial pollen data lie within the range of around $12 \pm 1.5^\circ\text{C}$ (lower part of sequence) and around $11 \pm 1.5^\circ\text{C}$ (higher part of sequence). High summer temperatures are ascribed in part to enhanced July insolation compared with present at the high latitude of the site.

Comparison with recently published, well-dated sediment sequences in eastern and western Finland suggests ice-free and warm conditions in a major part of eastern Fennoscandia at ~50 ka BP. Open birch forest seems to be registered in eastern Finland during part of the warming event. Direct evidence is lacking to reconstruct the total time span with ice-free conditions at the studied sites. It is argued that the Sokli site was glaciated during the overall colder late MIS 3. The absence of well-dated geological data in northern Sweden hampers a reconstruction of the total ice-marginal retreat in the continental sector of the Fennoscandian Ice Sheet during the early MIS 3 climate warming event. For more details on this study, see Helmens et al. (2007, 2009), Engels et al. (2008, 2010), Bos et al. (2009), Helmens (2009a) and Helmens and Engels (2010).

A warm climate during early MIS 3, such as reconstructed for northern Fennoscandia by e.g. Helmens (2009a), is in line with, and probably necessary for, a deglaciation of the large ice sheet that existed during MIS 4.

Middle MIS 3 (at 44 ka BP)

A comprehensive climate modelling study was performed to investigate climate extremes within which the climate in Fennoscandia may vary on a 100 ka time scale (Kjellström et al. 2009, including erratum dated Feb 2010). Three different periods were simulated, a cold glacial climate (at LGM, ~21 ka BP), a periglacial climate (at MIS 3, 44 ka BP) and a warm future climate dominated by global warming (a few thousands of years after present). In the present section, results from the periglacial climate simulation are presented. Results from the LGM climate simulation are presented below in the present section, under the heading “Late Weichselian including LGM (24–12 ka BP)”, whereas results from the global warming simulation are described in Section 3.3.6.

In order to give a detailed example of a modelled periglacial MIS 3 climate over northern Europe, climate modelling was performed using a global climate model (GCM) which produced boundary conditions for a regional climate model (RCM) (Kjellström et al. 2009). This model study was designed also to test whether a cold and dry climate favourable for permafrost growth would exist in the ice-free regions surrounding a Fennoscandian MIS 3 ice sheet with a restricted ice configuration. Based on forcing conditions for a selected period during MIS 3 (Greenland stadial 12 at 44 ka BP), a simulation of middle MIS 3 climate conditions was performed with the climate models. For the simulations performed and analysed within this study, atmospheric and land components of the CCSM3 used a grid spacing of approximately 2.8° in latitude and longitude. The vertical resolution is 26 levels in the atmosphere and 40 levels extending to 5.5-km depth in the ocean. The regional climate model used a horizontal resolution of 50 km and a time resolution of 30 minutes. For details on the models, how they were employed, and a discussion on climate model uncertainties, see Kjellström et al. (2009).

The choice of period to simulate for MIS 3 followed from a workshop on MIS 3 organised by SKB in September 2007 (Näslund et al. 2008) with the specific purpose of supporting this selection. Only limited and in some cases controversial, palaeo-information is available to reconstruct the extent of the Fennoscandian ice sheet during the different warm and cold intervals of MIS 3. We here assumed, in line with several recent studies, see above, that the southern part of Fennoscandia was ice free during some of the MIS 3 stadials.

The modelling activities included the use of; i) a fully coupled Atmosphere-Ocean General Circulation Model (AOGCM; Community Climate System Model version 3, CCSM3), ii) a Regional Climate Model (RCM; Rossby Centre Regional Climate Model, RCA3), and iii) a dynamic vegetation model (DVM; the LPJ-GUESS model). The AOGCM was used to simulate the global climate in steady-state simulation for the selected time period. Even though AOGCMs are powerful models they are relatively coarse in their resolution due to computational limitations. Therefore, the output from the AOGCM was used as input to a RCM that provides output at a relatively high horizontal resolution for Europe. Both global and regional climate models hold descriptions of the land surface, including vegetation. In the regional model, it is important to describe the vegetation cover with a high degree of regional detail. Such details are missing in available global fields and details of the vegetation cover have to be estimated, based on the global fields and consideration of, among other things, land/sea distribution. In order to improve the representation of the regional vegetation, a dynamic vegetation model was used to simulate the European vegetation resulting from the RCM-simulated climate. In a subsequent step, the new vegetation was used in a new RCM simulation that provided the final climate output. For the studied MIS 3 period, data on relevant climate parameters was extracted from the regional model for the Forsmark area.

The global model simulation of the periglacial MIS 3 climate used a CO₂ concentration in the atmosphere of 200 ppm (Kjellström et al. 2009). An ice sheet with a restricted configuration was assumed, and, in line with this, a simulated MIS 3 ice sheet configuration obtained from the Weichselian ice sheet reconstruction described in Section 2.3.4 was used (Kjellström et al. 2009). For a detailed description of the assumptions made in the modelling process, model forcing and initial conditions (such as astronomical and solar forcing, concentration of greenhouse gases and aerosols in the atmosphere, extents of ice sheets, distribution of land and sea, topography and vegetation), also see Kjellström et al. (2009).

In addition to the modelling activities, an effort was made to collect palaeoclimatic information by compiling various MIS 3 and LGM proxy data from different sources (Kjellström et al. 2009, Wohlfarth 2009). Part of this palaeoclimatic information was used to constrain the forcing conditions used in the climate models. Other proxy data were used for model evaluation purposes. Results from the global climate model were compared with proxy records of sea-surface temperatures and with terrestrial climate records. The regional climate model results have been compared with existing terrestrial palaeoclimate records from Europe.

Global climate

Figure 3-6 shows the simulated global climate from the middle MIS 3 simulation. Seasonal mean changes in temperature as compared with a simulation of the pre-industrial climate (with forcing conditions set at levels consistent with those preceding the 18th century) are also shown.

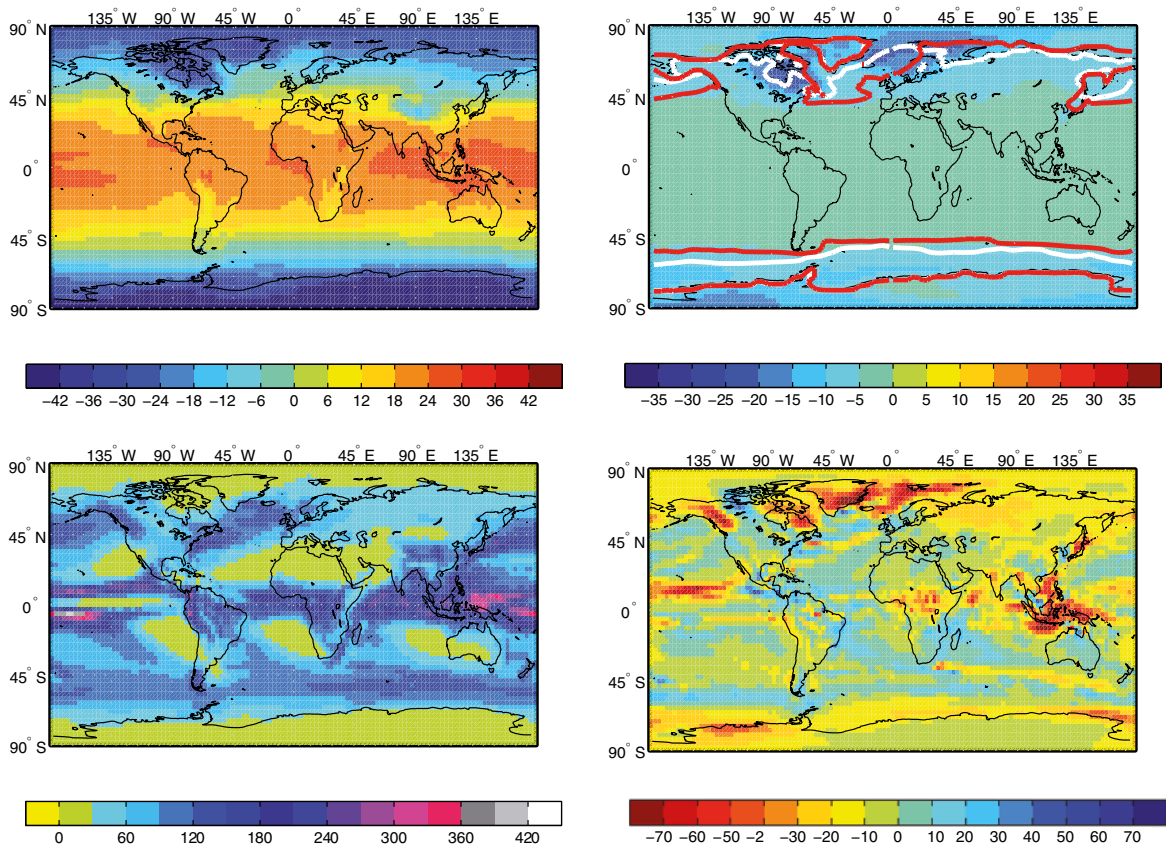


Figure 3-6. Annual mean near-surface air temperature in the MIS 3 simulation (upper left) and the difference compared with a simulated pre-industrial climate (upper right). Units are °C. Also shown is the annual mean sea ice edge (defined at 10% areal sea ice cover) for the pre-industrial simulation (white; upper right) and the MIS 3 simulation (red; upper right). The lower panels show the simulated precipitation (lower left) and the difference compared with the simulated pre-industrial climate (lower right). Units are mm/month. From Kjellström et al. (2009).

The annual mean surface cooling in the MIS 3 simulation as compared with pre-industrial conditions is most pronounced over the Laurentide and the Fennoscandian ice sheets and over the Greenland–Iceland–Norwegian Sea, with a maximum cooling of 25°C (Figure 3-6). A large portion of the cooling over the Fennoscandian and Laurentide ice sheets is due to the increased elevation over the ice sheet. The cooling amounts to 5–10°C north of 40°N in the Atlantic Ocean, the Arctic Ocean and over Antarctica and the Southern Ocean. The sea-ice extent is increased in the MIS 3 simulation in the North Atlantic and north Pacific as compared with the pre-industrial simulation (Figure 3-6).

Even though proxy data for the period around 44 ka BP are sparse, comparison with available sea surface temperature data shows that the globally modelled temperatures and proxy data are in reasonable agreement. For further results and discussion of the MIS 3 simulation from the global climate model, and for details about the comparison with MIS 3 climate proxy data, see Kjellström et al. (2009).

Climate in Europe and Sweden

The regional climate model was then used to downscale the model results of the global climate model in order to obtain a higher resolution data over Europe and Sweden. The resulting climate over Europe was used to produce a new vegetation distribution with the vegetation model. This vegetation was in turn, used as input to the regional climate model, to produce a climate in line with the new vegetation. An evaluation of the results from this iterative process is given in Kjellström et al. (2009). Figure 3-7 presents selected results on temperature and precipitation from the regional modelling.

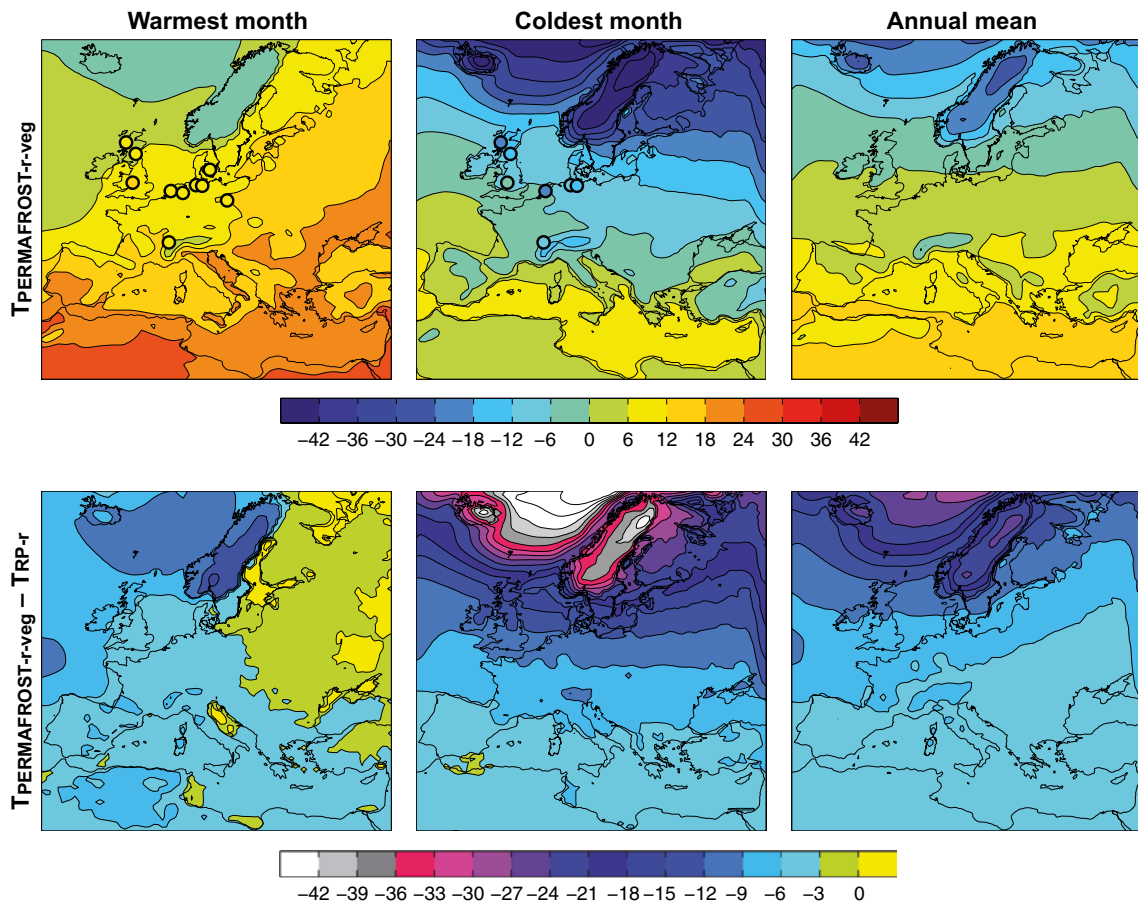


Figure 3-7. Mean air temperatures of the warmest month, coldest month and annual mean in the MIS 3 simulation (top). Shown also are temperature estimates based on proxy data as described in Kjellström et al. (2009, Section 2.4) (coloured circles). The lower row shows the differences between the simulated MIS 3 climate and a recent-past climate simulated for the period 1961–2000. From Kjellström et al. (2009).

During this part of the middle Weichselian, the simulated temperature is dominated by a very strong seasonal cycle (Figure 3-7) and a pronounced north–south gradient in the winter (Figure 3-7, upper row, middle panel). In the north, the effect of the Weichselian ice sheet is clearly seen in the isolines of temperature showing low temperatures in parts of Fennoscandia. The isotherm showing 0°C annual mean temperature goes south of Ireland, through England and the southern parts of Denmark, just south of Sweden and then eastwards (Figure 3-7, upper row, right panel). Compared with the present climate (1961–2000), the annual mean temperature in the MIS 3 simulation is ~5°C colder around the Mediterranean, 5–10°C colder in central Europe and more than 8°C colder in the ice-free parts of Fennoscandia (Figure 3-7, lower row, right panel). The same values as for difference in annual temperature apply for winter temperature in southern and central Europe. The winter temperature of the British Isles is 10–15°C colder and the southern tip of Fennoscandia around 15°C colder in comparison with the present climate (Figure 3-7, lower row, middle panel). Over the ice sheet in northern Fennoscandia, temperatures are at least 30°C colder than in the present climate (1961–2000) simulation. On Iceland and over the Norwegian Sea, the difference from the late 20th century is even larger. In summer, most of continental Europe is 0–5°C colder than in the late 20th century, western Europe and the British Isles are 5–10°C colder and northern Fennoscandia is 10–15°C colder than in the simulated present climate (Figure 3-7, lower row, left panel).

The annual mean precipitation in the MIS 3 simulation is characterised by considerably drier conditions than in the simulated present climate (1961–2000), by more than 360 mm/year in large parts of Fennoscandia and over the North Atlantic, and by an increase in precipitation of up to 360 mm/year in parts of the southwest (Figure 3-9, upper row right panel). In the rest of the model domain, differences are, with few exceptions, smaller.

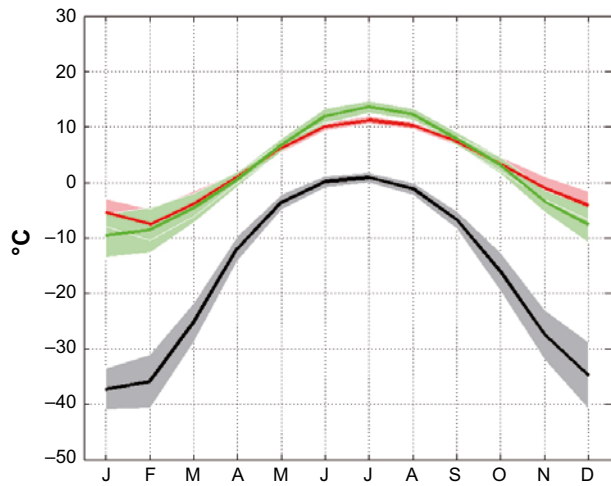


Figure 3-8. Annual temperature range in Sweden for MIS 3 (black), simulated present climate (red) and according to the CRU (Climate Research Unit, East Anglia) observational data for the time period 1961–1990 (green). Shaded areas in corresponding colours indicate the ± 1 standard deviation range of individual monthly averages in the three data sets. From Kjellström et al. (2009).

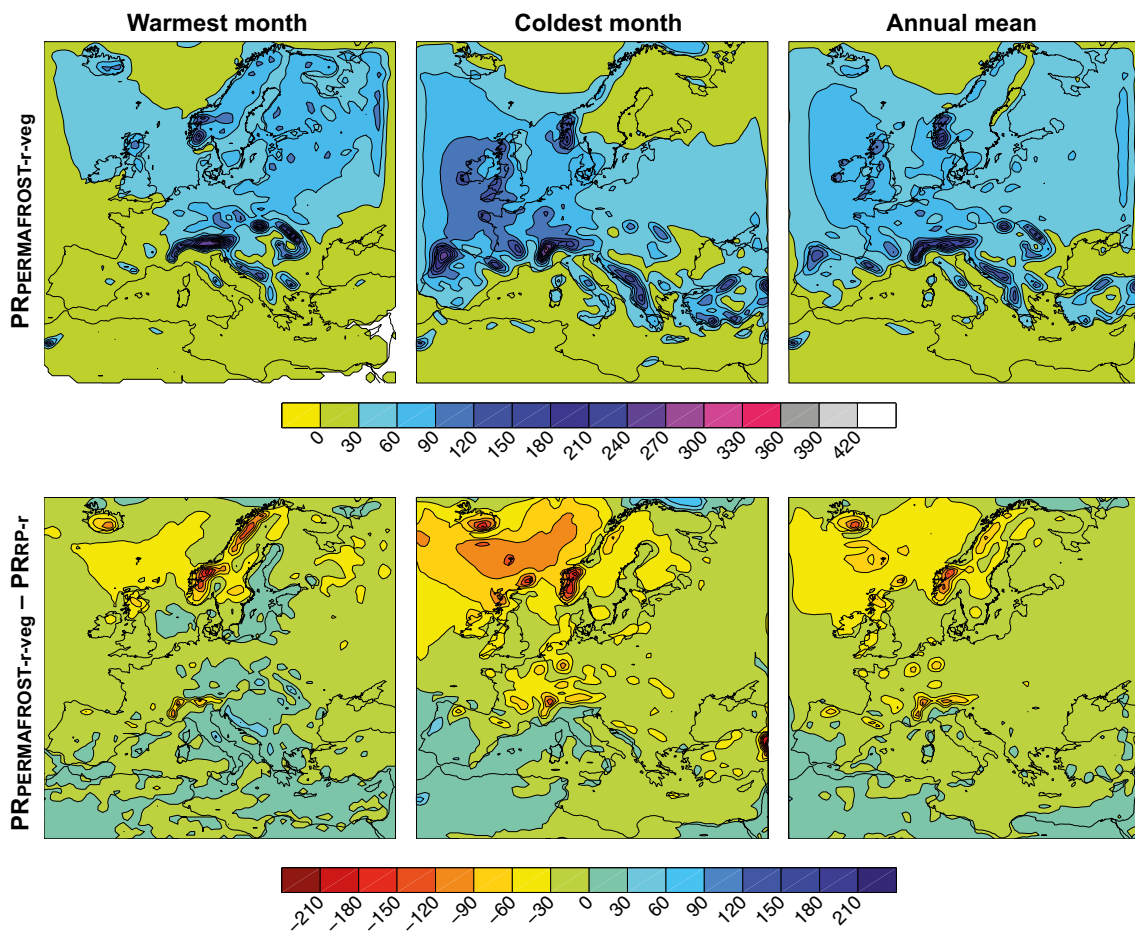


Figure 3-9. Mean precipitation of the warmest month, coldest month and annual mean in the MIS 3 climate simulation (upper row). Also shown are differences between MIS 3 simulation and the simulation of the present (1961–2000) climate. Units are mm/month. From Kjellström et al. (2009).

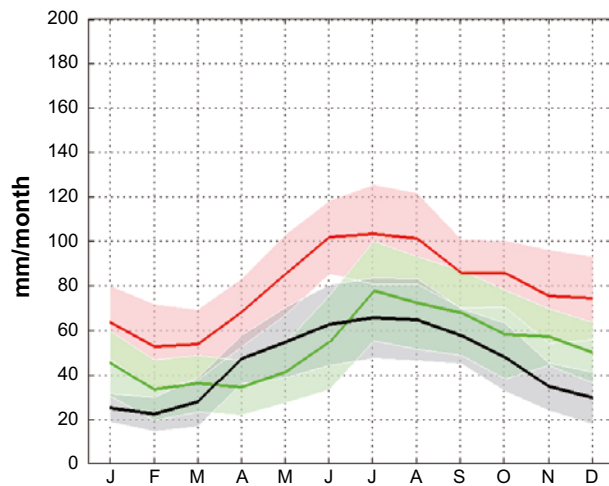


Figure 3-10. Annual precipitation range in Sweden in the MIS 3 simulation (black), present climate simulation (1961–2000) (red) and according to the CRU observational data (green). Shaded areas in corresponding colours indicate the ± 1 standard deviation range of individual monthly averages in the three data sets. From Kjellström et al. (2009).

The drier climate in northern Europe is reflected in the seasonal cycle of precipitation. For Sweden there is a reduction of more than a factor of two in winter and substantial reduction also during summer (Figure 3-10). Further south, the reduction is most evident in the winter half of the year, whereas in southernmost Europe the changes relative to the present climate are small for all months.

For further results, on the European scale, from the MIS 3 climate simulations, including results and discussion of the simulations of MIS 3 vegetation, comparisons with climate proxy data, and comparisons with other model simulations of MIS 3 climates, see Kjellström et al. (2009).

Do the results support a cold and dry climate favourable for permafrost growth? Heginbottom et al. (1995) examined the relation between ground temperature and permafrost continuity. An annual ground temperature of between -5 and -2°C is defined as the boundary for discontinuous permafrost (50–90% of landscape covered by permafrost) and -5°C and colder as the boundary for continuous permafrost (90–100%). However, it is also stated that a large fraction of areas with continuous permafrost has a ground temperature warmer than -5°C . Since the ground temperature differs from the near-surface air temperature by a few degrees, the simulated annual mean ground temperatures over Europe for MIS 3 are presented in Figure 3-11.

In central and northern Fennoscandia, outside of the prescribed ice sheet, the modelled MIS 3 annual average ground temperature is colder than -5°C (Figure 3-11), which suggests that the climate conditions are favourable for development of continuous permafrost. South of this, the modelled annual average ground temperature increases, reaching 0°C in the southernmost parts of Fennoscandia. The higher ground temperatures in the southern areas including northernmost Denmark, southern Sweden, Estonia and part of what today is the Baltic Sea and Gulf of Finland do not fulfil the thermal requirements for extensive permafrost. However, it is cold enough for sporadic permafrost (less than 50% of landscape covered), which may exist when the annual mean ground temperature is between 0 and -2°C . Based on these results of Kjellström et al. (2009) it is concluded that conditions were favourable for permafrost growth in the inferred ice-free parts of Fennoscandia.

Do the results support a restricted MIS 3 Fennoscandian ice sheet? The global and regional climate models do not include dynamical modelling of ice sheets and thus an ice sheet cannot form in the models, even if the climate conditions are favourable for ice sheet growth. The snowpack is, however, allowed to build up in the model. If the snow depth increases in time in a specific region, we can take this as an indication that an ice sheet would grow in this region if such processes were included in the model. However, the opposite situation, a lack of snow accumulation in front of, or at the margins of, a prescribed ice sheet, does not necessarily mean that the ice sheet would not grow (simply that the lowermost part of the ice sheet would have a net mass loss, which is typical for ice sheets ending on land). Growth of the ice sheet could still be possible if the precipitation over the ice sheet were large enough compared with its mass loss by melting, i.e. if conditions for the common pattern of ice-sheet growth were satisfied.

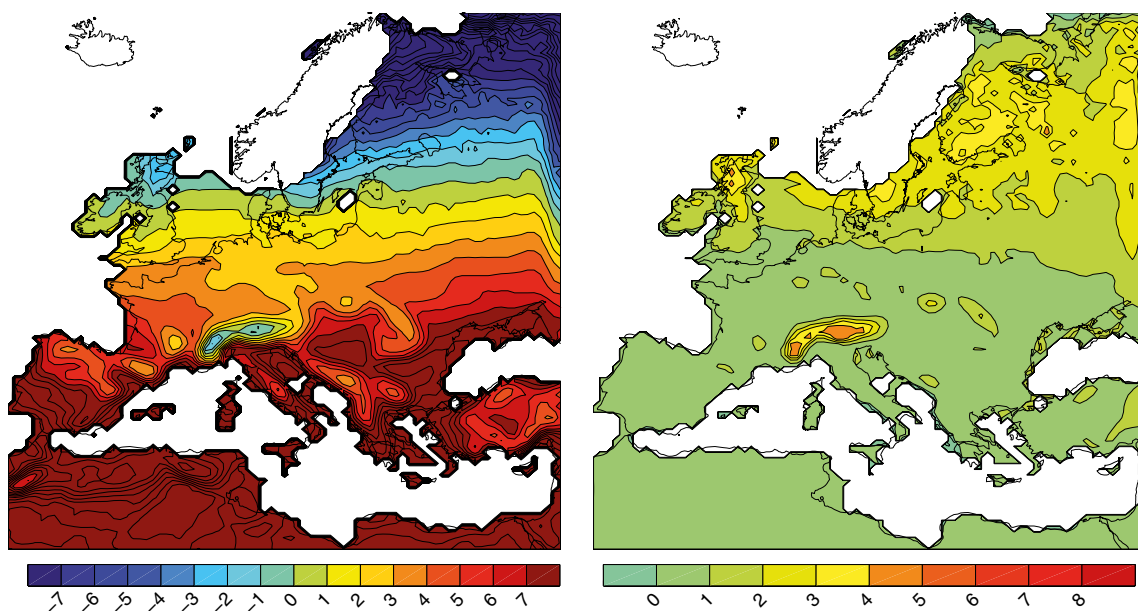


Figure 3-11. Annual mean ground temperature (left) and difference between near-surface air temperature and the ground temperature (right) in the MIS 3 simulation. Units are °C. White areas in Fennoscandia are covered by the prescribed restricted MIS 3 ice sheet. From Kjellström et al. (2009).

In the middle MIS 3 simulation, the snow depth in eastern Sweden, including the Forsmark region, does not increase in time. The annual minimum snow depth (occurring in September) is close to zero (varying from 0–0.02 m equivalent water depth). For the issue of whether the simulated climate is in line with the prescribed restricted middle MIS 3 ice sheet configuration, with ice-free conditions in e.g. the Forsmark region (Figure 3-11), one can therefore conclude that 1) an ice sheet would not grow locally from the local precipitation in front of the ice margin, 2) the modelled temperature and precipitation climate in front of the ice sheet is consistent with the assumed ice-free conditions and restricted ice-sheet coverage, but it does not exclude the possibility of a larger ice sheet.

Climate in the Forsmark region

Figure 3-12 and Figure 3-13 show average air temperature and precipitation for a 50 year period of the simulated MIS 3 climate, and a comparison with the climate simulated for present conditions. The results show that the climate is significantly colder and drier than at present, with arctic climate conditions prevailing in the Forsmark region.

The last step in the MIS 3 climate modelling study was to extract climatological data for the Forsmark region from these regional modelling results. Figure 3-14 show the grid boxes used for extraction of data. Information was extracted from the grid point located closest to the Forsmark site.

50-year average values from the regional MIS 3 climate simulation show that the annual mean air temperature in the Forsmark region is -7.6°C during the inferred ice-free stadial 44 ka ago. This is 12 degrees lower than in the simulated present climate (1961–2000). The largest difference compared with the simulated present climate in the seasonal cycle of temperature is seen in winter (Figure 3-15, upper row, second column).

The mean annual precipitation in the Forsmark region is 441 mm, which is 225 mm (or 30%) less compared with the simulated present climate. In this periglacial climate, the precipitation is lower than in the present climate for most parts of the year, and there is a very strong seasonal cycle in snow cover as the temperatures during summer get well above 0°C allowing complete snow melting (Figure 3-15, upper and lower row, second column). The length of the completely snow-free season is three months and there is a more or less constant snow cover during at least 3 months.

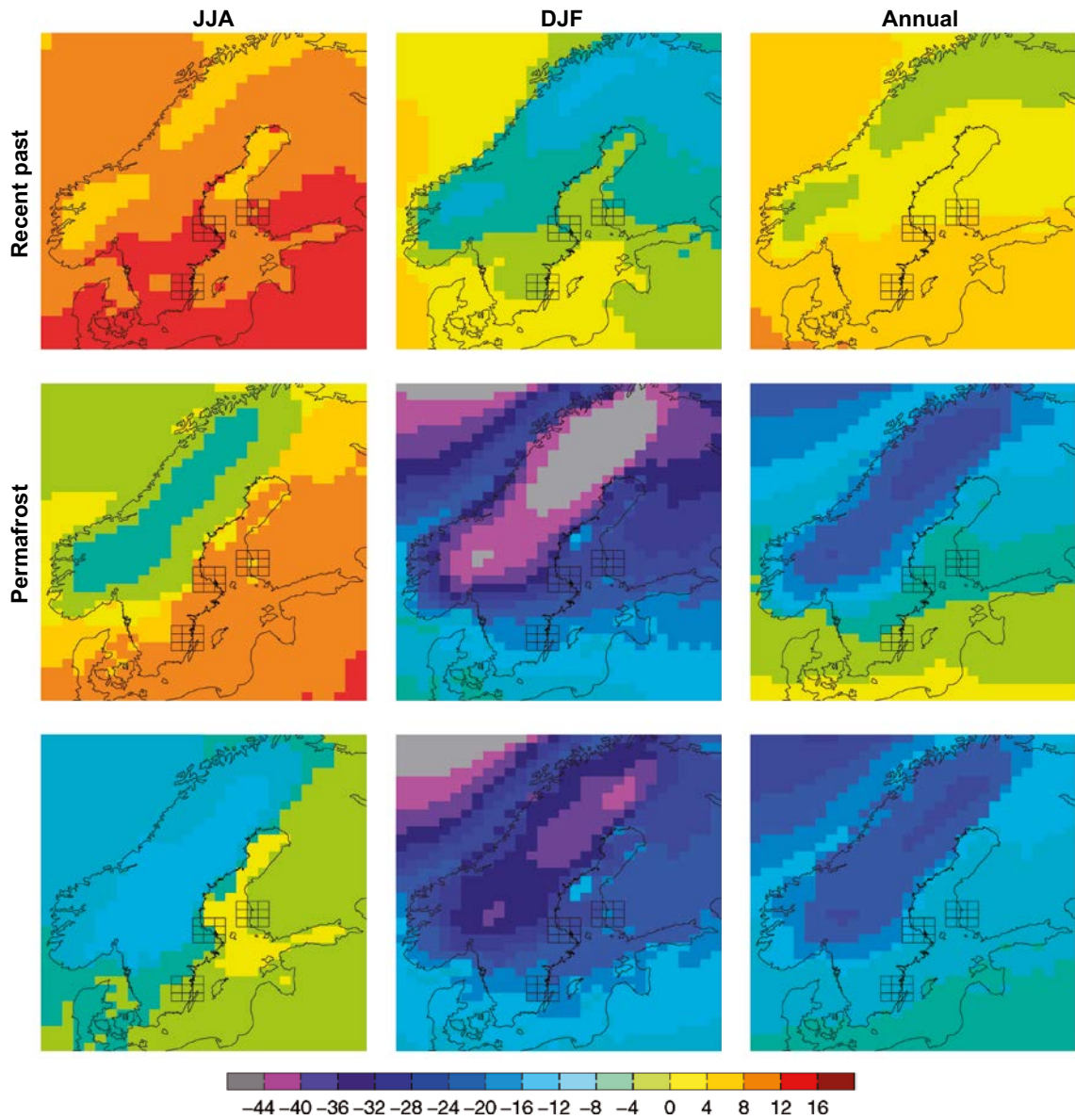


Figure 3-12. Seasonal and annual mean temperature for the present (1961–2000) (upper row) and MIS 3 (middle row) climate simulations. The lower row shows the difference between the two. Units are °C. From Kjellström et al. (2009).

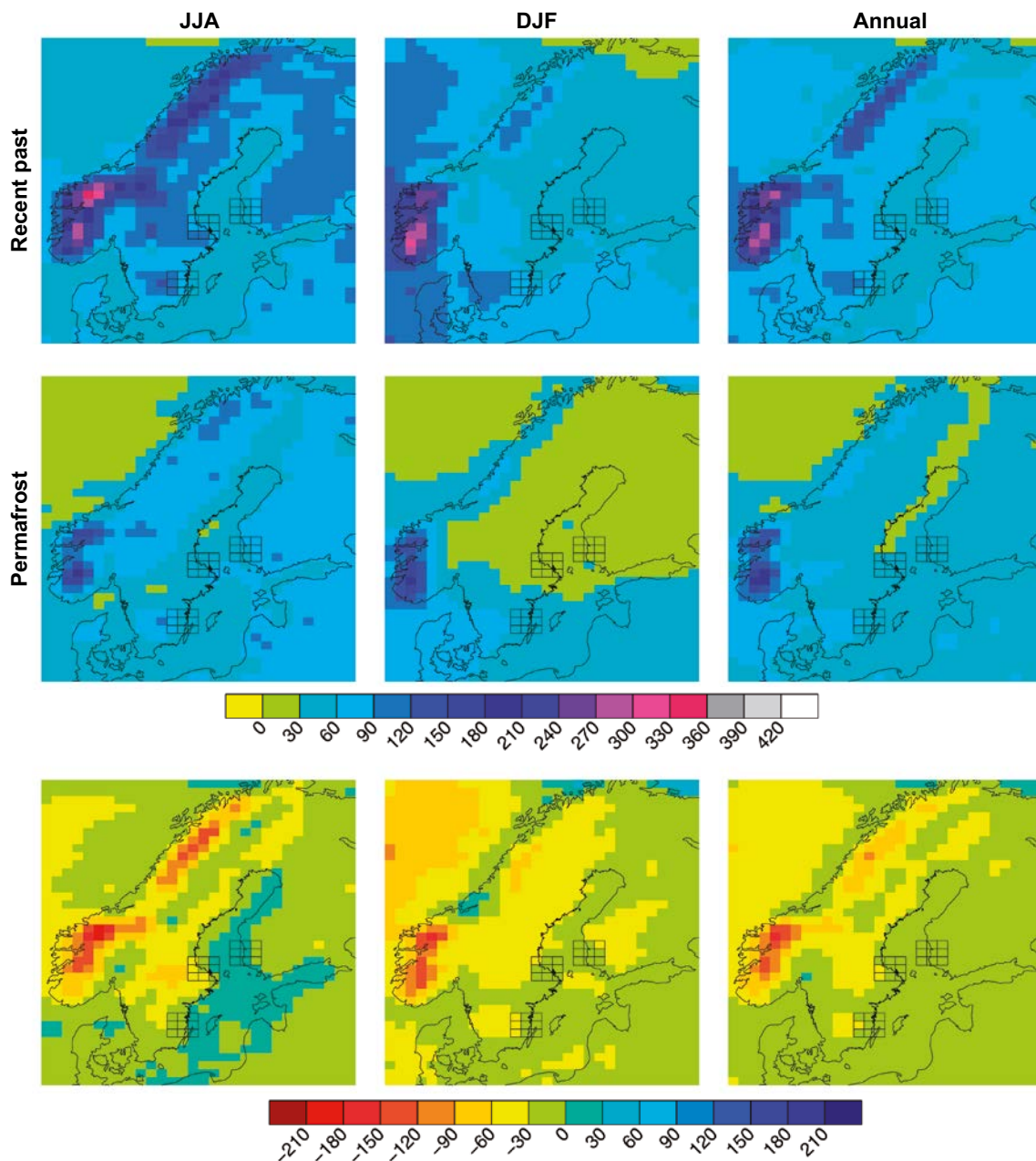


Figure 3-13. Seasonal and annual mean precipitation in the present (1961–2000) (upper row) and MIS 3 (middle row) climate simulation. The lower row shows the difference between the two. Units are mm/month. From Kjellström et al. (2009).

The annual surface runoff is 139 mm in this exemplified periglacial climate, which is somewhat less (36 mm/year) than in the simulated present climate. In the MIS 3 climate, there is a clear spring peak in runoff connected with the snow melt which is more extensive than in the simulated present climate, since more snow is accumulated on the ground during the winter. During the remaining part of the year, the runoff is fairly small, due to the cold conditions during winter and the relatively small amounts of precipitation during summer. Given the uncertainties and assumptions used in the climate modelling, the model results thus show that the MIS 3 climate in the Forsmark region may be characterised as being a significantly colder and drier climate than at present and also that the surface runoff is reduced.

The annual mean ground temperature is about -4°C in the Forsmark region (Figure 3-11). According to Heginbottom et al. (1995) this temperature indicates that climate conditions are favourable for discontinuous permafrost (covering 50–90% of the landscape). The cold and dry climate with partially snow-free conditions implies that the climate is very favourable for permafrost growth.

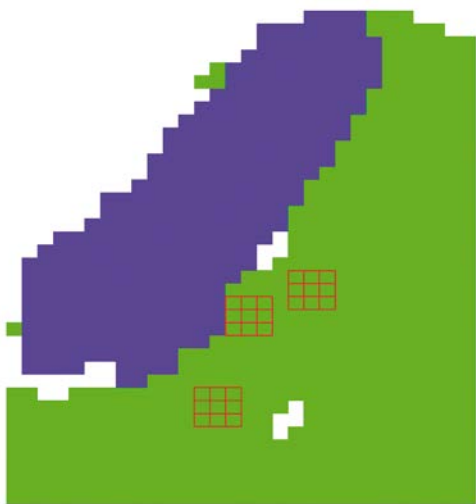


Figure 3-14. Land (green), ice sheet (blue) and sea extent (white) in the Fennoscandian region used for the MIS 3 climate simulation. The 3×3 -grids represent grid boxes covering the Forsmark, Oskarshamn and Olkiluoto sites (centre box) and the eight surrounding boxes. Grid boxes with a land fraction lower than 20% are not filled. Results from Oskarshamn and Olkiluoto are presented in Kjellström et al. (2009). From Kjellström et al. (2009).

In summary, the results from Kjellström et al. (2009, including erratum dated Feb 2010) show that i) the climate models produce a cold and dry arctic climate in the Forsmark region for a stadial during MIS 3, ii) the resulting climate is in agreement with ice-free conditions in south-central Fennoscandia and iii) that this climate is suitable for permafrost growth in the Forsmark region.

The major uncertainties in the climate simulation are related to uncertainties in forcing, model formulation and natural variability. These uncertainty aspects are discussed in detail in Kjellström et al. (2009). For further details on the setup, results, and discussion of the MIS 3 climate modelling results, see Kjellström et al. (2009 including erratum Feb 2010, 2010) and Brandefelt et al. (2011).

Following the very warm temperatures reconstructed for *early* MIS 3, described above, which are suggested to have resulted in ice-free conditions over large parts of Fennoscandia during MIS 3 (e.g. Helmens et al. 2009, Wohlfarth 2009, Wohlfarth and Näslund 2010), the low air temperatures simulated for Fennoscandia for the middle MIS 3 stadial (44 ka BP) are in line with the view that the Weichselian ice sheet needs to re-grow to attain the known large MIS 2 (LGM) ice configuration in a relatively short time.

Late Weichselian including LGM (24–12 ka BP)

As previously mentioned, all of Fennoscandia was covered by the Weichselian ice sheet during the Last Glacial Maximum, which occurred during the Late Weichselian. At that time, air temperatures were among the lowest of the last glacial cycle (Jouzel et al. 2007). In order to study the climate during the LGM in a consistent way with the simulation of a periglacial climate, the same models and modelling approach as for the periglacial climate modelling described above was used for LGM simulations. The LGM climate model simulations were set up to resemble conditions at the time of LGM in a way as similar as possible to what was done in the Palaeoclimate Modelling Intercomparison Project (Joussaume and Taylor 2000, Harrison et al. 2002). This choice facilitates comparisons with other GCM results. It also allowed the use of pre-existing long simulations with the general circulation model CCSM3 performed at the National Centre for Atmospheric Research (NCAR) in the USA (Otto-Bliesner et al. 2006), reducing the model spin-up time needed for this study. Further, as the LGM is part of the most recent Weichselian glacial period, there is a better possibility of finding climate proxy data than for earlier cold stadials during the Weichselian. The orbital year 21 ka BP and a CO_2 level of 185 ppm were used in the LGM simulation. Ice-sheet configurations were the same as in the PMIP-2 project (Harrison et al. 2002), which were based on the ICE-5G data (Peltier 2004). For a description of the set up of all other forcing conditions see Kjellström et al. (2009).

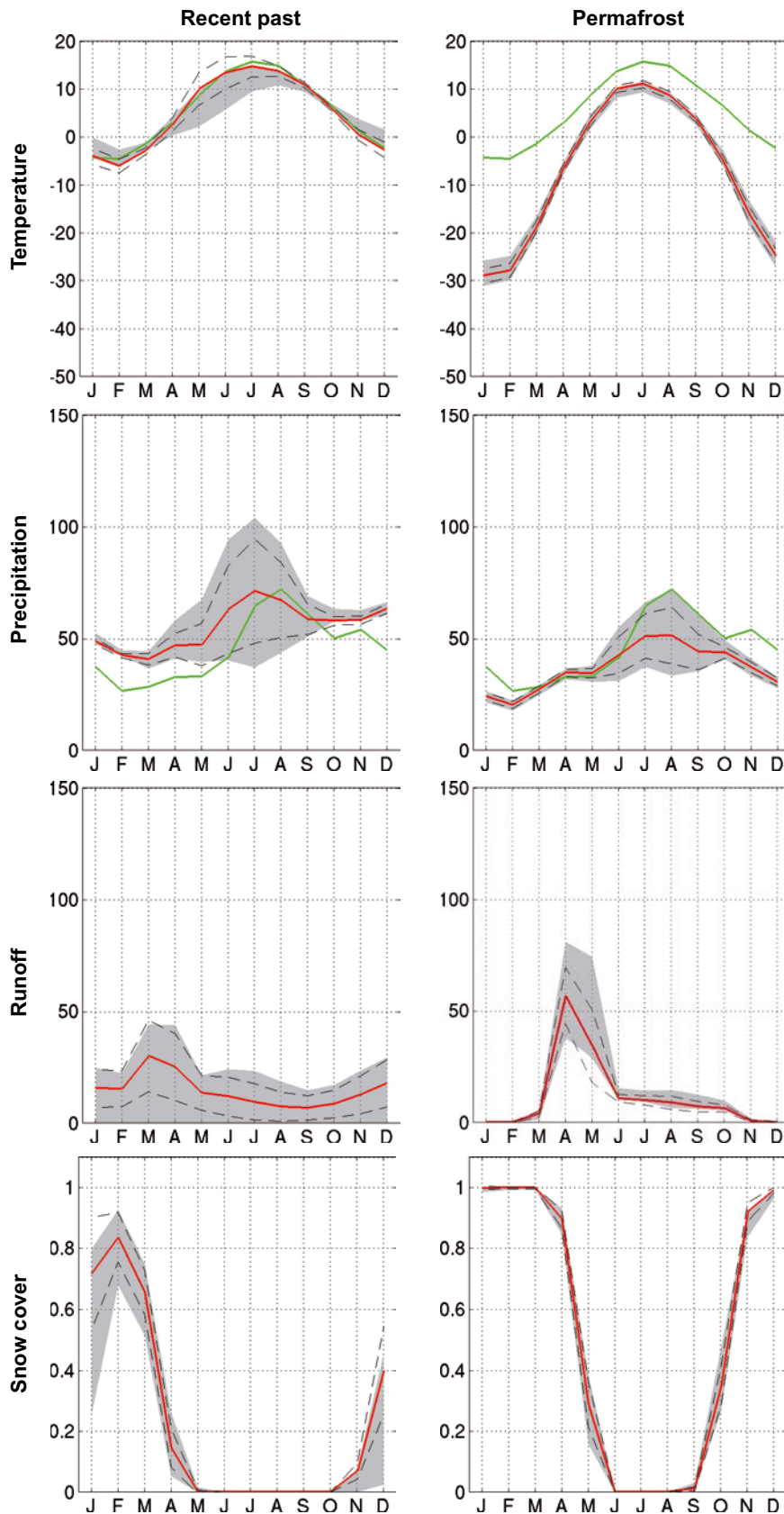


Figure 3-15. Simulated seasonal cycles of temperature (°C), precipitation (mm/month), runoff (mm/month) and snow fraction (dimensionless ranging from 0 to 1) at the grid box closest to the Forsmark site (red line). The spatial variability in the 3×3 -grids (Figure 4-13) is displayed with the dashed lines representing ± 1 standard deviation calculated from the 9 grid boxes, and the grey area representing the absolute maximum and minimum, of the 9 grid boxes. The green line for temperature and precipitation is the observed seasonal cycle from the CRU data set for the period 1961–1990, see Kjellström et al. (2009). From Kjellström et al. (2009).

Global climate

The global LGM simulation is a continuation of a LGM simulation performed at NCAR (Otto-Bliesner et al. 2006). The simulation was originally initiated from a simulation of pre-industrial climate, except for the ocean which was initiated by adding three-dimensional anomalies of ocean temperature and salinity derived from a LGM simulation with the Climate System Model version 1.4 (CSM1.4) (Shin et al. 2003) to the CCSM3 pre-industrial simulation. The simulation was first run for 400 years at NCAR, and was then continued for another 856 years within the present study. The annual global mean surface temperature reaches quasi-equilibrium after 100–150 years, after which it continues to cool and reaches a new quasi-equilibrium after a total of 750–800 years. This second quasi-equilibrium extends until the simulation is ended at model year 1,538 (Kjellström et al. 2009 erratum Feb 2010). The annual global mean surface temperature is 9.0°C in the first quasi-equilibrium and 7.9°C in the second LGM equilibrium, i.e. 4.5°C and 5.6°C colder than the corresponding simulated pre-industrial temperature (Kjellström et al. 2009, Brandefelt and Otto-Bliesner 2009). The second equilibrium also results in a 30% reduction in the strength of the Atlantic Meridional Overturning Circulation (AMOC) compared with the first quasi steady-state (Brandefelt and Otto-Bliesner 2009).

The global climate model LGM simulation thus shows that the global mean air temperature during the LGM could have been more than one degree colder than previously thought, and also that the variability in global mean temperature was larger. The variability is attributed to coupled ocean–atmosphere–sea ice variations in the North Atlantic region. The difference between globally warm and cold years is focussed over oceans in the Northern Hemisphere outside the tropics. The largest difference between cold and warm years is found over Greenland and Northern Europe, with a maximum of 6.8°C. The total amount of precipitation is up to 32% higher over the North Atlantic and North Pacific region in warm years than in cold years at the LGM. Furthermore, the sinking branch of the AMOC is shifted further north in globally warm years as compared with cold years. Further results, and discussions of their significance, are found in Kjellström et al. (2009, including erratum dated Feb 2010).

Significant effort was made to compile LGM climate proxy data for model validation. For the comparison between global LGM model results and marine and terrestrial LGM climate proxy data, see Kjellström et al. (2009, Section 3.2.1).

Climate over Europe and Sweden

A very cold LGM climate, with annual mean temperatures below 0°C in all of Europe north of about 50°N and also in high-altitude regions in southern Europe is clearly seen in the regional climate model results (Figure 3-16, upper row right). In winter, the situation is even more striking with the 0°C line encompassing basically all of continental Europe and monthly mean temperatures below –40°C over the northern parts of the ice sheet (Figure 3-16, upper row middle). During summer, the area with the lowest temperatures is more confined to the ice sheet, the extent of which is readily visible in Figure 3-16 (upper left). In winter when most parts of Europe are snow covered, the gradient is less pronounced as there is no abrupt shift from snow-covered to snow-free conditions. The annual mean temperature in the LGM simulation is 25–30°C lower than the simulated present climate. Over the southern parts of the ice sheet (British Isles, southern Fennoscandia) the annual mean temperature is around 15°C lower than today. At the edge of the ice sheet, there is a strong gradient towards smaller temperature differences. Central Europe is around 8°C colder than today and southern Europe around 6°C colder. In winter the temperature over the Fennoscandian ice sheet is around 40°C colder than present Fennoscandian temperatures.

Annual mean precipitation has its maximum over the North Atlantic and over parts of Western Europe (Figure 3-17, upper right). Relatively small amounts of precipitation are simulated in the northern parts of Fennoscandia and over the Mediterranean Sea and North Africa. Compared with the simulated present climate (1961–2000), Fennoscandia, the British Isles and Iceland are drier (Figure 3-17, lower right). More precipitation than at present is seen in southernmost Europe (the Iberian Peninsula, Italy) and northwest Africa. Fennoscandia and Western Europe receive less precipitation than in the present climate. The steep coastlines of western Fennoscandia and Scotland which today are facing the ocean and therefore get a lot of precipitation were, during the LGM, parts of the ice sheet that extended further westward. Without the strong orographic effect, precipitation is considerably smaller in this region during the LGM. In summer, as in winter, precipitation is less

than in the present climate in most parts of northern Europe. However, more precipitation in the LGM simulation is seen on the edge of the Weichselian ice sheet northwest of Fennoscandia and over the British Isles (Figure 4-16, upper and lower left panels). Another area with more precipitation than in the present climate is the area of what is today the Baltic Sea. During the LGM this area partly coincided with the most elevated parts of the ice sheet in which the regional climate model produces large amounts of precipitation during summer.

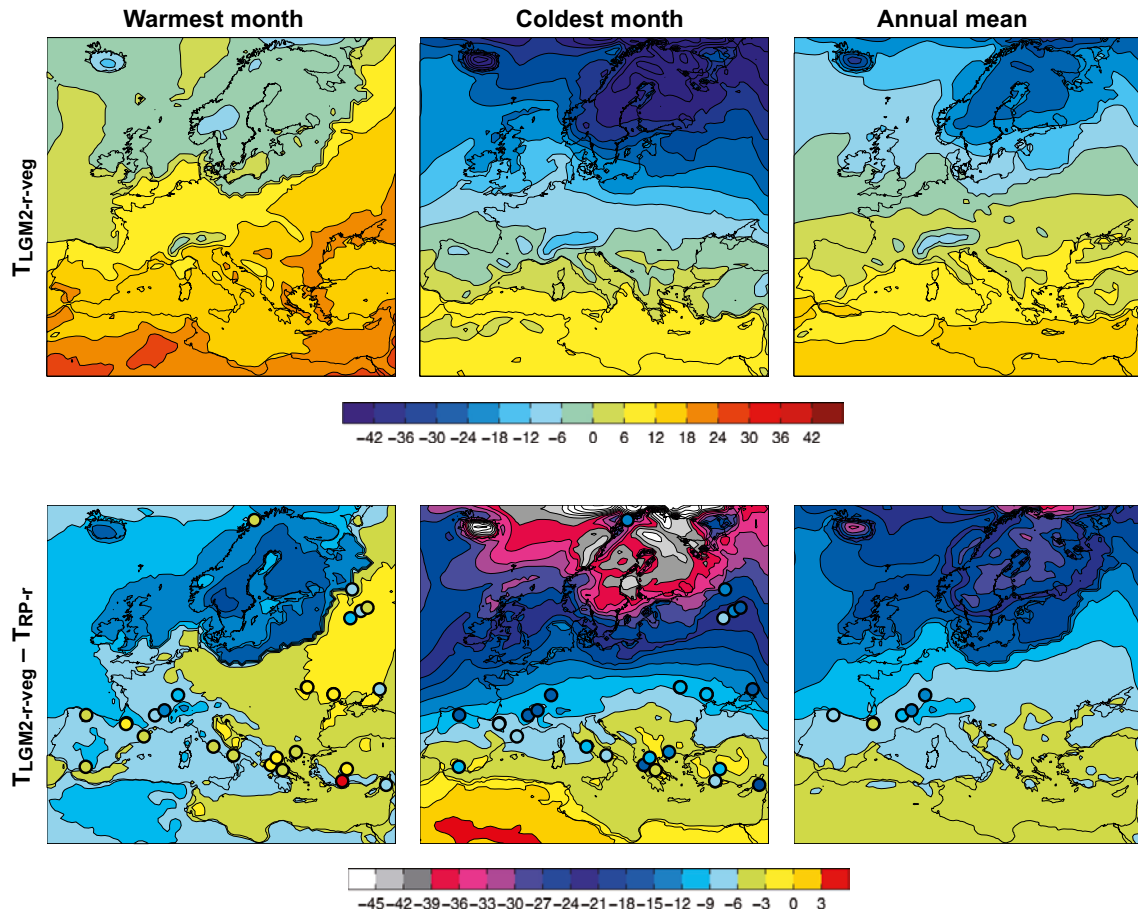


Figure 3-16. Mean temperatures of the warmest and coldest month and annual mean for the LGM simulation (denoted LGM2-r-veg) (upper row). Also shown are differences between the LGM simulation and the simulation of the present climate (years 1961–2000) (denoted RP-r) (lower row). Climate proxy based temperature reconstructions are denoted in the filled circles. Units are °C. From Kjellström et al. (2009).

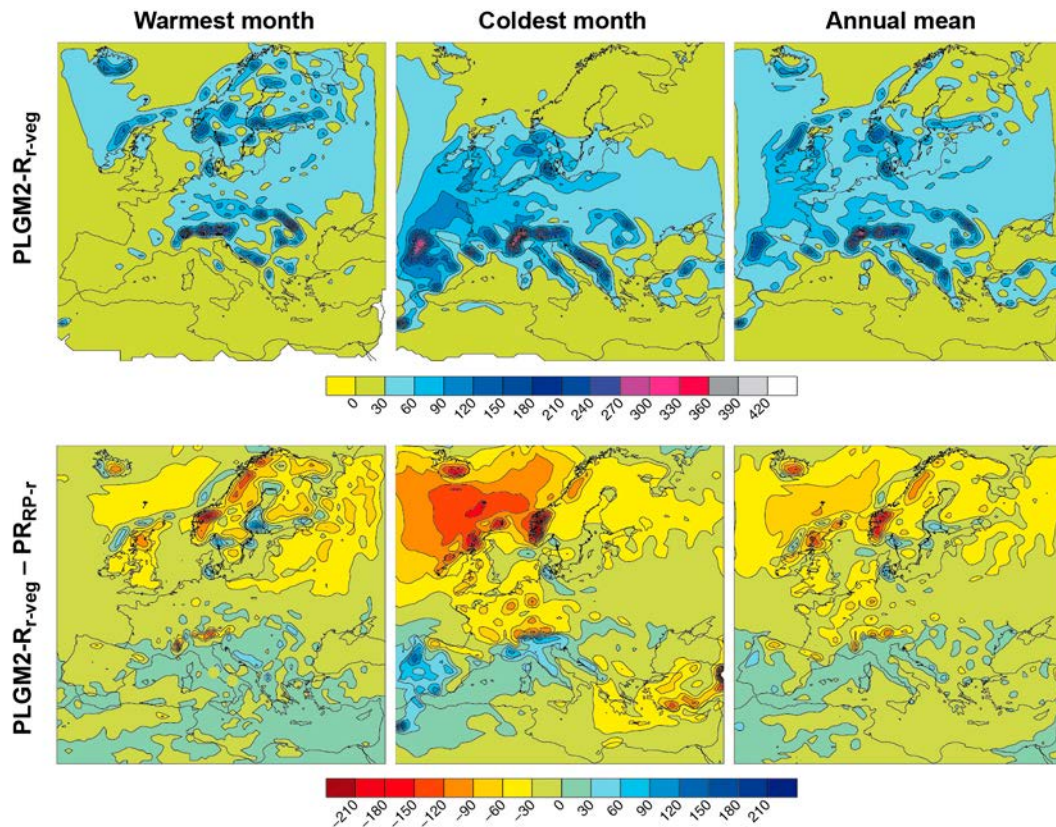


Figure 3-17. Mean precipitation of the warmest month, coldest month and annual mean in the LGM simulation (denoted PLGM2-r-veg) (upper row). Also shown are differences between the LGM simulation and the simulation of the present climate (year 1961–2000) (denoted RP-r) (lower row). Units are mm/month. From Kjellström et al. (2009).

Comparison to other model simulations

The simulated annual global mean temperature in the LGM simulation (i.e. the second quasi-equilibrium described in the beginning of this section) is 6.9°C lower than in the present climate. This is a stronger response than in most of the PMIP1 (full range is 1.85–9.17°C colder than in the present climate) and PMIP2 simulations (3.4–5.46°C colder than the pre-industrial climate) presented by Kageyama et al. (2006). The results indicate that much of the strong cooling is associated with low Sea Surface Temperatures (SSTs) (up to 6°C colder than some proxy data indicate) and extensive sea-ice cover in the North Atlantic and North Pacific.

These changes in sea-ice extent are a result of the changes in the temperature climate, but they also act to amplify the changes, as increased sea-ice extent leads to a colder climate through the feedback mechanisms involving increased surface albedo and reduced heat fluxes from the ocean to the atmosphere. This connection between low SSTs at high northern latitudes and the global mean temperature for the LGM simulation is in contrast with the PMIP simulations discussed by Kageyama et al. (2006). They find that winter and summer temperature changes over the North Atlantic, Europe and western Siberia do not relate closely to global temperature changes.

Regardless of possible biases in SSTs, the simulated changes in annual mean temperatures over Europe in the global model are similar to those obtained in the high-resolution atmosphere-only CCM3-simulations by Kim et al. (2008). In both our global and regional models, the coldest month of the year is warmer than proxy data indicate. This is a result also shown for the PMIP1 and PMIP2 simulations (Ramstein et al. 2007, Kageyama et al. 2006). However, even though the models are warmer than the proxy data indicates, Ramstein et al. (2007) conclude that they are within the confidence interval of the proxy based reconstructions. Wu et al. (2007) suggest that LGM winter temperatures were ~10–17°C lower than today outside the ice-sheet margin in Eurasia, with a more significant decrease in northern regions. This is in line with the results by Kjellström et al. (2009).

For a description of the results concerning using an improved representation of European vegetation for the regional LGM climate simulations, as well as for a detailed description of the comparison with climate proxy data, see Kjellström et al. (2009).

Just as for the simulation of a periglacial MIS 3 climate, results from the regional climate modelling were extracted for the Forsmark region also for the LGM simulation. However, for this situation, the results naturally show the climate conditions prevailing at the ice sheet surface, high above the over-riden Forsmark landscape. They are thus of less importance for the present report and are therefore not included here. The interested reader is referred to Kjellström et al. (2009).

Climate variability during the last glacial cycle

From the LGM climate modelling study described above, annual air temperatures in front of the southern sector of the ice sheet are around 9–12°C colder than at present (Figure 3-16, lower right) whereas further towards northeast, annual air temperatures are around 12–15°C lower than at present. The largest difference compared to present occurs during the winter season (Figure 3-16, middle).

In a similar way, the air temperatures simulated for an ice-free Forsmark region for a MIS 3 stadial (at 44 ka BP) are low, 12.5 degrees lower than at present (Figure 3-12, lower right). Also for this situation, the largest change compared to present occurs during the winter season. This seasonal trend is similar to the results from the climate proxy reviews undertaken by Wohlfarth (2013) and Helmens (2013) and discussed above in the present section.

As exemplified by the climate development around the modelled cold stadial at 44 ka BP, such cold events were relatively short lived, around a few thousands of years long, and alternated with warmer interstadials. Striking climate variability was found also in the simulated LGM climate (see above). These results, both from geological archives and from climate modelling, illustrate a typical feature of the last glacial cycle, namely that the climate was highly variable on both long and short time scales. This is also described in, for instance, the section on abrupt climate change in the description on paleoclimate characteristics in IPCC (2007). The last glacial cycle climate variability is also seen, for example, in the GRIP temperature proxy record (Figure 2-51). When severe cold conditions occur, these conditions do not persist for long periods of time. Such climate variability is observed also in frequency analyses of climate records (Moberg et al. 2005, Witt and Schumann 2005).

The climate variability seen during the last glacial cycle (e.g. Figure 2-51) was caused by the combined effect of variations in external orbital forcing (Section 3.1) and internal feedback mechanisms within and between the atmosphere, ocean, cryosphere and vegetation systems (Section 3.1). These mechanisms will continue to operate also in the future. Therefore, it is reasonable to assume that a similar climate variability to that characteristic of the last glacial cycle would be characteristic also for future glacial cycles.

For further descriptions of last glacial cycle temperatures, see SKB (2010a, Appendix 1).

3.2.3 Reconstructed last glacial cycle conditions at Forsmark

In this section, results from Sections 2.1.4, 2.2.4 and 2.3.4 are summarised to present key parameters (development of permafrost, shore-level and ice sheets) for the reconstruction of last glacial cycle conditions at Forsmark. Additional results from these simulations are presented in Section 4.4, where the results have been used for the construction of the Weichselian glacial cycle climate case. Section 4.4.6 also presents the resulting sequence of climate domains, as defined in Section 1.3.2.

Permafrost evolution

In Section 2.1.4 reconstructions of permafrost and freezing depths for the last glacial cycle at Forsmark were made using two permafrost models (Figure 3-18 and Figure 3-19). The simulations were made by employing the air temperature curve reconstruction for the last glacial cycle (SKB 2010a, Appendix 1 and Section 2.1.4) together with site-specific data on e.g. bedrock, soil, ground-water, lakes and shore-level development, see Section 2.1.4 and Hartikainen et al. (2010).

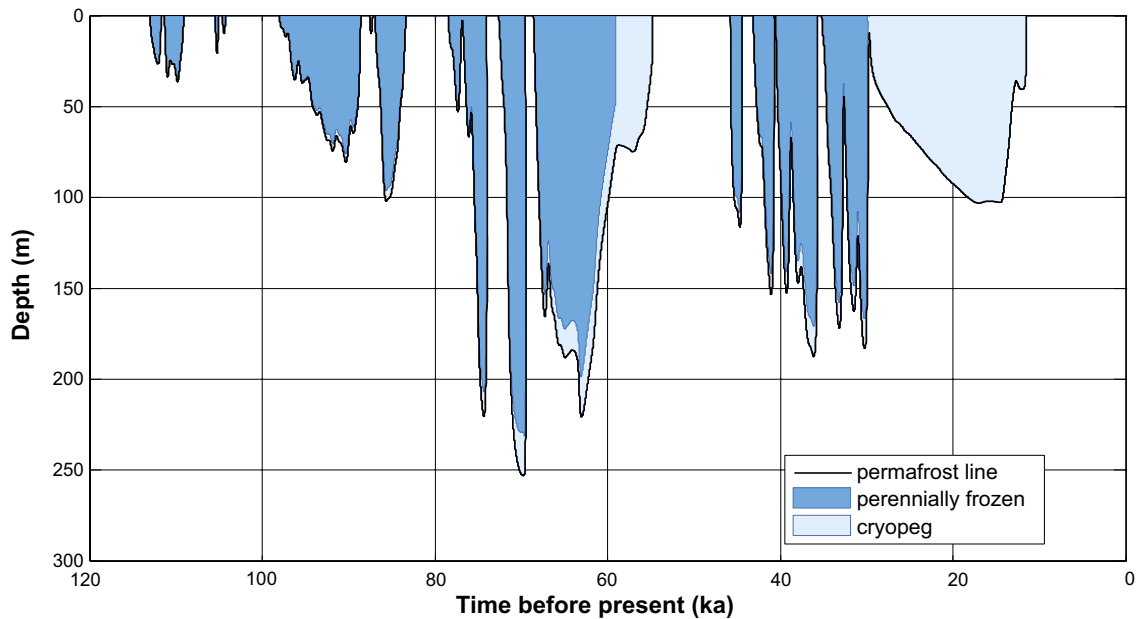


Figure 3-18. Evolution of permafrost and perennially frozen ground depth for the reconstruction of last glacial cycle conditions in Forsmark (spent nuclear fuel repository site). The results were obtained using a 1D permafrost model (Section 2.1.4). Due to the high sub-glacial pressure, a thick unfrozen cryopeg exists within the permafrost (defined by the 0°C isotherm) after 60 ka and after 30 ka before present (including the LGM). For the corresponding 2D modelling results see Figure 3-69 in SKB (2010a).

The maximum simulated Weichselian permafrost depth at the location of the repository for spent nuclear fuel is ~250 m, which occurs around 70 ka BP prior to the MIS 4 ice sheet advance over the region (Figure 3-18). The maximum permafrost depth in the surrounding region, here represented by a 15 km long profile, is ~300 m (Figure 3-19) and it occurs at the same time (Figure 3-19 lower part). At this time, the area is subject to continuous permafrost coverage (more than 90% spatial coverage) (Figure 3-19, upper part). During periods of ice-sheet coverage, permafrost declines, especially during periods when the ice sheet is warm-based (Figure 3-20). At the time of ice-sheet retreat and deglaciation, there is no permafrost or frozen ground present.

The estimated last glacial cycle air temperatures at ground level (2.1.4 and SKB 2010, Appendix 1) are typically 2–4°C lower than mean annual temperature in the uppermost part of the ground for the same climate, see Section 2.1.4 and Figure 3-11. As discussed in detail above, really low air temperatures during the last glacial cycle only prevailed during stadials that had a limited duration of some thousands of years. During cold ice-free periods, permafrost developed at the Forsmark site, but climate variability with alternating cold and warm periods, (e.g. Figures 3-53 and 3-65 in SKB 2010a), as well as the presence of the ice sheet (e.g. Figure 3-21), prevented permafrost from developing to great depths (Figure 3-18 and Figure 3-19) and Section 2.1.4. Further description and discussion of this permafrost evolution is given when these data are used to construct the *Weichselian glacial cycle climate case* (Section 4.4).

It should be noted that the reconstruction of last glacial cycle permafrost development was performed specifically to define a future climate evolution based on a repetition of the last glacial cycle for the safety assessment SR-Site. Therefore heat from the repository for spent nuclear fuel was included in the simulation. The difference between including and excluding heat from the repository was evaluated (see Figures 3-50, 3-87 of SKB 2010a as well as SKB 2006a, Figure 3-59). However, the influence of this heat for the location of the SFR repository is negligible in terms of influence on permafrost growth. All uncertainties related to the permafrost simulations are examined in detail in Section 2.1.4 and in Hartikainen et al. (2010).

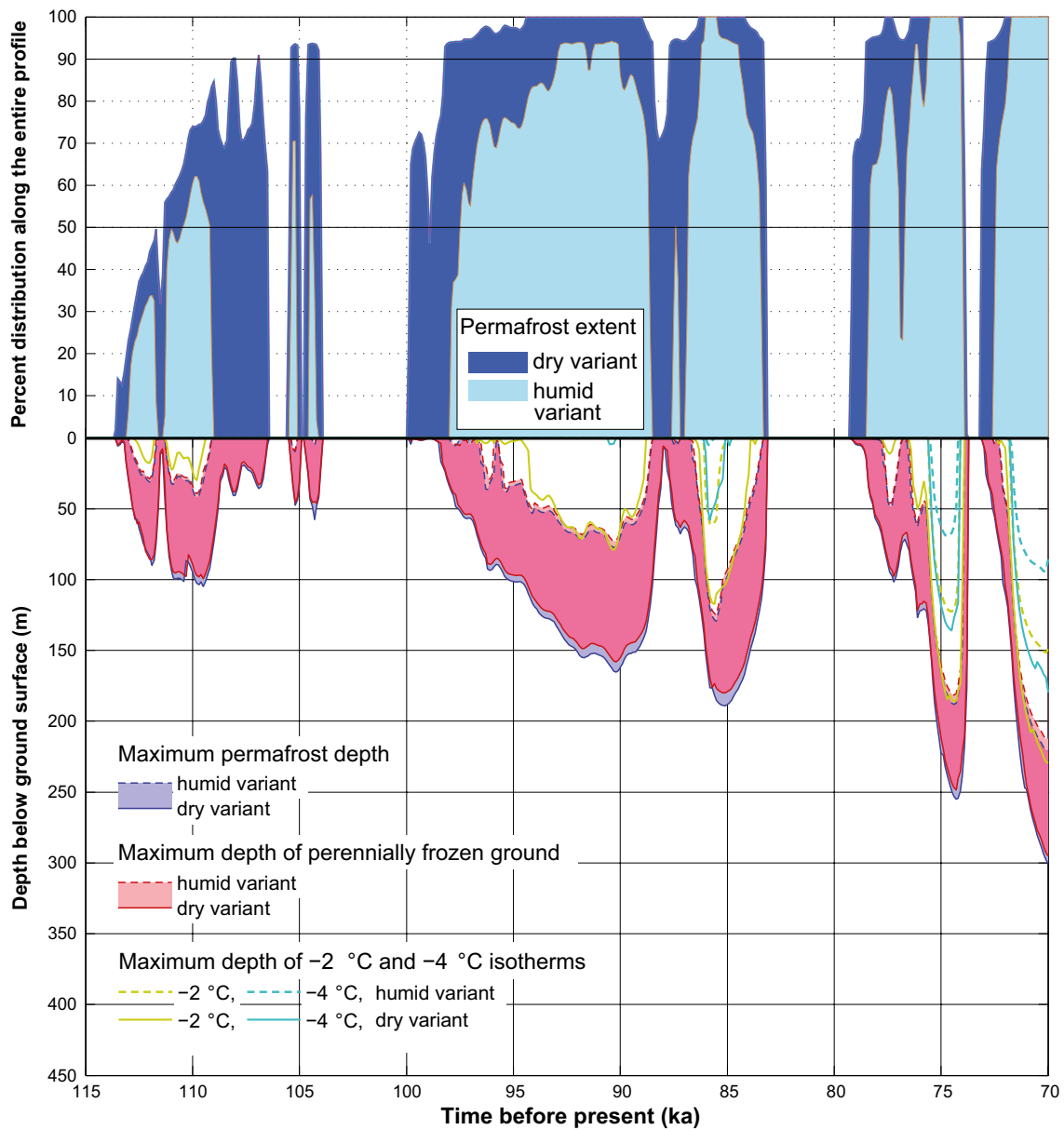


Figure 3-19. Reconstructed evolution of maximum permafrost depth, maximum freezing depth and percent permafrost distribution over a 15 km long transect over the Forsmark area for the first 50 ka of the last glacial cycle, see Section 2.1.4. Upper panel: the transition from sporadic to discontinuous permafrost occurs at 50% spatial coverage and from discontinuous to continuous permafrost at 90% coverage. Lower panel: the shaded area in blue and red represents the range obtained when considering one dry and one humid climate variant. The lilac colour indicates that the results for permafrost and perennially frozen ground overlap.

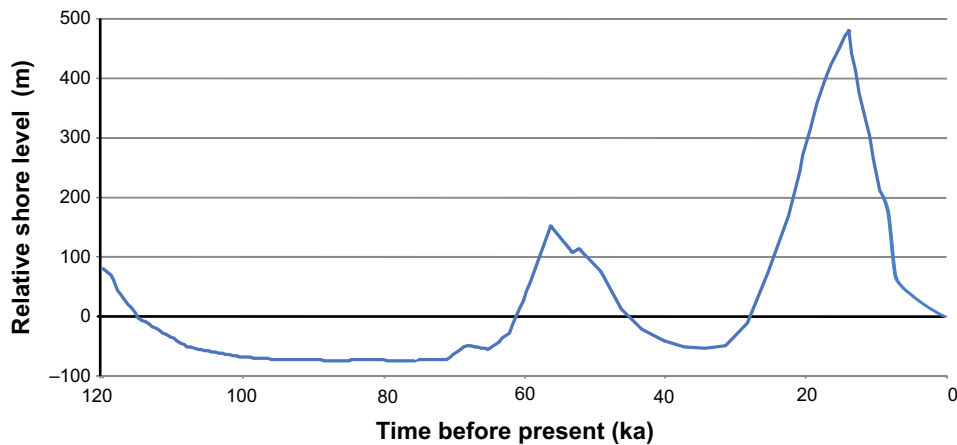


Figure 3-20. Reconstructed shore-level displacement at Forsmark for the last glacial cycle using GIA modelling (Section 2.2.4) and Holocene data (Påsse 2001). Positive values mean that the area is submerged under the contemporary level of the Baltic Sea. Note that during periods of maximum isostatic depression, the area is situated under the ice sheet.

Shoreline evolution

At times of maximum isostatic depression, the Forsmark region was covered by the Weichselian ice sheet. In Section 2.2.4, a GIA model was used to reconstruct changes in shore-level during the last glacial cycle, given input from various Earth models as well as the ice-load history from Section 2.3.4. Shore-level data were extracted for the Forsmark region (Figure 3-20) showing that the area was submerged after both reconstructed phases of ice-sheet coverage (Figure 3-21). The uncertainties in reconstructed levels are rather large (Section 2.2.4). Since the response to a specified ice load seems to be somewhat too large in the performed GIA simulations, this has resulted in the inferred water depth at Forsmark at the time of deglaciation (10,800 BP) in Figure 3-20 probably being too large. The results from the GIA modelling have for the following part of the Holocene been combined with results from other shore-level estimates (Påsse 2001) in order to decrease the uncertainty (Section 2.2.4).

Further description and discussion of this shore-level displacement, and the associated development of the Baltic Sea, is given when these data are used to construct the *Weichselian glacial cycle climate case* (Section 4.4). Uncertainties related to the GIA model simulation are discussed in Section 2.2.7.

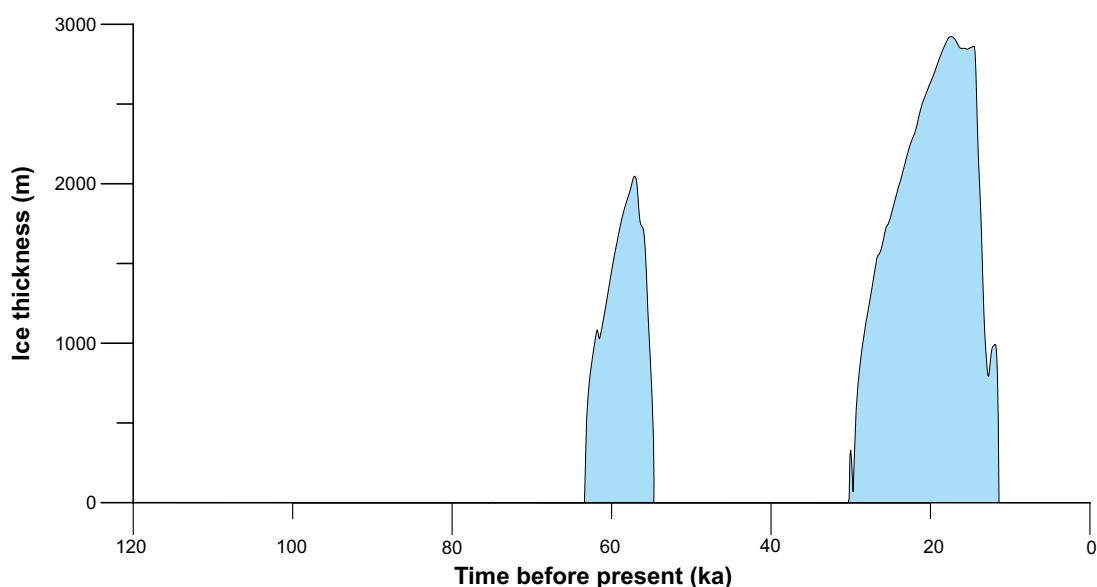


Figure 3-21. Reconstructed ice-sheet thickness over Forsmark for the last glacial cycle (Section 2.3.4).

Ice-sheet evolution

In Section 2.3.4, an ice-sheet model simulation of the Weichselian ice sheet was described, based on e.g. the temperature reconstruction of the last glacial cycle (SKB 2010a, Appendix 1). The modelled ice-sheet configurations during Weichselian stadials were calibrated against the known maximum ice margin positions for these periods. In the Weichselian ice-sheet reconstruction, the overall behaviour of the ice sheet can be characterised as being distinctly dynamic throughout the glacial cycle (Figure 2-51). For instance, during the MIS 3 period (which was *not* used for model calibration), large parts of Fennoscandia were modelled to be ice free (Figure 2-51), in line with several recent independent Quaternary geological studies (Section 3.2.1).

From the ice-sheet simulation, data on ice-sheet thickness were extracted for the Forsmark region (Figure 3-21). The Forsmark region was subject to two phases of ice-sheet coverage, during the cold stadials of MIS 4 and 2. During the last glacial maximum, the ice-sheet thickness reached ~2,900 m. Further description and discussion of this ice-sheet evolution is given when these data are used to construct the future SR-PSU *Weichselian glacial cycle climate case* (Section 4.4).

Combined reconstructed last glacial cycle parameters

Figure 3-22 shows the combined evolution of permafrost- and frozen ground depth, shore-level changes and ice sheet thickness at Forsmark as reconstructed in Sections 2.1.4, 2.2.4 and 2.3.4 and above. This reconstruction was used to construct the SR-PSU *Weichselian glacial cycle climate case* for the coming 120 ka (Section 4.4).

3.3 Projected future climate evolution

Due to incomplete knowledge of the dynamics and interactions of the Earth's climate system, the future evolution of Earth's climate cannot be predicted on the time scales of interest for safety assessments of nuclear waste repositories. Nonetheless, abundant knowledge exists and projections of future climate evolution based on this knowledge provide valuable information and a range of possible future climate evolutions. The climate cases used in this safety assessment (Chapter 4) were designed to cover the uncertainty range associated with future climate development. In this section, the current knowledge on the Earth's future climate evolution in the coming ~100 ka is described in terms of global average evolution and large-scale patterns of climate change. Implications for future climate evolution in the Forsmark region are also discussed.

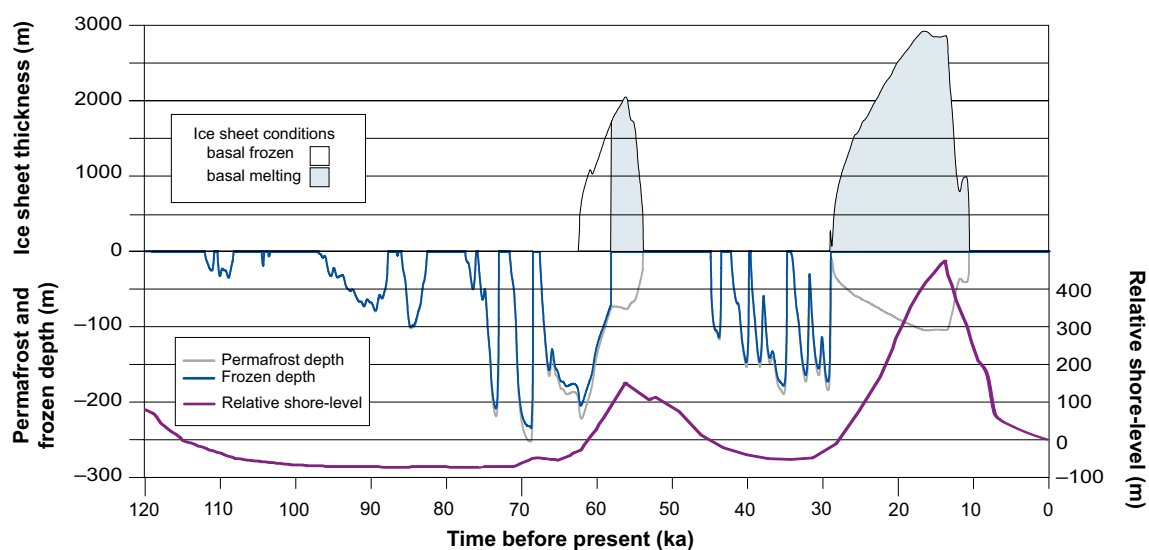


Figure 3-22. Reconstructed Weichselian evolution of ice sheet, shore-level, permafrost and frozen ground at Forsmark. This evolution was repeated and projected into the future in order to construct the SR-PSU *Weichselian glacial cycle climate case*.

Atmospheric greenhouse gas concentrations and insolation variations due to variations in astronomical parameters are the major drivers of global climate variability. In the following, current knowledge on future greenhouse gas concentrations (Section 3.3.1) and insolation variations (Section 3.3.2) is described.

Projections of future climate evolution are obtained using models of varying complexity ranging from Earth System Models (ESMs) through Atmosphere-Ocean General Circulation Models (AOGCMs), Earth System Models of Intermediate Complexity (EMICs) to Simple Climate Models (SCMs). In modelling studies of future climate evolution, assumptions regarding future variations in the forcing conditions, e.g. human carbon emissions, are made. In general terms, the range from ESMs to SCMs involves decreasing complexity of the model physics and dynamics of the different components of the climate system as compared to the real world, as well as decreasing spatial and temporal model resolution. The computational cost of state-of-the-art ESMs and AOGCMs prevents use of these models for modelling of more than a few centuries-millennia. To reflect both the complexity of the models used to assess the future evolution, and, the increased spread in possible future climate evolution, projected future climate evolution is described for the current century (Section 3.3.3), for the next 10 ka (Section 3.3.4) and for the next 100 ka (Section 3.3.5).

Climate evolution in a specific region, such as the Forsmark region in south-central Sweden, can differ from the global climate evolution. The annual average temperature increase in the Forsmark region until 2100 AD is for instance expected to exceed the global temperature increase due to stronger warming over land than over ocean and to stronger warming in the polar regions than in the tropics (IPCC 2013). Further, precipitation will increase in the Forsmark region in accordance with a general increase in the contrast in precipitation between wet and dry regions (IPCC 2013).

Another component of the climate system that influences regional climate is the ocean circulation which transports heat from low to mid and high latitudes. Changes in this circulation contribute to regional differences in the future climate evolution. For the North Atlantic region, including Sweden, the northward heat flow associated with the Atlantic Meridional Overturning Circulation (AMOC) is of primary importance for climate. It is very likely that the AMOC will weaken over the 21st century (IPCC 2013). It is, however, very unlikely that the AMOC will undergo an abrupt transition or collapse in the 21st century for the scenarios considered by the IPCC (2013). However, a collapse beyond the 21st century for large sustained warming cannot be excluded. Implications for regional climate in Forsmark of a possible strong reduction or collapse of the AMOC are discussed in Sections 3.3.3, 3.3.4 and 3.3.5.

3.3.1 Atmospheric greenhouse-gas concentrations

Global atmospheric concentrations of greenhouse gases have increased markedly as a result of human activities since 1750 and now far exceed pre-industrial values determined from ice cores spanning many thousands of years. Human greenhouse-gas emissions include both carbon dioxide (CO₂) and methane (CH₄), but CH₄ emitted to the atmosphere is converted to CO₂ after an average lifetime of only 12 years. Therefore, studies of future climate focus on CO₂. Recent studies with coupled climate-carbon cycle models have shown that the century-scale global mean temperature response to CO₂ emissions is independent of the emissions pathway (Eby et al. 2009, Zickfeld et al. 2009). Further, it has been demonstrated that global mean temperature remains approximately constant for several centuries after cessation of CO₂ emissions (e.g. Solomon et al. 2009). These results can be generalised to show that the ‘instantaneous’ global temperature response is proportional to cumulative carbon emissions (Matthews et al. 2009).

Humankind has up to now released c 300 Pg (10¹⁵ g) carbon to the atmosphere and the total cumulative emissions will surpass 1,000 Pg carbon before the end of this century under business-as-usual scenarios (Archer et al. 2009). The remaining fossil fuel reserve that it might be reasonable to extract under present economic conditions totals c 5,000 Pg carbon. Human emissions have so far increased the atmospheric CO₂ concentration from 280 ppmv in 1750 AD prior to industrialisation to 394 ppmv in 2012 AD (www.esrl.noaa.gov). A continued increase in the CO₂ concentration at the same rate as during the last decade (c 2 ppmv per year) would result in an atmospheric CO₂ concentration of c 570 ppmv in 2100 AD.

Until 2100 AD

To produce climate projections for the next few centuries, coordinated experiments, in which many climate models run a set of scenarios, have become the standard (Knutti and Sedláček 2013). A number of emission scenarios or scenarios for atmospheric concentrations are used in these multi-model ensembles, which sample uncertainties in emission scenarios, model uncertainty and initial condition uncertainty, and provide a basis to estimate projection uncertainties. The Coupled Model Intercomparison Project Phase 5 (CMIP5; Taylor et al. 2012), coordinated by the World Climate Research Programme in support of the Intergovernmental Panel on Climate Change Fifth Assessment Report (IPCC AR5, 2013) is the most recent of these activities. The fourth IPCC assessment report (IPCC AR4), which was based on the Coupled Model Intercomparison Project Phase 3 (CMIP3), was published 2007 (IPCC 2007) and the fifth IPCC assessment report, based on CMIP5, was released online in September 2013 (www.ipcc.ch) and the printed version is expected in early 2014. This report was written and reviewed by the experts in the field and it provides an up-to-date description of current knowledge on the future evolution of climate and climate-related processes, such as sea level, in the next centuries to millennium. The conclusions presented by IPCC (2013) are therefore used here, when applicable.

In CMIP3, the models were integrated until year 2100 AD using projected concentrations of long-lived greenhouse gases (CO₂ and CH₄) and emissions of SO₄ specified in a set of three emission scenarios defined in the Special Report on Emissions Scenarios (SRES; IPCC 2000). The emissions scenarios represent ‘low’ (B1), ‘medium’ (A1B) and ‘high’ (A2) emissions (IPCC 2007).

In CMIP5, ESMs were used for the first time in CMIP. These are AOGCMs coupled to biogeochemical components and, in some cases, also include interactive prognostic aerosol, chemistry, and dynamical vegetation components. These models have the capability of using time-evolving emissions of constituents from which concentrations can be computed interactively. The CMIP5 projections of climate change are driven by concentration or emission scenarios consistent with the representative concentration pathways (RCPs; Meinshausen et al. 2011). In contrast to the SRES scenarios used in CMIP3, which do not include policy intervention, the RCPs are mitigation scenarios that assume policy actions will be taken to achieve certain emission targets. For CMIP5, four RCPs have been formulated that are based on a range of projections of future population growth, technological development, and societal responses. The labels for the RCPs provide a rough estimate of the radiative forcing in the year 2100 (relative to preindustrial conditions). For example, the radiative forcing in RCP8.5 increases throughout the twenty-first century before reaching a level of about 8.5 Wm⁻² at the end of the century. In addition to this “high” scenario, there are two intermediate scenarios, RCP4.5 and RCP6, and a low so-called peak-and-decay scenario, RCP2.6, in which radiative forcing reaches a maximum near the middle of the twenty-first century before decreasing to an eventual nominal level of 2.6 Wm⁻².

Until 10 ka AP

The future atmospheric CO₂ evolution after human carbon emissions have stopped will depend on the cumulative emissions up to that point in time and on the processes that act to decrease the concentration (e.g. Zickfeld et al. 2012). Archer et al. (2009) performed a review and model inter-comparison of the atmospheric lifetime of fossil fuel CO₂ as predicted by nine different carbon cycle models and EMICs. The models were integrated for 10 ka starting from a pre-industrial CO₂ concentration of 280 ppmv and initial pulses of 1,000 Pg and 5,000 Pg carbon. Archer et al. (2009) concluded that 20–35% of the CO₂ remains in the atmosphere after equilibration with the ocean (200–2000 years). Further, they concluded that neutralisation by calcium carbonate draws the airborne fraction down further on timescales of 3 to 7 ka. After 10 ka of integration following a 1,000 Pg carbon initial pulse, 8–19% of the emissions remained in the atmosphere. After 10 ka of integration following a 5000 Pg carbon initial pulse, 10–33% of the emissions remained in the atmosphere. Archer et al. (2009) concluded that generally accepted modern understanding of the global carbon cycle indicates that climate effects of CO₂ releases to the atmosphere will persist for tens, if not hundreds, of thousands of years into the future.

Table 3-2. IPCC emission scenarios used in CMIP3 and CMIP5.

Emission scenario	SRES scenario used in CMIP3	RCP scenario used in CMIP5
Low	B1	RCP2.6
Medium	A1B	RCP4.5 and RCP6
High	A2	RCP8.5

Until 100 ka AP

Several modelling studies, described in Section 3.3.5, indicate that the atmospheric CO₂ concentration is of great importance for Earth's climate evolution in the next 100–200 ka. The future concentration is controlled by cumulative carbon emissions and the processes that act to reduce the atmospheric concentration, but also by the processes involved in the natural glacial–interglacial cycles in the last 800 ka (Lüthi et al. 2008; Figure 3-1). The results presented by Archer et al. (2009) strongly suggest that the atmospheric CO₂ concentration will remain above the pre-industrial 280 ppmv for the next 10 ka and possibly even the next 100 ka. However, past glacial–interglacial CO₂ cycles are not fully understood and future human carbon emissions are uncertain.

To obtain a lower limit of future atmospheric CO₂ concentration, an estimation of the fastest decline in the atmospheric CO₂ concentration that can be anticipated based on current knowledge is given in the following. The experiments analysed by Archer et al. (2009) were based on the assumption of continued human-induced emissions of carbon to the atmosphere. The absolutely most conservative assumption would be to assume that anthropogenic emissions are reduced to zero today and that the atmospheric concentration would start to decrease from the present level of 394 ppmv. This corresponds to total cumulative emissions of ~300 Pg carbon as compared to the 1,000 and 5,000 Pg carbon cumulative emissions used in the experiments presented by Archer et al. (2009). Assuming that the atmospheric CO₂ concentration would decrease at the same rate as in the fastest decreasing model for 1,000 Pg carbon cumulative emissions in Archer et al. (2009), 8% of the fossil fuel carbon (i.e. the CO₂ in excess of the preindustrial concentration of 280 ppmv) would remain in the atmosphere after 10 ka in this bounding case. The atmospheric CO₂ concentration would thus be c 290 ppmv at 10 ka AP. If conditions were favourable for initiation of ice-sheet build up at this point, a further decrease in CO₂ concentration by the processes responsible for previous interglacial to glacial reductions in atmospheric CO₂ could potentially further decrease the atmospheric CO₂ concentration.

For comparison, the rapid decrease of the atmospheric CO₂ concentration found in ice-core data during the last glacial inception (Lüthi et al. 2008) is estimated. The atmospheric CO₂ concentration decreased from interglacial levels of c 275 ppmv around 115.4 ka BP to c 228 ppmv around 108.0 ka BP, i.e. c 47 ppmv CO₂ in 7.4 ka. A similar rapid decrease from 10 ka AP and onwards would result in an atmospheric CO₂ concentration of c 240 ppmv around 17 ka AP.

In summary, atmospheric CO₂ concentrations at or below pre-industrial levels cannot be excluded after 10 ka AP if human emissions of CO₂ were reduced to zero in the near future. This improbable scenario can be regarded as a bounding case. Under more realistic scenarios for future anthropogenic carbon emissions, the atmospheric CO₂ concentration would be at or above 300 ppmv at 10 ka AP (Archer et al. 2009).

3.3.2 Insolation

As described in Section 3.1, glacial–interglacial cycles are believed to be driven by changes in insolation as a result of variations in the Earth's orbit around the Sun. Over the next 100 ka, the amplitude of insolation variations will be small, much smaller than during the Weichselian (Figure 3-1; Berger and Loutre 2002). For example, at 60°N in June, insolation will vary by less than 25 Wm⁻² over the next 25 ka, compared with 110 Wm⁻² between 125 ka and 115 ka BP (see Figure 3-1). Thus, from the standpoint of insolation, the Weichselian cannot be taken as an analog for the next millennia (Berger and Loutre 2002).

3.3.3 Climate evolution until 2100 AD

Atmospheric greenhouse-gas concentrations are expected to increase until 2100 AD at a rate mostly determined by human emissions (IPCC 2013). This increase is expected to result in an increased global average surface temperature (IPCC 2013).

Based on the CMIP5 simulations, IPCC (2013) draws the following conclusions.

- The global annual mean surface air temperature anomalies (SAT) for 2081–2100 relative to the 1986–2005 AD reference period range from 0.3°C–1.7°C for the RCP2.6 scenario (Table 3-2), to 1.1°C–2.6°C for the RCP4.5 scenario, 1.4°C–3.1°C for the RCP6.0 scenario and 2.6°C–4.8°C for the RCP8.5 scenario.
- Globally averaged SAT changes over land will exceed changes over the ocean at the end of the 21st century and the Arctic region is projected to warm most.
- Global precipitation will increase with increased global mean SAT.
- Changes in average precipitation will exhibit substantial spatial variation with an increase in the contrast of annual mean precipitation between dry and wet regions and between dry and wet seasons.

The spread of projected global mean temperature increase for the RCP scenarios used in CMIP5 is considerably larger (at both the high and low response ends) than for the three SRES scenarios used in CMIP3 as a direct consequence of the larger range of radiative forcing across the RCP scenarios compared with that across the three SRES scenarios (Collins et al. 2013).

Ocean circulation

Almost all climate model projections reveal an enhanced increase of high latitude temperature and high latitude precipitation (Meehl et al. 2007). Both of these effects tend to make the high latitude surface waters lighter and hence increase their stability. All the models included in CMIP5 show a weakening of the AMOC over the course of the 21st century (IPCC 2013). Once the radiative forcing is stabilised, the AMOC recovers, but in some models to less than its preindustrial rate of turnover. The recovery may include a significant overshoot if the anthropogenic radiative forcing is eliminated (Wu et al. 2011). The AMOC overshoot could give an extended period of anomalously strong northward heat transport, maintaining warmer northern high latitudes for decades after the atmospheric CO₂ concentration returns to preindustrial values.

Based on the assessment of the CMIP5 RCP simulations and of understanding from analysis of CMIP3 models, observations and understanding of physical mechanisms, IPCC (Collins et al. 2013) conclude that it is very likely that the AMOC will weaken over the 21st century. It is however very unlikely that the AMOC will undergo an abrupt transition or collapse in the 21st century (Collins et al. 2013). This was concluded taking both the high latitude temperature and precipitation increase and a possible rapid melting of the Greenland ice sheet into account. For a review of current knowledge please refer to IPCC (Collins et al. 2013, Section 12.5.5.2).

Implications of changes in AMOC for the Forsmark region

The weakening of the AMOC in the 21st century contributes to reducing the warming in Europe, but since the radiative forcing caused by increasing greenhouse gases would overwhelm the cooling associated with the AMOC reduction (IPCC 2007), the net effect would be continued warming in the Forsmark region. This internal climate feedback is included in the CMIP5 simulations.

Climate in Forsmark until 2100 AD

Multi-model CMIP5 ensemble average SAT change for 2081–2100 AD relative to the 1986–2005 AD reference period is displayed in Figure 12.11 of Collins et al. (2013). The SAT anomaly for the Forsmark region ranges from 1.0°C–1.5°C for the RCP2.6 scenario to 2°C–3°C for the RCP4.5 scenario, 3°C–4°C for the RCP6.0 scenario and 4°C–5°C for the RCP8.5 scenario. Note that the SAT ranges given here represent the shading interval in the figure and give no indication of the uncertainty in the projected change.

Multi-model CMIP5 ensemble average change for 2081–2100 AD in seasonal precipitation relative to the 1986–2005 AD reference period is displayed in Figure 12.22 of Collins et al. (2013) for the high emission scenario RCP8.5. The precipitation anomaly is in the range 20–30% in winter, and 10–20% in spring, summer and autumn. Again note that the precipitation ranges given here represent the shading interval in the figure and give no indication of the uncertainty in the projected change.

The CMIP5 results are in agreement with previous studies with regional climate models. Kjellström et al. (2011) analysed a six-member ensemble of simulations of European climate in response to increasing atmospheric greenhouse-gas concentrations until 2100 AD (A1B scenario; Table 3-2; Nakićenović and Swart 2000). The ensemble-mean winter SAT increased by c 4°C and precipitation increased by 20–30% at 2100 AD in the Forsmark region. The corresponding ensemble mean for the summer season indicated a SAT increase of 2–3°C and a precipitation increase of c 10%.

Relative sea-level evolution at Forsmark until 2100 AD

The area surrounding the SFR entrance tunnel is located ~3 m above the present mean sea level in Forsmark. Changes in relative sea level until 2100 AD, i.e. during the construction and operational phases of the SFR repository, are of importance to planning and construction. The *maximum possible* relative sea-level at 2100 AD in Forsmark, as can be deduced from present scientific literature, is therefore assessed here. This results in a pessimistic worst-case scenario, with low probability according to present knowledge, but it still constitutes a scenario that cannot be ruled out. The present analysis does not show the *most likely* scenarios for projected future sea-level rise, since the purpose is to provide input to e.g. construction planning. Such values can be found in the provided references. Relative sea-level is, per definition, zero at the present day (Section 2.2.1). The annual average sea level for the period 1986–2005 is chosen here to represent the mean sea level at the present day at Forsmark, since this period is used as the reference period in the latest IPCC report (IPCC 2013). Based on this choice, the mean sea level at Forsmark is +0.19 m expressed in the Swedish national elevation datum RH2000 (http://www.smhi.se/hfa_coord/BOOS/dbkust/mwreg_rh2000.pdf).

Worst-case scenarios for sea-level change at Forsmark for the year 2100 AD, must include contributions from both slow long-term processes, such as ocean thermal expansion, and fast short-term processes, such as storm surges. When considering constructing at near-coastal sites, such as the planned SFR3 repository, it is important to distinguish between the potential effect from slow long-term processes, which influence the mean sea-level, and fast temporary processes. A key point here is that it will be possible to monitor sea-level rise due to slow long-term processes over the coming decades. This gives the important opportunity to take further necessary measures if and when sea-level rise proves to be in the high range.

The relative sea level evolution in Forsmark is determined by the net effect of *eustatic* changes (i.e. sea-level rise associated with e.g. changes in the volume and spatial distribution of ocean water) and *isostatic* changes (at the Forsmark site manifested through glacial isostatic rebound with an uplift rate of c 8 mm a⁻¹). The present-day net effect of the two processes at the Forsmark site is a slow lowering and off-shore migration of the shoreline.

An up-to-date overview of scientific knowledge on past, present and future sea-level evolution was released by the IPCC AR5 (IPCC 2013, Church et al. 2013). The review presented by Church et al. (2013) includes the processes of thermal expansion of ocean water, melting of glaciers and ice sheets, rapid dynamics of ice sheets, and land water storage, which influence the sea-level. The estimates of maximum sea-level rise made by Church et al. (2013) have been used here, together with complementary information on regional and local effects, to estimate the maximum relative sea level at Forsmark at 2100 AD. The main conclusions related to eustatic sea-level change until 2100 AD presented by Church et al. (2013) are given here.

- Proxy and instrumental sea-level data indicate a transition in the late 19th to the early 20th century from relatively low mean rates of rise over the previous two millennia to higher rates of rise. It is likely that the rate of global mean sea-level rise has continued to increase since the early 20th century.
- Ocean thermal expansion and glacier melting have been the dominant contributors to 20th century global mean sea-level rise.
- Confidence in projections of global mean sea-level rise has increased since AR4 because of the improved physical understanding of the components of sea level, the improved agreement of process-based models with observations, and the inclusion of ice-sheet dynamical changes.
- There is high confidence in projections of thermal expansion, high confidence in projections of Greenland surface mass balance, and medium confidence in projections of Antarctic surface mass balance and glacier mass loss.

- It is very likely that the rate of global mean sea-level rise during the 21st century will exceed the rate observed during 1971–2010 for all RCP scenarios due to increased ocean warming and loss of mass from glaciers and ice sheets. For 2100 AD, compared to 1986–2005, global mean sea-level rise is likely to be in the 5–95% range of process-based models, which give 0.28–0.60 m for RCP2.6, 0.35–0.70 m for RCP4.5, 0.37–0.72 m for RCP6.0, and 0.53–0.97 m for RCP8.5.
- Based on current understanding, only the collapse of marine-based sectors of the Antarctic Ice Sheet, if initiated, could cause global mean sea level to rise substantially above the likely range during the 21st century. This potential additional contribution cannot be precisely quantified, but there is medium confidence that it would not exceed several tenths of a meter of sea-level rise during the 21st century.
- Some semi-empirical models project a range that overlaps the process-based likely range, whereas others project a median and 95-percentile that are about twice as large as the process-based model projections, but there is no consensus in the scientific community about their reliability and there is thus low confidence in their projections.
- Over decadal periods, the rates of regional sea-level change as a result of climate variability can differ from the global average rate by more than 100% of the global average rate.
- It is very likely that there will be a significant increase in the occurrence of sea level extremes by 2100. This increase will primarily be the result of an increase in mean sea level, with the frequency of a particular sea level extreme increasing by an order of magnitude or more in some regions by the end of the 21st century. There is low confidence in region-specific projections of storminess and associated storm surges.
- In general, there is low confidence in region-specific projections of changes in wave height due to the low confidence in storm projections, and to the challenge of downscaling future wind fields from coarse-resolution climate models.

The different processes contributing to maximum relative sea level at Forsmark at 2100 AD are summarised in Table 3-3 and Figure 3-27. Each contribution is discussed in the following.

Fast temporary sea-level change

Sea level at coastal sites, such as Forsmark, varies on short time-scales due to variations in atmospheric pressure and winds associated with temporary weather systems. The maximum relative sea level at Forsmark, with 100-year recurrence time, was estimated based on observations for the period 1976–2000 AD, to +1.46 m in RH2000 (Engqvist 2013, personal communication). This estimate, corresponding to +1.27 m above mean sea level for the period 1986–2005, is used here to represent the maximum storm surge level at Forsmark for 2000 AD (Table 3-3). It should be noted that a 100-year recurrence time means that there is a 63% probability that a sea-level rise of this magnitude or higher occurs once in a 100-year period. The sea level may thus occasionally rise above this value, as illustrated by the highest observed sea level in Forsmark, +1.45 m above mean sea level for the year (corresponding to +1.56 m in RH2000), which occurred during a storm surge in 2007. Storm surge levels were modelled for present-day conditions and for year 2100 AD by Meier (2006). Data from this study suggest that this contribution to temporarily high sea level in Forsmark will increase by 0.3 m from 2000 AD to 2100 AD (Table 3-3) (Meier 2006, Meier 2013, personal communication). The spatial resolution used by Meier (2006) does not resolve the detailed ocean dynamics off the coast at Forsmark. To account for this, the local effect of increasing wind speeds in a future climate on Forsmark extreme sea level was estimated for the Forsmark site by Nerheim (2008) (Table 3-3). An increase in storm surges within the North Sea area for 2100 AD was modelled by Woth et al. (2006) amounting at most to 0.07 m in the Skagerrak (Table 3-3). In order to estimate a pessimistic case, this episodic contribution was also included in the analysis, even though it is unlikely that it would occur with sufficient duration and at times that could accentuate extreme sea-levels in the Baltic Sea.

Slow long-term sea-level rise

The slow long-term processes that contribute to changes in global-mean sea-level include thermal expansion of ocean water, melting of glaciers and the Greenland and Antarctic ice sheets, rapid ice-sheet dynamics and changes in land water storage. Sea-level rise associated with these processes is distributed over the world oceans. However, the distribution is not uniform. Some regions experience less than the global-mean whereas the situation is the opposite for other regions. These regional

differences are due to gravitational effects, ocean dynamics, regional differences in water temperature and salinity, winds and air pressure, and air-sea heat and freshwater fluxes, see Church et al. (2013) and references therein.

Church et al. (2013) stated that there is low confidence in the projections made by semi-empirical models (e.g. Vermeer and Rahmstorf 2009), and also in kinematic constraints on ice-sheet melting (Pfeffer et al. 2008). However, for the purpose of the present assessment, the overall highest value for global average sea-level rise until 2100 AD given in the scientific literature (2.25 m by Srivier et al. 2012), is of interest. The study by Srivier et al. (2012) adds an additional uncertainty of 0.25 m of steric sea-level rise to the high-end value of 2.0 m global sea-level rise given by Pfeffer et al. (2008). The resulting value of 2.25 m encompasses all estimates by semi-empirical models, and it is included in the present analysis in order to obtain a worst-case scenario. This value represents maximum contributions from thermal expansion of ocean water, melting of glaciers and the Greenland and Antarctic ice sheets and rapid ice-sheet dynamics.

The calculation of the contribution to sea-level change until 2100 AD in Forsmark from slow long-term processes was performed as follows.

- The maximum global-average sea-level rise by 2100 AD reported by Church et al. (2013) for process-based models under the RCP8.5 emission scenario, +0.97 m, is used as a point of reference.
- Further, the maximum global-average sea-level rise by 2100 AD based on methods other than the process-based models, +2.25 m (Srivier et al. 2012, Pfeffer et al. 2008), is used to illustrate the highest value found in the scientific literature.

The maximum sea-level rise along the Baltic Sea coast at Forsmark associated with these two estimates of the maximum global-average sea-level rise is determined in steps. For the process-based models the steps were:

- Church et al. (2013) present maps of the regional distribution due to ocean dynamics and steric effects and the gravitational effects of the melting of glaciers and ice sheets. The data used to prepare these maps was obtained from Mark Carson (Carson 2013, personal communication). For the RCP 8.5 emission scenario, the sea-level rise in the North Sea is just below the global average rise of +0.97 m. It is therefore assumed to be equal to the global average value.
- The maximum sea-level rise along the Baltic coast can deviate from the rise in the North Sea by a maximum of +0.1 m due to differences in the atmospheric wind and run-off to the Baltic Sea (Meier 2013, personal communication). Based on this information the maximum sea-level rise along the Baltic Sea coast at Forsmark is estimated to be +1.07 m by 2100 AD based on process-based models.

For the semi-empirical projections and kinematic constraints on ice-sheet melting (Srivier et al. 2012, Pfeffer et al. 2008) the steps were:

- The authors present the contributions to the total sea-level rise separately. These were compared to the corresponding contributions to the RCP 8.5 scenario:
 - Greenland ice sheet: 24% (Pfeffer et al. 2008), 23% (Church et al. 2013)
 - Antarctic ice sheet: 28% (Pfeffer et al. 2008), 15% (Church et al. 2013)
 - glaciers and ice caps: 24% (Pfeffer et al. 2008), 23% (Church et al. 2013)
 - thermal expansion: 24% (Srivier et al. 2012), 32% (Church et al. 2013)
 - land water storage: 8% (Church et al. 2013).

The distribution among the different contributions is similar, though with a larger contribution from thermal expansion in Church et al. (2013) and larger contributions from the Antarctic ice sheet in Pfeffer et al. (2008). Based on this comparison, it is assumed that the relation between North Sea and global-average sea-level rise is similar for the semi-empirical projections and kinematic constraints on ice-sheet melting as for the process-based models. Thus it is assumed that North-Sea sea-level rise by 2100 AD is equal to the global-average +2.25 m.

- The difference of the maximum sea-level rise along the Baltic coast as compared to the North Sea is determined in the same way as for the process-based models (see above). Thus +0.1 m is added to the North Sea value resulting in a maximum sea-level rise along the Baltic Sea coast at Forsmark of 2.35 m by 2100 AD based on semi-empirical projections and kinematic constraints on ice-sheet melting.

Further note that the wave height has not been included in the present analysis, due to the difficulties in calculating proper wave heights at the precise settings along the coast line. However, for the constructional purposes of SFR, it may also be noted that the wave height close to the SFR entrance is significantly reduced due to the location of the pier, local bathymetry, detailed shore configuration and location of small islands. Waves from SSE need to bend in an s-shape before reaching SFR, which results in a reduction in wave energy and waves with lower amplitude than would otherwise be the case. In this context it is also worth noting that the local setting means that the contribution from a local maximum wave height cannot occur simultaneously with the local maximum in wind setup. Since the latter is included in the analysis, this partly compensates for the fact that wave heights are not included.

Isostatic change

The best known process of importance to relative sea-level change in Forsmark until 2100 AD is the glacial isostatic rebound. The isostatic rebound, interpolated to the Forsmark site from data of Lidberg et al. (2010), amounts to 0.84 m for the period 2000 to 2100 AD (Table 3-3). This contribution will compensate for a significant portion of projected eustatic sea-level rise at the Forsmark site by 2100 AD.

Resulting relative sea-level

The maximum mean sea-level rise at Forsmark by 2100 AD, as determined by process-based methods and reported in the latest IPCC report (Church et al. 2013), is moderate. Taking only slow long-term processes into account, the maximum mean sea-level rise at Forsmark by 2100 AD amounts to +0.23 m above the present-day mean sea-level (corresponding to +0.42 m in the RH2000 height system) (Table 3-3 and Figure 3-23 C1). This level represents the maximum rise of mean sea-level due to slow long-term processes as projected by process based methods (+1.07 m; Table 3-3), compensated for isostatic rebound (−0.84 m; Table 3-3 and Figure 3-23).

If the slow long-term processes are estimated based on non-process based models (e.g. Sriver et al. 2012) rather than process-based models (Church et al. 2013), the maximum mean sea-level rise at Forsmark by 2100 AD amounts to +1.51 m above the present-day mean sea-level (corresponding to +1.70 m in the RH2000 height system) (Table 3-3 and Figure 3-23 C2). This level represents the maximum possible rise of mean sea-level due to slow long-term processes as projected by non-process based methods (+2.35 m; Table 3-3), compensated for isostatic rebound (−0.84 m; Table 3-3). Figure 3-24 shows areas that will be permanently flooded at Forsmark at 2000 AD if the mean sea level reaches +1.51 m above the present-day sea level.

At 2100 AD, the sea level at Forsmark will temporarily rise above mean sea level due to fast temporary processes such as storm events, in a similar way as today. The contribution from these processes is estimated to be increased by 2100 AD (Figure 3-23 B). When these fast temporary contributions to high sea-levels are combined with the maximum rise of mean sea-level as determined by process-based methods (Church et al. 2013), the maximum sea-level at Forsmark by 2100 AD is +2.02 m above the present-day mean sea-level (corresponding to +2.21 m in the RH2000 height system) (Table 3-3 and Figure 3-23 D1). This level represents the sum of the maximum possible rise of mean sea-level due to slow long-term processes as projected by process-based methods (+1.07 m; Table 3-3) and the maximum sea-level rise due to fast temporary processes (1.79 m; Table 3-3), compensated for isostatic rebound (−0.84 m; Table 3-3 and Figure 3-23). Figure 3-25 shows areas that will be temporarily flooded at Forsmark at 2100 AD if the sea level, during short storm events, reaches +2.02 m above the present-day sea level. After such storm events, the sea level would decrease to the long-term mean value.

If the contribution from fast temporary storm processes instead are combined with the maximum rise of mean sea-level as estimated by non-process based models (e.g. Sriver et al. 2012), the maximum sea-level at Forsmark by 2100 AD is +3.30 m above the present-day mean sea-level (corresponding to +3.49 m in the RH2000 height system) (Table 3-3 and Figure 3-23 D2). This level represents the sum of the maximum possible rise in mean sea-level due to slow long-term processes as projected by non process-based methods (+2.35 m; Table 3-3) and the maximum sea-level rise due to fast temporary storm processes (+1.79 m; Table 3-3), compensated for the isostatic rebound (−0.84 m; Table 3-3 and Figure 3-23). This is a very pessimistic estimate, based on the highest inferred sea-level rise for the year 2100 AD published in the present scientific literature. Figure 3-26 shows

areas that will be temporarily flooded at Forsmark at 2100 AD if the sea level, during storm events, reaches +3.30 m above the present-day sea level. After such storm events, the sea level would decrease to the long-term mean value.

The lateral shoreline migration that would occur by 2100 AD at Forsmark if the mean sea-level would remain unchanged compared to the present day and only isostatic rebound would influence the shoreline displacement at Forsmark is shown in Figure 3-27. This map illustrates the lower limit of the uncertainty range for changes in mean sea-level at Forsmark until 2100 AD. In this case, the sea-level reaches -0.84 m below the present-day mean sea-level (corresponding to -0.65 m in the RH2000 height system) (Table 3-3). Note that the present rise in mean sea level amounts to c 1.1 mm/yr at Forsmark (see Section 2.2.3), why the assumption of no future mean sea-level rise is unrealistic.

The estimates on maximum sea-level presented in Table 3-3 and Figures 3-23, 3-24, 3-25 and 3-26 describe cumulative worst-case scenarios derived from considering the effects of possible future changes in processes spanning global-, regional- and local scales. However, it should again be emphasised that research on future global sea-level rise is in a very intensive phase, and that major uncertainties still exist in this field. Nevertheless, these uncertainties need to be considered when planning to build near the present-day coast-line.

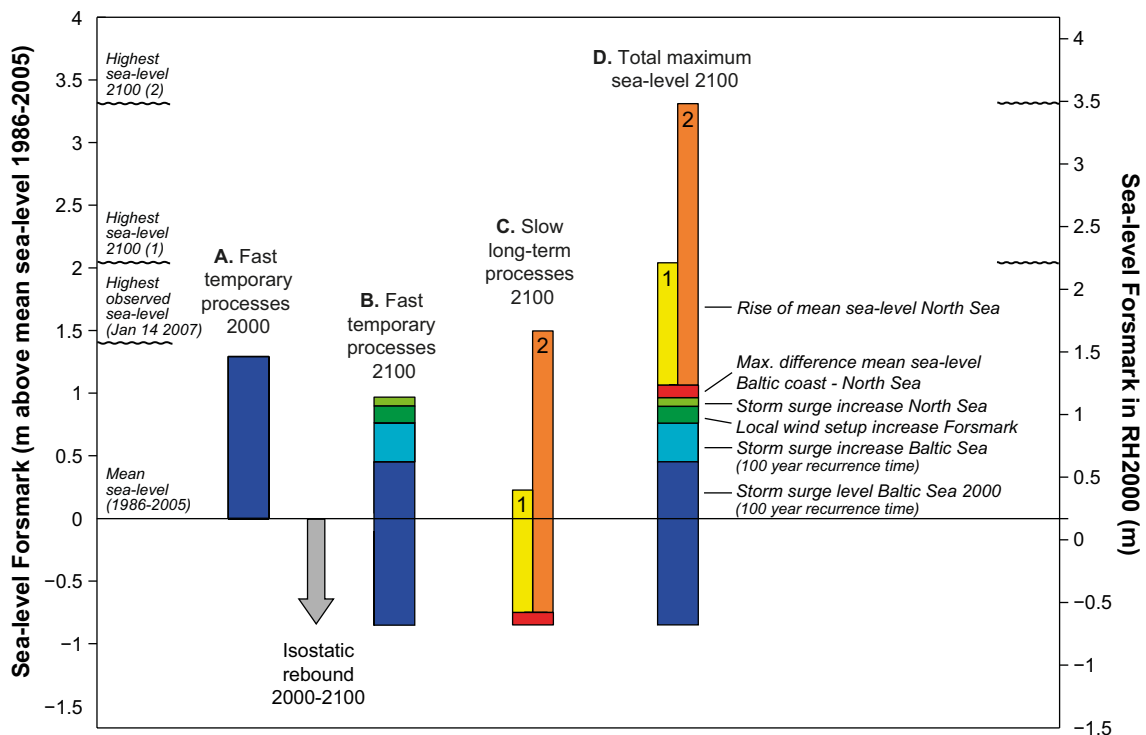


Figure 3-23. Estimated maximum possible sea level at Forsmark at 2100 AD (from Table 3-2). A: present day maximum sea-level rise due to fast temporary processes (e.g. storm surges), B: maximum sea-level rise in 2100 AD due to fast temporary processes, in part compensated for by isostatic rebound, C: sea-level rise at 2100 AD due to slow long-term processes, i.e. rise of mean sea level. (1: process-based projections (IPCC 2013), 2: from other methods (Srивer et al. 2012)), D: total maximum sea-level rise in the year 2100 when considering both the fast temporary processes and the slow long-term processes. The C2 value of Srивer et al. (2012) represents the upper, worst-case, value in a range of values estimated by non-process based models, e.g. semi-empirical models and kinematic constraints on ice-sheet melting. The isostatic rebound for the period 2000 to 2100 AD at the Forsmark site (0.84 m) compensates for a significant portion of the sea-level rise. The sea level is given in m above the present day mean sea level for the period 1986-2005 (corresponding to +0.19 m in RH2000) and in RH2000.

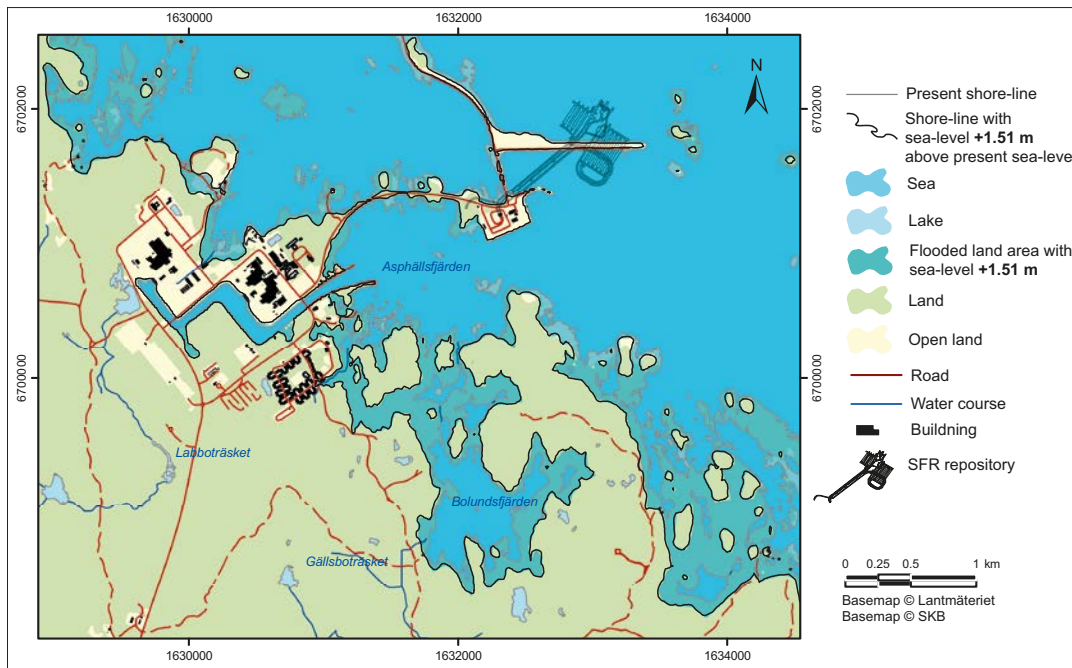


Figure 3-24. Areas at Forsmark which will be permanently flooded at 2100 AD if the sea-level reaches +1.51 m above the present-day mean sea-level (corresponding to +1.70 m in the RH2000 height system). This level represents the maximum possible mean sea-level rise due to slow long-term processes as projected by non-process based methods (+2.35 m; Table 3-3), compensated for the isostatic rebound (−0.84 m; Table 3-3). The present shore line is based on the Lantmäteriet Property map (www.lantmateriet.se). Note that the results describe a situation assuming cumulative worst-case effects of possible future processes spanning the global, regional and local scales.

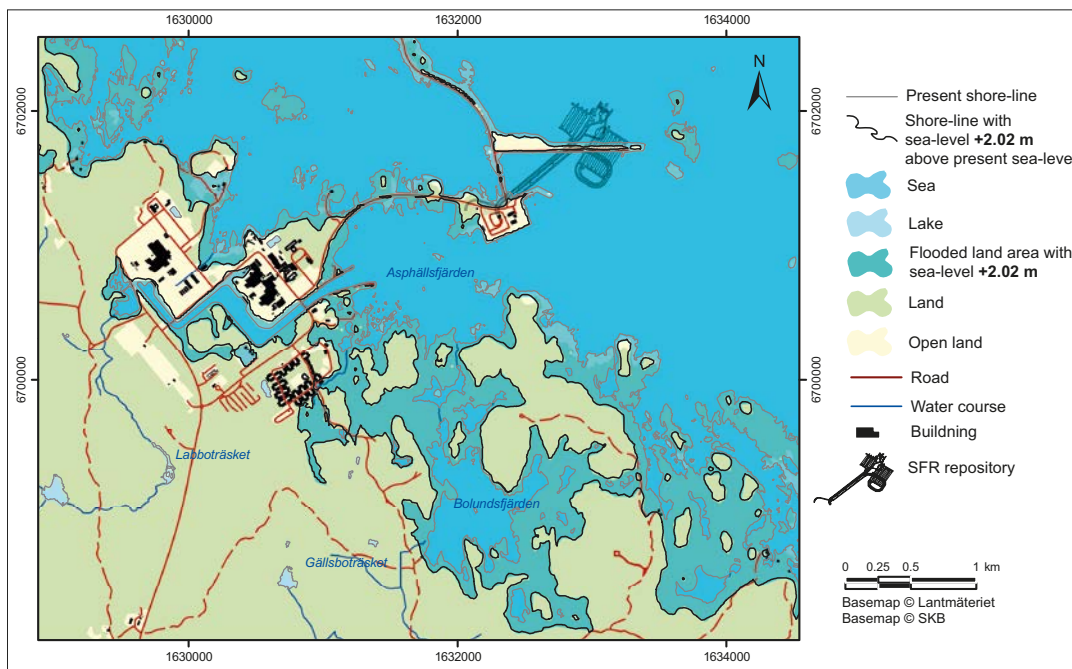


Figure 3-25. Areas at Forsmark which will be temporarily flooded at 2100 AD if the sea-level reaches the maximum possible level of +2.02 m above the present-day mean sea-level (corresponding to +2.21 m in the RH2000 height system). This level represents the sum of the maximum possible mean sea-level rise due to slow long-term processes as projected by process-based methods (+1.07 m; Table 3-3) and the maximum sea-level rise due to fast temporary processes (1.79 m; Table 3-3), compensated for the isostatic rebound (−0.84 m; Table 3-3). The present shore line is based on the Lantmäteriet Property map (www.lantmateriet.se). Note that the results describe a situation assuming cumulative worst-case effects of possible future processes spanning the global, regional and local scales, and that the number only applies for occasions of short duration during heavy storms.

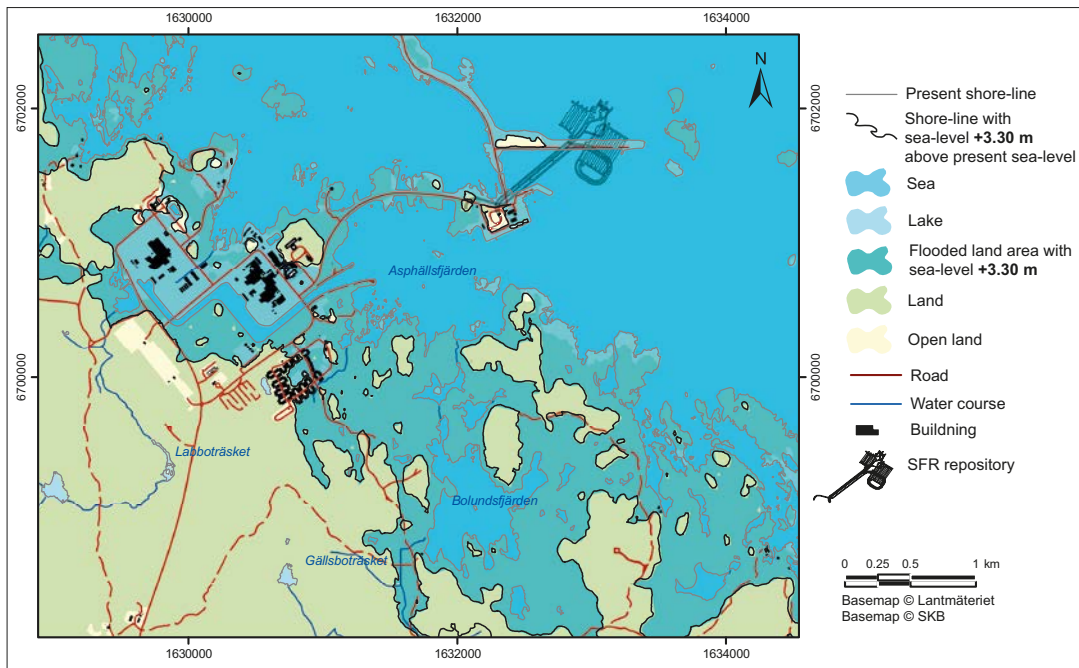


Figure 3-26. Areas at Forsmark which will be temporarily flooded at 2100 AD if the sea-level reaches the maximum possible level of +3.30 m above the present-day mean sea-level (corresponding to +3.49 m in the RH2000 height system). This level represents the sum of the maximum possible mean sea-level rise due to slow long-term processes as projected by non-process based methods (+2.35 m; Table 3-3) and the maximum sea-level rise due to fast temporary processes (1.79 m; Table 3-3), compensated for the isostatic rebound (−0.84 m; Table 3-3). The present shore line is based on the Lantmäteriet Property map (www.lantmateriet.se). Note that the results describe a situation assuming cumulative worst-case effects of possible future processes spanning the global, regional and local scales, and that the number only applies for occasions of short duration during heavy storms.

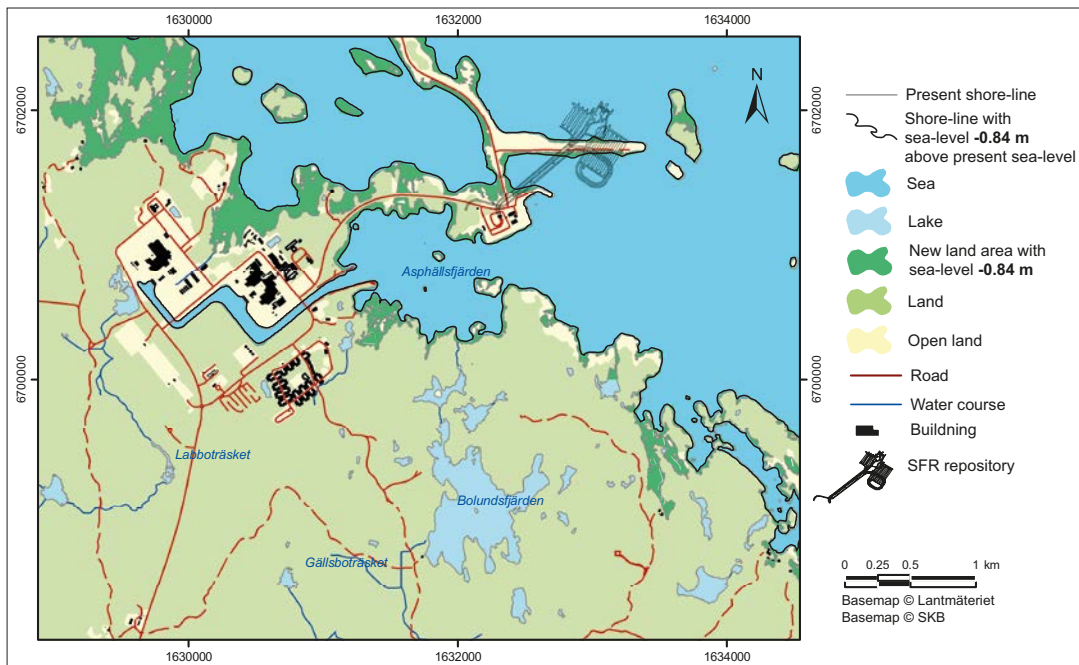


Figure 3-27. Areas at Forsmark which will have emerged from the sea at 2100 AD if the mean sea-level would remain unchanged compared to the present day and only isostatic rebound would influence the shoreline displacement at Forsmark. This map serves to illustrate the lower limit of the uncertainty range for mean sea-level change in Forsmark until 2100 AD. In this case, the sea-level reaches −0.84 m below the present-day mean sea-level (corresponding to −0.65 m in the RH2000 height system) (Table 3-3). The present shore line is based on the Lantmäteriet Property map (www.lantmateriet.se). Note that the mean sea level rises by c 1.1 mm/yr at Forsmark at present (see Section 2.2.3), why the assumption of no future mean sea-level rise is unrealistic.

Table 3-3. Contributions to the maximum possible relative sea level at Forsmark in 2100 AD, divided into slow long-term processes (i.e. mean sea-level rise) and fast temporary processes (e.g. storm surges). The sea level rise is given in relation to the present-day sea-level at Forsmark, which is defined as the mean sea level at Forsmark for the period 1986–2005 AD (corresponding to +0.19 m in the Swedish national elevation datum RH2000).

Type of contribution	Process	Reference	Contribution to sea-level rise at Forsmark 2100 AD (m)
Slow long-term eustatic contributions	Maximum sea-level rise in North Sea according to process-based projections	Determined based on Church et al. (2013) and Meier (2013, personal communication), see the text.	0.97
	Maximum sea-level rise in North Sea according to semi-empirical projections and kinematic constraints on ice-sheet melting	Determined based on Sriver et al. (2012), Pfeffer et al. (2008), and Church et al. (2013), see the text.	2.25
	Maximum difference between Baltic coast and North Sea	Meier (2013, personal communication)	0.10
Sum slow long-term eustatic contributions		Process-based projections	1.07 m
		Projections based on other methods	2.35 m
Fast temporary eustatic contributions	Storm surge level Baltic Sea 2000 AD (100 year return period)	Meier (2006), Meier (2013, personal communication)	1.27
	Increase in storm surge level Baltic Sea 2000–2100 (100 year return period)	Meier (2006), Meier (2013, personal communication)	0.30
	Increase in local wind setup 2100 AD	Nerheim (2008)	0.15
	Increase in storm surge North Sea (100 year return period)	Woth et al. (2006)	0.07
Sum fast temporary eustatic contributions			1.79 m
Slow long-term isostatic change	Isostatic rebound (2000 AD–2100 AD)	Modified from Lidberg et al. (2010), see the text.	–0.84
Total sum		Process-based projections	2.02 m (2.21 m in RH2000)
		Projections based on other methods	3.30 m (3.49 m in RH2000)

3.3.4 Climate evolution until 10 ka AP

CO₂ induced warming is projected to remain approximately constant for many centuries following a complete cessation of emissions. A large fraction of climate change is thus irreversible on a human time scale, except if net anthropogenic CO₂ emissions were strongly negative over a sustained period (Collins et al. 2013). For scenarios driven by CO₂ alone, the global average temperature is projected to remain approximately constant for many centuries following a complete cessation of emissions. The positive commitment from CO₂ may be enhanced by the effect of an abrupt cessation of aerosol emissions, which will cause warming. By contrast, cessation of emission of short-lived greenhouse gases will contribute a cooling.

In the last few years a number of modelling studies of the climate evolution in the next 1–10 ka have been performed. These studies were generally performed with models of less complexity and/or coarser resolution than the ESMs and AOGCMs used for CMIP3 and CMIP5. The studies were designed to study the long-term response to anthropogenic carbon emissions and do not include the effect of variations in insolation due to variations in the orbital parameters. These variations will be small as compared to the variations during the last glacial cycle (Berger and Loutre 2002), which is why anthropogenic carbon emissions are expected to be the primary forcing during the next 10 ka.

Recent modelling studies of the climate evolution in the next 1–10 ka are summarised in Table 3-4. The general shape of the global annual average SAT evolution is similar in the available studies (Eby et al. 2009, Huybrechts et al. 2011, Mikolajewicz et al. 2007, Vizcaíno et al. 2008). In all these studies, anthropogenic carbon emissions are assumed to occur in the current and next century followed by an instant or rather rapid decrease to zero emissions. Some studies include modelling of the global carbon cycle (Eby et al. 2009, Mikolajewicz et al. 2007, Vizcaíno et al. 2008), whilst others use prescribed atmospheric greenhouse gas concentrations (Huybrechts et al. 2011). Due to the slow equilibration of the ocean, the simulated annual global average SAT reaches a maximum level as compared to the present around 0.5–1 ka AP, i.e. a few centuries to a millennium *after* the maximum in atmospheric CO₂ concentration. Subsequently, the annual global average SAT slowly decreases until 10 ka AP. According to Eby et al. (2009), the lifetime of the SAT anomaly might be as much as 60% longer than the lifetime of anthropogenic CO₂ and two-thirds of the maximum temperature anomaly will persist for longer than 10 ka. A generalised evolution of the annual global average SAT in these studies is displayed in Figure 3-28. Decadal, centennial and millennial variability, with a maximum amplitude of c 1 to 2°C is superimposed on this slow evolution for any specific simulation of the next 10 ka. Such variability arises due to internal climate dynamics, e.g. the El Niño, the Atlantic Multi-decadal Oscillation and AMOC variability. Further, an increased greenhouse effect may result in changes in the mean state of these internal processes such as e.g. a reduction in the AMOC strength, see Section 3.3.3. The simulated evolution of the ocean circulation is described in the following subsection.

Ocean circulation

As described in Section 3.3.3, ocean circulation is expected to change in response to increasing atmospheric greenhouse-gas concentrations resulting in changes in the density distribution in the ocean. Changes in precipitation patterns and magnitudes, continental run-off including melting of land-based ice and evaporation at the ocean surface are the main processes responsible for changing the ocean water density in response to increasing atmospheric greenhouse-gas concentrations. Collins et al. (2013) conclude that it is very likely that the AMOC will weaken over the 21st century. It is however very unlikely that the AMOC will undergo an abrupt transition or collapse in the 21st century (Collins et al. 2013).

For an abrupt transition of the AMOC to occur, the sensitivity of the AMOC to forcing would have to be far greater than seen in current models (Collins et al. 2013). Alternatively, significant ablation of the Greenland ice sheet greatly exceeding even the most aggressive of current projections would be required (Hu et al. 2009, Swingedouw et al. 2007). While neither possibility can be excluded entirely, it is unlikely that the AMOC will collapse before the end of the 21st century because of global warming based on the models and range of scenarios considered.

Table 3-4. Summary of the range of future projected global annual average near-surface air temperature increase with respect to the present climate until 10 ka AP. The range represents uncertainty associated with inter-model differences and/or internal variability. Uncertainty ranges are expressed within square brackets.

Reference	Emission scenario/ Total carbon emissions	Max. ΔT^1 (°C)	Timing of max. T increase (ka AD)	ΔT 2100 AD (°C)	ΔT 3000 AD (°C)	ΔT 7000 AD (°C)	ΔT 12000 AD (°C)
Solomon et al. (2011)	1,000 PgC				1.6 [0.8–2.5]	1.0 [0.5–1.5]	0.9 [0.5–1.3]
	5,000 PgC				7.5 [4.3–10]	5.5 [2.8–8.0]	4.7 [2.5–7.5]
Mikolajewicz et al. (2007b)	B1 ²	2	2.5	1	1.3	1 ⁵	
	A1B ²	3.5	2.9	2	3.0	2 ⁵	
	A2 ²	5	3.0	2	4.9	4.2 ⁵	
Vizcaíno et al. (2008)	1% to 2x ³			1.7	2		
	1% to 3x ³			2.6	3.5		
	1% to 4x ³			2.8	4.1		
Plattner et al. (2008)	A1B ²			1.1–3.5	1.5–4.8		
	A1B ^{2,6}	1.2–3.8	2.3–2.7	1.0–3.3	1.0–3.6		
Eby et al. (2009)	460 PgC ⁴	0.2		0.2	0.2	0.2	0.2
	940 PgC ⁴	1.3	5.5	1.1	1	1	0.8
	2,580PgC ⁴	2.5	3.8	2.2	2	1.7	1.5
	2,860PgC ⁴	4.7	3	4.2	4.5	3.5	3.1
	5,420PgC ⁴	7.8	3.2	6.7	7.8	6.5	5.9
Huybrechts et al. (2011)	1% to 2x ³			1.5	1.6	1.8 ⁵	
	1% to 4x ³			2.5	2.8	3.5 ⁵	
Li et al. (2013)	1% to 4x ³	10.8	3.2	~2	~10.5	10.8	
Meehl et al. (2007)	B1			1.8 [1.1–2.9]			
	A1B			2.8 [1.7–4.4]			
	A2			3.4 [2.0–5.4]			
Collins et al. (2013)	RCP2.6			1.0 [0.3–1.7]			
	RCP4.5			1.8 [1.1–2.6]			
	RCP8.5			3.7 [2.6–4.8]			

¹ The maximum T increase is only given for studies that project the climate for sufficiently long into the future to obtain a decrease in global annual mean temperature following the peak.

² Emissions follow the SRES emission scenarios until 2100 AD. After 2100 AD emissions are reduced instantaneously to zero.

³ The atmospheric CO₂ concentration is increased by 1% per year and then stabilised at 2, 3 and 4 times the pre-industrial concentration.

⁴ Emissions follow observations until 2000 AD. At the beginning of 2001 AD, a pulse of CO₂ was applied over one year. The total C emissions given in this table were determined as 300 Pg + (pulse C emissions), where 300 Pg C are the total C emissions until 2000 AD.

⁵ Values are valid for 5000 AD.

⁶ Models include the global carbon cycle.

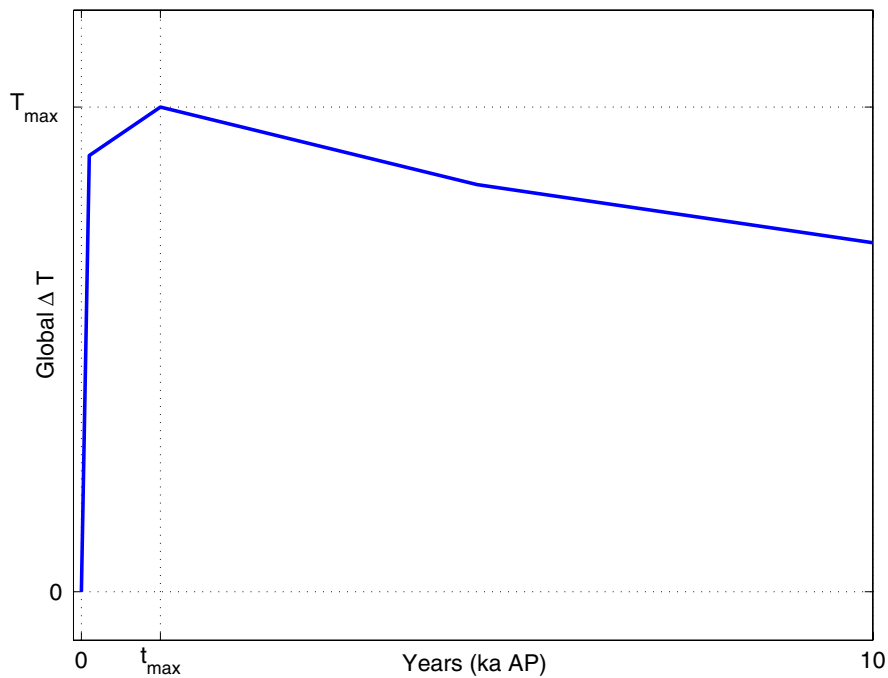


Figure 3-28. Generalised evolution of the global annual average surface air temperature displayed as the anomaly with respect to the year 2000 AD (ΔT). T_{max} is the maximum increase, which occurs at t_{max} ka AP.

Climate in Forsmark until 10 ka AP

A few studies provide data such that the future projected Forsmark region annual average near-surface air temperature can be assessed on a 10 ka timescale. Table 3-5 provides a summary of the range of future projected Forsmark region annual average near-surface air temperature increase, relative to the present climate, given by these studies. The highest emission scenarios presented by both Pimenoff et al. (2012) and Vizcaíno et al. (2008) show the regional effect of a substantial decrease of the AMOC, which leads to a smaller temperature increase in the North Atlantic region in these experiments than in the low and medium emission scenarios (Table 3-5).

The difference between Forsmark and global annual average temperature increase is given in Table 3-6. From these differences, it can be seen that the temperature increase for the Forsmark region is generally 0°C to 1.5°C higher than the global average temperature increase. This relation is however not valid for experiments in which the AMOC is substantially reduced and in these the Forsmark temperature is $1\text{--}5.5^{\circ}\text{C}$ lower than the global average (as is the case in the high cumulative emission experiments of both Pimenoff et al. (2012) and Vizcaíno et al. (2008)).

Another important difference between global changes and those at Forsmark is that the temporal evolution of the temperature increase in Forsmark is expected to have significantly higher variability on annual, decadal and centennial time scales. Regional climate is generally more variable than the global average, and also, Forsmark is located in the mid-latitude storm-track region. As an example of the temporal evolution in a specific region as simulated by one specific model, Figure 15 of Pimenoff et al. (2012) has been reproduced in Figure 3-29. In the high emission scenario, S1, the AMOC weakened and collapsed at $\sim 2150\text{--}2250$ AD, with dramatic effects for the Fennoscandian climate (Pimenoff et al. 2012). A temporary weakening of the AMOC was also simulated in the intermediate emission scenario, S3, around 2200–2300 AD (Pimenoff et al. 2012).

For a detailed example of how the climate in Forsmark may manifest itself a few thousand years into the future under a high emissions scenario, see Section 3.3.6.

Table 3-5. Summary of the range of future projected Forsmark annual average near-surface air temperature increases with respect to the present climate in the coming 10 ka.

Reference	Emission scenario / Tot. C emissions	Max. ΔT^1 (°C)	Timing of max. ΔT (ka AD)	ΔT 2100 AD (°C)	ΔT 3000 AD (°C)	ΔT 5000 AD (°C)	ΔT 9000 AD (°C)
Pimenoff ³ et al. (2012)	B1 ²	2.6	2.6	0.8	1.4	0.4	
	A1B ²	5.0	2.7	1.4	3.3	2.0	
	A2 ²	3.8	2.8	1.4	2.9	0.2	-0.1
Vizcaíno et al. (2008)	1% to 2x ³				2.0–3.0		
	1% to 3x ³				3.0–5.0		
	1% to 4x ³				2.0–3.0		
Meehl et al. (2007)	B1			2.5			
	A1B			3.0			
	A2			3.5			
Collins et al. (2013)	RCP2.6			1.0–1.5			
	RCP4.0			2–3			
	RCP8.5			4–5			

¹ The maximum temperature increase is only given for studies that project the climate sufficiently long into the future to obtain a decrease in global annual mean temperature following the peak.

² The projected temperature increase is based on Mikolajewicz et al. (2007) until 7000 AD and on Eby et al. (2008) for the period 7000 to 12,000 AD. The associated global annual average temperature increase for those studies is given in Table 1-2.

³ Pimenoff et al. (2012) present data for Olkiluoto in Finland. These have been corrected to represent Forsmark by taking into account that the present-day annual average near-surface temperature is 4.8°C in Olkiluoto as compared to 5.0°C in Forsmark.

Table 3-6. Difference between Forsmark region and global average annual near-surface air temperature increase.

Reference	Emission scenario / Tot. C emissions	Max. ΔT^1 (°C)	ΔT 2100 AD (°C)	ΔT 3000 AD (°C)	ΔT 5000 AD (°C)	ΔT 9000 AD (°C)
Pimenoff ¹ et al. (2012)	B1 ²	+0.6	+0.2	+0.4	-0.6	
	A1B ²	+1.5	+0.4	+0.3	0	
	A2 ²	-1.2	+0.4	-2.1	-4.0	-3.5
Vizcaíno et al. (2008)	1% to 2x ³			-1.0 to 0.0		
	1% to 3x ³			+0.5 to +1.5		
	1% to 4x ³			-2.1 to -1.1		
Meehl et al. (2007)	B1		+0.7			
	A1B		+0.3			
	A2		+0.4			
Collins et al. (2013)	RCP2.6		+0–0.5			
	RCP4.0		+0.2–1.2			
	RCP8.5		+0.3–1.3			

¹The Pimenoff study is based on data from Mikolajewicz et al. (2007).

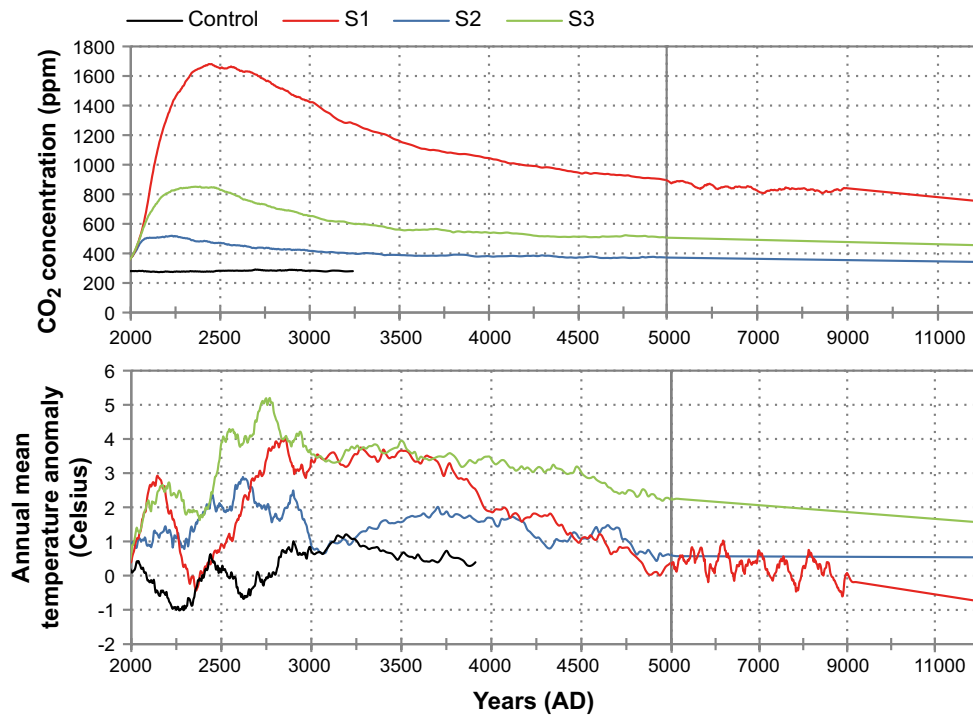


Figure 3-29. Evolution of the atmospheric CO₂ concentration (upper panel) and the annual mean temperature relative to Rauma Kuuskajaskari during 1961–1990 (4.8°C) (lower panel). Note the non-constant scale of the x-axis. Modified from Figure 15 of Pimenoff et al. (2012).

Relative sea-level evolution at Forsmark until 10 ka AP

The main conclusions related to sea level change beyond 2100 AD presented in IPCC AR5 (Church et al. 2013) are the following.

- It is virtually certain that global mean sea-level rise will continue beyond 2100 AD, with sea-level rise due to thermal expansion continuing for many centuries. Longer term sea-level rise depends on future emissions. The few available model results that go beyond 2100 AD indicate the global mean sea-level rise above the pre-industrial level by 2300 AD to be less than 1 m for a radiative forcing that corresponds to CO₂ concentrations that peak and decline and remain below 500 ppm, as in the scenario RCP2.6. For a radiative forcing that corresponds to a CO₂ concentration that is above 700 ppm but below 1,500 ppm, as in the scenario RCP8.5, the projected rise is 1 m to more than 3 m.
- The available evidence indicates that global warming greater than a certain threshold would lead to the near-complete loss of the Greenland ice sheet over a millennium or more, causing a global mean sea-level rise of about 7 m.
- Ocean heat uptake and thermal expansion take place not only while atmospheric greenhouse gas concentrations are rising, but continue for many centuries to millennia after stabilisation of radiative forcing, at a rate which declines on a centennial time scale.
- On a multi-millennial time scale, the range from Earth System Models of Intermediate complexity suggests that thermal expansion contributes between 0.20–0.63 m per °C of global mean temperature increase.

Sea-level change in association with increased global average SAT will influence the relative sea-level in the Forsmark region. As described in Section 3.3.3, the uncertainty in future sea-level response to global warming until 2100 AD is large. Sea-level change beyond 2100 AD is naturally associated with even larger uncertainties. To account for these uncertainties, a maximum sea-level rise at Forsmark until 10 ka AP is calculated here based on published estimates of the maximum contributions from ocean steric expansion, a complete melting of the Greenland and West Antarctic ice sheets and a complete melting of all glaciers and ice caps. In order to estimate the maximum possible

sea-level rise at Forsmark, the maximum contributions are all pessimistically assumed to occur within the next few centuries to the next millenium. The relative sea-level evolution in the SR-PSU climate cases is defined in order to cover the full uncertainty range associated with sea-level evolution (Chapter 4).

For a case of very strong global warming, Li et al. (2013) reported a global maximum steric sea-level rise of 5.8 m and a maximum global average SAT increase of 10.8°C (0.58 m per °C), including a strong and persistent reduction in AMOC. This value is used here to cover the large uncertainty.

As mentioned above, one crucial aspect of sea-level rise due to ice-sheet collapse is that the effect of the rising sea-level is not distributed evenly over the seas and along continental coasts. This is due to changes in the gravity field associated with the melting of ice sheets and water entering the ocean basins (e.g. Milne et al. 2009, Whitehouse 2009, Bamber and Riva 2010). For instance, a complete collapse of the Greenland ice sheet would result in gravitational changes that counteracts the sea-level rise in the near-field of the collapsed ice sheet, resulting in a *lower* sea-level, in the near field than when the ice sheet was present (Milne et al. 2009). This aspect is one key aspect of the GIA model used for safety assessment purposes for the Forsmark site. Milne et al. (2009) studied this spatially-variable change in sea-level assuming a complete melting of the Greenland ice sheet, and they predicted a ~0 mm/yr sea-level change in the region of Fennoscandia. The same effect in Forsmark was also seen in the GIA simulations performed for a future warmer climate described in Section 2.2.4.

Several studies have been published on the possible contribution to sea-level rise by the West Antarctic ice sheet (e.g. Mitrovica et al. 2009, Bamber et al. 2009, Ivins 2009, Rignot et al. 2008). A relatively recent study suggests that the potential maximum rise in global mean sea-level from the West Antarctic Ice Sheet is 3.3 m (Bamber et al. 2009). Another recent study suggested that during the penultimate interglacial, the Eemian, the Greenland ice sheet configuration was *not* drastically reduced although air temperatures over Greenland were 8 ± 4 degrees warmer than today (NEEM community members 2013). In order to close the global water budget, with 6–8 m higher global Eemian sea levels than today, this result suggests that the West Antarctic ice sheet needs to have contributed more to the Eemian sea-level rise, and in turn that the West Antarctic ice sheet might be more vulnerable to warming temperatures than previously thought (Schiermeier 2013). The effects of a collapse of the West Antarctic ice sheet were studied by Mitrovica et al. (2009) and Bamber et al. (2009). By using the traditional ice volume value for West Antarctica, corresponding to 5 m of global mean sea-level rise, Mitrovica et al. (2009) estimated that a collapse of the West Antarctic ice sheet would result in a sea-level rise around Fennoscandia of 5 ± 1 m, when including the gravitational effects associated with the ice-sheet collapse. However, information on the ice- and bed-topography of the West Antarctic ice sheet suggest that it has about 3.3 m of equivalent global sea level grounded on areas with downward sloping bedrock (Bamber et al. 2009). Using this estimate Bamber et al. (2009) suggested that melting of the West Antarctic ice sheet would give a sea-level rise around Fennoscandia of around 3 m, gravitational effects taken into account.

The timing of the maximum contributions to sea-level rise differs for the different processes. In general, the processes are slow, especially the thermosteric sea-level rise which may reach the maximum value in several thousands of years. Table 3-7 summarises the maximum possible contributions from different processes to mean sea-level rise, both globally and for the Baltic Sea.

Table 3-7. Long-term maximum contribution to eustatic sea-level rise from various processes. The contributions from thermal expansion as well as from melting of glaciers and ice caps are assumed to have a uniform global distribution.

Process	Maximum contribution to global mean sea level rise	Reference	Maximum contribution to sea level rise in the Baltic Sea	Reference
Melting of West Antarctic Ice Sheet	3.3 m	Bamber et al. (2009), Figure 3.	~3.4 m	Bamber et al. (2009), Figure 3.
Complete melting of Greenland ice sheet	7.3 m	Bamber et al. (2001)	0–0.7 m	Present report, Section 3.3.4 and Pimenoff et al. (2012)
Complete melting of all glaciers and ice caps	0.5 m	IPCC 2007	0.5 m	IPCC 2007
Thermosteric sea level rise	5.8	Li et al. 2013 (see Section 3.3.4)	5.8 m	Li et al. 2013 (see also Section 3.3.4)
		Sum	~10 m	

The contributions from thermal expansion and from melting of glaciers and ice caps are here assumed to have a globally uniform distribution, since regional data do not exist. This coarse assumption, especially for the larger contribution from thermal expansion, is made also in e.g. Mitrovica et al. (2001b). Furthermore, Table 3-7 only includes slow long-term processes. Short term temporary effects that do not add to the long-term rise of mean sea level (such as e.g. storm events) are not included. During such events, the sea level could temporarily rise higher, which may be exemplified with the situation at year 2100 (Figure 3-27).

When all contributions to sea-level rise are summed, unrealistically assuming that they all occur within the next centuries to millenium, the maximum total rise of the mean sea level in the Baltic is ~10 m (Table 3-7). This value is similar to that estimated for the Olkiluoto site on the other side of the Baltic Sea (8 m, Pimenoff et al. 2012). At the Forsmark site, as well as many other sites around the Baltic coast line, the position of the shoreline is determined by the combination of the local sea level and the ongoing, counteracting, post-glacial isostatic uplift. The present and near-future isostatic uplift rate at Forsmark is 8.4 mm/yr. This value, as well as the simulated future relative sea-level curve for Forsmark (which excludes steric sea-level rise and melting of ice other than from a collapsed Greenland ice sheet, see Section 2.1.4), shows that at around 1.2 ka AP the isostatic uplift at Forsmark would have exceeded the maximum sea level rise, i.e. the uplift would be larger than ~10 m. This shows that the longest additional period with submerged conditions at Forsmark, caused by a 10 m sea-level rise, is c 1.2 ka. After that, the situation would be similar as today, with the isostatic uplift slowly raising the repository site over the level of the Baltic Sea. However, in reality, this period would be shorter than 1.2 ka since this argumentation also assumes that all maximum contributions to sea level (Table 3-7) would occur in the next millenium. Thermal expansion of this magnitude, for instance, is expected to require a longer period to equilibrate.

In addition, the SFR repository is today covered by the Baltic Sea, with a maximum water depth of 7.2 m over SFR1 and 5.3 m over the planned SFR3 (layout L2). With the relative shore level change curve calculated for a future warm climate (see Section 2.2.4), the duration for a complete transformation to terrestrial conditions above the repository (SFR 1 and 3) is c 1200 years. The duration for 75% of the surface above SFR 1 and 3 to have become land is c 600 years and requires a relative sea level change of 3.8 m (see Section 2.2.4).

The uncertainty range associated with future sea-level rise is taken into account in the SR-PSU safety assessment in the *global warming climate case* (Section 4.1) and the *extended global warming climate case* (Section 4.3). The *global warming climate case* represents the lower end of the uncertainty range, with negligible effects of global sea-level rise (See Section 4.1.3), whereas the *extended global warming case* represents the upper end of the uncertainty range (see further Section 4.3.3). The two cases thus represent a minimum length period of submerged conditions above SFR in the *global warming climate case* as opposed to a maximum length period of submerged conditions above SFR in the *extended global warming climate case*.

3.3.5 Climate evolution until 100 ka AP

State-of-the-art AOGCMs and ESMs have not been applied for studies of climate evolution beyond 10 ka AP, since these models are too computationally expensive. Several modelling studies of climate evolution in the next 100 ka AP have however been performed with simplified models (SCMs and EMICs). A question that has engaged many scientists is the timing of the next glacial inception, i.e. initiation of ice-sheet build-up. For the purpose of the current safety assessment, this question, and the related question of when cold climate conditions may produce permafrost in the Forsmark region, is of importance.

For the coming ~100–200 ka, climate models are forced with the known future variations in insolation due to variations in the Earth's orbital parameters (Berger and Loutre 1991) and different hypothesised atmospheric CO₂ concentrations. For all models, the event of glaciation is crucially dependent on the atmospheric level of CO₂. As described in Section 3.3.1, the current atmospheric CO₂ concentration is c 394 ppmv (www.esrl.noaa.gov). If human emissions of CO₂ were reduced to zero in the near future, atmospheric CO₂ concentrations at or below pre-industrial levels cannot be excluded after 10 ka AP. This improbable scenario can be regarded as a bounding case. Under more realistic scenarios for future anthropogenic carbon emissions, the atmospheric CO₂ concentration would be at or above 300 ppmv

at 10 ka AP (Archer et al. 2009). In the following, published studies of Earth's climate in the coming 100–200 ka are briefly described, with a focus on the timing of glacial inception and maximum Northern Hemisphere ice volume. The results are summarised in Table 3-8 and Figure 3-30.

Loutre and Berger (2000) simulated the coming 130 ka with the Louvain-la-Neuve two-dimensional Northern Hemisphere climate model (LLN 2-D NH) forced by future variations in orbital parameters and a number of different constant atmospheric CO₂ concentrations. They found that, in their model, glaciation occurs 50 ka into the future in simulations with CO₂ concentration lower than 280 ppmv, whereas for CO₂ concentrations above this value glaciation is postponed beyond 50 ka into the future. For CO₂ concentrations lower than 220 ppmv glaciation inception was found to be imminent.

Berger and Loutre (2002) simulated the period 200 ka BP to 130 ka AP with the LLN 2-D NH model forced by future variations in orbital parameters and three different scenarios for future atmospheric CO₂ concentration; constant concentration of 210 ppmv, constant concentration of 280 ppmv, and an anthropogenic scenario with the concentration reaching 750 ppmv in 200 years from now and decreasing to 280 ppmv in 1000 years from now. In accordance with Loutre and Berger (2000), they found that glacial inception is imminent in the 210 ppmv scenario, whereas glacial inception occurs after ~50 ka in the 280 ppmv and the anthropogenic scenarios.

The BIOCLIM project (Texier et al. 2003) simulated the coming 200 ka with two EMICs, MoBidiC (an improved version of the LLN model) and CLIMBER-GREMLINS, forced by variations in orbital parameters and prescribed time-varying atmospheric CO₂. They found that the two EMICs responded quite differently to the imposed forcing conditions. MoBidiC produced ice sheets over North America from the start of the simulation when CO₂ was kept constant at 280 ppmv, whereas CLIMBER-GREMLINS produced no glaciation until after 50 ka AP. Under this scenario neither of the models produced ice sheets over Fennoscandia during the next 100 ka.

Table 3-8. Review of the timing of first Northern Hemisphere (NH) glacial inception and maximum NH ice volume. Note that glacial inception in this context indicates growth of NH ice to a substantially larger volume than at present, which can result in periglacial or glacial climate conditions in south-central Sweden depending on the extent of a Fennoscandian ice sheet.

Authors, model	Atmospheric CO ₂ concentration (ppmv)	Total cumulative emissions (Pg C)	Timing of first NH glacial inception (ka AP)	Timing of maximum NH ice volume (ka AP)
Loutre and Berger (2000)	210		0	~61
LLN 2-D NH	220		0	~22, ~62
	230		~40	
	240–270		~50	~60
	280, 290		>130	
Berger and Loutre (2002)	210		0	~60, ~100
LLN 2-D NH	280		~50	~60, ~100
	750→280		~50	~60, ~100
Texier et al. (2003) MoBidiC	280		0	~120
Texier et al. (2003) CLIMBER-GREMLINS	280		~50	~200
Archer and Ganopolski (2005) CLIMBER-2	280		~50	
		300	~50	
		1,000	~130	
		5,000	>500	
Cochelin et al. (2006)	≤270		0	~100
McGill Paleoclimate Model	280, 290		50	>100
	≥300		>100	
Crucifix and Rougier (2009)	Naturally varying		40	60
Pimenoff et al. (2011) CLIMBER-2	280		0	~20, ~60
	400		~50	~60

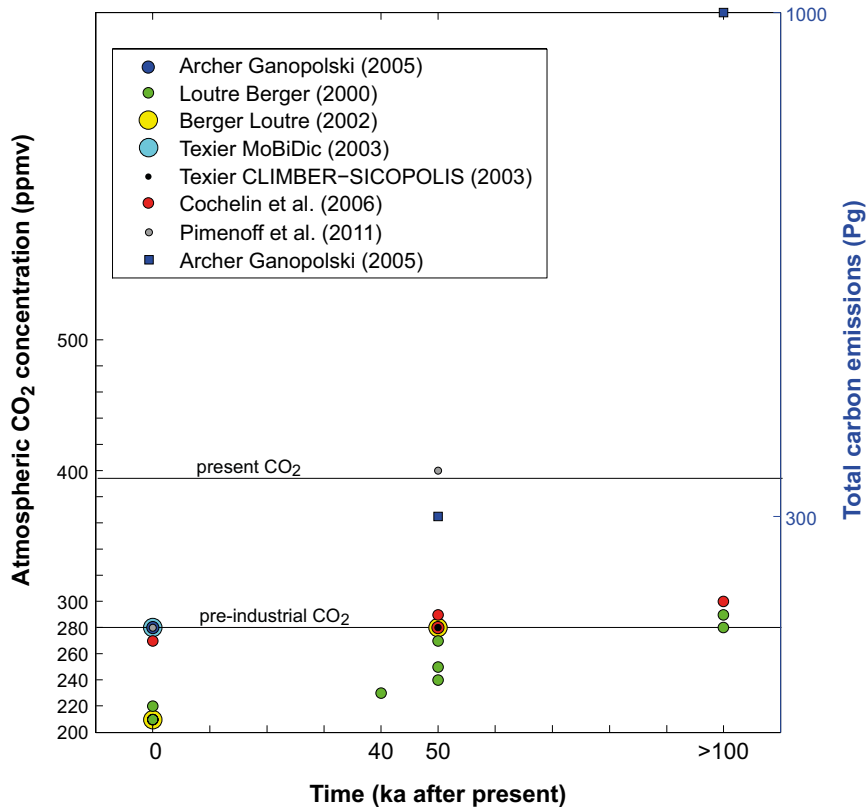


Figure 3-30. Approximate timing of glacial inception versus atmospheric CO₂ concentration in the studies summarised in Table 3-8 (circles and asterisk) and an approximate timing of glacial inception versus total carbon emissions (squares).

Based on simulations with the EMIC CLIMBER-2, forced with future insolation variations and a constant atmospheric CO₂ concentration, Archer and Ganopolski (2005) predicted that a carbon release from fossil fuels or methane hydrate deposits of 5,000 Pg carbon could prevent glaciation for the next 500 ka. For cumulative emissions of 300 Pg and 1,000 Pg carbon, glacial inception occurs after ~50 ka and ~130 ka respectively. Archer and Ganopolski (2005) pointed out that for an atmospheric CO₂ concentration of 280 ppmv, a slight shift in the model parameters can easily tip the simulation to onset of glaciation now rather than in 50 ka.

Cochelin et al. (2006) simulated the coming 100 ka with the McGill Paleoclimate Model (MPM) forced by variations in orbital parameters and prescribed atmospheric CO₂. Their model produced three types of evolution for the ice volume: an imminent glacial inception (low CO₂ levels), a glacial inception in 50 ka (CO₂ levels of 280 or 290 ppmv), or no glacial inception during the next 100 ka (CO₂ levels of 300 ppmv and higher).

Crucifix and Rougier (2009) utilised a 3D stochastic model to investigate the timing of the next glacial inception. The model simulates ice volume, atmospheric CO₂ concentration and deep-ocean temperature forced by the variations in insolation at 65°N at summer solstice. Their inference takes the form of a data assimilation of paleo proxy data and the model parameters are trained to match the past record. As stated by the authors, if phenomenological models are to be used to predict actual climate system behaviour, then we must take very careful account of the uncertainty introduced by their limitations. Their provisional results indicated that without anthropogenic intervention (i.e. only natural processes) peak glacial conditions would occur in 60 ka AP, with glacial inception starting at 40 ka AP. Predictability by their model after that point is said to be poor.

Pimenoff (2011) employs the CLIMBER-2 model with the thermo-mechanical ice-sheet model SICOPOLIS to study the future evolution of climate in Olkiluoto, the site selected for the Finnish repository for spent nuclear fuel. They simulated the coming 120 ka with a constant atmospheric CO₂ concentration of 280 ppmv and 400 ppmv respectively. The climate evolution differs substantially

between these two experiments, with an immediate glaciation occurring in the 280 ppmv experiment as opposed to very restricted glaciation during the coming 120 ka in the 400 ppmv experiment. The insolation minimum at about 17 ka AP causes a large ice sheet over northern Fennoscandia in the 280 ppmv scenario as opposed to only some ice in the Scandinavian mountain range in the 400 ppmv scenario. The following insolation minimum at about 54 ka AP produces an extensive ice sheet in the 280 ppmv scenario as opposed to a small ice sheet from the Scandinavian mountain range to Finnish Lapland and parts of Northern Ostrobothnia in the 400 ppmv scenario. In the 400 ppmv scenario, the mean temperatures at Olkiluoto are warmer than at present for most of the time. An exception is the insolation minimum at about 54 ka AP, when the mean temperatures are about the same as at present.

Vettoretti and Peltier (2011) investigated the impact of insolation, greenhouse-gas forcing and ocean circulation changes on glacial inception with the AOGCM CCSM3. Based on the seasonal and latitudinal distribution of insolation, they argue that MIS 11, ~420 ka BP, is a good analogue for the present interglacial. They simulate the climate for orbital year 10 ka AP, when obliquity is at a minimum and eccentricity is low. They conclude that this period is favourable for the full onset of the next glacial cycle, if atmospheric greenhouse-gas concentrations have reached pre-industrial or lower levels.

Tzedakis et al. (2012a) determine the natural length of the current Holocene interglacial. They argue that MIS 19c, ~780 ka BP, is a good analogue to the present interglacial. Assuming that ice growth mainly responds to insolation and CO₂ forcing, this analogy suggests that the end of the current interglacial would occur within the next 1500 years, if atmospheric CO₂ concentrations did not exceed 240 ± 5 ppmv. Tzedakis et al. (2012b) demonstrate the importance of obliquity, rather than summer insolation at high northern latitudes, for the timing of glacial inception. They conclude that glacial inception always takes place when obliquity is decreasing and never after the obliquity minimum. The phasing of precession and obliquity appear to influence the persistence of interglacial conditions over one or two insolation peaks, leading to shorter (~13 ka) and longer (~28 ka) interglacials (Tzedakis et al. 2012b). The onset of interglacials, on the other hand, occurs within 2 ka of the summer insolation maximum at high northern latitudes.

The latter two studies are not included in Table 3-8, but should be taken as an indication of the uncertainty in the current knowledge of the occurrence of the next Northern Hemisphere glaciation.

Ocean circulation

Due to large uncertainties, it is not feasible to assess the timing of ocean circulation variations beyond a few thousand years AP.

Climate in Forsmark until 100 ka AP

Modelling studies of climate evolution in the next 100 ka performed with simplified models (Table 3-8) do not generally include the level of detail required to assess the climate evolution in a specific region such as south-central Sweden. Further, the uncertainty in the global climate evolution illustrated in Table 3-8 and Figure 3-30, indicates that detailed assessment of climate evolution in the Forsmark region is not possible. Rather, the studies discussed here show a range of possible future climate evolutions including progressively colder climate conditions and ice-sheet build up starting after c 50 ka AP as well as warm climate conditions similar to the present climate prevailing until (at least) 100 ka AP.

3.3.6 Exemplified climate conditions for a future warm climate

In order to give a detailed example of the Forsmark climate under the influence of increased atmospheric greenhouse gas concentrations, a future temperate climate with increased greenhouse-gas concentrations in the atmosphere (750 ppm), a few thousands of years from now was simulated with global and regional climate models (Kjellström et al. 2009, including erratum Feb 2010).

The 750 ppm atmospheric CO₂ concentration used by Kjellström et al. (2009) can be compared with Archer et al. (2009), described in Section 3.3.1, to show that this concentration represents a scenario with large human carbon emissions, but less than the entire carbon reserve.

In the climate model simulations, a complete loss of the Greenland ice sheet was assumed. Since such a deglaciation may take up to a couple of thousand years, if it were to occur, it is very uncertain what other climate-related conditions may be prevailing at that time. According to climate-change scenarios from simulations with GCMs, irreversible melting of the Greenland ice sheet may start at a time when the global mean temperature has increased by about 1.9–5.1°C above today's conditions and the temperature over Greenland has increased by about 3–6.5°C (Gregory et al. 2004, Gregory and Huybrechts 2006). Some recent studies indicate that the Greenland ice sheet might be more sensitive to increased concentrations of atmospheric greenhouse gases than previously thought (Robinson et al. 2012, Stone et al. 2010a, b), whereas other recent studies indicate the opposite (NEEM community members 2013).

Increases in temperature that may be large enough for making the Greenland ice sheet collapse are projected by GCMs within the 21st century for some emission scenarios (Meehl et al. 2007). If such high temperatures persist for a long enough time (several hundreds to a couple of thousand years depending on the degree of warming), the Greenland ice sheet may potentially collapse and disappear. In this time perspective, CO₂ levels will start to decrease again (when emissions cease). Nevertheless, at one thousand years from now, the atmospheric CO₂ concentrations will remain considerably higher than today (Archer et al. 2009). Further, if the Greenland ice sheet does collapse and disappear, a regrowth of the ice sheet is difficult to envisage to be initiated without substantial cooling. Here, the time period for the global warming simulation was chosen as a compromise between a high level of CO₂ (needed to simulate a warm climate that melts the Greenland ice sheet), and not too high a CO₂ level (since it needs to be that which remains in the atmosphere a long time after the emissions have ceased). Thus, the simulations can be considered as representative of the climate a few thousand years into the future after a complete melting of the Greenland ice sheet and a partial recovery towards lower CO₂ concentrations.

For these simulations, a global GCM model (Community Climate System Model version 3, CCSM3), a regional climate model (Rossby Centre Regional Climate Model RCA 3) and a vegetation model (LPJ-GUESS) were used. For the simulations performed, atmospheric and land components of the CCSM3 used a grid spacing of approximately 2.8° in latitude and longitude. The vertical resolution is 26 levels in the atmosphere and 40 levels extending to 5.5-km depth in the ocean. The regional climate model used a horizontal resolution of 50 km and a time resolution of 30 minutes. For details on the models, how they were employed, and a discussion on model uncertainties, see Kjellström et al. (2009). As mentioned above, the simulation of the global warming climate used a CO₂ concentration in the atmosphere of 750 ppm. In order to include the effect of also other greenhouse gases in the RCA 3 model, a CO₂ equivalent value of 841 ppm was used (Kjellström et al. 2009). For a detailed description of the assumptions made in the modelling process, model forcing and initial conditions (such as astronomical and solar forcing, concentration of greenhouse gases and aerosols in the atmosphere, extents of ice sheets, distribution of land and sea, topography and vegetation), see Kjellström et al. (2009).

The simulated global warming climate should not be taken as a prediction or prognosis on how a future climate at Forsmark would manifest itself. Instead, it is a *detailed example* of how such a climate may be manifested. Given another forcing, for instance using a lower or higher CO₂ concentration, the resulting climate at this time would have been different. Further, given the same forcing conditions, differences between different climate model simulations exist (e.g. Kjellström et al. 2011). However, the model results are useful for exemplifying a climate affected by global warming as expressed at Forsmark. In this context, it is worth noting that the results of Kjellström et al. (2009) resemble those for many of the scenarios for the 21st century from the climate model inter-comparison project (CMIP3) (Meehl et al. 2007). For a detailed discussion and comparison with other climate model results, see Kjellström et al. (2009, Section 3.1.4).

Global climate

Figure 3-31 shows the simulated global warming climate from the GCM simulations. Seasonal mean changes in temperature in the global warming simulation as compared with a simulation of the present (1961–2000) climate are also shown in Figure 3-31. The removal of the Greenland ice sheet produces a strong heating of up to 17°C over Greenland in both summer and winter, resulting in summer near-surface air temperatures of 0–12°C in Greenland which prevent a regrowth of the Greenland ice sheet.

This heating is primarily due to a combination of i) the lowering of the surface by up to 3,000 m and ii) the decrease in surface albedo and changes in heat fluxes between the atmosphere and the ground produced by the replacement of the glacier ice surface by tundra (Kjellström et al. 2009). Similarly to all greenhouse warming scenarios presented in the IPCC AR4 report (Meehl et al. 2007), the Arctic region exhibits strong heating by up to 15°C in winter (due to a substantial decrease in the Arctic sea-ice cover and a decrease in the snow cover). The seasonal mean temperature is up to 5°C warmer in summer and up to 7.5°C warmer in winter over Fennoscandia in the global warming simulation as compared with the simulation of the present climate. Seasonal mean summer temperatures in Sweden vary in the range 12–18°C and winter temperatures vary in the range 0–6°C. Sensitivity to changes in vegetation in these GCM simulations is discussed in Kjellström et al. (2009).

The change in precipitation in the global warming simulation as compared with the simulation of the present climate is also shown in Figure 3-31. The removal of the Greenland ice sheet leads to a 25% decrease in precipitation, in particular over south-eastern Greenland in both summer and winter, indicating that much of the precipitation in that area in today's climate is triggered by the steep ice-sheet topography. Similarly to all greenhouse-warming scenarios presented in the IPCC AR4 report (Meehl et al. 2007), precipitation is increased over mid-latitude Northern Hemisphere continents and the Arctic. For Fennoscandia there is an increase in precipitation, most notably in the north.

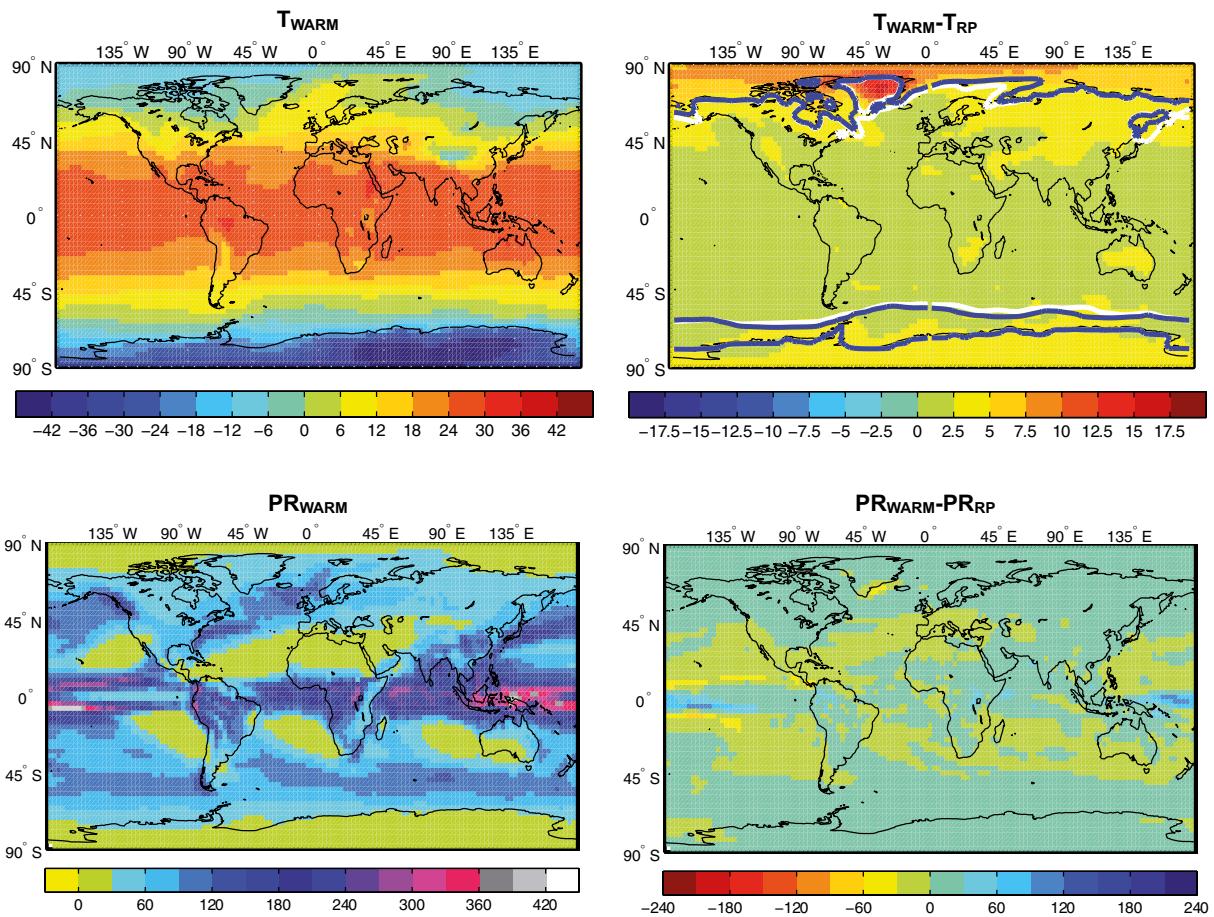


Figure 3-31. Upper panels: Simulated near-surface air temperature in the global warming simulation (T_{WARM}) and the difference compared with the simulated present climate (T_{RP}) (1961–2000). Units are °C. Also shown by isolines in the rightmost panels is the extent of sea-ice in the simulation of the present climate (white) and in the global warming simulation (blue). Lower panels: Precipitation in the global warming simulation (PR_{WARM}) and the difference compared with the simulated present climate (PR_{RP}). Units are mm/month. From Kjellström et al. (2009).

Climate in Europe and Sweden

The regional climate model was then used to downscale the results from the global climate model in order to obtain higher resolution data over Europe and Sweden. The resulting climate over Europe was used to produce a new vegetation distribution with the vegetation model. This vegetation was in turn, used as input to the regional climate model, to produce a climate in line with the new vegetation. An evaluation of the results from this iterative process is given in Kjellström et al. (2009). Figure 3-32, Figure 3-33 and Figure 3-34 present selected results on temperature and precipitation from the regional modelling.

In the regional global warming simulation, the warming compared with the simulated present climate (1961–2000) is strongest over northern Europe in winter. The simulated temperature increase for the coldest month is more than 5°C in northern Fennoscandia (Figure 3-32, second row, middle panel). In southern Europe, the warming is stronger in summer, where the temperature of the warmest month increases by more than 4°C over large areas (Figure 3-32, second row, left panel). The stronger warming in the areas of the Bothnian Bay, Bothnian Sea and in the Gulf of Finland in summer in this experiment is due to the land uplift converting sea to land in those areas. The same phenomenon is also responsible for the weaker warming in these areas in winter. Differences between the results of the global and regional model simulations are discussed in Kjellström et al. (2009).

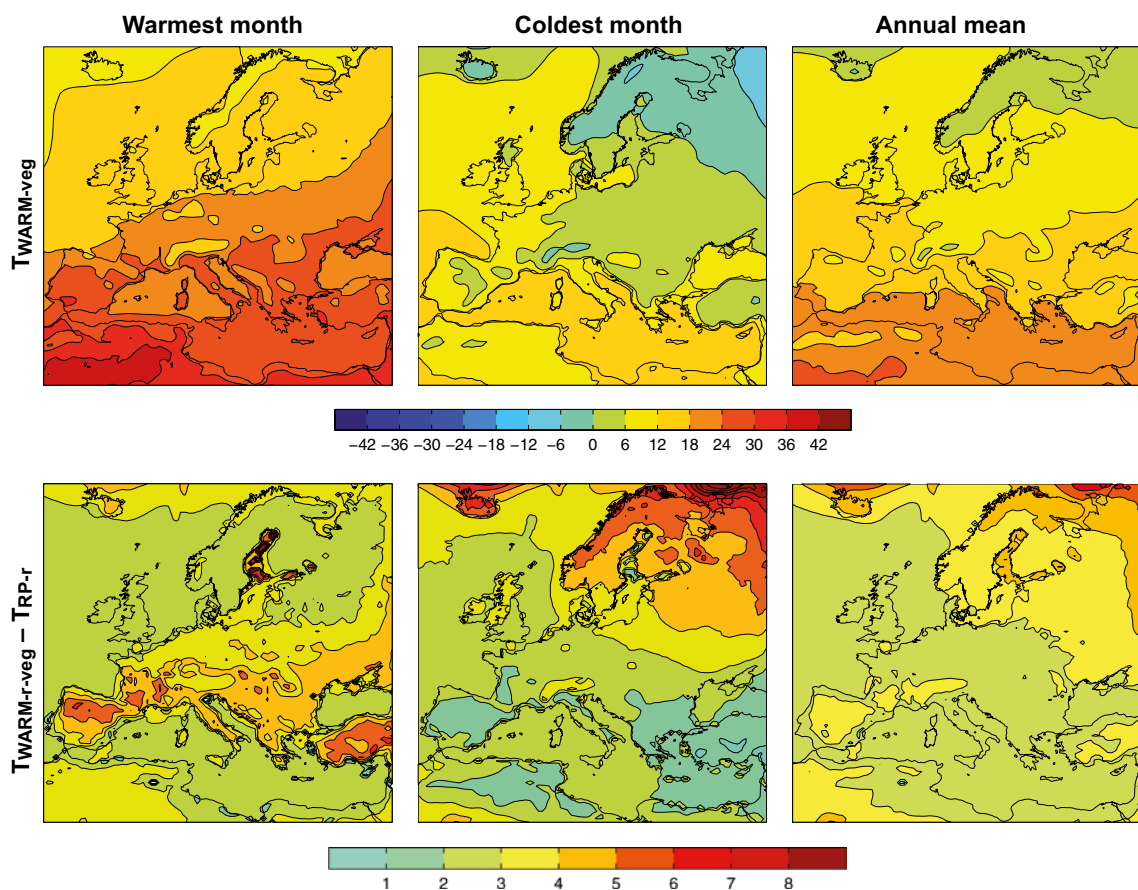


Figure 3-32. Mean near-surface air temperatures of the warmest month, coldest month and annual mean in the global warming simulation with improved vegetation (upper row). Also shown are differences between the global warming simulation and the simulations of the present climate (RP-r) (1961–2000) (lower row). Units are °C. From Kjellström et al. (2009).

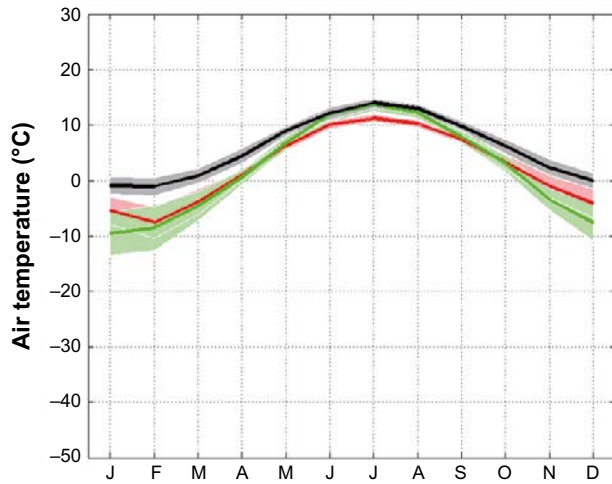


Figure 3-33. Annual cycle of temperature for Sweden in the global warming case (black line) and for the simulated present climate (1961–2000) (red line). Also shown is the CRU observational data from 1961–1990 (green line). Shaded areas in corresponding colours indicate the ± 1 standard deviation calculated for the range of individual monthly averages in the three data sets. From Kjellström et al. (2009).

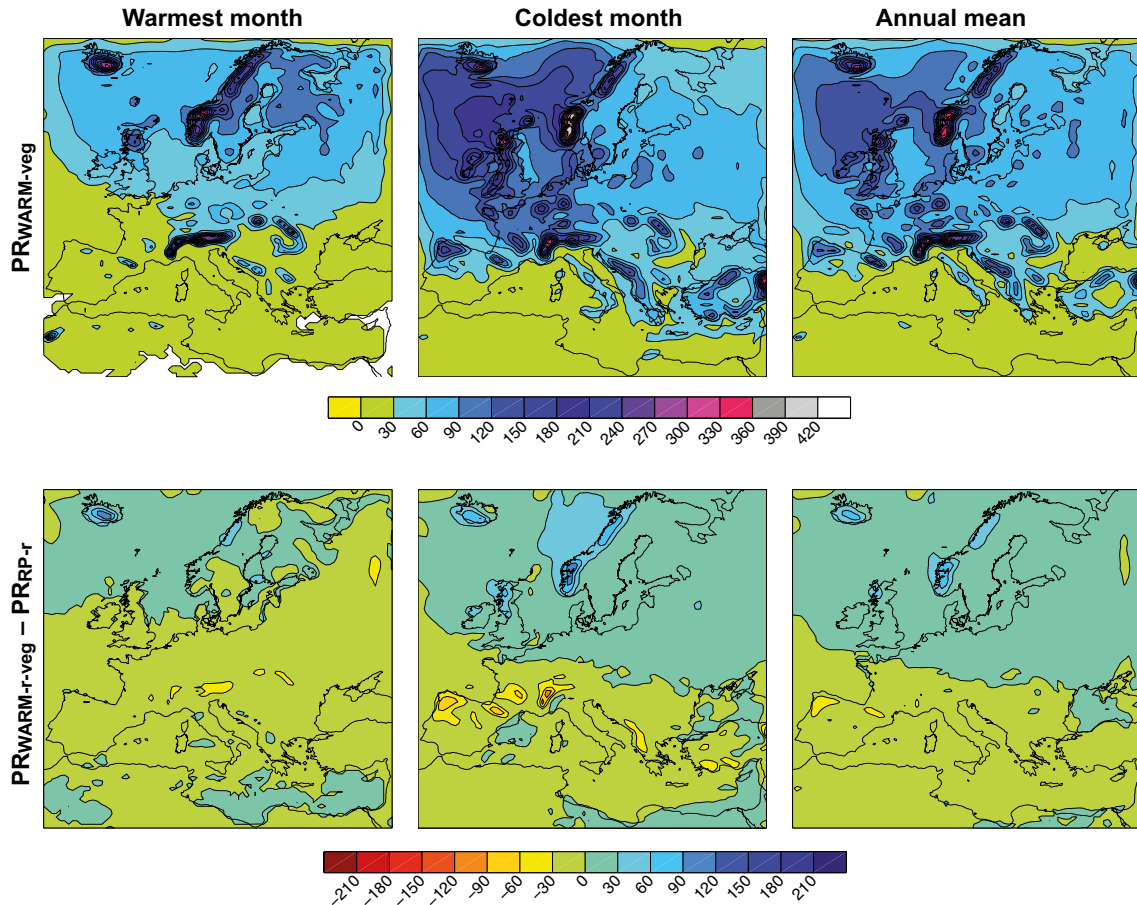


Figure 3-34. Mean precipitation of the warmest month, coldest month and annual mean in the global warming simulation. Also shown are differences between the global warming simulation and the simulated present climate (RP-r) (1961–2000). Units are mm/month. From Kjellström et al. (2009).

As expected, the simulated climate of the *global warming climate case* clearly resembles many of the scenarios for the 21st century from the climate model intercomparison project (CMIP3) as presented by IPCC (Meehl et al. 2007). Seasonal mean changes in precipitation and temperature from a large number of the CMIP3 scenarios have been analysed for Sweden by Lind and Kjellström (2008). Lind and Kjellström (2008) report increases in temperatures by 4–6°C by the end of the 21st century in northern Sweden and about 3°C in southern Sweden, relative to the 1961–1990 period. The corresponding increases in precipitation are about 25% in the north and only a small average increase in the south, albeit with a large spread between the models. These changes are annual averages over a range of different emission scenarios. As noted in Kjellström et al. (2009), the uncertainties related to the future forcing in the global warming simulation are large and substantially lower or higher greenhouse-gas concentrations than the one used cannot be ruled out. Considering the large spread between the emission scenarios and the uncertainty related to the climate models one cannot rule out that a future warmer climate can be warmer than the one simulated in Kjellström et al. (2009).

Clearly, the results from the regional model gives a climate change signal that is within the range defined by the global model results for southern Sweden compiled in Lind and Kjellström (2008), see Figure 3-15 in Kjellström et al. (2009). The climate-change signal for Sweden as a whole is +4°C in winter and +3.5°C in summer and the corresponding numbers for precipitation are +37% in winter and no change ($\pm 0\%$) in summer. Further model results and discussion for all of Sweden from the global and regional climate modelling and from the vegetation modelling are presented in Kjellström et al. (2009).

The vegetation simulated by LPJ-GUESS for the global warming climate is reported in the context of the biosphere studies (Lindborg 2010).

Here it is also worth noting that the Greenland summer temperatures are well above 0°C, clearly indicating that there is no chance of ice-sheet regeneration under these circumstances once the ice sheet has been removed. A similar result was obtained previously for the pre-industrial climate when the Greenland ice sheet was removed in the Hadley Centre HadCM3 coupled model (Toniazzi et al. 2004).

Climate in the Forsmark region

In the last step in the climate modelling study of the global warming climate, climatological data for the Forsmark region were extracted from the regional modelling. Figure 3-35 shows the grid boxes used for extraction of data. Information was extracted from the grid point located closest to the Forsmark site. As there is a high degree of spatial heterogeneity in land-sea distribution and topography, information from the surrounding eight grid boxes was also used to discuss uncertainties related to these inhomogeneities.

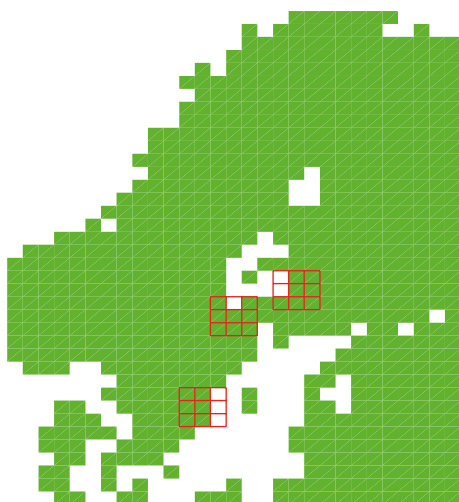


Figure 3-35. Land (green) sea extent (white) in the regional climate model in the Fennoscandian region used for the global warming climate simulation. The 3 × 3-grids represent grid boxes covering the Forsmark, Oskarshamn and Olkiluoto sites (centre box) and the eight surrounding boxes. Grid boxes with a land fraction lower than 20% are not filled. Results from Oskarshamn and Olkiluoto are presented in Kjellström et al. (2009).

In addition to the results from the modelled case, data from the simulation of the present climate (1961–2000) (RP-r) and from the CRU observations representing conditions in the late 20th century are also shown for the Forsmark region (Figure 3-36). In addition to this, results from three other climate-change simulations with RCA3 for the 21st century as described in Persson et al. (2007) are also shown. These simulations follow the A2, A1B and B2 emission scenarios (Nakićenović and Swart 2000). The A1B emission scenario leads to greenhouse gas concentrations close to the one in the *global warming climate case* by the end of the 21st century. The two other scenarios have more (A2) or less (B2) emissions than the A1B scenario.

The fairly small annual temperature range in the present climate is even smaller in the future global warming climate for the Forsmark region (Figure 3-36, upper row, first column). This reduction in the seasonal cycle of temperature is a consequence of the future warming being stronger in winter than in summer. The snow season is much shorter, or even totally absent, in the warm climate. The seasonality of the runoff is closely connected to the presence or absence of snow. In the warmer future climate, the spring peak in runoff is absent and there is a more widespread wintertime maximum related to the large amounts of precipitation for that season.

In the global warming simulation, the spread in the presented variables due to differences in geographical location is reduced compared with that in the simulation of the present climate. This is partly a result of the land uplift turning two of the Baltic Sea grid boxes east of Forsmark into land in the *global warming climate case*. Thereby, the surrounding area becomes more homogeneous than in the present-day situation. When including also the uncertainty ranges based on results from the three other climate simulations for the 21st century, also simulated with RCA3 (Persson et al. 2007), it is seen that the weakening of the annual cycle is a robust trend when going to a warmer climate.

50-year averages values from the regional global warming climate simulation show that the annual mean air temperature in the Forsmark region is +8.3°C. This is a temperature increase of 3.6°C compared with the simulated present climate (1961–2000). The future warming is stronger in winter than in summer and there is an associated reduction in the seasonal cycle amplitude in temperature. The mean annual precipitation in the region is 804 mm, which is an increase of 138 mm (or 20%) compared with the simulated present climate. Most of the precipitation increase occurs during the winter season (DJF). The snow season is much shorter than at present or even totally absent (Figure 3-36). Finally, the annual surface runoff is 337 mm in this exemplified global warming climate, which is an increase of 162 mm compared with the present climate. Given the uncertainties and assumptions used in the climate modelling, and the CO₂ level chosen, the model results thus show that the global warming climate in the Forsmark region, may be characterised by a clearly warmer and wetter climate than at present, and also that the surface runoff is significantly increased.

The major uncertainties in the climate simulation are related to uncertainties in forcing, model formulation and natural variability. These uncertainty aspects are discussed in detail in Kjellström et al. (2009).

Another recent study that focussed on regional climate modelling is described in Kjellström et al. (2011). In this study, changes in seasonal mean temperature, precipitation and wind over Europe were studied in an ensemble of 16 regional climate model (RCM) simulations for 1961–2100. The RCM took boundary conditions from six different global climate models under four different emission scenarios. The study focused on the A1B emission scenario (Nakićenović and Swart 2000) in which the CO₂ equivalents in RCA 3 reaches 902 ppm by year 2100, somewhat higher than the 841 ppm used in calculations in Kjellström et al. (2011). Six-member ensemble means of winter season (DJF) conditions suggest an increase in temperature by c 4°C and precipitation by 20–30% in south central Sweden, including the Forsmark region, by the period 2071–2100 as compared to the period 1961–1990. Corresponding model ensemble means for the summer season (JJA) indicate an air temperature increase of 2–3°C and a precipitation increase of c 10%. The study also showed that the climate-change signal gets stronger the larger the forcing becomes, i.e. more greenhouse-gas emissions lead to a stronger warming and larger changes in precipitation. The results of the A1B-scenario-simulations are thus in line with the detailed results described above from Kjellström et al. (2009). Similar results were obtained also in the SWECLIM project (Rummukainen 2003, Tjernström et al. 2003). Other modelling results that give similar pictures of future global warming climates are reported in BIOCLIM (2003), Lind and Kjellström (2008) and Meehl et al. (2007).

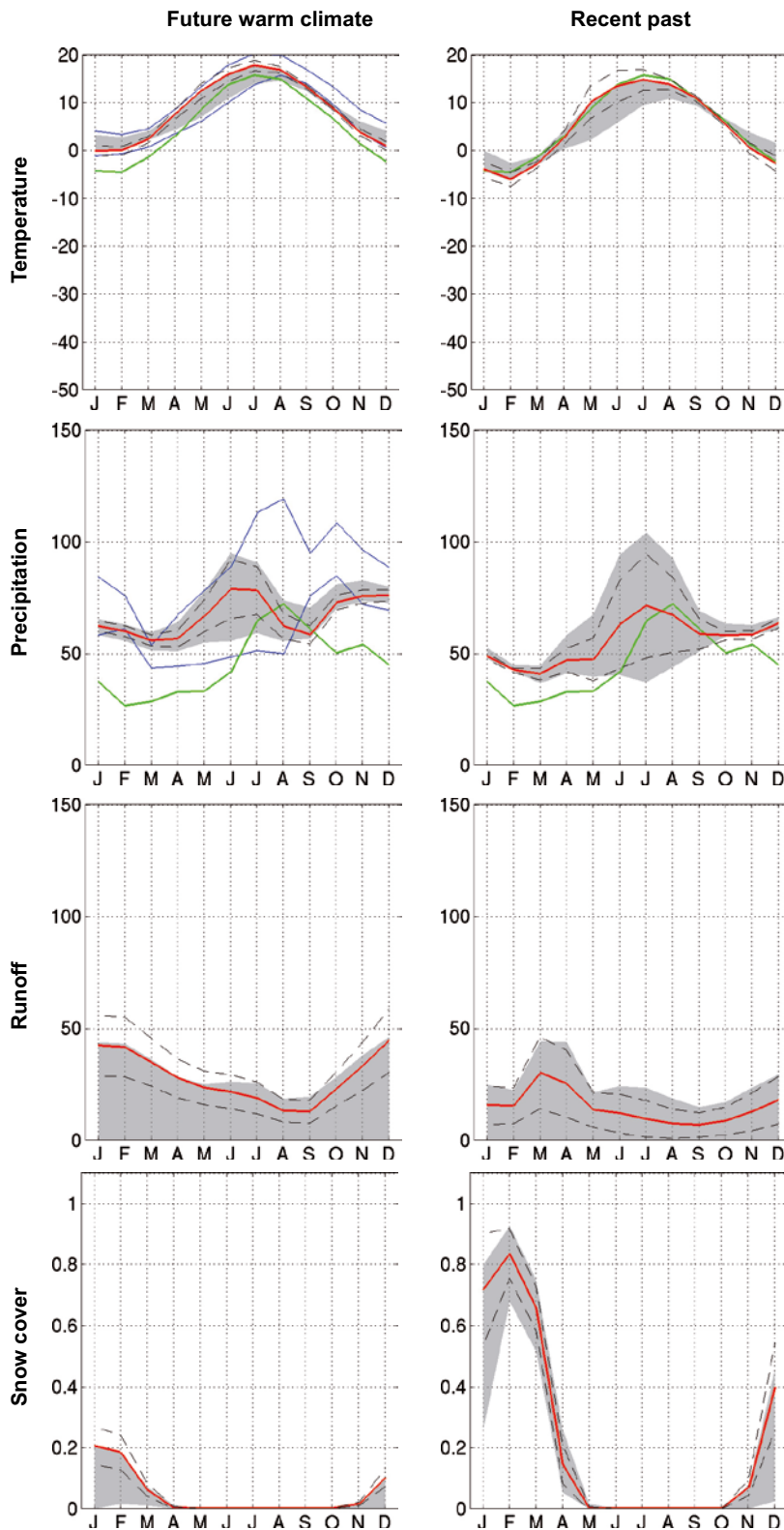


Figure 3-36. Simulated seasonal cycles of temperature ($^{\circ}\text{C}$), precipitation (mm/month), runoff (mm/month) and snow fraction (dimensionless ranging from 0 to 1) at the grid box closest to the Forsmark site (red line). The spatial variability in the 3×3 -grid (Figure 3-35) is displayed with the dashed lines representing ± 1 standard deviation calculated from the 9 grid boxes, and the grey area representing the absolute maximum and minimum, of the 9 grid boxes. The green line for temperature and precipitation is the observed seasonal cycle from the CRU data set in the period 1961–1990. In the exemplified future warm climate (left column), an additional uncertainty range defined by ± 1 standard deviations of the data calculated from the 9 surrounding grid boxes from three additional simulations for the 21st century with RCA3 is shown with blue full lines. From Kjellström et al. (2009).

4 Climate cases for the SR-PSU safety assessment

Rationale and general approach

In order to cover the uncertainty in future climate evolution in the next 100 ka, four different climate cases have been defined. The climate cases were defined as a basis for analysis of climate-related processes that can impact repository safety functions. These processes are:

- Ground freezing leading to sub-freezing temperatures at repository depth.
- Ground water recharge by meteoric water over prolonged periods affecting groundwater geochemistry.
- Shore-level displacement.
- Ice-sheet growth above the repository resulting in high hydrostatic pressure affecting repository structures.
- Glacial erosion resulting in the repository being located closer to the surface after de-glaciation.

As described in Section 3.3, present understanding of the global carbon cycle indicates that climate effects of carbon releases to the atmosphere may persist for tens, if not hundreds, of thousands of years into the future (Archer et al. 2009). Elevated CO₂, in combination with low amplitude variations in insolation in the next 100 ka, is expected to result in a prolonged period of warm climate (e.g. Berger and Loutre 2002, Plattner et al. 2008, Solomon et al. 2009). The next 100 ka is thus not expected to be similar to the last glacial cycle, which was characterised by a period of warm climate conditions lasting until c 115 ka BP followed by cold climate conditions in high northern latitudes with permafrost and ice-sheet development. Based on current knowledge, a similar evolution towards cold climate conditions is not realistic for the next 10 ka, and possibly not for the next 100 ka.

The four climate cases considered in the SR-PSU safety assessment are listed in Table 4-1. The first three are defined to span the range in future climate evolution associated with low, medium and high human carbon emissions. The *early periglacial climate case* represents low human carbon emissions and a relatively fast decrease in atmospheric CO₂ concentration. The *global warming climate case* represents medium human carbon emissions and the *extended global warming climate case* represents high human carbon emissions. A generalised time evolution of the near-surface temperature in Forsmark in these first three climate cases is displayed in Figure 4-1.

The last climate case is the *Weichselian glacial cycle climate case* which represents a repetition of the last glacial cycle. This climate case was included to span the uncertainty in the onset and speed of ice-sheet growth in the Northern Hemisphere and for comparison with earlier safety assessments for the SFR repository. It serves to illustrate the possible impact of ice-sheet growth and decay on the repository safety functions. The reconstructed last glacial cycle is further used to represent natural climate variability beyond the human-induced anomalous climate for the *global warming climate case* and the *early periglacial climate case*.

Table 4-1. Climate cases considered in the SR-PSU safety assessment.

Case number (section in present report)	Climate case	Description
1 (Section 4.1)	Global warming	Temperate conditions until 50 ka AP followed by natural variability and cooling of climate until 100 ka
2 (Section 4.2)	Early periglacial	As case 1 except for a 3 ka period of periglacial conditions centered at 17 ka AP
3 (Section 4.3)	Extended global warming	Temperate conditions until 100 ka AP
4 (Section 4.4)	Weichselian glacial cycle	Repetition of reconstructed last glacial cycle conditions

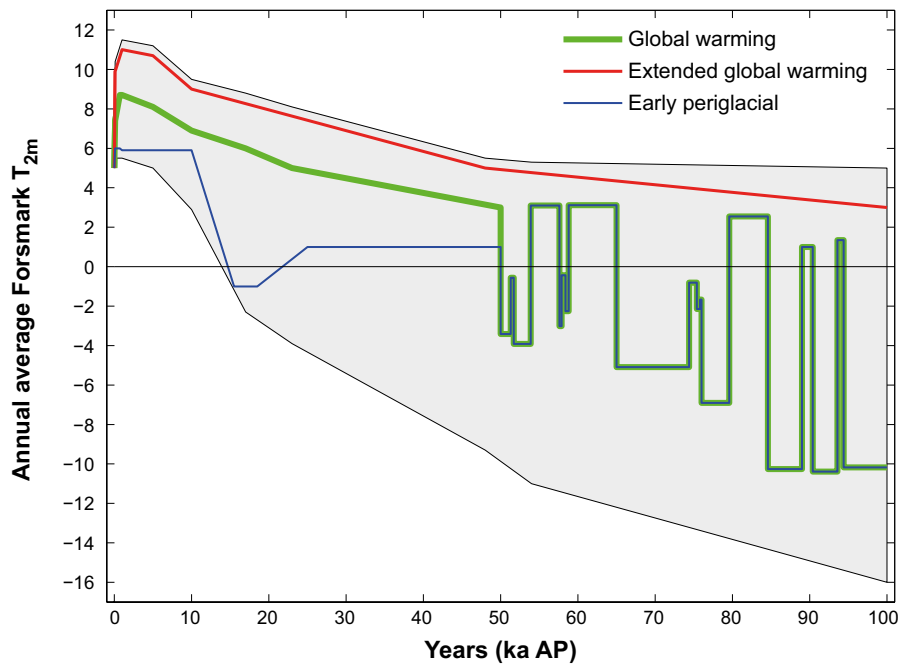


Figure 4-1. Generalised time evolution of annual average near-surface temperature (°C) in Forsmark in the first three climate cases, i.e. global warming, early periglacial and extended global warming climate cases. The grey shading indicates the uncertainty interval for the climate evolution in the next 100 ka. A motivation for the temperature evolution for each case is given in the respective Sections (4.1, 4.2 and 4.3).

Representative future projected global annual average near-surface air temperature evolutions have been constructed for low, medium and high cumulative carbon emissions (Table 3-2). The *early periglacial*, *global warming* and *extended global warming* climate cases correspond to the low, medium and high carbon emission scenarios, respectively. They are based on the review of current knowledge on future climate evolution until 10 ka AP (Section 3.3.4, Table 3-4, Table 3-5 and Table 3-6). The time evolutions are displayed in Figure 4-2. These time evolutions are associated with significant uncertainty associated with inter-model differences and internal variability, as indicated by the range of results in Table 3-4 and Table 3-5. The largest uncertainty is found for the *extended global warming climate case* due to uncertainty in the future evolution of the Atlantic meridional overturning circulation which may result in regionally cooler conditions in Scandinavia. They are *examples* of possible time evolutions of the future annual near-surface air temperature.

Representative future projected global annual average near-surface air temperature evolutions until 100 ka AP have also been constructed for the *early periglacial*, *global warming* and *extended global warming* climate cases (Figure 4-1). These time evolutions are associated with significant uncertainty and shall be interpreted as *examples* of possible time evolutions of the future annual near-surface air temperature. A total uncertainty range (grey area in Figure 4-1) for the future climate evolution until 100 ka AP has also been estimated based on the review of current knowledge on future climate evolution in Sections 3.3.3, 3.3.4 and 3.3.5.

For a description of the strategy for using and selecting climate cases, see the Section on *Strategy for handling evolution of climate and climate-related processes* (Section 1.3.2). The four climate cases are described in the following (Sections 4.1, 4.2, 4.3 and 4.4). For clarity, the same set of sub-sections is used for all climate cases. The starting point for all the climate cases is the present climate at Forsmark, which is briefly described below.

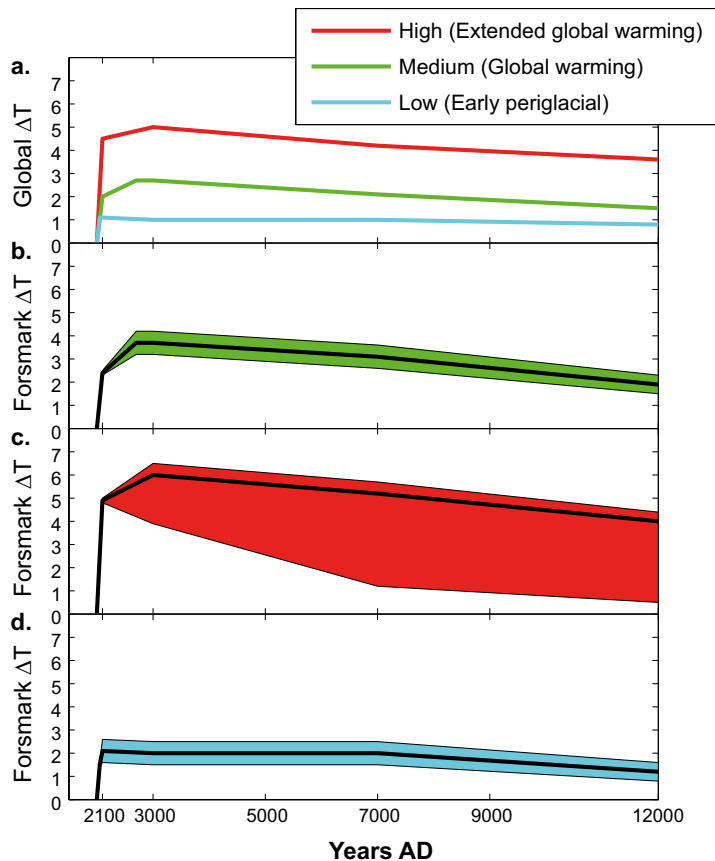


Figure 4-2. Plate (a) shows projected future global annual average near-surface temperature evolution for low (blue), medium (green) and high (red) cumulative carbon emissions. The low, medium and high scenarios correspond to the early periglacial, global warming and extended global warming climate cases respectively. Plate (b) shows the corresponding estimated temperature evolution for the Forsmark region for the global warming climate case (medium emission case), whereas plate (c) and (d) show the corresponding estimated Forsmark temperature evolution for the extended global warming climate case (high emission case) and the early periglacial climate case (low emission case). The temperature is expressed as an increase from the present annual air temperature. The figure also includes the uncertainty interval estimated for each case.

Present climate at Forsmark

The present climate in the Forsmark region has typical values for the climate on the Swedish east coast (Table 4-2), with a mean annual air temperature of c +5.5°C for the period 1961–1990 (Johansson et al. 2005). This can be compared to a mean annual air temperature of c 7°C (Werner et al. 2014) for the period 2004–2010. The difference between these values is likely due to an observed increase in the mean annual air temperature, but also to the short averaging period (7 years) used by Werner et al. (2014) which makes this value sensitive to natural climate variability.

Precipitation in the Forsmark area for the period 1961–1990 is represented here by the close-by stations Högmasten and Storskäret. Mean annual precipitation at these stations was 568 mm and 549 mm, respectively, for this period (Johansson 2008). This can be compared to a mean annual precipitation amount c 589 mm (Werner et al. 2014) for the period 2004–2010.

Table 4-2. Climate data for the Forsmark region (mean values for the period 1961–1990).

Site	Mean annual precipitation (mm/yr)	Mean annual air temperature (°C)
Forsmark	549–568	+5.5

As described in Section 2.2.3, Forsmark is in a region of ongoing shore-level change due to glacial isostatic uplift following the last glaciation, but also due to sea-level changes associated with human-induced global warming. The resulting shore-level change at Forsmark at present is c 6 mm/yr (Pässe 2001).

Transitions between climate domains

The climate cases represent a succession of climate domains at Forsmark. Depending on what spatial scale is considered, the transitions between climate domains need to be described differently. If considering a repository site only, or even a central part of a repository, the transitions between climate domains (temperate-, periglacial-, glacial domains and submerged conditions) may be described as more or less instantaneous in time. This is in line with the way the succession of climate domains is depicted in this chapter. The ice-sheet and GIA modelling used for the construction of climate cases were done on a coarser spatial scale. Therefore, the results from the larger model grid cells in these simulations are taken to represent the ice sheet- and shore-level development at the SFR repository location.

However, if looking at Forsmark on a site-scale, i.e. several hundreds of square km (e.g. Figure 4-12), the transition between climate domains is of a gradual nature, both spatially and temporally. Examples of the duration of the main transitions within the reconstructed last glacial cycle (3.2.3) which occur when the site goes from i) temperate climate domain to periglacial climate domain, ii) periglacial climate domain to glacial climate domain, iii) glacial domain to submerged conditions and finally iv) from submerged conditions back to temperate climate domain are given in the following paragraphs.

The transient nature of the change from a temperate climate domain to a periglacial climate domain is illustrated in Figure 3-19, which shows permafrost evolution in the *Weichselian glacial cycle climate case*, which is a repetition of the reconstruction of the last glacial cycle. Sporadic permafrost starts to grow more or less simultaneously over the site. Subsequently, if climate allows, the permafrost may develop to a discontinuous- and continuous spatial coverage. The duration of such a full transition in the reconstruction of the last glacial cycle, i.e. the development from a landscape without permafrost to a landscape with permafrost coverage of 90% or more at the Forsmark site, is approximately between 2 and 5 ka (Figure 3-19).

The transition from a periglacial- to a glacial climate domain manifests itself as an ice-sheet margin that advances over the site. A spatially transient change takes place in one specific direction over the Forsmark site, by which the periglacial climate domain is replaced with glacial climate domain following the advance of the ice-sheet front. In the reconstruction of the last glacial cycle, the ice-sheet margin advances over the site at a speed of ~50 m/year. The duration of this transition, i.e. the time it takes for the ice sheet to advance over the Forsmark site, is around 250 years. Note that permafrost may still exist under the ice sheet for some of the time that the site is assigned to the glacial climate domain.

The transition from glacial to submerged conditions constitutes the deglaciation phase of the site, when ice-sheet conditions are replaced by submerged conditions. The retreat rate of the ice sheet margin during deglaciation of the Forsmark site is, in the reconstructed last glacial cycle, ~300 m/year. The duration of this transition, i.e. the time during which one deglaciation occurs over the Forsmark site in the Weichselian glacial cycle climate case, is around 50 years. It should be noted, as previously described, that during both advancing and retreating phases, there is a possibility of having the ice sheet margin oscillating over the site due to climate variability. However, such a case should be regarded as an exception from the more common situation of having a continuously advancing or retreating margin.

According to the model reconstruction of the last phase of ice sheet coverage in the Forsmark area (Section 2.3.4), the ice-flow direction during the MIS 2 ice-sheet advance was approximately from the north, whereas the ice-flow direction during the deglaciation was from the north-west. This is in line with the interpretation of glacial striae, with a northerly direction recorded both in the oldest glacial striae and the oldest documented directional transport of the till material as recorded in clast fabric analysis (Sundh et al. 2004), and with an overall dominating younger striae system showing transport and deposition from the north-west (Sohlenius et al. 2004). This demonstrates that the transition to and from the glacial climate domain may be spatially different during phases of ice-sheet growth and decay.

The transition from submerged conditions to the temperate climate domain is manifested by the shore-level displacement caused by the isostatic rebound that follows deglaciation. The duration of this transition in the reconstructed last glacial cycle, i.e. the time it takes from the very first appearance of land at the site (SKB 2010a, Figure 4-37) until the last remnants of sea have disappeared from the site is around 12 ka (Lindborg 2010). This is the transition that is occurring at the Forsmark site at present, manifested by the slow movement of the shoreline across the site and indeed across the SFR repository. The transient nature of shore-level displacement over the site is further described in Lindborg (2010).

The durations of the four transitions above are summarised in Table 4-3.

Given the climate evolution of the reconstructed last glacial cycle, the assumptions made in all modelling exercises (Section 2), and the physiographical characteristics of the site, the glacial processes result in the fastest transition between climate domains (Table 4-3). The transition from glacial climate domain to submerged conditions for the Forsmark site is around 50 years. The transition from periglacial to glacial climate domain is about five times slower. These two fastest transitions relate to the glacial climate domain, i.e. to the relatively fast processes of ice-sheet advance and decay. The transition from a temperate- to a periglacial climate domain with continuous permafrost is 40 to 100 times slower than the transition from a glacial climate domain to submerged conditions (Table 4-9). The slowest transition is the one from submerged conditions back to a temperate climate domain, which, in the reconstructed last glacial cycle, is around 240 times slower than the transition from glacial climate domain to submerged conditions. This is due to very slow glacial isostatic adjustment of the Earth's crust to the unloading associated with deglaciation (Section 2.2).

Note that for any given time during these transitions, the Forsmark site (Figure 4-12) contains more than one type of climate domain. For instance, parts of the site may be subject to the periglacial climate domain, having permafrost conditions without an ice sheet, at the same time as another part of the site may be overridden by an ice sheet and thus be subject to the glacial climate domain. Also note that the transition from one climate domain to another over the site does not need to be a full transition (as in the above examples). For instance, discontinuous permafrost may start to form within the site due to lower air temperatures, transforming the affected areas to periglacial climate domain. Thereafter, the climate may become warmer, such that permafrost (and the periglacial climate domain) diminishes and disappears.

Table 4-3. Approximate durations of full transitions between climate domains over the Forsmark site for the reconstructed last glacial cycle (Section 3.2.3). In order to compare the duration of the transitions from and to various climate domains, the relative durations of the transitions are expressed as numbers compared to the duration of deglaciation of the site.

Transition	Approximate duration in the reconstructed last glacial cycle	Relative duration of transition
Temperate- to periglacial climate domain with continuous permafrost coverage	~2,000 to ~5,000 years	40 to 100
Periglacial- to glacial climate domain	~250 years	5
Glacial climate domain to submerged conditions (deglaciation)	~50 years	1
Submerged conditions to temperate climate domain	~12,000 years	240

4.1 Global warming climate case

4.1.1 Background

The *global warming climate case* describes a situation with moderate carbon emissions in the current and next century (corresponding to IPCC scenarios A1B and RCP4.6; see Table 3-2) followed by a slow decrease in atmospheric CO₂ concentration such that glacial inception, i.e. growth of Northern Hemisphere ice sheets, starts around 50 ka AP. It was defined to represent the results of the modelling studies described in Section 3.3.5 which conclude that glacial inception would commence around 50 ka AP if the atmospheric CO₂ concentration had decreased to a pre-industrial value (c 280 ppmv).

For the period from 50 ka AP to 100 ka AP, the global climate is assumed to cool gradually with intermittent ice-sheet build up in the Northern Hemisphere. Similar to previous glacial cycles substantial climate variability produced by internal climate dynamics is expected, superimposed on the gradual cooling. This variability is not predictable, which is why a realistic variability is defined based on the reconstructed Weichselian glacial cycle described in Section 3.2.3. The period from 113 ka BP to 63 ka BP in the reconstructed Weichselian glacial cycle is used to define the *global warming climate case* for 50 ka AP to 100 ka AP. This period starts with periglacial climate conditions for 1.3 ka, which is followed by a succession of temperate and periglacial climate periods of a few centuries to almost 10 ka.

4.1.2 Ice-sheet evolution

The Fennoscandian ice sheet does not reach Forsmark during the next 100 ka in the *global warming climate case*. In the reconstructed Weichselian glacial cycle (Section 3.2.3), the Fennoscandian ice sheet first reaches Forsmark at c 60 ka BP. This corresponds to c 100 ka AP in the *global warming climate case*. This timing is defined, somewhat arbitrarily, by the choice of using this specific 50 ka period of the reconstructed Weichselian glacial cycle to represent climate in Forsmark in this climate case. It is, however, in general agreement with the timing of maximum Northern Hemisphere ice-sheet volume in the studies described in Section 3.3.5 (Table 3-8). To take the uncertainty in the timing of the first occurrence of an ice sheet in Forsmark into account, an ice sheet that reaches Forsmark within the next 100 ka is analysed in the *Weichselian glacial cycle climate case* (Section 4.4).

4.1.3 Shore-level evolution

One of the main processes of importance for repository safety in the temperate climate domain is changes in Baltic Sea shore-level. The surface above the SFR repository is currently between 0 and 7.2 m below sea level. The location of the repository in relation to the shore level will vary in time due to variations in the eustatic (related to ocean volume) and isostatic (related to land movement) sea level. As described in Section 3.3, the projected future sea-level rise due to thermal expansion and glacier and ice-sheet melt is expected to be slow, extending over several millennia. The *global warming climate case* was defined based on the GIA modelling of a future warm climate described in Section 2.2.4. In this modelling, a complete melting of the Greenland ice sheet in the next 1 ka was assumed. Due to gravitational effects, the global average sea-level increase of in total 7 m does not result in a sea-level rise in the Forsmark region (Section 2.2.4). The use of this shore-level evolution in the *global warming climate case* is therefore equivalent to assuming that the future eustatic contribution to shore-level change does not exceed the present eustatic contribution.” This assumption is made in order to cover the full uncertainty associated with future sea-level changes. The *global warming climate case* represents the lower end of the uncertainty range, with negligible effects of global sea-level rise, whereas the *extended global warming case* represents the upper end of the uncertainty range (see further Section 4.3.3). The two cases thus represent a minimum length period of submerged conditions above SFR in the *global warming climate case* as opposed to a maximum length period of submerged conditions above SFR in the *extended global warming climate case*. The shore-level evolution at Forsmark for the *global warming climate case* is shown in Figure 4-6.

The SFR repository is today covered by the Baltic Sea, with a maximum water depth of 7.2 m over SFR1 and 5.3 m over the planned SFR3 (layout L2). With the relative shore-level change curve for the *global warming climate case* (Figure 2-37), the duration for 100% of the surface above SFR 1 and 3 to have become land is c 1200 years (see Section 2.2.4). The duration for 75% of the surface

above SFR 1 and 3 to have become land is c 600 years. Based on this simplistic approach, the *global warming climate case* is defined with an initial submerged period of c 0.6 ka at Forsmark. This simplistic approach is however not used in e.g. the landscape evolution modelling (see **SR-PSU Biosphere report**), for which the temporal shore-level evolution, shown in Figure 4-6, is used.

4.1.4 Permafrost evolution

As described in Section 4.1.1, the *global warming climate case* was designed with temperate conditions in the Forsmark region until 50 ka AP. For the period from 50 ka AP to 100 ka AP, a realistic variability is defined based on the reconstructed Weichselian glacial cycle described in Section 3.2.3. The permafrost starts to develop in Forsmark at around 50 ka AP. After that, progressively longer periods of permafrost conditions and shorter periods of temperate climate conditions generally occur. The maximum permafrost depth in this climate case is c 260 m (with a maximum uncertainty interval down to c 460 m) and it occurs c 100 ka AP. The depth of the frozen ground is somewhat shallower than the permafrost depth, due to the hydrostatic pressure and groundwater salinity; 245 m (with a maximum uncertainty interval down to 420 m). These depth values relate to the location of the planned KBS-3 repository for spent nuclear fuel. The heat from this repository has been included in the permafrost simulations, whereas no heat is produced from SFR. The reduction in permafrost and freezing depths over SFR, introduced by the presence of the nearby KBS-3 repository, are however not large (Figure 4-15 and 4-16), on the order of a few tens of m at maximum. The 0°C isotherm reaches c 60 m depth at the location of SFR around 70 ka AP and the -4°C isotherm reaches c 60 m depth at the location of SFR around 87 ka AP.

4.1.5 Surface denudation

Glacial erosion is identified as the most important denudation process in the reconstructed Weichselian glacial cycle, with the largest contribution to the total denudation rate (Section 2.4.4). The Fennoscandian ice sheet does not reach the Forsmark region in the *global warming climate case*, and hence glacial erosion does not occur in this climate case.

In the *global warming climate case*, the annual air temperature and precipitation are expected to increase in Forsmark during the initial part of the temperate climate domain, as described in Section 3.3.3. For the first tens of thousands of years of this climate case, increased precipitation results in increased surface runoff, see above and Kjellström et al. (2009), which may lead to increased fluvial erosion. The resulting amount of fluvial erosion is somewhat limited by the fact that fluvial erosion cannot erode deeper than the level of the Baltic Sea and that the site is located at sea-level today. The period of increased precipitation is accompanied by a slowly regressing, stationary or even transgressing sea-level (2.2.4), which precludes deep fluvial erosion during the period influenced by increased precipitation. However, the remaining amount of shoreline displacement amounts to around 70 m (Figure 4-3), i.e. in the same order of magnitude as the present day depth of SFR 1. On the other hand, there will be no major rivers located above SFR when the sea has left the area, strongly indicating that any increase in fluvial erosion will not result in deep fluvial erosion specifically above SFR.

Due to the low relief and proximity to base level, the long-term non-glacial denudation rate in the Forsmark region has been estimated to be low in the past (up to 10 m/Ma) (Olvmo 2010). Increased temperatures could lead to somewhat higher weathering rates. However, given the absence of glacial erosion, and small expected effect of increased weathering rates, the feedback mechanisms between climate, weathering and vegetation, are not further treated in this climate case.

Since periglacial conditions have a shorter duration in this climate case than in the reconstruction of the Weichselian cycle, aeolian erosion is expected to contribute even less to the total denudation in this climate case than in the *Weichselian glacial cycle climate case*.

All in all, the total denudation in Forsmark in the *global warming climate case* is more restricted than in the reconstruction of the Weichselian glacial cycle. The one process that could give a relevant contribution to increased denudation, fluvial erosion, is limited by the near-sea-level location of the site and by the fact that no major water drainage pathways will be located above the repository.

4.1.6 Evolution of climate domains

The development of climate domains for the *global warming climate case* is shown in Figure 4-3. The temperate climate domain dominates. Temperate conditions prevail for c 69 ka (69% of the time), periglacial conditions for c 31 ka (31% of the time) and submerged conditions prevail for c 0.6 ka (<1% of the time).

A considerable variation in the temperature and precipitation is expected in the initial 50 ka period of temperate climate conditions, ranging from air temperatures and precipitation rates considerably higher than at present in the first millennia to lower than at present. A detailed example of the characteristics of a climate dominated by increased atmospheric greenhouse gas concentrations is given below, derived from the climate modelling study by Kjellström et al. (2009). In time, the high temperatures slowly decrease, as a response to the slow decrease in atmospheric CO₂ concentrations. During the initial long temperate period, climate varies within a range that is larger than that during the preceding parts of the Holocene. As described in Section 4.1.1, the length of the initial period of temperate climate domain is defined here based on studies of future climate and the next glacial inception. Large uncertainty exists in the future climate evolution though, as discussed in Section 3.3.5, and thus the initial period of temperate climate domain could be shorter or longer than that described here. To cover this uncertainty, two alternative cases are included in the safety assessment. The *early periglacial climate case* describes a future evolution with a more rapid return to pre-industrial atmospheric CO₂ concentrations than in the *global warming climate case* resulting in periglacial climate domain in Forsmark at c 15 ka AP, see Section 4.2. The *extended global warming climate case* on the other hand describes a future evolution with a longer duration of temperate climate conditions, see Section 4.3.

Between c 50 ka AP and 100 ka AP, periods of periglacial conditions with permafrost occur and get, in general, progressively more severe (Figure 4-3). Table 4-4 summarises the sequence of events for the *global warming climate case*.

Table 4-4. Sequence of climate-related events for the global warming climate case.

Event	Transition date	Climate domain
Deglaciation /start of the Holocene interglacial (locally defined)	10.8 ka BP	–
Holocene interglacial	–	Temperate climate domain (incl. submerged conditions)
End of Holocene interglacial (locally defined)	c 50 ka AP	–
Periglacial conditions (progressively longer periods of permafrost conditions)	–	Periglacial climate domain (incl. progressively shorter phases of temperate climate conditions)
End of periglacial conditions Start of glacial conditions	100 ka AP	–

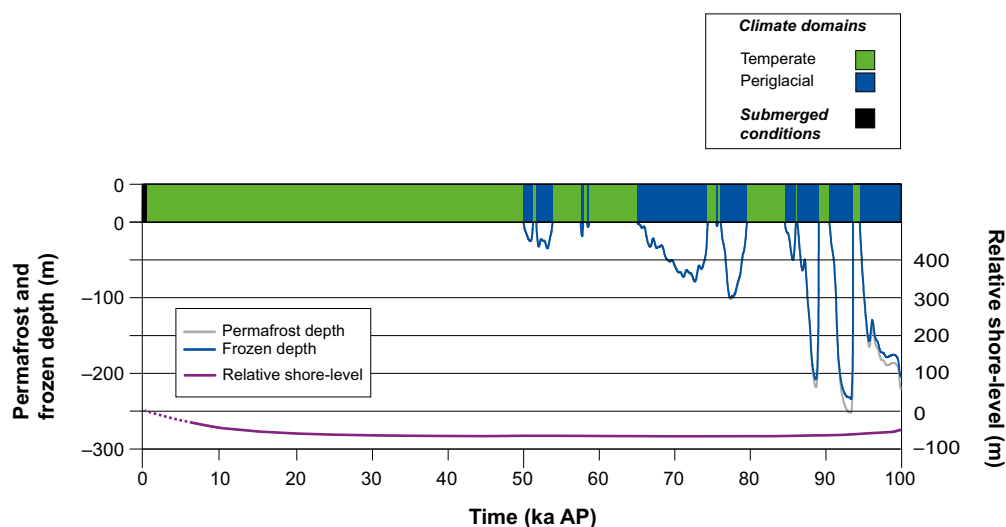


Figure 4-3. Evolution of climate-related conditions at Forsmark as a time series of climate domains and submerged periods for the *global warming climate case*.

In the *global warming climate case*, the initial warm annual mean air temperatures do not affect repository safety functions. Furthermore, the increase in precipitation would not affect groundwater formation significantly, since, on a regional scale, the major part of the groundwater aquifer is filled already by present-day precipitation rates. Instead surface-runoff is increased, discussed further under the section on surface denudation. However, low groundwater salinity due to persistent infiltration of meteoric water during the initial temperate period may have a potential effect on the function of clay components in the repository (see further SKB 2014d).

4.2 Early periglacial climate case

4.2.1 Background

As described in the beginning of the present chapter, climate effects of carbon releases to the atmosphere are expected to persist for tens, if not hundreds, of thousands of years into the future (Archer et al. 2009). The *early periglacial climate case* represents the lower end of the uncertainty range associated with the amount of human and natural carbon emissions to the atmosphere, the global carbon cycle, and with the climate system response to the carbon emissions. It thus represents low human carbon emissions and a relatively fast decrease in atmospheric CO₂ concentration.

The *early periglacial climate case* is defined as a variant of the *global warming climate case* with a faster decrease in atmospheric CO₂ concentration resulting in climate conditions cold enough for permafrost development in Forsmark in the period of the minimum in incoming summer solar radiation at high northern latitudes around 17 ka AP. After this period, the Forsmark climate is assumed to return to the temperate climate domain. As in the *global warming climate case*, the atmospheric CO₂ concentration is assumed to further decrease such that glacial inception, i.e. growth of Northern Hemisphere ice sheets, starts around 50 ka AP.

Beyond 50 ka AP, the *early periglacial climate case* is identical to the *global warming climate case* with a period of periglacial climate conditions starting at 50 ka AP, which is followed by a succession of temperate and periglacial climate periods of a few centuries to almost 10 ka.

4.2.2 Ice sheet evolution

As in the *global warming climate case*, a Fennoscandian ice sheet does not reach Forsmark during the next 100 ka in the *early periglacial climate case*. This choice is in general agreement with the timing of maximum Northern Hemisphere ice sheet volume in the studies described in Section 3.3.5 (Table 3-8). However, to take the uncertainty in the timing of the first occurrence of an ice sheet in Forsmark into account, an ice sheet that reaches Forsmark within the next 100 ka is analysed in the *Weichselian glacial cycle climate case* (Section 4.4).

4.2.3 Shore-level evolution

The same assumptions regarding eustatic and isostatic changes in Forsmark are made in the *early periglacial climate case* as in the *global warming climate case* (Section 4.1.3), resulting in the same shore-level evolution.

4.2.4 Permafrost evolution

Brandefelt et al. (2013) analysed the potential for cold climate conditions and permafrost in Forsmark in the next 60 ka, with emphasis on the periods of minimum summer insolation at high northern latitudes around 17 ka and 54 ka AP. A range of EMIC and ESM simulations with a wide range of atmospheric CO₂ concentrations and insolation distributions for the next 60 ka was performed. The results of these climate simulations were combined with estimates of the uncertainty in the results due to future glacier and ice-sheet growth, inter-model differences, internal variability and future atmospheric greenhouse gas concentrations, in order to estimate the coldest feasible near-surface air temperature in Forsmark in the 17 ka AP and 54 ka AP periods. The resulting temperature is listed in Table 4-5 and Table 4-6 as a function of the atmospheric CO₂ concentration.

Table 4-5. The minimum annual average bias-corrected Forsmark T_{2m} when all uncertainties are taken into account for orbital year 17 ka AP (Data from Brandefelt et al. 2013).

Atmospheric CO ₂ concentration (ppmv)	180	200	240	280	320
Minimum annual average bias-corrected Forsmark T_{2m} (°C)	-7.4	-5.9	-2.3	0.3	0.8

Table 4-6. The minimum annual average bias-corrected Forsmark T_{2m} when all uncertainties are taken into account for orbital year 54 ka AP (Data from Brandefelt et al. 2013).

Atmospheric CO ₂ concentration (ppmv)	180	200	240	280	320
Minimum annual average bias-corrected Forsmark T_{2m} (°C)	-11	-9.5	-6.5	-3.1	-2.6

The near-surface air temperature from one of the climate simulations was also used as input to a site-specific 2D permafrost model for Forsmark. In accordance with previous permafrost simulations for Forsmark (e.g. Hartikainen et al. 2010), the permafrost model was set up under the assumption of dry climate conditions and dry surface conditions to promote permafrost at the site. A number of sensitivity simulations were performed to investigate the potential for frozen ground when the uncertainties in simulated Forsmark near-surface air temperature are taken into account.

The results of the permafrost modelling performed by Brandefelt et al. (2013) are summarised in Figure 4-4, which shows the maximum depth of the 0°C, -3°C and -5°C isotherms at the SFR repository location after 10,000 years of permafrost model integration as a function of the annual average near-surface air temperature in Forsmark. In combination with the climate modelling results including uncertainties, Brandefelt et al. (2013) discussed the implications for the potential for permafrost in Forsmark in these periods. The atmospheric CO₂ concentration is a key factor. As discussed in 3.3.1, the atmospheric CO₂ concentration is expected to be larger than the pre-industrial value of 280 ppmv for at least the next 10 ka. To estimate the minimum feasible atmospheric CO₂ concentration around 17 ka AP, Brandefelt et al. (2013) utilised the atmospheric CO₂ data from ice cores. When the previous interglacial ended at c 115 ka BP, the atmospheric CO₂ concentration decreased from interglacial levels of c 275 ppmv around 115.4 ka BP to c 228 ppmv around 108.0 ka BP, i.e. c 47 ppmv CO₂ in 7.4 ka. If the processes that produced this natural decrease in CO₂ were to set in around 10 ka AP, an atmospheric CO₂ concentration of c 230 ppmv could be reached by 17 ka AP. The minimum annual average Forsmark near-surface temperature for this CO₂ concentration is c -3.2°C (linear interpolation from Table 4-5). For this annual average Forsmark near-surface temperature, the 0°C isotherm is located at about 150 m depth (i.e. below SFR3) and the -2°C isotherm is located at c 60 m depth, i.e. at SFR1 depth.

Under the assumptions made in their study, Brandefelt et al. (2013) concluded that frozen ground (a bedrock temperature of less than 0°C) cannot be excluded at c 60 m and c 110 m depth at 17 ka AP or at 54 ka AP. Furthermore, they concluded that it is very unlikely that a bedrock temperature of -3°C or less, relevant for analysis of freezing of concrete repository structures, would occur at c 60 m and c 110 m depth at 17 ka AP, but that this possibility cannot be excluded at 54 ka AP. The main reason for the different conclusions for the two time periods is the expected decrease in atmospheric CO₂ concentration between those periods.

4.2.5 Surface denudation

The *early periglacial climate case* differs from the *global warming climate case* in the period 15.5 ka AP to 18.5 ka AP when periglacial conditions prevail in the *early periglacial climate case* as compared to a temperature conditions in the *global warming climate case*. Based on the same considerations as for the *global warming climate case* (see Section 4.1.5), the total denudation in Forsmark in the *early periglacial climate case* is therefore more restricted than in the reconstruction of the Weichselian glacial cycle.

4.2.6 Evolution of climate domains

The development of climate domains for the *early periglacial climate case* is shown in Figure 4-5. The temperate climate domain dominates. Temperate conditions prevail for c 66 ka (66% of the time), periglacial conditions for c 34 ka (34% of the time) and submerged conditions prevail for c 0.6 ka (<1% of the time).

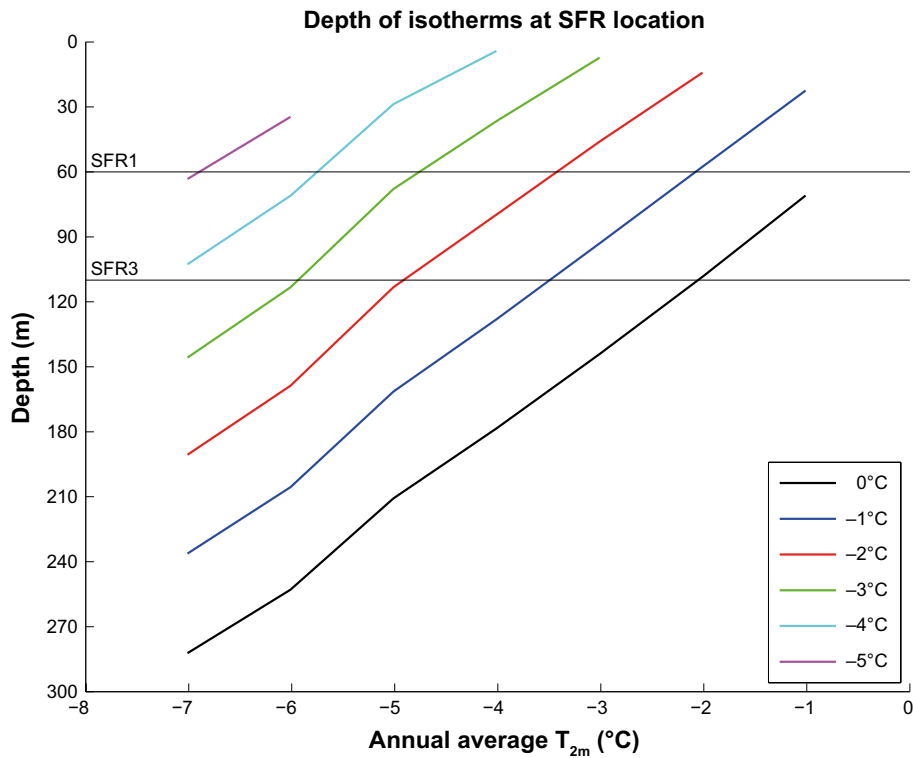


Figure 4-4. Depth (m) of the 0, -1, -2, -3, -4° and -5°C isotherms as a function of the annual average near-surface air temperature (T_{2m}) in Forsmark. The depths of the existing SFR1 repository (c 60 m) and planned SFR3 repository (c 110 m) are indicated with black lines.

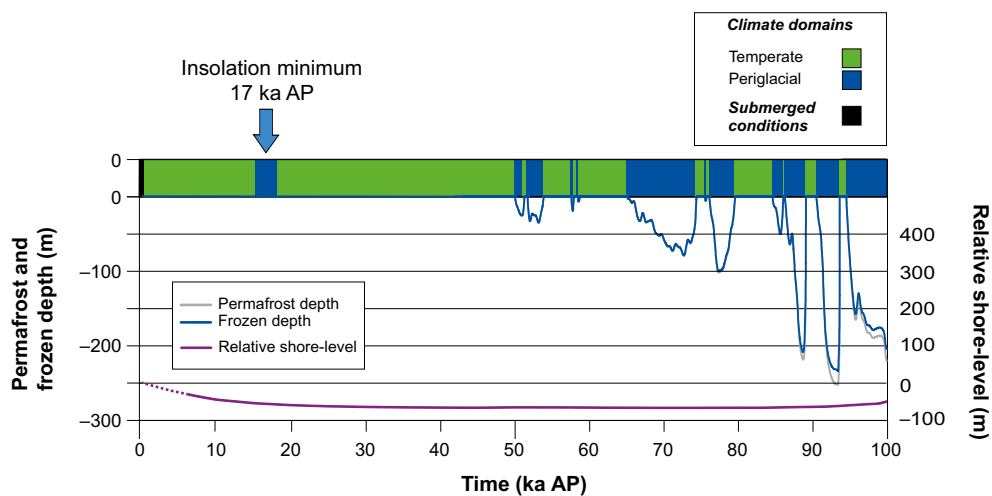


Figure 4-5. Evolution of climate-related conditions at Forsmark as a time series of climate domains and submerged periods for the early periglacial climate case. Note that permafrost and frozen ground evolution is not shown for the period 0 to 50 ka AP. Permafrost and frozen ground can however not be excluded to a depth of about 150 m for the periglacial period from 15.5 to 18.5 ka AP (see Section 4.2.4).

A considerable variation in the temperature and precipitation is expected in the initial 50 ka period of temperate climate conditions, ranging from air temperatures and precipitation rates considerably higher than at present in the first millennia to temperatures and precipitation rates lower than at present. A detailed example of the characteristics of a climate dominated by increased atmospheric greenhouse gas concentrations is given in Section 3.3.6, derived from the climate modelling study by Kjellström et al. (2009). In time, the high temperatures slowly decrease, as a response to the slow decrease in atmospheric CO_2 concentrations. During the initial long temperate period, climate varies within a range that is larger than that during the preceding parts of the Holocene. In this climate case,

Table 4-7. Sequence of climate-related events for the early periglacial climate case.

Event	Transition date	Climate domain
Deglaciation /start of the Holocene interglacial (locally defined)	10.8 ka BP	–
Holocene interglacial	–	Temperate climate domain (incl. submerged conditions)
End of Holocene interglacial (locally defined)	c 15.5 ka AP	–
Periglacial conditions around minimum in summer insolation	–	Periglacial climate domain
End of periglacial period	c 18.5 ka AP	–
End of temperate climate period	c 50 ka AP	–
Periglacial conditions (progressively longer periods of permafrost conditions)	–	Periglacial climate domain (incl. progressively shorter phases of temperate climate conditions)
End of periglacial conditions Start of glacial conditions	100 ka AP	–

a 3 ka period of periglacial climate domain centered around the minimum in northern hemisphere summer insolation at 17 ka AP (i.e. between 15.5 and 18.5 ka AP) is assumed. After this period, a temperate climate is assumed to prevail in Forsmark until 50 ka AP. Identically to the *global warming climate case*, a realistic variability based on the reconstructed Weichselian glacial cycle is assumed for the period 50 ka AP to 100 ka AP.

In the *early periglacial climate case*, the warmer annual mean air temperatures do not affect repository safety functions. Furthermore, the increase in precipitation would not affect groundwater formation significantly, since, on a regional scale, the major part of the groundwater aquifer is filled already by present-day precipitation rates. Instead surface-runoff is increased, discussed further under the section on surface denudation. However, low groundwater salinity due to persistent infiltration of meteoric water during the initial temperate period may have a potential effect on the function of clay components in the repository (see further SKB 2014d).

4.3 Extended global warming climate case

4.3.1 Background

The *extended global warming climate case* describes a situation with high carbon emissions in the current and next century (corresponding to IPCC scenarios A2 and RCP8.5; see Table 3-2) followed by a slow decrease in atmospheric CO₂ concentration such that glacial inception, i.e. growth of Northern Hemisphere ice sheets, starts around 100 ka AP. It was defined to represent the results of the modelling studies described in Section 3.3.5 which concluded that glacial inception is not expected until around 100 ka AP if the atmospheric CO₂ concentration stays well above the pre-industrial value (c 280 ppmv).

4.3.2 Ice sheet evolution

No ice sheets are present in the Forsmark region during the next 100 ka in this climate case, since glacial inception is assumed to occur around 100 ka AP.

4.3.3 Shore-level evolution

One of the main processes of importance for repository safety in the temperate climate domain is changes in Baltic Sea shore-level. The surface above the SFR repository is currently between 0 and 7.2 m below sea level. The location of the repository in relation to the shore level will vary in time due to variations in the eustatic (related to ocean volume) and isostatic (related to land movement) sea level. As described in Section 3.3, the projected future sea-level rise due to thermal expansion and glacier and ice-sheet melt is expected to be slow, extending over several millennia. To cover the wide range of uncertainty in the magnitude and timing of future global sea-level rise due to ocean steric and glacier and ice-sheet processes the *extended global warming climate case* was defined to represent the upper end of this uncertainty range.

In this climate case, the maximum contributions to sea-level rise in the Forsmark region from various processes are added, pessimistically and unrealistically assuming that they all occur within the next millennium. The resulting total mean sea level rise in the Baltic is c 10 m (3.3.4 and Table 3-7). This value is similar to that estimated for the Olkiluoto site on the other side of the Baltic Sea (8 m, Pimenoff et al. 2012). It would take c 1.2 ka for the isostatic uplift in Forsmark, which is 8.4 mm/yr for the present and near future (Lidberg et al. 2010), to compensate for a sea-level rise of c 10 m. At 1.2 ka AP, the shore level at Forsmark is located in about the same location as at present. After that, the situation is assumed to be similar to today, with the isostatic uplift slowly raising the repository site over the level of the Baltic Sea. The shore-level evolution at Forsmark is shown in Figure 4-6 for the *extended global warming climate case*, in comparison to the *global warming climate case*. As described in Section 4.1.3, the duration for a complete transformation from present conditions to terrestrial conditions above the repository (SFR 1 and 3) is c 1200 years. The third quartile, when 75% of the surface above SFR 1 and 3 has become land takes c 600 years and requires a relative sea level change of 3.8 m. Based on this simplistic approach, the *extended global warming climate case* is defined with an initial submerged period of c 1.8 ka (1200+600 years) at Forsmark. This simplistic approach is however not used in e.g. the landscape evolution modelling (see **SR-PSU Biosphere report**), for which the temporal shore-level time, shown in Figure 4-6, is used.

As described in Section 4.1.3, the *global warming* and the *extended global warming climate cases* are thus defined to describe the full range of uncertainty in future sea level rise. The *global warming climate case* represents the lower end of the uncertainty range, with negligible effects of global sea-level rise, whereas the *extended global warming case* represents the upper end of the uncertainty range. The two cases thus represent a minimum length period of submerged conditions above SFR in the *global warming climate case* as opposed to a maximum length period of submerged conditions above SFR in the *extended global warming climate case*.

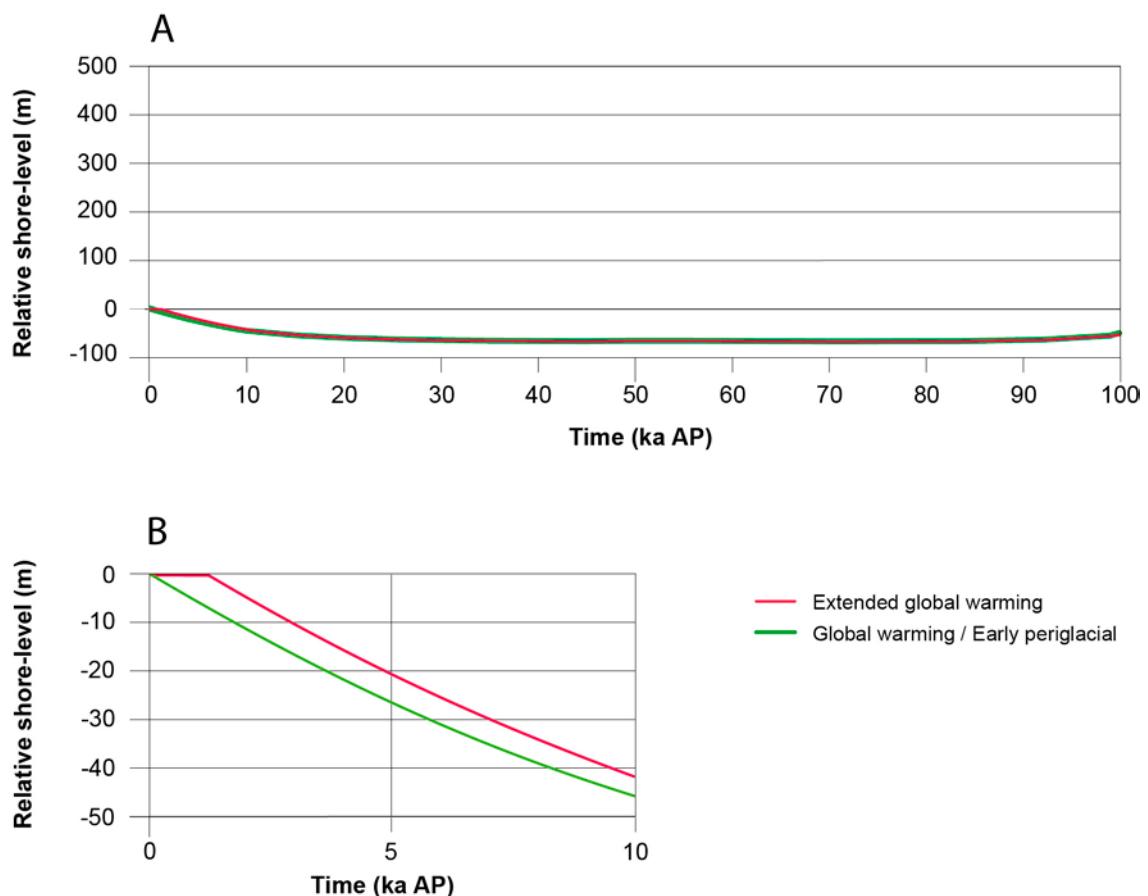


Figure 4-6. Shore-level evolution data from the present (A.) to 100,000 years after present and (B.) to 10,000 years after present for the global warming and early periglacial climate cases (green line) and the extended global warming climate case (red line).

It should be emphasised that the assumptions made in the definition of the *extended global warming climate case* of maximum contributions from thermal expansion, GIS and WAIS complete melting and complete melting of all glaciers and ice caps within the next millennium is regarded as unrealistic based on current knowledge (Section 3.3). These assumptions are motivated by large uncertainties and are intended for analysis of a maximum duration of submerged conditions for long-term safety of the SFR repository in Forsmark.

4.3.4 Permafrost evolution

No permafrost develops in Forsmark during the next 100 ka in this climate case. Cold climate conditions in Forsmark, required for permafrost development, are assumed to first occur around 100 ka AP.

4.3.5 Surface denudation

Since the *extended global warming climate case* is defined to represent larger carbon emissions and a stronger climate response than in the *global warming climate case*, fluvial erosion and chemical weathering in the wetter and warmer climate are anticipated to be more efficient than in the *global warming climate case* (Section 4.1.5). For a description of denudation processes of importance in a temperate climate, see the description of denudation under the *global warming climate case*.

Even though fluvial erosion and chemical weathering in this climate case is expected to exceed that found in the reconstructed last glacial cycle (Section 2.4), the *extended global warming climate case* comprises temperate climate conditions for the entire 100 ka, and consequently completely excludes the most efficient denudation process (glacial erosion) as defined in Section 2.4.1. Given this, the expected total amount of denudation for this climate case is considered smaller, or at least not larger, than in the *Weichselian glacial cycle climate case*. Surface denudation is therefore not described or treated further in the *extended global warming climate case*.

4.3.6 Evolution of climate domains

The development of climate domains for the *extended global warming climate case* is shown in Figure 4-7. The temperate climate is assumed to prevail until 100 ka AP, and thus temperate conditions prevail for 100% of the time.

Table 4-8. Sequence of climate-related events for the extended global warming climate case.

Event	Transition date	Climate domain
Deglaciation /start of the Holocene interglacial (locally defined)	10.8 ka BP	–
Holocene interglacial	–	Temperate climate domain (incl. submerged conditions)
End of Holocene interglacial (locally defined)	c 100 ka AP	

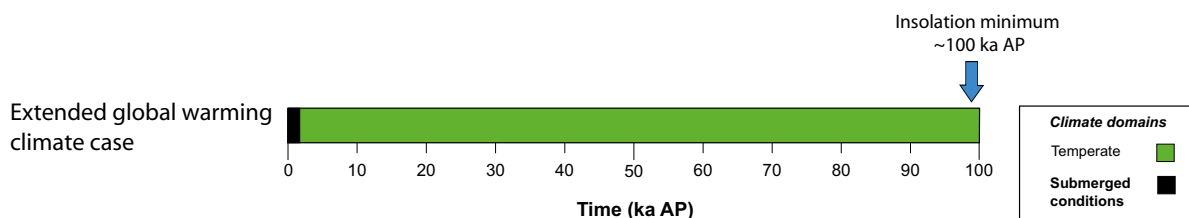


Figure 4-7. Evolution of climate-related conditions at Forsmark as a time series of climate domains and submerged periods for the extended global warming climate case.

A considerable variation in the temperature and precipitation is expected in the 100 ka period of temperate climate conditions, ranging from air temperatures and precipitation rates considerably higher than at present in the first millennia to lower than at present. A detailed example of the characteristics of a climate dominated by increased atmospheric greenhouse gas concentrations is given in Section 3.3.6, derived from the climate modelling study by Kjellström et al. (2009). In time the high temperatures are slowly reduced, as a response to the slow decrease in atmospheric CO₂ concentrations.

In the *extended global warming climate case*, the warmer annual mean air temperatures do not affect repository safety functions. Furthermore, the increase in precipitation would not affect groundwater formation significantly, since, on a regional scale, the major part of the groundwater aquifer is filled already by present-day precipitation rates. Instead surface-runoff is increased, discussed further under the section on surface denudation. Dispersion of bentonite clay during extended periods (100 ka) of meteoric groundwater recharge has been judged as not posing a problem for the SFR repository (Barrier process report, SKB 2014d, section 7.4.12).

4.4 Weichselian glacial cycle climate case

4.4.1 Background

The *Weichselian glacial cycle climate case* describes a climate evolution fully governed by natural climate variability, i.e. without anthropogenic influence on climate. It is constructed by repeating the reconstructed conditions for the last glacial cycle described in Section 3.2.3. The length of the present temperate interglacial period is assumed to be within the range of interglacial durations as observed within the past 800 ka (Tzedakis et al. 2009), see further Section 4.4.6.

Current scientific knowledge, described in Section 3.3, indicates that the Earth's climate evolution during the next 100 ka will deviate significantly from this reconstruction of the last glacial cycle climate. Due to human-induced increases in atmospheric greenhouse gas concentrations and small variations in insolation over the next 50 ka, the current interglacial is expected to last longer than previous interglacials (e.g. Berger and Loutre 2002). Since the timing of the first future period of periglacial climate conditions supporting permafrost was not an important question for the SR-Site safety assessment, for which this climate case originally was developed, efforts were, at the time, not made to obtain a timing of this occurrence in accordance with current knowledge. Therefore, the *Weichselian glacial cycle climate case*, and its first permafrost occurrence in Forsmark at c 7 ka AP should *not* be used for this specific purpose in studies where the timing of first permafrost is of importance, such as in SR-PSU. Instead and as previously mentioned, the *Weichselian glacial cycle climate case* is included in the present safety assessment in order to cover the remaining uncertainties regarding the development of an ice sheet during the coming 100 ka.

The *Weichselian glacial cycle climate case* is defined for the coming 120 ka, rather than 100 ka as for the other climate cases. This is done in order to include the full phase of glacial conditions that occurs around 100 ka AP in the *Weichselian glacial cycle climate case*.

4.4.2 Ice-sheet evolution

In the *Weichselian glacial cycle climate case*, the lowering of air temperature during the onset of the glacial results in ice-sheet inception. Following the ice-sheet evolution in the model reconstruction of the Weichselian glacial, see Section 3.2.3, the evolution of ice-covered area and ice volume for the *Weichselian glacial cycle climate case* are shown in Figure 4-8. The corresponding ice configurations for selected time slices, depicting future stadial and interstadial configurations in the *Weichselian glacial cycle climate case* are shown in Figure 4-9. During the glacial cycle, the ice sheet grows progressively larger in a number of distinct growth phases, with intervening phases of more restricted ice coverage. The Glacial Maximum (corresponding to the LGM of the Weichselian glaciation), is reached at around 100 ka into the future. As described in Section 3.2, the overall behaviour of the ice sheet can be characterised as being distinctly dynamic throughout the glacial cycle.

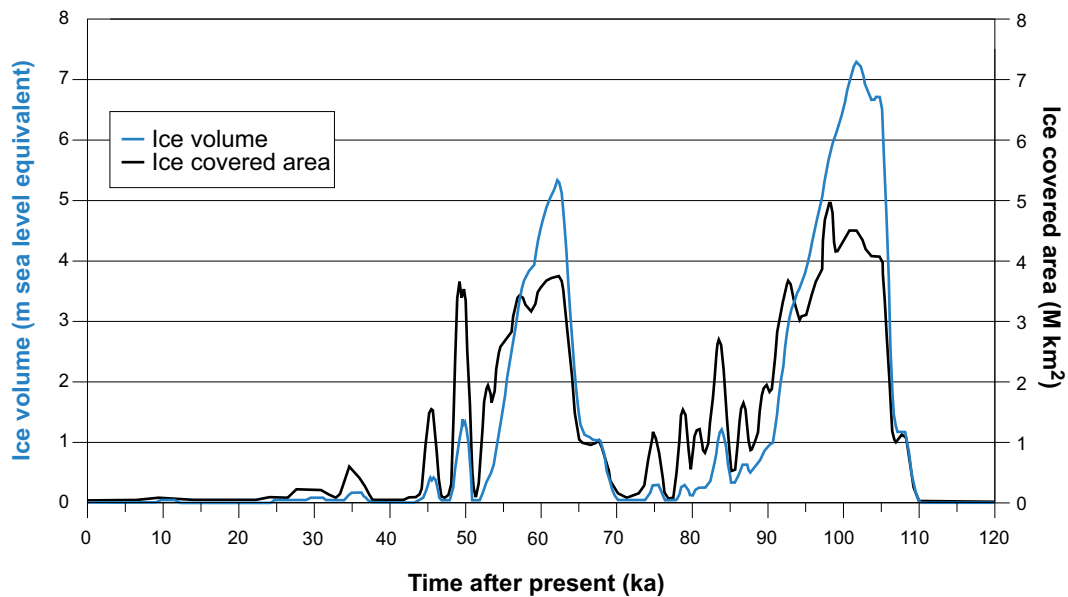


Figure 4-8. Ice sheet volume and ice covered area for the Weichselian glacial cycle climate case.

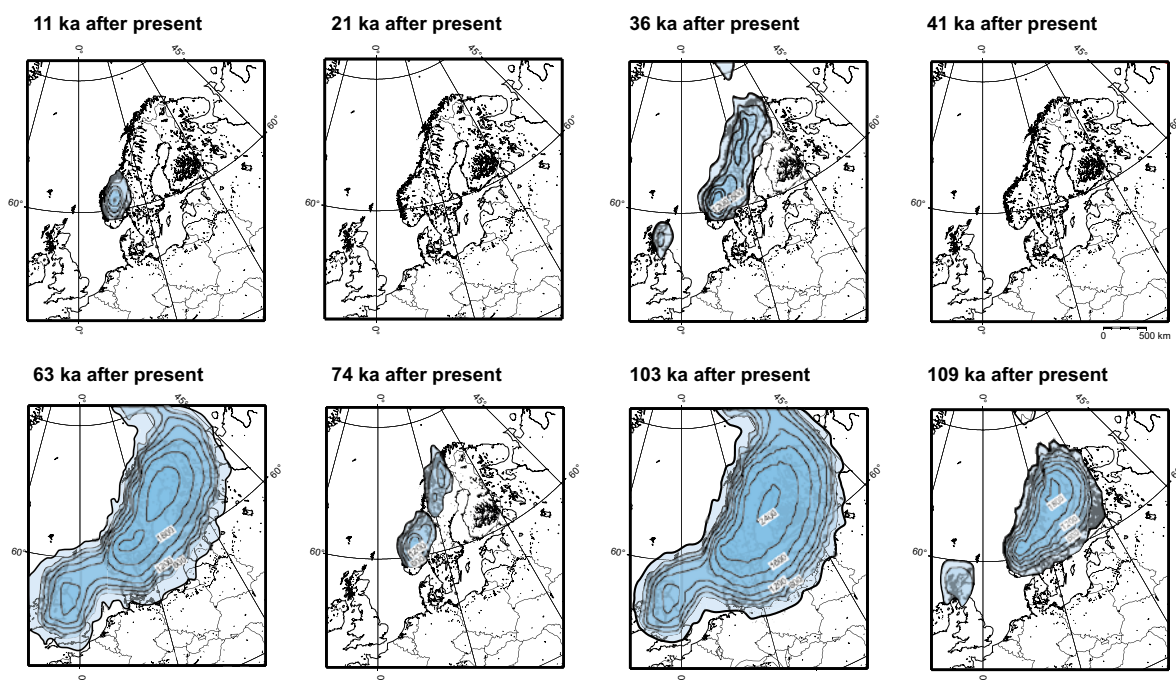


Figure 4-9. Ice-sheet configurations at stadials and interstadials for the Weichselian glacial cycle climate case. Contour lines show ice-surface elevation with a 300 m interval. All maps show present day shoreline position.

The dynamic behaviour of the ice sheet is seen also at the Forsmark site. The site is covered by ice during the cold stadials at around 60 and 100 ka AP (Figure 4-10). Between these stadials, the site experiences ice-free warmer interstadial conditions (corresponding to Marine Isotope Stage 3 in the reconstructed Weichselian glacial cycle). Ice-sheet advances during stadials around 14 and 38 ka AP do not reach the Forsmark site (Figure 4-9), although the ice-sheet margin is close to Forsmark during the latter stage. Note that even though an ice sheet is present in Fennoscandia during most of the glacial cycle (Figure 4-8), the Forsmark site, located in south-central Sweden, is not covered by the ice sheet for the majority of the time (Figure 4-10). This is in line with results of Kleman et al. (2008, Figure 9) who showed that for the period of the Quaternary that is dominated by 100 ka long glacial cycles, the Forsmark region has been covered by ice sheets for ~10% of the time.

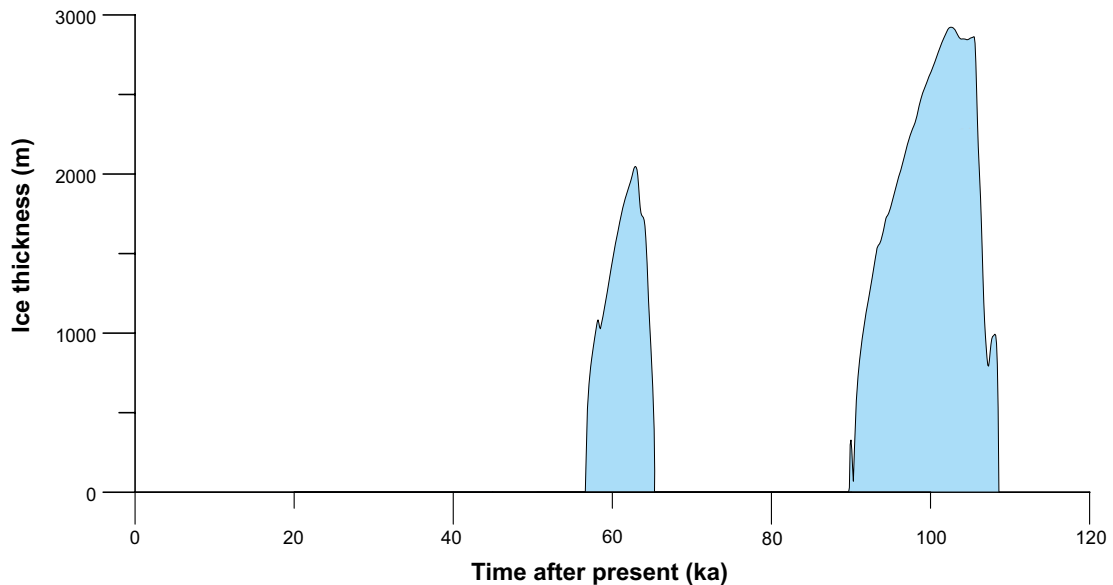


Figure 4-10. Development of ice-sheet thickness at the Forsmark site in the Weichselian glacial cycle climate case. Note that even though an ice sheet is present in Fennoscandia during most of the glacial cycle (Figure 4-8) the Forsmark site, located in south-central Sweden, is not covered by the ice sheet for the majority of the time.

In the *Weichselian glacial cycle climate case*, the Forsmark region is covered by the ice sheet for a total time of ~30 ka. For most of the ice-covered time, the numerical ice sheet modelling suggests that the site is covered by warm-based ice with free water present at the ice-bed interface. Forsmark is covered by wet-based ice for ~23 ka, corresponding to about 75% of the ice-covered time. This means that during most of the time when the ice sheet covers the site in the *Weichselian glacial cycle climate case*, meltwater is present at the ice-sheet bed, typically produced at rates of a few mm/year, up to ~10 mm/year, as seen from ice sheet modelling (e.g. Näslund et al. 2005), and hence groundwater recharge by glacial meltwater takes place.

The short periods of cold-based conditions, with no basal water production, always follow immediately after each time the site becomes ice covered. During these periods, as well as during deglaciation periods when the site is close to becoming ice free, water from *surface* melting may still reach the bed. However, in cases when the ice-sheet margin is located over permafrost ground, this melt water would not contribute significantly to groundwater recharge.

During the glacial maximum of the *Weichselian glacial cycle climate case*, at around 100 ka AP, the maximum ice-sheet thickness over Forsmark is ~2,900 m (Figure 4-10). It is worth noting that the modelled ice sheet reaches a significant thickness over the site not only during the glacial maximum, but also during the cold stadial at around 60 ka AP. At that time, the modelled maximum ice thickness is ~2,000 m.

The groundwater pressure at repository depth is, for non-glacial conditions, determined by the depth of the repository, and for glacial conditions by the repository depth as well as an additional pressure induced by the ice load. The ice-sheet thickness sets a limit to the maximum hydrostatic pressure that may occur at the ice sheet/bed interface. The additional hydrostatic pressure related to the maximum thickness in the *Weichselian glacial cycle climate case* (Figure 4-10) is 26 MPa for Forsmark.

Although not the case during the deglaciation of the Weichselian ice sheet, or in the *Weichselian glacial cycle climate case*, future periods of ice sheet-frontal stillstands cannot be excluded for the Forsmark site during ice advance, maximum or retreat phases, given suitable climate conditions. Such situations are described in SKB (2010a, Section 4.5.1). In line with the treatment of glacial erosion (Section 2.4.1), it is also here worth noting that for the shallow SFR repository it is not meaningful, or requested by the regulators, to try and describe how the repository evolves during and after ice sheet coverage. It is however requested to assess the radiological *consequences* of a potential repository collapse, following ice sheet coverage. In this context, the consequences of

a repository affected by a stillstand of the ice margin above the SFR repository, and the associated increase in groundwater flux, is covered by the safety assessment scenarios analysed in SR-PSU that include a case that assumes completely degraded concrete and no geosphere retention (SKB 2014a).

4.4.3 Shore-level evolution

At the start of a GIA model run, the Earth is assumed to be in isostatic equilibrium. In reality, the Earth is unlikely to reach such a state if glaciations occur with similar periodicity as in the past. To correct for this, the GIA-modelling, Section 2.2.4, was initiated by a glacial loading history yielding shore-levels comparable to those reported by Funder et al. (2002) at the peak of marine inundation in the Early Eemian about 130 ka before present. This gives shore-levels similar to those of the present at the early phase of the *Weichselian glacial cycle climate case*. However, during the first 1 ka AP, and for the analysis of biosphere and hydrological evolution during the initial period of temperate climate domain, the shore-level evolution is extrapolated from shore-level data (Påsse 2001). From about 8 ka AP to the end of the *Weichselian glacial cycle climate case*, the shore-level evolution is based on the GIA modelling described in Section 2.2.4.

The evolution of the Baltic Sea

During the initial phase of the *Weichselian glacial cycle climate case*, when climate is getting colder and ice sheets expand globally, global sea-levels fall. At the same time, the rate of isostatic rebound from the last glacial cycle decreases. However, even if the rate is low, the amount of remaining uplift for parts of Fennoscandia is significant. For the central parts of the Fennoscandian ice sheet it has been estimated to be ~100 m, and in the distal parts to be ~25 m. As long as the Baltic Sea is connected to the Atlantic, the relative shore-level along the Baltic Sea coast is determined by isostatic rebound and global sea-level change. If and when the relative sea-level at the Darss sill, in the southern Baltic Sea south of Denmark, falls below the sill depth (at present 18 m below mean sea-level), the Baltic Sea is transformed into a lake. The surface level of this lake is determined by the altitude of the contemporary Darss sill.

In the *Weichselian glacial cycle climate case*, results from the GIA simulations (Section 2.2.4) indicate that the Baltic Sea is isolated from the Atlantic at around 9 ka AP. However, due to the uncertainties in the GIA modelling, discussed in Section 2.2.4, it is likely that the suggested timing for this isolation is too early. Given these uncertainties, the salinity of the Baltic Sea could remain high for a considerably longer period than 9 ka AP. If extrapolation of present observed relative sea-level trends (Påsse 2001) is made, it seems unlikely that isolation of the Baltic Sea from the Atlantic would occur at all, even excluding the possibility of a considerable future global sea-level rise due to global warming.

In addition, the northern part of the Baltic Sea, i.e. the Gulf of Bothnia on which the Forsmark site is located, will be isolated from the rest of the Baltic Sea due to the remaining isostatic uplift. This occurs around 25 ka AP (Lindborg 2010), i.e. well before the onset of the first phase of glacial conditions in the Forsmark region in the *Weichselian glacial cycle climate case* (after 60 ka AP) (see Figure 4-10). The salinity in the Gulf of Bothnia is reduced as a consequence of this isolation, since the Gulf at this stage constitutes a large lake fed by freshwater from surrounding terrestrial regions. This freshwater stage is formed regardless of the isostatic and eustatic conditions in the southern Baltic Sea (Darss sill). Note that, at this stage, the Forsmark site is situated far from the shoreline of the Gulf of Bothnia due to land uplift (Lindborg 2010).

In the *Weichselian glacial cycle climate case*, the isostatic load from the first major ice sheet advance, at ~60 ka AP (Figure 4-10), most likely depresses the Gulf of Bothnia lake threshold so that the Gulf of Bothnia regains contact with the southern part of the Baltic Sea. However, it is uncertain if the Baltic Sea has contact with the Atlantic or not at this stage. The uncertainties in the GIA simulations for the southern Baltic Sea region are too large to give useful information for that region at this time. However, according to modelling studies by Lambeck et al. (2010), the Baltic may have constituted a freshwater lake during MIS 3 of the Weichselian, which corresponds to the period following the deglaciation of the first glacial period of the *Weichselian glacial cycle climate case*.

Following the deglaciation of the second and larger ice sheet coverage, at around 110 ka AP (Figure 4-10) the Baltic regains contact with the Atlantic. Given that the *Weichselian glacial cycle climate case* is based on the repetition of conditions reconstructed for the last glacial cycle (including the Holocene), the development of the Baltic Sea for this future post-glacial period is envisaged to follow the Holocene development, which includes both saline and freshwater stages. After this deglaciation, large parts of southern Sweden are submerged by a predominantly saline Baltic Sea. At the end of the *Weichselian glacial cycle climate case*, and as isostatic rebound proceeds, the Baltic Sea is transformed to an inland brackish sea, similar to today's situation.

Shore-level displacement in Forsmark

For the first 30–40 ka of the *Weichselian glacial cycle climate case*, the Forsmark site continues to rise due to post-glacial isostatic uplift. When the isostatic uplift is completed, the site is, according to the GIA simulations (Section 2.2.4), elevated ~70 m above the contemporary sea-level (Figure 4-11).

During the first glaciated period of the *Weichselian glacial cycle climate case*, at 60–70 ka AP, the Forsmark site is isostatically depressed by the weight of the ice sheet (Figure 4-10). The glacial phase is followed by interstadial ice-free conditions around 65–90 ka AP. In connection with the deglaciation that follows the first glaciated period, the isostatic depression results in the Forsmark site being situated below the Baltic Sea water level, at around 70 ka AP (Figure 4-11). In line with the description of the development of the Baltic Sea above, it is uncertain if the site during this stage is submerged by a freshwater lake only, or if the water is more saline as a result of a contact with the Atlantic.

Subsequently during this future interstadial, isostatic recovery results in the Forsmark site rising above the Baltic water level, after 75 ka AP. At this time in the *Weichselian glacial cycle climate case*, the Forsmark site is situated above sea-level, and is free of ice, for approximately 15 ka.

During the second and main phase of glaciated conditions around 100–110 ka AP (Figure 4-10) the Forsmark site is again isostatically depressed (Figure 4-11). After the deglaciation that follows this glaciated period, at around 110 ka AP, the Baltic Sea is in contact with the Atlantic and the Forsmark site is submerged by a saline sea. In line with the development of the Baltic Sea presented above, the development of salinity over the Forsmark site during this submerged period follows that of the Holocene. The site finally rises above the Baltic Sea-level again during a brackish phase at around 120 ka AP (corresponding to present-day conditions).

During periods of maximum salinity in the Baltic Sea, generally following sometime after periods of maximum glaciation, the Forsmark site is submerged (Figure 4-11).

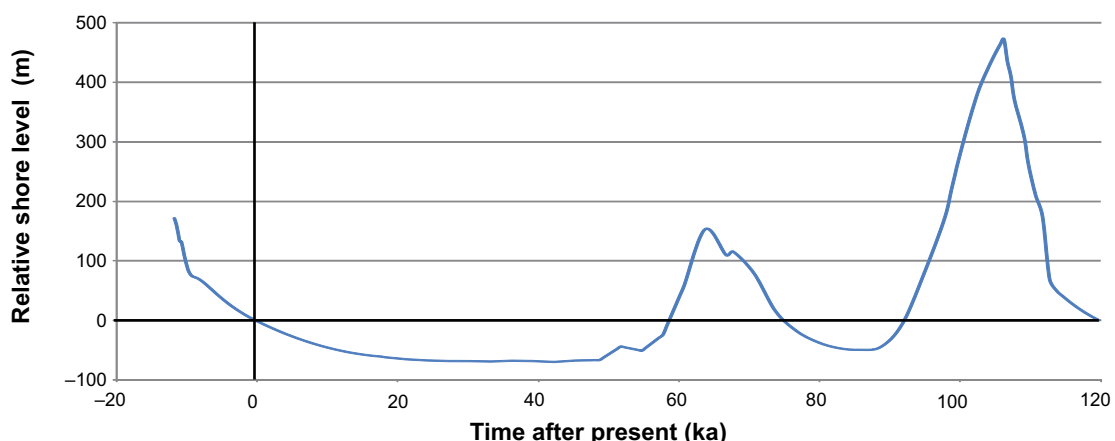


Figure 4-11. Shore-level evolution at Forsmark during the *Weichselian glacial cycle climate case*. The first c 8 ka of the future period is based on observed relative sea-level data (Påsse 2001) whereas the following part of the time series is constructed from Glacial Isostatic Adjustment modelling (Section 2.2.4). The shore-level is expressed relative to the contemporary Baltic sea-level. Positive numbers indicate that the site is submerged and vice versa. Note that for most of the time when the figure shows submerged conditions, the site is covered by an ice sheet (Figure 4-10). The figure also includes the relative shore-level from the time of deglaciation up to present, used in e.g. the SR-Site biosphere programme.

The most important factor affecting modelled shore-level displacement is the Earth structure and ice-loading history, primarily the near-field history, in this case the ice loading history of the Fennoscandian and Greenland ice sheets. The uncertainty in modelled shore-level mainly manifests itself in that reported relative sea-level values are too high, resulting from an overestimation of isostatic depression during glaciated periods, see Section 2.2.4. The size of the uncertainty varies over the modelled glacial cycle. Postulating that the ice-sheet evolution is correct, the mean overestimation of relative sea-level over the whole glacial cycle may be up to 45 m for Forsmark.

4.4.4 Permafrost evolution

The permafrost modelling is described in Section 2.1.4. The input data for geological, hydro-geological, geothermal, geochemical and geo-mechanical properties are based on site-specific descriptions and are summarised in SKB (2006a) and Hartikainen et al. (2010). In the reconstruction of last glacial cycle conditions, permafrost develops during the progressively colder phases of the glacial cycle. When the ice sheet subsequently comes to cover an area of permafrost, the permafrost typically stops developing and starts to slowly diminish. When the ground is re-exposed to cold climate conditions permafrost starts to grow again.

The permafrost model simulations used to define the *Weichselian glacial cycle climate case* were performed for the location of the planned repository for spent nuclear fuel, including the heat from the spent nuclear fuel. The timing of onset and termination of periglacial climate conditions is however representative also for the SFR location, due to small horizontal gradients in the ground temperature (Hartikainen et al. 2010). Further as described in Section 2.1.4, the timing of onset and termination of periglacial climate conditions is not significantly influenced by the heat from the planned repository for spent nuclear fuel.

In the *Weichselian glacial cycle climate case*, the development of permafrost at Forsmark starts about 7 ka AP (Figure 4-13 and Figure 4-14). However, this timing is not in accordance with present knowledge on future climate development, see Section 4.1.1.

When permafrost starts to grow over the site, it starts as sporadic permafrost (i.e. with a spatial coverage less than 50%). As the climate gets colder, discontinuous permafrost (with a spatial coverage between 50 and 90%) and continuous permafrost (more than 90% spatial coverage) form over the site. During periods of permafrost an unfrozen active layer develops above the permafrost during summer conditions. The thickness of the active layer could typically be c 40–70 cm, depending on the vegetation and soil. For a bare surface, the active layer thickness is greater, up to ~1 m.

During the permafrost development prior to the first ice-sheet advance, unfrozen taliks are formed under the two future lakes that are located along the profile (Figure 4-12). This may be exemplified by the dry climate variant of the *Weichselian glacial cycle climate case* (Figure 4-17). The upper panel shows the situation at 25 ka AP when the taliks have formed 9 and 15 km from the south-western starting point of the profile. Groundwater recharge and/or discharge are likely to occur in such taliks. The lower panel of Figure 4-17 shows the situation at 46 ka AP. At this time, permafrost growth has developed further and none of the taliks reach through the permafrost anymore. In this situation groundwater flow is heavily reduced or stopped.

The permafrost and frozen ground depth reach a maximum prior to the first major glacial advance, at about 50 ka AP. At this time, the maximum modelled permafrost depth reaches ~260 m at Forsmark (Figure 4-13 and Figure 4-14). The perennially frozen depth is, at the same time, a few tens of metres shallower. When the ice sheet advances over the site, the permafrost stops developing and instead starts to diminish, for example around 60 ka AP. Subsequently, permafrost develops again at the site during the ice-free interstadial period between the two major ice-covered periods, but at this time to a somewhat shallower depth, about 180 m (Figure 4-13). During the major phase of ice coverage, including the ice-sheet maximum at more than 100 ka AP, the maximum permafrost depth (defined by the 0°C isotherm) is around 100 m at Forsmark. Note that, at this time, the permafrost consists only of a completely unfrozen cryopeg due to the insulation effect of the ice sheet and due to the high pressure induced by the ice load. Hence all bedrock is at this time at the pressure melting point temperature (Figure 4-13).

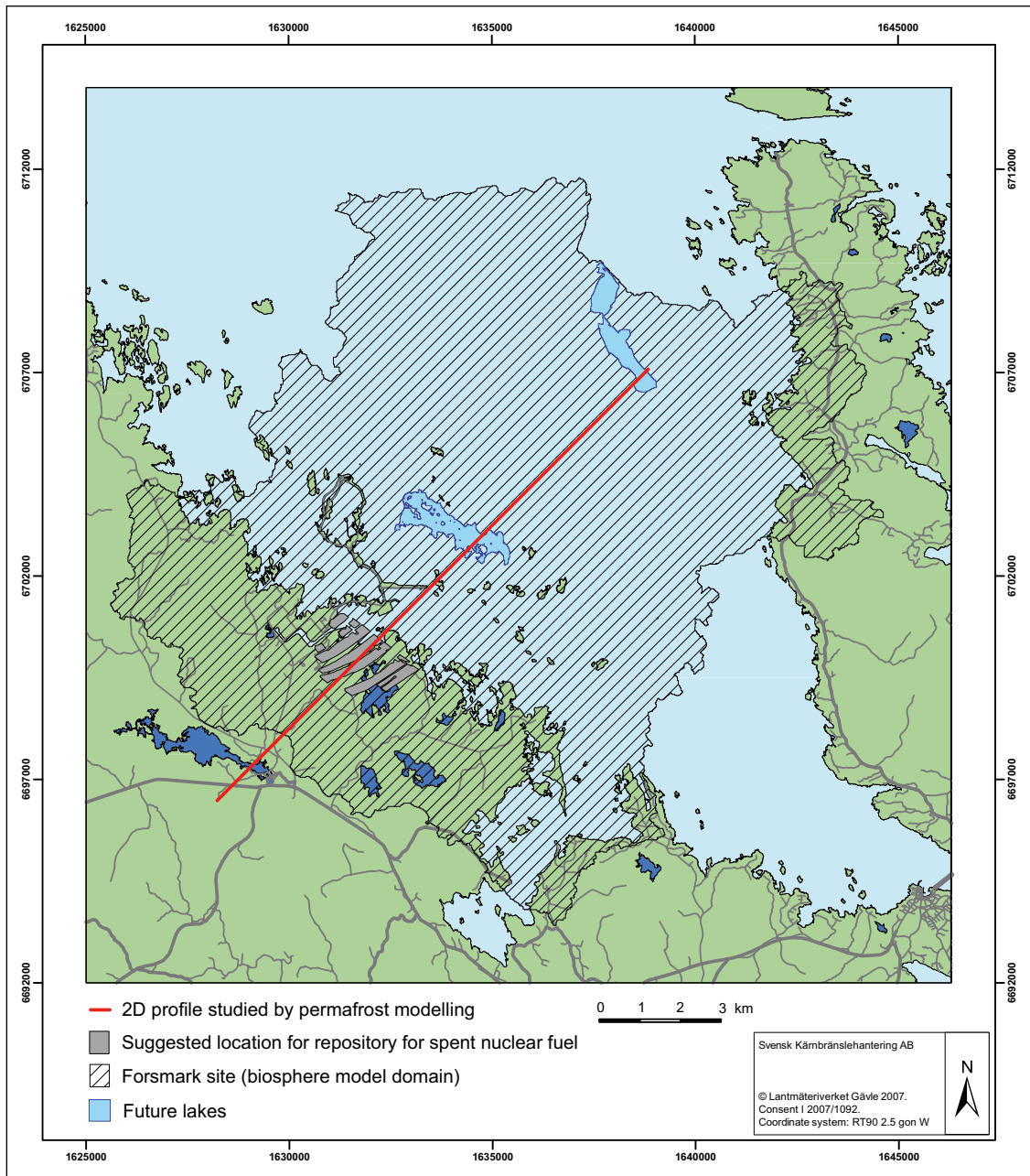


Figure 4-12. 2D profile studied in permafrost simulations, location of SFR repository and location of major future lakes along the profile.

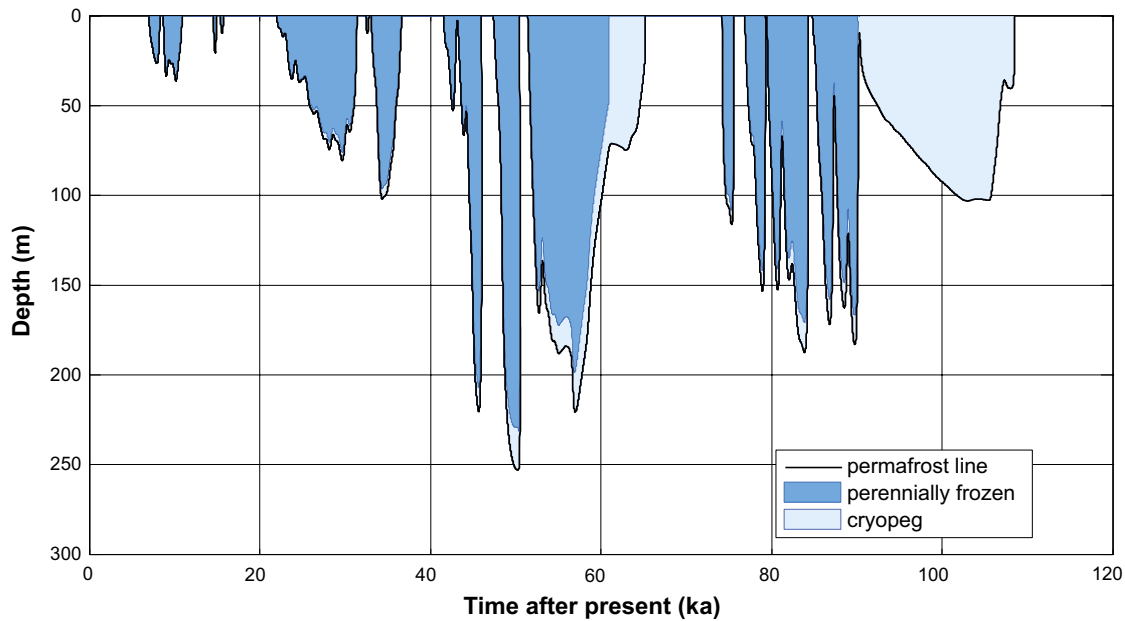


Figure 4-13. Evolution of permafrost and perennially frozen ground depth at Forsmark for the Weichselian glacial cycle climate case. The results were obtained using a 1D permafrost model (Section 2.1.4) for the location of the planned repository for spent nuclear fuel. Due to the high pressure from the ice sheet, a thick unfrozen cryopeg exists within the permafrost (defined by the 0°C isotherm) after 60 ka and 90 ka AP.

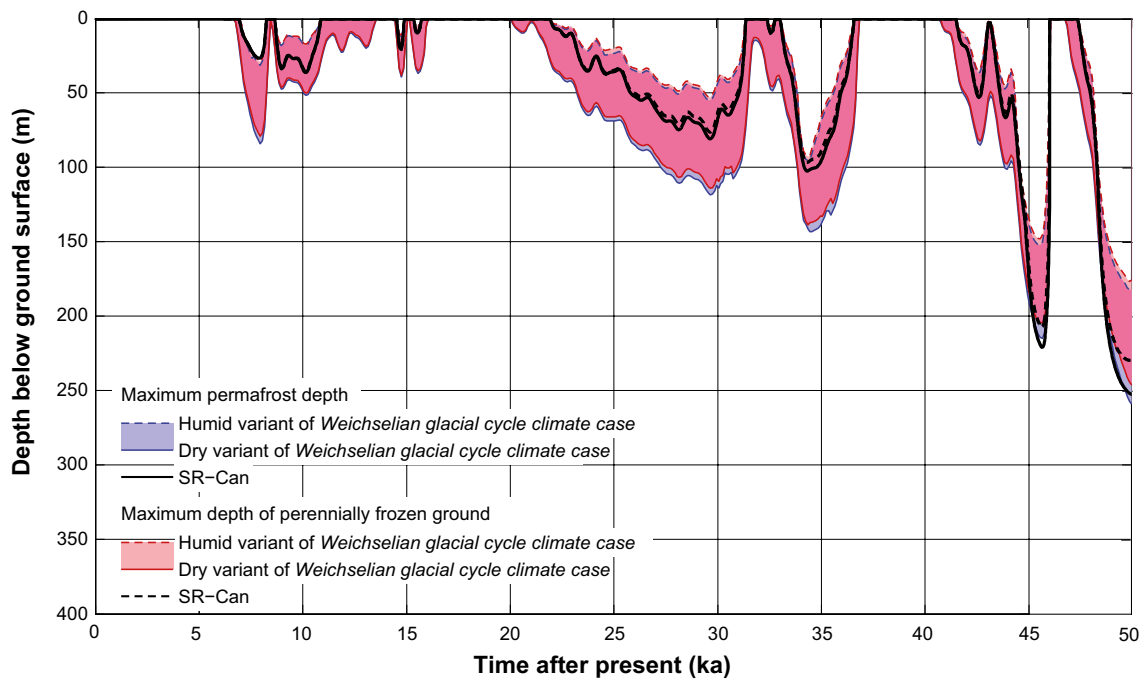


Figure 4-14. Evolution of permafrost and perennially frozen ground depth for the location of the planned repository for spent nuclear fuel the first 50 ka of the Weichselian glacial cycle climate case as simulated by the 2D and 1D permafrost models (Section 2.1.4). The shaded area in blue and red represents the range obtained from the 2D modelling when considering one dry and one humid climate variant. Further uncertainties in the permafrost modelling are discussed in Section 2.1.4. Both model simulations show that the maximum permafrost depth is ~250 m around 50 ka AP.

Some of the input data for the permafrost simulations are associated with significant uncertainty. A major uncertainty relates to the air temperature time series reconstructed for the Forsmark site for last glacial cycle, an uncertainty estimated up to $\pm 6^{\circ}\text{C}$ (SKB 2010a, Appendix 1). If this uncertainty in air temperature is combined with the uncertainty in climate humidity, the permafrost (e.g. 0°C isotherm) uncertainty range in the *Weichselian glacial cycle climate case* reach a maximum depth of ~ 410 m, while the uncertainty range for the perennially frozen ground reaches ~ 380 m (SKB 2010a, Figure 3-79).

Uncertainties related to other surface conditions (vegetation type, surface wetness, snow cover) and subsurface conditions (thermal conductivity and diffusivity, and geothermal heat flow) have a smaller impact on the simulated permafrost results. If they all are combined with the uncertainty in climate humidity, they result in a permafrost uncertainty interval down to between ~ 170 to ~ 290 m depth (SKB 2010a, Figure 3-85). This range was calculated based on the air temperature time series reconstructed for the Forsmark site for last glacial cycle excluding its uncertainty.

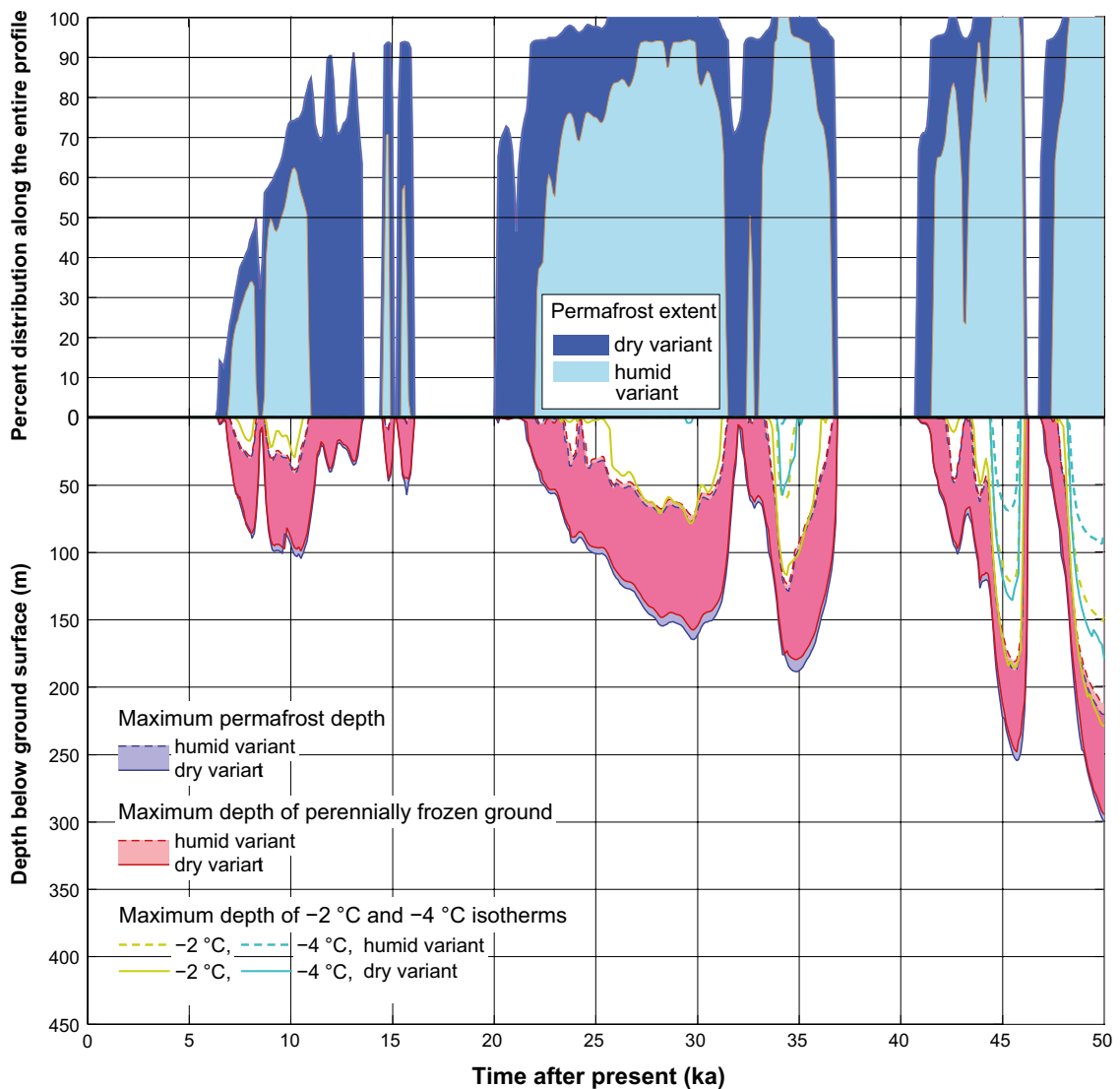


Figure 4-15. Evolution of maximum permafrost depth, maximum freezing depth and percent permafrost distribution over the entire investigated profile (Figure 4-12) for the first 50 ka of the Weichselian glacial cycle climate case. Upper part: the transition from sporadic to discontinuous permafrost occurs at 50% spatial coverage and from discontinuous to continuous permafrost at 90% coverage. Lower part: the shaded area in blue and red represents the range obtained when considering one dry and one humid climate variant of the Weichselian glacial cycle climate case. The lilac colour indicates that the results for permafrost and perennially frozen ground overlap.

Setting *all* known uncertainties (in air temperature, climate humidity, surface wetness, vegetation, snow cover, bedrock thermal conductivity and diffusivity, and geothermal heat flux) at their most extreme values favourable for permafrost growth, the permafrost uncertainty range reaches a maximum depth of ~460 m, whereas the uncertainty range for the perennially frozen ground reaches a maximum depth of ~420 m (SKB 2010a, Figure 3-86). It must be noted, however, that this most extreme combination of uncertainties is quite unrealistic. For a more detailed description of e.g. individual contributions of uncertainty from various parameters affecting permafrost growth, see Section 2.1.4 and Hartikainen et al. (2010).

The climate that may prevail in the Forsmark region during periods of periglacial climate domain was studied and exemplified by climate modelling (Kjellström et al. 2009, including erratum Feb 2010), see Section 3.2.2.

The results show that, during the interstadial between the two phases of ice-sheet coverage (Figure 4-10), the climate at Forsmark is subject to dry and cold periglacial conditions at the end of the interstadial. For the selected modelled time period (44 ka BP), the climate in the Forsmark region is considerably colder and drier than at present. The modelled mean annual air temperature is 12°C colder than at present whereas the precipitation is reduced by more than 30% (Section 3.2.2). The results of the study thus show that, when projecting the conditions from the Weichselian into the future *Weichselian glacial cycle climate case*, climate conditions are clearly favourable for permafrost growth during this cold stadial. This climatological description and several other climatic parameters reported in Kjellström et al. (2009), together give a detailed example of the climatic characteristics that may prevail at the Forsmark site during periods of periglacial climate domain. In addition to the climate modelling performed by Kjellström et al. (2009), the same study also simulated vegetation types associated with the different climate cases studied. The results of the vegetation simulations for e.g. the periglacial climate case are reported in Kjellström et al. (2009) and Lindborg (2010).

Some general conclusions about the site-specific evolution of permafrost and perennially frozen ground for the *Weichselian glacial cycle climate case* can be drawn.

- If climate permits, permafrost (i.e. the 0°C isotherm) and frozen ground gradually grows from small patches spread over the Forsmark landscape to a more persistent coverage, until a continuous cover of permafrost and frozen ground has developed. The last parts of the landscape to freeze constitute areas below major lakes, where unfrozen taliks may persist also under severe Arctic climate conditions.
- The development of permafrost at Forsmark starts about 7 ka AP and reaches a maximum depth of ~90 m around 7.5 ka AP (Figure 4-13 and Figure 4-14). It should however be noted that this timing is not in accordance with present knowledge on future climate development, see Section 4.1.1.
- The uncertainties in the input data do not significantly alter the timing of the initiation and termination of permafrost growth.
- Permafrost reaches a maximum depth of ~250 m in the *Weichselian glacial cycle climate case*.
- If considering the extreme and unrealistic combination of setting *all* known uncertainties (in air temperature, air humidity, surface wetness, vegetation, snow cover, bedrock thermal conductivity and diffusivity, and geothermal heat flux) at their values most favourable for permafrost growth, the uncertainty range for the maximum permafrost depth reaches a depth of ~460 m and for the perennially frozen ground ~420 m.

4.4.5 Surface denudation

For the *Weichselian glacial cycle climate case*, the total amount of surface denudation, i.e. the combined effect of surface erosion and weathering, is expected to be 1–2.6 m for the SFR repository location in Forsmark (Section 2.4, Table 2-8).

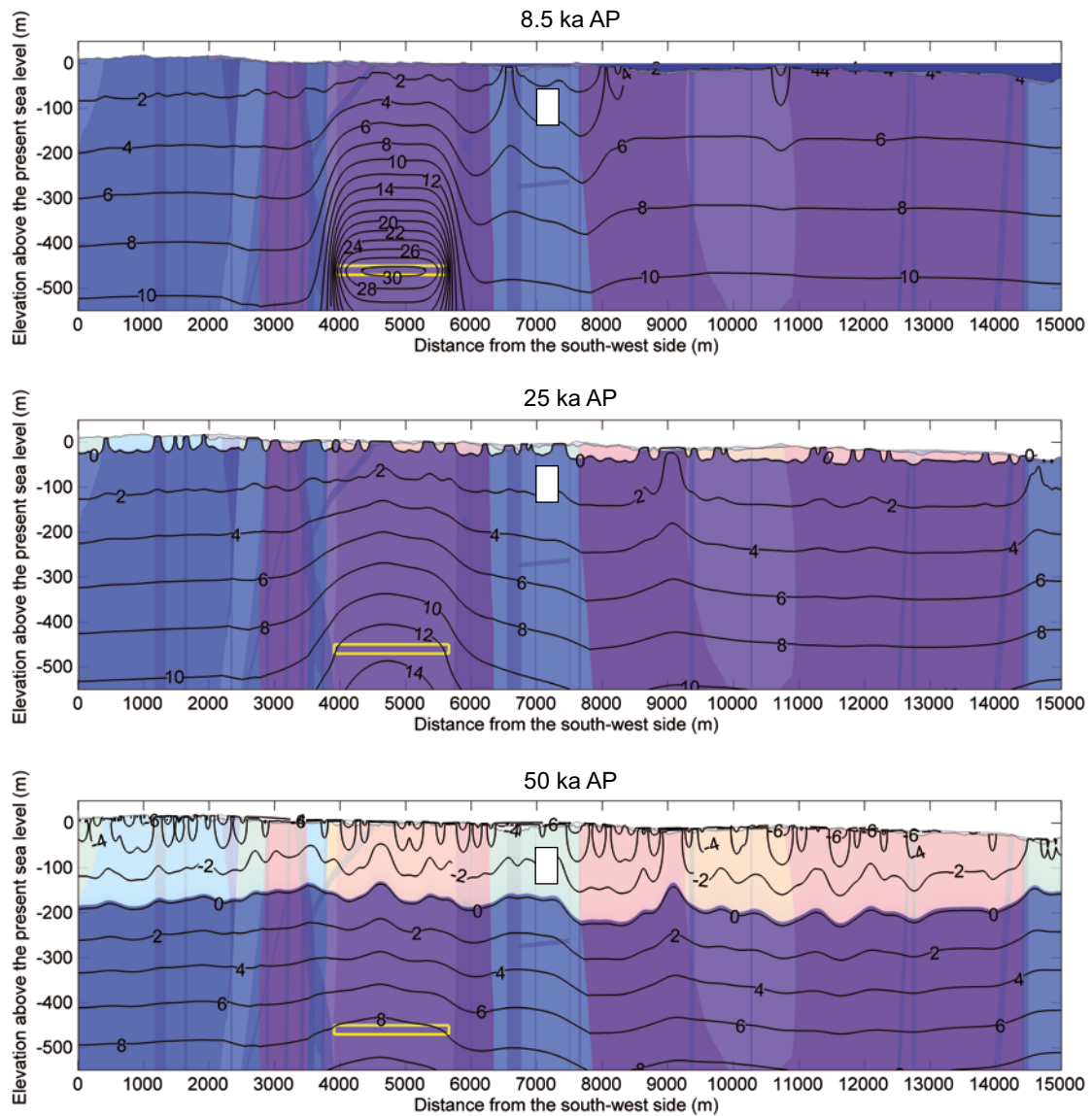


Figure 4-16. Temperature contours in (°C) and the extent of perennially frozen ground (light colour) and permafrost (0°C isotherm) at 8.5, 25 and 50 ka AP for the Weichselian glacial cycle climate case (humid climate variant, see Section 2.1.4). Blue colour on the top of the profile at 8.5 ka AP shows the Baltic Sea. The white rectangle indicates the location of the SFR repository (the box encompasses all SFR1 and SFR3 structures) and the yellow rectangle indicates the planned location of the repository for spent nuclear fuel. Vertical areas with various light colours denote different rock domains. At 8.5 ka AP (upper panel) a subarctic climate prevails. At this time, the profile is partially submerged and the exposed ground surface is partially underlain by permafrost (too thin to be seen in the figure). At 25 ka AP (middle panel) a subarctic climate prevails and discontinuous permafrost is developing. At 50 ka AP (lower panel) an arctic climate prevails and continuous permafrost reaches its maximum depth in this humid climate variant of the Weichselian glacial cycle climate case. In the dry climate variant, the permafrost grows deeper (Figure 4-15 and Figure 4-17).

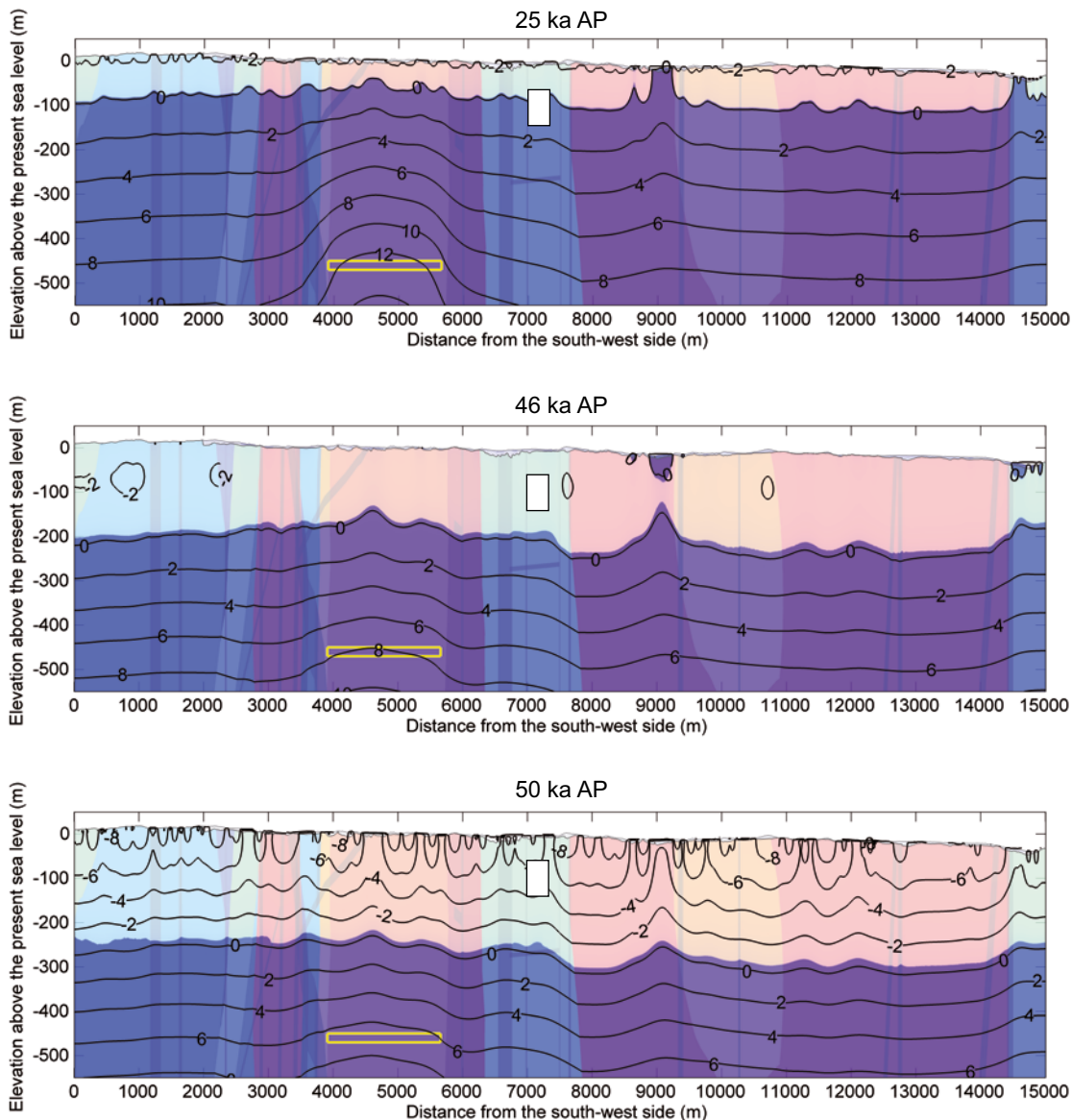


Figure 4-17. Temperature contours in ($^{\circ}\text{C}$) and the extent of perennially frozen ground (light colour) and permafrost (0°C isotherm) at 25, 46 and 50 ka AP for the Weichselian glacial cycle climate case (dry climate variant, see Section 2.1.4). The white rectangle indicates the location of the SFR repository (the box encompasses all SFR1 and SFR3 structures) and the yellow rectangle indicates the planned location of the repository for spent nuclear fuel. Vertical areas with various light colours denote different rock domains. At 25 ka AP (Upper panel) a subarctic climate prevails and continuous permafrost has developed. Two major taliks have formed under the future lakes located at c 9,000 and 14,600 m along the profile (Figure 4-12). At 46 ka AP (middle panel), the taliks are shallow, and not in contact with the deep groundwater. At 50 ka AP (lower panel) an arctic climate prevails and continuous permafrost reaches its maximum depth in the Weichselian glacial cycle climate case. The maximum permafrost depth is shallower in the humid climate variant (Figure 4-15 and Figure 4-16).

The major part of this denudation is a result of glacial erosion, occurring during phases of warm-based ice-sheet coverage. These warm-based periods of glacial erosion occur after 60 ka, and between 90 and 110 ka into the *Weichselian glacial cycle climate case* (Figure 4-18). The amount of glacial erosion at the repository location is estimated to 1–2 m for this glacial cycle (Table 2-8). This relatively low amount of expected glacial erosion is a result of the very flat topography in the area, and that the erosional capacity of the ice sheet is relatively small (compared with considerably more active erosion by more active ice sheets or smaller glaciers in other climatological and topographic settings, such as along the Norwegian coast or alpine environments). For examples of various glacial erosion rates from different climatological and topographic environments see Olvmo (2010) and references therein.

The non-glacial component of surface denudation, resulting from all other active erosion and weathering processes, such as weathering and fluvial erosion during temperate- and periglacial climate conditions, is estimated to be up to 0.6 m for the *Weichselian glacial cycle climate case* (Table 2-8).

All in all, the total denudation for the *Weichselian glacial cycle climate case* is estimated to be limited at Forsmark (less than 3 m), since the area is dominated by the well-preserved sub-Cambrian peneplain (Section 2.4). The dissected area with sometimes considerable relief in the coastal areas, some 25 km south-east of Forsmark, may experience considerably more efficient glacial erosion during a glaciation. In this area, glacial erosion of more than 10 m is expected locally in low topographic positions. However, this is not the case for Forsmark.

4.4.6 Evolution of climate domains

Based on the above evolutions of ice sheet, shore-level and permafrost, the temporal evolution of the climate domains is presented in Figure 4-18. Considering that the development of permafrost in Figure 4-18 has been simulated specifically for the location of the planned repository for spent nuclear fuel (Section 2.1.4 and 4.4.4), the development of climate domains in Figure 4-18 also refers specifically to this location. The main difference between the locations is that the SFR repository is currently submerged, while the location for the planned repository for spent nuclear fuel is not. For a description of the spatial representativity and development of the climate domains, see the Section on *Rationale and general approach* for the SR-PSU climate cases.

At Forsmark, periods with periglacial climate domain correspond to 34% of the total time of the *Weichselian glacial cycle climate case* (Table 4-9), whereas periods with temperate climate domain occupies 26%, the glacial climate domain 24% and periods with submerged conditions 16% of the *Weichselian glacial cycle climate case*, see also Table 4-9.

The climate succession bar in Figure 4-18 shows that the Forsmark site is dominated by temperate climate conditions for the first ~25 ka of the *Weichselian glacial cycle climate case*, although shorter periods of periglacial climate domain occur around 10 ka AP. Subsequently, up to the first period of glacial climate domain, temperate conditions are gradually replaced by periglacial conditions.

Table 4-9. Duration of climate domains in the Weichselian glacial cycle climate case.

Climate domain	Duration (% of Weichselian glacial cycle climate case)	Duration (years)
Temperate climate domain	26%	31,200
Periglacial climate domain	34%	40,800
Glacial climate domain	24%	28,200
Submerged conditions	16%	19,200

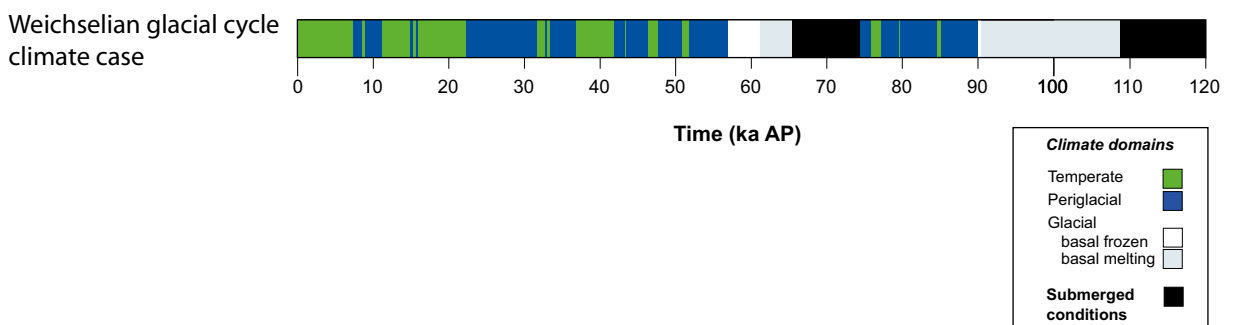


Figure 4-18. Evolution of important climate-related variables at Forsmark for the coming 120 ka in the *Weichselian glacial cycle climate case*.

The ice-free interstadial period around 80–90 ka AP is dominated by permafrost conditions. The general trend with gradually more dominating permafrost conditions is a natural result of the progressively colder climate during the glacial cycle. An exception to this trend is the short period after the submerged phase that follows the final deglaciation, at the very end of the scenario. At that time, ice-free conditions are again dominated by temperate conditions in a warm interglacial climate. Yet another effect of the progressively colder climate during the glacial cycle is the increasing length of the periods with glacial climate domain.

Periods of temperate climate domain occur in Forsmark in the early phase of the glacial cycle, during short periods of the interstadial between the two major ice advances, and during the interglacial period following the glacial maximum. The periods of temperate climate domain in the early phases of the *Weichselian glacial cycle climate case* are generally warmer and longer than those occurring during interstadials in the later part of the glacial.

During the first 50 ka of the *Weichselian glacial cycle climate case*, and in the period between the two ice advances, the increasingly colder climate results in progressively longer periods of periglacial conditions. The total duration of the periglacial climate domain at Forsmark is about 41 ka (Table 4-9). During the most severe permafrost periods in the *Weichselian glacial cycle climate case*, at around 70 ka BP (Figure 4-18), the permafrost at the repository location develops to between ~180 and ~250 m depth depending on assumed ground cover. The corresponding depths of perennially frozen conditions are between ~180 and ~250 m. The maximum permafrost depth along the entire profile investigated for permafrost development (Figure 3-19) is between 220 and 300 m for the same simulation. The maximum depth of perennially frozen ground along the profile is from 210 to 300 m. The uncertainties related to the simulated permafrost depths are described in Section 2.1.4 and 3.2.3.

Forsmark is exposed to two major ice advances and retreats during the *Weichselian glacial cycle climate case*, the first advance occurs around 60 ka AP and the second after about 90 ka AP (Figure 4-18). Prior to both of these glaciated periods, the Forsmark site is situated above sea-level with prevailing permafrost conditions when the ice sheet advances towards and over the site. A period of basal frozen conditions initiates the first major period of glacial climate domain. The period of basal frozen conditions is ~4 ka long.

After the first glacial period, the site is submerged under the Baltic Sea (Figure 4-18). Following from the warm climate conditions reconstructed for the first part of MIS 3 during the Weichselian (Section 3.2.2), with present-day air temperatures during summer in northern Fennoscandia, temperate climate conditions are envisaged to prevail at Forsmark during the first several thousands of years of the submerged period (not seen in Figure 4-18). That is, if the site were not submerged after the first glacial period, due to a thinner ice sheet and less isostatic depression, subaerial temperate climate conditions would prevail at the site for considerable amount of time after ~66 ka AP.

The landscape is in a state of continuous permafrost coverage during the time of the first ice advance over the site, at around 70 ka AP (Figure 4-15 and Figure 4-18). At this time, all present and future lakes at the Forsmark site are infilled (Lindborg 2010), and hence there are no taliks present under lakes.

When the ice sheet expands over the site, it insulates the ice-sheet bed from the cold air temperatures and in time induces ice-sheet basal melting conditions. During periods of ice sheet coverage, the development of subglacial permafrost is more restricted than permafrost development during ice-free conditions (Figure 4-18). The total length of periods of glacial climate domain in the *Weichselian glacial cycle climate case* is 28 ka at Forsmark (Table 4-9). During this time, basal melting conditions dominate.

For detailed examples of how the climate may be characterised in Sweden and in the Forsmark region under periglacial and glacial conditions, see the exemplified climates of the Weichselian glacial cycle in Section 3.2.2.

The climate simulations (Kjellström et al. 2009) show that there is a large range in possible climates for the Fennoscandian region in a 100 ka time perspective. Excluding the situation when the region is covered by an ice sheet, annual mean air temperatures for the Forsmark region vary from the simulated cold MIS 3 stadial climate (Section 3.2.2) to the future warm climate (Section 3.3.6) by 12–15°C. Correspondingly, annual mean precipitation is almost a factor two higher in the future warm climate compared with MIS 3 at these sites.

The sequence of main climate-related events for the *Weichselian glacial cycle climate case*, including times of transitions between events and corresponding climate domains, is summarised in Table 4-10.

Table 4-10. Sequence of climate-related events for the Weichselian glacial cycle climate case, including the full Holocene. The same sequence of events is seen in Figure 4-18.

Event	Time for transition between events	Climate domain
Deglaciation / start of the Holocene interglacial (locally defined)	10.8 ka BP (8800 BC)	–
Holocene interglacial	–	Temperate climate domain (incl. submerged conditions)
Present	0 BP	
End of Holocene interglacial (locally defined as first occurrence of permafrost in Weichselian glacial cycle climate case)	7 ka AP (9000 AD)	–
Periglacial and temperate conditions (progressively longer periods of permafrost conditions)	–	Periglacial- and temperate climate domains (progressively shorter phases of temperate climate conditions)
End of periglacial and temperate conditions. Start of glacial conditions	57.6 ka AP (59,600 AD)	–
First phase with glacial conditions	–	Glacial climate domain
Deglaciation at site. Start interstadial conditions	66.2 ka AP (68,200 AD)	–
Interstadial conditions	–	Mainly periglacial climate domain (incl. submerged conditions and short temperate periods)
End of interstadial conditions. Start of glacial conditions	90.8 ka AP (92,800 AD)	–
Second and main phase with glacial conditions	–	Glacial climate domain
Deglaciation/start of interglacial (locally defined as time of deglaciation of Forsmark)	109.5 ka AP (111,500 AD)	–

4.5 Summary of climate cases for the SR-PSU safety assessment

As stated in Section 1.3.2, a single most likely future climate evolution cannot be predicted on the SR-PSU assessment time-scale. This 100 ka time scale corresponds to the glacial cycle time scale during the past 900 ka. The selected approach in previous safety assessments for spent nuclear fuel (SR-Can and SR-Site) and for low- and intermediate-level waste (SAR-08) was therefore to define one climate case as a repetition of conditions reconstructed for the last glacial cycle. This climate case was complemented with a number of alternative future climate evolutions with potentially different impacts on repository safety. Due to the specific questions to be answered in the SR-PSU safety assessment, the strategy for defining relevant climate cases is partly different. Specifically, the question of the timing of the first future period of permafrost and freezing conditions is of interest for SR-PSU, whereas the maximum freezing depth is not. This is a fundamental difference compared to SR-Site where the situation was the opposite. The repository concept (barrier material, repository depth etc) and total assessment time (100 ka or 1 Ma) means that the questions to be answered, and the climate cases built to answer them, need to be different between e.g. SR-Site and SR-PSU, see also Näslund et al. (2013).

Current scientific knowledge on future climate evolution, reviewed in Section 3.3, suggests that the combination of human intervention and relatively small-amplitude variations in insolation will lead to a global climate evolution in the next 100,000 years which is significantly different from previous glacial cycles. Therefore, the *Weichselian glacial cycle climate case* is not suitable for the analysis of e.g. timing of the first future freezing of SFR. Instead, it has been included in the safety assessment in order to cover remaining uncertainties regarding the presence of an ice sheet during the next 100 ka after the analysis of the other climate cases *and* also as point of reference for the other climate cases.

Figure 4-19 and Table 4-11 summarise the climate developments included in the SR-PSU safety assessment. These cases are based on the processes that have been identified as important for long-term repository safety and on the present scientific knowledge and uncertainties of future climate development with focus on these processes. The climate cases in Figure 4-19 are used as input to the description and analysis of various SR-PSU safety assessment scenarios, see Figure 1-4 and SKB (2014a).

The *global warming climate case* (Section 4.1) represents a potential future climate evolution under intermediate carbon emissions, as defined by the IPCC, to the atmosphere. In this climate case, the current interglacial is extended to 50 ka AP. Subsequently, the climate variability of the reconstructed last glacial cycle is assumed.

The *early periglacial climate case* (Section 4.2) represents a potential future climate evolution under low carbon emissions, as defined by the IPCC, to the atmosphere. In this climate case, the current interglacial is interrupted at 15.5 ka AP by a shorter period of periglacial climate conditions. Temperate climate conditions are then assumed to prevail until 50 ka AP and natural climate variability is assumed after this.

The *extended global warming climate case* (Section 4.3) represents a potential future climate evolution under high carbon emissions, as defined by the IPCC, to the atmosphere. In this climate case, the current interglacial is extended to 100 ka AP due to human intervention. This climate case represents temperate climate conditions in Forsmark for the complete 100 ka assessment period, including an initial period with the warmest and wettest climate conditions, highest sea-level, as well as longest period of groundwater composition defined by precipitation.

The *Weichselian glacial cycle climate case* (Section 4.4) is defined as a repetition of the climate evolution reconstructed for the last glacial cycle.

These climate cases together cover the expected maximum range within which climate and climate-related conditions of importance for long-term repository safety may vary within the 100 ka time scale analysed in the SR-PSU safety assessment.

The approach in the SR-PSU safety assessment is to handle *all* possible future climate developments relevant to repository safety. Therefore, the probability of each climate case is not quantified. A distinction is however made for the *Weichselian glacial cycle climate case*, which is not considered relevant, in terms of the first occurrence of periglacial conditions, on a 100 ka time scale based on current scientific knowledge. The four climate cases presented here span the uncertainty range for the future climate evolution in Forsmark in the next 100 ka.

Table 4-11. Summary of duration of climate domains for the four climate cases in SR-PSU. For definitions of the climate domains, see Section 1.3.2.

Climate case	Temperate climate domain [ka] (percent of assessment period)	Periglacial climate domain [ka] (percent of assessment period)	Glacial climate domain [ka] (percent of assessment period)	Submerged conditions [ka] (percent of assessment period)
<i>Extended global warming</i> (Section 4.3)	100 ka (100%)	0 ka (0%)	0 yrs (0%)	1.8 ka (2%)
<i>Global warming</i> (Section 4.1)	69 ka (69%)	31 ka (31%)	0 ka (0%)	0.6 ka (< 1%)
<i>Early periglacial</i> (Section 4.2)	66 ka (66%)	34 ka (34%)	0 ka (0%)	0.6 ka (<1%)
<i>Weichselian glacial cycle</i> (Section 4.4)	31 ka (26%)	41 ka (34%)	28 ka (24%)	19 ka (16%)

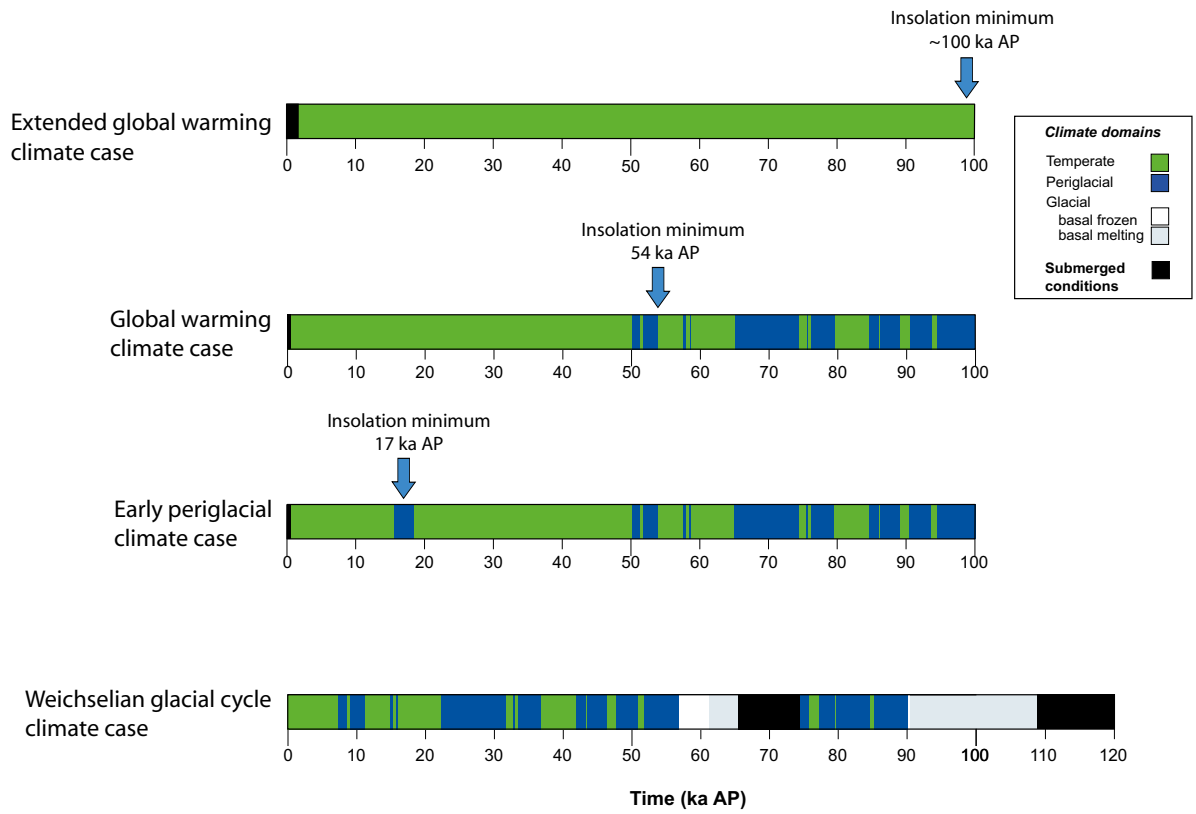


Figure 4-19. Summary of future climate cases analysed in the SR-PSU safety assessment. The cases go from warmer/wetter climates at the top to colder/dryer climates at the bottom.

5 List of abbreviations

Except expressions in equations, chemical expressions and common units

1D	One dimensional
2D	Two dimensional
3D	Three dimensional
A1B	IPCC emission scenario
A2	IPCC emission scenario
AD	Anno Domini
AMOC	Atlantic Meridional Overturning Circulation
AOGCM	Atmosphere-Ocean General Circulation Model
AP	After Present
AR4	Fourth Assessment Report of IPCC
AR5	Fifth Assessment Report of IPCC
B2	IPCC emission scenario
BC	Before Christ
BIFROST	Baseline Inferences for Fennoscandian Rebound, Sea-level, and Tectonics
BIOCLIM	Modelling sequential BIOSphere systems under CLIMate change for radioactive waste disposal
BP	Before Present
CCSM3	Community Climate System Model 3
CRU	Climate Research Unit (East Anglia)
CMIP3	Climate Model Intercomparison Project, phase 3
CMIP5	Climate Model Intercomparison Project, phase 5
DEM	Digital Elevation Model
DJF	December, January, February (winter season)
EAIS	East Antarctic Ice Sheet
EISMINT	European Ice Sheet Modeling Initiative
ELA	Equilibrium Line Altitude
EMIC	Earth System Model of Intermediate Complexity
EPICA	European Project for Ice Coring in Antarctica
ESM	Earth System Model
ETOP02	Global Digital Elevation Model
FEP	Features, Events and Processes
GAP	Greenland Analogue Project
GCM	General Circulation Model, Global Circulation Model
GI	Greenland Interstadial
GIA	Glacial Isostatic Adjustment
GIS	Geographical Information System
GISP2	Greenland Ice Sheet project 2
GPS	Global Positioning System
GRACE	Gravity Recovery and Climate Experiment
GRIP	European Greenland Ice Core Project
GS	Greenland Stadial
HadCM3	Hadley Centre Coupled Climate Model, version 3
HFD	Heat Flow Density <i>or</i> geothermal heat flow
ICE-3G	Global ice sheet reconstruction
ICE-5G	Global ice sheet reconstruction
InSAR	Interferometric Synthetic Aperture Radar
IPCC	Intergovernmental Panel on Climate Change
JJA	June, July, August (summer season)
ka	kilo annum (thousands of years)
KBS-3	Kärnbränslesäkerhet 3 (method for final storage of spent nuclear fuel)

KTH	Royal Institute of Technology (Stockholm)
LGM	Last Glacial Maximum
LLN 2-D NH	the Louvain-la-Neuve two-dimensional Northern Hemisphere climate model
LOVECLIM	LOch–Vecode-Ecbilt-CLio-agIsm Model
LPJ-GUESS	A dynamic vegetation model
Ma	Mega annum (millions of years)
MIS	Marine Isotope Stage
MPa	Mega Pascal (million Pascal)
NAC	North Atlantic Cold event
NAW	North Atlantic Warm event
NCAR	National Center for Atmospheric Research (USA)
NEA	Nuclear Energy Agency
NEEM	The North Greenland Eemian Ice Drilling
NGRIP	North Greenland Ice core Project
NH	Northern Hemisphere
NSF	National Science Foundation (USA)
NWMO	Nuclear Waste Management Organization (Canada)
PMIP	Paleoclimate Modelling Intercomparison Project
PREM	Preliminary Reference Earth Model
QA	Quality Assurance
RCA 3	Rosby Centre Regional Climate Model
RCM	Regional Climate Model
RCP2.6	IPCC representative concentration pathway
RCP4.5	IPCC representative concentration pathway
RCP6	IPCC representative concentration pathway
RCP8.5	IPCC representative concentration pathway
RH70	Rikets höjdsystem 1970 (national elevation system in Sweden)
RP	Recent Past
RP-r	RCA3 simulation of the present climate
RT-90	Rikets Triangelnät 1990 (national coordinate system in Sweden)
RH2000	Rikets höjdsystem 2000 (national elevation system in Sweden)
SAR-08	Long-term safety assessment for the repository for low- and intermediate-level waste, SFR (SKB 2008)
SAT	Surface air temperature
SCAR	Scientific Committee on Antarctic Research
SCM	Simple Climate Model
SFR	Repository for short-lived low- and intermediate level waste
SGU	Geological Survey of Sweden
SKB	Swedish Nuclear Fuel and Waste Management Company
SMHI	Swedish Meteorological and Hydrological Institute
SRES	Special Report on Emission Scenarios
SR-Can	Long-term safety assessment for the final repository for spent nuclear fuel (SKB 2006)
SR-Site	Long-term safety assessment for the final repository for spent nuclear fuel at Forsmark (SKB 2011)
SSE	South south east
SST	Sea Surface Temperature
SWECLIM	Swedish Regional Climate Modelling Programme
THM	Thermo-Hydro-Mechanical
TWI	Topographic Wetness Index
UMISM	University of Maine Ice Sheet Model
UNFCCC	United Nation's Framework Convention on Climate Change
WAIS	West Antarctic Ice Sheet

References

SKB's (Svensk Kärnbränslehantering AB) publications can be found at www.skb.se/publications.

- Abe-Ouchi A, Saito F, Kawamura K, Raymo M E, Okuno J, Takahashi K, Blatter H, 2013.** Insolation-driven 100,000-year glacial cycles and hysteresis of ice-sheet volume. *Nature* 500, 190–193.
- Ahonen L, 2001.** Permafrost: occurrence and physicochemical processes. Helsinki: Posiva.
- Allen D, Michel F, Judge A, 1988.** Paleoclimate and permafrost in the Mackenzie Delta. In Proceedings of the fifth international conference on permafrost. Trondheim, 2–5 August 1988. Vol 1. Trondheim: Tapir.
- Alley R B, 1992.** Flow-law hypotheses for ice-sheet modeling. *Journal of Glaciology* 38, 245–256.
- Andersen B G, Mangerud J, 1989.** The last interglacial-glacial cycle in Fennoscandia. *Quaternary International* 3–4, 21–29.
- Andrews J T, Barber D C, 2002.** Dansgaard-Oeschger events: is there a signal off the Hudson Strait Ice Stream? *Quaternary Science Reviews* 21, 443–454.
- Archer D, Ganopolski A, 2005.** A movable trigger: Fossil fuel CO₂ and the onset of the next glaciation. *Geochemistry, Geophysics, Geosystems* 6, Q05003. doi:10.1029/2004GC000891
- Archer D, Eby M, Brovkin V, Ridgwell A, Cao L, Mikolajewicz U, Caldeira K, Matsumoto K, Munhoven G, Montenegro A, Tokos K, 2009.** Atmospheric lifetime of fossil fuel carbon dioxide. *Annual Review of Earth and Planetary Sciences* 37, 117–134.
- Árnadóttir T, Lund B, Jiang W, Geirsson H, Björnsson H, Einarsson P, Sigurdsson T, 2009.** Glacial rebound and plate spreading: results from the first countrywide GPS observations in Iceland. *Geophysical Journal International* 177, 691–716.
- Artemieva I M, Mooney W D, 2001.** Thermal thickness and evolution of Precambrian lithosphere: a global study. *Journal of Geophysical Research* 106, 16387–16414.
- Balling N, 1984.** Gravity and isostasy in the Baltic Shield. In Galson D A, Mueller S, Munch B (eds). Proceedings of the first workshop on the European Geotraverse Project (EGT): The northern segment. Strasbourg: European Science Foundation, 53–66.
- Bamber J L, Riva R E M, 2010.** The sea-level fingerprint of 21st century ice mass flux. *The Cryosphere Discussions* 4, 1593–1606.
- Bamber J L, Riva R E M, Vermeersen B L A, LeBrocq A M, 2009.** Reassessment of the potential sea-level rise from a collapse of the West Antarctic ice sheet. *Science* 324, 901–903.
- Bard E, Hamelin B, Fairbanks R G, 1990.** U-Th ages obtained by mass spectrometry in corals from Barbados: sea-level during the past 130,000 years. *Nature* 346, 456–458.
- Bard E, Hamelin B, Arnold M, Montaggioni L, Cabioch G, Faure G, Rougerie F, 1996.** Deglacial sea-level record from Tahiti corals and the timing of global meltwater discharge. *Nature* 382, 241–244.
- Bassett S E, Milne G A, Mitrovica J X, Clark P U, 2005.** Ice sheet and solid Earth influences on far-field sea-level histories. *Science* 309, 925–928.
- Bauder A, Mickelson D M, Marshall S J, 2003.** Modelling ice sheet permafrost interaction around the southern Laurentide ice sheet. EGS - AGU - EUG Joint Assembly. Abstracts from the meeting held in Nice, France, 6–11 April 2003, abstract 12348.
- Beardmore G R, Cull J P, 2001.** Crustal heat flow: a guide to measurement and modelling. Cambridge: Cambridge University Press.
- Benn D I, Evans D J A, 1998.** *Glaciers & glaciation*. London: Arnold.
- Bennett M R, Waller R I, Midgley N G, Huddart D, Gonzalez S, Cook S J, Tomio A, 2003.** Subglacial deformation at sub-freezing temperatures? Evidence from Hagafellsjökull-Eystrí, Iceland. *Quaternary Science Reviews* 22, 915–923.

- Berger A, 1978.** Long-term variations of daily insolation and Quaternary climatic changes. *Journal of the Atmospheric Sciences* 35, 2362–2367.
- Berger A, Loutre M F, 1991.** Insolation values for the climate of the last 10 million years. *Quaternary Science Reviews* 10, 297–317.
- Berger A, Loutre M F, 2002.** An exceptionally long interglacial ahead? *Science* 297, 1287–1288.
- Bills B G, James T S, 1996.** Late Quaternary variations in relative sea level due to glacial cycle polar wander. *Geophysical Research Letters* 23, 3023–3026.
- BIOCLIM, 2003.** Deliverable D7. Continuous climate evolution scenarios over western Europe (1000 km scale). Work package 2: Simulation of the future evolution of the biosphere system using the hierarchical strategy. Châtenay-Malabry: Andra.
- Birch F, Roy R F, Decker E R, 1968.** Heat flow and thermal history in New England and New York. In Zen E-an (ed). *Studies of Appalachian geology: northern and maritime*. New York: Interscience, 437–451.
- Björck S, 1995.** A review of the history of the Baltic Sea, 13.0–8.0 ka BP. *Quaternary International* 27, 19–40.
- Bos J A A, Helmens K F, Bohncke S J P, Seppä H, Birks H J B, 2009.** Flora, vegetation and climate at Sokli, northeastern Fennoscandia, during the Weichselian Middle Pleniglacial. *Boreas* 38, 335–348.
- Bosson E, Lindborg T, Berglund S, Gustafsson L-G, Selroos J-O, Laudon H, Claesson L L, Destouni G, 2013.** Water balance and its intra-annual variability in a permafrost catchment: hydrological interactions between catchment, lake and talik. *Hydrology and Earth System Sciences Discussions* 10, 9271–9308.
- Boulton G S, Clark C D, 1990.** The Laurentide Ice Sheet through the last glacial cycle: the topology of drift lineations as a key to the dynamic behaviour of former ice sheets. *Transactions of the Royal Society of Edinburgh: Earth Sciences* 81, 327–347.
- Boulton G S, Payne A, 1992.** Simulation of the European ice sheet through the last glacial cycle and prediction of future glaciation. SKB TR 93-14, Svensk Kärnbränslehantering AB.
- Boulton G S, Kautsky U, Morén L, Wallroth T, 2001.** Impact of long-term climate change on a deep geological repository for spent nuclear fuel. SKB TR-99-05, Svensk Kärnbränslehantering AB.
- Braconnot P, Otto-Bliesner B, Harrison S, Joussaume S, Peterchmitt J-Y, Abe-Ouchi A, Crucifix M, Driesschaert E, Fichefet T, Hewitt C D, Kageyama M, Kitoh A, Laíné A, Loutre M-F, Marti O, Merkel U, Ramstein G, Valdes P, Weber S L, Yu Y, Zhao Y, 2007.** Results of PMIP2 coupled simulations of the Mid-Holocene and Last Glacial Maximum – Part 1: experiments and large-scale features. *Climate of the Past* 3, 261–277.
- Brandefelt J, Otto-Bliesner B L, 2009.** Equilibrium and variability in a Last Glacial Maximum climate simulation with CCSM3. *Geophysical Research Letters* 36, L19712 doi:10.1029/2009GL040364
- Brandefelt J, Kjellström E, Näslund J-O, Strandberg G, Voelker A H L, Wohlfarth B, 2011.** A coupled climate model simulation of Marine Isotope Stage 3 stadial climate. *Climate of the Past* 7, 649–670.
- Brandefelt J, Zhang Q, Hartikainen J, Näslund J-O, 2013.** The potential for cold climate conditions and permafrost in Forsmark in the next 60,000 years. SKB TR-13-04, Svensk Kärnbränslehantering AB.
- Brydsten L, Engqvist A, Näslund J-O, Lindborg T, 2009.** Expected extreme sea levels at Forsmark and Laxemar-Simpevarp up until year 2100. SKB TR-09-21, Svensk Kärnbränslehantering AB.
- Calcagnile G, 1982.** The lithosphere asthenosphere system in Fennoscandia. *Tectonophysics* 90, 19–35.
- Čermák V, Balling N, Kukkonen I, Zui V I, 1993.** Heat flow in the Baltic Shield – results of the lithospheric geothermal modelling. *Precambrian Research* 64, 53–65.
- Chapman M R, Shackleton N J, 1999.** Global ice-volume fluctuations, North Atlantic ice-rafting events, and deep-ocean circulation changes between 130 and 70 ka. *Geology* 27, 795–798.

- Chappell J, Polach H, 1991.** Post-glacial sea-level rise from a coral record at Huon Peninsula, Papua New Guinea. *Nature* 349, 147–149.
- Chappell J, Omura A, Esat T, McCulloch M, Pandolfi J, Ota Y, Pillans B, 1996.** Reconciliation of late Quaternary sea levels derived from coral terraces at Huon Peninsula with deep sea oxygen isotope records. *Earth and Planetary Science Letters* 141, 227–236.
- Church J A, Clark P U, Cazenave A, Gregory J M, Jevrejeva S, Levermann A, Merrifield M A, Milne G A, Nerem R S, Nunn P D, Payne A J, Pfeffer W T, Stammer D, Unnikrishnan A S, 2013.** Sea level change. In Stocker T F, Qin D, Plattner G-K, Tignor M, Allen S K, Boschung J, Nauels A, Xia Y, Bex V, Midgley P M (eds). *Climate change 2013: the physical science basis: Working Group I Contribution to the Fifth Assessment Report of the Intergovernmental Panel on Climate Change*. Cambridge: Cambridge University Press, 1137–1216. (The report has to be read in conjunction with the document entitled “Climate change 2013: the physical science basis. Working Group I Contribution to the IPCC 5th Assessment Report – Changes to the underlying scientific/technical assessment”. Available at: <http://www.ipcc.ch>.)
- Clarhäll A, 2011.** SKB studies of the periglacial environment – report from field studies in Kangerlussuaq, Greenland 2008 and 2010. SKB P-11-05, Svensk Kärnbränslehantering AB.
- Clark J A, Farrell W E, Peltier W R, 1978.** Global changes in postglacial sea level: a numerical calculation. *Quaternary Research* 9, 265–287.
- Clark P U, Mix A C, 2002.** Ice sheets and sea level of the Last Glacial Maximum. *Quaternary Science Reviews* 21, 1–7.
- Clark P U, Alley R B, Keigwin L D, Licciardi J M, Johnsen S J, Wang H X, 1996.** Origin of the first global meltwater pulse following the Last Glacial Maximum. *Paleoceanography* 11, 563–577.
- Clauser C, Huenges E, 1995.** Thermal conductivity of rocks and minerals. In Ahrens T J (ed). *Rock physics and phase relations: handbook of physical constants*. Washington, DC: American Geophysical Union, 105–126.
- Cochelin A-S B, Mysak L L, Wang Z, 2006.** Simulation of long-term future climate changes with the green McGill paleoclimate model: the next glacial inception. *Climatic Change* 79, 381–401.
- Collins M, Knutti R, Arblaster J M, Dufresne J-L, Fichetef T, Friedlingstein P, Gao X, Gutowski W J, Johns T, Krinner G, Shongwe M, Tebaldi C, Weaver A J, Wehner M, 2013.** Long term climate change: projections, commitment and irreversibility. In Stocker T F, Qin D, Plattner G-K, Tignor M, Allen S K, Boschung J, Nauels A, Xia Y, Bex V, Midgley P M (eds). *Climate change 2013: the physical science basis: Working Group I Contribution to the Fifth Assessment Report of the Intergovernmental Panel on Climate Change*. Cambridge: Cambridge University Press, 1029–1136. (The report has to be read in conjunction with the document entitled “Climate change 2013: the physical science basis. Working Group I Contribution to the IPCC 5th Assessment Report – Changes to the underlying scientific/technical assessment”. Available at: <http://www.ipcc.ch>.)
- Collinson J, 2005a.** Erosional sedimentary structures. In Selley R C, Cocks L R M, Plimer I R (eds). *Encyclopedia of geology*. Amsterdam: Elsevier Academic Press.
- Collinson J, 2005b.** Depositional sedimentary structures. In Selley R C, Cocks L R M, Plimer I R (eds). *Encyclopedia of geology*. Amsterdam: Elsevier Academic Press.
- Crowley T J, Hyde W T, 2008.** Transient nature of late Pleistocene climate variability. *Nature* 456, 226–230.
- Crucifix M, Rougier J, 2009.** On the use of simple dynamical systems for climate predictions. *The European Physical Journal Special Topics* 174, 11–31.
- Cuffey K M, Conway H, Gades A M, Hallet B, Lorrain R, Severinghaus J P, Steig E J, Vaughn B, White J W C, 2000.** Entrainment at cold glacier beds. *Geology* 28, 351–354.
- Danielson E W, Levin J, Abrams E, 2003.** *Meteorology*. 2nd ed. New York: McGraw-Hill.
- Dansgaard W, Johnsen S J, Clausen H B, Dahl-Jensen D, Gundestrup N S, Hammer C U, Hvidberg C S, Steffensen J P, Sveinbjörnsdóttir A E, Jouzel J, Bond G, 1993.** Evidence for general instability of past climate from a 250-kyr ice-core record. *Nature* 364, 218–220.

- Davis J L, Mitrovica J X, 1996.** Glacial isostatic adjustment and the anomalous tide gauge record of eastern North America. *Nature* 379, 331–333.
- Davis J L, Mitrovica J X, Scherneck H G, Fan H, 1999.** Investigations of Fennoscandian glacial isostatic adjustment using modern sea level records. *Journal of Geophysical Research* 104, 2733–2747.
- Denton G H, Hughes T J (eds), 1981.** The last great ice sheets. New York: John Wiley.
- Drewry D, 1986.** Glacial geologic processes. London: Arnold.
- Duval P, Ashby M F, Anderman I, 1983.** Rate-controlling processes in the creep of polycrystalline ice. *Journal of Physical Chemistry* 87, 4066–4074.
- Dziewonski A M, Anderson D L, 1981.** Preliminary reference earth model. *Physics of the Earth and Planetary Interiors* 25, 297–356.
- Ebert K, 2009.** Cenozoic landscape evolution in northern Sweden: geomorphological interpretation within a GIS-framework. PhD thesis. Department of Physical Geography and Quaternary Geology, Stockholm University.
- Eby M, Zickfeld K, Montenegro A, Archer D, Meissner K J, Weaver A J, 2009.** Lifetime of anthropogenic climate change: millennial time scales of potential CO₂ and surface temperature perturbations. *Journal of Climate* 22, 2501–2511.
- Ehlers J, Gibbard P L (eds), 2004.** Quaternary glaciations: extent and chronology. Part I: Europe. Amsterdam: Elsevier. (Developments in quaternary science 2)
- Ekman M, 1991.** A concise history of postglacial land uplift research (from its beginning to 1950). *Terra Nova* 3, 358–365.
- Engelhardt H, Kamb B, 1998.** Basal sliding of Ice Stream B, West Antarctica. *Journal of Glaciology* 44, 223–230.
- Engelhardt H, Humphrey N, Kamb B, Fahnestock M, 1990.** Physical conditions at the base of a fast moving Antarctic ice stream. *Science* 248, 57–59.
- Engels S, Bohncke S J P, Bos J A A, Brooks S J, Heiri O, Helmens K F, 2008.** Chironomid-based palaeotemperature estimates for northeast Finland during Oxygen Isotope Stage 3. *Journal of Palaeolimnology* 40, 49–61.
- Engels S, Helmens K F, Väiliranta M, Brooks S J, Birks H J B, 2010.** Early Weichselian (MIS 5d and 5c) temperatures and environmental changes in northern Fennoscandia as recorded by chironomids and macroremains at Sokli, northeast Finland. *Boreas* 39, 689–704.
- Engström J, Kukkonen I, Ruskeeniemi T, Claesson Liljedahl L, Lehtinen A, 2012.** Temperature measurements providing evidence for permafrost thickness and talik occurrences in Kangerlussuaq, West Greenland. 30th Nordic Geological Winter Meeting, Reykjavik, Iceland, 9–12 January 2012. Abstract EC3-5. Available at: http://www.congress.is/reg_logos/NGWM_2012_Abstract_vol.pdf
- Eronen M, Gluckert G, Hatakka L, van de Plassche O, van der Plicht J, Rantala P, 2001.** Rates of Holocene isostatic uplift and relative sea-level lowering of the Baltic in SW Finland based on studies of isolation contacts. *Boreas* 30, 17–30.
- Fairbanks R G, 1989.** A 17,000-year glacio-eustatic sea level record: influence of glacial melting rates on the Younger Dryas event and deep-ocean circulation. *Nature* 342, 637–642.
- Farrell W E, Clark J A, 1976.** On postglacial sea level. *Geophysical Journal of the Royal Astronomical Society* 46, 647–667.
- Fastook J L, 1990.** A map-plane finite-element program for ice sheet reconstruction: a steady-state calibration with Antarctica and a reconstruction of the Laurentide ice sheet for 18,000 BP. In Brown H U (ed). *Computer assisted analysis and modelling on the IBM 3090*. White Plains, NY: IBM Scientific and Technical Computing Department.
- Fastook J L, 1994.** Modeling the Ice Age: the finite-element method in glaciology. *Computing Science and Engineering* 1, 55–67.
- Fastook J L, Chapman J E, 1989.** A map plane finite-element model: three modeling experiments. *Journal of Glaciology* 35, 48–52.

- Fastook J L, Holmlund P, 1994.** A glaciological model of the Younger Dryas event in Scandinavia. *Journal of Glaciology* 40, 125–131.
- Fastook J L, Prentice M, 1994.** A finite-element model of Antarctica: sensitivity test for meteorological mass-balance relationship. *Journal of Glaciology* 40, 167–175.
- Fischer U H, Haeblerli W, 2010.** Glacial erosion modelling: results of a workshop held in Unterägeri, Switzerland, 29 April – 1 May 2010. Nagra Arbeitsbericht NAB 10-34, Nagra, Switzerland.
- Fischer U H, Haeblerli W (eds), 2012.** Glacial overdeepening. Nagra Arbeitsbericht NAB 12-48, Nagra, Switzerland.
- Fjeldskaar W, 1994.** The amplitude and decay of the glacial forebulge in Fennoscandia. *Norsk Geologisk Tidsskrift* 74, 2–8.
- Fleming K, Johnston P, Zwartz D, Yokoyama Y, Lambeck K, Chappell J, 1998.** Refining the eustatic sea-level curve since the Last Glacial Maximum using far- and intermediate-field sites. *Earth and Planetary Science Letters* 163, 327–342.
- Forsström P-L, Sallasmaa O, Greve R, Zwinger T, 2003.** Simulation of fast-flow features of the Fennoscandian ice sheet during the Last Glacial Maximum. *Annals of Glaciology* 37, 383–389.
- Fotiev S M, 1997.** Permafrost groundwater Russian Literature Review. In Haldorsen S, Liebman M, Nelson G, van Everdingen R O, Boike J, 1997: State-of-the-art report on saturated water movement in permafrost areas. Report No 4/97 (Inr 54). Ås: Norges landbrukshøgskole.
- Fredén C (ed), 2002.** Sveriges nationalatlas. Berg och Jord. Stockholm: SNA publishing. (In Swedish.)
- French H M, 2007.** The periglacial environment. 3rd ed. Chichester: Wiley.
- Fronval T, Jansen E, 1996.** Late Neogene paleoclimates and paleoceanography in the Iceland-Norwegian Sea: evidence from the Iceland and Vøring plateaus. In Thiede J, Myhre A M, Firth J V, Johnson G L, Ruddiman W F (eds). *Proceedings of the Ocean Drilling Program, Scientific results* 151, 455–468.
- Funder S, Demidov I, Yelovicheva Y, 2002.** Hydrography and mollusc faunas of the Baltic and the White Sea-North Sea seaway in the Eemian. *Palaeogeography, Palaeoclimatology, Palaeoecology* 184, 275–304.
- Furlong K P, Chapman D S, 1987.** Crustal heterogeneities and the thermal structure of the continental crust. *Geophysical Research Letters* 14, 314–317.
- Ganopolski A, Calov R, Claussen M, 2010.** Simulation of the last glacial cycle with a coupled climate ice-sheet model of intermediate complexity. *Climate of the Past* 6, 229–244.
- Garisto F, Avis J, Chshyolkova T, Gierszewski P, Gobien M, Kitson C, Melnyk T, Miller J, Walsh R, Wojciechowski L, 2010.** Glaciation scenario: safety assessment for a deep geological repository for used fuel. NWMO TR-2010-10, Nuclear Waste Management Organization, Canada.
- Gascoyne M, 2000.** A review of published literature on the effects of permafrost on the hydrogeochemistry of bedrock. SKB R-01-56, Svensk Kärnbränslehantering AB.
- Giovinetto M B, Zwally H J, 2000.** Spatial distribution of net surface accumulation on the Antarctic ice sheet. *Annals of Glaciology* 31, 171–178.
- Glen J W, 1955.** The creep of polycrystalline ice. *Proceedings of the Royal Society of London, Series A*, 228, 519–538.
- Global Warming Art, 2007.** Five Myr climate change. Figure prepared by Robert A. Rohde / Global Warming Art. Available at: http://www.globalwarmingart.com/wiki/File:Five_Myr_Climate_Change_Rev_png. [26 November 2010].
- Goodrich L E, 1978.** Some results of a numerical study of ground thermal regimes. In *Proceedings of the Third International Conference on Permafrost*, Edmonton, Alberta, Canada, 10–13 July 1978. Ottawa: National Research Council of Canada, 30–34.
- Gregory J M, Huybrechts P, 2006.** Ice-sheet contributions to future sea-level change. *Philosophical Transactions of the Royal Society A* 364, 1709–1731.

- Gregory J M, Huybrechts P, Raper S C B, 2004.** Threatened loss of the Greenland ice sheet. *Nature* 428, 616.
- Greve R, Hutter K, 1995.** Polythermal three-dimensional modelling of the Greenland ice sheet with varied geothermal heat flux. *Annals of Glaciology* 21, 8–12.
- Hallet B, Hunter L, Bogen J, 1996.** Rates of erosion and sediment evacuation by glaciers: a review of field data and their implications. *Global and Planetary Change* 12, 213–235.
- Hambrey M J, Barrett P J, Ehrmann W U, Larsen B, 1992.** Cainozoic sedimentary processes on the Antarctic continental margin and the record from deep drilling. *Zeitschrift für Geomorphologie, Suppl.* 86, 77–103.
- Han D, Wahr J, 1989.** Post-glacial rebound analysis for a rotating Earth. In Cohen S, Vanicek P (eds). *Slow deformations and transmission of stress in the Earth*. Washington, DC: American Geophysical Union. (AGU Monograph Series 49), 1–6.
- Hanebuth T, Stattegger K, Grootes P M, 2000.** Rapid flooding of the Sunda Shelf: a late-glacial sea-level record. *Science* 288, 1033–1035.
- Haq B U, Hardenbol J, Vail P R, 1987.** Chronology of fluctuating sea levels since the Triassic. *Science* 235, 1156–1165.
- Harper J, Hubbard A, Ruskeeniemi T, Claesson Liljedahl L, Lehtinen A, Booth A, Brinkerhoff D, Drake H, Dow C, Doyle S, Engström J, Fitzpatrick A, Frape S, Henkemans E, Humphrey N, Johnson J, Jones G, Joughin I, Klint K E, Kukkonen I, Kulessa B, Landowski C, Lindbäck K, Makahnouk M, Meierbachtol T, Pere T, Pedersen K, Pettersson R, Pimentel S, Quincey D, Tullborg E-L, van As D, 2011.** The Greenland Analogue Project. Yearly report 2010. SKB R-11-23, Svensk Kärnbränslehantering AB.
- Harrison S P, Braconnot P, Joussaume S, Hewitt C, Stouffer R J, 2002.** Comparison of palaeoclimate simulations enhances confidence in models. *Eos* 83, 447.
- Hartikainen J, 2004.** Permafrost modeling in DECOVALEX III for BMT3. In Eloranta E (ed). *DECOVALEX III, 1999–2003. An international project for the modelling of coupled thermo-hydro-mechanical processes for spent fuel disposal*. Finnish national contributions. STUK-YTO-TR 209, Finnish Centre for Radiation and Nuclear Safety (STUK), Helsinki.
- Hartikainen J, 2013.** Simulations of permafrost evolution at Olkiluoto. Posiva Working Report 2012-34, Posiva Oy, Finland.
- Hartikainen J, Kouhia R, Wallroth T, 2010.** Permafrost simulations at Forsmark using a numerical 2D thermo-hydro-chemical model. SKB TR-09-17, Svensk Kärnbränslehantering AB.
- Hays J D, Imbrie J, Shackleton N, 1976.** Variations in the Earth's orbit: pacemaker of the ice ages. *Science* 194, 1121–1132.
- Heginbottom J A, Dubreuil M A, Harker P A, 1995.** Canada – Permafrost. In *National Atlas of Canada*. 5th ed. Ottawa: National Atlas Information Service, Natural Resources Canada.
- Heinrich H, 1988.** Origin and consequences of cyclic ice rafting in the northeast Atlantic Ocean during the past 130,000 years. *Quaternary Research* 29, 142–152.
- Helmens K F, 2009a.** Climate, vegetation and lake development at Sokli (northern Finland) during early MIS 3 at ~50 kyr: Revising earlier concepts on climate, glacial and vegetation dynamics in Fennoscandia during the Weichselian. SKB TR-09-16, Svensk Kärnbränslehantering AB.
- Helmens K F, 2009b.** Late Quaternary climate variability in high latitude northern Europe: data-model comparison. 4th BBCC (Bert Bolin Climate Centre, Stockholm University) annual meeting, Stockholm, Sweden, 14–15 September 2009.
- Helmens K, 2013.** The last interglacial-glacial cycle (MIS 5-2) re-examined based on long proxy records from central and northern Europe. SKB TR-13-02, Svensk Kärnbränslehantering AB.
- Helmens K F, Engels S, 2010.** Ice-free conditions in eastern Fennoscandia during early Marine Isotope Stage 3: lacustrine records. *Boreas* 39, 399–409.

- Helmens K F, Bos J A A, Engels S, Van Meerbeeck C J, Bohncke S J P, Renssen H, Heiri O, Brooks S J, Seppä H, Birks H J B, Wohlfarth B, 2007.** Present-day temperatures in northern Scandinavia during the last glaciation. *Geology* 35, 987–990.
- Helmens K F, Risberg J, Jansson K N, Weckström J, Berntsson A, Kaislahti Tillman P, Johansson P W, Wastegård S, 2009.** Early MIS 3 glacial lake evolution, ice-marginal retreat pattern and climate at Sokli (northeastern Fennoscandia). *Quaternary Science Reviews* 28, 1880–1894.
- Helmens K F, Väliranta M, Engels S, Shala S, 2012.** Large shifts in vegetation and climate during the Early Weichselian (MIS 5d-c) inferred from multi-proxy evidence at Sokli (northern Finland). *Quaternary Science Reviews* 41, 22–38.
- Henton J A, Craymer M R, Ferland R, Dragert H, Mazotti S, Forbes D L, 2006.** Crustal motion and deformation monitoring of the Canadian landmass. *Geomatica* 60, 173–191.
- Hindmarsh R C A, Boulton G S, Hutter K, 1989.** Modes of operation of thermo-mechanically coupled ice sheets. *Annals of Glaciology* 12, 57–69.
- Hohmann M, 1997.** Soil freezing – the concept of soil water potential. State of the art. *Cold Regions Science and Technology* 25, 101–110.
- Holmlund P, Fastook J, 1995.** A time dependent glaciological model of the Weichselian ice sheet. *Quaternary International* 27, 53–58.
- Holmlund P, Jansson P, 2003.** *Glaciologi*. Stockholm: Stockholm University and the Swedish Research Council. (In Swedish.)
- Hooke R LeB, 1977.** Basal temperatures in polar ice sheets: a qualitative review. *Quaternary Research* 7, 1–13.
- Hooke R LeB, 1991.** Positive feedbacks associated with erosion of glacial cirques and overdeepenings. *Geological Society of America Bulletin* 103, 1104–1108.
- Hooke R LeB, 2004.** *Principles of glacier mechanics*. 2nd ed. Cambridge: Cambridge University Press.
- Houmark-Nielsen M, 2009.** MIS 3 interstadial climate and rapid ice advances in the south-western Baltic. SKB P-09-10, Svensk Kärnbränslehantering AB.
- Hu A, Meehl G A, Han W, Yin J, 2009.** Transient response of the MOC and climate to potential melting of the Greenland ice sheet in the 21st century. *Geophysical Research Letters* 36. doi:10.1029/2009GL037998
- Huybers P, 2011.** Combined obliquity and precession pacing of late Pleistocene deglaciations. *Nature* 480, 229–232.
- Huybers P, Wunsch C, 2005.** Obliquity pacing of the late Pleistocene glacial terminations. *Nature* 434, 491–494.
- Huybrechts P, 1986.** A three dimensional time-dependent numerical model for polar ice sheets: some basic testing with a stable and efficient finite difference scheme. Report 86-1, Geografisch Instituut, Vrije Universiteit Brussel, Belgium.
- Huybrechts P, 1990.** A 3D model for the Antarctic ice sheet: a sensitivity study on the glacial-interglacial contrast. *Climate Dynamics* 5, 79–92.
- Huybrechts P, 2006.** Numerical modeling of ice sheets through time. In Knight P G (ed). *Glacier science and environmental change*. Malden: Blackwell Publishing, 406–412.
- Huybrechts P, T'siobbel S, 1995.** Thermomechanical modelling of northern hemisphere ice sheets with a two-level mass-balance parameterization. *Annals of Glaciology* 21, 111–116.
- Huybrechts P, Payne A J, EISMINT Intercomparison Group, 1996.** The EISMINT benchmarks for testing ice-sheet models. *Annals of Glaciology* 23, 1–12.
- Huybrechts P, Goelzer H, Janssens I, Driesschaert E, Fichefet T, Goosse H, Loutre M-F, 2011.** Response of the Greenland and Antarctic ice sheets to multi-millennial greenhouse warming in the earth system model of intermediate complexity LOVECLIM. *Surveys in Geophysics* 32, 397–416.

- Imbrie J, Boyle E A, Clemens S C, Duffy A, Howard W R, Kukla G, Kutzbach J, Martinson D G, McIntyre A, Mix A C, Molfino B, Morley J J, Peterson L C, Pisias N G, Imbrie J, Hays J D, Martinson D G, McIntyre A, Mix A C, Morley J J, Pisias N G, W L Prell, Shackleton N J, 1984.** The orbital theory of Pleistocene climate: support from a revised chronology of the marine $\delta^{18}\text{O}$ record. In Berger A L, Imbrie J, Hays J D, Kukla G, Saltzman B (eds). *Milankovitch and climate: understanding the response to astronomical forcing*. Dordrecht: Reidel, 269–305.
- Imbrie J Z, Imbrie-Moore A, Lisiecki L E, 2011.** A phase-space model for Pleistocene ice volume. *Earth and Planetary Science Letters* 307, 94–102.
- IPCC, 2000.** Emissions scenarios: summary for policymakers: a special report of IPCC Working Group III. Geneva: World Meteorological Organization.
- IPCC, 2001.** Climate change 2001: the scientific basis. Contribution of Working Group I to the Third Assessment Report of the Intergovernmental Panel on Climate Change. New York: Cambridge University Press.
- IPCC, 2007.** Climate change 2007: the physical science basis. Contribution of Working Group I to the Fourth Assessment Report of the Intergovernmental Panel on Climate Change. Cambridge: Cambridge University Press.
- IPCC, 2013.** Climate change 2013: the physical science basis: summary for policymakers. Contribution of Working Group I to the Fifth Assessment Report of the Intergovernmental Panel on Climate Change. Available at: <http://www.ipcc.ch>.
- Isaksen K, Holmlund P, Sollid J L, Harris C, 2001.** Three deep alpine-permafrost boreholes in Svalbard and Scandinavia. *Permafrost and Periglacial Processes* 12, 13–26.
- Iverson N R, 1991.** Potential effects of of subglacial water-pressure fluctuations on quarrying. *Journal of Glaciology* 37, 27–36.
- Iverson N R, 1993.** Regelation of ice through debris at glacier beds: implications for sediment transport. *Geology* 21, 559–562.
- Iverson N R, 2000.** Sediment entrainment by a soft-bedded glacier: a model based on regelation into the bed. *Earth Surface Processes and Landforms* 25, 881–893.
- Iverson N R, Hanson B, Hooke R LeB, Jansson P, 1995.** Flow mechanism of glaciers on soft beds. *Science* 267, 80–81.
- Ivins E R, 2009.** Ice sheet stability and sea-level. *Science* 324, 888–889.
- Jansen E, Sjøholm J, 1991.** Reconstruction of glaciation over the past 6 Myr from ice-borne deposits in the Norwegian Sea. *Nature* 349, 600–603.
- Jansson P, Näslund J-O, 2009.** Spatial and temporal variations in glacier hydrology on Storglaciären, Sweden. SKB TR-09-13, Svensk Kärnbränslehantering AB.
- Jaquet O, Siegel P, 2006.** Regional groundwater flow model for a glaciation scenario. Simpevarp subarea – version 1.2. SKB R-06-100, Svensk Kärnbränslehantering AB.
- Jaquet O, Rabah N, Pascal S, Jansson P, 2012.** Groundwater flow modelling under ice sheet conditions in Greenland (phase II). SKB R-12-14, Svensk Kärnbränslehantering AB
- Johansson J M, Davis J L, Scherneck H-G, Milne G A, Vermeer M, Mitrovica J X, Bennett R A, Jonsson B, Elgered G, Elósegui P, Koivula H, Poutanen M, Rönnäng B O, Shapiro I I, 2002.** Continuous GPS measurements of postglacial adjustment in Fennoscandia. 1. Geodetic results. *Journal of Geophysical Research* 107, 400–428.
- Johansson P-O, 2008.** Description of surface hydrology and near-surface hydrogeology at Forsmark. Site descriptive modelling, SDM-Site Forsmark. SKB R-08-08, Svensk Kärnbränslehantering AB.
- Johansson P-O, Werner K, Bosson E, Berglund S, Juston J, 2005.** Description of climate, surface hydrology, and near-surface hydrogeology. Preliminary site description Forsmark area – version 1.2. SKB R-05-06, Svensk Kärnbränslehantering AB.

- Johnsen S J, Clausen H B, Dansgaard W, Fuhrer K, Gundestrup N, Hammer C U, Iversen P, Jouzel J, Stauffer B, Steffensen J P, 1992.** Irregular glacial interstadials recorded in a new Greenland ice core. *Nature* 359, 311–313.
- Johnsen S J, Dahl-Jensen D, Dansgaard W, Gundestrup N, 1995.** Greenland palaeotemperatures derived from GRIP bore hole temperature and ice core isotope profiles. *Tellus* 47B, 624–629.
- Johnson J, 1994.** A basal water model for ice sheets. Ph D. thesis. University of Minnesota.
- Johnson J, 2004.** Estimating basal melt rate in Antarctica. International Symposium on Ice and Water Interactions: processes across the phase boundary. Portland, Oregon, 26–30 July 2004.
- Johnston, P, 1993.** The effect of spatially non-uniform water loads on predictions of sea-level change. *Geophysical Journal International* 114, 615–634.
- Joughin I, Tulaczyk S, 2002.** Positive mass balance for the Ross Ice Streams, West Antarctica. *Science* 295, 476–480.
- Joughin I, Abdalati W, Fahnestock M, 2004.** Large fluctuations in speed on Greenland's Jakobshavn Isbræ glacier. *Nature* 432, 608–610.
- Joussaume S, Taylor K E, 2000.** The paleoclimate modeling intercomparison project. In Braconnot P (ed). Proceedings of the third Paleoclimate Modelling Intercomparison Project (PMIP) workshop. La Huardière, Canada, 4–8 October 1999. (WCRP-111, WMO/TD-1007)
- Jouzel J, Stievenard M, Johnsen S J, Landais A, Masson-Delmotte V, Sveinbjornsdottir A, Vimeux F, von Grafenstein U, White J W C, 2007.** The GRIP deuterium-excess record. *Quaternary Science Reviews* 26, 1–17.
- Kageyama M, Laine A, Abe-Ouchi A, Braconnot P, Cortijo E, Crucifix M, de Vernal A, Guiot J, Hewitt C D, Kitoh A, Kucera M, Marti O, Ohgaito R, Otto-Bliesner B, Peltier W R, Rosell-Melé A, Vettoretti G, Weber S L, Yu Y, MARGO project members, 2006.** Last Glacial Maximum temperatures over the North Atlantic, Europe and western Siberia: a comparison between PMIP models, MARGO sea-surface temperatures and pollen-based reconstructions. *Quaternary Science Reviews* 25, 2082–2102.
- Kamb B, 2001.** Basal zone of the West-Antarctic ice streams and its role in their rapid motion. In Alley R B, Bindschadler R A (eds). *The West Antarctic ice sheet: behavior and environment*. Washington D.C.: American Geophysical Union, 157–200.
- Kaufmann G, Lambeck K, 2002.** Glacial isostatic adjustment and the radial viscosity profile from inverse modeling. *Journal of Geophysical Research* 107, 2280. doi:10.1029/2001JB000941
- Kaufmann G, Wu P, 1998.** Lateral asthenospheric viscosity variations and postglacial rebound: a case study for the Barents Sea. *Geophysical Research Letters* 25, 1963–1966.
- Kaufmann G, Wu P, 2002.** Glacial isostatic adjustment in Fennoscandia with a three-dimensional viscosity structure as an inverse problem. *Earth and Planetary Science Letters* 197, 1–10.
- Kaufmann G, Wu P, Li G Y, 2000.** Glacial isostatic adjustment in Fennoscandia for a laterally heterogeneous earth. *Geophysical Journal International* 143, 262–273.
- Kendall R A, Mitrovica J X, Milne G A, 2005.** On post-glacial sea level – II. Numerical formulation and comparative results on spherically symmetric models. *Geophysical Journal International* 161, 679–706.
- Kim S-J, Crowley T J, Erickson D J, Govindasamy B, Duffy P B, Lee B Y, 2008.** High-resolution climate simulation of the last glacial maximum. *Climate Dynamics* 31, 1–16.
- King L, 1984.** Permafrost in Skandinavien: Untersuchungsergebnisse aus Lappland, Jotunheimen und Dovre/Rondane. Heidelberg: Geographisches Institut der Univ. (Heidelberger geographische Arbeiten 76)
- Kjellström E, Strandberg G, Brandefelt J, Näslund J-O, Smith B, Wohlfarth B, 2009.** Climate conditions in Sweden in a 100,000-year time perspective. SKB TR-09-04, Svensk Kärnbränslehantering AB.

- Kjellström E, Brandefelt J, Näslund J-O, Smith B, Strandberg G, Voelker A H L, Wohlfarth B, 2010.** Simulated climate conditions in Europe during a Marine Isotope Stage 3 stadial. *Boreas* 39, 436–456.
- Kjellström E, Nikulin G, Hansson U, Strandberg G, Ullerstig A, 2011.** 21st century changes in the European climate: uncertainties derived from an ensemble of regional climate model simulations. *Tellus A* 63, 24–40.
- Kleman J, 1994.** Preservation of landforms under ice sheets and ice caps. *Geomorphology* 9, 19–32.
- Kleman J, Glasser N F, 2007.** The subglacial thermal organisation (STO) of ice sheets. *Quaternary Science Reviews* 26, 585–597.
- Kleman J, Hättestrand C, 1999.** Frozen-based Fennoscandian and Laurentide ice sheets during the last glacial maximum. *Nature* 402, 63–66.
- Kleman J, Stroeven A P, 1997.** Preglacial surface remnants and Quaternary glacial regimes in northwestern Sweden. *Geomorphology* 19, 35–54.
- Kleman J, Hättestrand C, Borgström I, Stroeven A, 1997.** Fennoscandian palaeoglaciology reconstructed using a glacial geological inversion model. *Journal of Glaciology* 43, 283–299.
- Kleman J, Stroeven A, Lundqvist J, 2008.** Patterns of Quaternary ice sheet erosion and deposition in Fennoscandia and a theoretical framework for explanation. *Geomorphology* 97, 73–90.
- Kleman J, Fastook J, Ebert K, Nilsson J, Caballero R, 2013.** Pre-LGM Northern Hemisphere paleo-ice sheet topography. *Climate of the Past Discussions* 9, 2557–2587.
- Knutti R, Sedláček J, 2013.** Robustness and uncertainties in the new CMIP5 climate model projections. *Nature Climate Change* 3, 369–373.
- Koppes M N, Montgomery D R, 2009.** The relative efficacy of fluvial and glacial erosion over modern to orogenic timescales. *Nature Geoscience* 2, 644–647.
- Kukkonen I, 1989.** Terrestrial heat flow and radiogenic heat production in Finland, the central Baltic Shield. *Tectonophysics* 164, 219–230.
- Kukkonen I T, Šafanda J, 2001.** Numerical modelling of permafrost in bedrock in northern Fennoscandia during the Holocene. *Global and Planetary Change* 29, 259–274.
- Lachenbruch A H, 1968.** Preliminary geothermal model of the Sierra Nevada. *Journal of Geophysical Research* 73, 6977–6989.
- Lagerbäck R, 1988a.** The Veiki moraines in northern Sweden – widespread evidence of an Early Weichselian deglaciation. *Boreas* 17, 469–486.
- Lagerbäck R, 1988b.** Periglacial phenomena in the wooded areas of northern Sweden – relicts from the Tärenö Interstadial. *Boreas* 17, 487–499.
- Lagerbäck R, Robertsson A-M, 1988.** Kettle holes – stratigraphical archives for Weichselian geology and palaeoenvironment in northernmost Sweden. *Boreas* 17, 439–468.
- Lambeck K, 1995.** Late Devensian and Holocene shorelines of the British Isles and North Sea from models of glacio-hydroisostatic rebound. *Journal of the Geological Society* 152, 437–448.
- Lambeck K, 1999.** Shoreline displacements in southern-central Sweden and the evolution of the Baltic Sea since the last maximum glaciation. *Journal of the Geological Society* 156, 465–486.
- Lambeck K, Chappell J, 2001.** Sea level change through the last glacial cycle. *Science* 292, 679–686.
- Lambeck K, Nakada M, 1990.** Late Pleistocene and Holocene sea-level change along the Australian coast. *Palaeogeography, Palaeoclimatology, Palaeoecology* 89, 143–176.
- Lambeck K, Smither C, Johnston P, 1998.** Sea-level change, glacial rebound and mantle viscosity for northern Europe. *Geophysical Journal International* 134, 102–144.
- Lambeck K, Yokoyama Y, Purcell T, 2002.** Into and out of the Last Glacial Maximum: sea-level change during Oxygen Isotope Stages 3 and 2. *Quaternary Science Reviews* 21, 343–360.

- Lambeck K, Purcell A, Zhao J, Svensson N-O, 2010.** The Scandinavian Ice Sheet: from MIS 4 to the end of the Last Glacial Maximum. *Boreas* 39, 410–435.
- Lambert A, Courtier N, Sasagawa G S, Klopping F, Winester D, James T S, Liard J O, 2001.** New constraints on Laurentide postglacial rebound from absolute gravity measurements. *Geophysical Research Letters* 28, 2109–2112.
- Landström O, Larsson, S Å, Lind G, Malmqvist D, 1979.** Geothermal investigations in the Bohus granite area in southwestern Sweden. *Tectonophysics* 64, 131–162.
- Latychev K, Mitrovica J X, Tamisiea M E, Tromp J, Moucha R, 2005a.** Influence of lithospheric thickness variations on 3D crustal velocities due to glacial isostatic adjustment. *Geophysical Research Letters* 32, L01304. doi:10.1029/2004GL021454
- Latychev K, Mitrovica J X, Tromp J, Tamisiea M E, Komatitsch D, Christara C C, 2005b.** Glacial isostatic adjustment on 3D Earth models: a finite-volume formulation. *Geophysical Journal International* 161, 421–444.
- Lemieux J-M, Sudicky E A, Peltier W R, Tarasov L, 2008a.** Dynamics and groundwater recharge and seepage over the Canadian landscape during the Wisconsinian glaciation. *Journal of Geophysical Research* 113, F01011. doi:10.1029/2007JF000838
- Lemieux J-M, Sudicky E A, Peltier W R, Tarasov L, 2008b.** Simulating the impact of glaciations on continental groundwater flow systems: 1. Relevant processes and model formulation. *Journal of Geophysical Research* 113, F03017. doi:10.1029/2007JF000928
- Lemieux J-M, Sudicky E A, Peltier W R, Tarasov L, 2008c.** Simulating the impact of glaciations on continental groundwater flow systems: 2. Model application to the Wisconsinian glaciation over the Canadian landscape. *Journal of Geophysical Research* 113, F03018. doi:10.1029/2007JF000929
- Li C, von Storch J-S, Marotzke J, 2013.** Deep-ocean heat uptake and equilibrium climate response. *Climate Dynamics* 40, 1071–1086.
- Lidberg M, 2007.** Geodetic reference frames in presence of crustal deformations. PhD thesis. Department of Radio and Space Science, Chalmers University of Technology.
- Lidberg M, Johansson J M, Scherneck H-G, Milne G A, 2010.** Recent results based on continuous GPS observations of the GIA process in Fennoscandia from BIFROST. *Journal of Geodynamics* 50, 8–18.
- Lide D R (ed), 1999.** CRC handbook of chemistry and physics: a ready-reference book of chemical and physical data. 80th ed. Cleveland, Ohio: CRC Press.
- Lidmar-Bergström K, 1995.** Relief and saprolites through time on the Baltic shield. *Geomorphology* 12, 45–61.
- Lidmar-Bergström K, 1997.** A long-term perspective on glacial erosion. *Earth Surface Processes and Landforms* 22, 297–306.
- Lidmar-Bergström K, Näslund J-O, 2002.** Landforms and uplift in Scandinavia. In Doré A G, Cartwright J A, Stoker M S, Turner J P, White N (eds). *Exhumation of the North Atlantic margin: timing, mechanisms, and implications for petroleum exploration*. London: Geological Society. (Special publication 196), 103–116.
- Lidmar-Bergström K, Näslund J-O, 2005.** Major landforms and bedrock. In Seppälä M (ed). *The physical geography of Fennoscandia*. Oxford: Oxford University Press.
- Lidmar-Bergström K, Olsson S, Olvmo M, 1997.** Palaeosurfaces and associated saprolites in southern Sweden. In Widdowson M (ed). *Palaeosurfaces: recognition, reconstruction and palaeo-environmental interpretation*. London: Geological Society. (Special publication 120), 95–124.
- Lind P, Kjellström E, 2008.** Temperature and precipitation changes in Sweden: a wide range of model-based projections for the 21st century. Norrköping: Sveriges meteorologiska och hydrologiska institut (Swedish Meteorological and Hydrological Institute). (SMHI reports. *Meteorology and Climatology* 113)
- Lindborg T (ed), 2010.** Landscape Forsmark, SR-Site Biosphere. SKB TR-10-05, Svensk Kärnbränslehantering AB.

- Lisiecki L E, 2010.** Links between eccentricity forcing and the 100,000-year glacial cycle. *Nature Geoscience* 3, 349–352.
- Lisiecki L E, Raymo M E, 2005.** A Pliocene-Pleistocene stack of 57 globally distributed benthic $\delta^{18}\text{O}$ records. *Paleoceanography* 20. doi:10.1029/2004PA001071
- Lisiecki L E, Raymo M E, 2007.** Plio–Pleistocene climate evolution: trends and transitions in glacial cycle dynamics. *Quaternary Science Reviews* 26, 56–69.
- Lokrantz H, Sohlenius G, 2006.** Ice-marginal fluctuations during the Weichselian glaciation in Fennoscandia, a literature review. SKB TR-06-36, Svensk Kärnbränslehantering AB.
- Loutre M F, Berger A, 2000.** Future climatic changes: are we entering an exceptionally long interglacial? *Climatic Change* 46, 61–90.
- Lunardini V J, 1978.** Theory of n-factors and correlation of data. In *Proceedings of the 3rd International Conference on Permafrost*. Edmonton, Alta, 10–13 July 1978. Ottawa: National Research Council of Canada, Vol 1, 40–46.
- Lunardini V J, 1995.** Permafrost formation time. CRREL Report 95-8, U.S. Army Cold Regions Research and Engineering Laboratory.
- Lund B, Näslund J-O, 2009.** Glacial isostatic adjustment: implications for glacially induced faulting and nuclear waste repositories. In Connor C B, Chapman N A, Connor L J (eds). *Volcanic and tectonic hazard assessment for nuclear facilities*. Cambridge: Cambridge University Press, 142–155.
- Lund B, Schmidt P, Hieronymus C, 2009.** Stress evolution and fault stability during the Weichselian glacial cycle. SKB TR-09-15, Svensk Kärnbränslehantering AB.
- Lundqvist J, 1992.** Glacial stratigraphy in Sweden. *Geological Survey of Finland Special Paper* 5, 43–59.
- Lundqvist J, 2007.** Surging ice and break-down of an ice dome – a deglaciation model for the Gulf of Bothnia. *Geologiska Föreningens i Stockholm Förhandlingar* 129, 329–336.
- Lundqvist J, Wohlfarth B, 2000.** Timing and east-west correlation of south Swedish ice-marginal lines during the Late Weichselian. *Quaternary Science Reviews* 20, 1127–1148.
- Lundqvist J, Lundqvist T, Lindström M, Calner M, Sivhed U, 2011.** *Sveriges geologi från urtid till nutid*. 3rd ed. Lund:Studentlitteratur. (In Swedish.)
- Lüthi D, Le Floch M, Bereiter B, Blunier T, Barnola J-M, Siegenthaler U, Raynaud D, Jouzel J, Fischer H, Kawamura K, Stocker T F, 2008.** High-resolution carbon dioxide concentration record 650,000–800,000 years before present. *Nature* 453, 379–82.
- Mackay J R, 1997.** A full-scale field experiment (1978–1995) on the growth of permafrost by means of lake drainage, western Arctic coast: a discussion of the method and some results. *Canadian Journal of Earth Sciences* 34, 17–33.
- Mai H, Thomsen T, 1993.** Permafrost studies in Greenland. In *Proceedings of the sixth international conference on permafrost*. Beijing, 5–9 July 1993. Guangzhou: South China University of Technology, Vol 2.
- Malmqvist D, Larson S Å, Landström O, Lind G, 1983.** Heat flow and heat production from the Malingsbo granite, central Sweden. *Bulletin of the Geological Institutions of the University of Uppsala* 9, 137–152.
- Mangerud J, Gyllencreutz R, Lohne O, Svendsen J I, 2011.** Glacial history of Norway. In Ehlers J, Gibbard P L, Hughes P D (eds). *Quaternary glaciations – extent and chronology: a closer look*. Amsterdam: Elsevier. (Developments in Quaternary Sciences 15), 279–298.
- Marchant D R, Denton G H, Sugden D E, Swisher C C, 1993.** Miocene glacial stratigraphy and landscape evolution of the western Asgard Range, Antarctica. *Geografiska Annaler* 75A, 303–330.
- Marcott S A, Shakun J D, Clark P U, Mix A C, 2013.** A reconstruction of regional and global temperature for the past 11,300 years. *Science* 339, 1198–1201.
- Marshall S J, Clarke G K C, 1997.** A continuum mixture model of ice stream thermodynamics in the Laurentide Ice Sheet. 1. Theory. *Journal of Geophysical Research* 102, 20599–20614.

- Matthews H D, Gillett N P, Stott P A, Zickfeld K, 2009.** The proportionality of global warming to cumulative carbon emissions. *Nature* 459, 829–832.
- McConnell R K, 1968.** Viscosity of the mantle from relaxation time spectra of isostatic adjustment. *Journal of Geophysical Research* 73, 7089–7105.
- McIntyre K, Delaney M L, Ravelo A C, 2001.** Millennial-scale climate change and oceanic processes in the late Pliocene and early Pleistocene. *Paleoceanography* 16, 535–543.
- McManus J F, Bond G C, Broecker W S, Johnsen S, Labeyrie L, Higgins S, 1994.** High-resolution climate records from the North-Atlantic during the last interglacial. *Nature* 371, 326–329.
- Meehl G A, Stocker T F, Collins W D, Friedlingstein P, Gaye A T, Gregory J M, Kitoh A, Knutti R, Murphy J M, Noda A, Raper S C B, Watterson I G, Weaver A J, Zhao Z-C, 2007.** Global climate projections. In IPCC, 2007. *Climate change 2007: the physical science basis. Contribution of Working Group I to the fourth assessment report of the Intergovernmental Panel on Climate Change.* Cambridge: Cambridge University Press.
- Meier H E M, 2006.** Baltic Sea climate in the late twenty-first century: a dynamical downscaling approach using two global models and two emission scenarios. *Climate Dynamics* 27, 39–68.
- Meinshausen M, Smith S J, Calvin K, Daniel J S, Kainuma M L T, Lamarque J-F, Matsumoto K, Montzka S A, Raper S C B, Riahi K, Thomson A, Velders G J M, van Vuuren D P P, 2011.** The RCP greenhouse gas concentrations and their extensions from 1765 to 2300. *Climatic Change* 109, 213–241.
- Mikolajewicz U, Gröger M, Maier-Reimer E, Schurgers G, Vizcaíno M, Winguth A M E, 2007.** Long-term effects of anthropogenic CO₂ emissions simulated with a complex earth system model. *Climate Dynamics* 28, 599–633.
- Milne G A, 1998.** Refining models of the glacial isostatic adjustment process. PhD thesis. University of Toronto.
- Milne G A, Mitrovica J X, 1998.** Postglacial sea-level change on a rotating Earth. *Geophysical Journal International* 133, 1–19.
- Milne G A, Mitrovica J X, Davis J L, 1999.** Near-field hydro-isostasy: the implementation of a revised sea-level equation. *Geophysical Journal International* 139, 464–482.
- Milne G A, Davis J L, Mitrovica J X, Scherneck H-G, Johansson J M, Vermeer M, Koivula H, 2001.** Space-geodetic constraints on glacial isostatic adjustment in Fennoscandia. *Science* 291, 2381–2385.
- Milne G A, Mitrovica J X, Schrag D P, 2002.** Estimating past continental ice volume from sea-level data. *Quaternary Science Reviews* 21, 361–376.
- Milne G A, Mitrovica J X, Scherneck H G, Davis J L, Johansson J M, Koivula H, Vermeer M, 2004.** Continuous GPS measurements of postglacial adjustment in Fennoscandia: 2. Modeling results. *Journal of Geophysical Research* 109, B02412. doi:10.1029/2003JB002619
- Milne, G A, Gehrels W R, Hughes C W, Tamisiea M E, 2009.** Identifying the causes of sea-level change. *Nature Geoscience* 2, 471–478.
- Mitrovica J X, 2003.** Recent controversies in predicting post-glacial sea-level change. *Quaternary Science Reviews* 22, 127–133.
- Mitrovica J X, Forte A M, 1997.** Radial profile of mantle viscosity: results from the joint inversion of convection and postglacial rebound observables. *Journal of Geophysical Research* 102, 2751–2769.
- Mitrovica J X, Forte A M, 2004.** A new inference of mantle viscosity based upon joint inversion of convection and glacial isostatic adjustment data. *Earth and Planetary Science Letters* 225, 177–189.
- Mitrovica J X, Milne G A, 2002.** On the origin of late Holocene sea-level highstands within equatorial ocean basins. *Quaternary Science Reviews* 21, 2179–2190.
- Mitrovica J X, Milne G A, 2003.** On post-glacial sea level: I. General theory. *Geophysical Journal International* 154, 253–267.

- Mitrovica J X, Peltier W R, 1991.** On post-glacial geoid subsidence over the equatorial oceans. *Journal of Geophysical Research* 96, 20053–20071.
- Mitrovica J X, Davis J L, Shapiro I I, 1994.** A spectral formalism for computing three-dimensional deformations due to surface loads. 2. Present-day glacial isostatic-adjustment. *Journal of Geophysical Research* 99, 7075–7101.
- Mitrovica J X, Milne G A, Davis J L, 2001a.** Glacial isostatic adjustment on a rotating earth. *Geophysical Journal International* 147, 562–579.
- Mitrovica J X, Tamisiea M E, Davis J L, Milne G A, 2001b.** Recent mass balance of polar ice sheets inferred from patterns of global sea-level change. *Nature* 409, 1026–1029.
- Mitrovica J X, Wahr J, Matsuyama I, Paulson A, 2005.** The rotational stability of an ice-age Earth. *Geophysical Journal International* 161, 491–506.
- Mitrovica J X, Gomez N, Clark P U, 2009.** The sea-level fingerprint of West Antarctic Collapse. *Science* 323, 753.
- Moberg A, Sonechkin D M, Holmgren K, Datsenko N M, Karlén W, 2005.** Highly variable Northern Hemisphere temperatures reconstructed from low- and high-resolution proxy data. *Nature* 433, 613–617.
- Montagnat M, Duval P, 2000.** Rate controlling processes in the creep of polar ice, influence of grain boundary migration associated with recrystallization. *Earth and Planetary Science Letters* 183, 179–186.
- Müller U C, Kukla G J, 2004.** North Atlantic Current and European environments during the declining stage of the last interglacial. *Geology* 32, 1009–1012.
- Mysak L A, 2008.** Glacial inception: past and future. *Atmosphere-Ocean* 46, 317–341.
- Mäkinen J, Engfeldt A, Harsson B G, Routsalainen H, Strykowski G, Oja T, Wolf D, 2005.** The Fennoscandian land uplift gravity lines 1966–2003. In Jekeli C, Bastos L, Fernandes J (eds). *Gravity, geoid and space missions*. Berlin: Springer. (International Association of Geodesy symposia 129), 328–332.
- Mörner N-A, 1977.** Past and present uplift in Sweden: glacial isostasy, tectonism and bedrock influence. *Geologiska föreningen i Stockholms förhandlingar* 99, 48–54.
- Mörner N-A, 1979.** The Fennoscandian uplift and Late Cenozoic geodynamics: geological evidence. *GeoJournal* 3, 287–318.
- Nakada M, Lambeck K, 1989.** Late Pleistocene and Holocene sea-level change in the Australian region and mantle rheology. *Geophysical Journal International* 96, 497–517.
- Nakićenović N, Swart R (eds), 2000.** Special report on emissions scenarios. A Special Report of Working Group III of the Intergovernmental Panel on Climate Change. Cambridge: Cambridge University Press.
- NEEM community members, 2013.** Eemian interglacial reconstructed from a Greenland folded ice core. *Nature* 493, 489–494.
- Nerheim S, 2008.** Extrema vattenstånd för ett högt klimatscenario perioden 2071–2100 för Forsmark och Oskarshamn. SMHI rapport 2008–80, Sveriges meteorologiska och hydrologiska institut (Swedish Meteorological and Hydrological Institute). (In Swedish.)
- NorthGRIP community members, 2004.** High-resolution record of the Northern Hemisphere climate extending into the last interglacial period. *Nature* 431, 147–151.
- Näslund J-O, 1997.** Subglacial preservation of valley morphology at Amundsenisen, western Dronning Maud Land, Antarctica. *Earth Surface Processes and Landforms* 22, 441–455.
- Näslund J-O, 1998.** Ice sheet, climate, and landscape interactions in Dronning Maud Land, Antarctica. PhD thesis. Department of Physical Geography, Stockholm University.
- Näslund J-O, 2001.** Landscape development in western and central Dronning Maud Land, East Antarctica. *Antarctic Science* 13, 302–311.

- Näslund J-O, Fastook J L, Holmlund P, 2000.** Numerical modelling of the ice sheet in western Dronning Maud Land, East Antarctica: impact of present, past, and future climates. *Journal of Glaciology* 46, 54–66.
- Näslund J-O, Rodhe L, Fastook J L, Holmlund P, 2003.** New ways of studying ice sheet flow directions and glacial erosion by computer modelling – examples from Fennoscandia. *Quaternary Science Reviews* 22, 245–258.
- Näslund J-O, Jansson P, Fastook J L, Johnson J, Andersson L, 2005.** Detailed spatially distributed geothermal heat-flow data for modeling of basal temperatures and meltwater production beneath the Fennoscandian ice sheet. *Annals of Glaciology* 40, 95–101.
- Näslund J-O (ed), Wohlfarth B (ed), Alexanderson H, Helmens K, Hättestrand M, Jansson P, Kleman J, Lundqvist J, Brandefelt J, Houmark-Nielsen M, Kjellström E, Strandberg G, Knudsen K L, Krogh Larsen N, Ukkonen P, Mangerud J, 2008.** Fennoscandian paleo-environment and ice sheet dynamics during Marine Isotope Stage (MIS) 3. Report of a workshop held September 20–21, 2007 in Stockholm, Sweden. SKB R-08-79, Svensk Kärnbränslehantering AB.
- Näslund J-O, Fastook J, Jansson P, 2010.** A numerical model reconstruction of the Weichselian ice sheet. SKB TR-09-19, Svensk Kärnbränslehantering AB.
- Näslund J-O, Brandefelt J, Claesson Liljedahl L, 2013.** Climate considerations in long-term safety assessments for nuclear waste repositories. *Ambio* 42, 393–401.
- Odén, M, Follin, S, Öhman J and Vidstrand P, 2013.** SR-PSU Bedrock hydrogeology. Groundwater flow modelling methodology, setup and results. SKB R-13-25, Svensk Kärnbränslehantering AB.
- Olvmo M, 2010.** Review of denudation processes and quantification of weathering and erosion rates at a 0.1 to 1 Ma time scale. SKB TR-09-18, Svensk Kärnbränslehantering AB.
- Olvmo M, Johansson M, 2002.** The significance of rock structure, lithology, and pre-glacial deep weathering for the shape of intermediate-scale glacial erosional landforms. *Earth Surface Processes and Landforms* 27, 251–268.
- Olvmo M, Lidmar-Bergström K, Ericson K, Bonow J M, 2005.** Saprolite remnant as indicators of pre-glacial landform genesis in southeast Sweden. *Geografiska annaler* 87A, 447–460.
- O’Neill K, Miller R D, 1985.** Exploration of rigid ice model of frost heave. *Water Resources Research* 21, 281–296.
- Otto-Bliesner B L, Brady E C, Clauzet G, Thomas R, Levis S, Kothavala Z, 2006.** Last glacial maximum and Holocene climate in CCSM3. *Journal of Climate* 19, 2526–2544.
- Paananen M, Ruskeeniemi T, 2003.** Permafrost at Lupin: Interpretation of SAMPO electromagnetic soundings at Lupin. Report YST-117, Geological Survey of Finland.
- Padilla F, Villeneuve J-P, 1992.** Modelling and experimental studies of frost heave including solute effects. *Cold Regions Science and Technology* 20, 183–194.
- Paterson W S B, 1994.** The physics of glaciers. 3rd ed. Oxford: Pergamon.
- Pattyn F, 2003.** A new three-dimensional higher-order thermomechanical ice sheet model: basic sensitivity, ice-stream development, and ice flow across subglacial lakes. *Journal of Geophysical Research* 108, 2382. doi:10.1029/2002JB002329
- Pattyn F, Huybrechts P, Declair H, 1989.** Modelling glacier fluctuations in the Sør Rondane, Dronning Maud Land, Antarctica. *Zeitschrift für Gletscherkunde und Glazialgeologie* 25, 33–47.
- Paulson A, Zhong S, Wahr J, 2005.** Modelling post-glacial rebound with lateral viscosity variations. *Geophysical Journal International* 163, 357–371.
- Payne A J, 1995.** Limit cycles in the basal thermal regime of ice sheets. *Journal of Geophysical Research* 100, 4249–4263.
- Payne A J, Baldwin D J, 1999.** Thermomechanical modelling of the Scandinavian ice sheet: implications for ice-stream formation. *Annals of Glaciology* 28, 83–89.
- Payne A J, Dongelmans P W, 1997.** Self-organization in the thermomechanical flow of ice sheets. *Journal of Geophysical Research* 102, 12219–12234.

- Payne A J, Huybrechts P, Abe-Ouchi A, Calov R, Fastook J L, Greve R, Marshall S J, Marsiat I, Ritz C, Tarasov L, Thomassen M P A, 2000.** Results from the EISMINT model intercomparison: the effects of thermomechanical coupling. *Journal of Glaciology* 46, 227–238.
- Peltier W R, 1994.** Ice age palaeotopography. *Science* 265, 195–201.
- Peltier W R, 1998.** Postglacial variations in the level of the sea: implications for climate dynamics and solid-earth geophysics. *Reviews of Geophysics* 36, 603–689.
- Peltier W R, 2002.** On eustatic sea level history: Last Glacial Maximum to Holocene. *Quaternary Science Reviews* 21, 377–396.
- Peltier W R, 2004.** Global glacial isostasy and the surface of the ice-age Earth: the ICE-5G (VM2) model and GRACE. *Annual Review of Earth and Planetary Science* 32, 111–149.
- Peltier W R, 2005.** On the hemispheric origins of meltwater pulse 1a. *Quaternary Science Reviews* 24, 1655–1671.
- Peltier W R, Drummond R, 2002.** A “broad-shelf effect” upon postglacial relative sea level history. *Geophysical Research Letters* 29, 1169. doi:10.1029/2001GL014273
- Peltier W R, Farrell W E, Clark J A, 1978.** Glacial isostasy and relative sea level: a global finite element model. *Tectonophysics* 50, 81–110.
- Pérez-Gussinyé M, Lowry A R, Watts A B, Velicogna I, 2004.** On the recovery of effective elastic thickness using spectral methods: examples from synthetic data and from the Fennoscandian Shield. *Journal of Geophysical Research* 109, B10409. doi:10.1029/2003JB002788
- Person M, McIntosh J, Bense V, Remenda V H, 2007.** Pleistocene hydrology of North America: the role of ice sheets in reorganizing groundwater flow systems. *Reviews of Geophysics* 45, RG3007. doi:10.1029/2006RG000206
- Persson G, Barring L, Kjellström E, Strandberg G, Rummukainen M, 2007.** Climate indices for vulnerability assessments. Norrköping: Sveriges meteorologiska och hydrologiska institut (Swedish Meteorological and Hydrological Institute). (SMHI reports. Meteorology and Climatology 111)
- Pfeffer W T, Harper J T, O’Neel S, 2008.** Kinematic constraints on glacier contributions to 21st-century sea-level rise. *Science* 321, 1340–1343.
- Pimenoff N, Venäläinen A, Järvinen H, 2011.** Climate scenarios for Olkiluoto on a time-scale of 120,000 Years. Posiva 2011-04, Posiva Oy, Finland.
- Pimenoff N, Venäläinen A, Järvinen H, 2012.** Climate and sea level scenarios for Olkiluoto for the next 10,000 years. Posiva 2012-26, Posiva Oy, Finland.
- Placidi L, Greve R, Seddik H, Faria S H, 2010.** Continuum-mechanical, Anisotropic Flow model for polar ice masses, based on an anisotropic Flow Enhancement factor. *Continuum Mechanics and Thermodynamics* 22, 221–237.
- Plattner G-K, Knutti R, Joos F, Stocker T F, von Bloh W, Brovkin V, Cameron D, Driesschaert E, Dutkiewicz S, Eby M, Edwards N R, Fichfet T, Hargreaves J C, Jones C D, Loutre M F, Matthews H D, Mouchet A, Müller S A, Nawrath S, Price A, Sokolov A, Strassmann K M, Weaver A J, 2008.** Long-term climate commitments projected with climate–carbon cycle models. *Journal of Climate* 21, 2721–2751.
- Pollack H N, Hurter S J, Johnson, J R, 1991.** A new global heat flow compilation. Available at: http://www.wdcb.ru/sep/data/hdata/hf_global.dat.
- Pollack H N, Hurter S J, Johnson J R, 1993.** Heat flow from the Earth’s interior: analysis of the global data set. *Reviews of Geophysics* 31, 267–280.
- Porter S C, 1989.** Some geological implications of average Quaternary glacial conditions. *Quaternary Research* 32, 245–261.
- Poudjom Djomani Y H, Fairhead J D, Griffin W L, 1999.** The flexural rigidity of Fennoscandia: reflection of the tectonothermal age of the lithospheric mantle. *Earth and Planetary Science Letters* 174, 139–154.

- Påsse T, 2001.** An empirical model of glacio-isostatic movements and shore-level displacement in Fennoscandia. SKB R-01-41, Svensk Kärnbränslehantering AB.
- Påsse T, 2004.** The amount of glacial erosion of the bedrock. SKB TR-04-25, Svensk Kärnbränslehantering AB.
- Radtke U, Grün R, Schwarcz H P, 1988.** Electron spin resonance dating of the Pleistocene coral reef tracts of Barbados. *Quaternary Research* 29, 197–215.
- Ramstein G, Kageyama M, Guiot J, Wu H, Hély C, Krinner G, Brewer S, 2007.** How cold was Europe at the Last Glacial Maximum? A synthesis of the progress achieved since the first PMIP model-data comparison. *Climate of the Past* 3, 331–339.
- Raymo M E, Ganley K, Carter S, Oppo D W, McManus J, 1998.** Millennial-scale climate instability during the early Pleistocene epoch. *Nature* 392, 699–702.
- Raymond C F, Harrison W D, 1975.** Some observations on the behaviour of the liquid and gas phases in temperate glacier ice. *Journal of Glaciology* 14, 213–234.
- Reiche P, 1950.** Survey of weathering processes and products. (University of New Mexico publications in geology 3)
- Remy F, Minster J F, 1993.** Precise altimetric topography in ice-sheet flow studies. *Annals of Glaciology* 17, 195–200.
- Richardson C, 2004.** Spatial characteristics of snow accumulation in Dronning Maud Land, Antarctica. *Global and Planetary Change* 42, 31–43.
- Riddihough R P, 1972.** Regional magnetic anomalies and geology in Fennoscandia: a discussion. *Canadian Journal of Earth Sciences* 9, 219–232.
- Rignot E, Bamber J L, van den Broeke M R, Davis C, Li Y, van de Berg W J, van Meijgaard E, 2008.** Recent Antarctic ice mass loss from radar interferometry and regional climate modelling. *Nature Geoscience* 1, 106–110.
- Riis F, 1996.** Quantification of Cenozoic vertical movements of Scandinavia by correlation of morphological surfaces with offshore data. *Global and Planetary Change* 12, 331–357.
- Riseborough D W, Shiklomanov N, Etzelmüller B, Gruber S, Marchenko S, 2008.** Recent advances in permafrost modelling. *Permafrost and Periglacial Processes* 19, 137–156.
- Ritz C, Fabre A, Letreguilly A, 1996.** Sensitivity of a Greenland ice sheet model to ice flow and ablation parameters: Consequences for evolution through the last climatic cycle. *Climate Dynamics* 13, 11–24.
- Robinson A, Calov R, Ganopolski A, 2012.** Multistability and critical thresholds of the Greenland ice sheet. *Nature Climate Change* 2, 429–432.
- Rudberg S, 1954.** Västerbottens berggrundsmorfologi: ett försök till rekonstruktion av preglaciala erosionsgenerationer i Sverige. PhD thesis. Uppsala University. (In Swedish.)
- Rummukainen M, 2003.** The Swedish regional climate modeling program, SWECLIM, 1996–2003. Final report. Norrköping: Sveriges meteorologiska och hydrologiska institut (Swedish Meteorological and Hydrological Institute). (SMHI Meteorologi 104)
- Ruskeeniemi T, Paananen M, Ahonen L, Kaija J, Kuivamäki A, Frape S, Moren L, Degnan P, 2002.** Permafrost at Lupin: report of Phase I. Report YST-112, Geological Survey of Finland.
- Ruskeeniemi T, Ahonen L, Paananen M, Frape S, Stotler R, Hobbs M, Kaija J, Degnan P, Blomqvist R, Jensen M, Lehto K, Moren L, Puigdomenech I, Snellman M, 2004.** Permafrost at Lupin: report of Phase II. Report YST-119, Geological Survey of Finland.
- Sánchez Goñi M F, 2007.** Introduction to climate and vegetation in Europe during MIS 5. In Sirocco F, Claussen M, Sánchez Goñi M F, Litt T (eds). *The climate of past interglacials*. Amsterdam: Elsevier. (Developments in Quaternary Sciences 7), 197–205.
- Sánchez Goñi M F, Landais A, Fletcher W J, Naughton F, Desprat S, Duprat J, 2008.** Contrasting impacts of Dansgaard-Oeschger events over a western European latitudinal transect modulated by orbital parameters. *Quaternary Science Reviews* 27, 1136–1151.

SCAR, 2007. A need for more realistic ice-sheet models. SCAR report 30, Scientific Committee on Antarctic Research.

Scherneck H-G, Johansson J M, Vermeer M, Davis J L, Milne G A, Mitrovica J X, 2001. BIFROST project: 3D crustal deformation rates derived from GPS confirm postglacial rebound in Fennoscandia. *Earth Planets Space* 53, 703–708.

Schiermeier Q, 2013. Greenland defied ancient warming. *Nature* 493, 459–460.

Seipold U, 1995. The variation of thermal transport properties in Earth's crust. *Journal of Geodynamics* 20, 145–154.

Selby M J, 1993. Hillslope materials and processes. 2nd ed. Oxford: Oxford University Press.

Selroos J-O, Cheng H, Painter S, Vidstrand P, 2013. Radionuclide transport during glacial cycles: comparison of two approaches for representing flow transients. *Physics and Chemistry of the Earth, Parts A/B/C* 64, 32–45.

Shackleton N J, Kennett J P, 1975. Paleotemperature history of the Cenozoic and the initiation of Antarctic glaciation: oxygen and carbon isotopic analyses in DSDP sites 277, 279, and 281. In Kennett J P, Houtz R (eds). *Initial reports of the Deep Sea Drilling Project* 29, 743–755.

Sharp R P, 1960. *Glaciers*. Eugene: University of Oregon Press. (Condon lectures 1960).

Shin S-I, Liu Z, Otto-Bliesner B, Brady E C, Kutzbach J E, Harrison S P, 2003. A simulation of the Last Glacial Maximum climate using the NCAR-CSM. *Climate Dynamics* 20, 127–151.

Siddall M, Rohling E J, Almogi-Labin A, Hemleben C, Meischner D, Schmelzer I, Smeed D A, 2003. Sea-level fluctuations during the last glacial cycle. *Nature* 423, 853–858.

Siegert M J, Dowdeswell J A, 1996. Spatial variations in heat at the base of the Antarctic ice sheet from analysis of the thermal regime above subglacial lakes. *Journal of Glaciology* 42, 501–509.

Simons M, Hager B H, 1997. Localization of the gravity field and the signature of glacial rebound. *Nature* 390, 500–504.

SKB, 2005. Preliminary site description. Forsmark area – version 1.2. SKB R-05-18, Svensk Kärnbränslehantering AB.

SKB, 2006a. Climate and climate-related issues for the safety assessment SR-Can. SKB TR-06-23, Svensk Kärnbränslehantering AB.

SKB, 2006b. Geosphere process report for the safety assessment SR-Can. SKB TR-09-19, Svensk Kärnbränslehantering AB.

SKB, 2008. Safety analysis SFR 1. Long-term safety. SKB R-08-130, Svensk Kärnbränslehantering AB.

SKB, 2010a. Climate and climate-related issues for the safety assessment SR-Site. SKB TR-10-49, Svensk Kärnbränslehantering AB.

SKB, 2010b. Model summary report for the safety assessment SR-Site. TR-10-51, Svensk Kärnbränslehantering AB.

SKB, 2010c. Geosphere process report for the safety assessment SR-Site. SKB TR-10-48, Svensk Kärnbränslehantering AB.

SKB, 2010d. Biosphere analyses for the safety assessment SR-Site – synthesis and summary of results. SKB TR-10-09, Svensk Kärnbränslehantering AB.

SKB, 2010e. The Greenland Analogue Project. Yearly report 2009. SKB R-10-59, Svensk Kärnbränslehantering AB.

SKB, 2011. Long-term safety for the final repository for spent nuclear fuel at Forsmark. Main report of the SR-Site project. SKB TR-11-01, Svensk Kärnbränslehantering AB.

SKB, 2014a. Safety analysis for SFR. Long-term safety. Main report for the safety assessment SR-PSU. SKB TR-14-01, Svensk Kärnbränslehantering AB.

SKB, 2014b. FEP report for the safety assessment SR-PS. SKB TR-14-07, Svensk Kärnbränslehantering AB.

- SKB, 2014c.** Model summary report for the safety assessment SR-PSU. SKB TR-14-11, Svensk Kärnbränslehantering AB.
- SKB, 2014d.** Engineered barrier process report for the safety assessment SR-PSU. SKB TR-14-04, Svensk Kärnbränslehantering AB.
- SKB, 2014e.** Data report for the for the safety assessment SR-PSU. SKB TR-14-10, Svensk Kärnbränslehantering AB.
- SKB, 2014f.** Biosphere synthesis report for the safety assessment SR-PSU. SKB TR-14-06, Svensk Kärnbränslehantering AB.
- SKB, 2014g.** Input data report for the safety assessment SR-PSU. SKB TR-14-12, Svensk Kärnbränslehantering AB.
- Slater A G, Lawrence D M, 2013.** Diagnosing present and future permafrost from climate models. *Journal of Climate* 26, 5608–5623.
- Sohlenius G, Hedenström A, Rudmark L, 2004.** Forsmark site investigation. Mapping of unconsolidated Quaternary deposits 2002–2003. Map description. SKB R-04-39, Svensk Kärnbränslehantering AB.
- Solomon S, Plattner G-K, Knutti R, Friedlingstein P, 2009.** Irreversible climate change due to carbon dioxide emissions. *Proceedings of the National Academy of Sciences of the United States of America* 106, 1704–1709.
- Solomon S, Battisti D, Doney S, Hayhoe K, Held I M, Lettenmaier D P, Lobell D, Matthews H D, Pierrehubert R, Raphael M, Richels R, Root R L, Steffen K, Tebalidi C, Yohe G W, 2011.** *Climate stabilization targets: emissions, concentrations, and impacts over decades to millennia.* Washington, DC: National Academies Press.
- Spada G, Antonioli A, Cianetti S, Giunchi C, 2006.** Glacial isostatic adjustment and relative sea-level changes: the role of lithospheric and upper mantle heterogeneities in a 3D spherical Earth. *Geophysical Journal International* 165, 692–702.
- Srifer R L, Urban N M, Olson R, Keller K, 2012.** Towards a physically plausible upper bound of sea-level rise projections. *Climatic Change* 115, 893–902.
- Staiger J K W, Gosse J C, Johnson J V, Fastook J, Gray J T, Stockli D F, Stockli L, Finkel R, 2005.** Quaternary relief generation by polythermal glacier ice. *Earth Surface Processes and Landforms* 30, 1145–1159.
- Steffen H, Wu P, 2011.** Glacial isostatic adjustment in Fennoscandia – A review of data and modeling. *Journal of Geodynamics* 52, 169–204.
- Stone E J, Lunt D J Rutt I C, Hanna E, 2010a.** The effect of more realistic forcings and boundary conditions on the modelled geometry and sensitivity of the Greenland ice-sheet. *The Cryosphere Discussion* 4, 233–285.
- Stone E J, Lunt D J, Rutt I C, Hanna E, 2010b.** Investigating the sensitivity of numerical model simulations of the modern state of the Greenland ice sheet and its future response to climate change. *The Cryosphere* 4, 379–417.
- Stroeven A P, Fabel D, Hättstrand C, Harbor J, 2002a.** A relict landscape in the centre of Fennoscandian glaciation: cosmogenic radionuclide evidence of tors preserved through multiple glacial cycles. *Geomorphology* 44, 145–154.
- Stroeven A P, Fabel D, Hättstrand C, Kleman J, 2002b.** Quantifying the erosional impact of the Scandinavian ice sheet in the Torneträsk-Narvik corridor, northern Sweden, based on cosmogenic radionuclide data. *Geografiska Annaler* 84A, 275–287.
- Stumm D, 2010.** Deep glacial erosion – Review with focus on tunnel valleys in northern Europe. *Nagra Arbeitsbericht NAB 10-33*, Nagra, Switzerland.
- Sugden D E, 1977.** Reconstruction of the morphology, dynamics and thermal characteristics of the Laurentide ice sheet at its maximum. *Arctic and Alpine Research* 9, 27–47.
- Sugden D E, 1978.** Glacial erosion by the Laurentide ice sheet. *Journal of Glaciology* 20, 367–391.

- Sugden D E, John B S, 1976.** *Glaciers and landscape: a geomorphological approach.* London: Arnold.
- Sundberg J, 1988.** Thermal properties of soils and rocks. PhD thesis. Chalmers University of Technology.
- Sundberg J, Back P-E, Ländell M, Sundberg A, 2009.** Modelling of temperature in deep boreholes and evaluation of geothermal heat flow at Forsmark and Laxemar. SKB TR-09-14, Svensk Kärnbränslehantering AB.
- Sundh M, Sohlenius G, Hedenström A, 2004.** Forsmark site investigation. Stratigraphical investigation of till in machine cut trenches. SKB P-04-34, Svensk Kärnbränslehantering AB.
- Svendsen J I, Mangerud J, 1987.** Late Weichselian and Holocene sea-level history for a cross-section of western Norway. *Journal of Quaternary Science* 2, 113–132.
- Swantesson J O H, 1992.** Recent micro-weathering phenomena in southern and central Sweden. *Permafrost and Periglacial Processes* 3, 275–292.
- Swingedouw D, Braconnot P, Delecluse P, Guilyardi E, Marti O, 2007.** Quantifying the AMOC feedbacks during a $2\times\text{CO}_2$ stabilization experiment with land-ice melting. *Climate Dynamics* 29, 521–534.
- Tamisiea M E, Mitrovica J X, Milne G A, Davis J L, 2001.** Global geoid and sea level changes due to present-day ice mass fluctuations. *Journal of Geophysical Research* 106, 30849–30863.
- Tamisiea M E, Mitrovica J X, Davis J L, Milne G A, 2003.** Long wavelength sea level and solid surface perturbations driven by polar ice mass variations: fingerprinting Greenland and Antarctic ice sheet flux. *Space Science Reviews* 108, 81–93.
- Taylor K E, Stouffer R J, Meehl G A, 2012.** An overview of CMIP5 and the experiment design. *Bulletin of the American Meteorological Society* 93, 485–498.
- Texier D, Degnan P, Loutre M, Paillard D, Thorne M, 2003.** Modelling sequential BIOSphere systems under CLIMate change for radioactive waste disposal. Project BIOCLIM. In Proceedings of the International High-Level Waste Management Conference, Las Vegas, 30 March–2 April 2003. Available at: <http://www.andra.fr/bioclim/publications/LasVegas.pdf>
- Thomas M F, 1994.** *Geomorphology in the tropics: a study of weathering and denudation in low latitudes.* Chichester: Wiley.
- Tjernström M, Rummukainen M, Bergström S, Rodhe J, Persson G, 2003.** Klimatmodellering och klimatscenarier ur SWECLIMS perspektiv. Norrköping: Sveriges meteorologiska och hydrologiska institut (Swedish Meteorological and Hydrological Institute). (SMHI reports. Meteorology and Climatology 102) (In Swedish.)
- Toniazzo T, Gregory J M, Huybrechts P, 2004.** Climatic impact of a Greenland deglaciation and its possible irreversibility. *Journal of Climate* 17, 21–33.
- Turkington A V, Phillips J D, Campbell S W, 2005.** Weathering and landscape evolution. *Geomorphology* 67, 1–6.
- Tushingham A M, Peltier W R, 1991.** ICE-3G: a new global model of Late Pleistocene deglaciation based upon geophysical predictions of post-glacial relative sealevel change. *Journal of Geophysical Research* 96, 4497–4523.
- Tzedakis P C, Raynaud D, McManus J F, Berger A, Brovkin V, Kiefer T, 2009.** Interglacial diversity. *Nature Geoscience* 2, 751–755.
- Tzedakis P C, Channell J E T, Hodell D A, Kleiven H F, Skinner L C, 2012a.** Determining the natural length of the current interglacial. *Nature Geoscience* 5, 138–141.
- Tzedakis P C, Wolff E W, Skinner L C, Brovkin V, Hodell D A, McManus J F, Raynaud D, 2012b.** Can we predict the duration of an interglacial? *Climate of the Past* 8, 1473–1485.
- UNEP/GRID-Arendal, 2005.** Permafrost distribution in the Arctic. UNEP/GRID-Arendal Maps and Graphics Library. Available at: <http://maps.grida.no/go/graphic/permafrost-distribution-in-the-arctic>. [26 November 2010].

- Van Tatenhove F G M, Huybrechts P, 1996.** Modelling of the thermal conditions at the Greenland ice sheet margin during Holocene deglaciation: boundary conditions from moraine formation. *Geografiska Annaler* 78A, 83–99.
- Vermeer M, Rahmstorf S, 2009.** Global sea level linked to global temperature. *Proceedings of the National Academy of Sciences of the United States of America* 106, 21527–21532.
- Vettoretti G, Peltier W R, 2011.** The impact of insolation, greenhouse gas forcing and ocean circulation changes on glacial inception. *The Holocene* 21, 803–817.
- Vidstrand P, 2003.** Surface and subsurface conditions in permafrost areas – a literature review. SKB TR-03-06, Svensk Kärnbränslehantering AB.
- Vidstrand P, Follin S, Zugec N, 2010.** Groundwater flow modelling of periods with periglacial and glacial conditions – SR-Site Forsmark. SKB R-09-21, Svensk Kärnbränslehantering AB.
- Vidstrand P, Follin S, Selroos J-O, Näslund J-O, Rhén I, 2013.** Modeling of groundwater flow at depth in crystalline rock beneath a moving ice-sheet margin, exemplified by the Fennoscandian Shield, Sweden. *Hydrogeology Journal* 21, 239–255.
- Vizcaíno M, Mikolajewicz U, Gröger M, Maier-Reimer E, Schurgers G, Winguth A M E, 2008.** Long-term ice sheet–climate interactions under anthropogenic greenhouse forcing simulated with a complex Earth System Model. *Climate Dynamics* 31, 665–690.
- Väliranta M, Birks H H, Helmens K F, Engels S, Piirainen M, 2009.** Early-Weichselian interstadial (MIS 5c) summer temperatures were higher than today in northern Fennoscandia. *Quaternary Science Reviews* 28, 777–782.
- Waddington E D, 1987.** Geothermal heat flux beneath ice sheets. In Waddington E D, Walder J S (eds). *The physical basis of ice sheet modelling*. Wallingford, Oxfordshire: International Association of Hydrological Sciences. (IAHS Publication 170), 217–226.
- Waelbroeck C, Labeyrie L, Michel E, Duplessy J C, McManus J F, Lambeck K, Balbon E, Labracherie M, 2002.** Sea-level and deep water temperature changes derived from benthic foraminifera isotopic records. *Quaternary Science Reviews* 21, 295–305.
- Waller R I, 2001.** The influence of basal processes on the dynamic behaviour of cold-based glaciers. *Quaternary International* 86, 117–128.
- Wallroth T, Lokrantz H, Andrius R, 2010.** The Greenland Analogue Project (GAP). Literature review of hydrogeology/hydrogeochemistry. SKB R-10-34, Svensk Kärnbränslehantering AB.
- Washburn A L, 1979.** *Geocryology: a survey of periglacial processes and environments*. 2nd ed. London: Arnold.
- Watts A B, 2001.** *Isostasy and flexure of the lithosphere*. Cambridge: Cambridge University Press.
- Werner K, Sassner M, Bosson E, 2014.** Hydrology and near-surface hydrogeology at Forsmark – synthesis for the SR-PSU project. SKB R-13-19, Svensk Kärnbränslehantering AB.
- Whalley W B, Warke P A, 2005.** Weathering. In Selley R C, Cocks L R M, Plimer I R (eds.) *Encyclopedia of geology*. Amsterdam: Elsevier.
- Whitehouse P, 2009.** Glacial isostatic adjustment and sea-level change. State of the art report. SKB TR-09-11, Svensk Kärnbränslehantering AB.
- Whitehouse P, Latychev K, Milne G A, Mitrovica J X, Kendall K, 2006.** Impact of 3D Earth structure on Fennoscandian glacial isostatic adjustment: Implications for space-geodetic estimates of present-day crustal deformations. *Geophysical Research Letters* 33, L13502. doi:10.1029/2006GL026568
- Williams P J, Smith M W, 1989.** *The frozen earth: fundamentals of geocryology*. Cambridge: Cambridge University Press.
- Witt A, Schumann A Y, 2005.** Holocene climate variability on millennial scales recorded in Greenland ice cores. *Nonlinear Processes in Geophysics* 12, 345–352.
- Wohlfarth B, 2009.** Ice-free conditions in Fennoscandia during Marine Oxygen Isotope Stage 3? SKB TR-09-12, Svensk Kärnbränslehantering AB.

- Wohlfarth B, 2010.** Ice free conditions in Sweden during Marine Oxygen Isotope Stage 3? *Boreas* 39, 377–398.
- Wohlfarth B, 2013.** A review of Early Weichselian climate (MIS 5d-a) in Europe. SKB TR-13-03, Svensk Kärnbränslehantering AB.
- Wohlfarth B, Näslund J-O (eds), 2010.** Fennoscandian ice sheet in MIS 3. *Boreas* 39, 325–456.
- Woth K, Weisse R, von Storch H, 2006.** Climate change and North Sea storm surge extremes: an ensemble study of storm surge extremes expected in a changed climate projected by four different regional climate models. *Ocean Dynamics* 56, 3–15.
- Wu H, Guiot J, Brewer S, Guo Z, 2007.** Climatic changes in Eurasia and Africa at the last glacial maximum and mid-Holocene: reconstruction from pollen data using inverse vegetation modelling. *Climate Dynamics* 29, 211–229.
- Wu P, Peltier W R, 1983.** Glacial isostatic adjustment and the free air gravity anomaly as a constraint on deep mantle viscosity. *Geophysical Journal of the Royal Astronomical Society* 74, 377–449.
- Wu P, Wang H, Schotman H, 2005.** Postglacial induced surface motions, sea-levels and geoid rates on a spherical, self-gravitating laterally heterogeneous earth. *Journal of Geodynamics* 39, 127–142.
- Wu P, Jackson L, Pardaens A, Schaller N, 2011.** Extended warming of the northern high latitudes due to an overshoot of the Atlantic meridional overturning circulation. *Geophysical Research Letters* 38. doi:10.1029/2011GL049998
- Yershov E D, 1998.** *General Geocryology*. Cambridge: Cambridge University Press.
- Yokoyama Y, Lambeck K, De Deckker P, Johnston P, Fifield L K, 2000.** Timing of the last glacial maximum from observed sea level minima. *Nature* 406, 713–716.
- Zickfeld K, Eby M, Matthews H D, Weaver A J, 2009.** Setting cumulative emissions targets to reduce the risk of dangerous climate change. *Proceedings of the National Academy of Sciences of the United States of America* 106, 16129–16134.
- Zickfeld K, Arora V K, Gillett N P, 2012.** Is the climate response to CO₂ emissions path dependent? *Geophysical Research Letters* 39. doi:10.1029/2011GL050205
- Zweck C, Huybrechts P, 2003.** Modeling the marine extent of northern hemisphere ice sheets during the last glacial cycle. *Annals of Glaciology* 37, 173–180.